IFPRI
International Fine Particle Research Institute

Model Assisted Design of Granular Products

Linking Process and Product Models for Wet Granulation

Rachel Smith
Peyman Mostafei

The University Of Sheffield.
Chemical and Biological Engineering

Help Transform Tomorrow.

Particle Technology Group @ Sheffield

Dr Rachel Smith

Prof Jim Litster

Dr Kate Pitt

(Soon to be)
Dr Jake Entwhistle

Dr Li-Ge Wang

The University Of Sheffield.

Chemical and Biological Engineering

Help Transform Tomorrow.

Project Brief

Model-Assisted Design of Granular Products

- *Develop multi-dimensional process models of binder agglomeration*
- *Output the appropriate particle properties (likely distributed), linked to associated product models to predict product performance.*

Proposal

Model Assisted Design of Granular Products: Linking Process and Product Models for Wet Granulation

- *Develop a modeling framework for product performance driven process design*
- *Deployable to industry*
- *Demonstrate the potential of this strategy with two case studies: fluidised bed spray granulation and high shear granulation.*

The University Of Sheffield. Chemical and Biological Engineering

IFPRI International Fine Particle Research Institute

Project Overview

- Project Commenced in October 2019
- PhD student Peyman Mostafei joined as the primary researcher in November 2019
- IFPRI Liasons:
  - Poul Bach
  - Christophe Grosjean
  - Joris Salari

Linking Process and Product Models

Wet granulation model

e.g. fluidised bed [1]

Process Model output

Product Model input

Product model

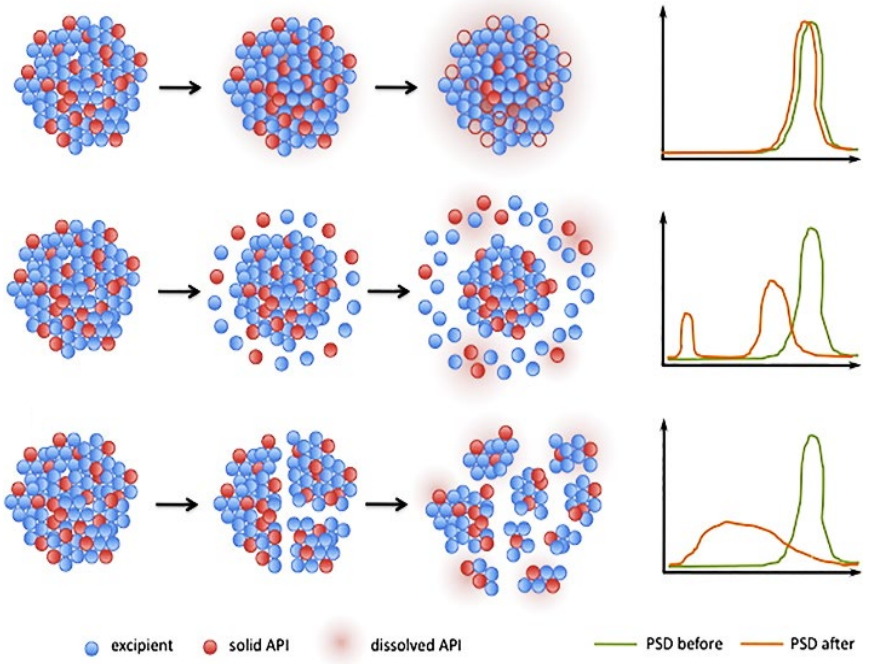

e.g. Dissolution and disintegration model [2]

[1] GlattGroup, Glatt Top-Spray granulation process by fluidized bed. (2013).
[2] D. Smrčka, J. Dohnal, F. Štěpánek, European Journal of Pharmaceutics and Biopharmaceutics, 106 (2016).

Linking Process and Product Models

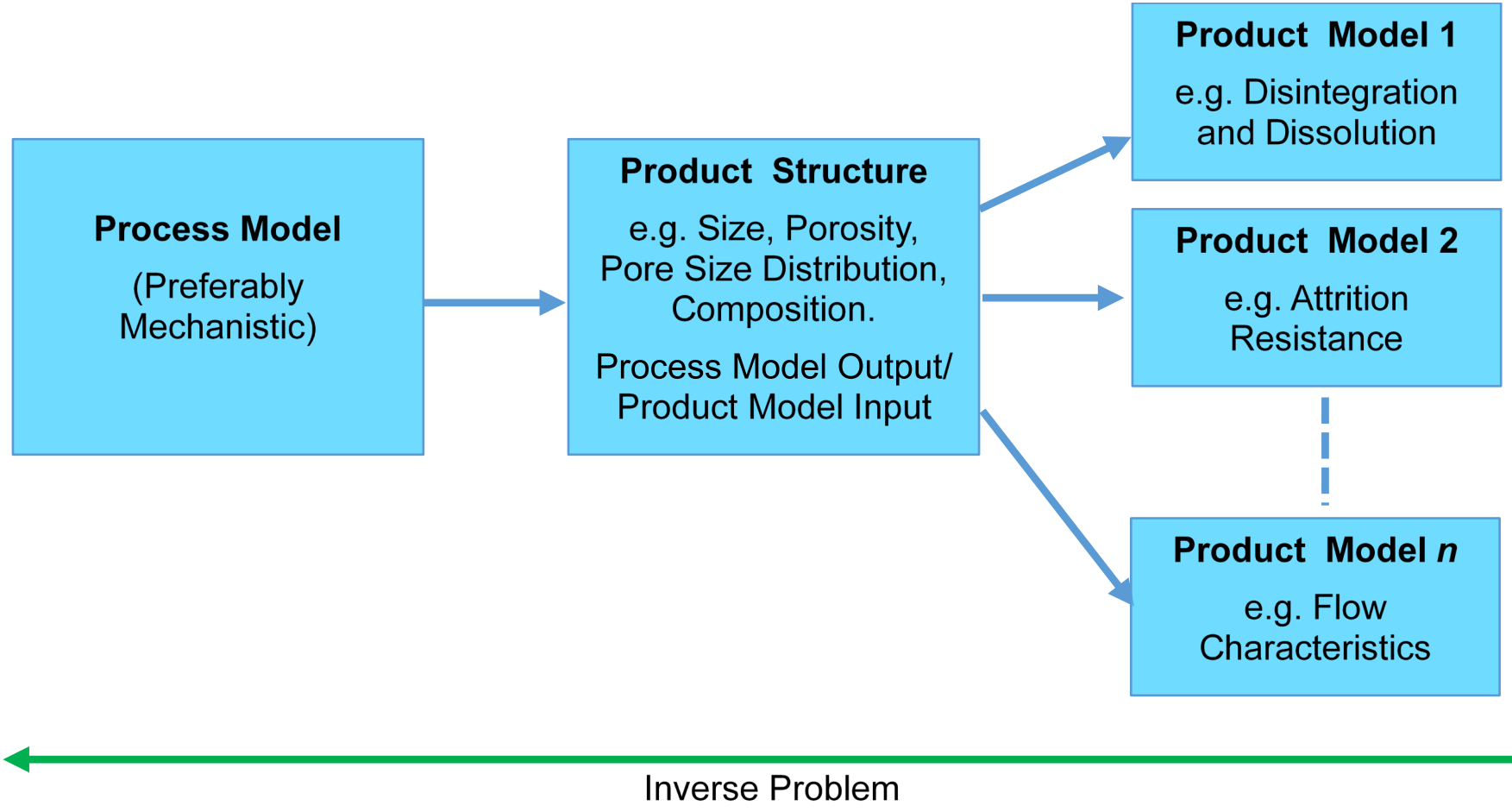

1st Year Objectives

- Complete a comprehensive literature survey of process and product modeling for wet granulation.
- Prepare a review paper based on the literature survey for publication
- Identify exemplar product model/s for development/modification, and commence development of these model/s to work cooperatively with process models. → Chose Disintegration/Dissolution
- Commence development and modification of Sheffield PBM High Shear and Fluidised Bed Granulation Models, to work with identified product models.
- Develop initial framework for co-operative process and product models
- A proposal submitted to the EPSRC for complementary project funding, to leverage this work, and increase project positive outcomes.

Creating a Product Model (PBM): Granule Dissolution and Disintegration

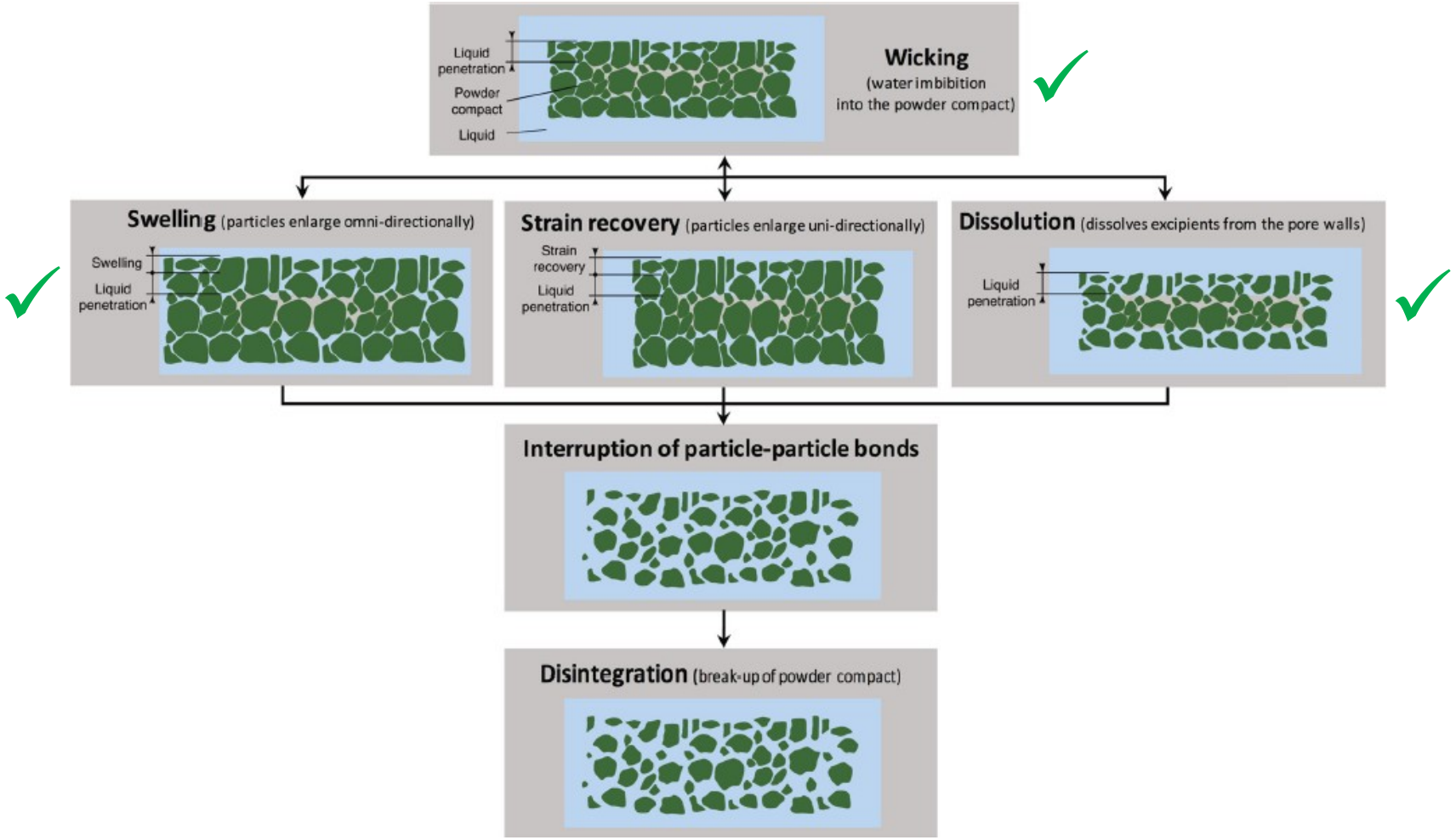

[3] D. Markl, J.A. Zeitler, A Review of Disintegration Mechanisms and Measurement Techniques, Pharm. Res., 34 (2017).

Liquid Penetration (Wicking/Hydration)

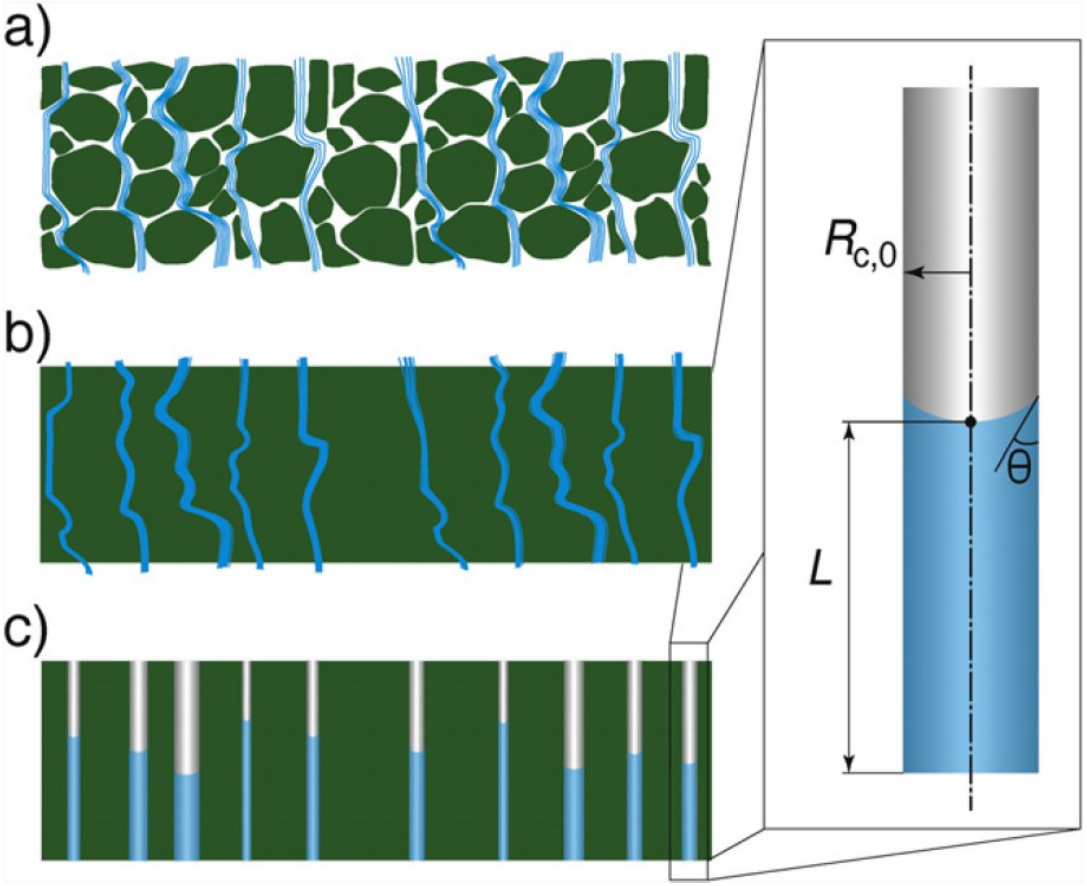

- Very fast in immediate release formulations
- Can affect other variables such as porosity and permeability

[4] D. Markl *et al.*, S. Yassin, D.I. Wilson, D.J. Goodwin, A. Anderson, J.A. Zeitler, Mathematical modelling of liquid transport in swelling pharmaceutical immediate release tablets, International Journal of Pharmaceutics, 526 (2017).

Useful Hydration Models/Descriptors

Darcy's Law: $$q = -\frac{K}{\mu}\frac{\Delta P}{L(t)}$$

Depth of Liquid Penetration: (adapted from [5])
$$L(t) = 2\sqrt{\frac{\gamma\cos(\theta)}{\varepsilon_{f0}\mu}\int_0^t K(t')/R_c(t')\,dt'}$$

Pressure difference [5]: $$\Delta P = \frac{2\gamma\cos(\theta)}{R_c}$$

q is flow rate; K is the permability; μ is the viscosity; ΔP is the pressure difference; $L(t)$ is the depth of liquid penetration at time t; γ is the surface tension; θ is the solid-liquid contact angle; ε_{f0} is the initial porosity; R_c is the capillary radius.

[5] R. Masoodi, K.M. Pillai, Darcy's Law-Based Model for Wicking in Paper-Like Swelling Porous Media, Aiche J., 56 (2010) 2257-2267.

Swelling

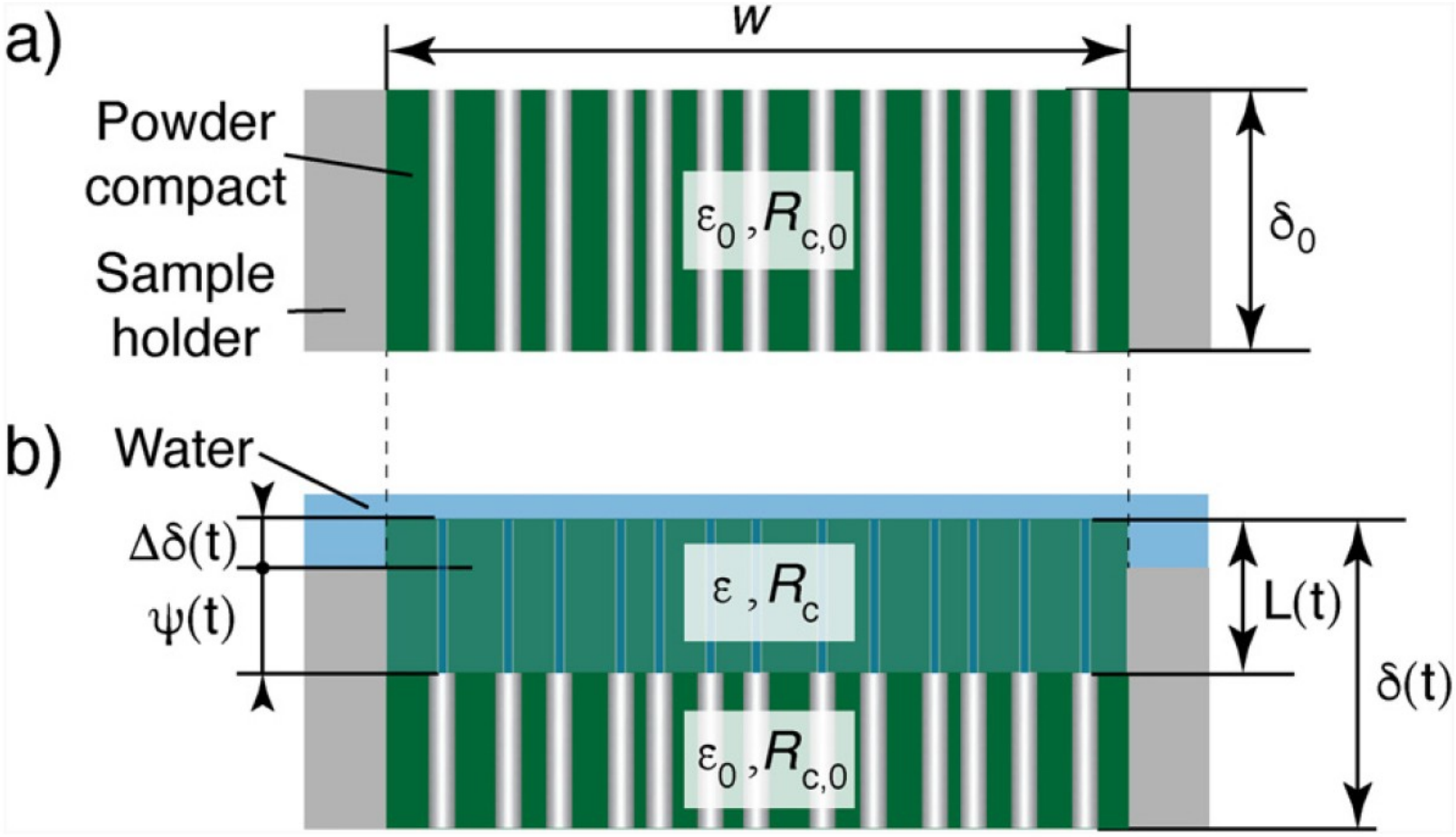

[4] D. Markl *et al.*, S. Yassin, D.I. Wilson, D.J. Goodwin, A. Anderson, J.A. Zeitler, Mathematical modelling of liquid transport in swelling pharmaceutical immediate release tablets, International Journal of Pharmaceutics, 526 (2017).

Swelling

- Very quick in formulations which incorporate disintegrants
- There are competing actions which can both aid and hinder release of components
  - Swelling creates pressure in the granule/tablet, which can promote breakup (links to agglomerate strength)
  - Swelling reduce capillary size, and can hinder liquid penetration and dissolution
- Need to consider the competing mechanisms of component swelling and agglomerate strength

Preliminary Model for Swelling

Model developed from work of Masoodi and Pillai [5]

Boundary Conditions:

$$\begin{cases} \dfrac{\partial p}{\partial r} = 0, \quad r = 0 \\ p = p_{atm}, \quad r = R, \quad 0 < \phi < \dfrac{\pi}{2} \\ p = p_{atm} - p_{cap}, \quad r = R, \quad \dfrac{\pi}{2} < \phi < \pi \end{cases}$$

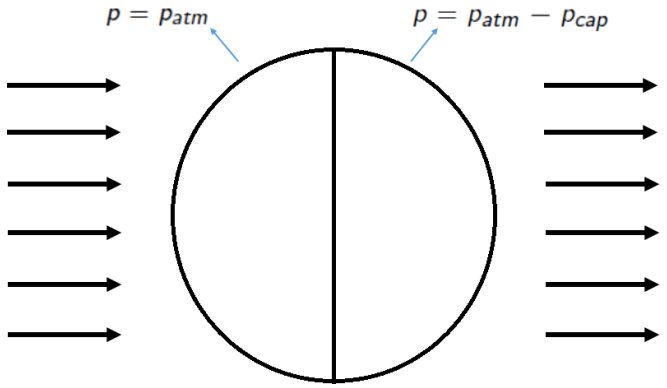

Solution:

$$p(r,\phi) = p_{atm} - \frac{p_{cap}}{2} + \frac{\mu}{6K}(1-b)\frac{d\varepsilon}{dt}(r^2 - R^2) + p_{cap}\sum_{n=0}^{\infty} A_n \left(\frac{r}{R}\right)^{2n+1} P_{2n+1}(\cos\phi)$$

[5] R. Masoodi, K.M. Pillai, Darcy's Law-Based Model for Wicking in Paper-Like Swelling Porous Media, Aiche J., 56 (2010) 2257-2267.

Preliminary Model for Swelling

Relationship with agglomerate's radius:

$$\frac{dR}{dt} = \int_0^{\pi/2} \frac{K}{\mu\varepsilon_{sur}} \frac{\partial p}{\partial r}_{r=R} \sin\phi d\phi = \frac{R(1-b)}{3\varepsilon_{sur}} \frac{d\varepsilon}{dt} + \frac{Kp_{cap}}{\mu R\varepsilon_{sur}} \sum_{n=0}^{\infty} (2n+1)A_n^2$$

Solution of Radius:

$$R^2 = R_0^2 \varepsilon^{\frac{2}{3}(1-b)} + \frac{\sum_{n=0}^{\infty}(2n+1)A_n^2}{\mu} \int_0^t \left(\frac{\varepsilon(t)}{\varepsilon(t')}\right)^{\frac{2}{3}(1-b)} \frac{K(t')p_{cap}(t')}{\varepsilon(t')} dt$$

Swelling vs Strength

Challenge: agglomerate strength changes with liquid imbibition

- Wet agglomerate strength has proven difficult to model
- Changing agglomerate strength is also difficult to measure experimentally

Challenge: what measure of agglomerate strength do we use?

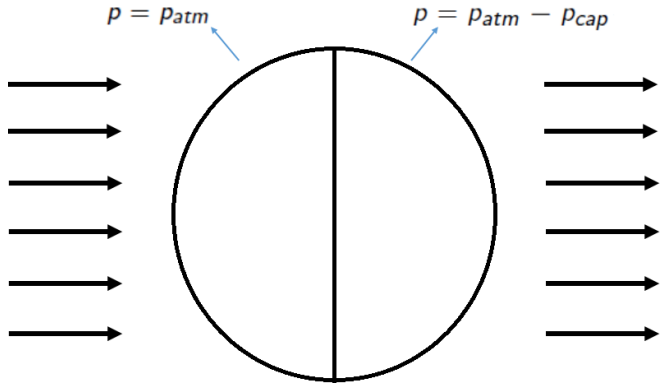

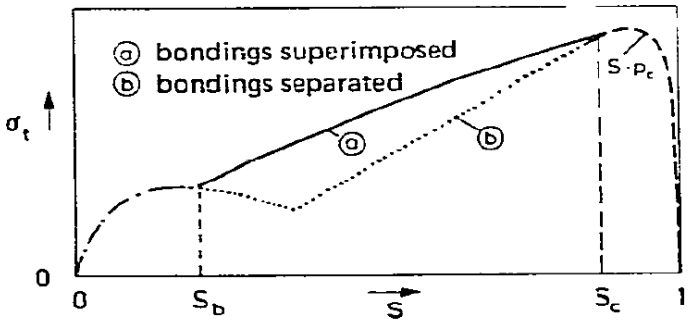

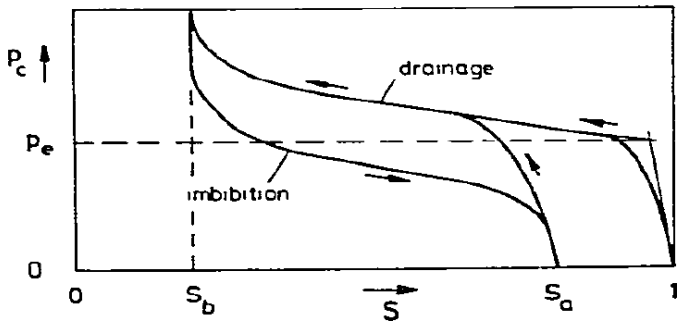

[6] H. Schubert, Tensile strength of agglomerates, Powder Technol., 11 (1975) 107-119.

Dissolution

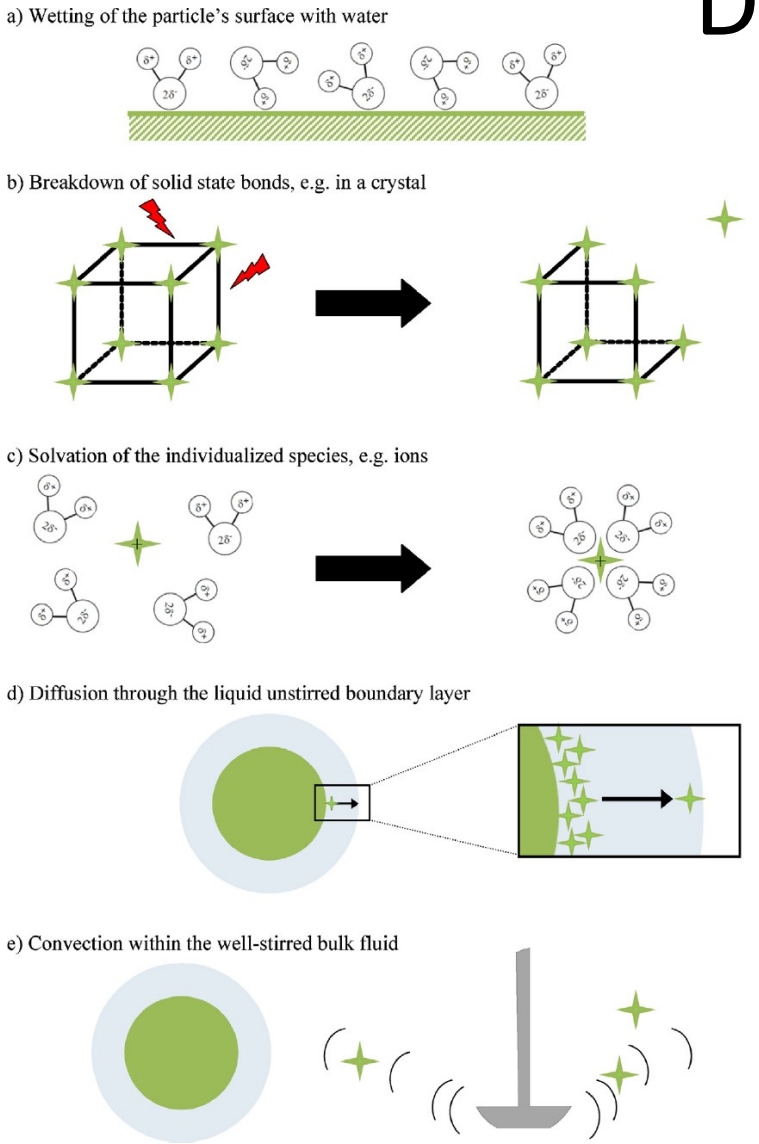

- Many approaches available in the literature
  - Noyes–Whitney equation
  - Nernst–Brunner equation
  - Hixson–Crowell equation

[7] J. Siepmann, F. Siepmann, Mathematical modeling of drug dissolution, International Journal of Pharmaceutics, 453 (2013) 12-24.

Dissolution and Disintegration Model Development

- Complex problem
- Will require extensive experimental validation
- Propose to use simplified systems
  - 3 components maximum
  - Reduce the number of “significant” mechanisms (e.g. eliminate non-swelling components, or non-dissolving components)
  - Include non-mechanistic elements where necessary

Key Progress 2020

1. Recruited PhD student Peyman Mostafei
2. Made significant progress in reviewing the literature
3. Dissolution/Disintegration chosen as the case study product model, and key mechanisms identified
4. Progress towards identifying and modifying mechanistic expressions for hydration, swelling dissolution

Looking Forward 2020

1. Complete a comprehensive literature survey of process and product modeling for wet granulation
2. Make decisions on mechanism inclusion and complementary experimental systems for disintegration model (effectively eliminate mechanisms)
3. Develop a granule disintegration/dissolution model designed to work cooperatively with process models (intermediate structure link).
4. Develop initial product model validation methodology
5. Initiate process model modification
6. Develop initial framework for co-operative process and product models

The University Of Sheffield.

Chemical and Biological Engineering

IFPRI
International Fine Particle Research Institute

I look forward to your questions ☺

Help Transform Tomorrow.



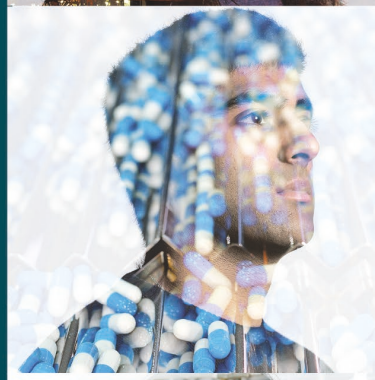


Modeling of screw feeder performance

Prabhu R Nott

Aashish Kumar Gupta

Indian Institute of Science
Bangalore

IFPRI funded project commenced on 21 October 2019

A brief history of screw conveyors/feeders

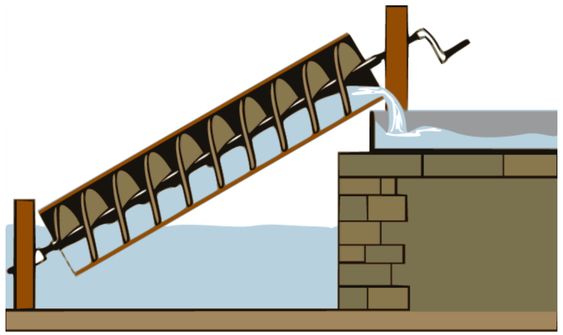

Dates back to ancient Egypt (~ 3rd century BC) for drawing water

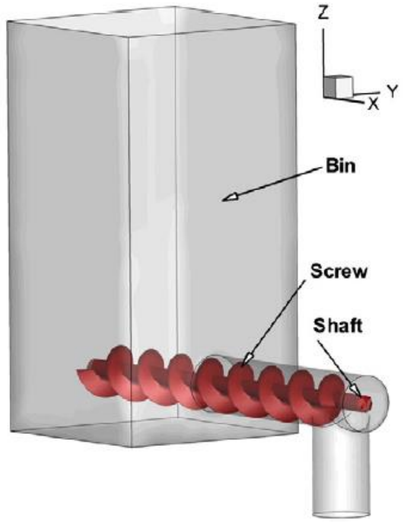

Remarkably, there is no analytical solution for even a Newtonian fluid!

Currently used widely for conveying of particulate materials in food, pharmaceutical, construction and mineral processing industries

Overview of the current work

- Develop of a simple mechanics-based model for the discharge rate through a screw feeder, under simple simplifying assumptions*.
- Understand the flow inside the feeder using simulations by the Discrete Element Method (DEM), and relax the simplifying assumptions.
- Study the stress variation on the surfaces of the feeder.

*Simplifying assumptions

- The space between the screw and the casing is completely filled with grains.
- Material inside the feeder moves as a plug.
- Gravity and centrifugal effects are neglected.

A simplistic analysis of the discharge rate

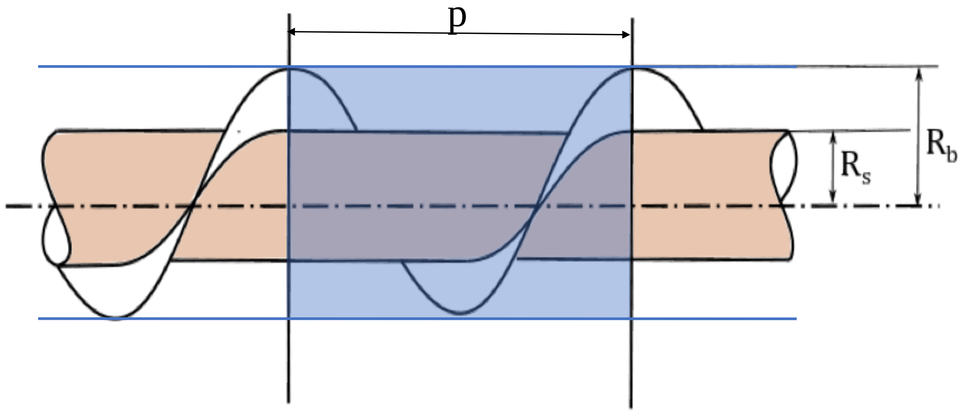

$$Q = \nu f \underline{p \pi (R_b^2 - R_s^2)}$$

v: solids fraction
f : rotation frequency
p: screw pitch

Roberts, A. W., *Powder Technol.* **104**(1) (1999).

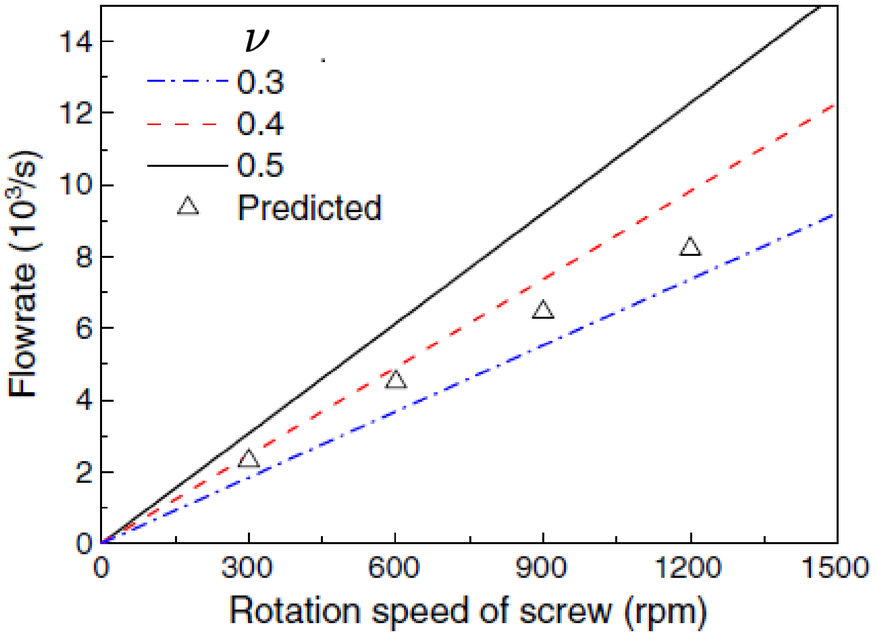

We will see that this a gross overestimate

Describing the screw surface

Screw surface: one parameter set of helices of pitch *p*

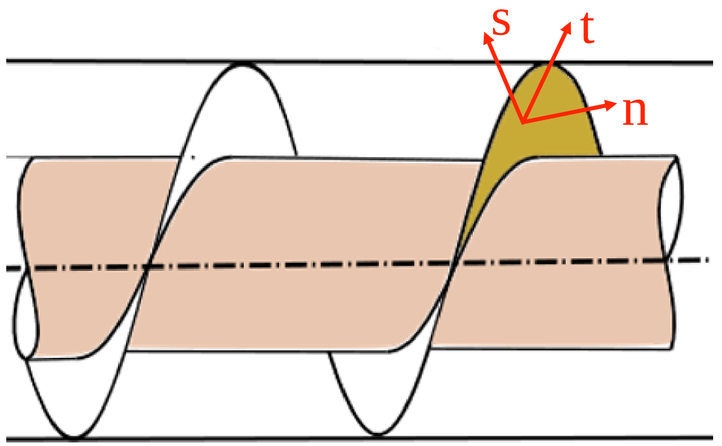

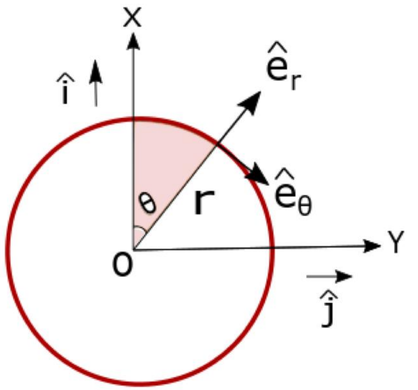

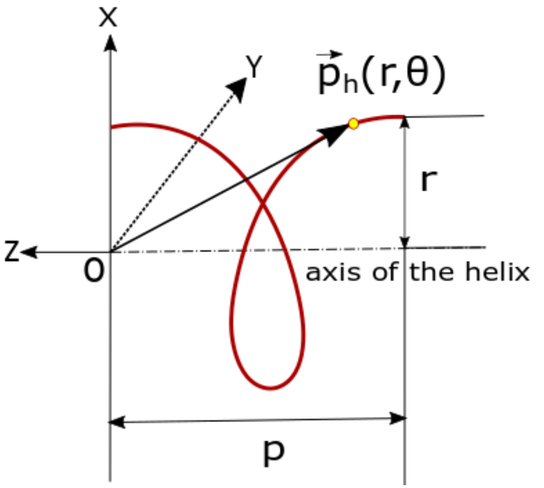

Equation of a helix: $\vec{P_h}(r,\theta) := (r\cos\theta)\hat{i} + (r\sin\theta)\hat{j} - \left(\frac{p\theta}{2\pi}\right)\hat{k}$

$$\hat{t}_h(r,\theta) = \left(\frac{\partial \vec{P_h}(r,\theta)}{\partial\theta}\right) \div \left|\frac{\partial \vec{P_h}(r,\theta)}{\partial\theta}\right| = \cos\alpha\,\hat{e}_\theta - \sin\alpha\,\hat{k}$$

$$\tan\alpha(r) = \frac{p}{2\pi r}$$

$$\hat{s}_h(r,\theta) = \left(\frac{\partial \vec{P_h}(r,\theta)}{\partial r}\right) \div \left|\frac{\partial \vec{P_h}(r,\theta)}{\partial r}\right| = \hat{e}_r$$

$$\hat{n}_h(r,\theta) = \hat{t}_h \times \hat{s}_h = -\sin\alpha\,\hat{e}_\theta - cos\alpha\,\hat{e}_k$$

General expression for discharge rate

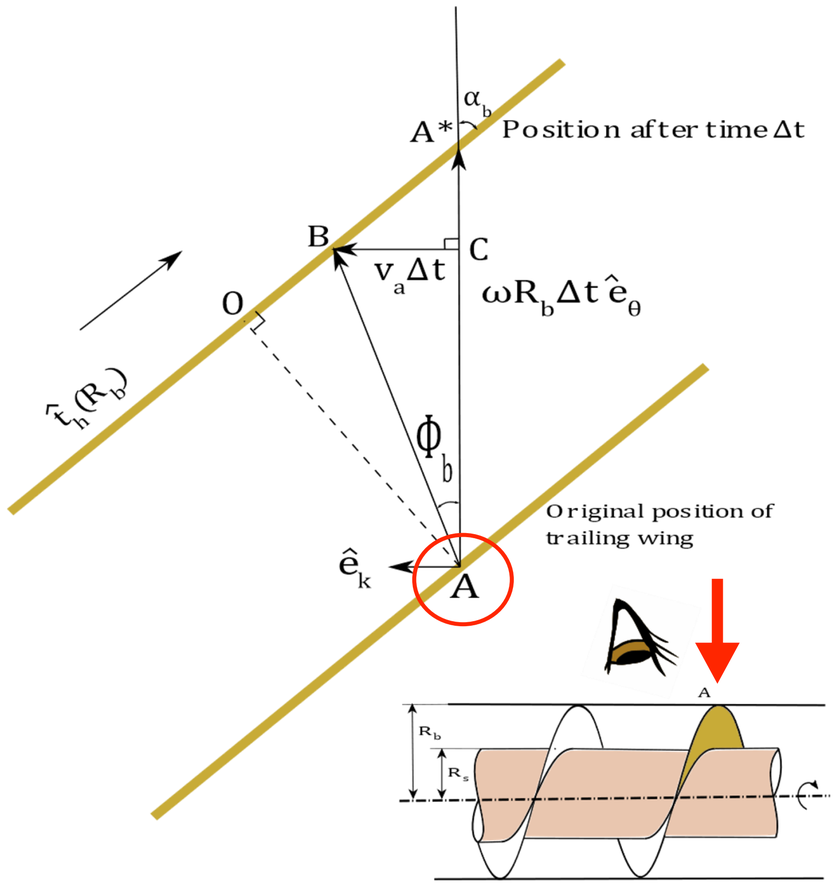

$$Q = \nu V_a \pi (R_b^2 - R_s^2)$$

$$\frac{V_a}{V_b} = \frac{BC}{AA^*} = \frac{BC}{AC+CA^*} = \frac{1}{\frac{1}{\tan\phi_b} + \frac{1}{\tan\alpha_b}}$$

$$V_a = V_b \frac{\tan\phi_b \tan\alpha_b}{\tan\alpha_b + \tan\phi_b}$$

$$V_b = \omega R_b$$

$$\boxed{Q = \nu\, \omega R_b \frac{\tan\phi_b \tan\alpha_b}{\tan\alpha_b + \tan\phi_b} \pi \left(R_b^2 - R_s^2\right)}$$

Wu, C. C. (1978), Masters thesis, Kansas State Univ.

Mechanics: forces on the sub-elements

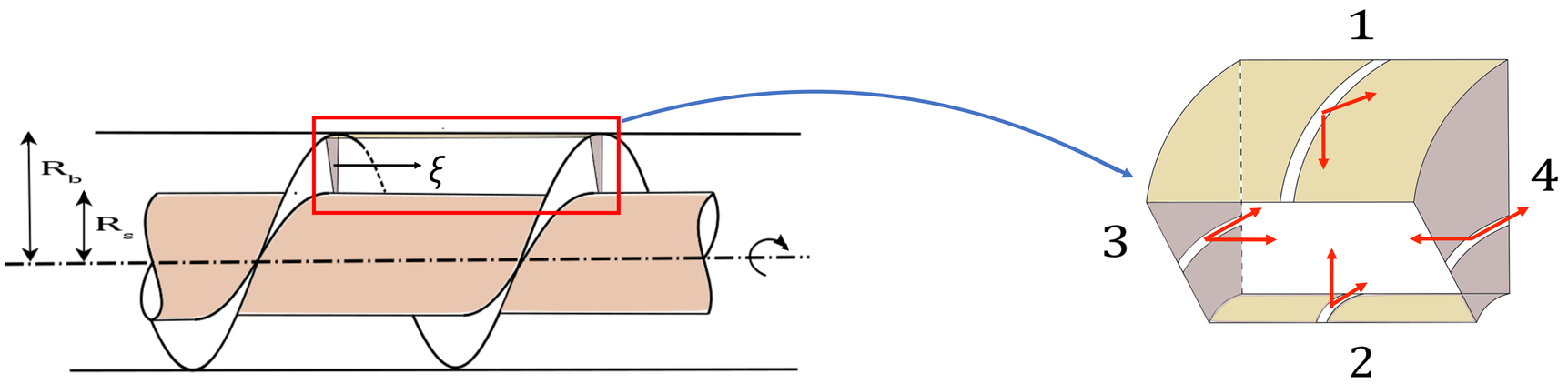

Force	Direction
$dF_{1n} = P_b(R_b d\theta d\xi)$	$-\hat{e}_r$
$dF_{1f} = \mu_b P_b(R_b d\theta d\xi)$	$-\cos\phi_b\,\hat{e}_\theta - \sin\phi_b\,\hat{e}_k$
$dF_{2n} = P_s(cR_b d\theta d\xi)$	$\hat{e}_r$
$dF_{2f} = \mu_s P_s(cR_b d\theta d\xi)$	$\hat{t}_h(R_s) = \cos\alpha_s\,\hat{e}_\theta - \sin\alpha_s\,\hat{e}_k$

Force	Direction
$dF_{3n} = P_{lw}\left(\left(\frac{rd\theta}{\cos\alpha}\right)dr\right)$	$\hat{n}_h(r,\theta) = -\sin\alpha\,\hat{e}_\theta - \cos\alpha\,\hat{e}_k$
$dF_{3f} = \mu_w P_{lw}\left(\left(\frac{rd\theta}{\cos\alpha}\right)dr\right)$	$\hat{t}_h(r) = \cos\alpha\,\hat{e}_\theta - \sin\alpha\,\hat{e}_k$
$dF_{4n} = P_{tw}\left(\left(\frac{rd\theta}{\cos\alpha}\right)dr\right)$	$-\hat{n}_h(r,\theta) = \sin\alpha\,\hat{e}_\theta + \cos\alpha\,\hat{e}_k$
$dF_{4f} = \mu_w P_{tw}\left(\left(\frac{rd\theta}{\cos\alpha}\right)dr\right)$	$\hat{t}_h(r) = \cos\alpha\,\hat{e}_\theta - \sin\alpha\,\hat{e}_k$

Linear Momentum Balances

Along $\hat{e}_r$

$$c\overline{P_s(\xi)} - \overline{P_b(\xi)} + 2\overline{P} = 0$$

Along $\hat{e}_\theta$

$$-\cos\phi_b\,\mu_b R_b \overline{P_b(\xi)} + c\mu_s R_b \overline{P_s(\xi)}\cos\alpha_s - \frac{p}{2\pi}\overline{P_{lw}(r)}$$

$$+\mu_w\left(\overline{rP_{lw}(r)}\right) + \frac{p}{2\pi}\overline{P_{tw}(r)} + \mu_w\left(\overline{rP_{tw}(r)}\right) = 0$$

Along $\hat{e}_k$

$$-\mu_b R_b \sin\phi_b\,\overline{P_b(\xi)} - \mu_s c R_b \sin\alpha_s \overline{P_s(\xi)} - \overline{rP_{lw}(r)}$$

$$-\frac{p\mu_w}{2\pi}\,\overline{P_{lw}(r)} + \overline{rP_{tw}(r)} - \frac{p\mu_w}{2\pi}\,\overline{P_{tw}(r)} = 0$$

$$\overline{\phi(x)} = \int_{x_i}^{x_f} \phi(x)\,dx$$

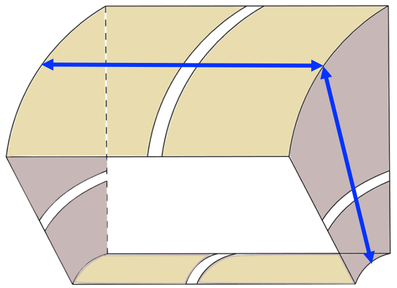

Angular Momentum Balances

All the moments are taken about a point on the axis of the shaft translated by $-\frac{p\theta}{2\pi}\hat{e}_k$ from the origin.

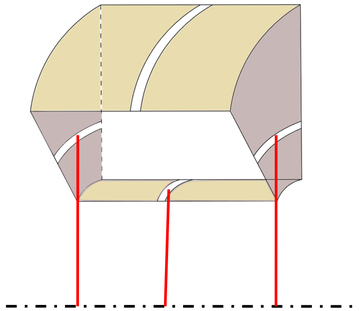

Along $\hat{e}_r$

$$-\cos\phi_b\mu_b R_b\overline{\xi P_b(\xi)} + \cos\alpha_s\mu_s cR_b\overline{\xi P_s(\xi)} + \frac{p^2}{2\pi}\overline{P_{tw}(r)} + p\mu_w\overline{rP_{tw}(r)} = 0$$

Along $\hat{e}_\theta$

$$R_b\overline{\xi P_b(\xi)} + R_b^2\sin\phi_b\mu_b\overline{P_b(\xi)} - cR_b\overline{\xi P_s(\xi)} + \sin\alpha_s\mu_s c^2R_b^2\overline{P_s(\xi)}$$

$$+\overline{r^2P_{lw}(r)} + \tfrac{p}{2\pi}\mu_w\overline{rP_{lw}(r)} - \overline{r^2P_{tw}(r)} + \tfrac{p}{2\pi}\mu_w\overline{rP_{tw}(r)} = 0$$

Along $\hat{e}_k$

$$-R_b^2\cos\phi_b\mu_b\overline{P_b(\xi)} + \mu_s\cos\alpha_s c^2R_b^2\overline{P_s(\xi)} - \tfrac{p}{2\pi}\overline{rP_{lw}(r)}$$

$$+\mu_w\overline{r^2P_{lw}(r)} + \tfrac{p}{2\pi}\overline{rP_{tw}(r)} + \mu_w\overline{r^2P_{tw}(r)} = 0$$

Number of unknowns and equations

More variables (11) than equations (6)!

- $\boxed{\phi_b}$
- $\overline{P(\xi, r)}$
- $\overline{P_s(\xi)}, \quad \overline{\xi P_s(\xi)}$
- $\overline{P_b(\xi)}, \quad \overline{\xi P_b(\xi)}$
- $\overline{P_{tw}(r)}, \quad \overline{rP_{tw}(r)}, \quad \overline{r^2 P_{tw}(r)}$
- $\overline{P_{lw}(r)}, \quad \overline{rP_{lw}(r)}, \quad \overline{r^2 P_{lw}(r)}$

Not surprising, as we do not have a constitutive relation for the stress.

However, we can get a solution when μ_s and $\mu_w = 0$

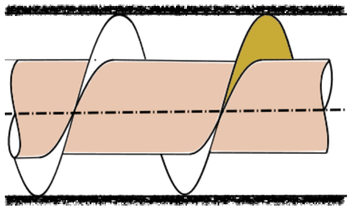

Screw and shaft surfaces frictionless

Linear momentum balance along $\hat{e}_k$ reduces to

$$-\mu_b R_b \sin\phi_b \overline{P_b(\xi)} - \overline{rP_{lw}}(r) + \overline{rP_{tw}(r)} = 0$$

Angular momentum balance along $\hat{e}_k$ reduces to

$$-R_b^2 \cos\phi_b \mu_b \overline{P_b(\xi)} - \frac{p}{2\pi}\overline{rP_{lw}(r)} + \frac{p}{2\pi}\overline{rP_{tw}(r)} = 0$$

Solving the above equations, we get:

$$\cot\phi_b = \frac{p}{2\pi R_b} = \tan\alpha_b$$

The expression for discharge rate simplifies to

$$Q = \nu\omega R_b \underbrace{\left[\frac{2\pi\,(p/R_b)}{(2\pi)^2 + (p/R_b)^2}\right]}_{f(p/R_b)} \pi(R_b^2 - R_s^2)$$

Dimensionless flow rate when μ_s and $\mu_w = 0$

$$Q = \nu\omega R_b f(p/R_b)\pi(R_b^2 - R_s^2)$$

Simplistic analysis of Roberts (slide 4)

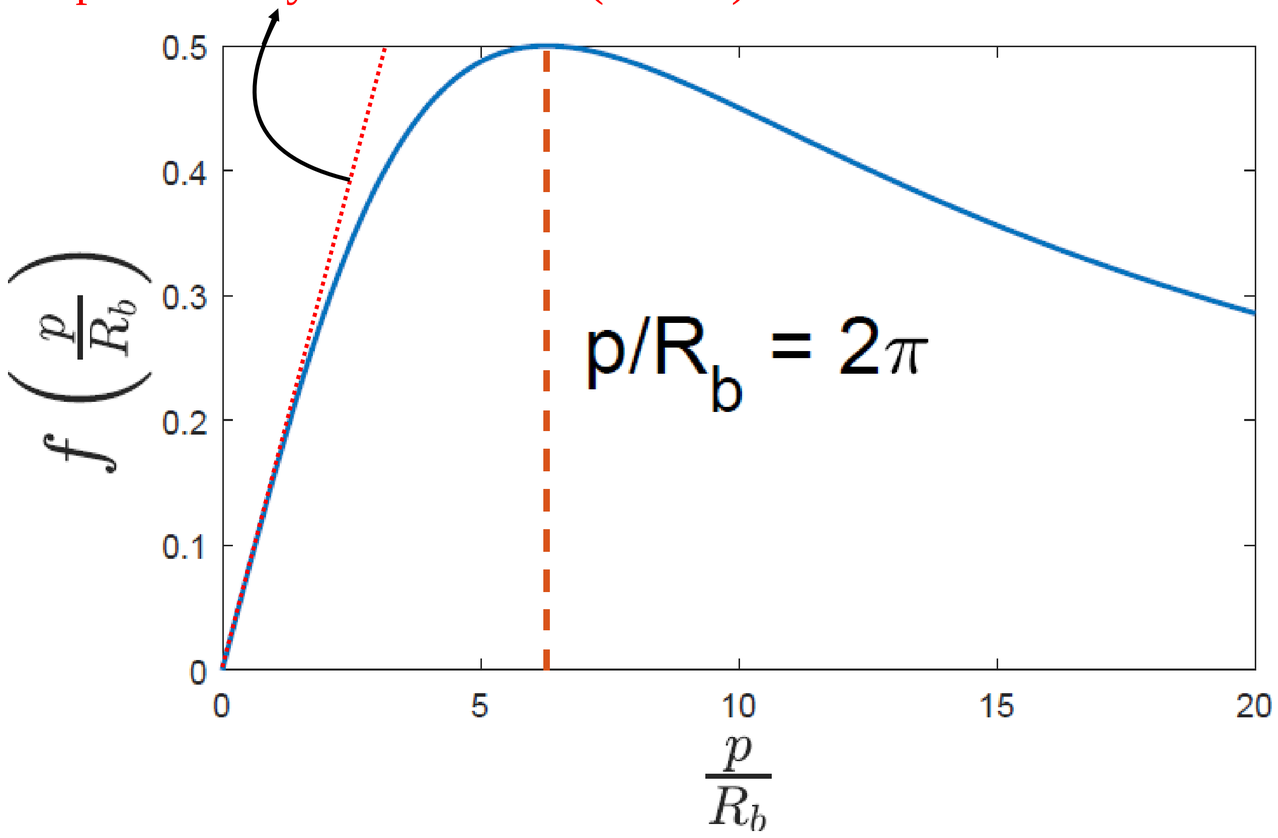

There is an optimum p/R_b at which discharge rate is maximum

DEM simulations of flow in a screw feeder

Verify predictions of simple model; relax simplifying assumptions; get details of the flow

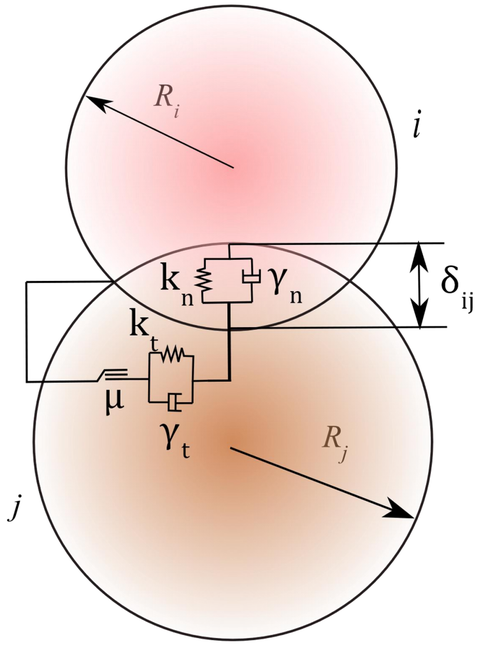

$$\mathbf{F}_n^{(i)} = k_n \delta \mathbf{n} - m_{eff} \gamma_n \mathbf{v}_n$$

$$\mathbf{F}_t^{(i)} = \begin{cases} -k_t \Delta \mathbf{s} - m_{eff} \gamma_t \mathbf{v}_t, & \left| \frac{\mathbf{F}_t}{\mathbf{F}_n} \right| < \mu \\ -\mu |\mathbf{F}_n^{(i)}| \frac{\mathbf{v}_t}{|\mathbf{v}_t|} & \text{otherwise} \end{cases}$$

$$m_i \frac{d\mathbf{v}_i}{dt} = m_i \mathbf{F}_i{}^b + \mathbf{F}_i{}^c$$

$$I_i \frac{d\omega_i}{dt} = \mathbf{T}_i{}^c$$

$$\mathbf{F}_i{}^c = \sum_{\substack{j=1 \\ j \neq i}}^{N} (\mathbf{F}_{ij}{}^n + \mathbf{F}_{ij}{}^t)$$

$$\mathbf{T}_i{}^c = \sum_{\substack{j=1 \\ j \neq i}}^{N} (R_i \mathbf{n}) \times (\mathbf{F}_{ij}{}^t)$$

Cundall, PA, & Strack, OD Geotechnique **29**, 47-65 (1979).

Simulation process overview

Carried out using the open source LIGGGHTS package

Geometric parameters in the DEM set-up

Geometric parameters	**category I**	**category II**
screw-shaft radius (R_s)	6.5 d_p	6.5 d_p
barrel radius (R_b)	19 d_p	(19 , 25.25, 31.5) d_p
pitch (p)	(38, 76, 114, 152, 190) d_p	38 d_p
blade thickness (t_b)	1 d_p	1 d_p

Creation of boundaries

Screw, shaft and casing surfaces created by triangulation

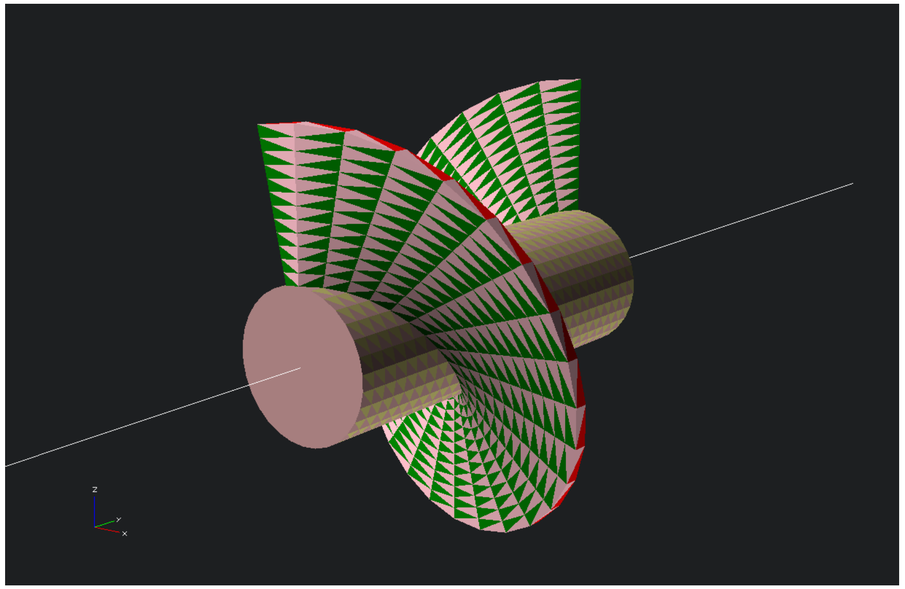

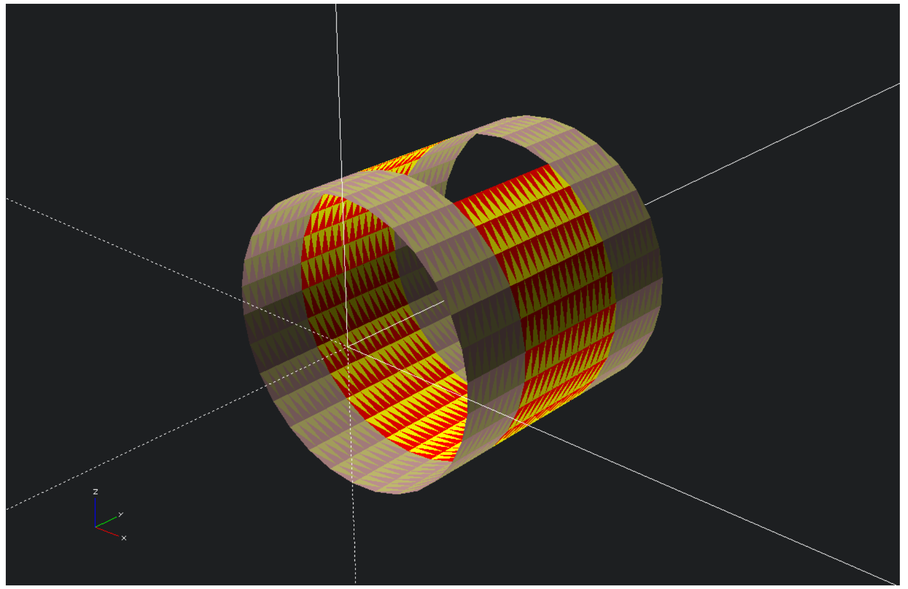

Averaging in the bulk and the surfaces

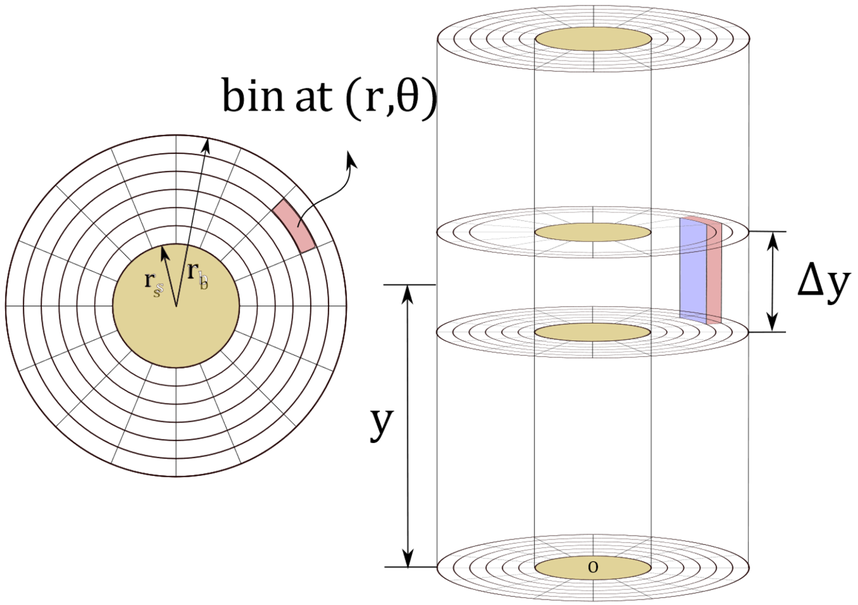

Annular ring
elements in the bulk

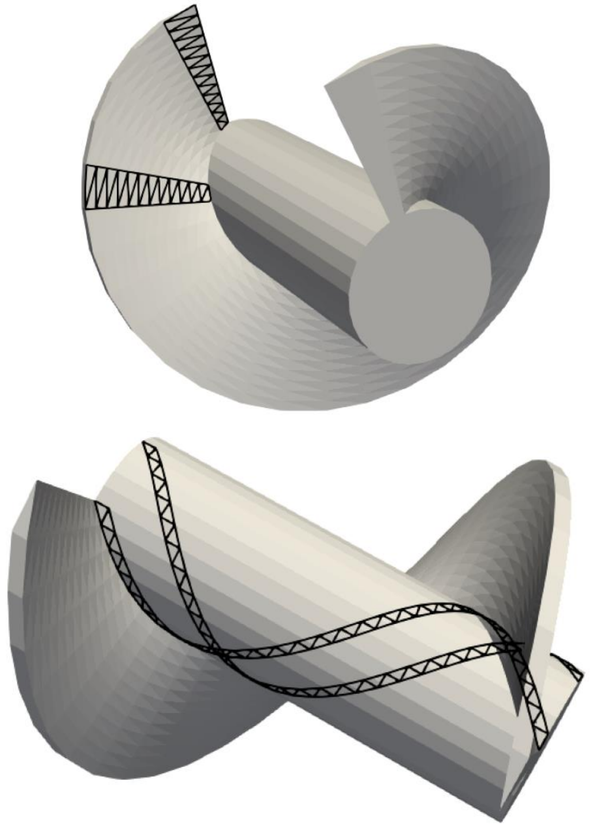

Triangular element
sets on the screw and
shaft surfaces

Variation of solid fraction and pressure in the bulk

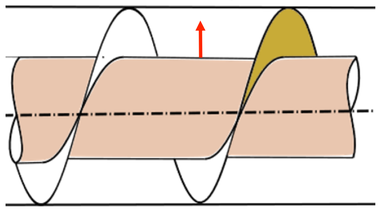

Solids fraction

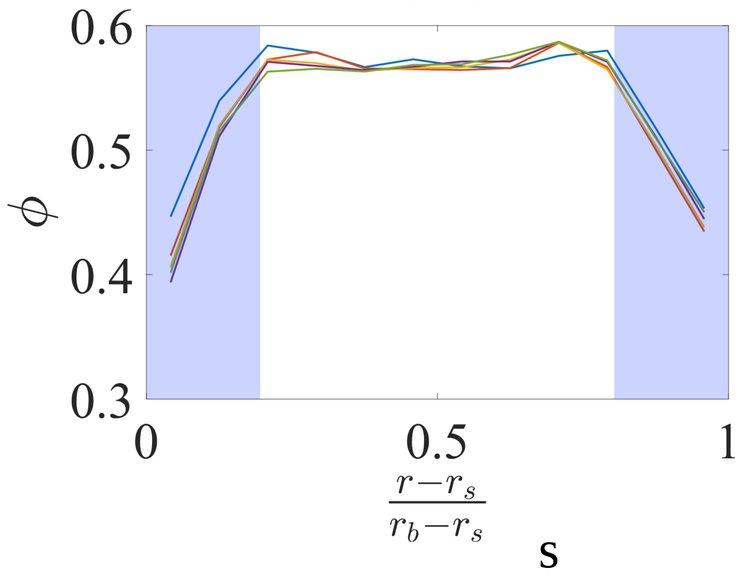

Pressure

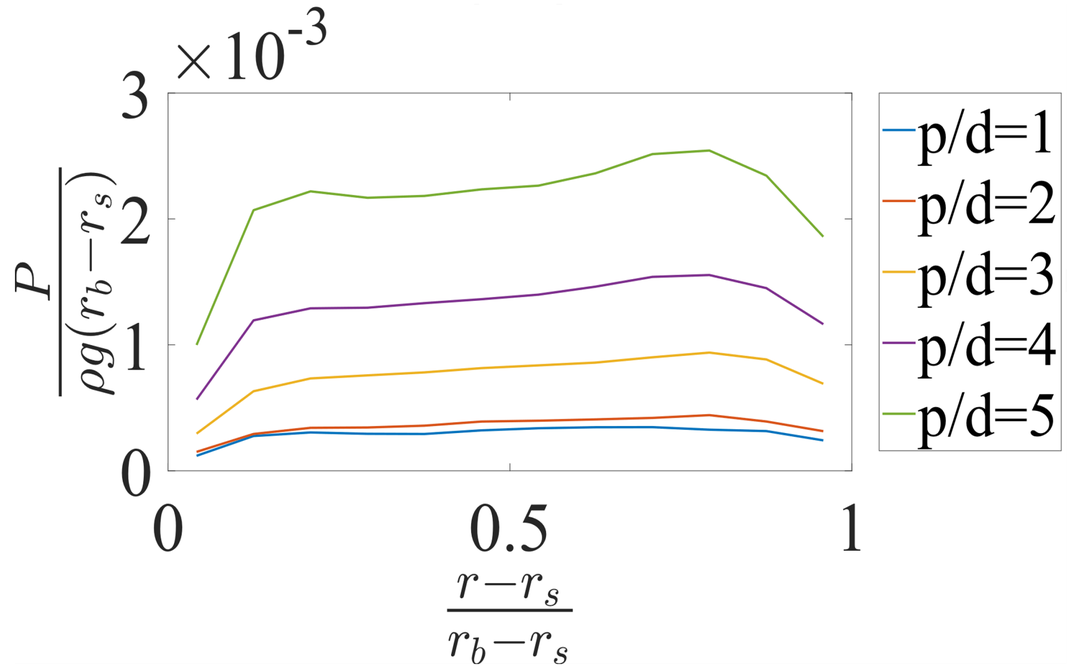

Lower solids fraction near the boundaries

Azimuthal and axial velocities

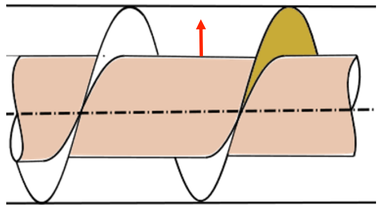

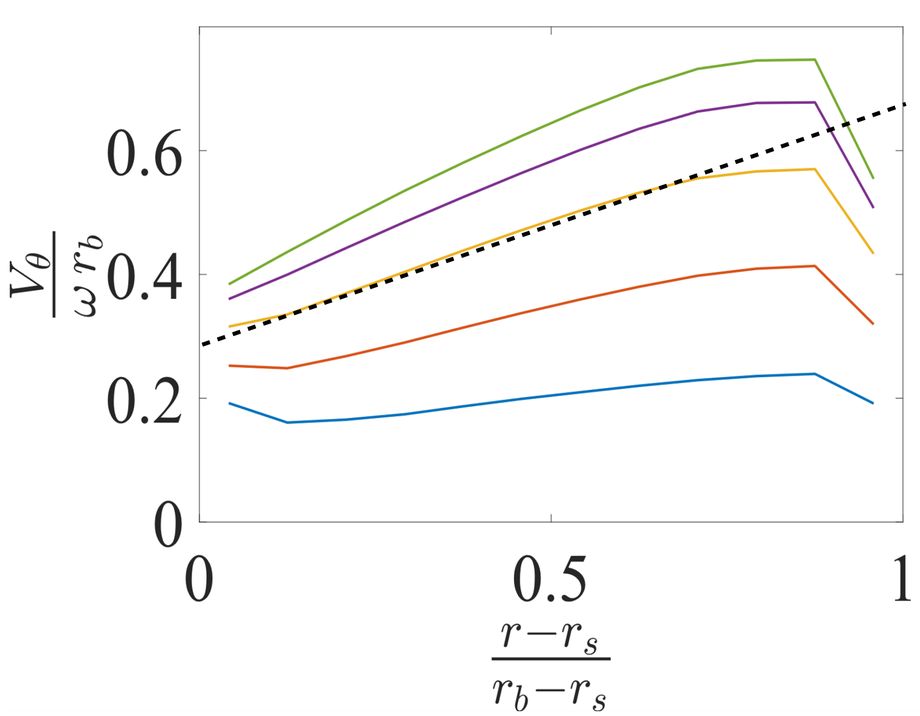

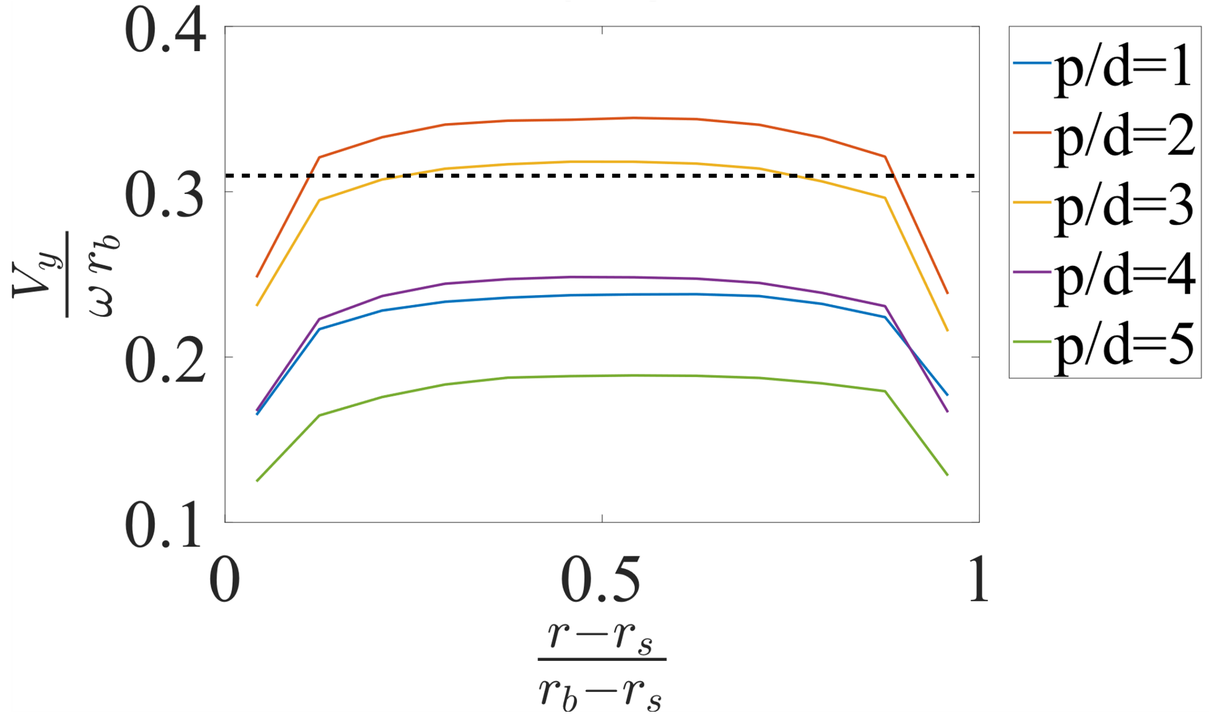

Motion nearly like that a rigid plug, except near the boundaries

Stresses on the barrel

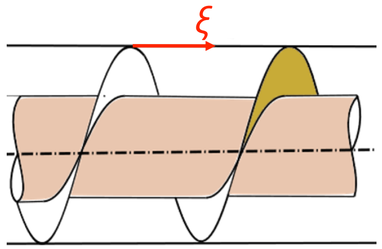

Normal stress

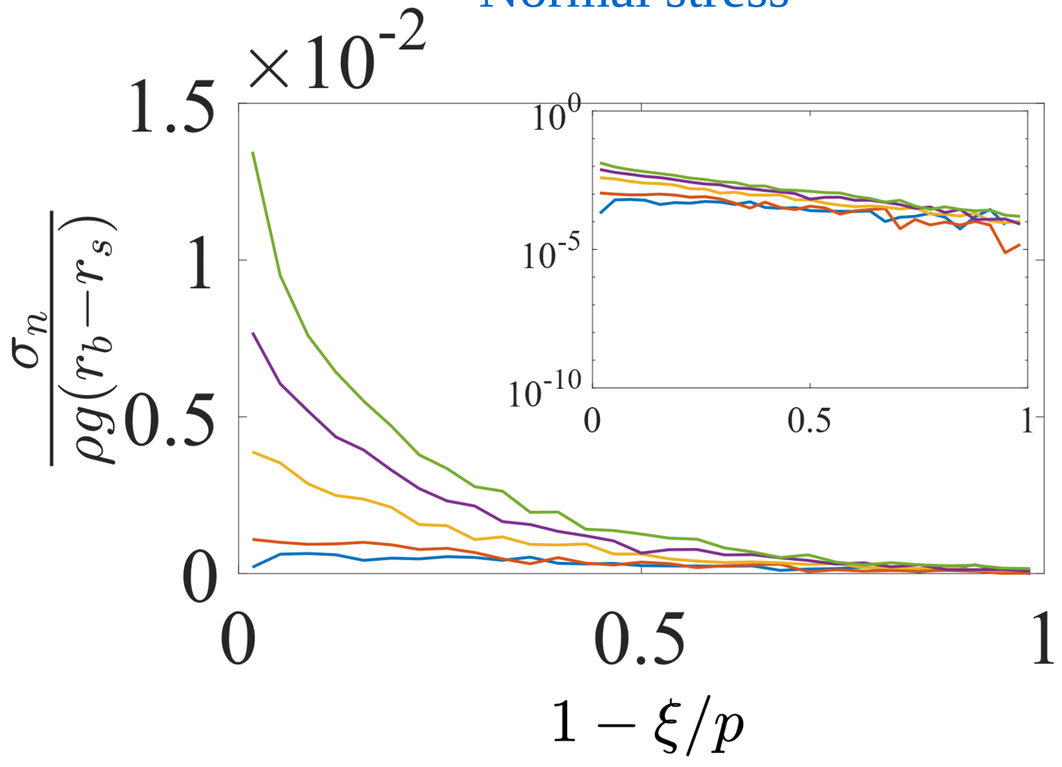

Shear stress

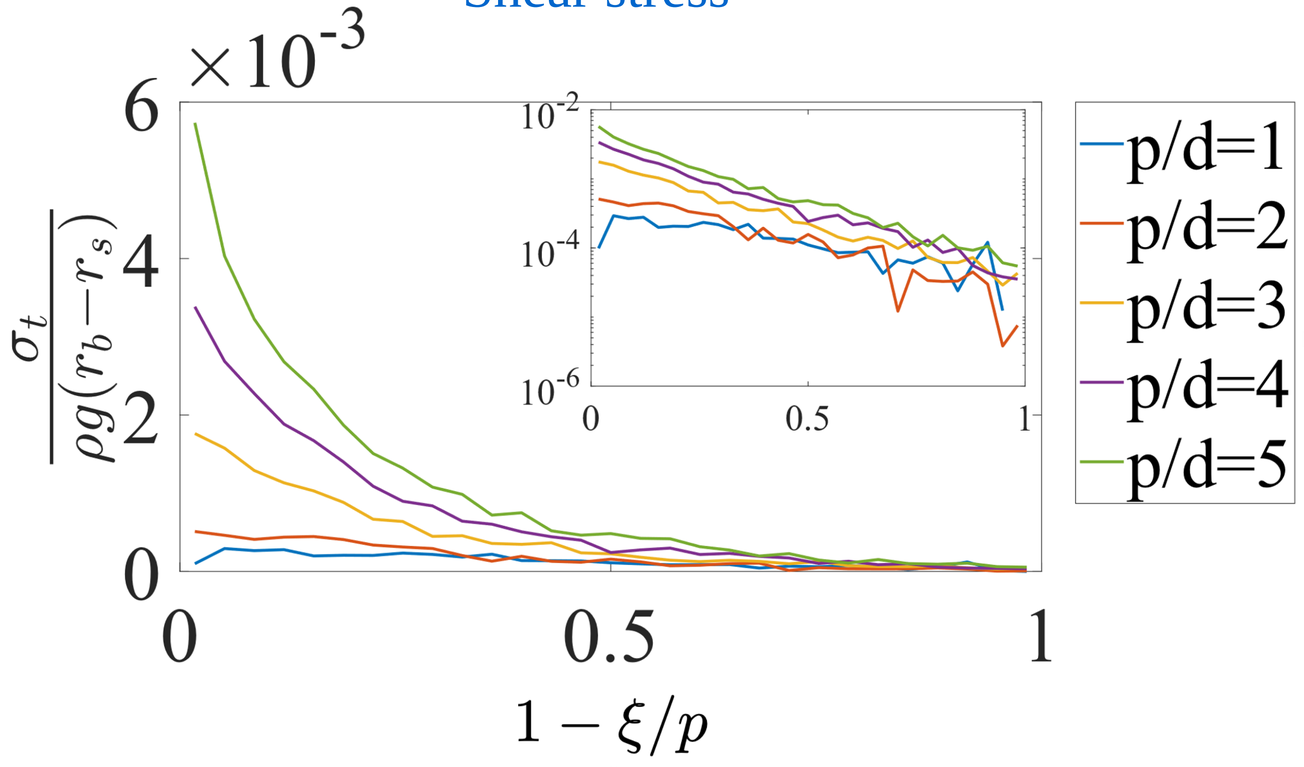

Exponential decay: similar to the Janssen saturation of stress in silos

Summary of the stress of surfaces in the absence of gravity

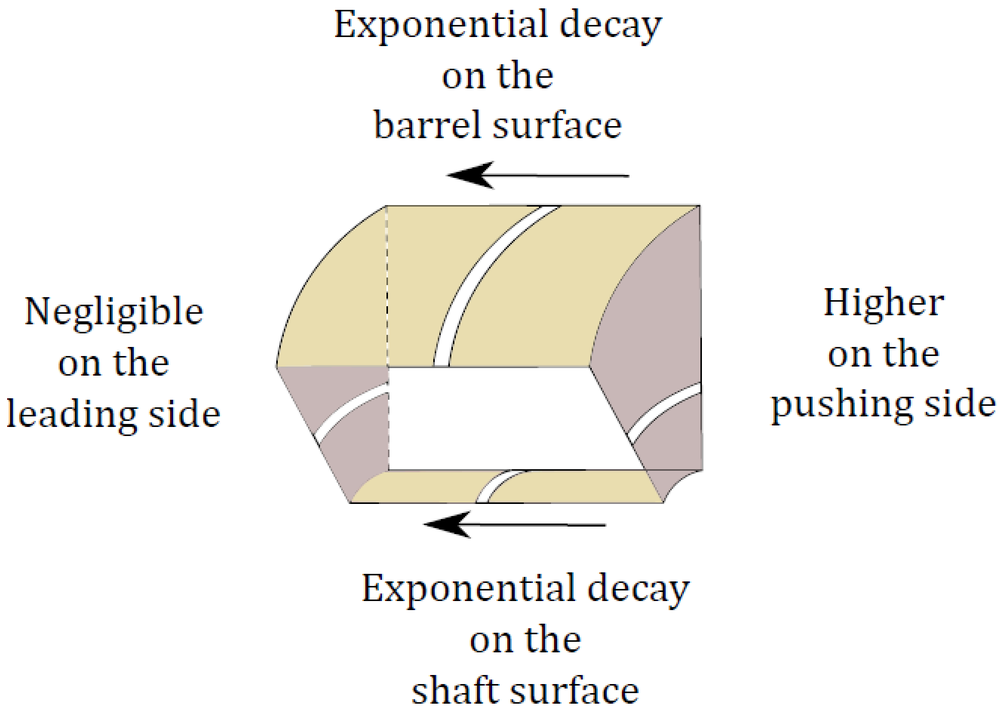

Results from DEM simulation under gravity

Pressure

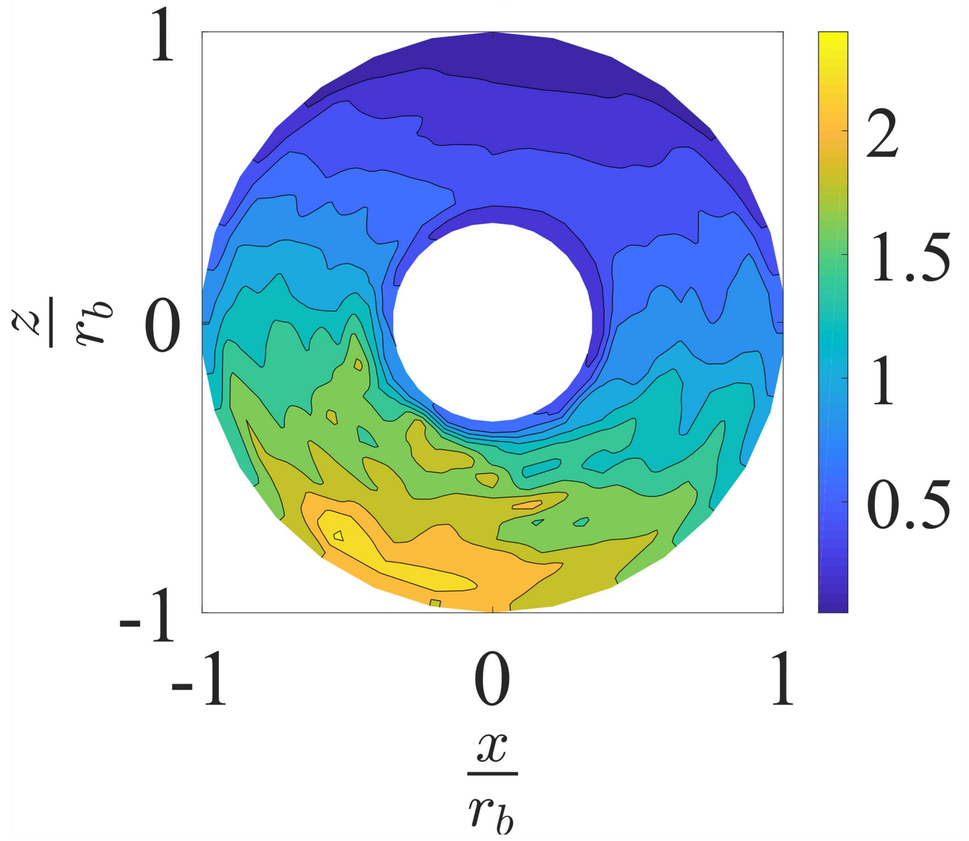

Solid fraction

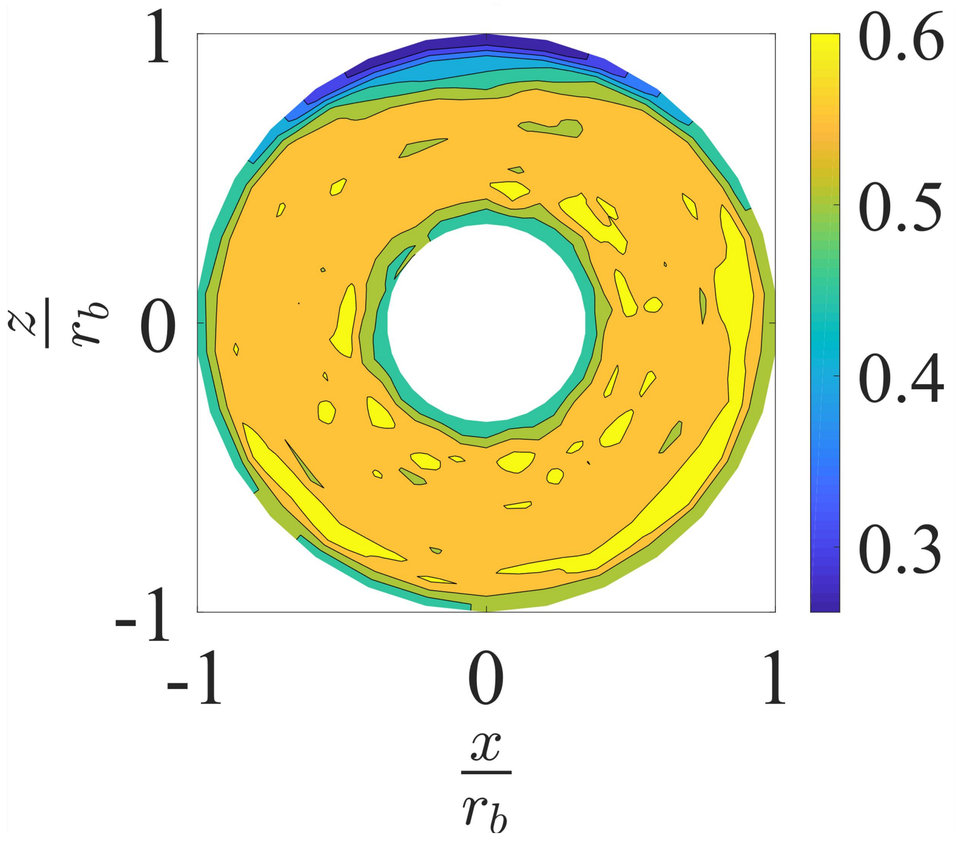

Results from simulations under gravity (Contd..)

Axial velocity

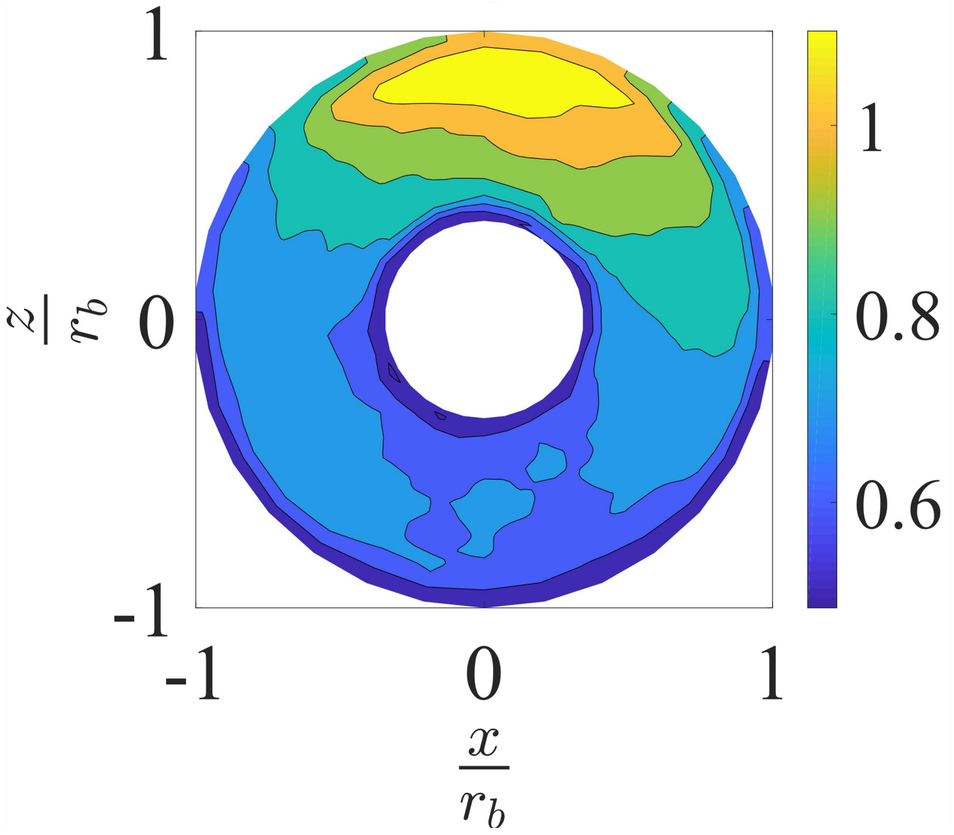

Azimuthal velocity

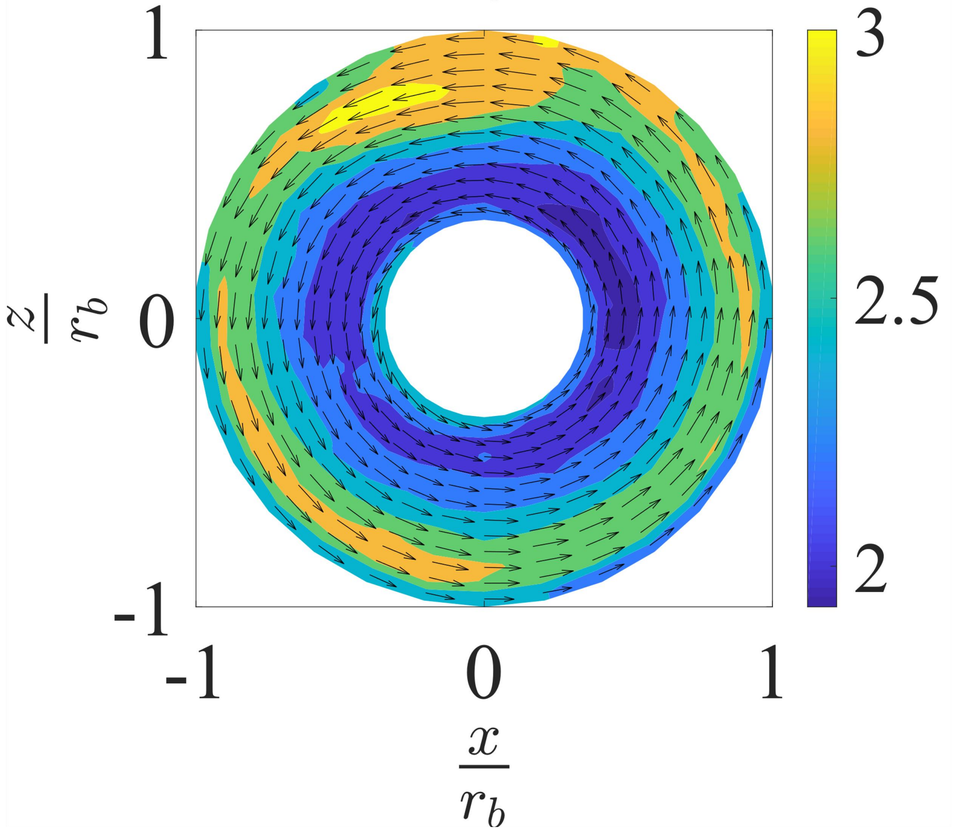

Comparison of DEM result with theory

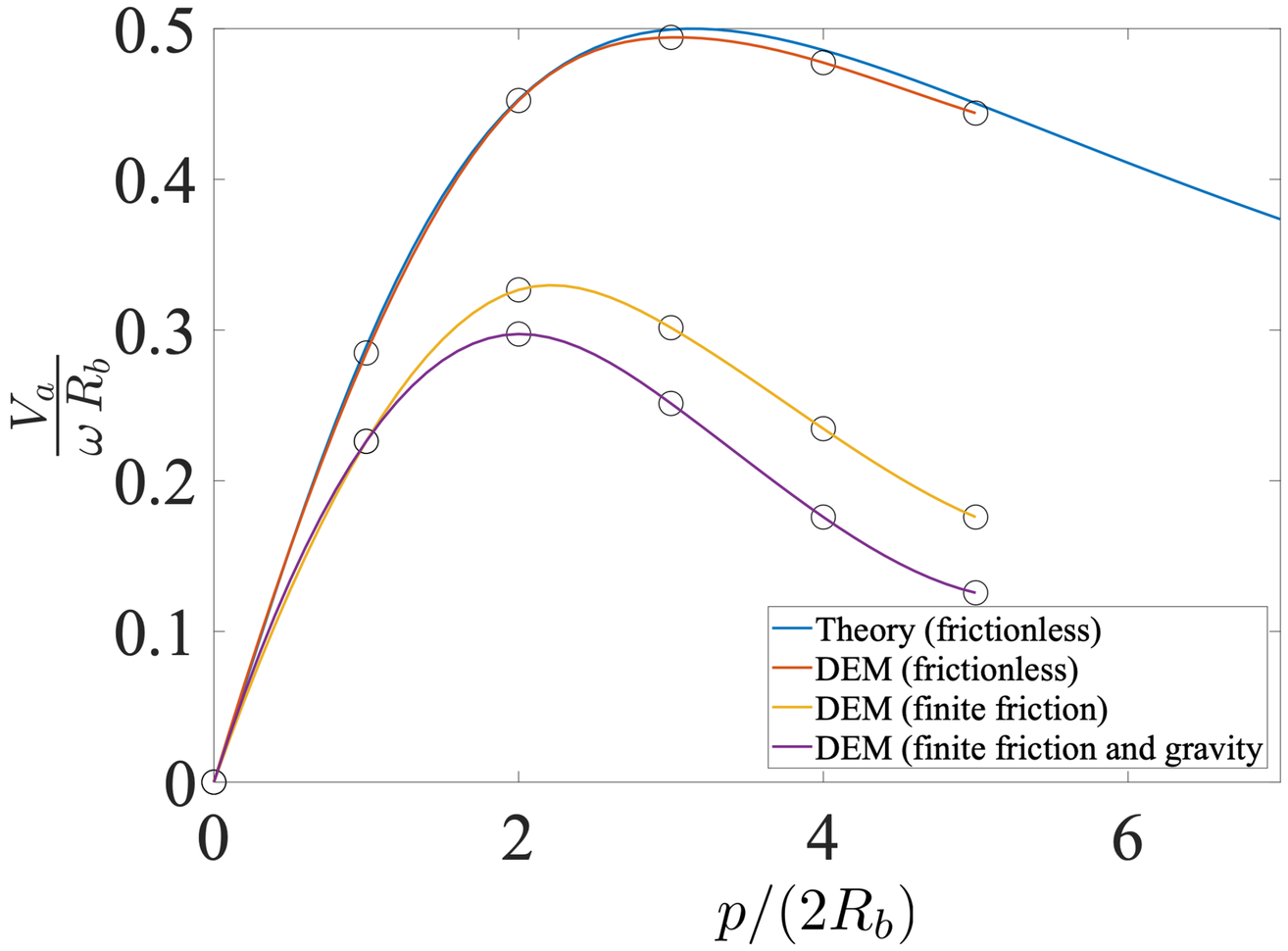

- Excellent agreement for frictionless screw surface
- Same qualitative trend for frictional surface, and when gravity is present
- There is always an optimum value of p/R_b at which discharge rate is maximum

Conclusion

- A mechanistic model for powder flow through a screw feeder developed.
- Balances of linear and angular momentum in the limit of vanishing friction coefficient on the screw surface solved to obtain maximum discharge rate.
- DEM simulations conducted to verify model predictions, relax assumptions, and provide insight. Excellent agreement with model predictions.
- The qualitative behavior of the average axial velocity curve doesn't change with the introduction of gravity.
- Ongoing and future work: experiments, extension to twin screw feeders, use more sophisticated models to determine density variation and discharge rate.

ETH zürich

Simplified industrial dispersions

Luico Isa and Jan Vermant

Department of Materials. ETH Zürich - ETH Zürich, CH

Gabriele Colombo

Chiao-Peng Hsu

Roberta Massaro
(visiting student)

Florence Müller

Vincent Niggel

Laura Stricker

Pierre Lehericy

Complexity in model systems

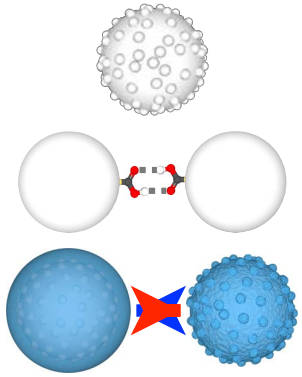

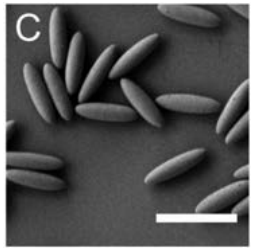

Simplified industrial dispersions

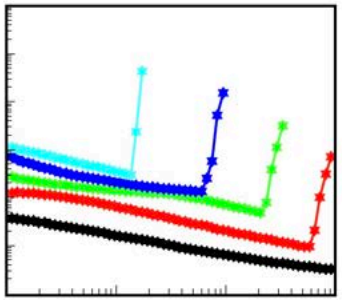

shear thickening

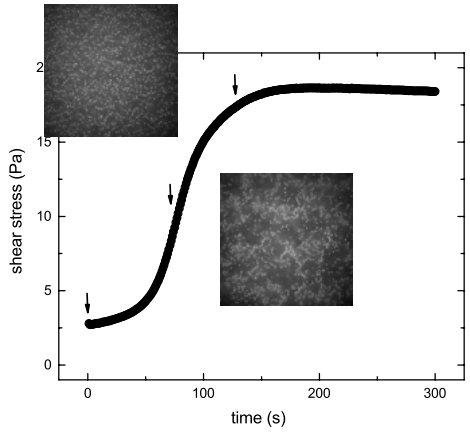

thixotropy

Analytical, structural and rheological
methods tailored to interrogate structure

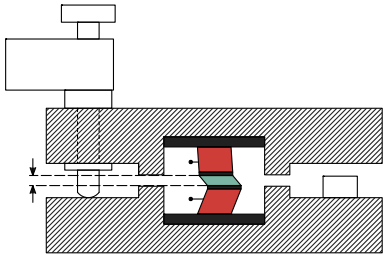

stress deconvolution

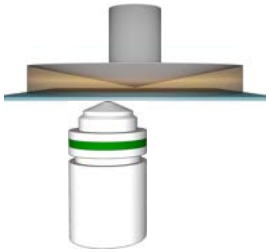

4D-imaging

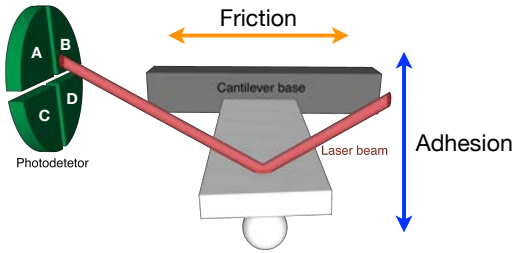

local scale tribology

- Objectives
- Shear thickening : roughness and adhesion
- Thixotropy : strength and adhesion
- Conclusions / outlook

Model rough colloids

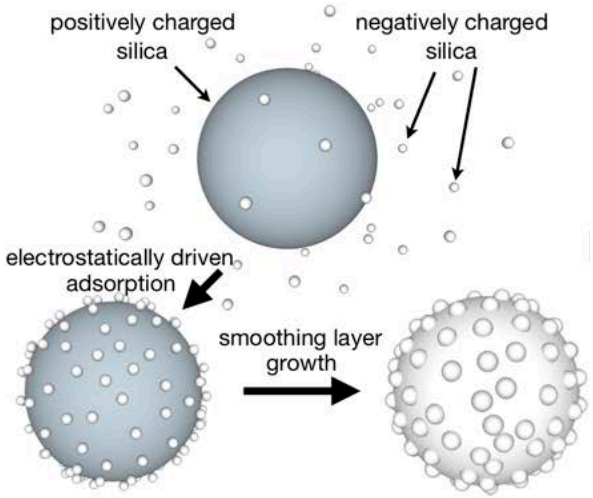

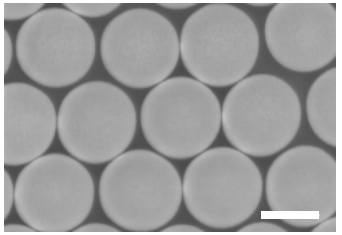

≈0

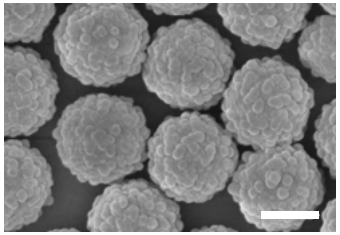

0.25±0.028

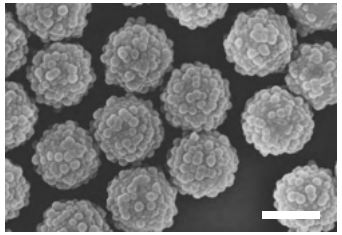

0.31±0.035

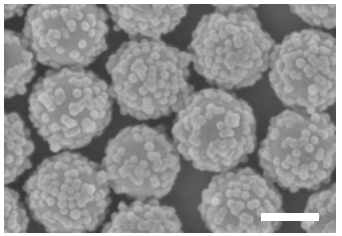

0.36±0.039

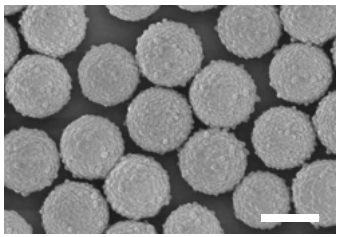

0.45±0.049

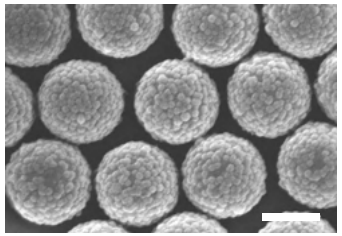

0.53±0.047

Scale bars = 500 nm

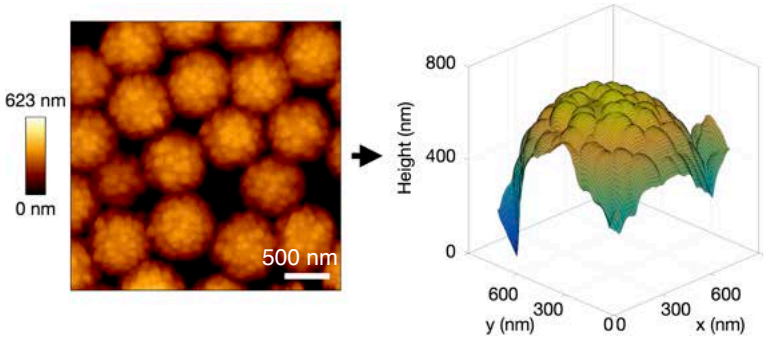

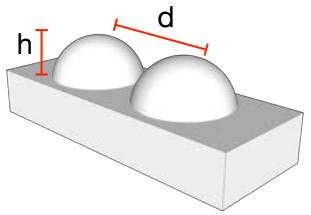

h: asperity height
d: inter-asperity distance

Dimensionless roughness parameter h/d

C. P. Hsu *et al.*, *PNAS* 115, (2018).

Sedimentation

characterization

ϕ_m, frictional packing fraction

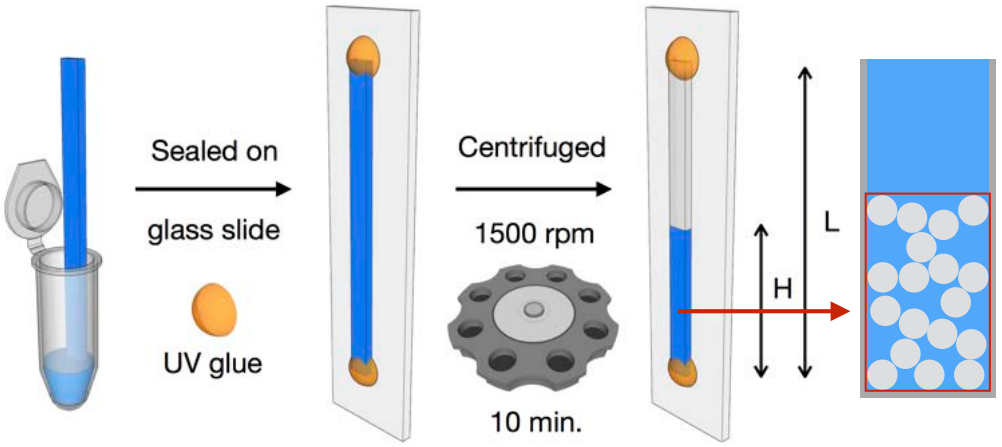

After centrifugation
H/L = ϕ_m

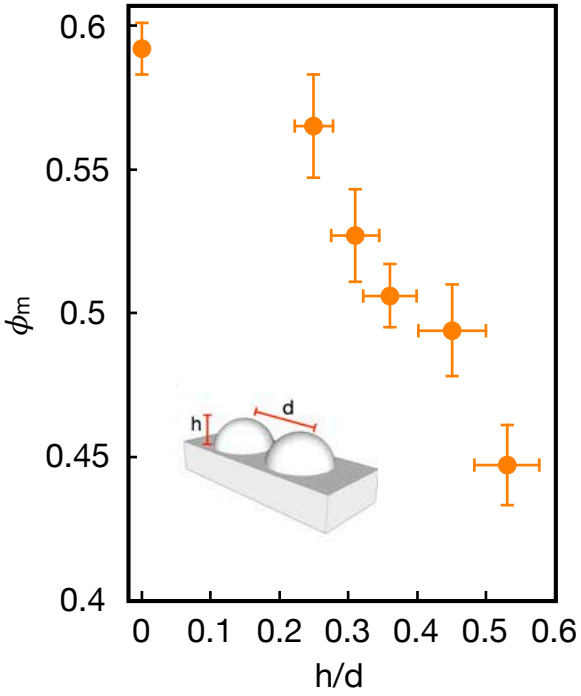

Higher h/d ➡
Lower ϕ_m

C. P. Hsu *et al.*, *PNAS* 115,

Rheology Meets Tribology

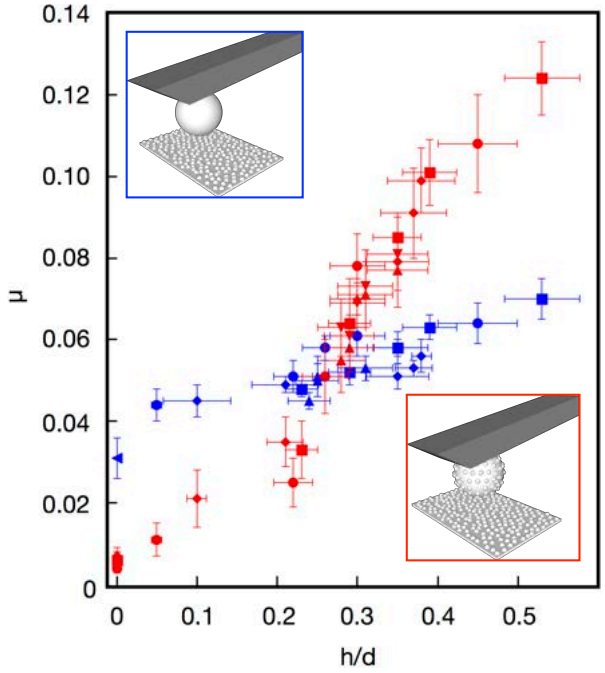

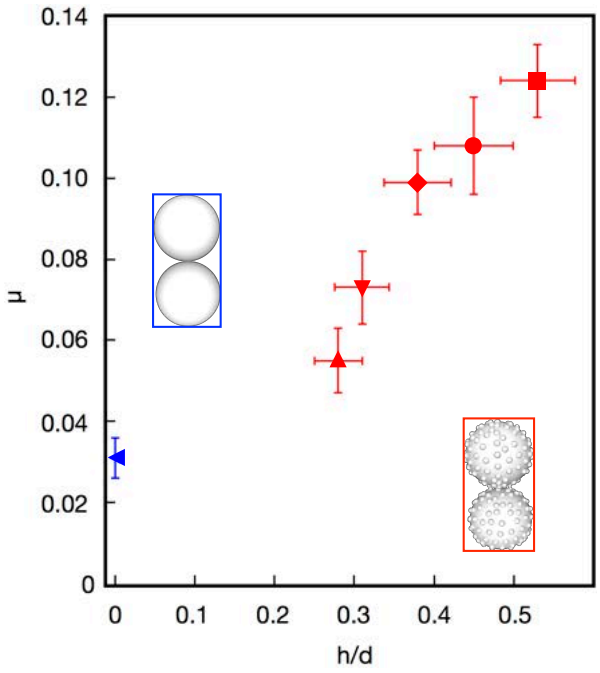

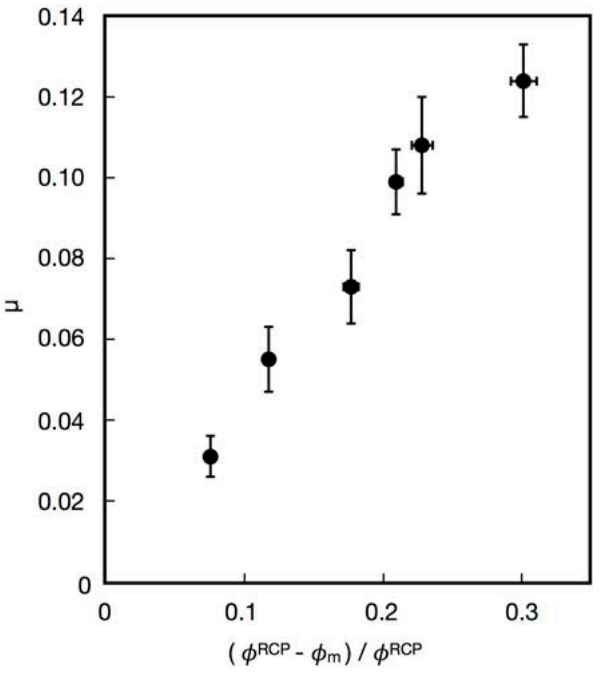

C. P. Hsu *et al.*, *PNAS* 115, (2018).

characterization : AFM

surprisingly simple relation

(topographic friction)

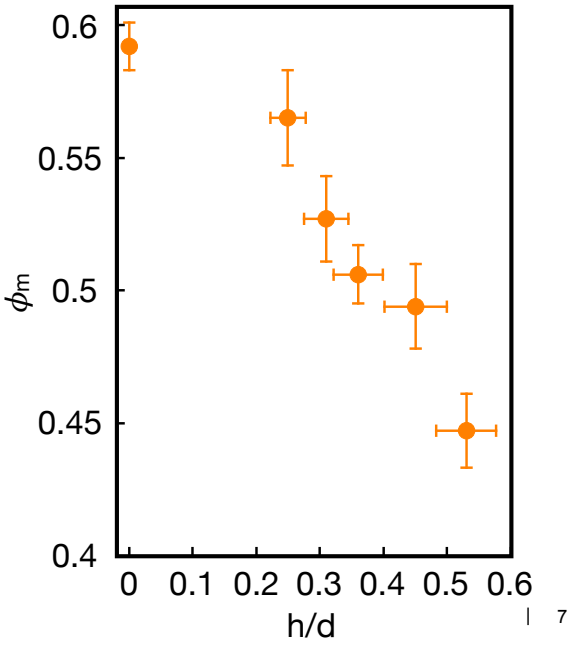

Smooth, ϕ_m = 59.2%

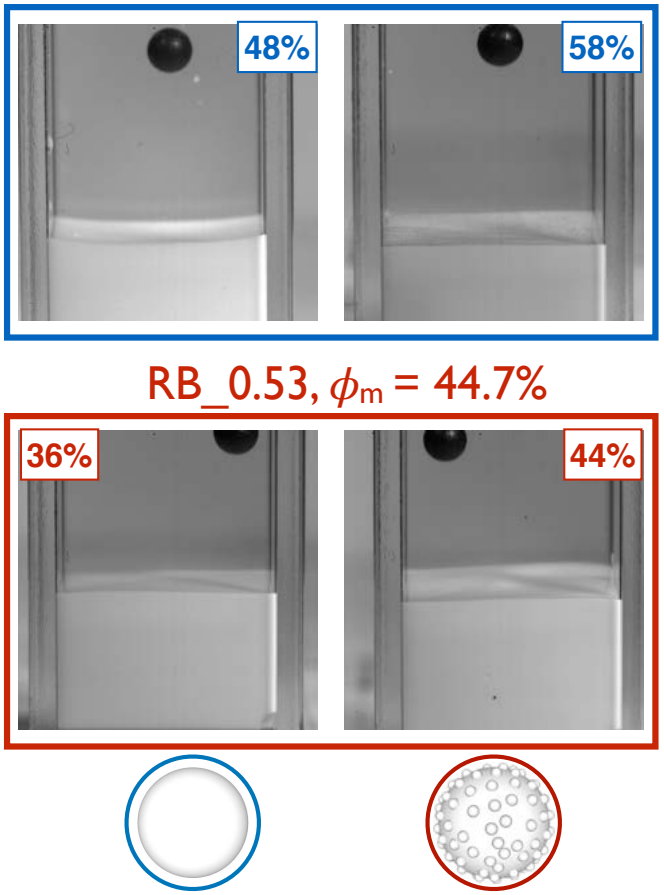

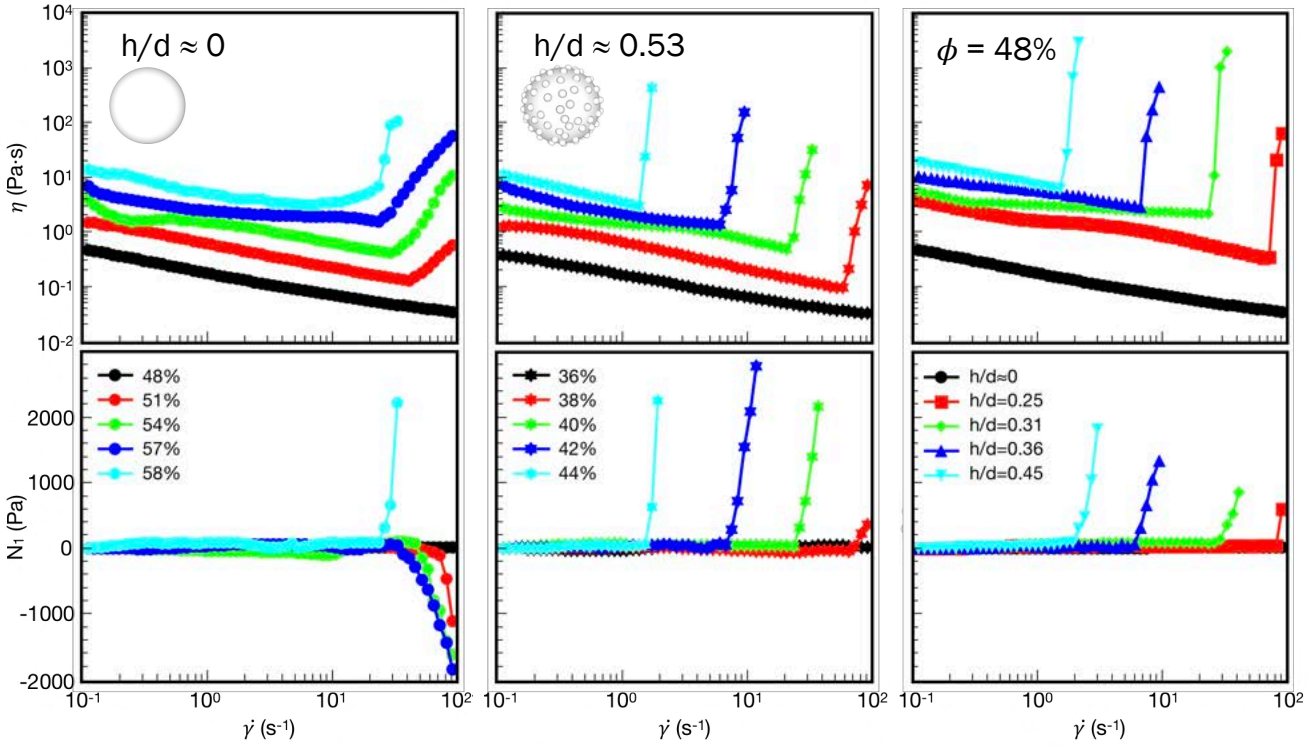

CST to DST

No CST

C. P. Hsu *et al.*, *PNAS* 115,

Rheology Meets Tribology

Friction between particles

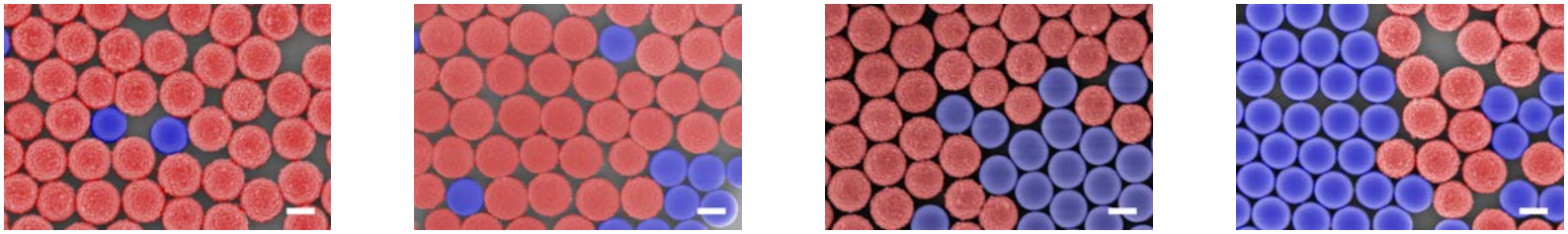

Scale bars = 500 nm

Vol% of smooth particles

Large increase in ϕ_m

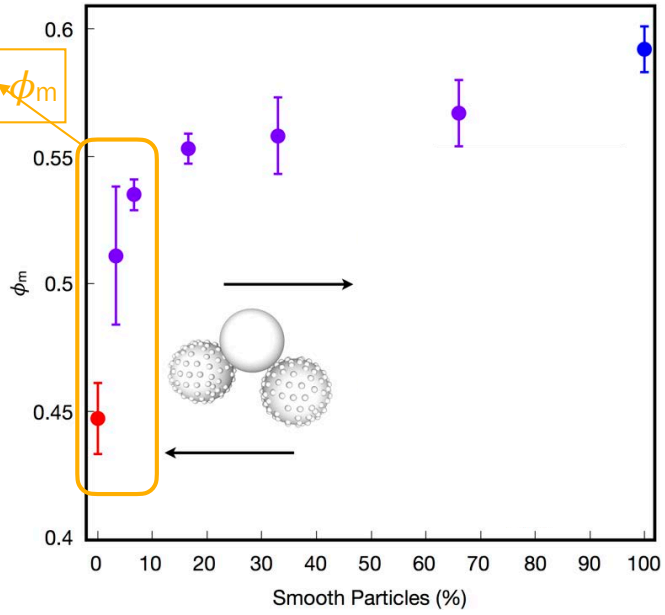

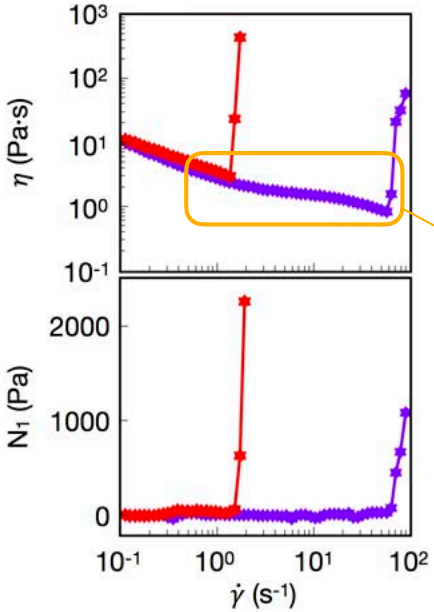

Large increase in $\dot{\gamma}_c$

Interparticle Hydrogen Bounding

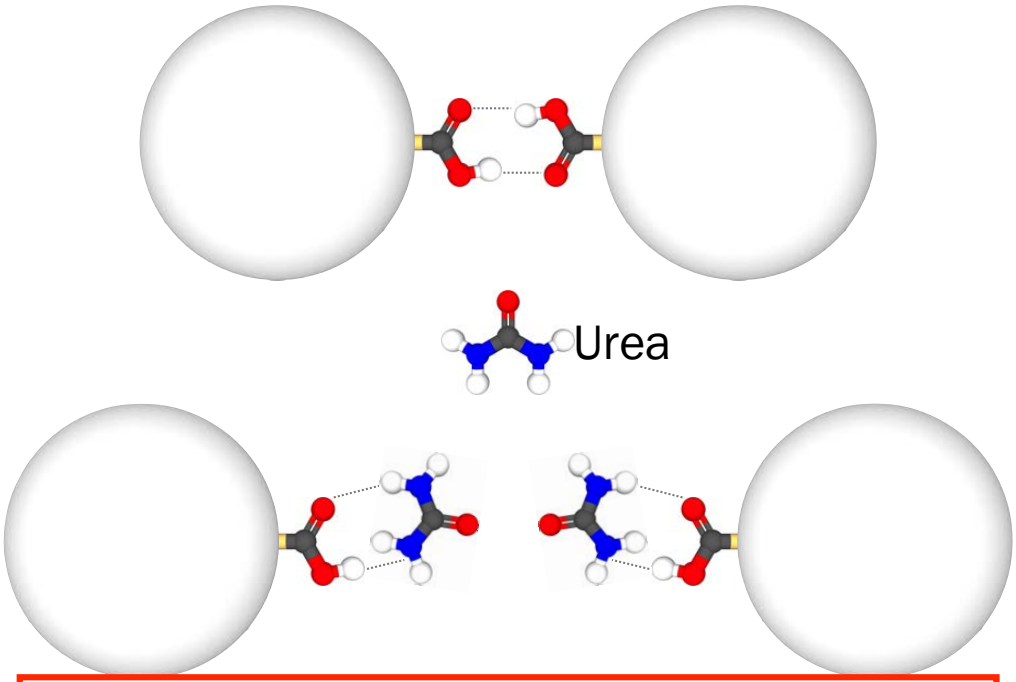

What is the role of adhesion introduced by interparticle hydrogen bonding?

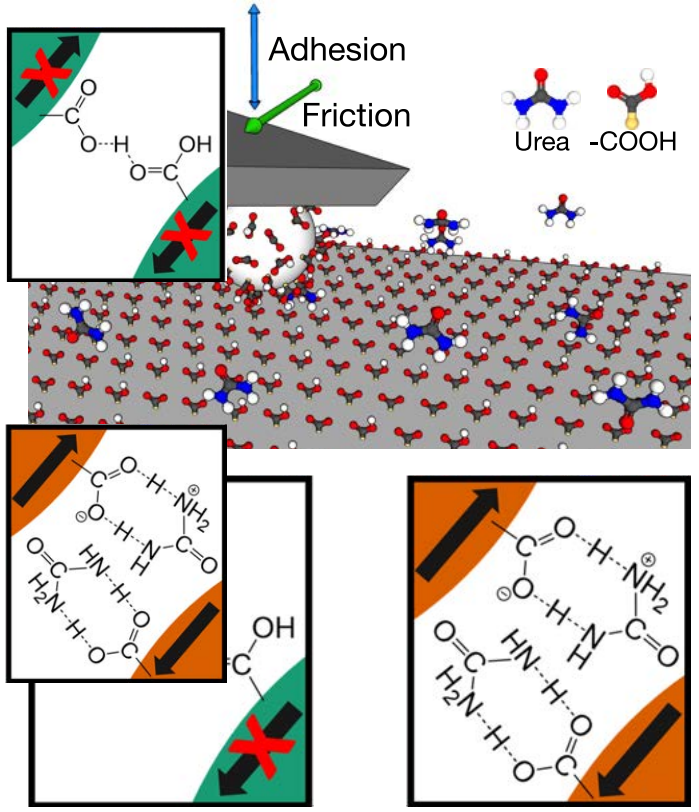

N. James & C. P. Hsu *et al.*, *JPCL* 10, (2019).

Adhesion ↔ Friction

1 hr equilibration
in 69% (v/v) glycerol/water

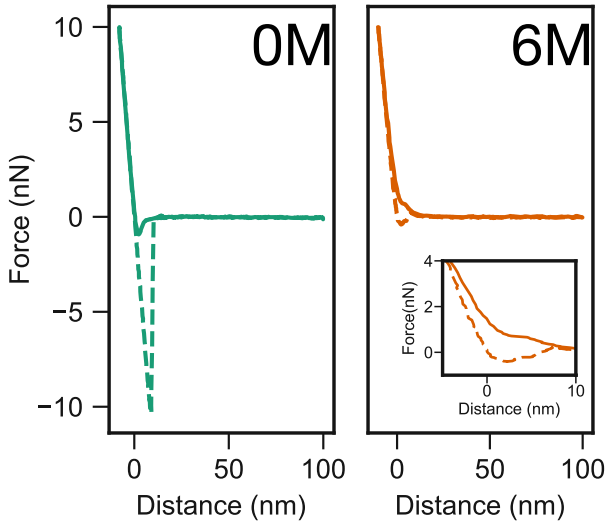

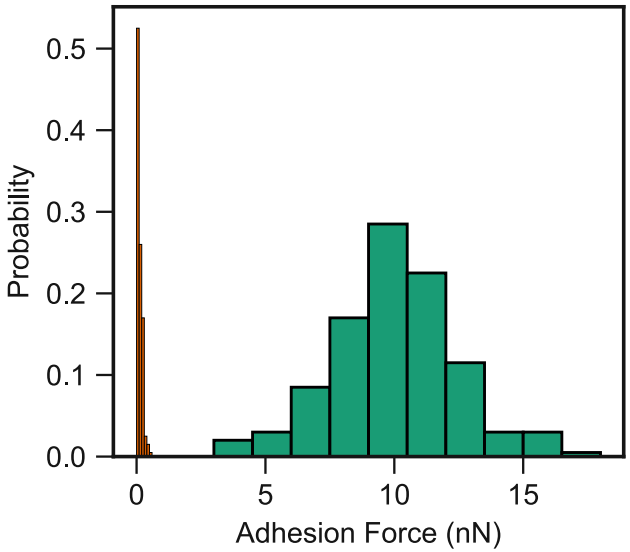

F_{ad} = 10.0 ± 2.5 nN
F_{ad} ≈ 0.1 nN

$F_{friction} = F_0 + \mu \cdot L$

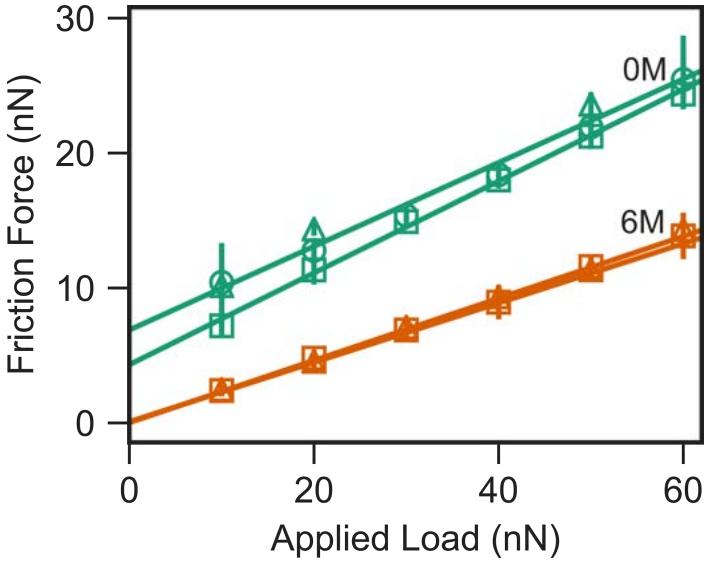

μ = 0.33 μ = 0.22

N. James & C. P. Hsu *et al.*, *JPCL* 10, (2019).

Connection to Bulk Rheology

High-shear rheology ↔ frictional interparticle interactions

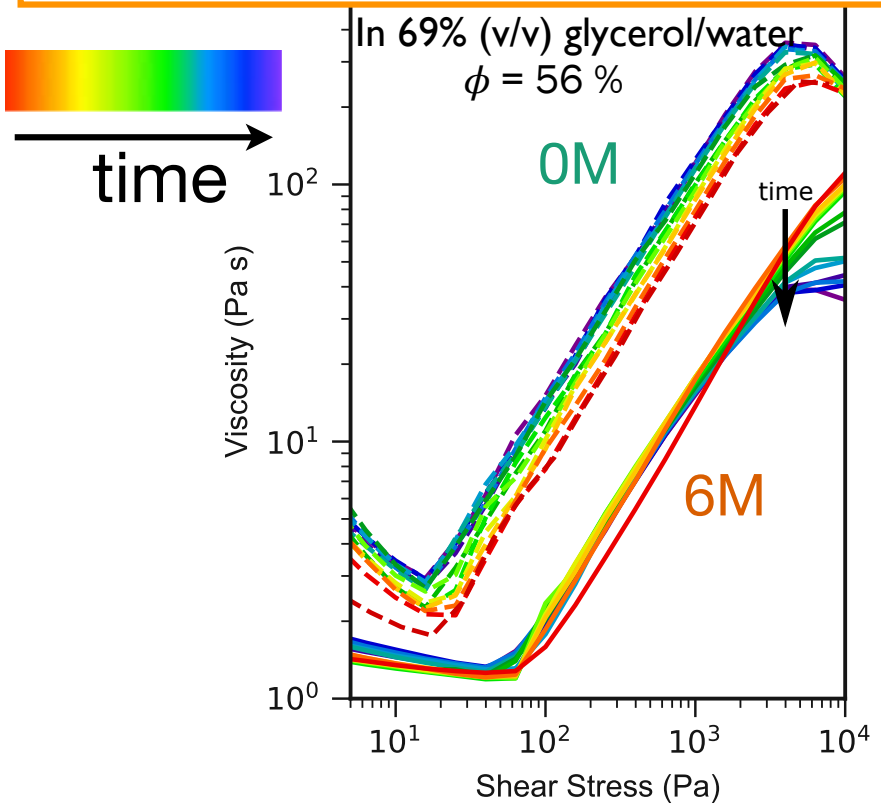

N. James & C. P. Hsu *et al.*, *JPCL* 10,

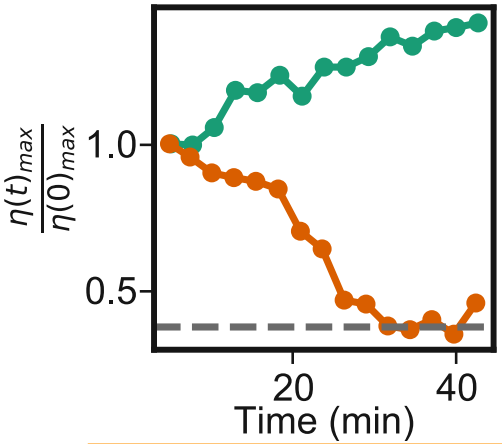

Krieger-Dougherty relation

$$\eta = \eta_0 \cdot (1 - \frac{\phi}{\phi_m})^{-\alpha}$$

Urea sorption onto the particle surface

μ ⬇, F_0 ⬇

ϕ_m ⬆, η_{max} ⬇

PNIPAM-grafted Model Colloids

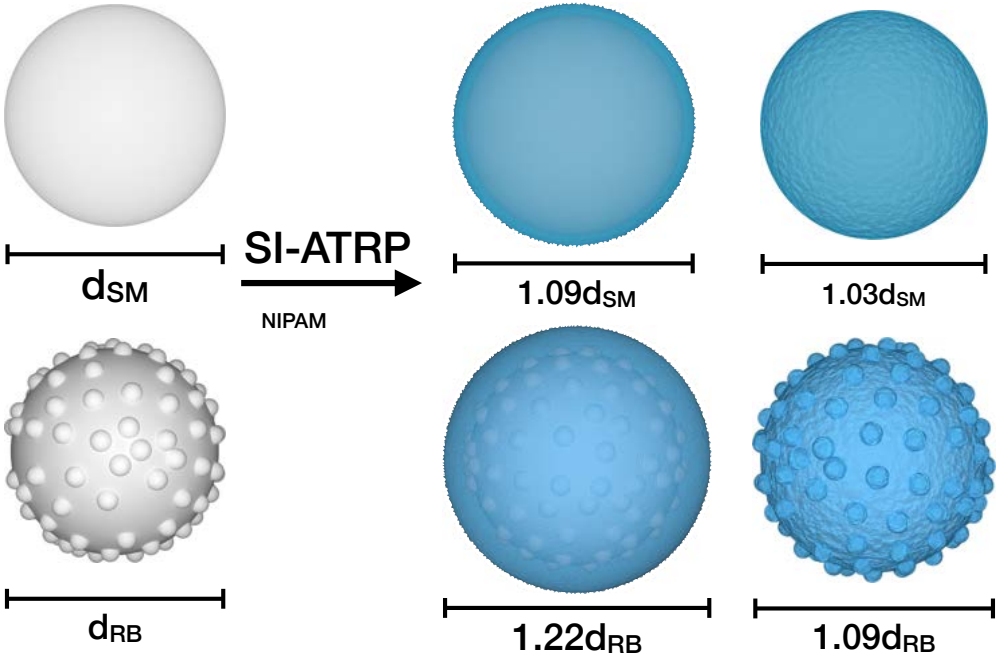

SM_PNIPAM
31 ± 3 nm

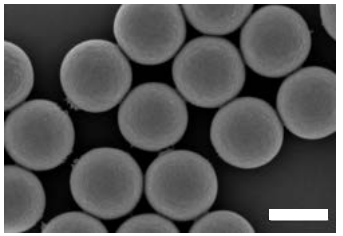

12 ± 2 nm

RB_0.36_PNIPAM
80 ± 5 nm

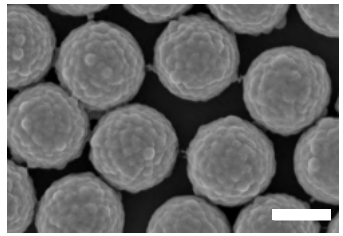

31 ± 5 nm

RB_0.46_PNIPAM
85 ± 6 nm

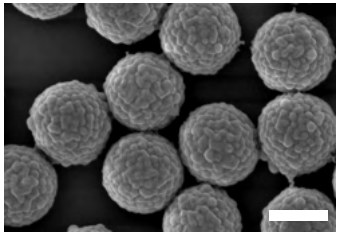

33 ± 3 nm

RB_0.52_PNIPAM
84 ± 6 nm

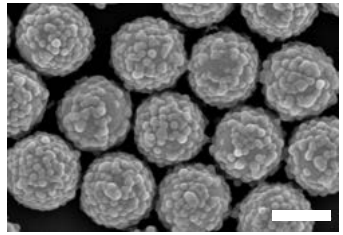

35 ± 4 nm

Scale bars = 500 nm

C. P. Hsu *et al.*, *arXiv:2004.05970*, (2020).

Friction ↔ Adhesion

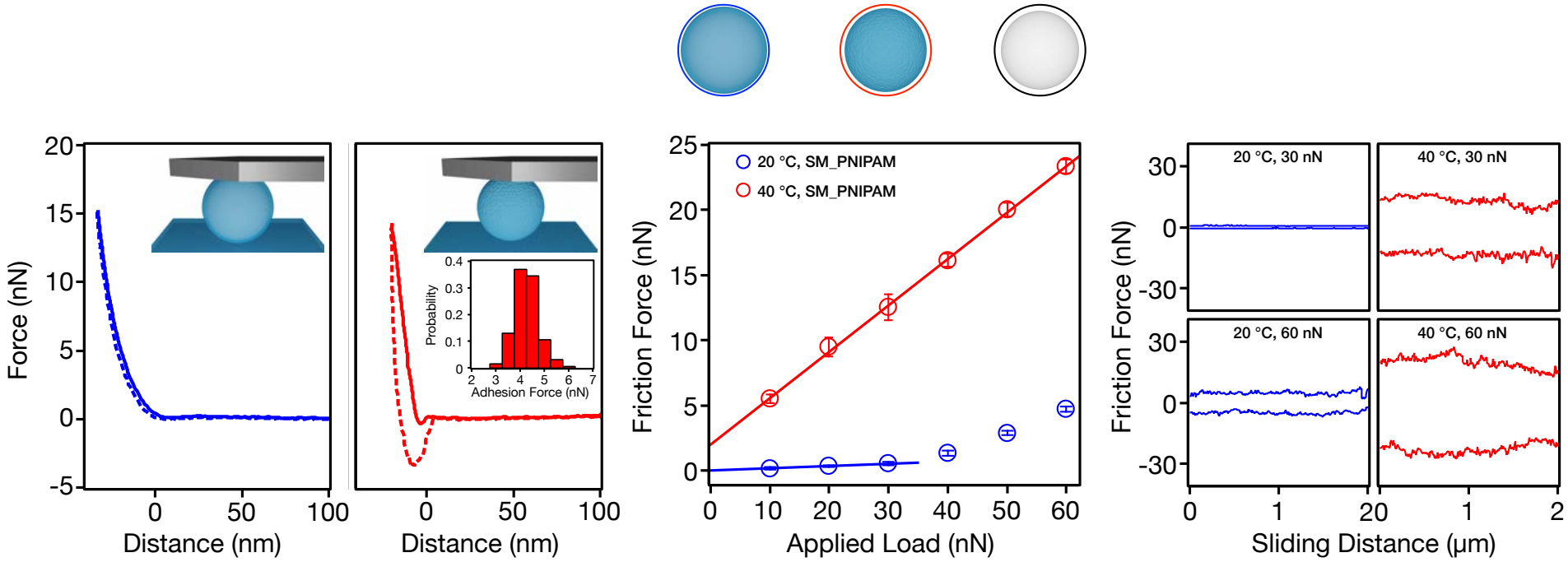

F_{ad} = 4.2 ± 0.9 nN

C. P. Hsu *et al.*, *arXiv:2004.05970*, (2020).

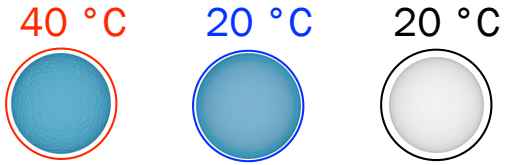

ϕ(T)

Friction ⬆ Adhesion ✔

⇕

Friction ⬇ Adhesion ✖

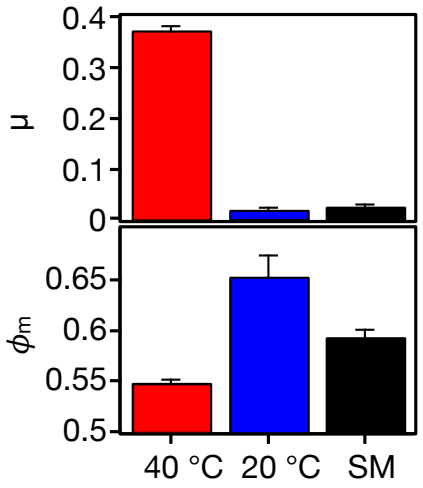

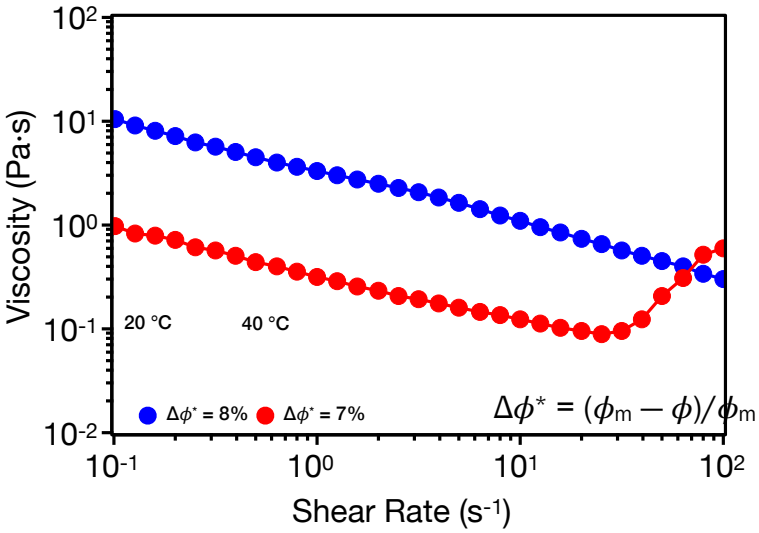

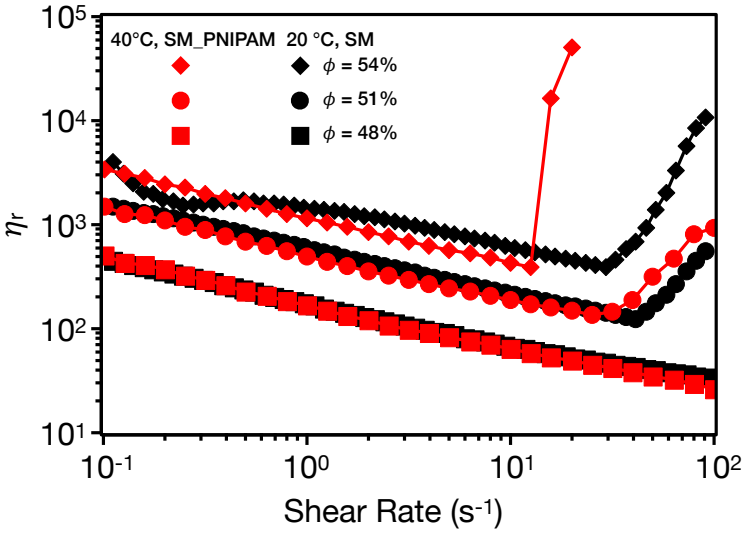

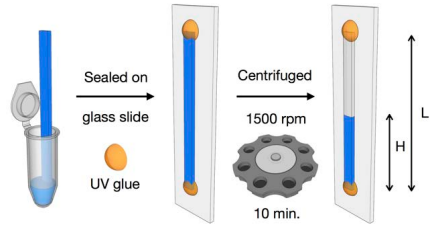

C. P. Hsu *et al.*,

- ☑ Objectives
- ☑ Shear thickening : roughness and adhesion
- ☐ Thixotropy : strength and adhesion
- ☐ Conclusions / outlook

Model system

Rhodamine B

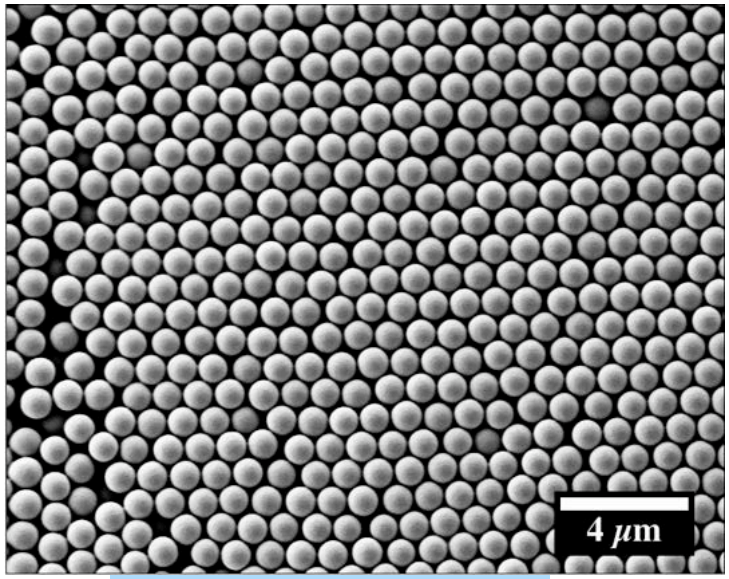

PMMA-g-PHSA (4)

$2a = 1.2\mu m$

Antl et al., *Colloids Surf.*, (1986) **17** , 67 -78
Palangetic, et al. (2016) *Faraday Discuss.* 191, 325

80% cyclobromohexane 20% cis-decalin

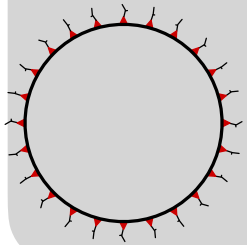

+ PS

$M_w = 925kDa$

$R_g = 41nm$

$\xi = 0.07$

Dissociation of Cyclobromohexane
creates HBR
Weak acid - induces charging

C. P. Royall, M. E. Leunissen, A. van Blaaderen *J. Phys.: Condens. Matter* **15** 3581 (2003)

Supplier	Treatment	σ [nS/cm]	Appearance
Sigma Aldrich	as received	0.9	colorless
Sigma Aldrich	stored 2 years	2.1	colorless
Alfa Aesar	as received	6.4	colorless
Acros Organics	as received	3.1	yellowish
Acros Organics	alumina cleaned	0.05	colorless
Acros Organics	cleaned, saturated HBr	146.3	colorless
Acros Organics	cleaned, saturated HBr, 50x diluted	12.2	colorless

Control initial charge + Screen charges
tetrabutylammonium chloride or bromide
TBAC or TBAB

Interaction potential

Asakura-Oosawa + $$\Phi_{\mathrm{Y}}(r) = \frac{Z^2}{1+\kappa a}\frac{\lambda_{\mathrm{B}}}{2a}\frac{\exp(-\kappa 2a[r/2a-1])}{r/2a}$$

Debye length from conductivity, Z estimated from zeta potential

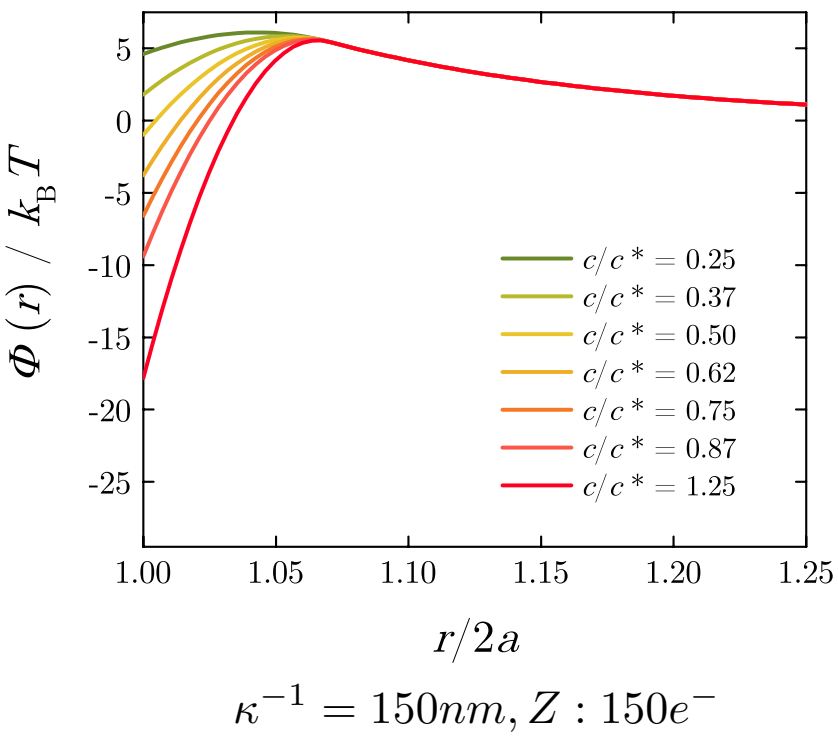

$\kappa^{-1} = 150nm, Z : 150e^-$

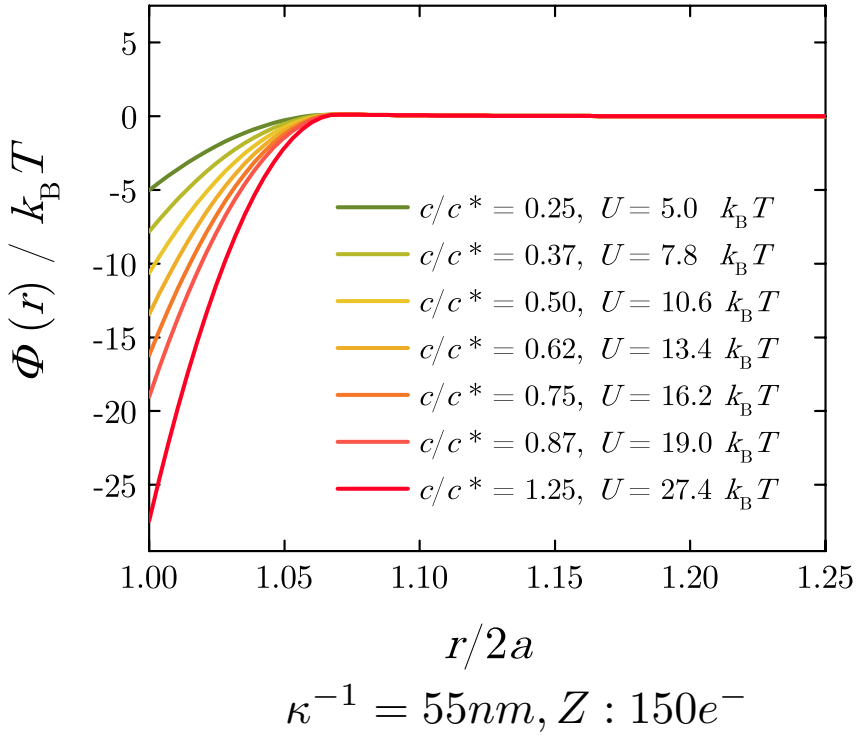

$\kappa^{-1} = 55nm, Z : 150e^-$

U

Lekkerkerker, H. N., & Tuinier, R. (2011). *Colloids and the depletion interaction* (Vol. 833). Springer.

near field - steric repulsion / weak screening hydrodynamics

Schroyen, B., Hsu, C. P., Isa, L., Van Puyvelde, P., & Vermant, J. (2019). Stress Contributions in Colloidal Suspensions: The Smooth, the Rough, and the Hairy. *Physical Review Letters*, *122*(21), 218001.

Slow, DC quenches

FOV:
100x100 µm

Φ = 0.2 (always)

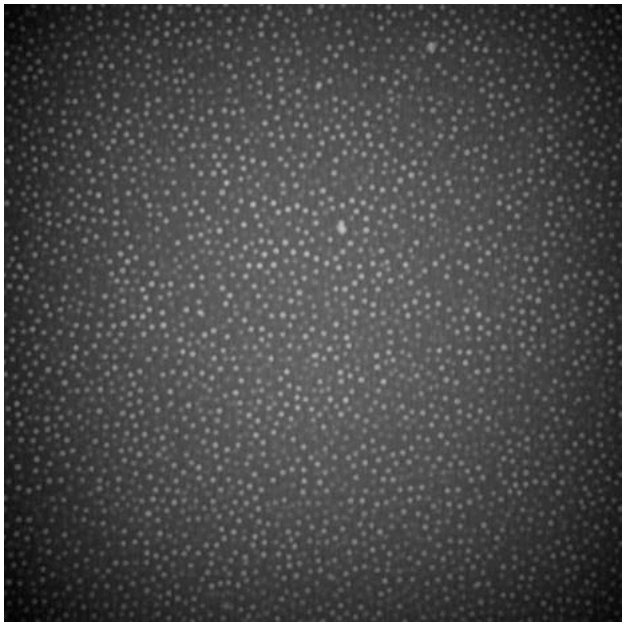

c/c* = 0.2
90 min timelapse

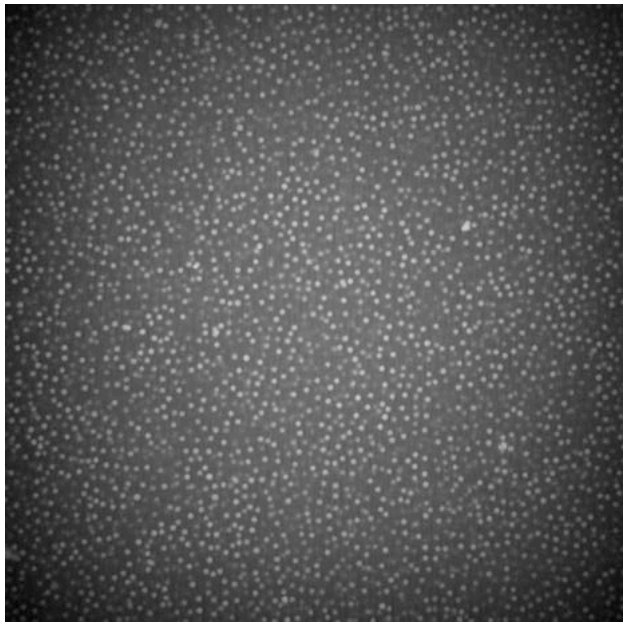

c/c* = 0.4
35 min timelapse

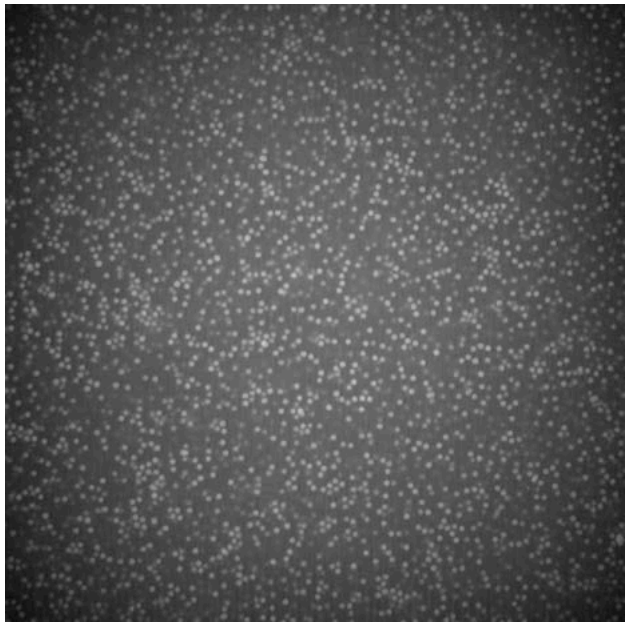

c/c* = 0.6
30 min timelapse

Charge-stabilized
colloid-polymer mixture

Diffusion of an organic salt
TBAC

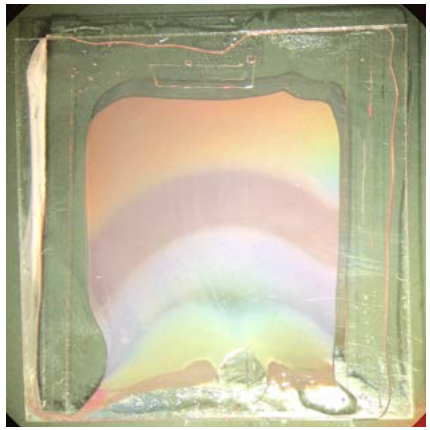

FOV: 100x100 µm

ETH zürich Structural illumination multiarray rheo-confocal

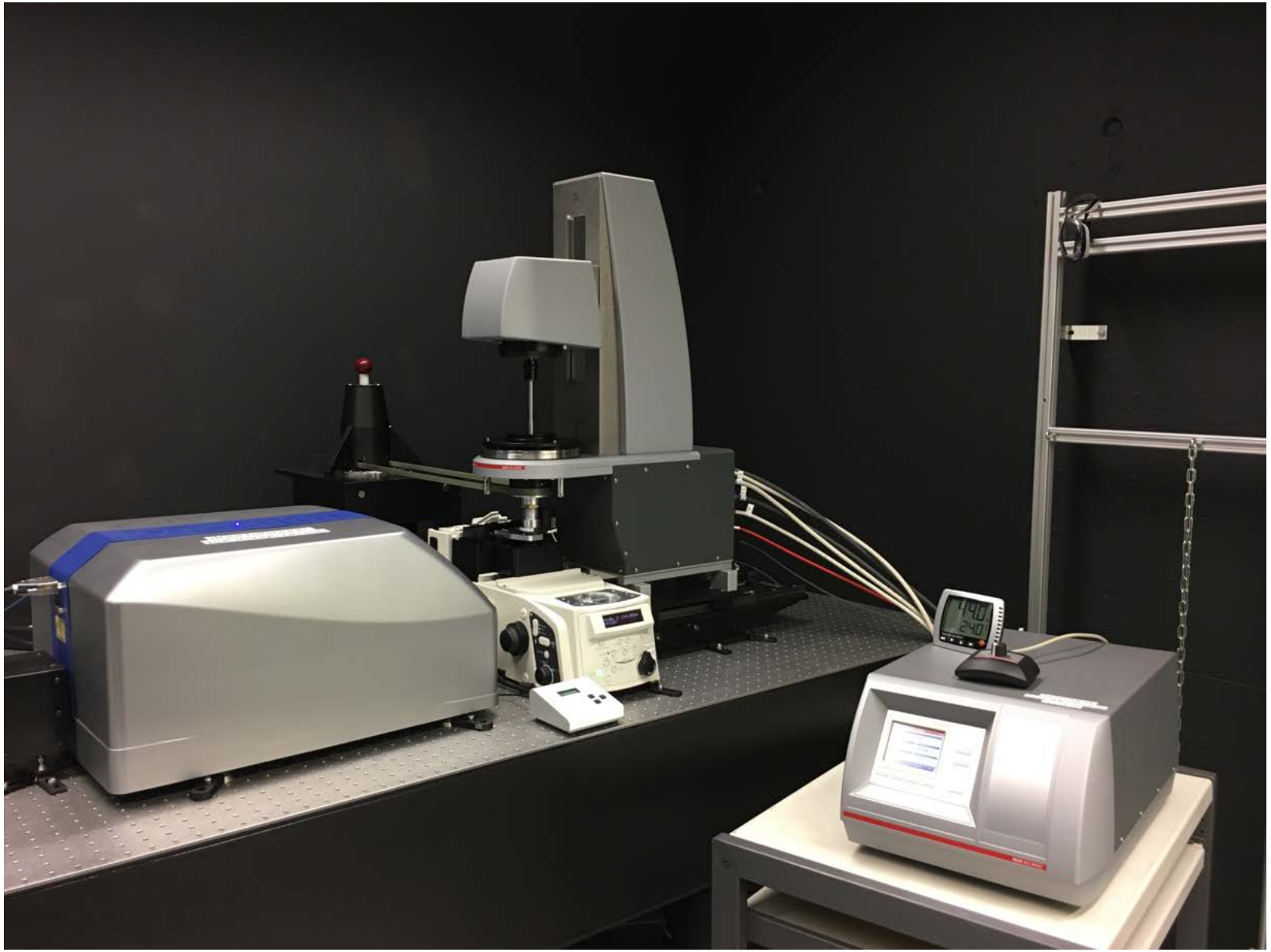

Steady state structures

$c/c^* = 0.7$

FOV: 150x150 µm

Pe = 40
real-time

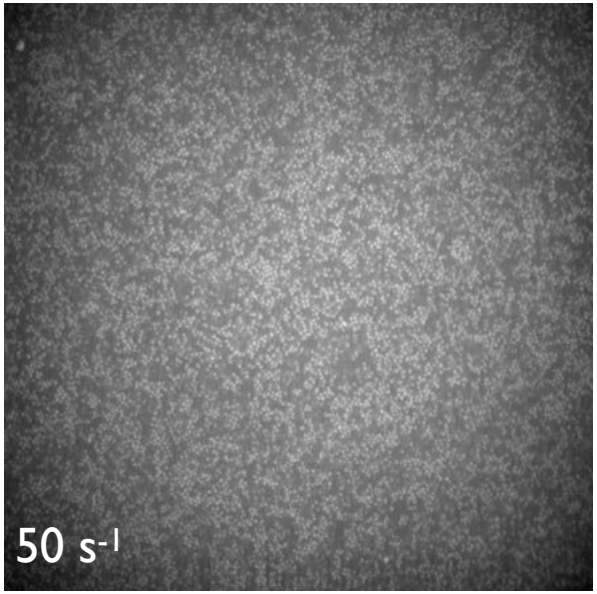

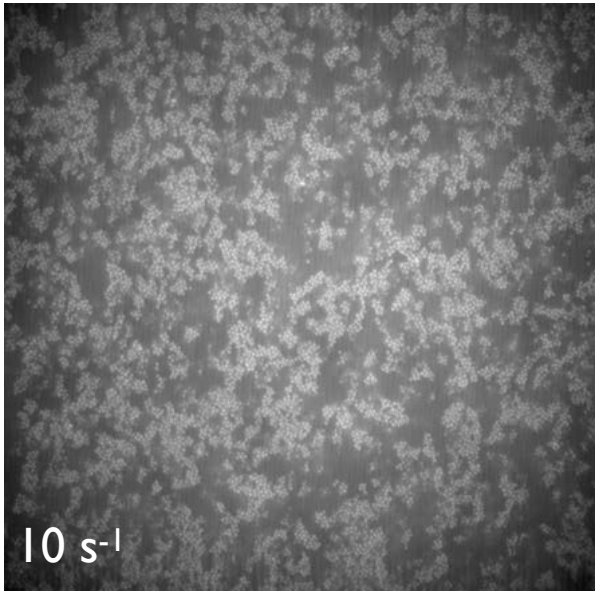

real-time

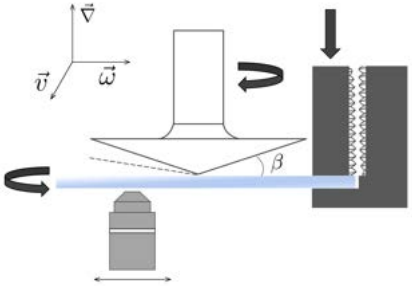

real-time

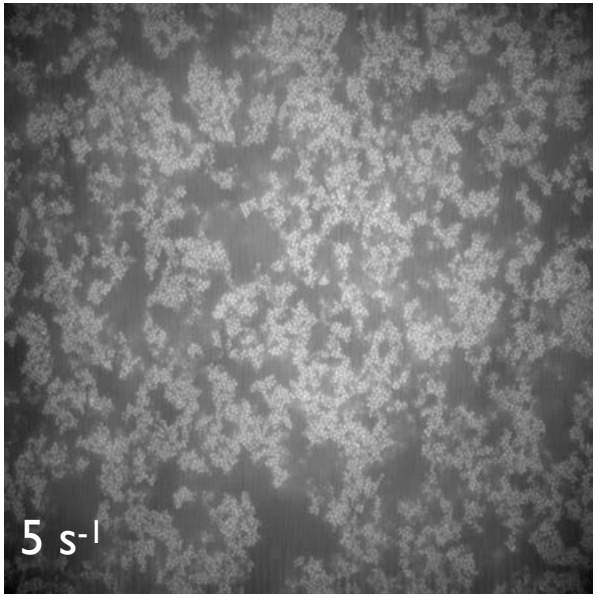

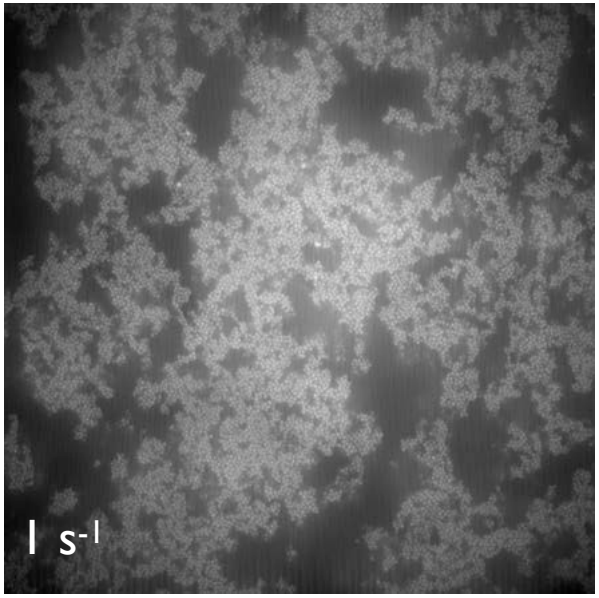

sped up 2x

Mason number scaling

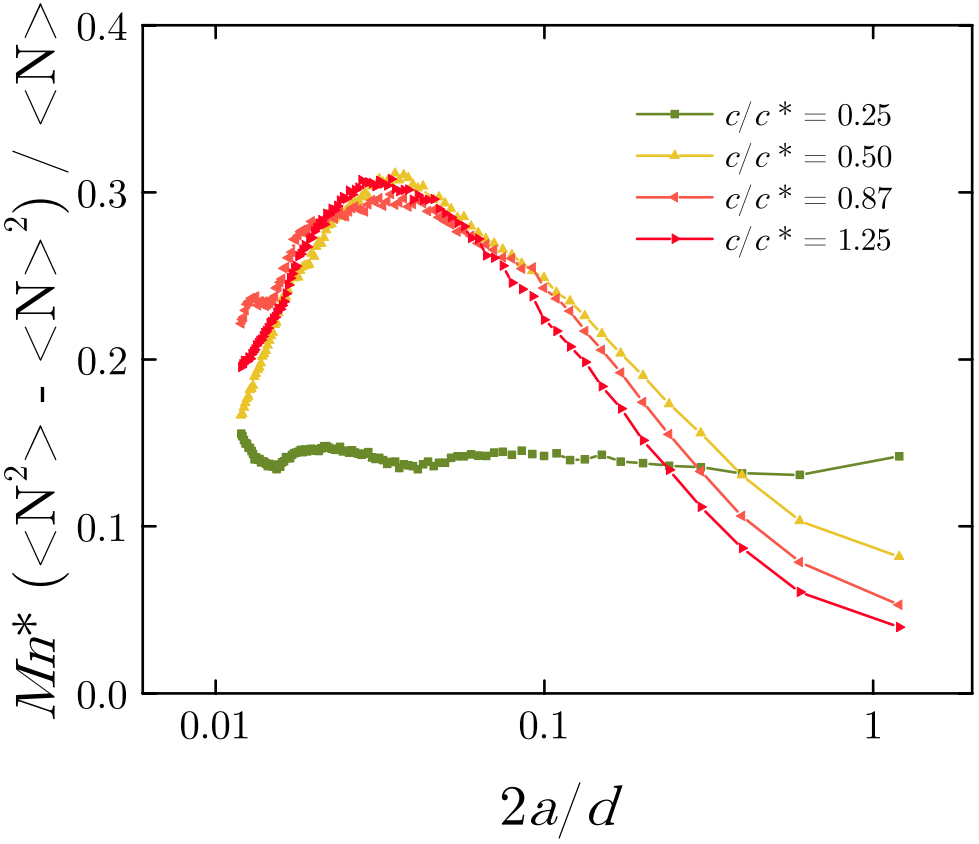

$$Mn^* = MnU/(f^*\xi)$$

Z Varga, JW Swan Large scale anisotropies in sheared colloidal gels
Journal of Rheology 62 (2), 405-418

Scaling with Mn also for 2DSANS - Min Kim, J., et al.. Journal of Rheology, 58(5), 1301-1328. (2014)

Rheological stress deconvolution methods

Stress jump experiments

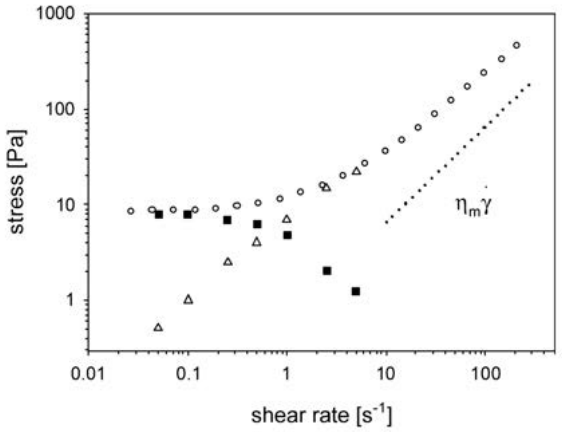

Fig. 3. Elastic (■) and viscous (△) contributions to the total steady stress (○) as a function of the shear rate (2.9 vol% fumed silica dispersion); the dotted line represents the medium contribution ($\eta_m\dot{\gamma}$).

K. Dullaert, J. Mewis, *J. Colloid Interface Sci.* **287** 542 (2005)

Orthogonal superposition rheometry

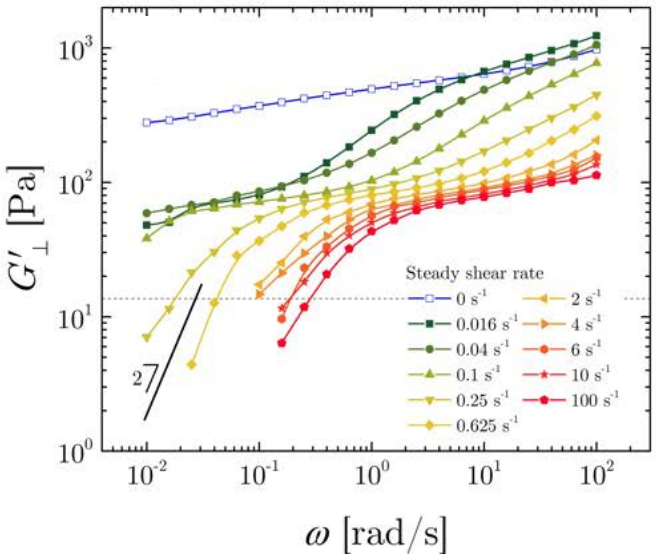

G. Colombo et al. *J. Rheol.* **61** 1035 (2017)

HF rheology non-ideal systems

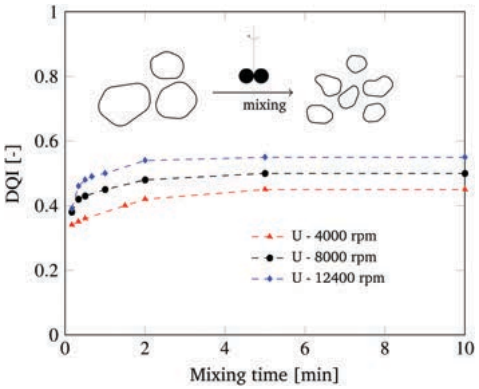

Schroyen, Swan, Van Puyvelde, Vermant (**2017**), *Soft Matter* 13, 7897

Flow reversals experiments

10 vol % PMMA in Newtonian (PDMS) matrix

$\dot{\gamma}$ = 0.025 s^{-1}

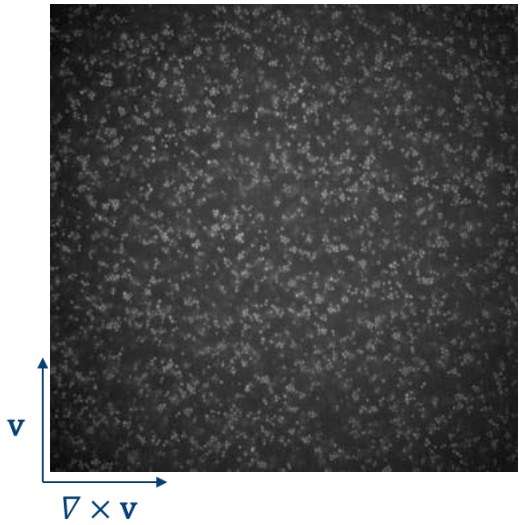

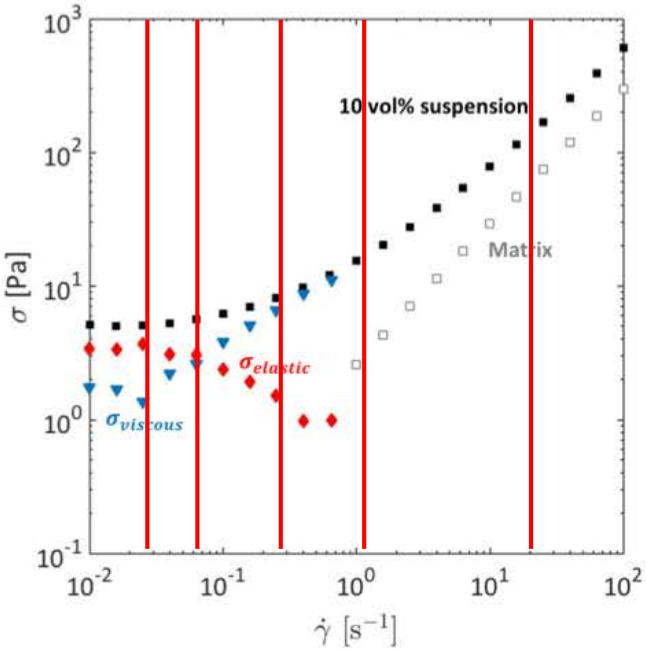

$\dot{\gamma}$ = 20s^{-1}

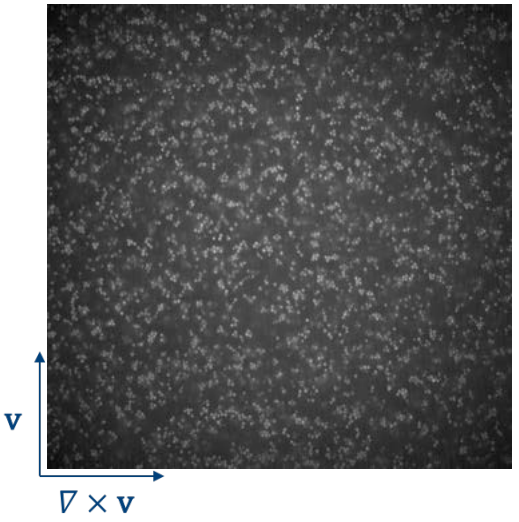

$\dot{\gamma}$ = 0.063 s^{-1}

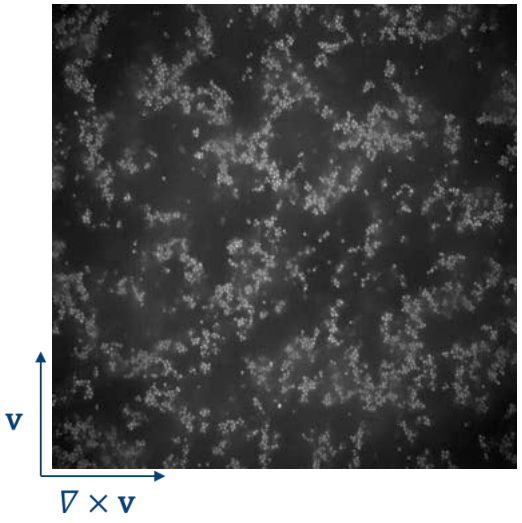

$\dot{\gamma}$ = 0.25 s^{-1}

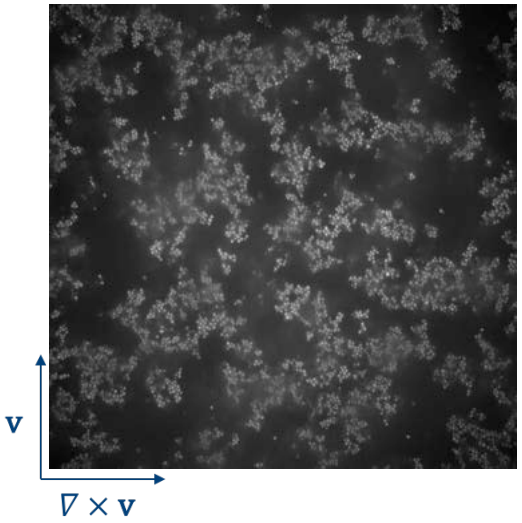

$\dot{\gamma}$ = 1s^{-1}

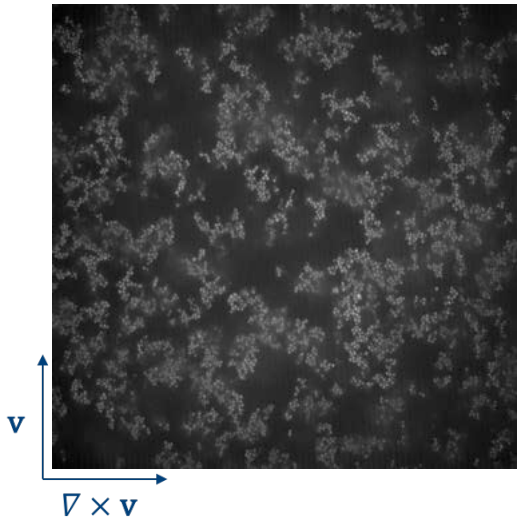

10 vol % PMMA in VE (PDMS) matrix

$\dot{\gamma}$ = 0.025 s^{-1}

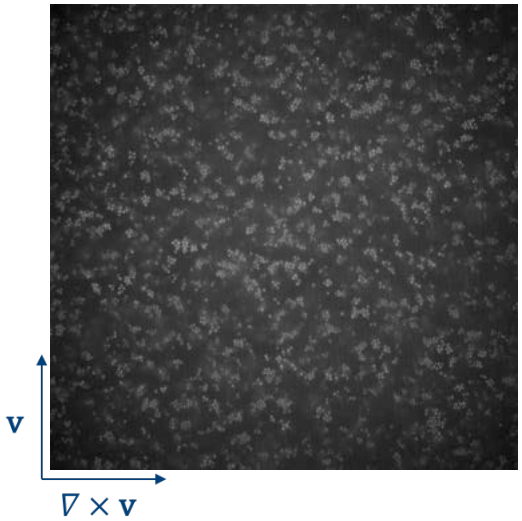

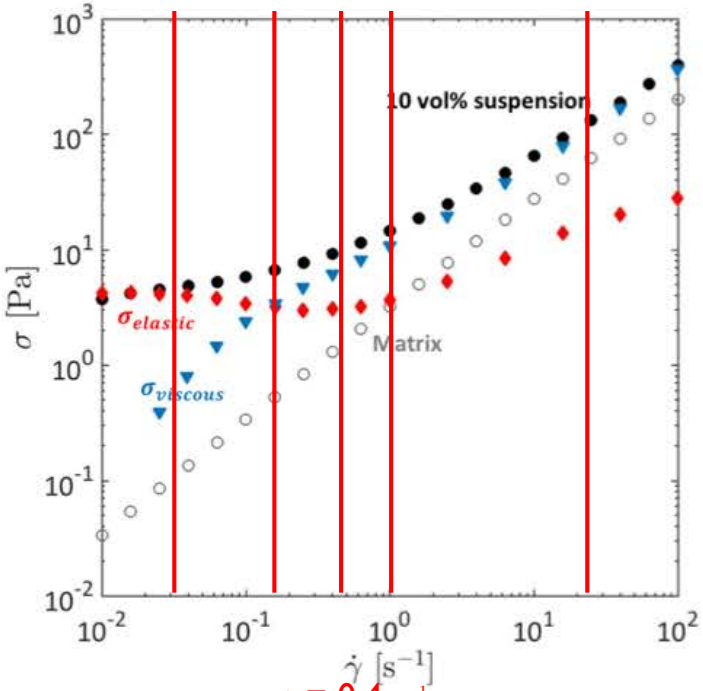

$\dot{\gamma}$ = 20 s^{-1}

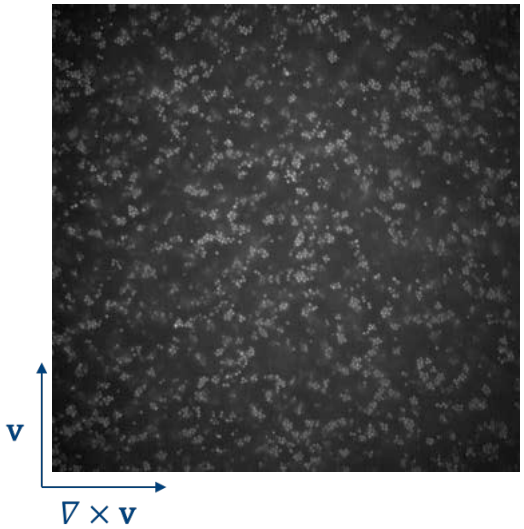

$\dot{\gamma}$ = 0.16 s^{-1}

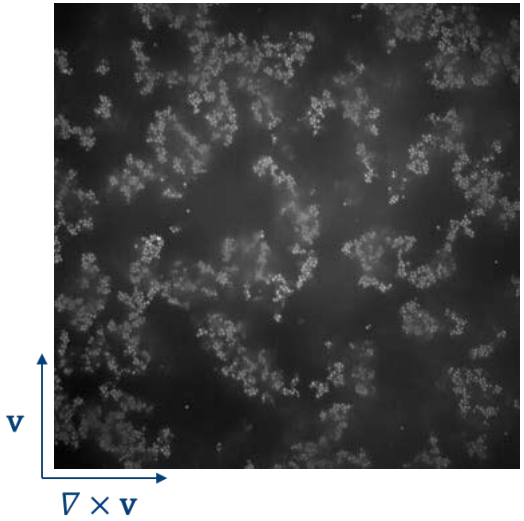

$\dot{\gamma}$ = 0.4 s^{-1}

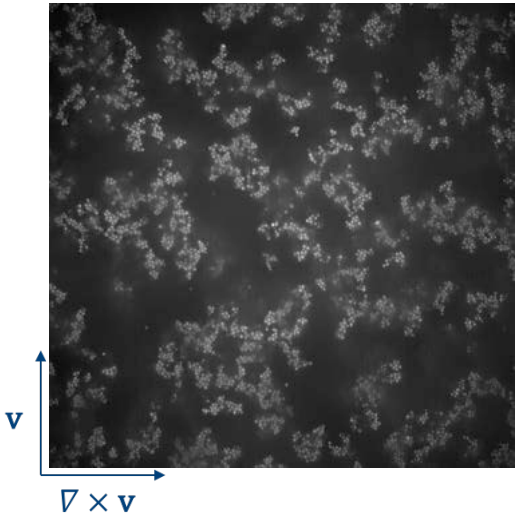

$\dot{\gamma}$ = 1 s^{-1}

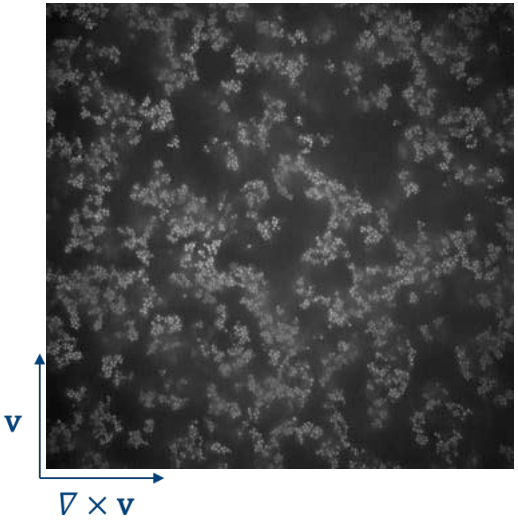

Suspension in linear matrix

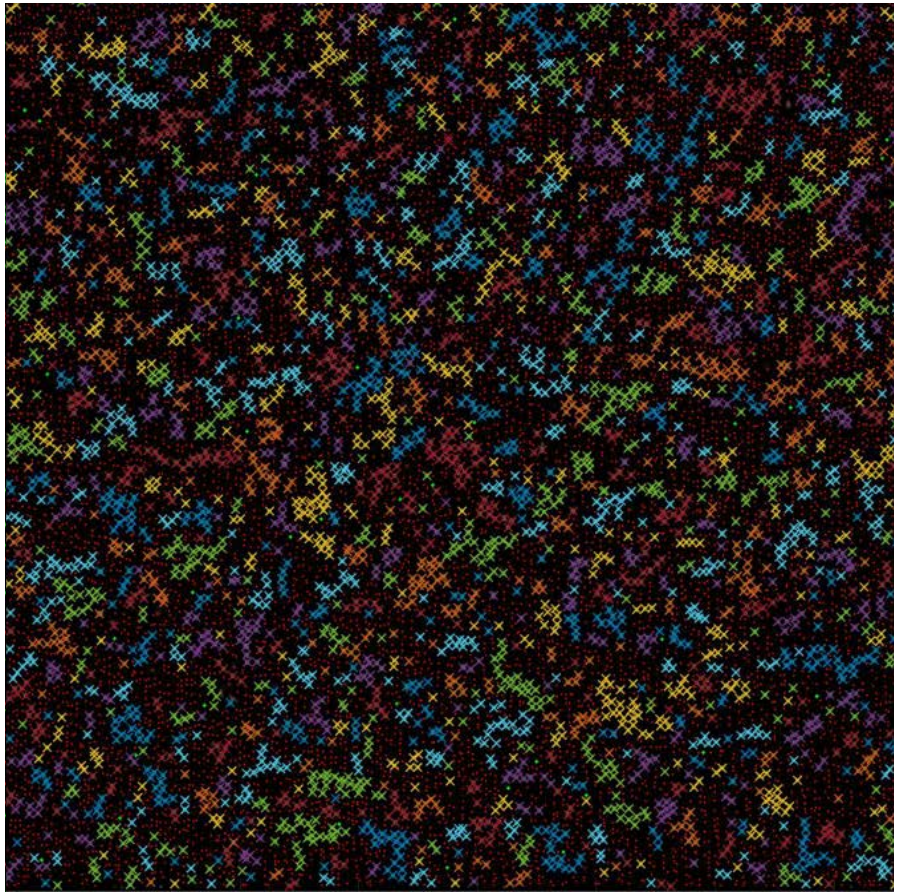

ϕ_{eff}= 0.3

$\dot{\gamma}$ =20 s^{-1}
154x154µm

Suspension in branched matrix

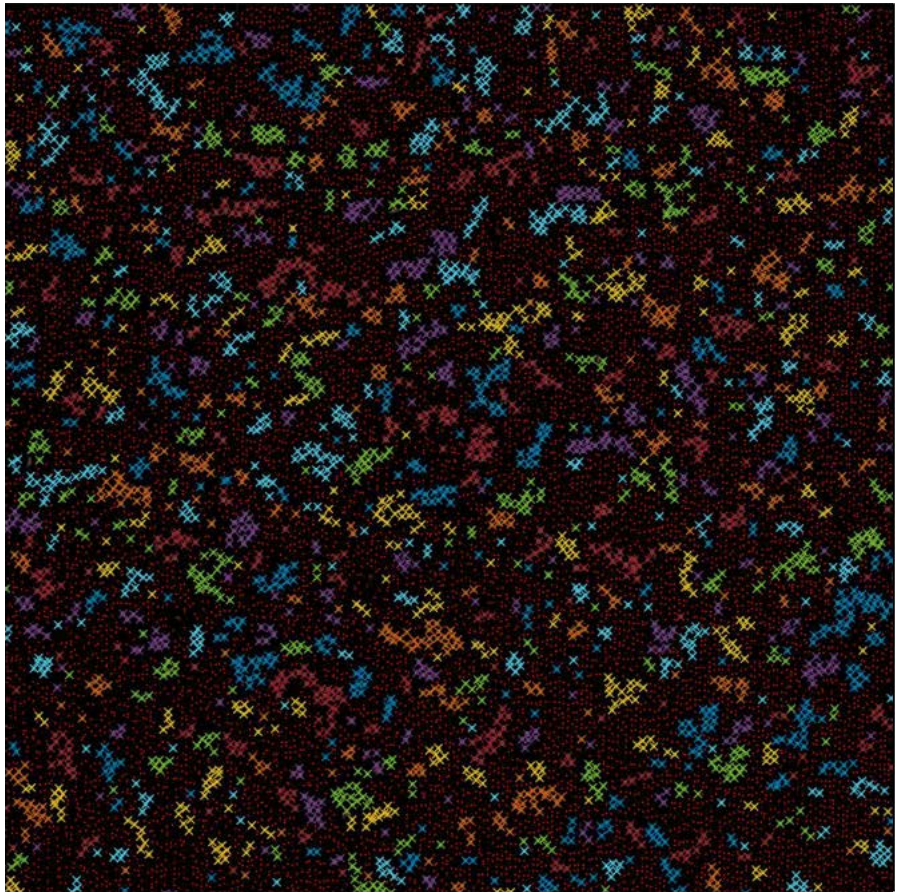

ϕ_{eff}= 0.25

$\dot{\gamma}$ = 20 s^{-1}
154x154µm

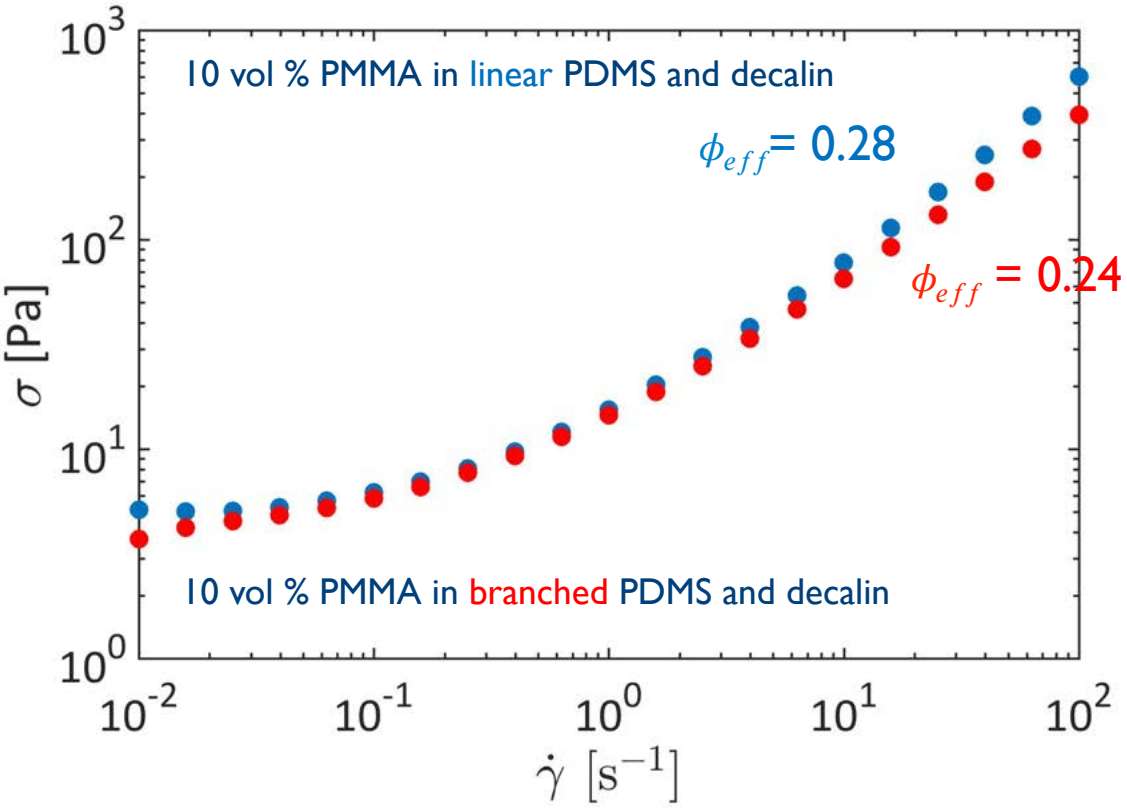

$$\eta_r = \left(1 - \frac{\phi}{\phi_{max}}\right)^{-[\eta]\rho\phi_{max}}$$

I. M. Krieger and T. J. Dougherty, *Trans Soc Rheol.* 3 (1959), 137

- ☑ Objectives
- ☑ Shear thickening : roughness and adhesion
- ☑ Thixotropy : strength and adhesion
- ☐ Conclusions / outlook

Toolbox for colloidal gel understanding and design:

- ☑ model systems which enable us to interrogate mechanisms
- ☑ rheological techniques which deconvolute the contributions to the stress
- ☑ structural techniques which probe pertinent time and length scales

Challenges:

- ☐ non-model systems and yet interrogate mechanisms
- ☐ complex flows
- ☐ HF during flow/processing

Feedback requested :

- rheological profiles/problems (IFPRI members)
- selected industrial systems

Instrument : Rheo-confocal setup, Obj = 60 x
Particles on the coverslip: PMMA of 75-90 µn in diameter (Cospheric)
Sample: 10 vol% PMMA in CHB, cis- decalin and PS

100% upper motor, $\dot{\gamma} = 10\ s^{-1}$

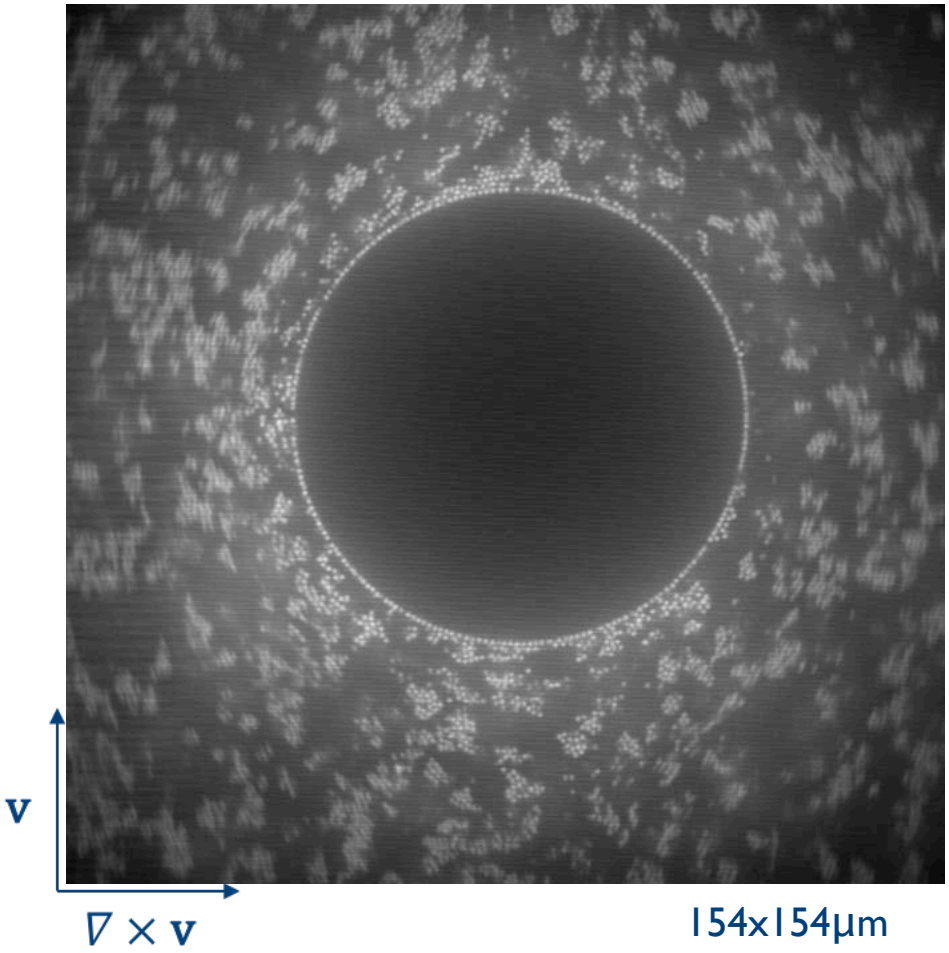

- ✓ Compressional flow before single bead
- ✓ Rotational flow around the sphere
- ✓ Extensional flow after the bead

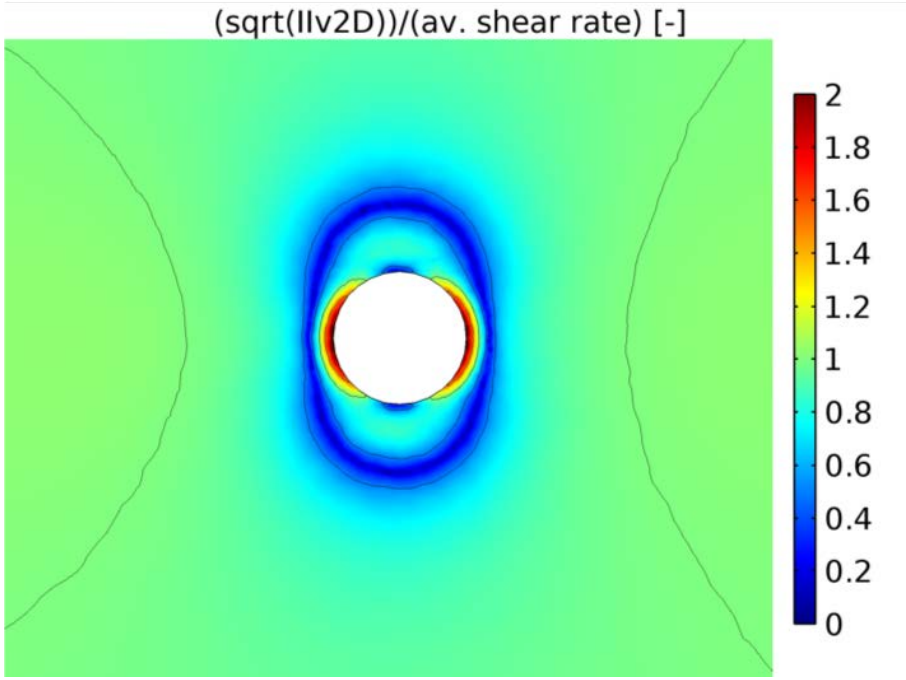

Technische Universität Braunschweig

iPAT
Institut für Partikeltechnik




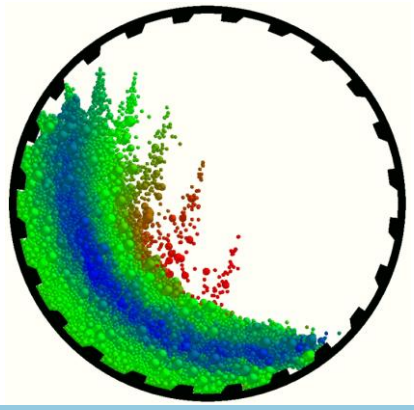


IFPRI

A Systems Engineering Approach to Dry-Milling with Grinding Aid Additives

Anderson Chagas, Sandra Breitung-Faes, Arno Kwade

Team at Institute for Particle Technology (iPAT)

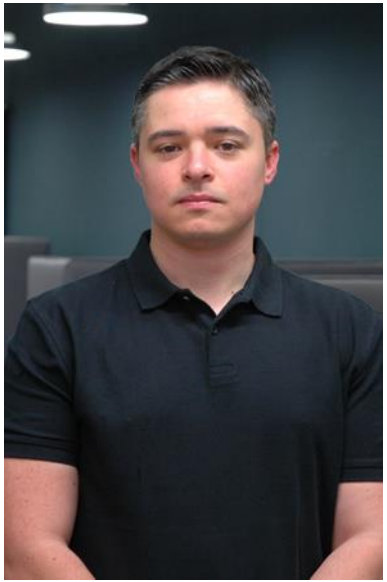

M.Sc. Anderson Chagas

Dr. -Ing. Sandra Breitung-Faes

Prof. Dr. -Ing. Arno Kwade

Project introduction

Objectives:

I. Develop a system engineering approach for optimizing and scaling industrial dry fine grinding processes.

II. Obtain numerical relations about the effect of grinding aids additives and humidity on material behaviour, process aspects and energy flows.

First phase (first 3-year-period):

I. Focus on the grinding aid and humidity impacts on the grinding aspects inside the ball mill, and the transfer of batch grinding results to closed circuit processes.

II. Those information will be used to predict particle size distributions and energy consumptions.

Materials and methods

iPAT
Institut für Partikeltechnik

Materials

- Calcinated alumina (Almatis)
  [x_{50} = 83.8 µm]
- Calcium carbonate (Imerys)
  [x_{50} = 10.7 µm]

Grinding aid additives

- Glycol ➔ Diethylene glycol (DEG)
- Acid ➔ Heptanoic acid (HepAc)
- Alcohol ➔ 1-Hexanol (HexOH)

Test equipment

Grinding process modelling

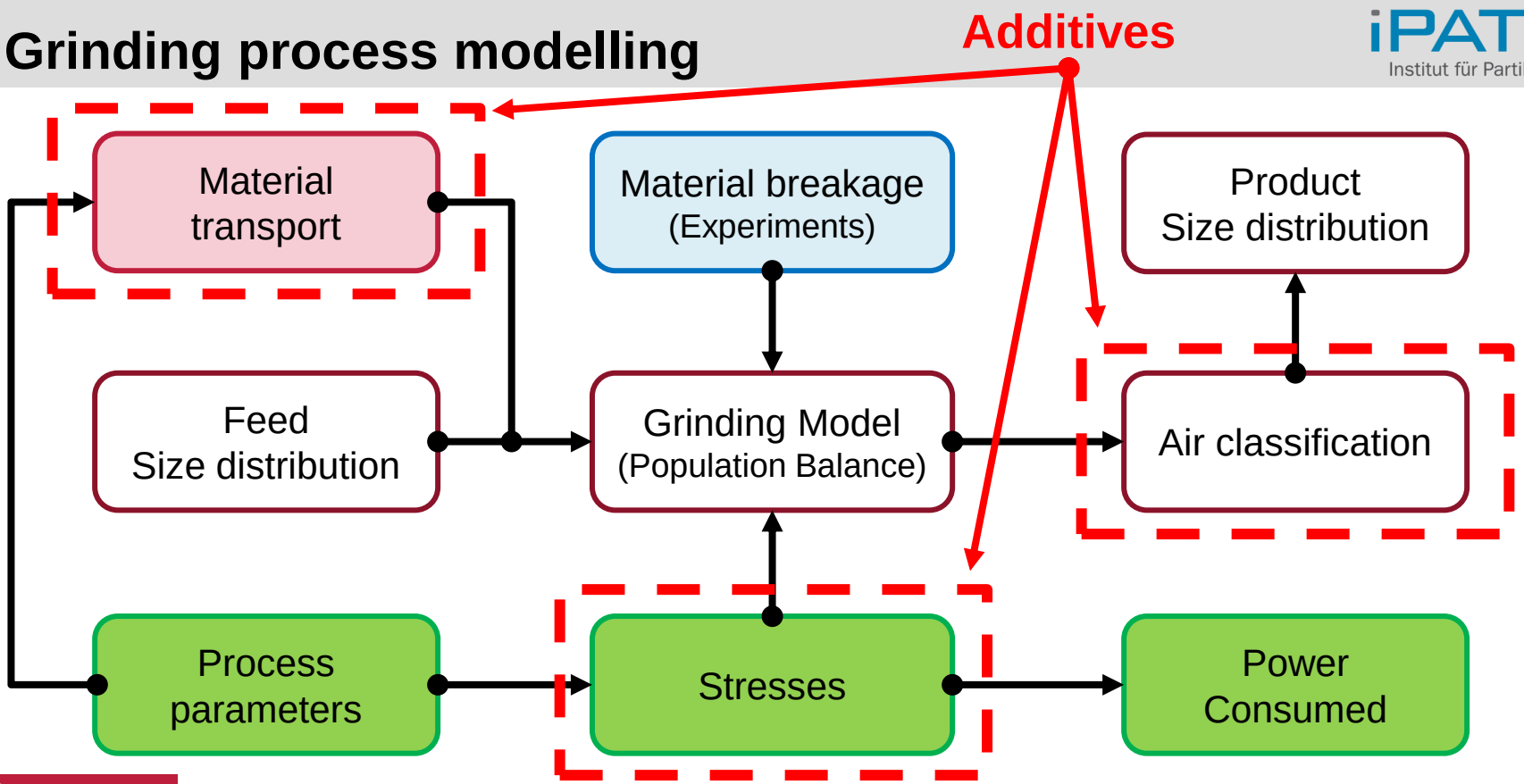

Effect of additive on stress transfer

- Additives will affect:
  - **Particle capturing between balls**
  - **Energy dissipation**
  - Material transport
  - Residence time (mill holdup)
  - Process efficiency

High flowabilty
(↓ captured mass)

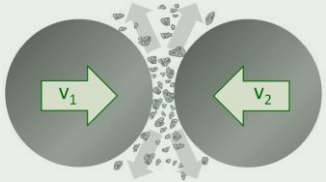

Low flowability
(↑ captured mass)

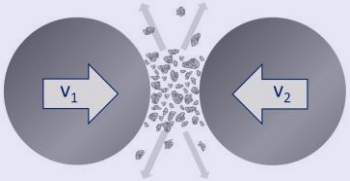

- Experiments:
  - Drop-weight-test – high stress rate
  - Slow compression – low stress rate
  - Hardgrove test – rolling grinding media over bed of particles

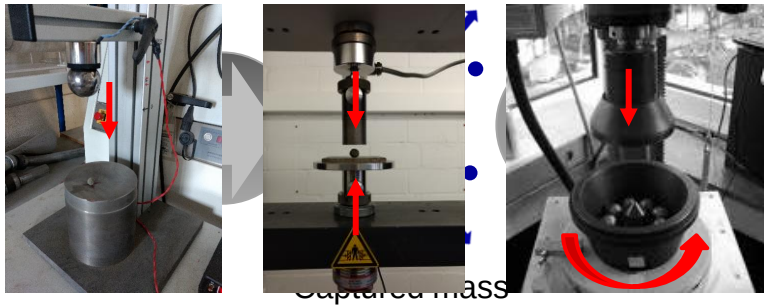

Effect of additive on material transport

- Additives will affect:
  - Particle capturing between balls
  - Energy dissipation
  - **Material transport**
  - **Residence time (mill holdup)**
  - **Process efficiency**

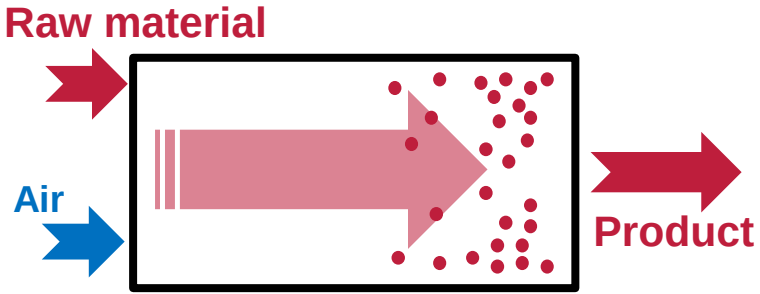

- Experiments:
  - Ring shear tester
  - Powder rheometer
  - Dynamic angle of repose

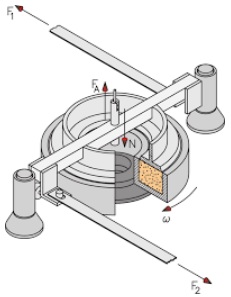

Preliminary Ring Shear tests

- Samples preparation:
  - Pre-mixing with additive
  - Grinded in batch mill for 240 min
- Preliminary observations:
  - Glycol presented small effect on flowabilty, although with good results for batch grinding
  - This result would indicate that Glycol would present similar grinding results as with no additive

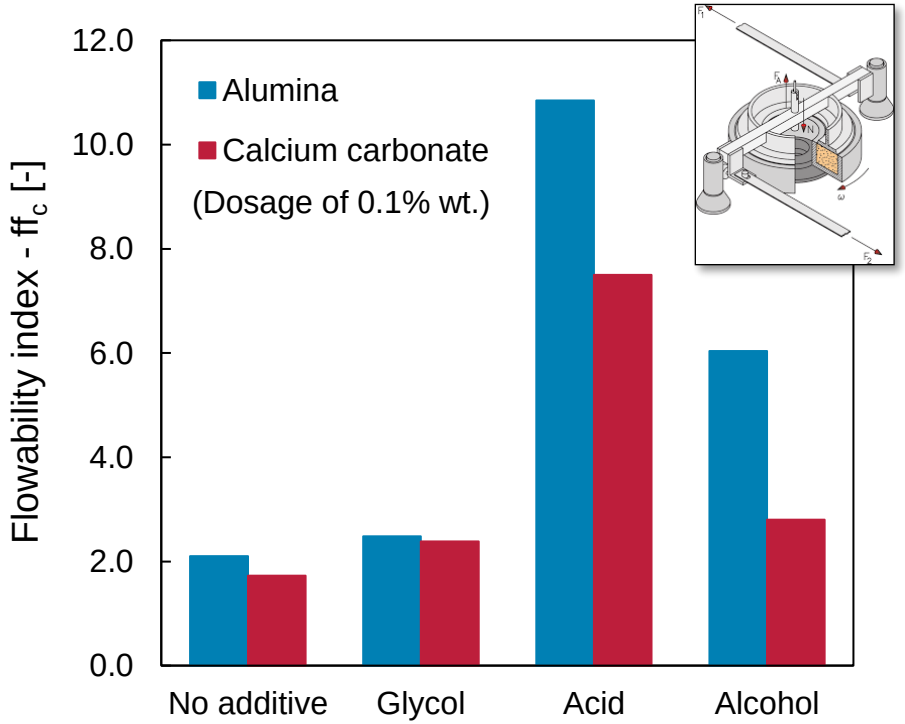

Preliminary batch grinding tests

- Transport can be ignored

- Process parameters:
  - Batch milling at 4l mill
  - Mill speed – 70% c.s.
  - Media filling – 30% of mill volume
  - Media: 10 mm alumina beads

- Preliminary observations:
  - Is it clear that the additives affect differently the grinding efficiency.
  - Highest flowability does not provide the best results.

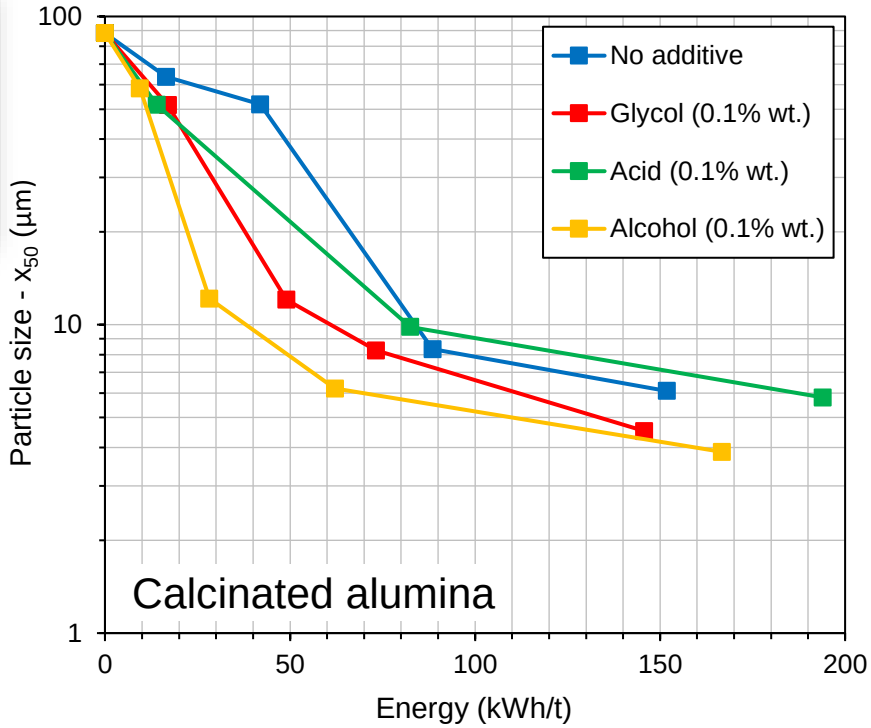

Preliminary batch grinding tests

- Transport can be ignored

- Process parameters:
  - Batch milling at 4l mill
  - Mill speed – 70% c.s.
  - Media filling – 30% of mill volume
  - Media: 10 mm alumina beads

- Preliminary observations:
  - In contrast to alumina, the additives presented similar effect among each other
  - Mechanisms such as breakage and transport must be understood independently

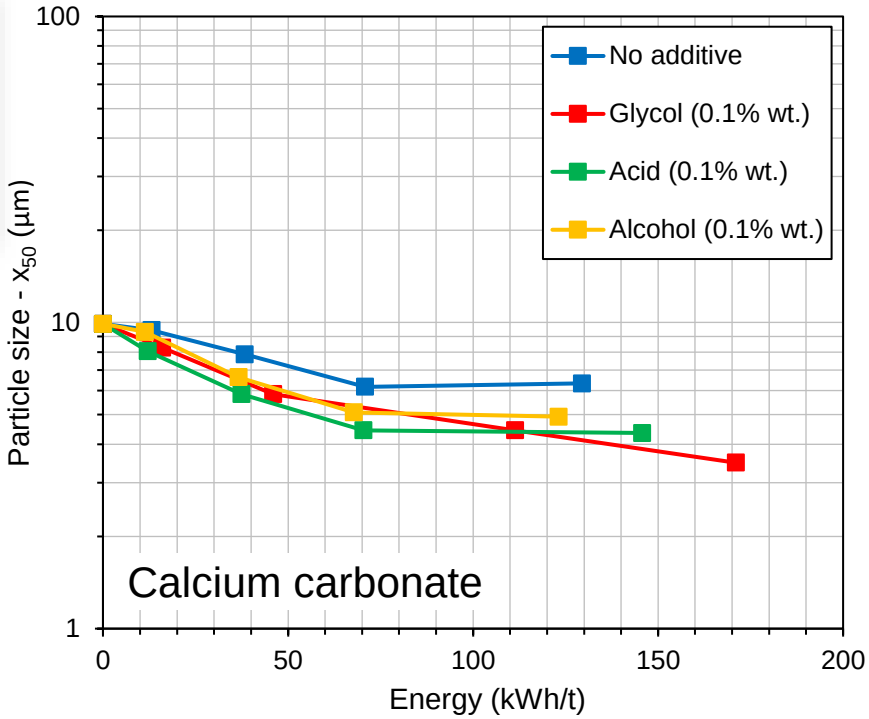

Open questions and future steps

Open questions

- An additional type of experiment should be included?
- How to model air classification considering the variety of classifiers design?
- How the temperature of the powder would impact the combined action of Grinding aids + humidity?

Outlook for the next 12 months

- Quantitative description of additives effects on dry grinding mechanisms
- Inclusion on modelling of batch grinding process

Outlook for the next 24 months

- Investigations on material transport and air classification
- Inclusion on modelling of closed-circuit grinding process

Acknowledgements

IFPRI
International Fine Particle Research Institute

For financing the project

Advisory board:

- Jarrod Hart (Imerys)
- Charles Compson (Almatis)
- Bas van Laarhoven (DFE Pharma)
- Eric Gulliver (Lincoln Electric)
- Marion Schnabel (Almatis)

For technical and scientific support

A MULTISCALE STUDY OF POWDER RECONSTITUTION

Claire GAIANI & Jeremy PETIT

Tristan FOURNAISE

Pr. Claire GAIANI - Université de Lorraine
LIBio – Laboratoire d'Ingénierie des Biomolécules
2 avenue de la Forêt de Haye - BP 20163
54505 Vandœuvre-lès-Nancy - FRANCE
Tél. : +33(0)3 72 74 41 11 - Fax : +33(0)3 83 59 57 72
claire.gaiani@univ-lorraine.fr
http://libio.univ-lorraine.fr/

1 Planning of PhD work and achieved deliverables

1. Screening of a large variety of powders

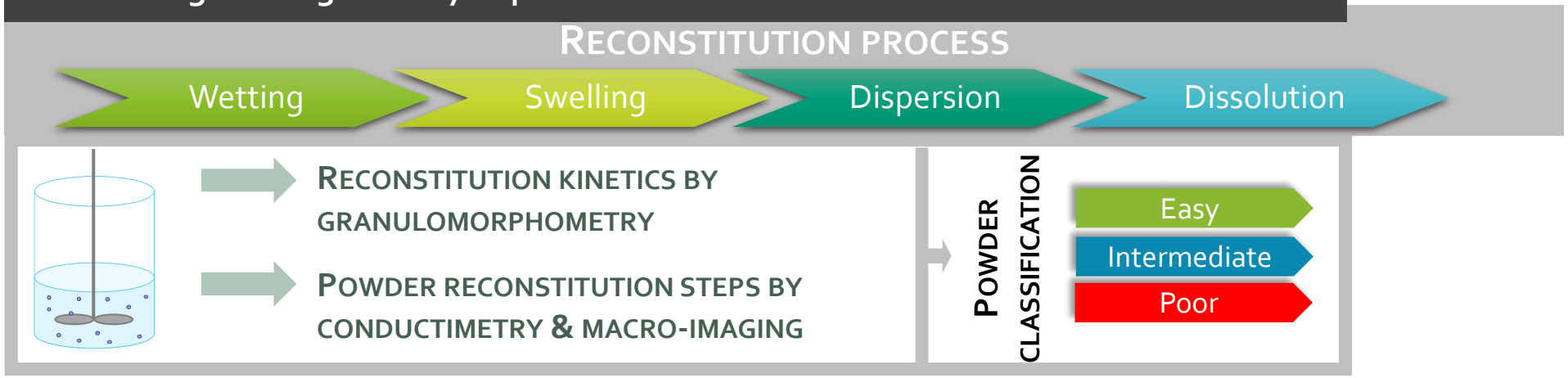

Year 1 (January 2019 – January 2020)

(1) Powder classification according to their reconstitution behavior
(2) For selected powders: reconstitution kinetics in different conditions of temperature, stirring…
(3) Statistical correlations between the numerous powder characteristics and their reconstitutability

1. Screening of a large variety of powders

RECONSTITUTION PROCESS

Wetting → Swelling → Dispersion → Dissolution

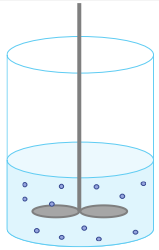

- RECONSTITUTION KINETICS BY GRANULOMORPHOMETRY
- POWDER RECONSTITUTION STEPS BY CONDUCTIMETRY & MACRO-IMAGING

POWDER CLASSIFICATION

- Easy
- Intermediate
- Poor

2. Surface composition (micro & molecular scale)

Selection of representative powders from each class of reconstituability

SUGAR COATING

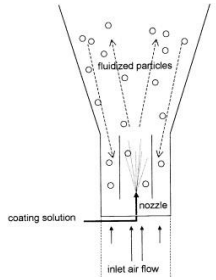

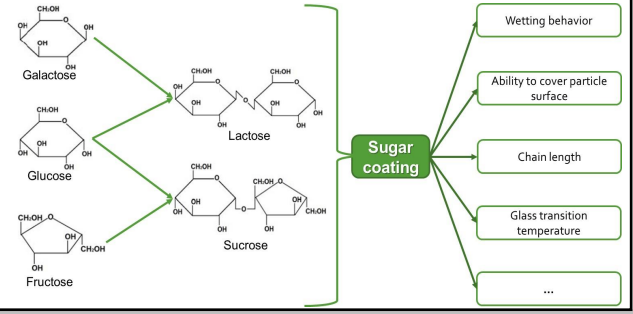

SURFACE MAPPING

Atomic force microscopy (AFM) : topography, chemical forces, nanoindentation

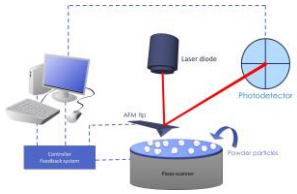

SURFACE COMPOSITION

X-ray photoelectron spectroscopy (XPS) : surface elemental composition

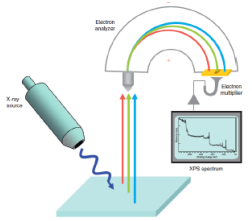

Year 2
(January 2020 – January 2021)
ongoing

LIBio Laboratoire d'Ingénierie des Biomolécules

1. Screening of a large variety of powders

RECONSTITUTION PROCESS

Wetting → Swelling → Dispersion → Dissolution

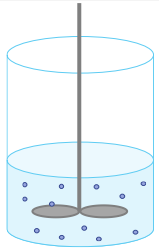

- RECONSTITUTION KINETICS BY GRANULOMORPHOMETRY
- POWDER RECONSTITUTION STEPS BY CONDUCTIMETRY & MACRO-IMAGING

POWDER CLASSIFICATION

- Easy
- Intermediate
- Poor

2. Surface composition (micro- & molecular scale)

Selection of representative powders from each class of reconstituability

SUGAR COATING

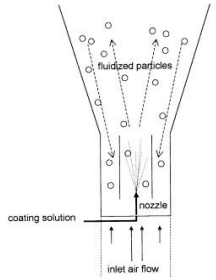

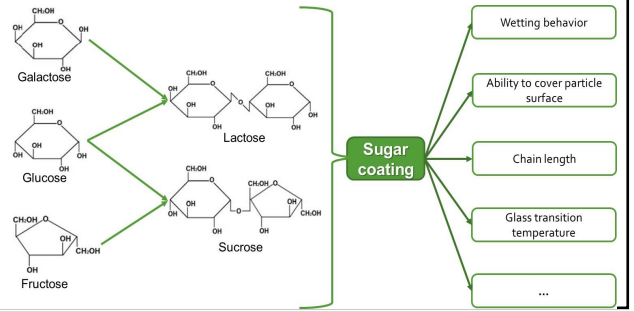

SURFACE MAPPING

Atomic force microscopy (AFM) : topography, chemical forces, nanoindentation

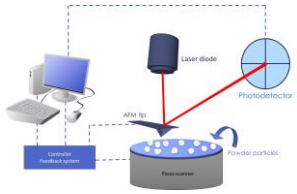

SURFACE COMPOSITION

X-ray photoelectron spectroscopy (XPS) : surface elemental composition

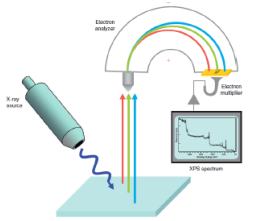

MOLECULES PARTICLES POWDES

Nano- Micro- Macro-

MULTISCALE STUDY

Semi-empirical models

Experimental data from 1. & 2.

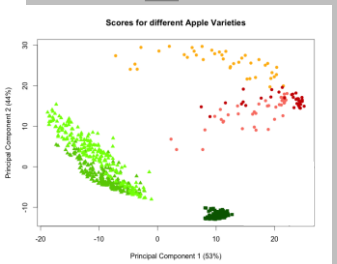

3. Development of a reconstituability index, in order to predict reconstitution times

Year 3 (January 2021 – January 2022)

HD WORK AND ERABLES

2

Powder classification according to their reconstitutability (year #1: 2019)

SCREENING OF A LARGE VARIETY OF POWDERS

About **50 food powders** were selected :
- Sugar: icing, fine, granular,
- Pea proteins: normal and micronized,
- Polenta: fine and large,
- Instant coffee: fine and large,
- Carboxymethylcellulose, flour,
- Fumed silica,
- Starch,
- Cocoa powders: medium and high fat content, alkalized or not

…

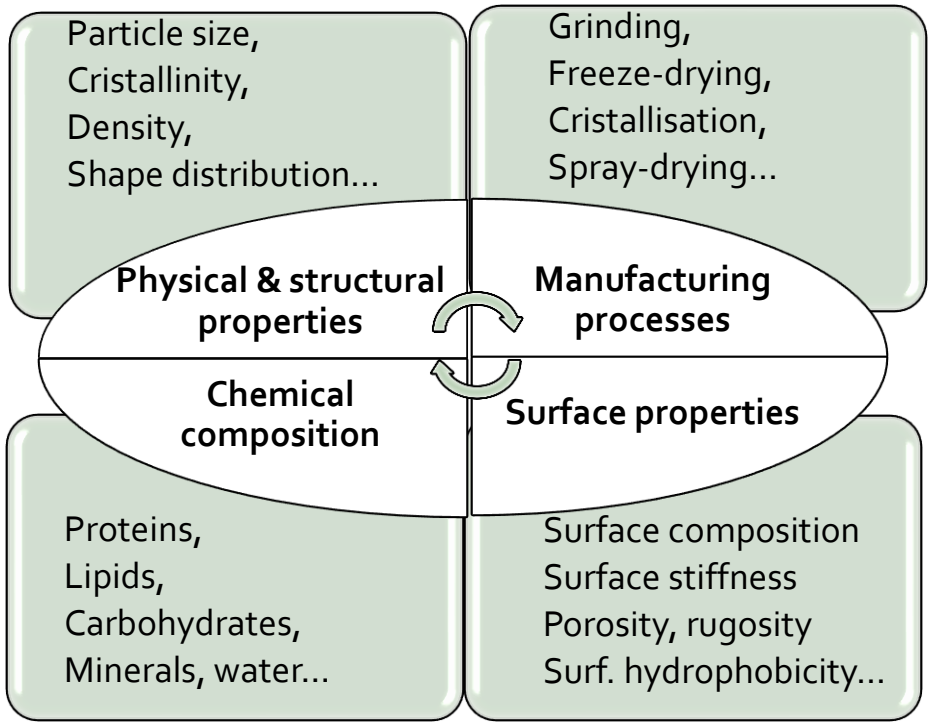

…

RECONSTITUTABILITY FOLLOWED BY CONDUCTIMETRY

1 - Powder reconstitution kinetics followed by conductimetry

- thermostated jacketed glass reactor
- mechanical stirring with a 5.08 cm diameter impeller
- powder added by a vibratory feeder

Powder reconstitution experiments were performed with distilled water at 25.0 ± 0.2 °C in the following conditions: 10.0 % (w/w) powder/water mass ratio with a total mass (powder + water) fixed at 2.650 kg, 800 rpm stirring rate and 3.6 $g.s^{-1}$ feeding rate.

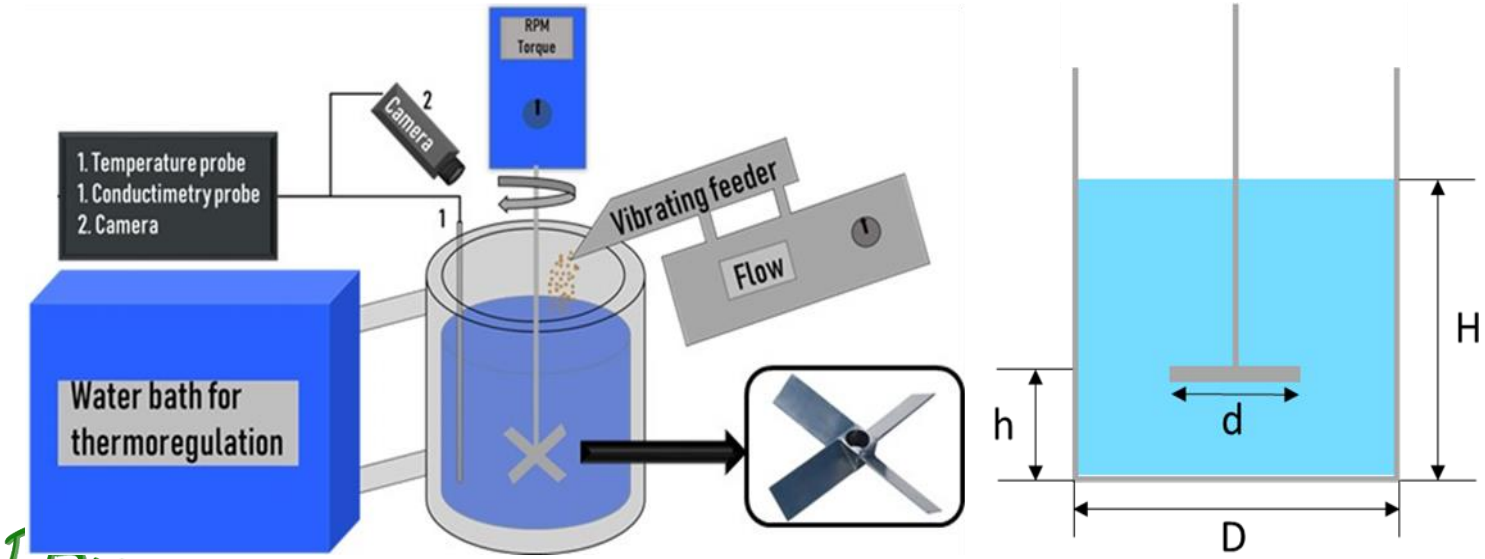

Reactor design and reconstitution conditions based on the literature

(Galet et al., 2004; Goalard et al., 2006; Mitchell et al., 2015, 2019; Schober & Fitzpatrick, 2005)

RECONSTITUTABILITY FOLLOWED BY CONDUCTIMETRY

2 - Conductivity normalization

- Conductivity evolved from an almost null initial value (real value inferior to the conductimeter sensitivity) to a final value that depended from powder nature.
- Averaged conductivity values were normalized according to:

$$c(t) = \frac{\kappa(t)-\kappa_{ini}}{\kappa_{fin}-\kappa_{ini}}$$

With: c(t) designates normalized conductivity (-);
$\kappa(t)$ stands for conductivity at time t ($\mu S.cm^{-1}$);
κ_{ini} represents the initial conductivity, i.e. distilled water conductivity, almost null ($\mu S.cm^{-1}$);
κ_{fin} corresponds to the final conductivity ($\mu S.cm^{-1}$).

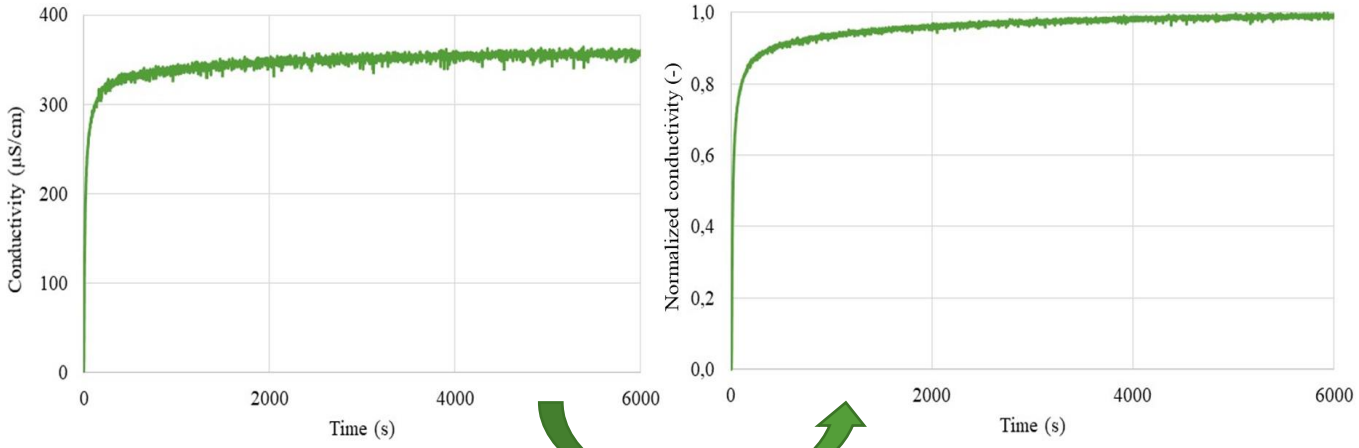

Before normalization (mean of three repetitions)

After normalization

RECONSTITUTABILITY FOLLOWED BY CONDUCTIMETRY

3 - Curve fitting

The normalized conductivity curves were fitted using the least squares method solved by the Levenberg Marquardt iteration algorithm with the Hill model :

$$c(t) = c_0 + (c_\infty - c_o)\frac{t^n}{k^n + t^n}$$

With: c_0, initial normalized conductivity (%);
c_∞, final normalized conductivity (%);
t, time (s);
k (s) and n (-), Hill model parameters.

Initial and final normalized conductivities being equal to 0 and 1, respectively, the Hill model could simply be rewritten as :

$$c(t) = \frac{t^n}{k^n + t^n}$$

k corresponds to the time needed to reach 50 % normalized conductivity. The slope of normalized conductivity curve at $t = k$ was found to be equal to $\frac{n}{4k}$, then it can be considered that the model parameter *n* gives an indication of the powder reconstitution rate once wetted/sinked, i.e. in the dispersion/solubilization steps of powder reconstitution. Last, powder reconstitution time was deduced from obtained Hill model by taking the time needed to reach 95 % normalized conductivity, it was then noted $t_{95\%}$.

RECONSTITUTABILITY FOLLOWED BY CONDUCTIMETRY

Instant coffee powder

Ground instant coffee powder

Impact of particle size on reconstitutability

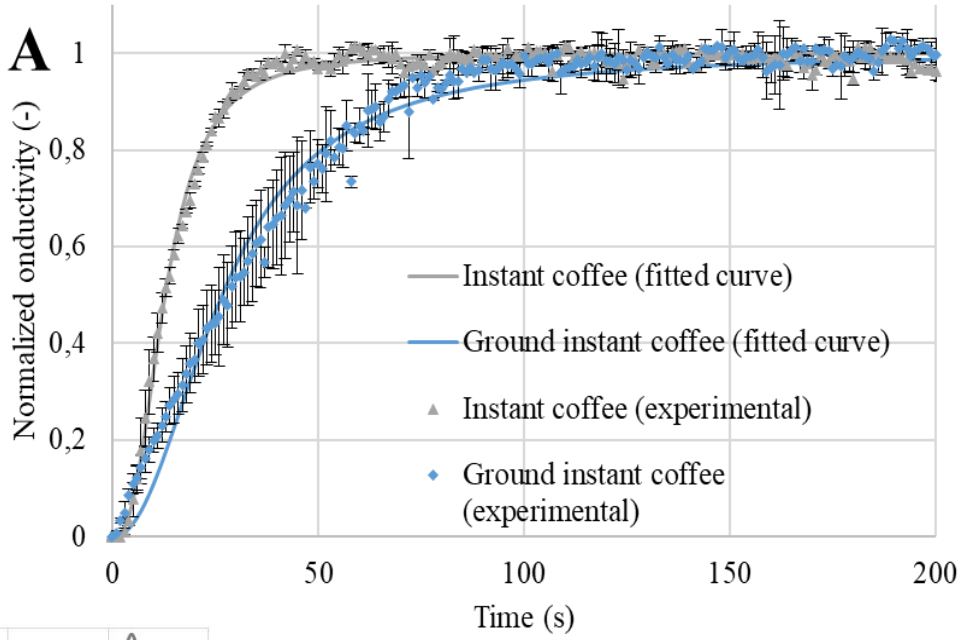

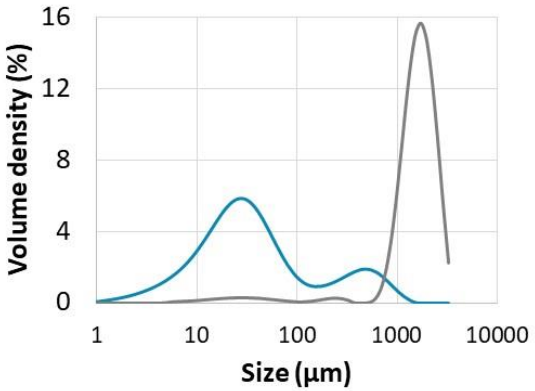

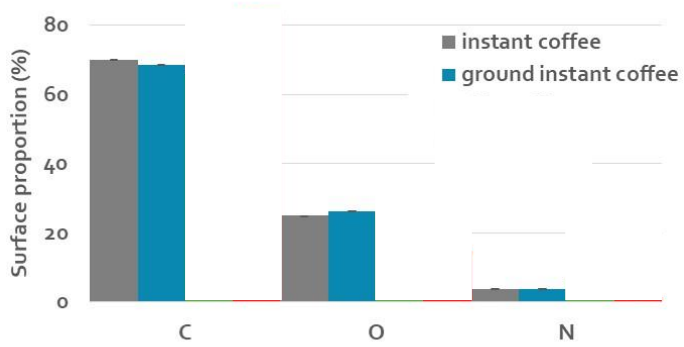

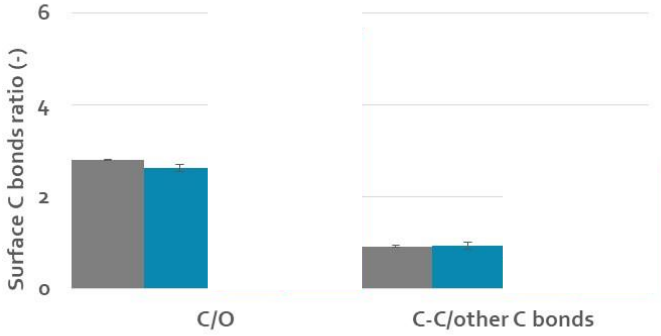

LIBio Laboratoire d'Ingénierie des Biomolécules

RECONSTITUTABILITY FOLLOWED BY CONDUCTIMETRY

Instant coffee powder

Ground instant coffee powder

Impact of particle size on reconstitutability

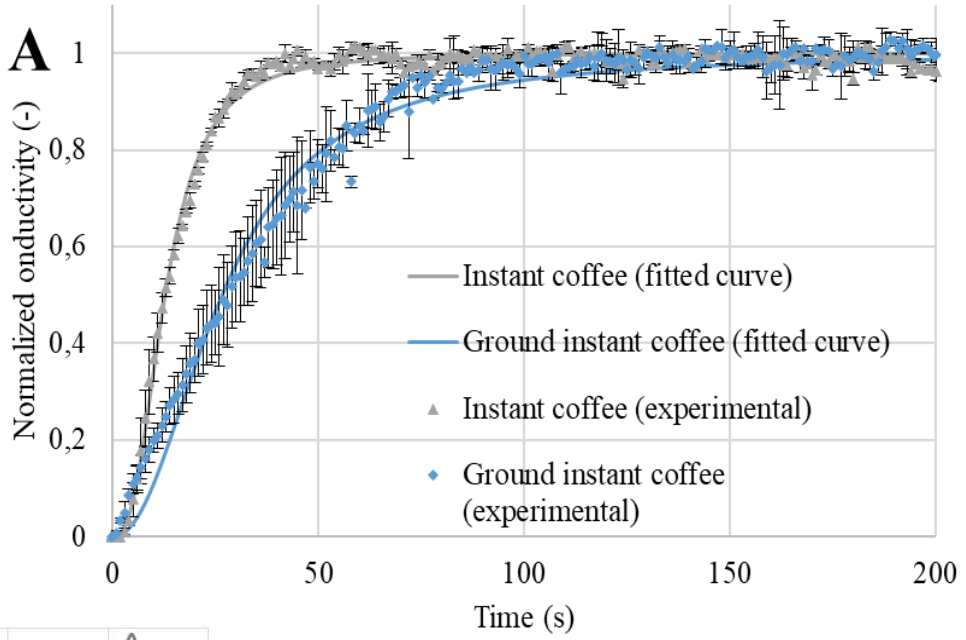

Impact of fat content on reconstitutability

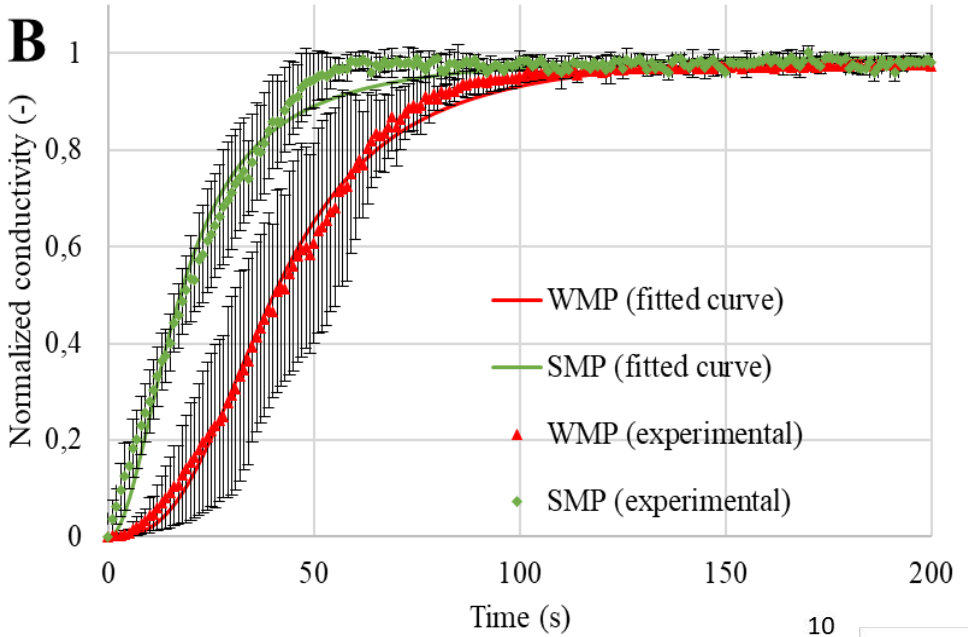

Whole milk powder

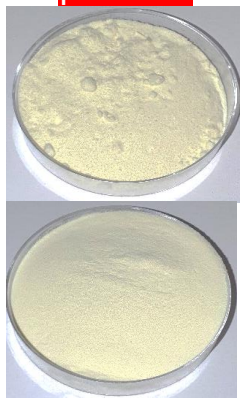

Skim milk powder

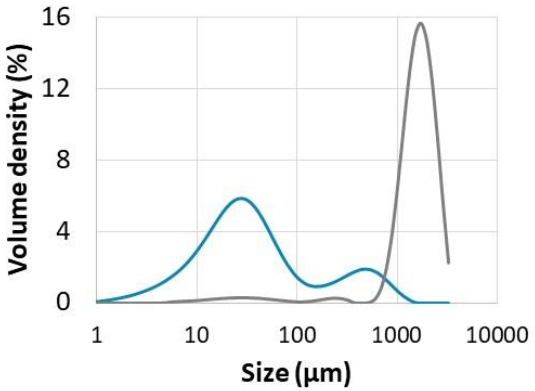

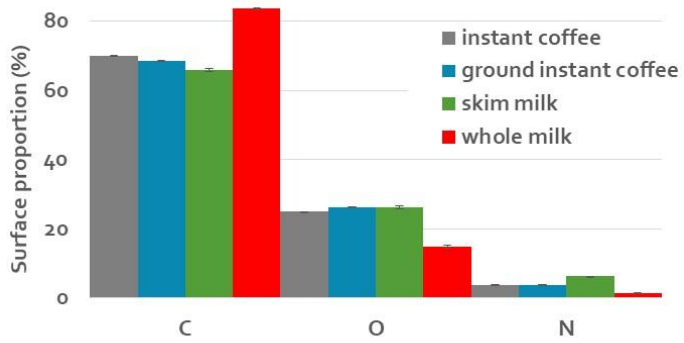

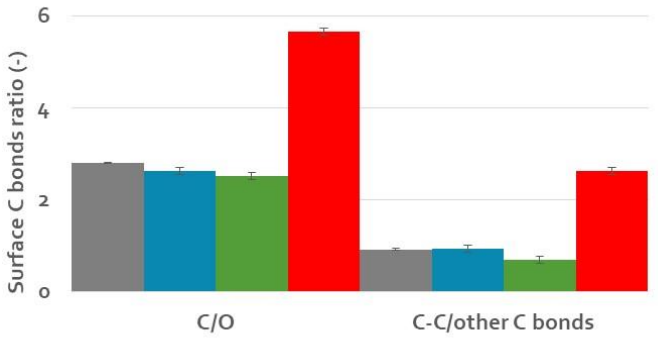

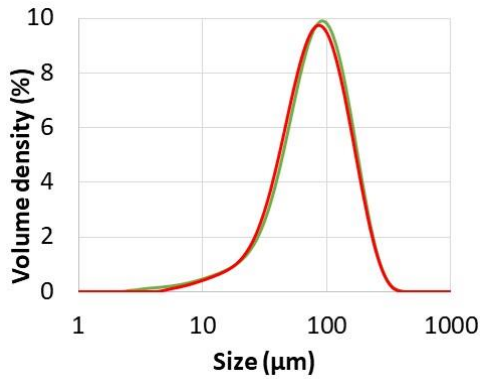

LIBio Laboratoire d'Ingénierie des Biomolécules

RECONSTITUTABILITY FOLLOWED BY CONDUCTIMETRY

Impact of particle size on reconstitutability

Instant coffee

Ground instant coffee

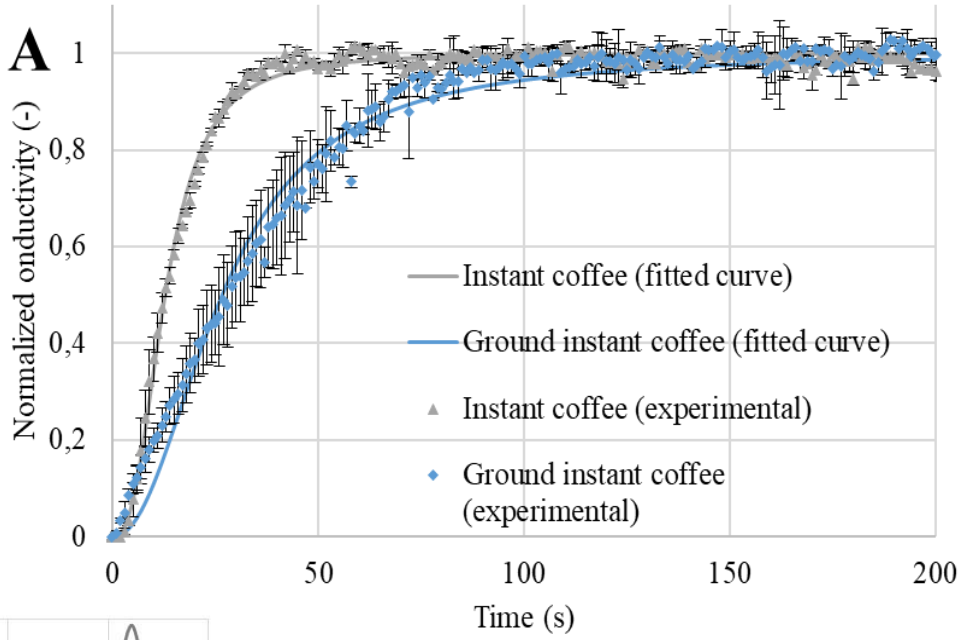

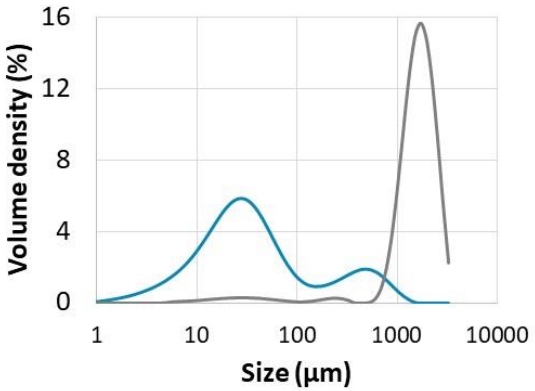

Impact of fat content on reconstitutability

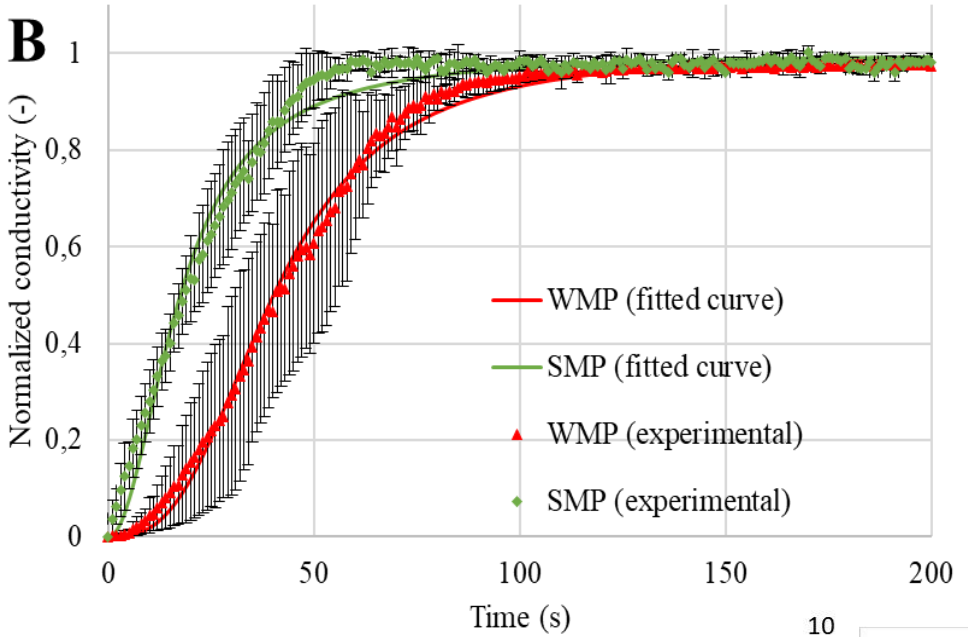

Whole milk powder

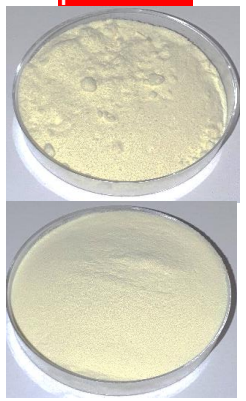

Skim milk powder

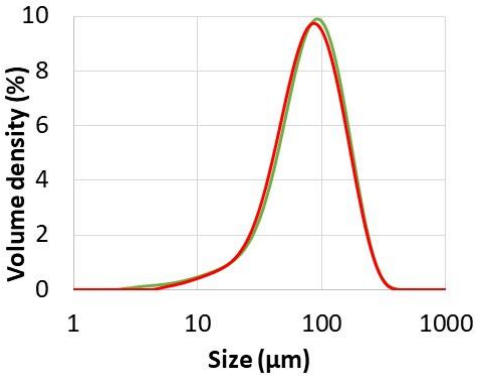

	Wetting time (s)	$t_{95\%}$ (s)	k (s)	n (-)	R^2
Skim milk powder	35.0	76.3	17.46	2.00	0.95
Whole milk powder	68.1	112.0	40.13	2.87	0.98
Instant coffee	22.5	38.9	12.8	2.65	0.98
Ground instant coffee	51.5	105.2	26.64	2.14	0.98

LIBio Laboratoire d'Ingénierie des Biomolécules

TAKE-HOME MESSAGE FROM YEAR #1

Physicochemical characteristics of powders were correlated with the **wetting** and **reconstitution times** of fifty food powders by principal component analysis (PCA). Four powder categories were identified based on wetting and reconstitution times.

Green group: short wetting and reconstitution times,
Yellow group: long wetting time and short reconstitution time,
Orange group: short wetting time and long reconstitution time,
Red group: long wetting and reconstitution times.

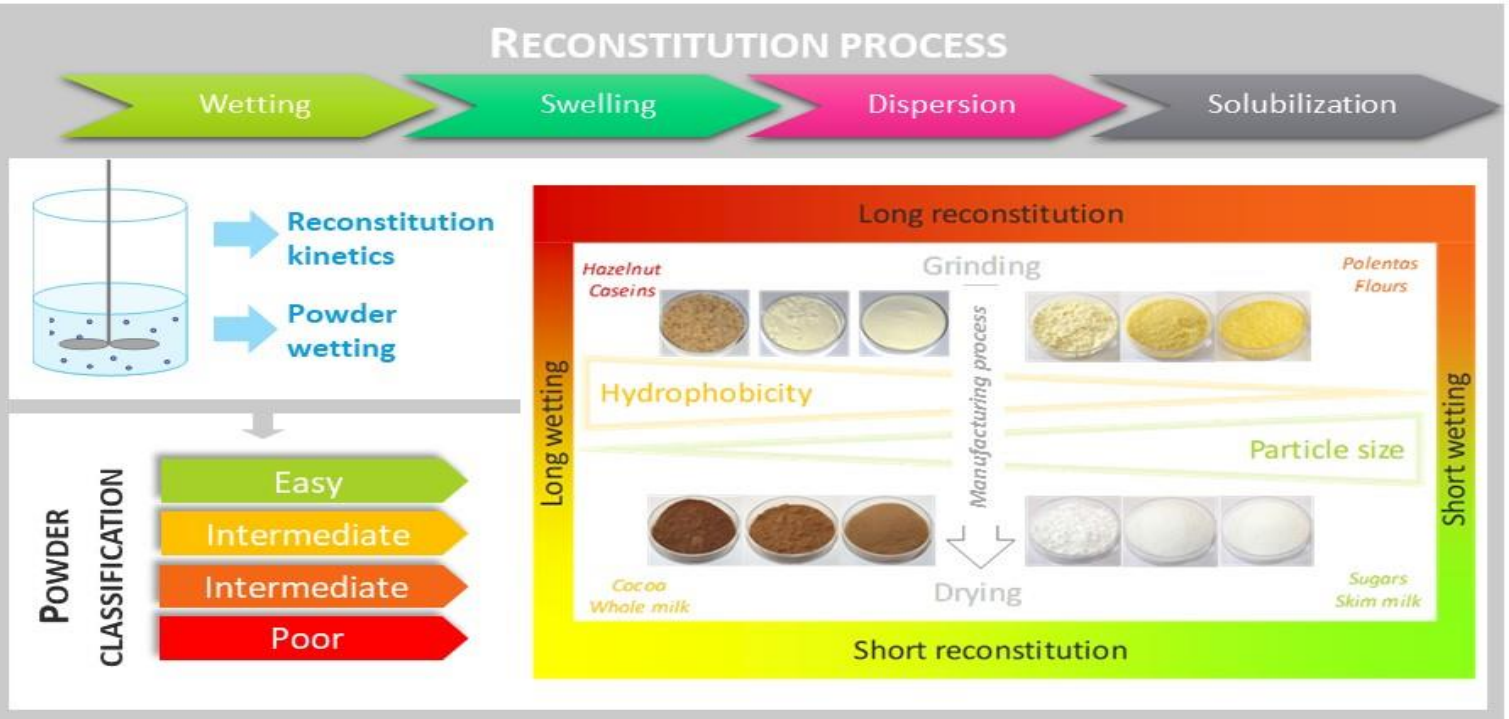

Powder classification according to their reconstitution behavior :

- **Long wetting times** associated to high particle surface hydrophobicity, small median particle size, as well as high protein and fat contents in the powder bulk.

Horizontal axis (PC1)

- **Long reconstitution times** linked to the powder manufacturing process (powders obtained by grinding of solid materials led to poorer reconstitution behavior than spray-dried powders) and low sugar content in the powder bulk.

Vertical axis (PC2)

3 New knowledge about powder reconstitutability thanks to a focus on particle surface (year #2: 2020)

Laboratory closure from mid march until mid may 2020…
The remote working was focused on data treatment and paper writting.

LIBio
Laboratoire d'Ingénierie des Biomolécules

FOCUS ON SOME POWDERS FROM EACH CLASS OF RECONSTITUTABILITY

Whey powder coating with sugar solutions (validated with IFPRI)

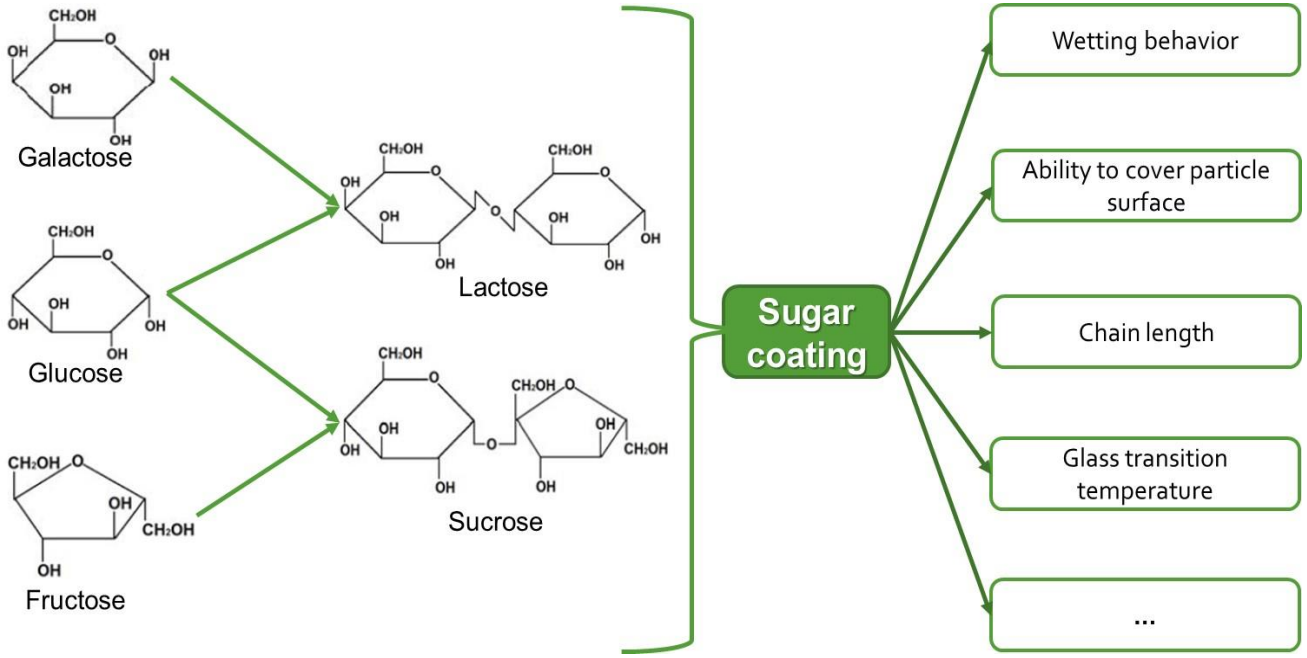

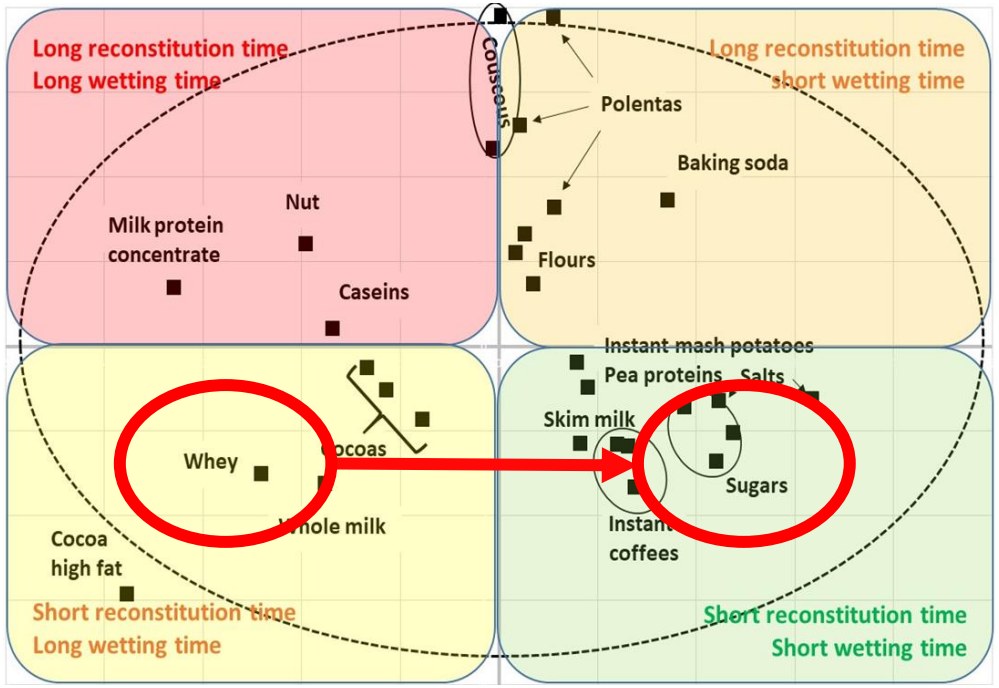

- Determination of the minimal sugar proportion necessary to improve whey powder wettability
- Impact of sugar nature
- Impact of powder surface (stiffness, rugosity, surface coverage…)

Whey powder
Non-wettable

Sugar powders
Easily wettable

LIBio
Laboratoire d'Ingénierie des Biomolécules

FIRST SUGAR COATINGS

- One day course training with Glatt application specialist (in February)
- Various process conditions and formulations were tested:
  - Coating duration from 5 to 15 min
  - Coating with sucrose solutions at concentrations from 0 to 45 %
  - Flow rate of 0.80 $g.s^{-1}$

Experiment code	Time (min)		
Sucrose (%)	5	10	15
0	#1	#2	#3
15	#1-1	#2-1	X
30	X	#2-2	X
45	X	X	X

First line: Reference powders = whey powder + process impact (attrition)

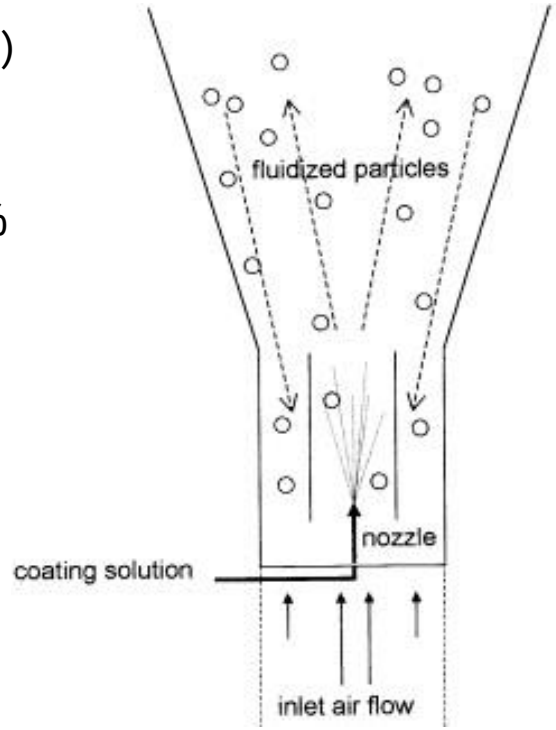

Mini-Glatt fluid bed coater (Würster design)

QUANTIFICATION OF SUGAR CONTENT IN COATED POWDERS

Example for sucrose coating

Sucrose quantification

Sample acid hydrolysis + Sucrose standards → Reaction with DNS → Absorbance at 530 nm

Samples	Sucrose g / 100 g
Whey powder	0
15 % sucrose; 5 min (#1-1)	1.11 ± 0.42
15 % sucrose; 10 min (#2-1)	1.97 ± 0.51
30 % sucrose; 10 min (#2-2)	3.84 ± 0.65
Sucrose powder	100

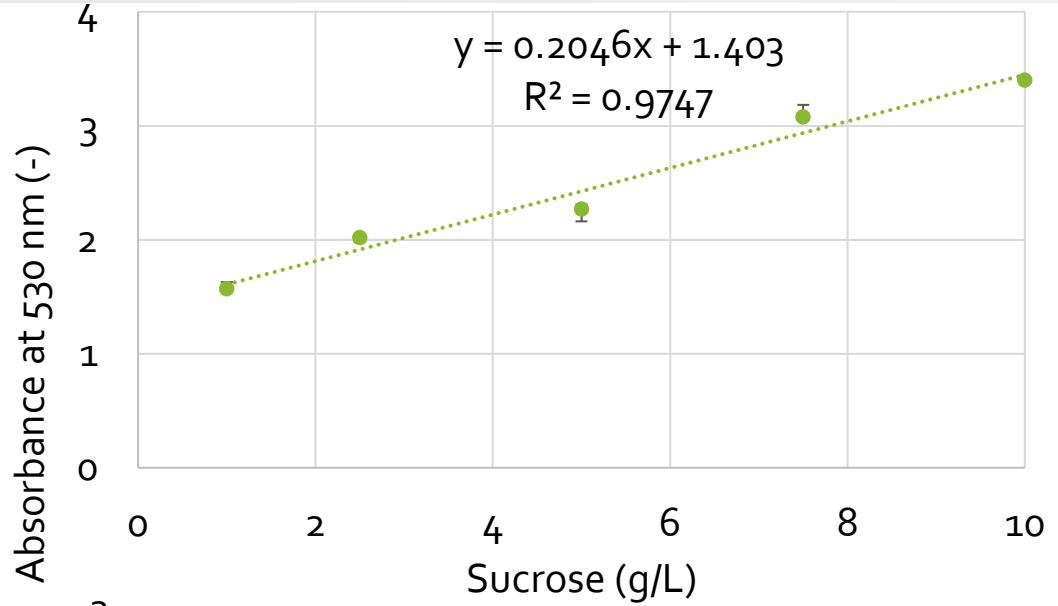

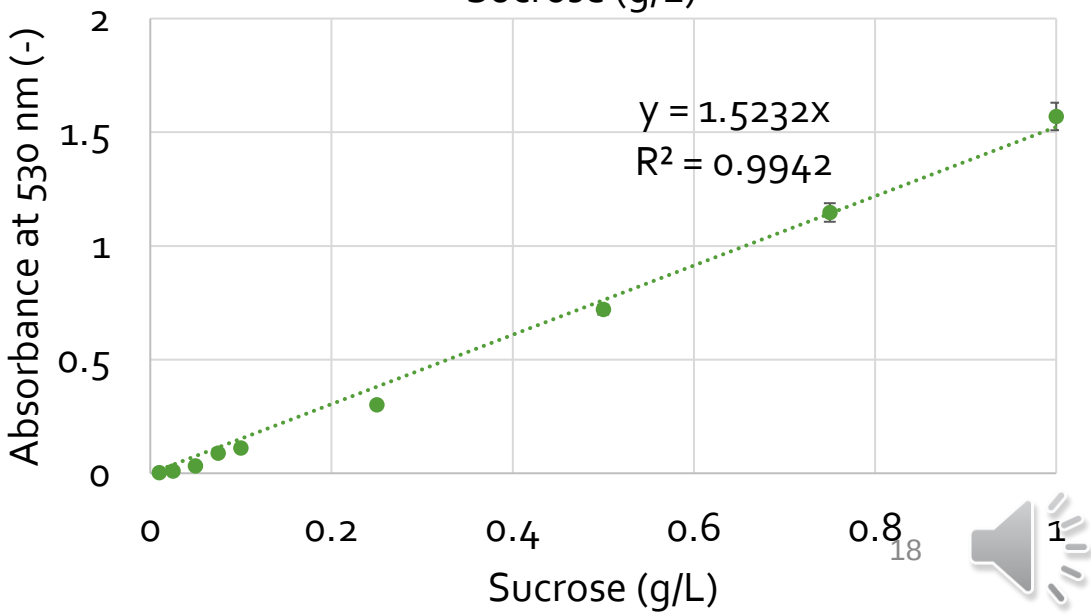

PHYSICOCHEMICAL CHARACTERIZATION

Particle size distribution

- No significant differences between uncoated and sucrose-coated whey powders
- No agglomeration induced by coating
- Fine and regular sucrose coverage

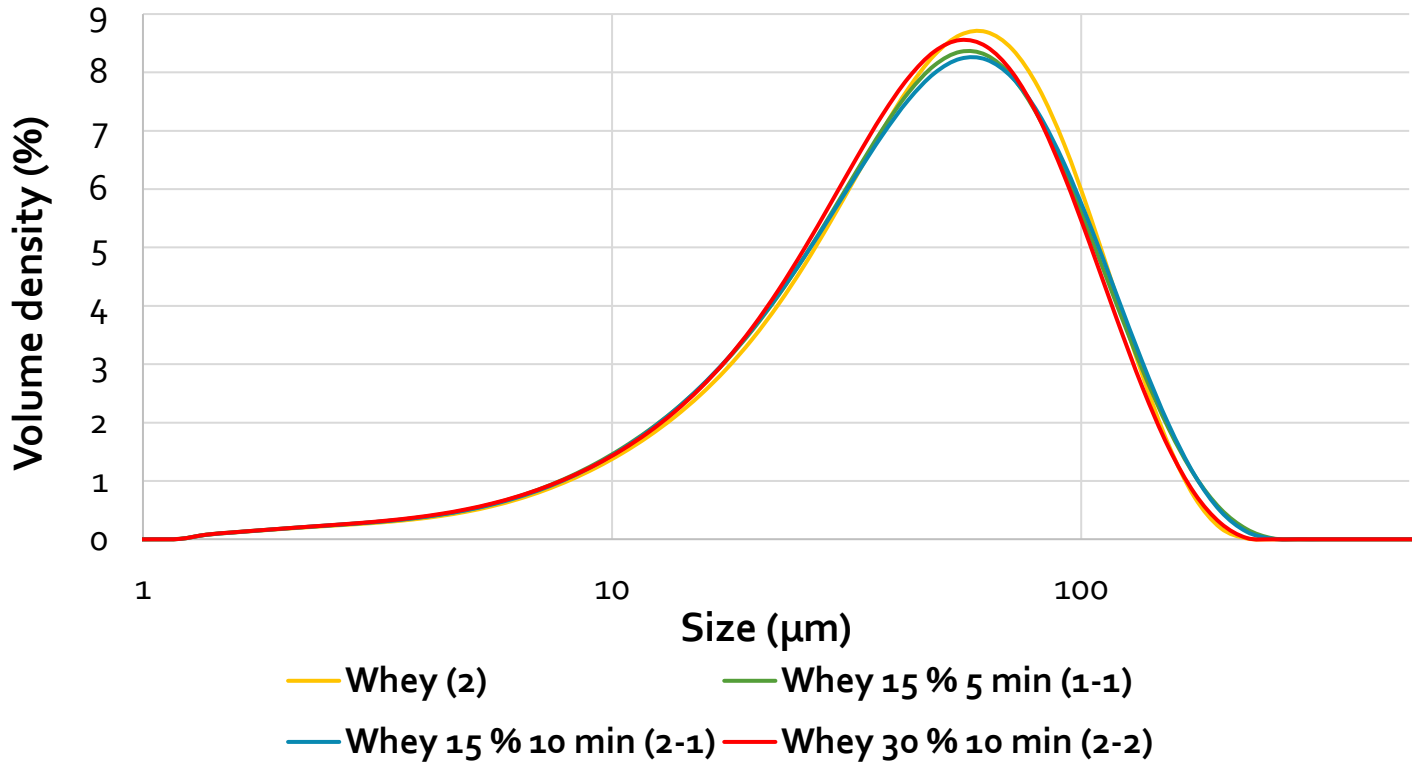

	D_{10} (µm)	D_{50} (µm)	D_{90} (µm)	Span (-)
#2	14.1 ± 0.0	48.3 ± 0.1	105.5 ± 0.7	1.9 ± 0.0
#1-1	13.6 ± 0.1	47.2 ± 0.1	107.5 ± 0.7	2.0 ± 0.0
#2-1	13.6 ± 0.0	47.5 ± 0.1	108.5 ± 0.7	2.0 ± 0.0
#2-2	13.6 ± 0.0	46.3 ± 0.4	103.5 ± 0.7	1.9 ± 0.0

LIBio Laboratoire d'Ingénierie des Biomolécules

RECONSITUTABILITY

- Wetting time (IDF standard)

Samples	Wetting time (s)	Sucrose (g/100 g)
Whey	1 217 ± 11	0
#1-1	1 090 ± 4	1.1
#2-1	1 068 ± 17	2.0
#2-2	1 032 ± 8	3.8

Powder 100 % sucrose

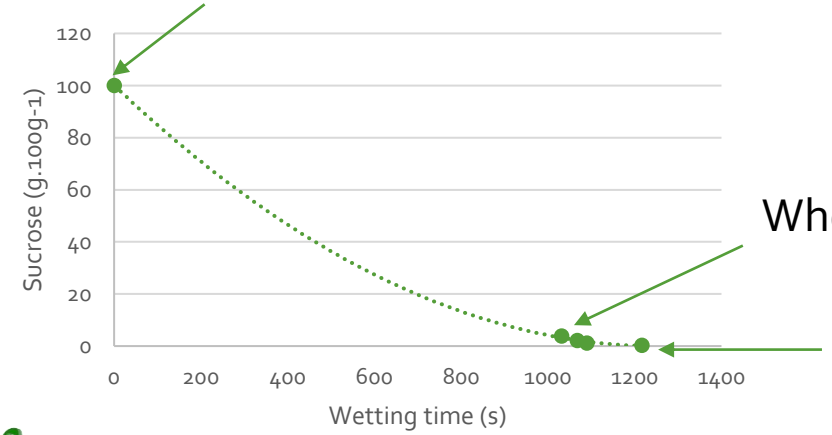

Whey powders coated with sucrose

Uncoated whey powder

- Reconstitution monitored by conductimetry

Ongoing

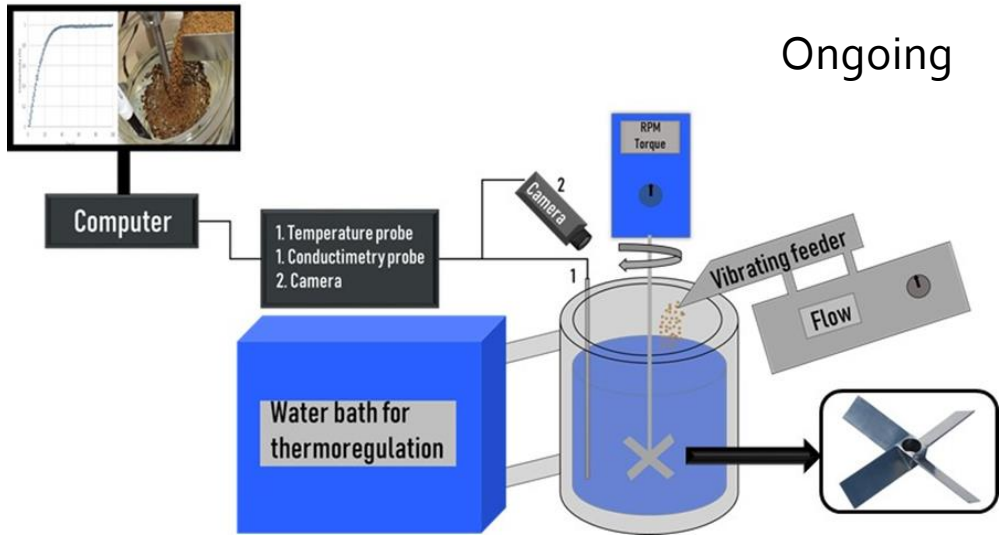

Only slight powder wetting improvement; in further experiments, longer coating durations and higher sugar concentrations will be used

LIBio Laboratoire d'Ingénierie des Biomolécules

SURFACE CHARACTERIZATION

- Surface topography and roughness

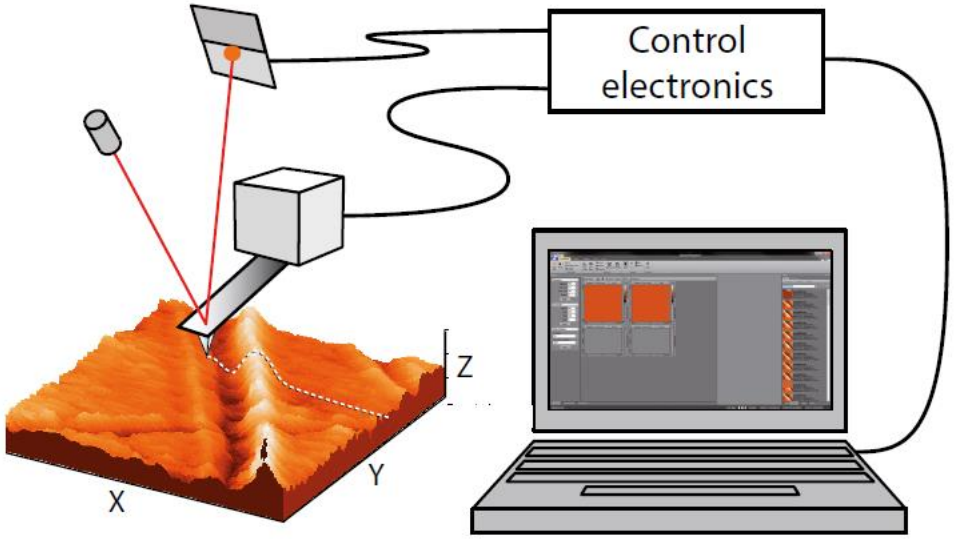

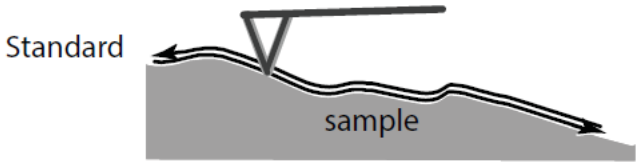

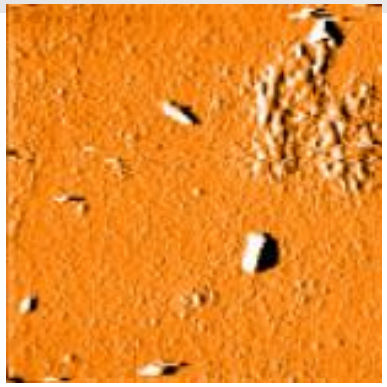

Powder 2 (5 x 5 µm²)
Reference whey powder

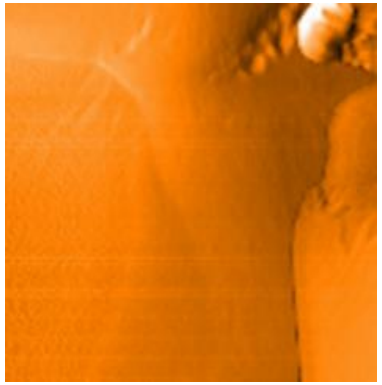

Powder #2-1 (5 x 5 µm²)
Whey powder coated during 10 min with 15 % sucrose solution

AFM Nanosurf Flex-Axiom

ONGOING - Roughness

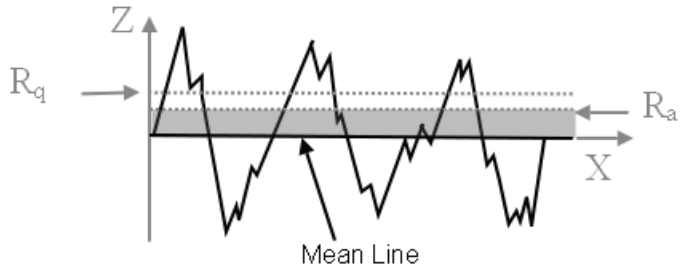

Image analysis for roughness calculation: Rq & Ra

LIBio Laboratoire d'Ingénierie des Biomolécules

SURFACE CHARACTERIZATION

- Surface mechanical properties (nanoindentation)

Expected results based on the results of other studies already performed by the laboratory

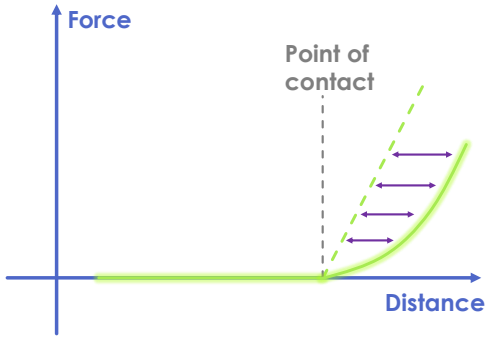

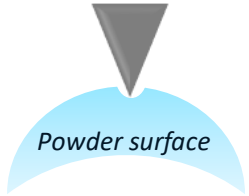

Soft surface

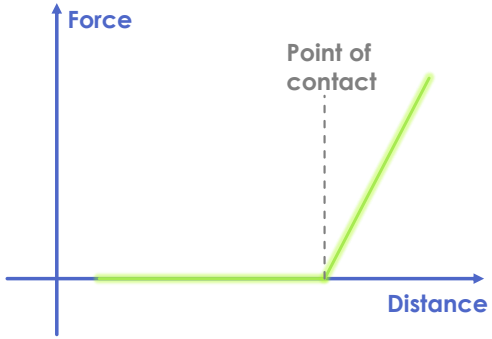

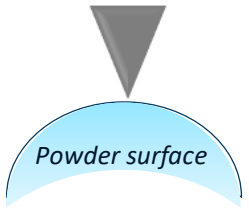

Stiff surface

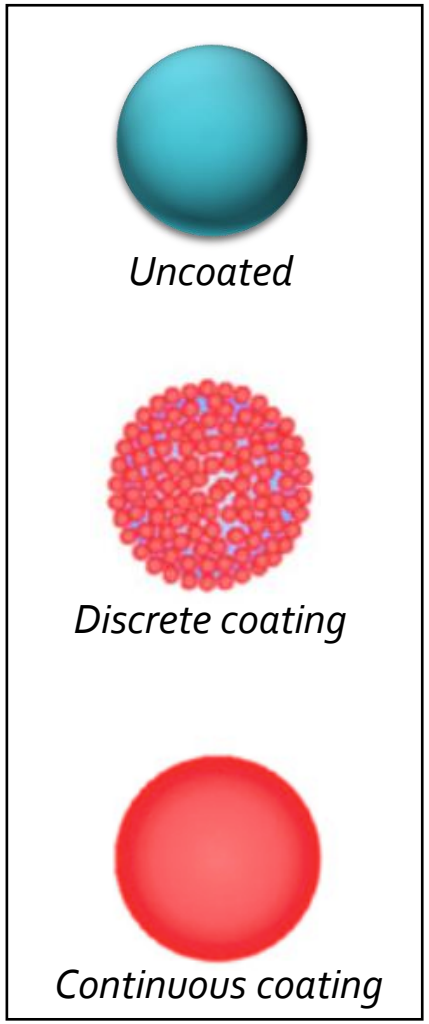

AFM Nanosurf Flex-Axiom

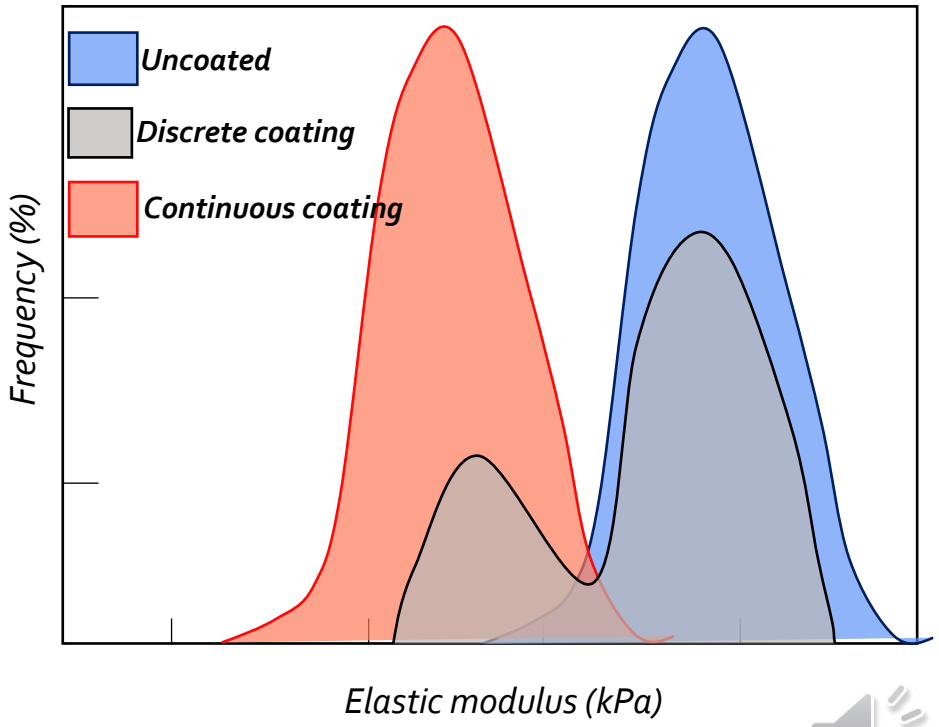

4 Perspectives

Year #2 ongoing…

- Coating with various sugars
- Surface characterization
- Functional properties

LIBio
Laboratoire d'Ingénierie des Biomolécules

FIRST SCIENTIFIC PAPER FROM YEAR 1

1 **Main physicochemical powder characteristics influencing their**

2 **reconstitution behavior**

3 **Tristan Fournaise[1], Jérémy Petit[1], Claire GAIANI[1]**

4 [1]Université de Lorraine, LIBio, F-54000 Nancy, France

5

6 **Abstract**

7 Sixty food powders corresponding to a wide range of physicochemical characteristics (chemical
8 bulk and surface composition, particle size, span) and manufacturing processes (grinding,
9 freeze-drying, spray-drying, crystallization) were investigated. A wide range of reconstitution
10 profiles were measured by conductivity measurements and analyzed thought data fitting.
11 Physicochemical characteristics of powders were correlated with the wetting and reconstitution
12 of sixty food powders by principal component analysis (PCA). Four powder categories were
13 identified based on wetting and reconstitution times; i.e. *Green group*: short wetting and

Draft sent to industrial project members
Waiting for comments/corrections from IFPRI members

Possible journals :
- Journal of Food Engineering
- Food Hydrocolloids

SECOND SCIENTIFIC PAPER FROM YEAR 1

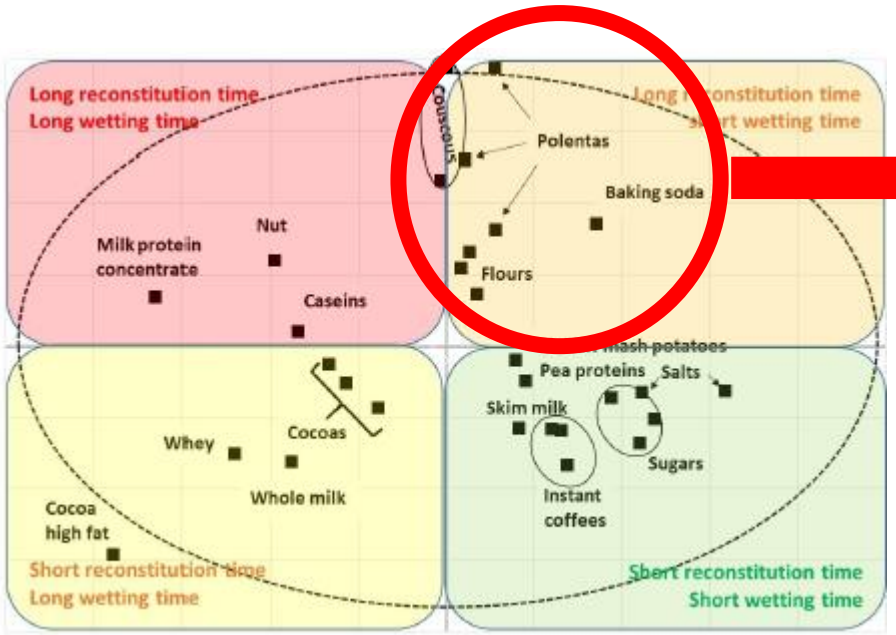

Naïma GAUDEL – 3 months Post doc focused on cereal powders reconstitution (couscous, flours, etc.):

- Swelling step
- Attrition step

Reconstitution kinetics at different stirring rates
Impact of particle size

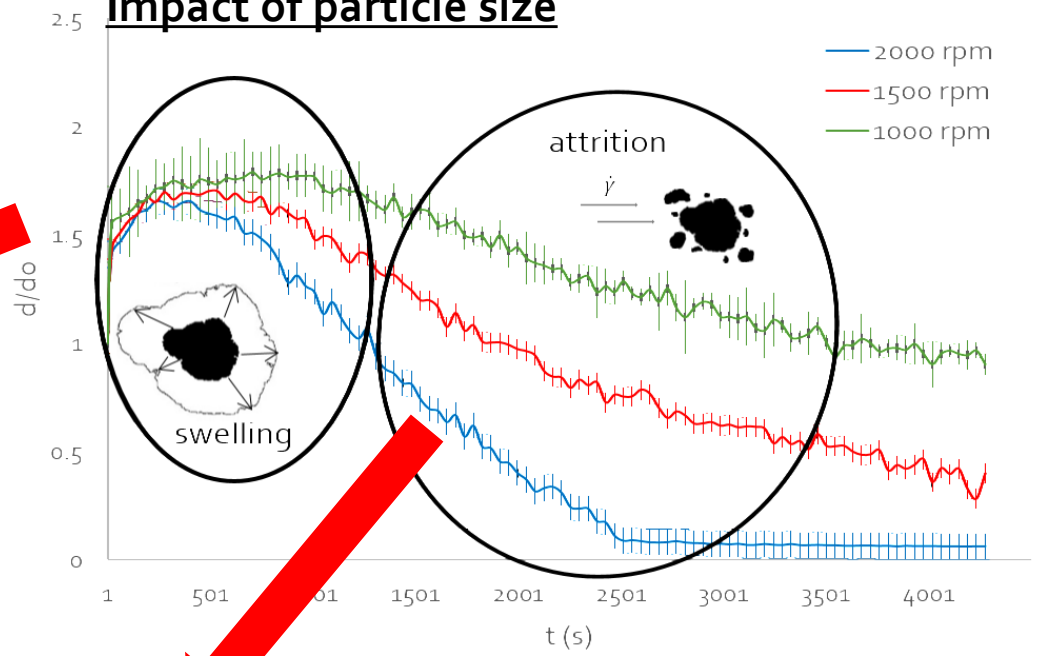

Swelling rates vs stirring rate for two mean particle sizes

Attrition rates (µm.s^{-1}) vs shear (for 2 grain sizes)

	2000 rpm	1500 rpm	1000 rpm
Attrition rate for fine powder	0.77 ± 0.01	0.48 ± 0.04	0.26 ± 0.01
Attrition rate for medium powder	2.19 ± 0.16	1.14 ± 0.04	0.52 ± 0.03

Draft sent to industrial project members
Waiting for comments/corrections from IFPRI members
Possible journals :

- Journal of Food Engineering
- Food Hydrocolloids
- Powder Technology

THANK YOU FOR YOUR ATTENTION !

Pr. Claire GAIANI - Université de Lorraine
LIBio – Laboratoire d'Ingénierie des Biomolécules
2 avenue de la Forêt de Haye - BP 20163
54505 Vandœuvre-lès-Nancy - FRANCE
Tél. : +33(0)3 72 74 41 11 - Fax : +33(0)3 83 59 57 72
claire.gaiani@univ-lorraine.fr
http://libio.univ-lorraine.fr/

LIBio
Laboratoire d'Ingénierie des Biomolécules

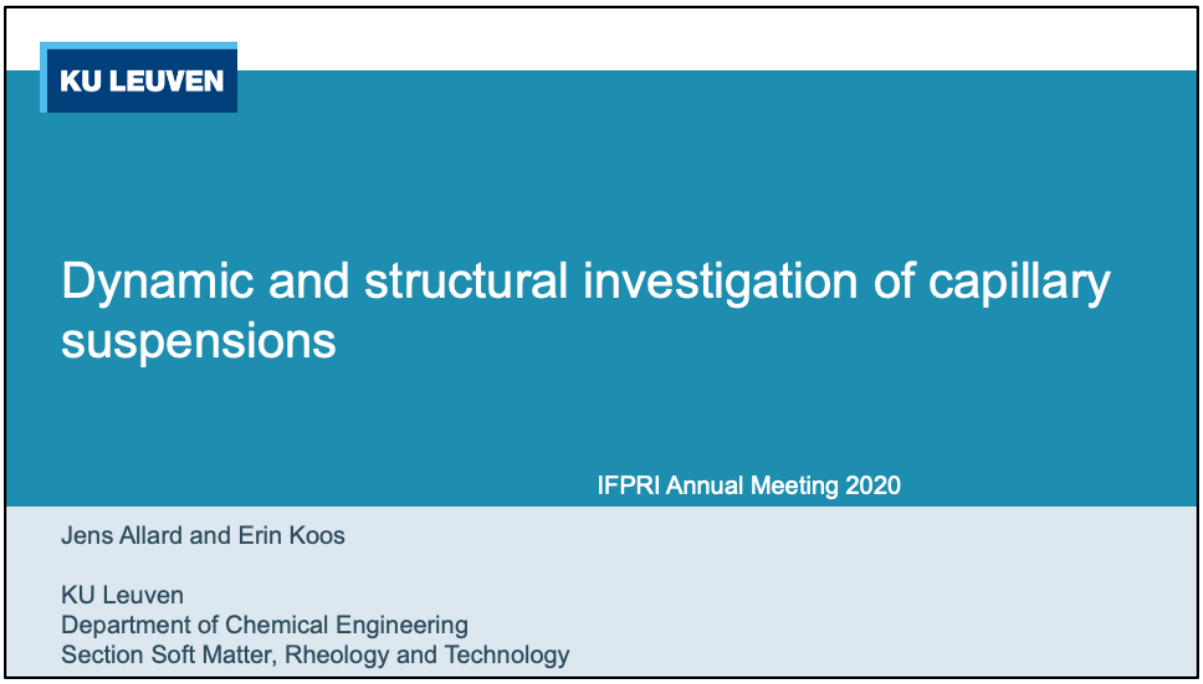

Hello and thank you for listening to (reading) this online version of our presentation at the IFPRI Annual Meeting 2020.

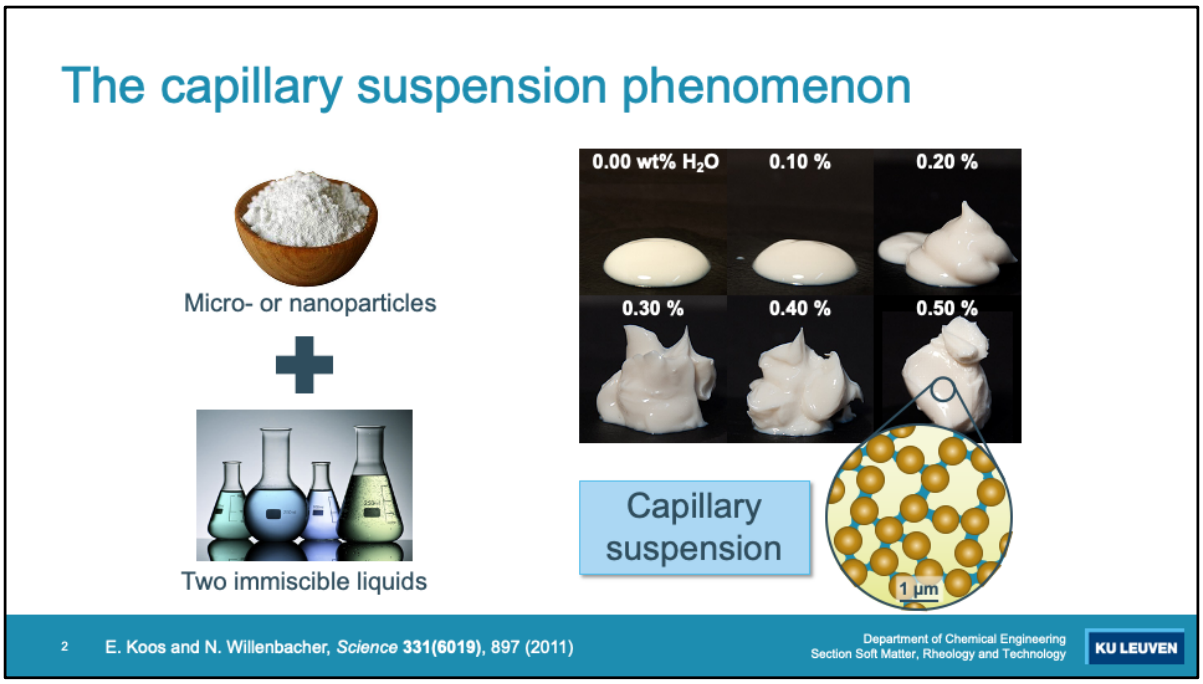

To start, let us quickly remind you about capillary suspensions. Capillary suspensions are solid-liquid-liquid systems, typically formed when a small amount of a secondary liquid is added to a suspension of micro- or nanoparticles. The two liquids must be (partial) immiscible and the secondary fluid is often present in only a few percent. This secondary liquid leads to the formation of a sample-spanning particle network caused by the capillary attraction between the particles. This is like the addition of small amounts of water to the grains of sand in a sandcastle, but here our grains are much smaller, the air is replaced by a liquid, and we usually have a much lower particle loading.

As can be seen in the example on the right, a dramatic change in the bulk properties of the materials occurs with very small amounts of liquid. In this case, using a suspension of calcium carbonate in an oil with small amounts of water, less than 0.5% water by weight increases the yield stress and viscosity by several orders of magnitude.

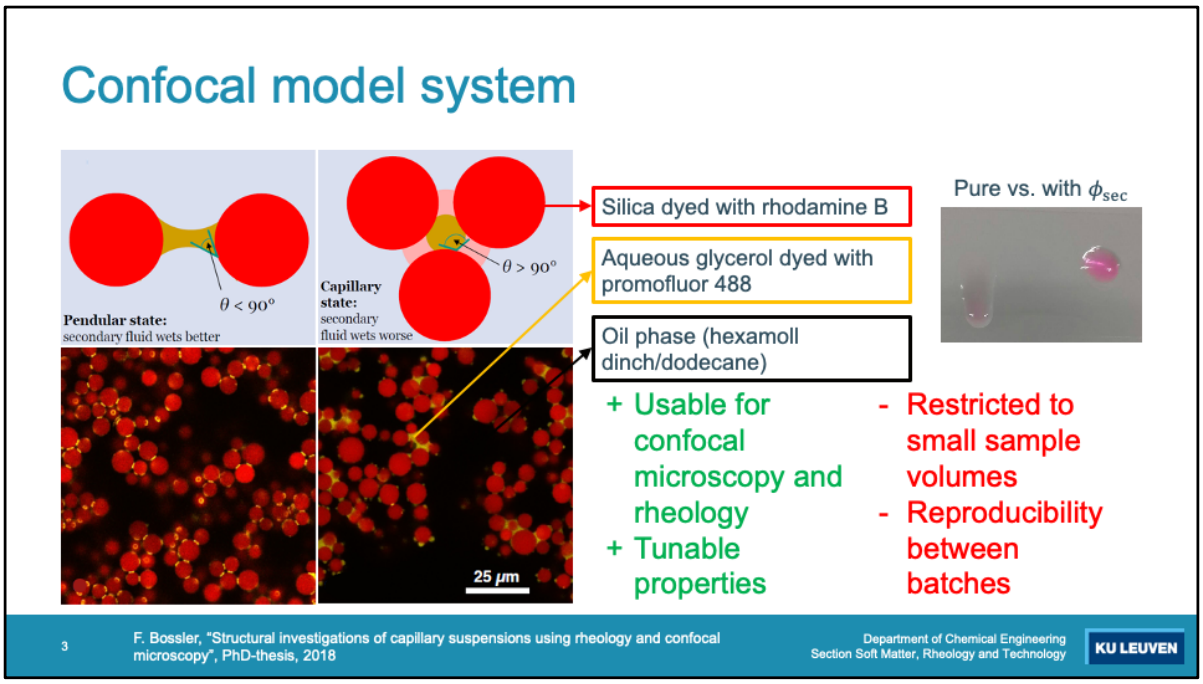

To investigate the structure of these networks, we use a confocal model system composed of silica particles dyed with rhodamine B isothiocyanate. These particles (at least in this part of the project) are porous and the dye is covalently bonded to both the particle interior and exterior. The aqueous phase, which is usually the secondary phase in these experiments, is a mixture of water and glycerol dyed with promofluor 488. In the confocal images on the left, the particles are shown in red and the secondary fluid in yellow. The oil phase is undyed and appears black on the images. Without secondary liquid, the pure suspension freely flows (upper right image) whereas it shows gel-like properties with a volume of added secondary liquid ϕ_{sec}. By using silica particles, we can change the three-phase contact angle θ through silanization. This lets us switch between the pendular state $\theta < 90°$ where the secondary liquid preferentially wets the particles, forming binary bridges between the particles, and the capillary state $\theta > 90°$ where the particles from small clusters surrounding the secondary liquid droplets.

This index-matched system is applicable to both confocal microscopy and can also be used for simple rheological measurements. We have carefully controlled the mixing procedure to ensure that the samples are uniform. Thus, the structure should be identical throughout the sample volume and we won't make mistakes by inferring changes in the material structure when it's only an error caused by the sampling location. Furthermore, we can tune the sample properties: the ratio of the three components and the contact angle.

…

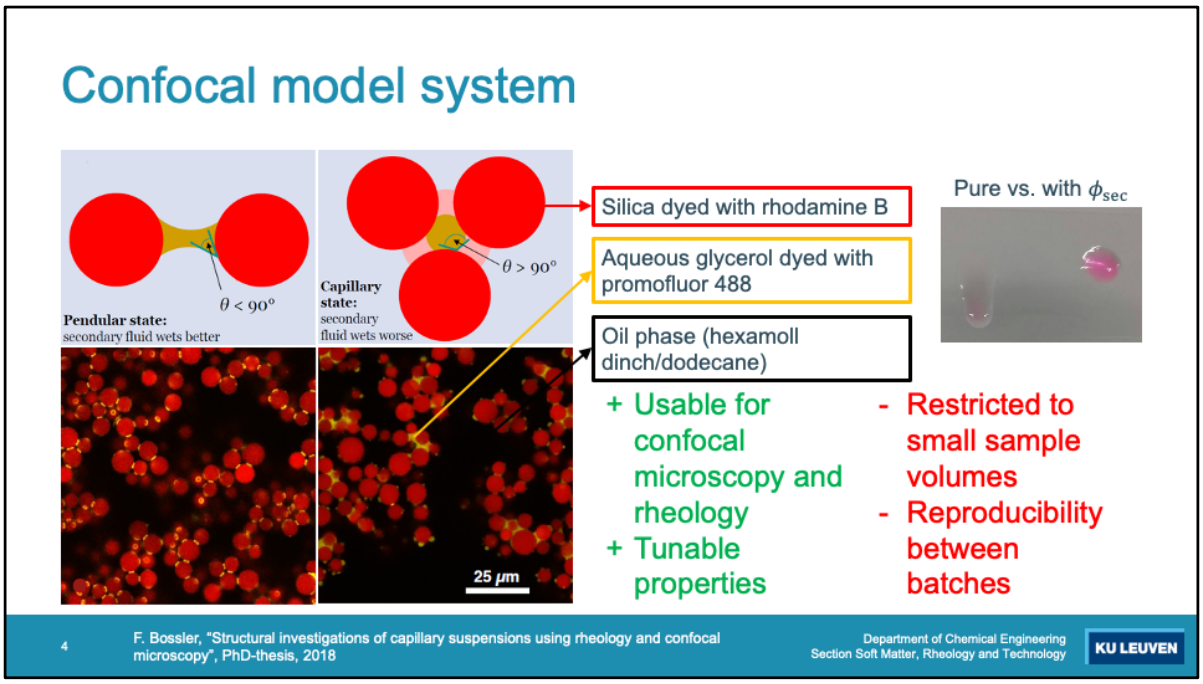

This isn't the perfect model system, however. The mixing procedure used to create uniform samples restricts us to sample sizes less than 1 ml. This means we can make rheological measurements using a small plate-plate geometry, but not a Couette cell or vane. The silanization process also lacks in reproducibility; the exact same processing steps and amounts can result in a change in the contact angle by more than 10º. Therefore, experiment runs are limited by the batch size.

Despite these drawbacks, this is still the best system we have been able to use to study the connection between rheology and structure.

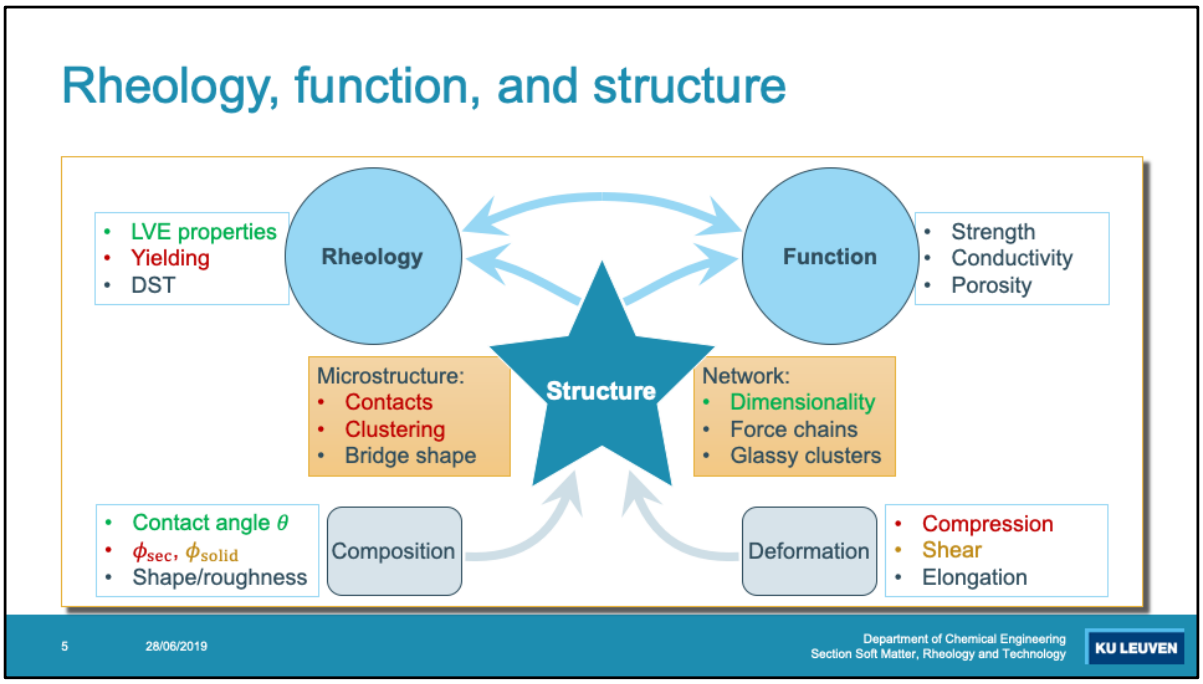

The goal of this project is to connect rheology (for example, the properties in the linear viscoelastic region, yielding, and shear thickening) and function (e.g. strength, conductivity porosity) through the structure of these samples. This structure depends on the sample composition and external deformation. If we can understand these relations, we can predict the behavior and design better materials. Typically, we think about structure at two extreme length scales: the microstructure at the size of the particles and the network structure at length scales much larger than the particle size. In this project, we also want to determine which length scale is important and to find rigorous measures that work at many different length scales.

We started this process previously, looking at the influence of the solid loading ϕ_{solid} and contact angle θ on the linear viscoelastic LVE properties and using this to design new materials. These properties were connected to the material structure through the network dimensionality. This year, we have concentrated on the influence of the secondary fluid content ϕ_{sec} using microstructural measures such as the number of contacts and clustering coefficient. We also investigated the influence of compression and shear on the material properties at different solid loadings.

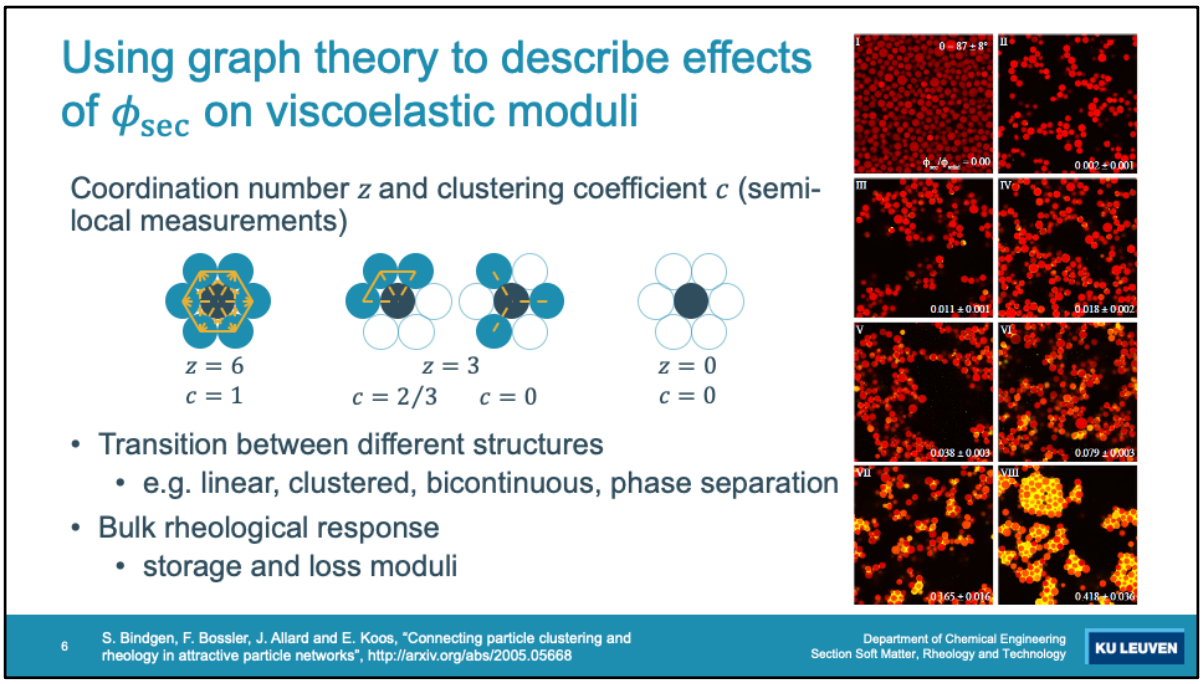

If we take, for instance, the influence of the secondary fluid volume fraction, you can see a wide variety of different structures that can be created. Without added liquid, there is no interaction between the particles and a granular pile forms. At point II, were only a small amount of aqueous glycerol is added, you can see a dramatic change in the structure. Even though there are no clear bridges shown here – they are much smaller than the size of the particles – the attractive force is sufficient to prevent particle sedimentation. As the amount of secondary liquid is increased, these bridges grow and merge to create small clusters. At point VII, you can clearly see these bridges connecting multiple particles. While there is undoubtedly a sample-spanning network in this sample, the clusters are still isolated from each other with binary bridges in between. This is termed the funicular state. At point VIII, the particle-secondary fluid clusters become fully connected and a bicontinuous structure is formed. Finally, the sample will phase separate into a single dense cluster if more secondary liquid is added.

Since network-level measures such as the dimensionality are clearly insufficient to describe each and every ϕ_{sec} point in this sample, we must use a different measure. The number of neighbors, the coordination number z, which can be readily calculated from confocal images, provides some insights, but has a tenuous link to rheology. We therefore propose supplementing this measure with another measure from graph theory, namely the clustering coefficient, as shown in the sketch.

…

Using graph theory to describe effects of ϕ_{sec} on viscoelastic moduli

Coordination number z and clustering coefficient c (semi-local measurements)

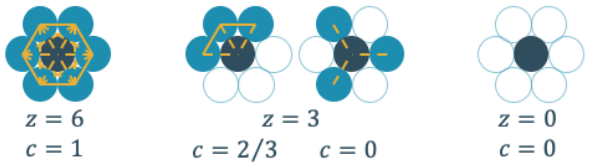

- Transition between different structures
  - e.g. linear, clustered, bicontinuous, phase separation
- Bulk rheological response
  - storage and loss moduli

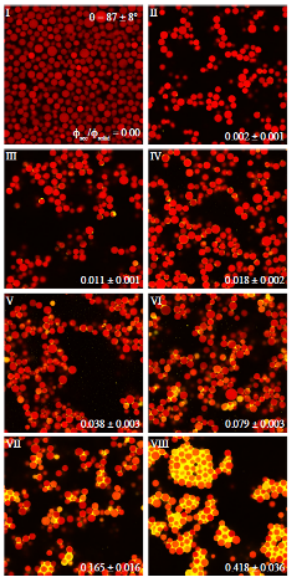

7 S. Bindgen, F. Bossler, J. Allard and E. Koos, "Connecting particle clustering and rheology in attractive particle networks", http://arxiv.org/abs/2005.05668

Department of Chemical Engineering
Section Soft Matter, Rheology and Technology
KU LEUVEN

The local clustering coefficient is defined as

$$c = \frac{2e}{z(z-1)},$$

where the number of bonds between neighbors (dashed lines) is z and the connections between these neighbors (solid lines) is e. An alternative definition of the clustering coefficient can be achieved by counting the number of triangles through a node (particle) compared to the number of neighbors

As illustrated in the sketch intermediate coordination numbers can either have low clustering ($c \to 0$) or high clustering ($c \to 1$) with clear implications of the mechanical response of the cluster. Although the upper limit of the clustering coefficient is $c = 1$, as shown in the non-physical packed structure on the left, real, e.g., biological networks, almost never reach this limit and $c > 0.5$ is considered as high clustering.

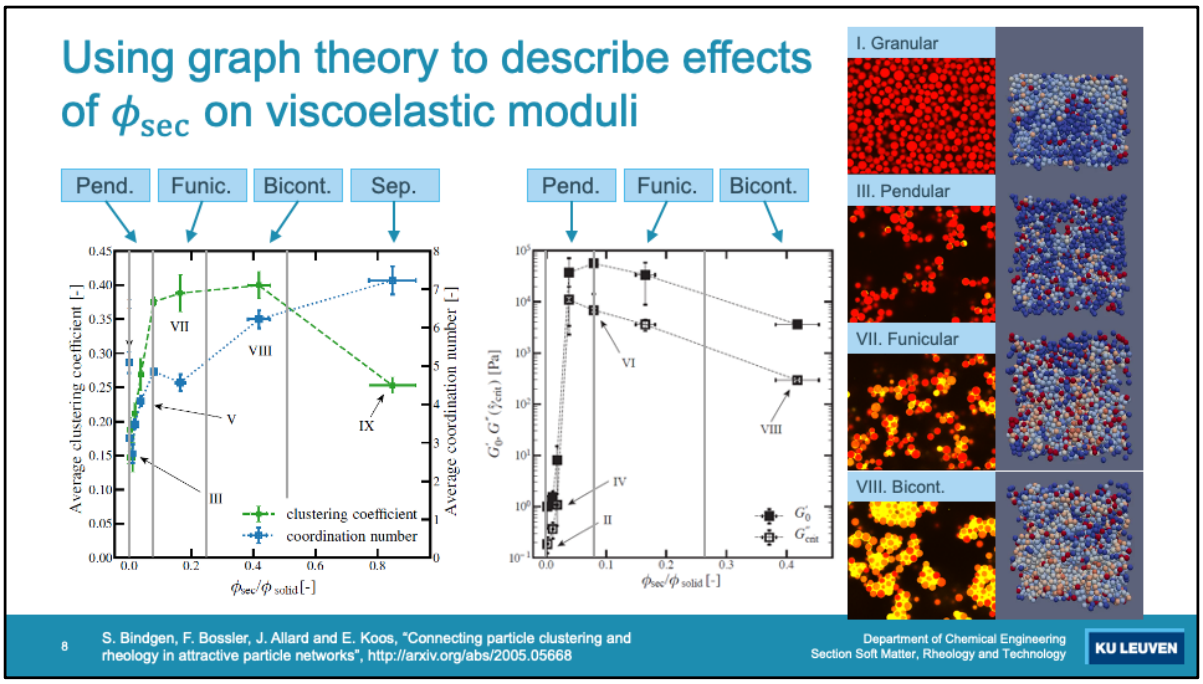

In a paper we recently placed on arXiv (and submitted to a journal for review), we used these measures to compare samples at two different contact angles, one in the pendular state and one in the capillary state. Changes in both the average $\bar{z}$ and $\bar{c}$ as well as in their distribution (captured here for a few key samples in the videos showing the networks where the particles are colored by their local clustering coefficient) can be quantified and correlated to rheological measurements. While the average values give some indication for the changes in the network structure, key transitions can be hidden by subtle changes in the average values.

A broad distribution of coordination numbers can be seen for the sample without added secondary liquid (top) with a mean value of $\bar{z} = 5.1$. The mean value of the clustering coefficient is $\bar{c} = 0.15$. A lot of particles with a clustering coefficient around the theoretical minimum of $c = 0$ can be observed, indicating particles without tight clustering. These values are characteristic for a loosely packed sedimented bed. That means there is a random arrangement of particles present where polydispersity of the particles can lead to a lot of isolated particles or particles with only one neighbor. This low clustering can indicate a metastable structure. Indeed, the structure of this sample changed slightly during the measurements, either due to the small movements of the objective or very slow sedimentation.

…

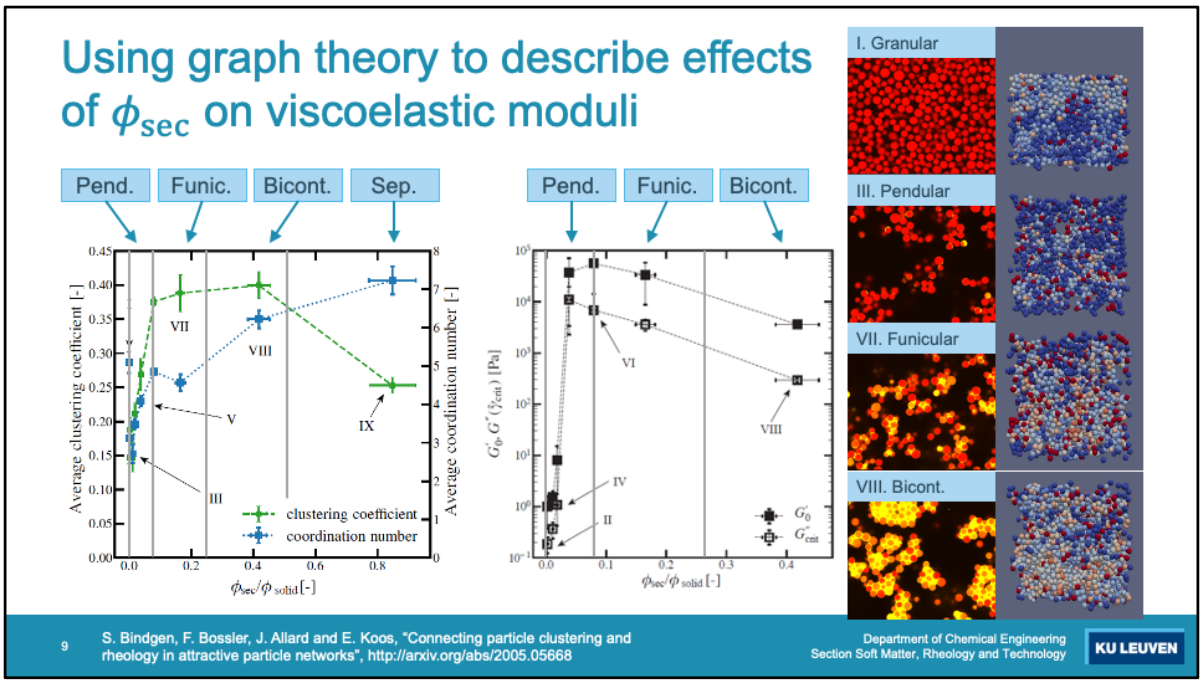

With the addition of secondary fluid to point III, we can see the structural arrangements due to the filling of the particle asperities. Particles are connected to each other via binary bridges leading to a lower average contact number of $\bar{z} = 2.7$ while the average clustering coefficient rises to $\bar{c} = 0.15$. This rise is caused by an increase in the number of particles with intermediate ($c = 0.3$) and high ($c = 1$) clustering. This is consistent with particles in a partially reinforced backbone chain. We conclude from the corresponding histogram that there is a change from the random sediment arrangement into an open network with many short, linear branches of two or three. Indeed, the amount of particles with a coordination number of $z = 2$ reaches its global maximum compared with the other histograms at point III. These values are consistent with the formation of a weak gel structure dominated by binary contacts and some tightly arranged clusters formed by trimers or other low number particle groups.

As the structure changes towards a funicular, or clustered, state (point IV), the coordination number increases. The average clustering coefficient also increases, but this change in the average is quite modest. The histogram shows a clearer loss in the number of particles with very low clustering and an increase in the intermediate clustering. This change is caused by the addition of particles to already existing clusters, leading to their increase in size and not by the formation of entirely new groups of particles.

…

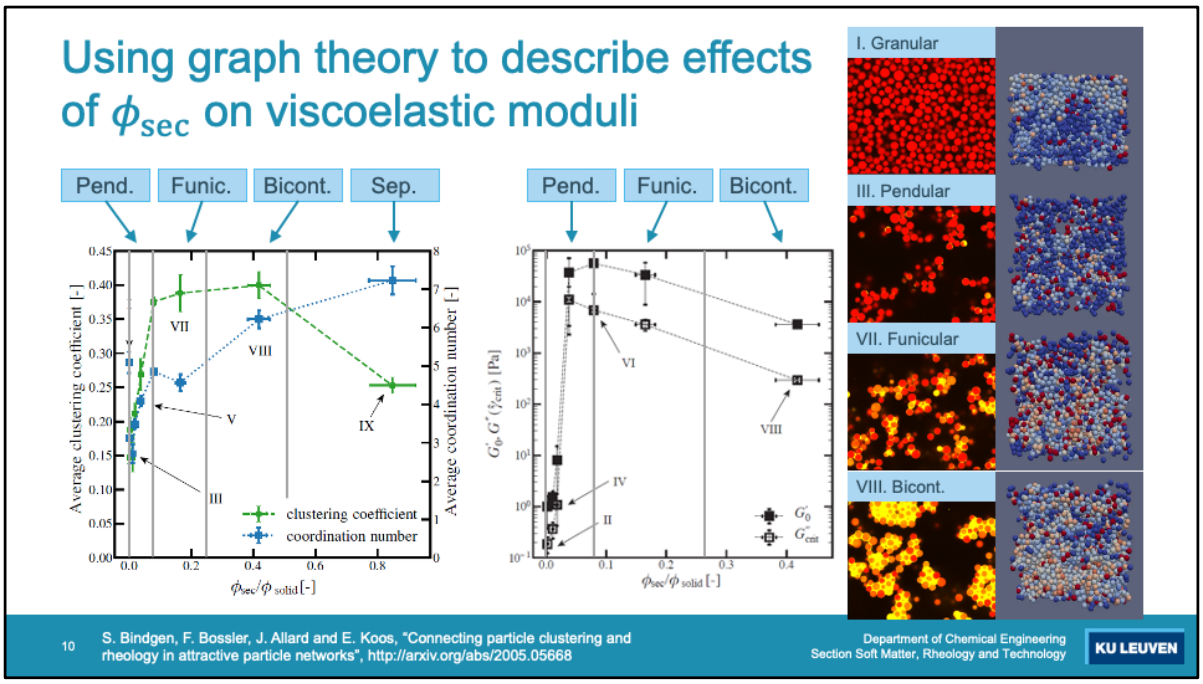

As the structure changes towards a funicular, or clustered, state (point IV), the coordination number increases. The average clustering coefficient also increases, but this change in the average is quite modest. The histogram shows a clearer loss in the number of particles with very low clustering and an increase in the intermediate clustering. This change is caused by the growth of clusters rather than the formation of entirely new groups of particles.

For the bicontinuous structure (point VII), the average coordination number has a value of $\bar{z} = 4.6$ while the clustering coefficient approaches a plateau with average values $\bar{c} = 0.39$. These are values that are typical of small-world phenomena in graph theory. Small world graphs have nodes that are not direct neighbors (low z or degree) but are only separated from each other by a few hops (a few particles). Put another way, these graphs are composed of tight cliques with few connections between cliques. A look at the confocal images reveals the presence of particle groups that become more and more isolated.

With the final addition of secondary fluid, the structure phase separates. This is indicated by the clustering coefficient decreasing towards the initial sedimented bed state. However, the structure seems to be denser than the initial sediment, as shown by the increased clustering coefficient and coordination number. This can be explained by the fact that the secondary liquid is solely present between the sedimented particles, pulling them together more tightly. This means that the arrangement of particles is not as random as in the first state without secondary liquid added. This structure should be more resilient to external deformation.

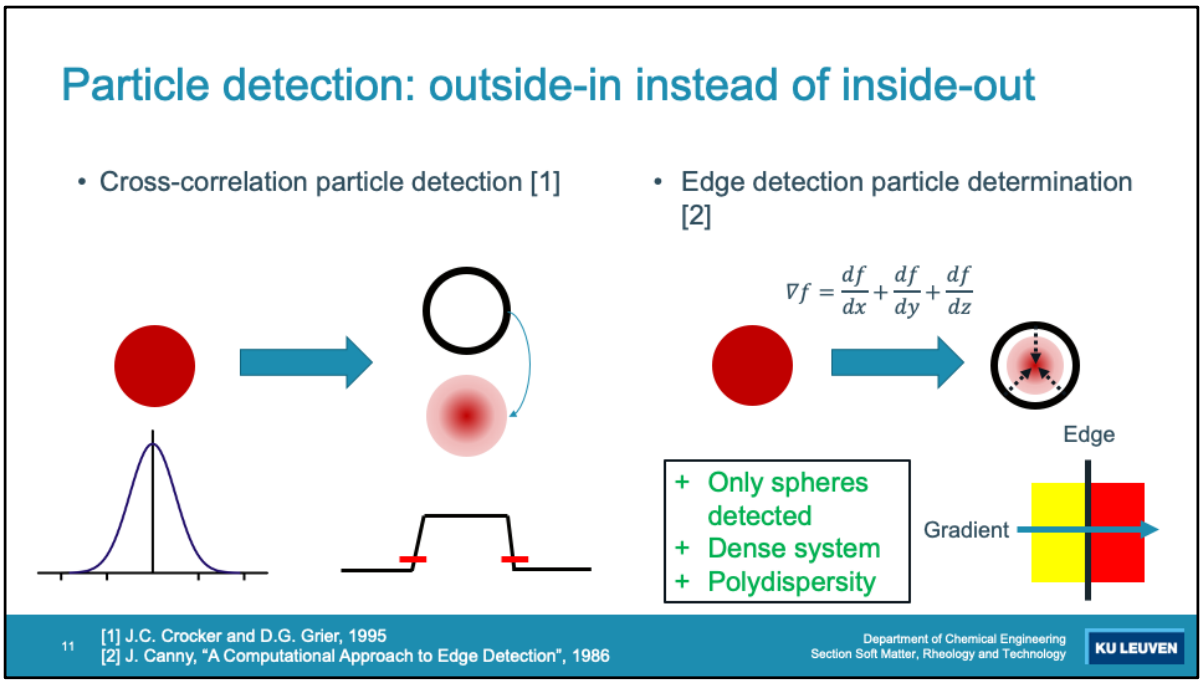

Moving on to the particle detection part, we see on the left a schematic of our previous approach based on the most widely-used particle detection program of Crocker and Grier. The image is convoluted with a Gaussian blur filter, which ideally transforms a particle in a bright center. These bright centers are detected in the next step with a cross-correlation mask. The radius is then determined by using a minimum cut-off intensity. The detection efficiency is very sensitive towards the size chosen for the Gaussian blur and the detection mask. Especially for a concentrated, polydisperse system, accidents are bound to happen: detecting two particles as one, or the other way around.

This is why the edge detection approach on the right was chosen. At the edge of the particle, a jump in intensity occurs. Thus, taking the image gradient, leaves us with these particle edges. For spheres, we have a huge advantage, in the sense that all gradients will point towards the center of the sphere. Next we vary the radius and let the edge pixels cast a vote in the direction of their gradient. The particle centers will be the pixels with the largest number of votes and will appear as bright centers. This process is called Hough transform (pronounced like tough). These bright centers can again be detected using the Crocker and Grier algorithm. Knowing the center and edge pixels, we can perform a least-squares fit of a sphere to determine the radius. For polydisperse samples, this approach is substantially more accurate.

To give you an illustration of how the edge detection works, Jens added a picture of himself (on the right). In this picture, the grass, for example, is bright so it has a high pixel value, while the darker shadows and the black dog have a low pixel value. Calculating the image gradient reveals the edges, which are the starting point for the detection. By the way, a lot of things are possible at this point. For example, you could try to extract from the right image the location of the laptop by looking for straight lines using the Hough transform. You can imagine though that in 3D, the computational cost of finding such specific shapes increases drastically.

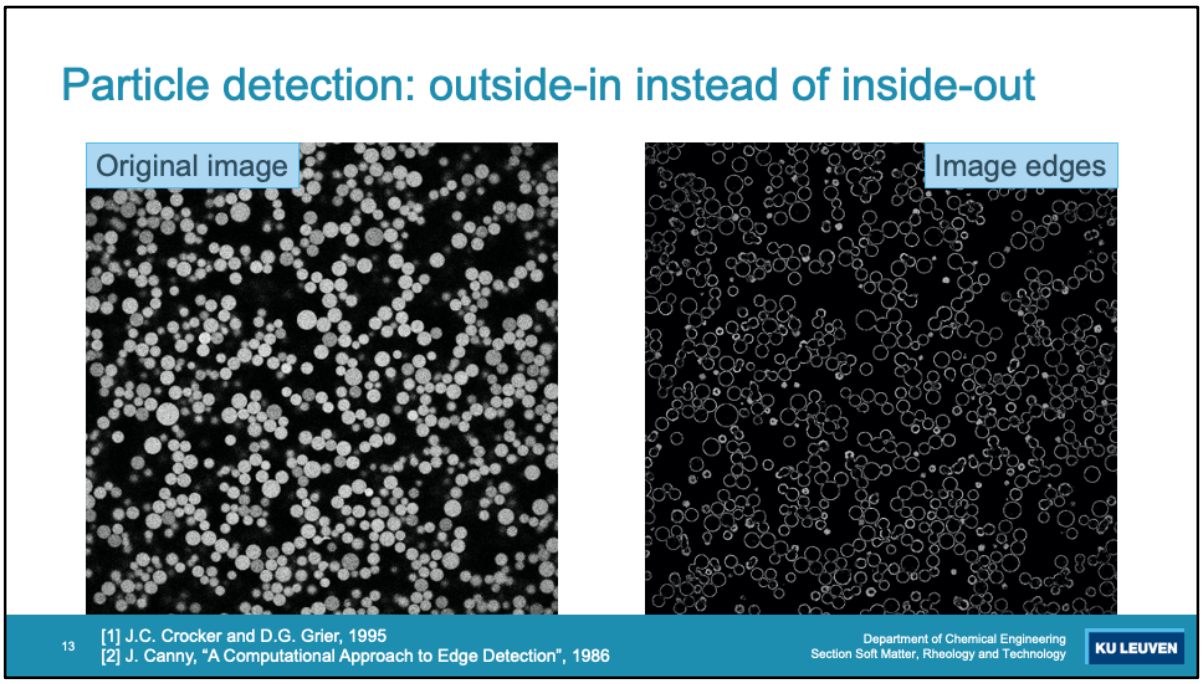

Luckily, as I mentioned before, the spherical particles greatly simplify the Hough transform step. All the pixels that remain on the right image point towards the center of their respective particle. By using a varying radius, we can find particle centers for this polydisperse, dense system.

Maybe I should make a short clarification for those of you wondering about the 3D detection. This is one 2D slice of the 3D image, which consists of taking 2D images at different heights in the sample. The particles which are not in focus on the left image, will be in focus on another slice. For the particle detection, this means their gradients point towards 2D slices above or below this one.

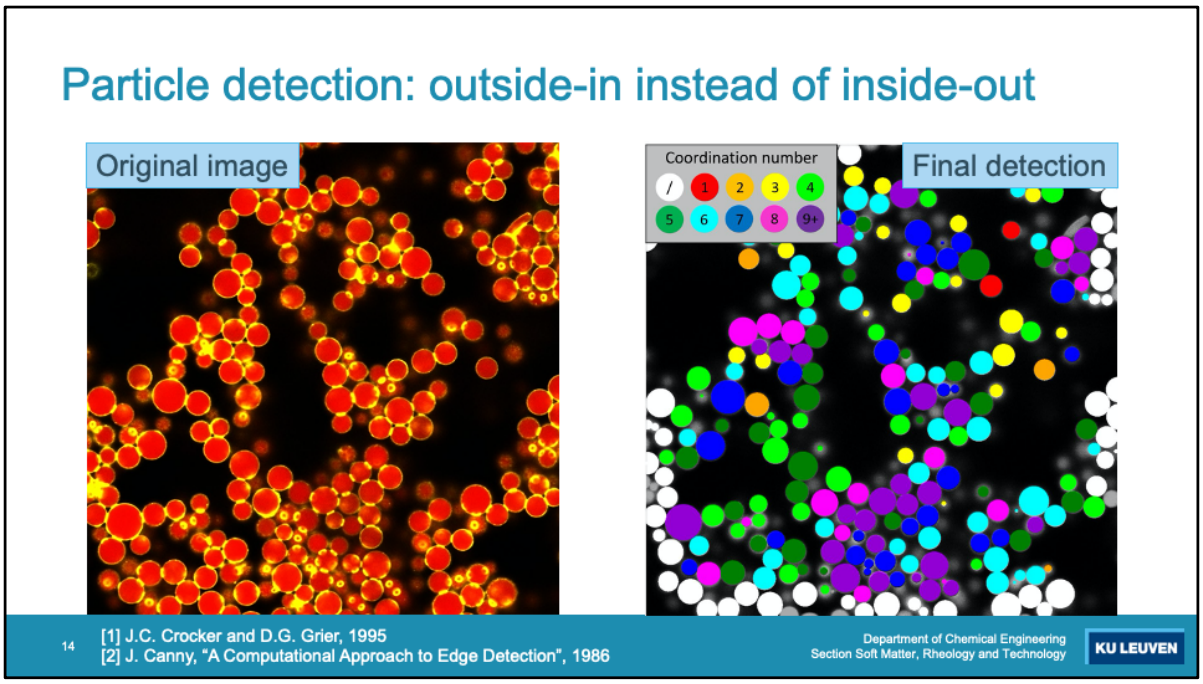

So to summarize, we start from a confocal image consisting of two colour channels: a yellow secondary fluid channel, which we don't really use for detection at this point, and a red particle channel. Using the edge detection and Hough transform we determine particle positions and radii. Once these are known, we can analyze the network using graph theory, for example with the coordination number. The image on the right shows particles with a low coordination number in red and orange, while high coordination numbers are shown in blue and purple. Particles at the edges are marked white, since we can't know their real coordination number. We considered two particles in contact, if their mutual distance falls below a threshold value. In reality, neighbouring particle connected by a bridge are in contact, but due to the resolution of the microscope and the accuracy of the detection, we chose the threshold equal to 6 pixels (0.85 µm).

A valuable upgrade to this code, would be to detect the bridge size and shape using the secondary fluid channel. This way, we can give a weight to each bond which will respresent the bond strength. When bonds start breaking under shear, we can quantify if the bond breaks due to low strength or its position in the network.

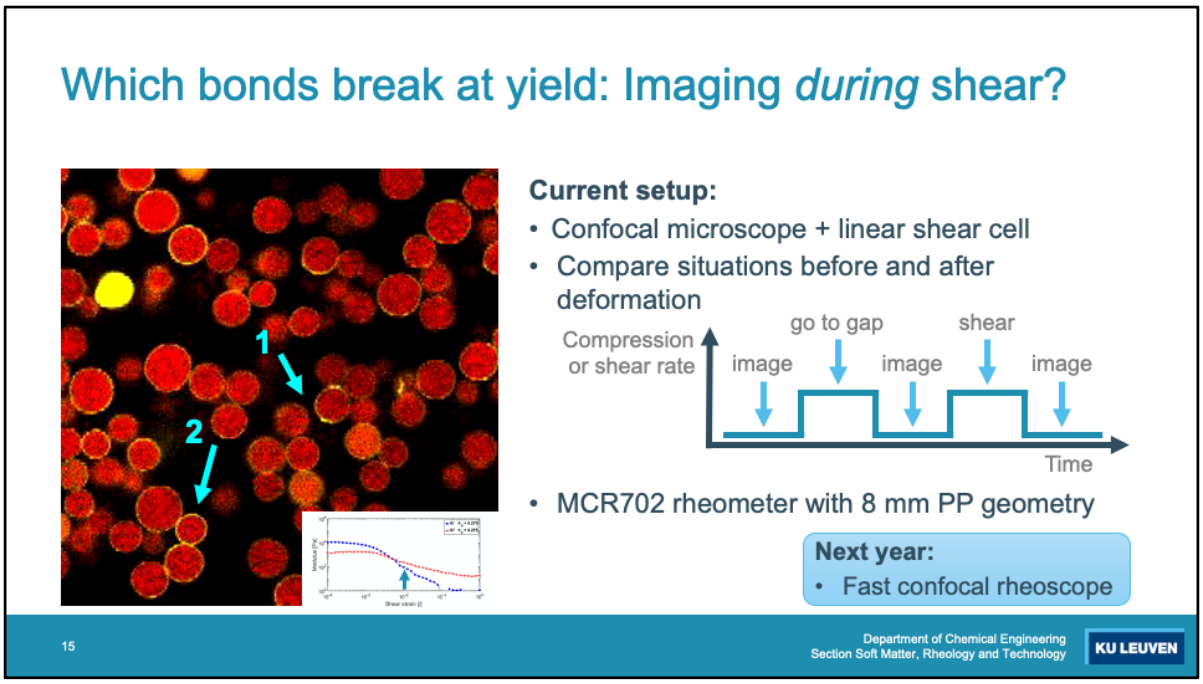

In this project, we want to go beyond the static measurements to investigate how the structure changes in response to external shear. In the video on the left, you can see the particle network deform and rearrange. There are two separate re-arrangement events. In 1, the particle attaches with its neighbor at about 6 seconds. In 2, the bond between these particles breaks at about 9 seconds. It's interesting to note that this video is taken just above the material flow point (crossover between G' and G''). If the material flows at this point, why do we only see two small events? Is this because most of the deformation happens in another location or are these two events critical in breaking the network structure?

To answer this question, we need to image the full network in 3D, ideally taking large images encompassing many particles. In our current setup, we have a linear shear cell attached to the confocal. The linear shear cell uses two microscope plates to deform the sample linearly, meaning that deformation is uniform regardless of the local x- and y-position. However, the speed of the confocal limits the size and deformation we can measure without distorting the image. To overcome this limitation, we have chosen to alternate between deforming and imaging. Since there is a sample-spanning network preventing particle motion in the absence of shear, we do not expect this periodic deformation profile to greatly affect the sample. Further, if the deformation is small, we can track the motion of the individual particles. Since the linear shear cell uses piezoelectric actuators, we cannot obtain stress measurements during deformation, so we must supplement this data with measurements on the rheometer.

Next year, we plan to attach a rheometer to our fast (sheet) confocal to take simultaneous deformation and stress measurements.

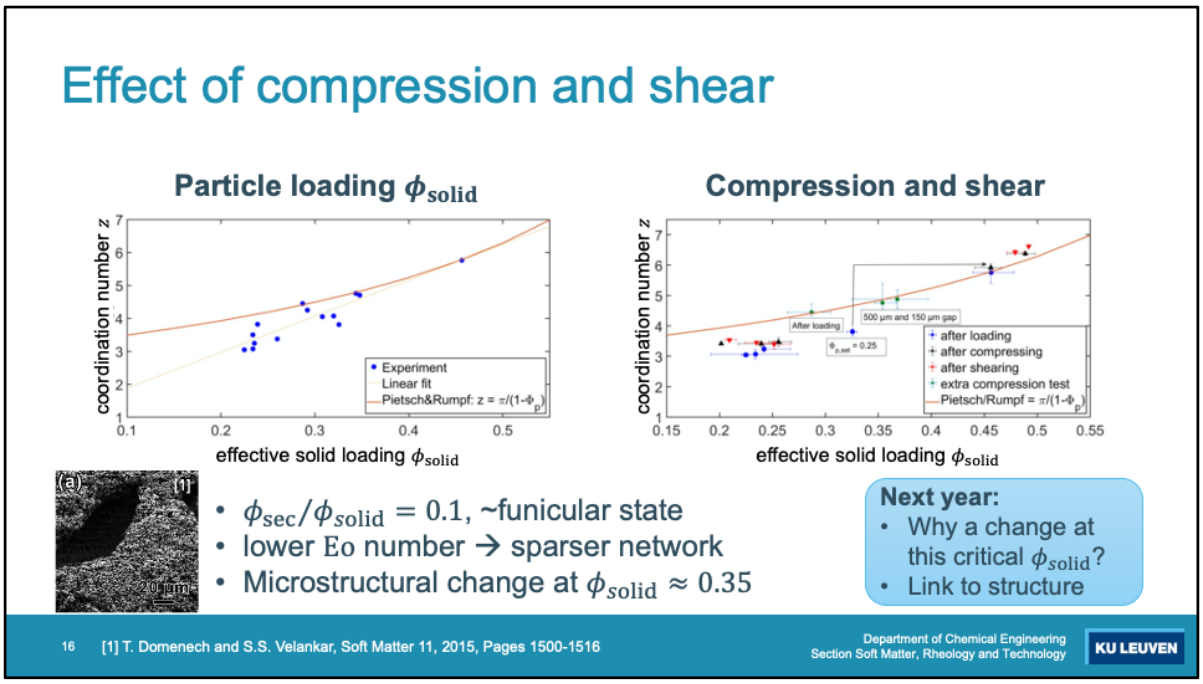

With our existing setup, we can still obtain a lot of information about the sample. Here, we show the effect of both particle loading and subsequent compression and shear on the coordination number z.

The coordination number obtained for different effective particle loadings is shown on the left for at $\phi_{sec}/\phi_{solid} = 0.1$ (near the funicular transition). The coordination number fits the trend proposed by Pietsch & Rumpf, $z = \pi/(1-\phi_{solid})$, at high loading. At lower solids, the coordination number deviates from this granular prediction and is shown with a linear fit. The Eötvös (or Bond) number, the ratio of capillary to gravitational forces, is typically smaller than unity ($\mathrm{Eo} \approx 0.01$ to 0.1) in granular matter but is much larger than for capillary suspensions ($\mathrm{Eo} \approx 10^{-5}$ to 10^{-6}). This produces sparser network in capillary suspensions. When the particle loading is high, however, the total weight of the clusters overcomes the capillary force to produce denser packings with more neighbors. The transition between the capillary-like and granular-like systems occurs at a volume fraction around $\phi_{solid} \approx 0.35$. This matches the results of Domenech and Velankar who observed large, capillary clusters (image) at $\phi_{solid} = 0.4$.

With compression and then shearing, the coordination number increases slightly, but there is no shift in the effective volume fraction ϕ_{solid} denoting compaction of the network for the sparse networks. At an initial volume fraction of $\phi_{solid,set} = 0.25$, however, the solid fraction increases dramatically to a value $\phi_{solid} = 0.46$. The even higher set volume fraction of $\phi_{solid,set} = 0.46$ also increases during the compression step. While these two points exhibit a strong resistance (high normal force) during the compression, they still compact more than the capillary-like samples. The shift in these

higher volume fraction samples follows the prediction of Pietsch and Rumpf.

…

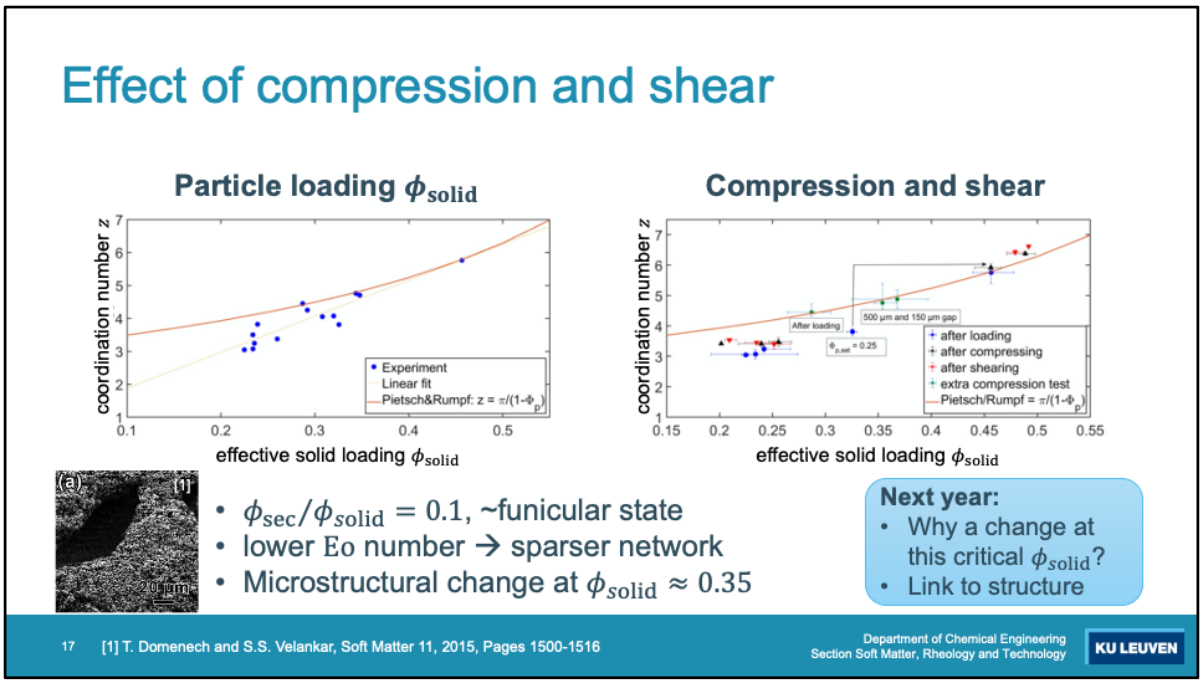

Interestingly, we conducted an extra experiment at a slightly lower set volume fraction of $\phi_{\text{solid,set}} = 0.3$. Unlike the previous experiment, the initial coordination number is higher, fitting to the granular prediction. This increases with compression to a gap of 500 µm and then subsequent compression to a gap of 150 µm, but the change is less pronounced than the previous transitional sample.

To understand the differences between the capillary-like and granular-like systems and to understand why at transition is observed at this critical ϕ_{solid}, we will continue these experiments this next year. We want to make a clear link with the structure and want to understand why two networks, both in the transitional region, behaved so differently.

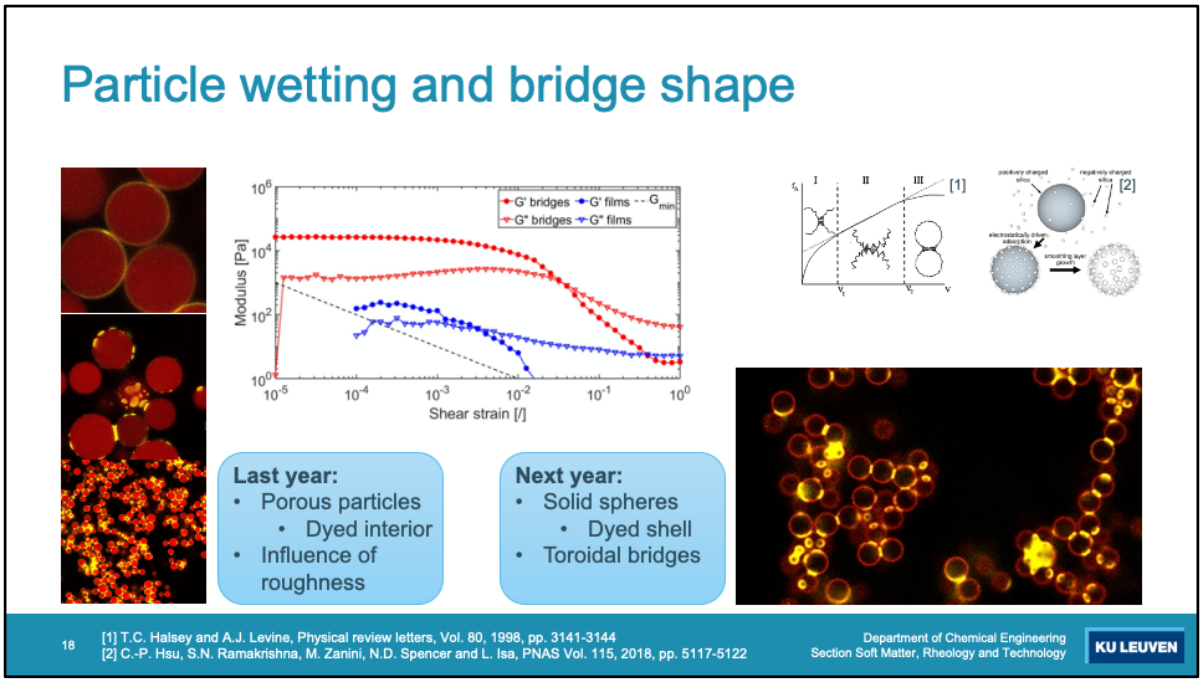

All the experiments performed so far, started from the same porous particles. After dyeing the particles, these pores are partially sealed off with a modified Stöber reaction to prevent, usually, the secondary fluid from being absorbed into the particles. However, as you see on the left, this resulted in different wetting behaviors which we assume to be caused by the surface roughness that remains after the pore closing reaction. At the top, we have a batch where only the surface asperities are wetted, forming a liquid film around the particles, without capillary bridges visible in the micrographs. In the middle, we see some sort of liquid patches on the particle surface, but not the toroidal or cylindrical bridge shape we ideally expect. The bottom image shows a funicular sample which did have toroidal bridges. Consistently, getting toroidal bridges proved to be difficult, due to the irreproducibility of the particle processing steps.

The rheological data shows the huge difference in moduli between proper bridges and films. The red data is obtained by making the same particles used for the blue data slightly more hydrophobic. Theoretically, a higher contact angle should correspond to a decrease in strength. However, this made it so the particles changed their wetting behavior from films to bridges, increasing both moduli by 2 orders of magnitude. The flow point is shifted to the right, since the liquid bridges are able to stretch before breaking, while this is much lesser the case for the film particles. The coordination number data shown earlier, was mostly obtained with film wetted particles.

…

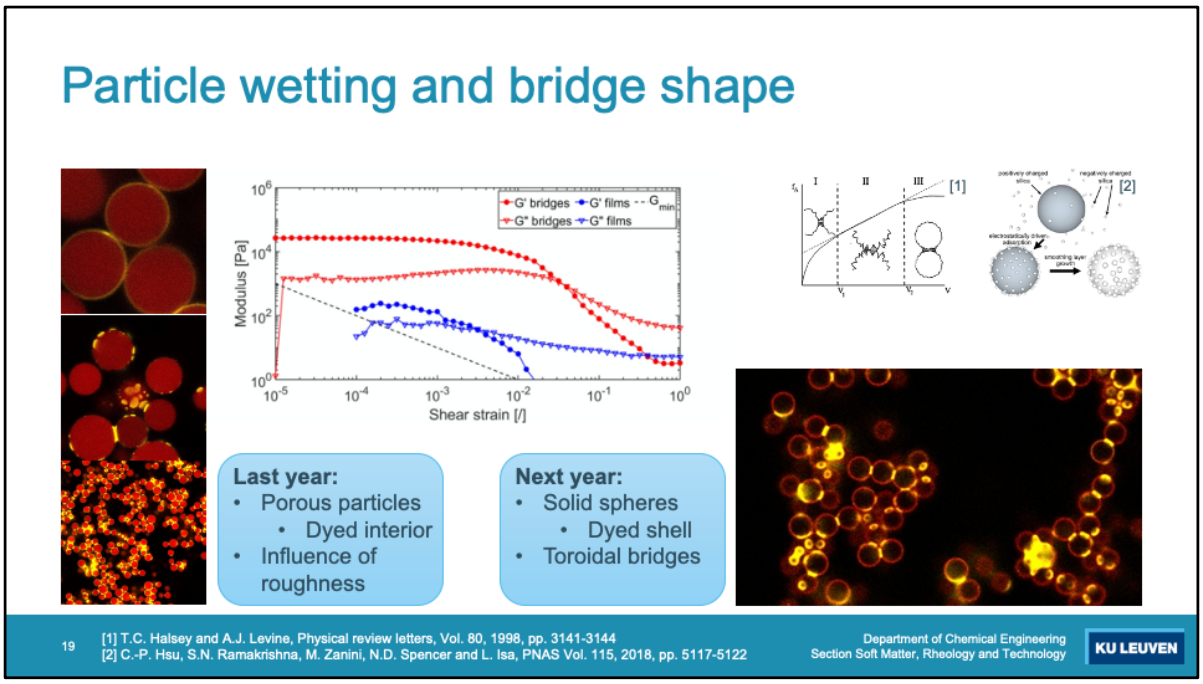

The possibly crucial influence of surface roughness will be investigated in detail next year by a Master thesis student. In this project, silica nanospheres will be adsorbed onto a micron-sized particle to create raspberry-like particles with varying roughness. We can hopefully recreate the three wetting behaviors on the left purposely, and identify the transitions from asperity wetting, to roughness wetting and finally toroidal bridges for which the surface roughness does not matter anymore compared to the curvature of the particle.

An obvious way to avoid the roughness problem is to switch to non-porous particles with a dyed shell. A batch of these was recently bought, and a confocal micrograph is shown on the bottom right picture. As you can see, the interior of the particles is no longer dyed. If we recall the two main particle detection methods, the cross-correlation Crocker/Grier algorithm would not be able to detect these particles. On the other hand, with edge detection and Hough transform, this becomes possible, but might introduce some difficulties which are shown on the next slide. These particles should however always show the same wetting behavior.

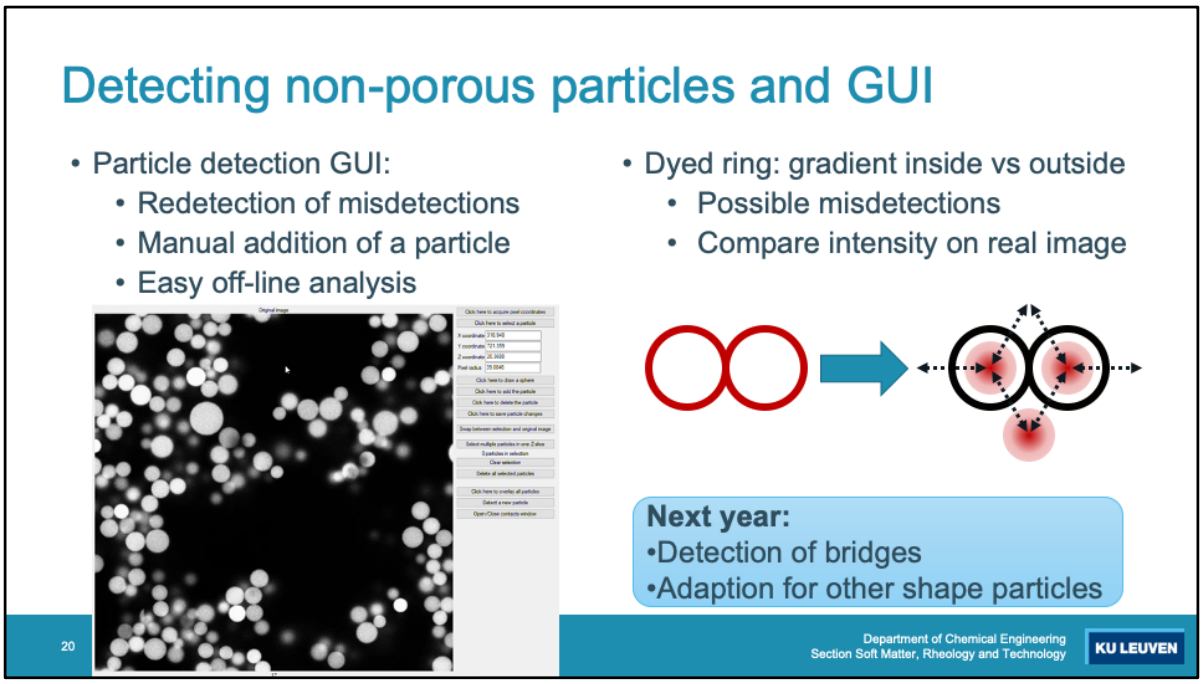

During the laboratory shutdown, we have had a chance to improve the particle detection. First, we have improved the detection of particles. These misdetections occur when small particles are detected as a single larger particle or larger particles are split into multiple smaller particles. One of the ways we have improved this detection is by implementing a GUI (shown in the video) where we can select particles, either redetecting their radii and centers, or manually select an approximate particle center and size to improve the detection. This GUI also lets us easily analyze the networks offline and better visualize the connections between particles so that we can understand the changes in the networks and link these changes to an applied deformation.

The switch to particles with a dyed ring, while it will undoubtedly be better to control the structure, presents some challenges in the detection of the particles. With the fully dyed particles, there is a clear gradient between the inside and the outside of the particles. This may result in possible misdetections where the gradient vector – which can now point both ways – can lead to phantom particle being detected near the intersection of two particles. To prevent this error, we can compare the intensity differences in the real images, looking for specific shaped (e.g. round) particles and use the secondary fluid channel to further give information about the inside or outside of the particle.

Next year, we will expand this detection algorithm to detect the size and shape of the bridges, a task that is again easier when we use the nonporous particles since the particle volume does not need to be “subtracted” from the bridges. We can also adapt the algorithm to adapt particles of different shapes. This detection should be more straightforward than the cross-correlation method since we will not have to use masks

with many different orientations.

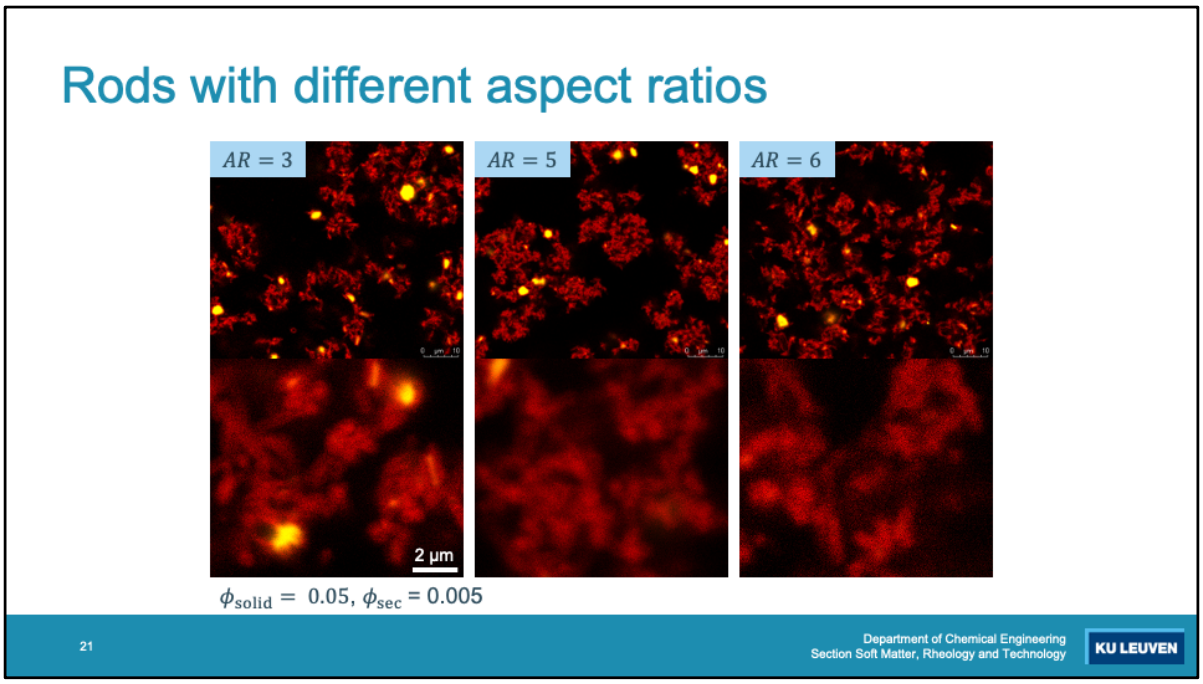

With the help of an exchange student from Delaware finishing her Master thesis in Leuven, we have also had the chance to start investigating the structures formed by rods with different aspect ratios. Here, we can see three examples of networks made with the same solid and secondary fluid fractions. At first glance, you can see the clusters with the lower aspect ratio form denser clusters than the higher aspect ratio. This result is consistent with experiments with particles with other attractive interactions where rods tend to percolate at lower volume fractions than spheres and pack into less dense clusters.

Although these experiments point to an interesting phenomenon, we haven't had the chance to finish due to the shutdown of the labs. Once we get a chance to continue, we will probably opt for slightly larger rods since these particles are too small to detect properly and any, slight mismatch in the index of refraction causes diffraction making such detection even more difficult. While we certainly anticipated this might be a problem, the synthesis route was easier.

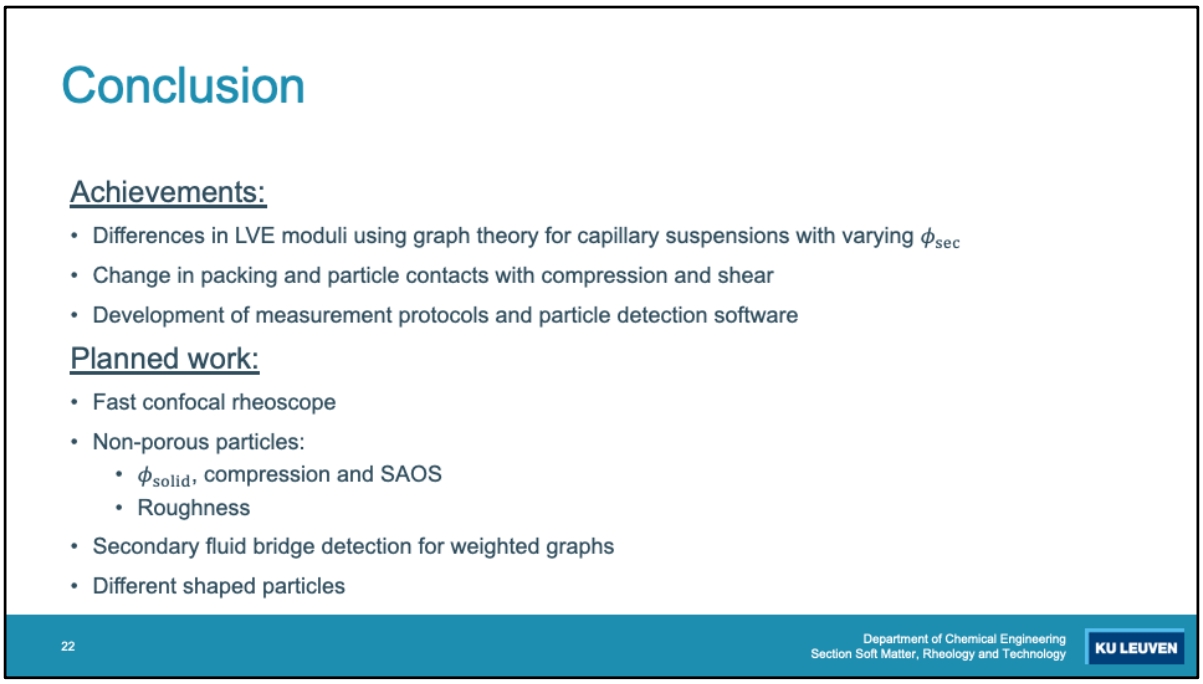

This year we were able to finish the analysis of previous experiments, which showed how measures from graph theory can be used to quantify the transitions that occur with increasing amounts of secondary fluid and can be used to predict the rheological properties of these materials in the linear viscoelastic region. We also conducted initial experiments on samples with different volume fractions, denoting a change from capillary-like behavior at low ϕ_{solid} to granular-like behavior at high loading.

We also used the shutdown period to further improve the measurement protocols and particle detection software. We now have much more accurate detection of the particles with fewer misdetections. These misdetections, caused by intensity differences within the larger particles, will be further improved in the next year when we switch to non-porous particles.

We also observed a curious behavior this year where the roughness of the behavior influenced the bridge type that could be formed. A master student will more rigorously investigate this influence next year. We will also use the non-porous particles to repeat the experiments at different solid fractions and, by including the detection of the secondary fluid bridges to create weighted graphs, we should hopefully link this to the forces between particles and clusters.

Finally, using a fast confocal rheoscope, we can get more information about the dynamic changes in these networks during the shear, more closely linking the stress measurements with the structure.

With that, we want to thank you for listening to (or reading) this presentation. If you have any questions, please feel free to contact me at erin.koos@kuleuven.be

Finally, we would like to welcome you – in better times – to come visit us in Leuven. We are happy to host the ECIS general meeting next year and promise that Willie will not want for good beer.

Characterization of Spray Drying Nozzles at Industrially Relevant Conditions

Jerry (Siyu) Chen

Nasser Ashgriz

Isaac Jackiw

ARR-02-15

May 25, 2020

UNIVERSITY OF TORONTO | Department of Mechanical and Industrial Engineering

IFPRI International Fine Particle Research Institute

Project Objectives

UNIVERSITY OF TORONTO

1. **Develop benchmark data for spray characteristics at different:**
   - Fluid properties: viscosity and polymeric effects
   - Pressures
   - Orifice diameters
   - Nozzle types:
     (1) Pressure Swirl Nozzles and
     (2) Twin-Fluid Nozzles

2. **Develop correlations for spray characteristics**
   - Physics based models based on observation and classification of the near nozzle primary atomization processes at different operating conditions.
     - Sheet preformation-based model for swirl nozzles
     - Droplet breakup-based model for twin fluid nozzles

3. Develop correlations for the effect of ambient temperature

(1) Pressure Swirl Nozzle

Jerry (Siyu) Chen

Testing Facility

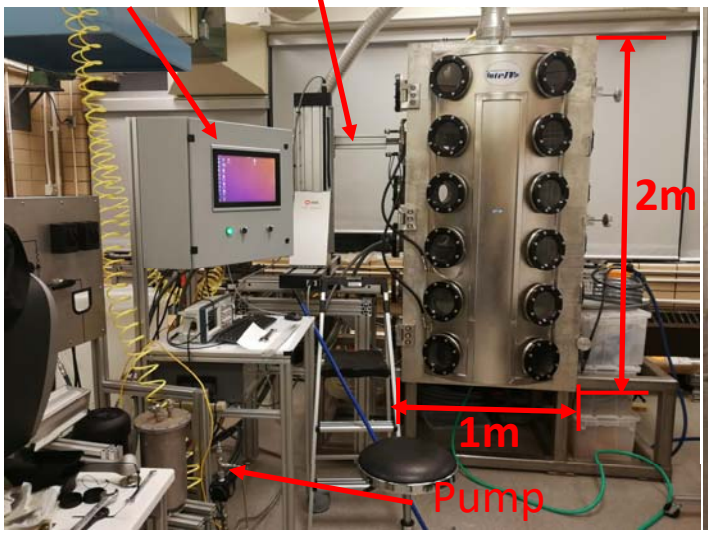

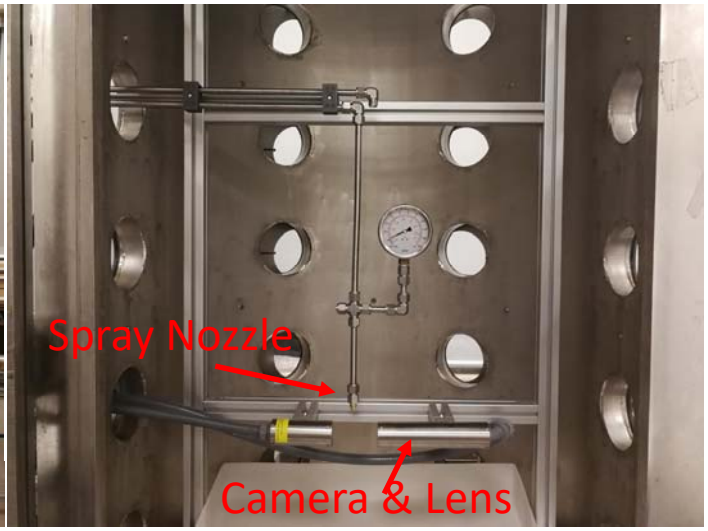

Swirl Nozzle with Swirl Insert

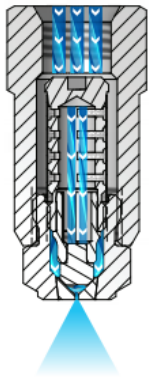

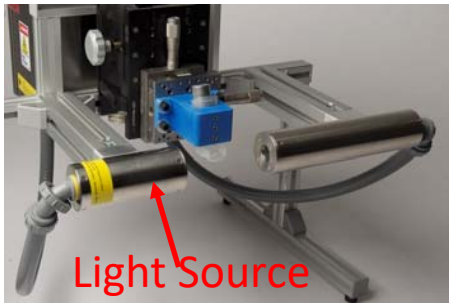

Imaging System
5μm resolution,
50 nanosecond flash

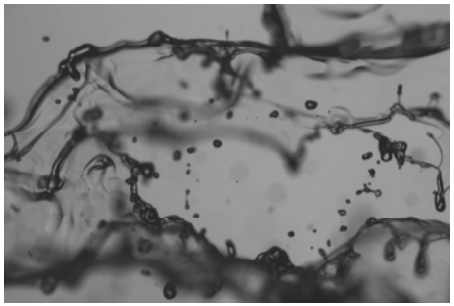

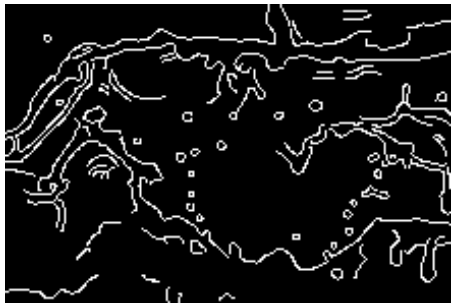

Imaging & image processing to determine droplet sizes and ligament thicknesses.

Swirl Nozzle with Tangential Inlet

Image based Characterization

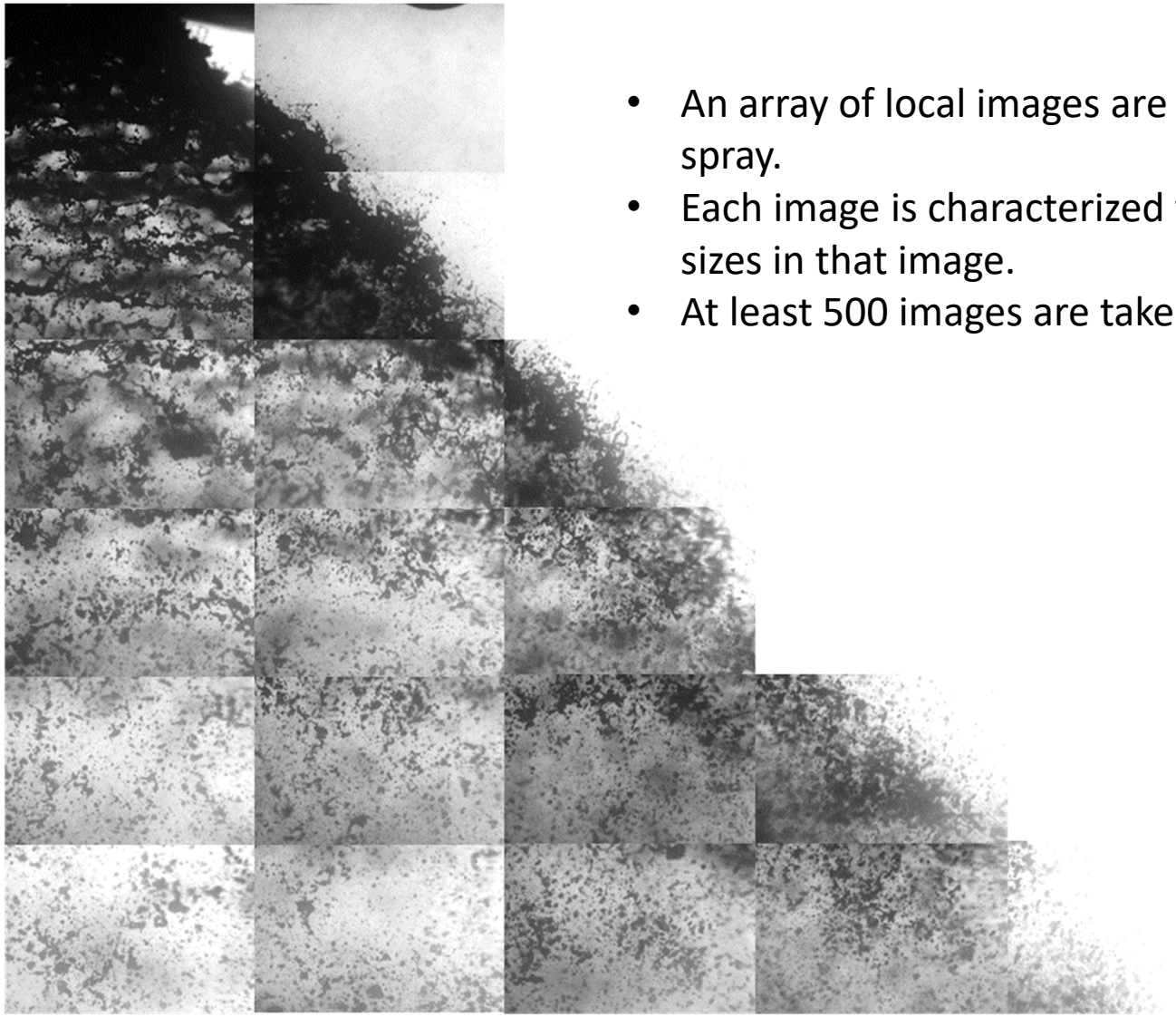

- An array of local images are taken to form the whole spray.
- Each image is characterized to determine the droplet sizes in that image.
- At least 500 images are taken for each position.

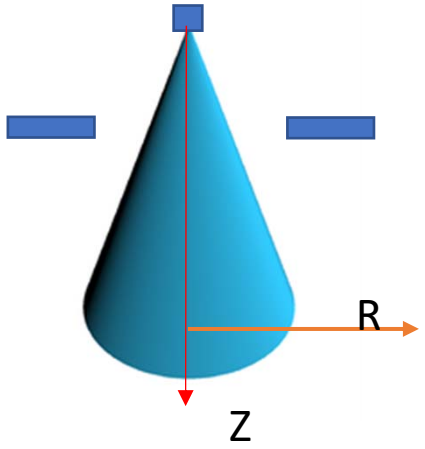

Testing Parameters

Nozzle Type (Orifice size)	Orifice Diameter
Spraying Systems Fine Spray Nozzle (FSN) (Swirl Insert)	0.02“ (0.5mm), 0.028” (0.7mm), 0.042” (1.1mm)
Spraying Systems SKH Nozzle (Swirl Insert)	0.02“ (0.5mm), 0.028” (0.7mm)
Spraying Systems WhirlJet Nozzle (WJN) (Tangential Inlet)	0.094“ (2.39mm), 0.109” (2.77), 0.129” (3.28mm)
Schlick 121V Nozzle (S121VN) (Swirl Insert)	0.014“ (0.36mm) 0.02” (0.5mm)

Fluid	Viscosity (cp)
Water	0.89
Acetone	0.316
60% glycerine	10.8
80% glycerine	60.1
5% HPMCAS/Acetone Solution	~5
10% HPMCAS/Acetone Solution	~30
Maltodextrin/Water Solution	60 to 308

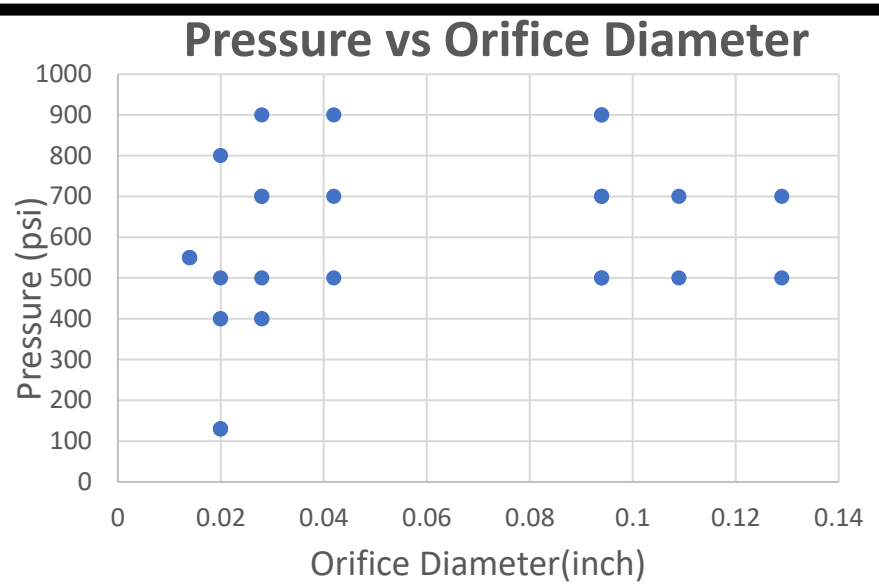

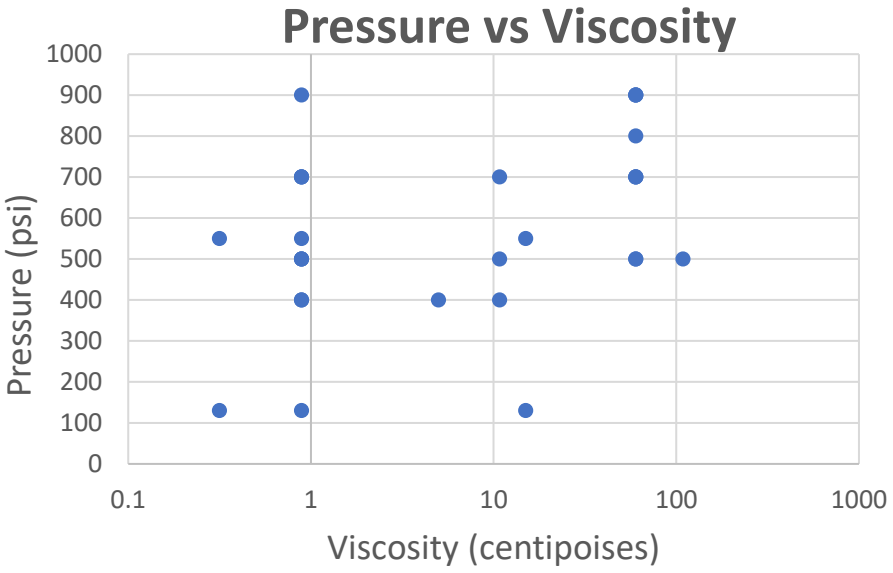

SMD in Radial Direction-WhirlJet Nozzle

$$SMD \downarrow \& \alpha \downarrow as\ P \uparrow$$
$$SMD \uparrow \& \alpha \downarrow as\ D_{nozzle} \uparrow$$

For the same nozzle and the same fluid, SMD_{max} reduces with increase in pressure, and the reduction is more at higher pressures.

Spray angle does not provide the location of SMD_{max}.

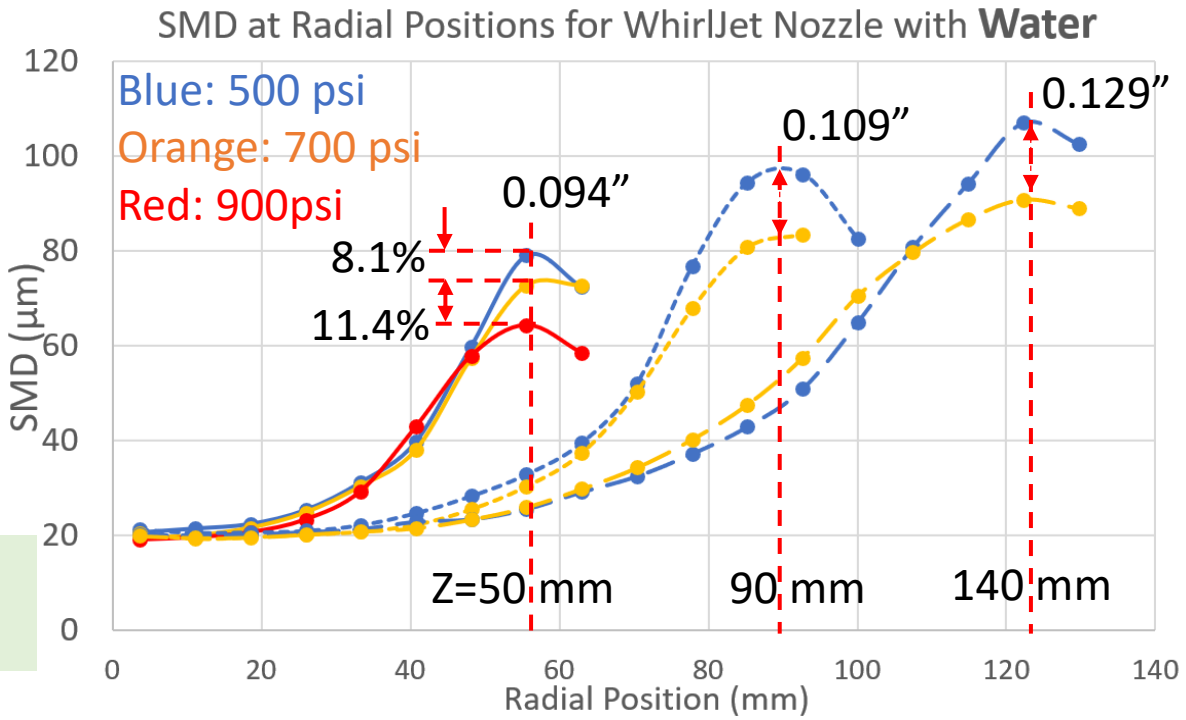

Orifice \ Pressure	SMD_{max} 500psi	SMD_{max} 700psi	SMD_{max} 900psi	Spray Angle 500psi	Spray Angle 700psi	Spray Angle 900psi
0.094”(2.39 mm)	79.1µm	72.7µm (-8.1%)	64.4µm (-11.4%)	89	82.2	75.4
0.109”(2.77 mm)	96.2µm	83.5µm (-13.2%)		81	77.4	
0.129”(3.28 mm)	107.3µm	90.8µm (-15.4%)		80	76	

Effect of Viscosity in WhirlJet Nozzle

$SMD \uparrow as\ \mu \uparrow$

At 900 psi,

SMD_{max} 64.4µm at μ=0.89cp to 146.09µm at μ= 60cp, (126%)

SMD_{global} 41µm at μ=0.89cp to 98µm at μ= 60cp (140%).

For high viscosity fluids, the location of SMD_{max} can change significantly

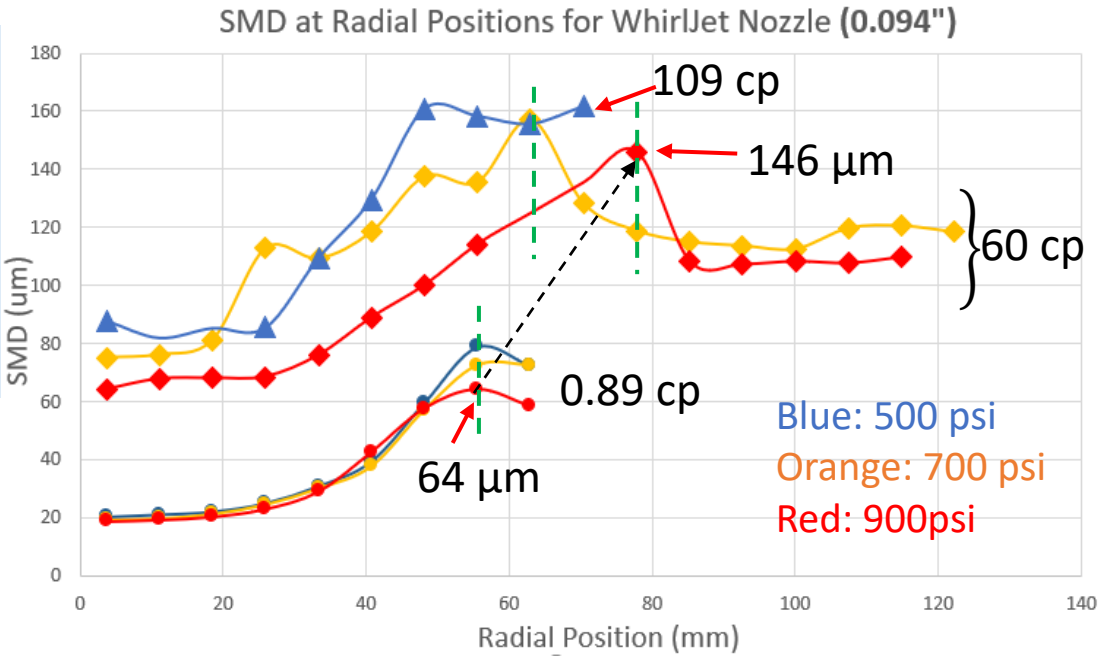

SMD_{max} and % of SMD reduced (in brackets) from the previous pressure level.

Orifice \ Pressure	Measuring Position	500psi	700psi	900psi
0.094”(0.89cp)	50 mm	79.1µm	72.7µm (-8.1%)	64.4µm (-11.4%)
0.094”(60.1cp)	200 mm		157.21µm	146.09µm (-7.1%)
0.094”(109cp)	135 mm	160.75µm		

Effect of Nozzle Diameter -FSN Nozzles

Whereas for low μ fluids:

$\boldsymbol{SMD \uparrow as\ D_{nozzle} \uparrow}$

For high μ fluids:

$\boldsymbol{SMD \downarrow as\ D_{nozzle} \uparrow}$

Poor atomization at **60 cp**

700 psi	SMD_{max}	SMD_{CL}
0.028”	112.3µm	110 µm
0.042”	108µm	76µm

For small nozzles & low $\boldsymbol{\mu}$, SMD_{max} does not reduce significantly as $\boldsymbol{P}$ ↑:
For 0.028” & 10.8cp: SMD_{max} reduces by 1% when P increases from 500 to 700psi, and SMD_{global} reduces from 58.39µm to 53.15µm, by 9%.

For high viscosity liquids, increase in pressure, reduces SMD_{max} more significantly, and more so for larger orifice nozzles.

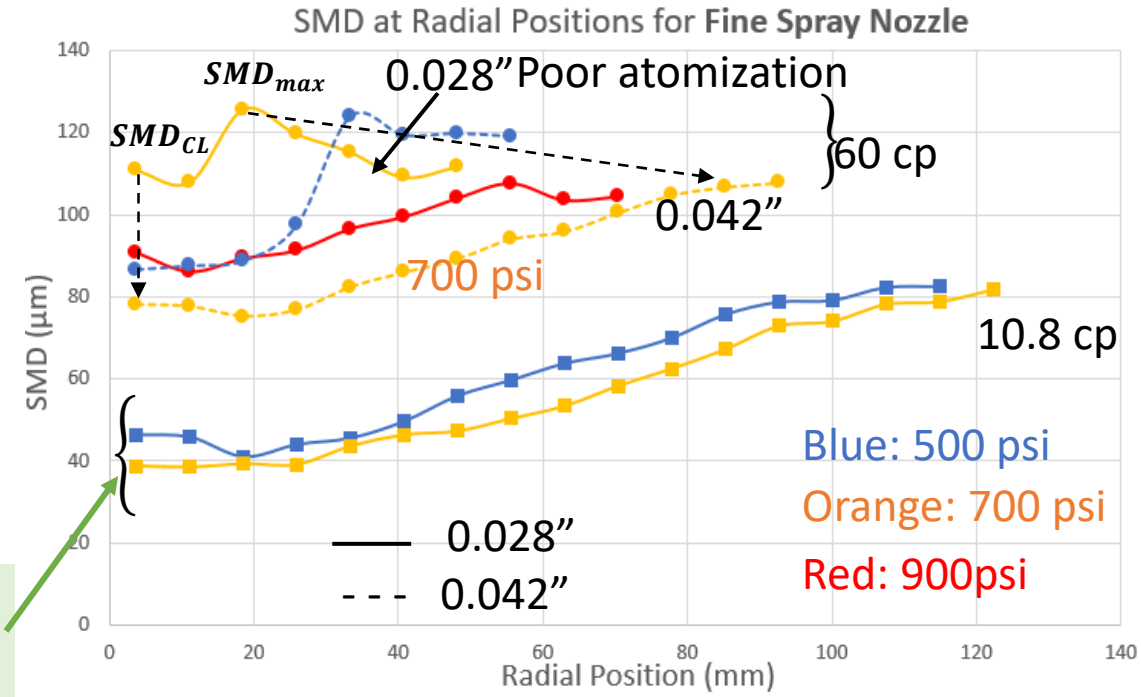

Measurements are at Z=200 mm

$\boldsymbol{SMD_{max}}$

Orifice \ Pressure	500psi	700psi	900psi
0.028”(10.8cp)	82.5µm	82µm (-0.85%)	
0.028”(60.1cp)		112.3µm	108µm(-4.2%)
0.042”(60.1cp)	120µm	108µm (-12%)	

Atomization Quality

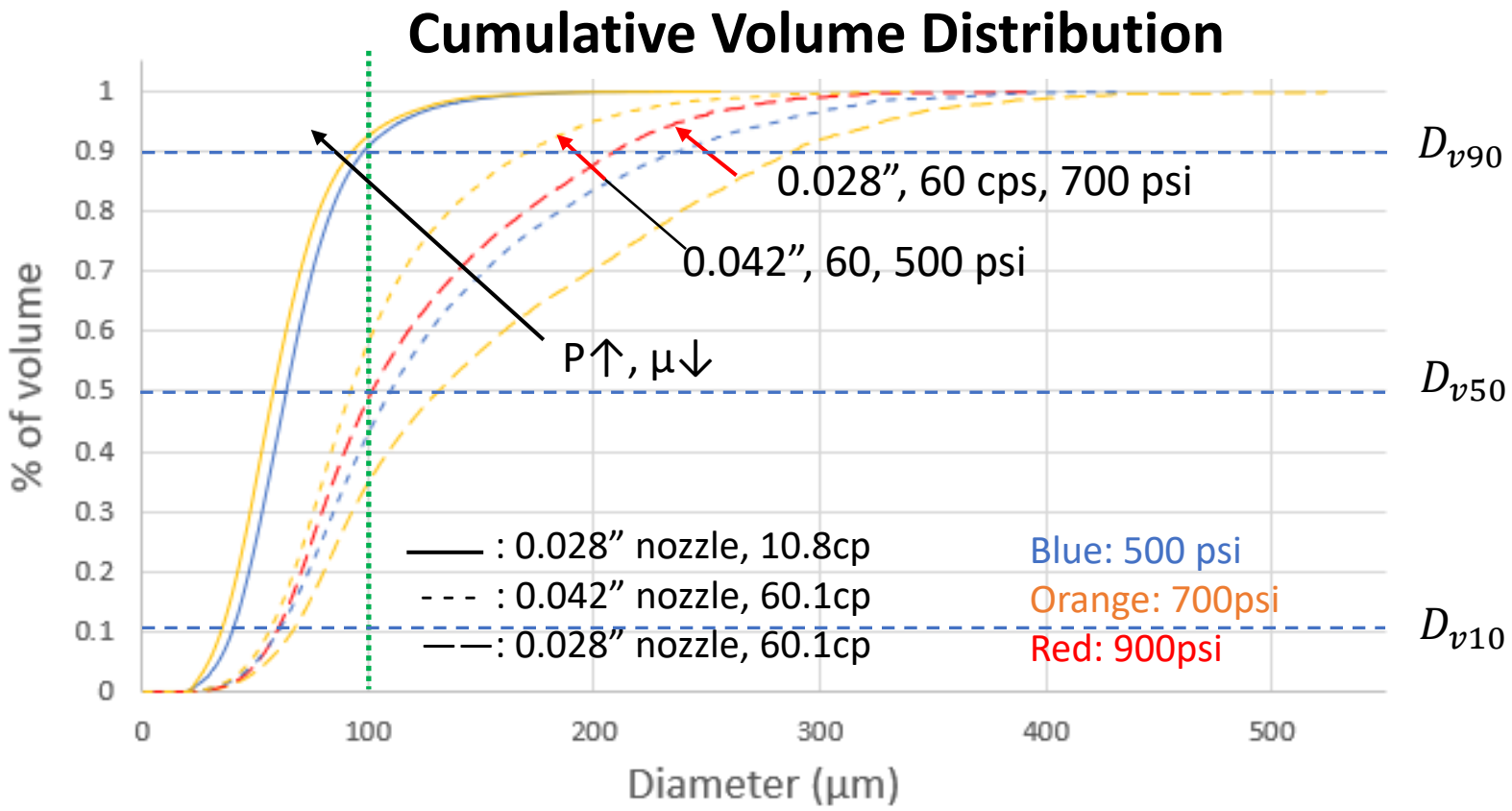

- Increase in pressure makes the droplet size distribution more uniform: More smaller droplets.
- For 0.028 nozzle with 10.8 cp fluid, droplets less than 100 µm take up 90% of the total volume, indicating a good atomization quality.

Particle Size Distribution

Viscosity influences the form of the size distribution function.

If the droplet sizes are categorizes as small, medium and large, as pressure increases, the number of large droplets decreases and number of small droplets increase. This is observed for curves for 10.8 cp fluids atomized at 500 psi and 700 psi, respectively.
The span of the PDF curve decreases as well.

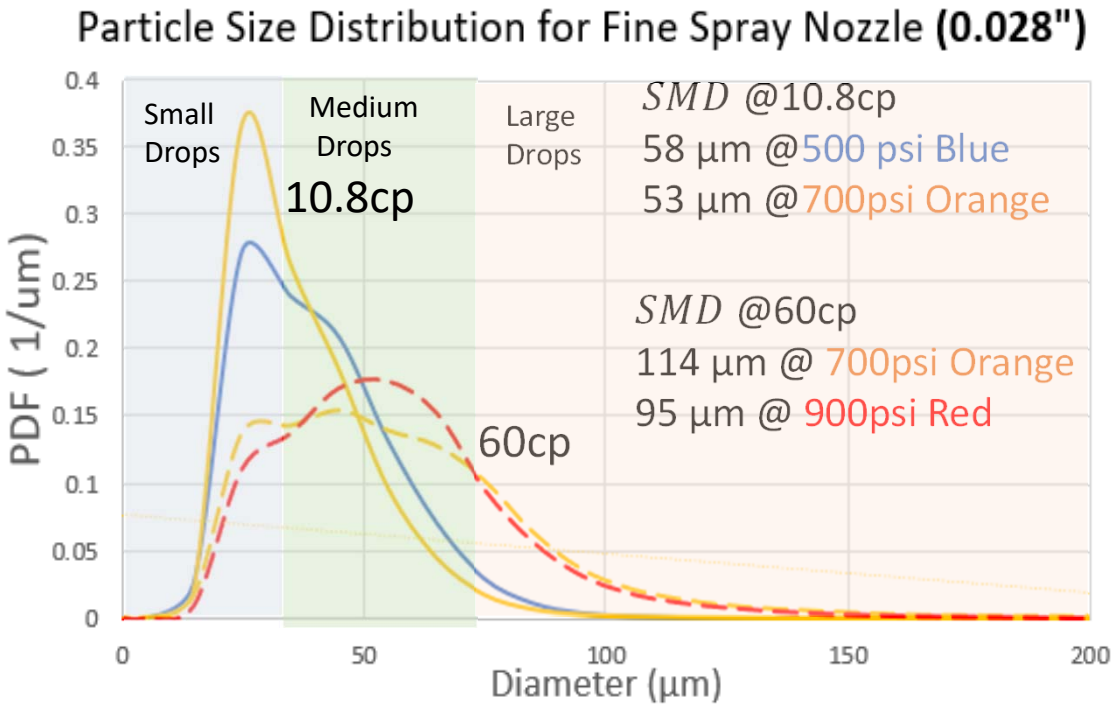

As viscosity increases, the number of large and medium size droplets increase, and the number of small droplets decreases (shown for 60.1 cp fluids atomized at 700 psi and 900 psi).

Effect of Pressure in high Viscosity Fluid Atom

UNIVERSITY OF TORONTO

- Generally, $SMD \downarrow as\ P \uparrow$
- However, size distribution change is not monotonic.
- The span of the distribution decreases at higher pressures: Span = $(\frac{D_{90}-D_{10}}{D_{50}})$:
- For 0.042" with 60.1 cp fluid, the span reduces from 1.42 to 1.12 as pressure increases from 500 psi to 700 psi.

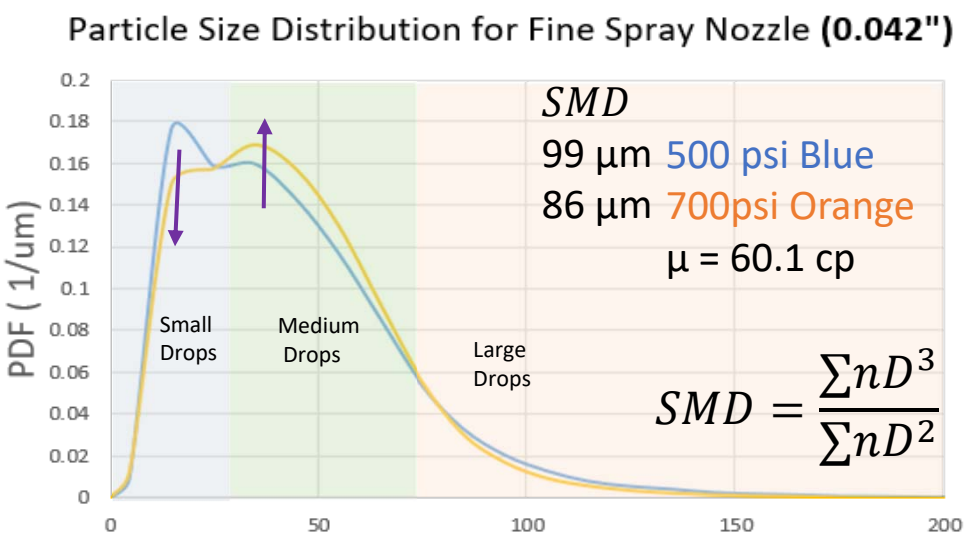

- The cumulate number distribution shows that the number of droplets below 64 µm are the same under both pressures. Above that, the curve for 700 psi increases faster than that of 500 psi.
- Since large droplets have much larger effect on the volume distribution and SMD, the SMD of 700 psi becomes smaller.

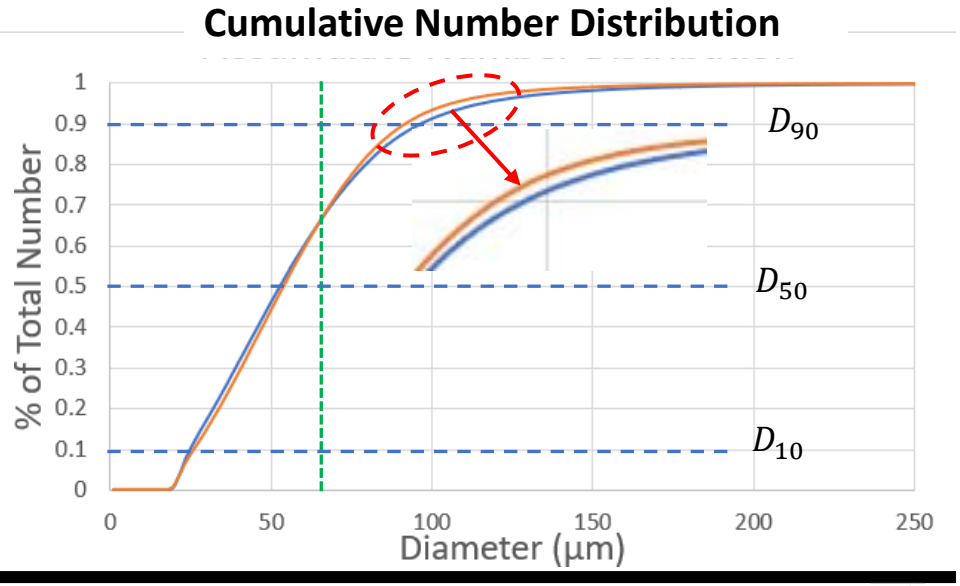

Breakup Mechanism

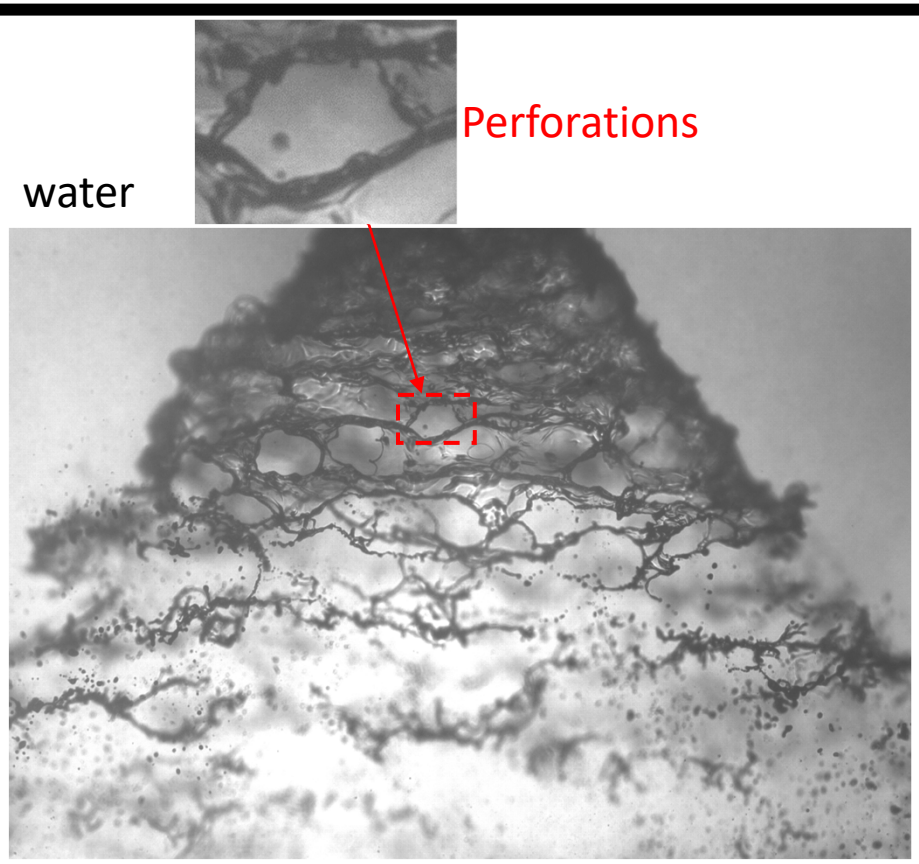

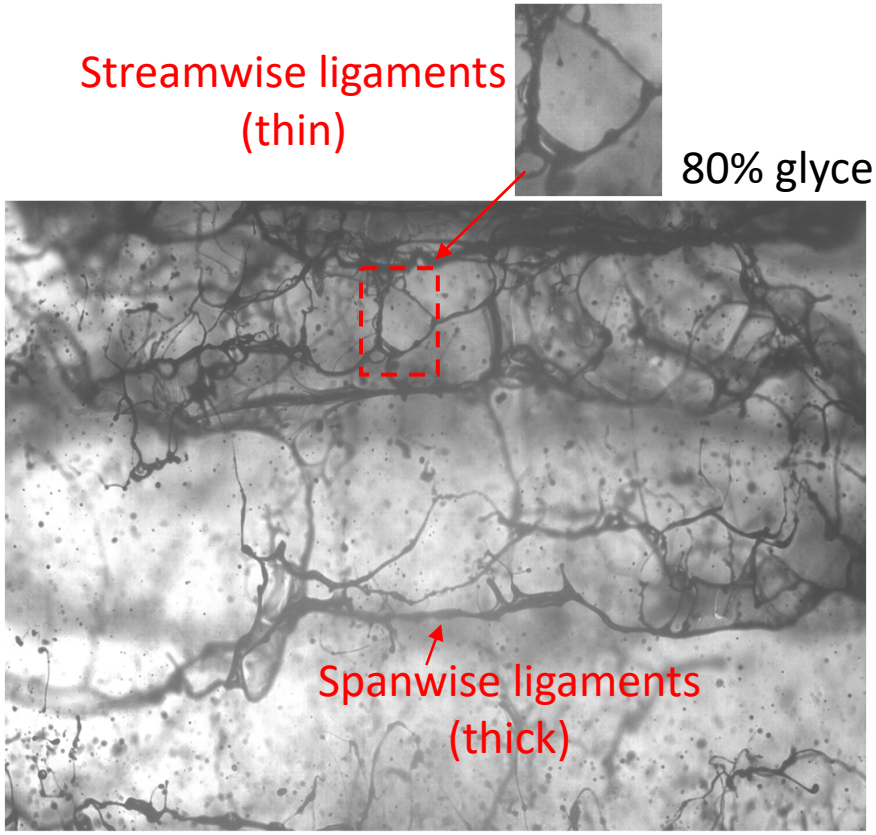

- Images show formation of surface waves; fluid accumulation at the wave crests and troughs, and a thin liquid sheet in between them.
- The liquid sheet thins out and eventually perforates.
- The wave crests and troughs form spanwise ligaments and collapse of thin sheets form streamwise ligaments.

Sheet Perforation-Based Model

- Kelvin-Helmholtz waves are generated on the conical sheet.
- Liquid accumulates on the wave crests and troughs, whose mass at the breakup is m_c, which will generate large ligaments and droplets with diameter:

$$D_L = \sqrt{\frac{4m_c}{\pi^2 D_b}}$$

D_b=Cone diameter at the breakup

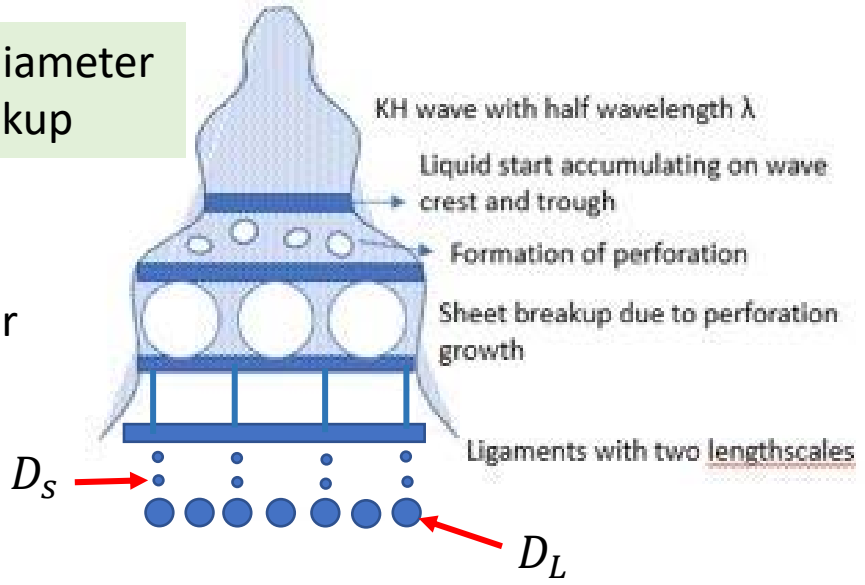

- Thin sheets form in between crests and troughs.
- Perforations occurs on these thin sheets.
- Perforations grow and form ligaments, which later breakup forming small droplets with diameter

$$D_s = \sqrt{\frac{4(m - m_c)}{\pi n \lambda}}$$

- Therefore, there are two different characteristic sizes in the spray. Each size is used to form a Gamma distribution. The overall PDF of droplets is the addition of both distributions:

Compound Distribution Model

$$PDF(d) = \underbrace{\frac{m_c}{m}\frac{1}{\kappa D_L}\frac{\nu^\nu}{\Gamma(\nu)}\left(\frac{d}{\kappa D_L}\right)^{\nu-1}\exp\left(-\nu\frac{d}{\kappa D_L}\right)}_{\boldsymbol{\Gamma_1}} + \underbrace{\left(1-\frac{m_c}{m}\right)\frac{1}{\kappa D_s}\frac{\nu^\nu}{\Gamma(\nu)}\left(\frac{d}{\kappa D_s}\right)^{\nu-1}\exp\left(-\nu\frac{d}{\kappa D_s}\right)}_{\boldsymbol{\Gamma_2}}$$

ν = f(We, Re, based on sheet thickness),
κ =f(wavelength of disturbance)

m_c, mass in the crests and troughs
n is the number of perforations.

The maximum number of perforations is given by $n_{max} = floor\left(\frac{\pi D_b}{\lambda}\right)$

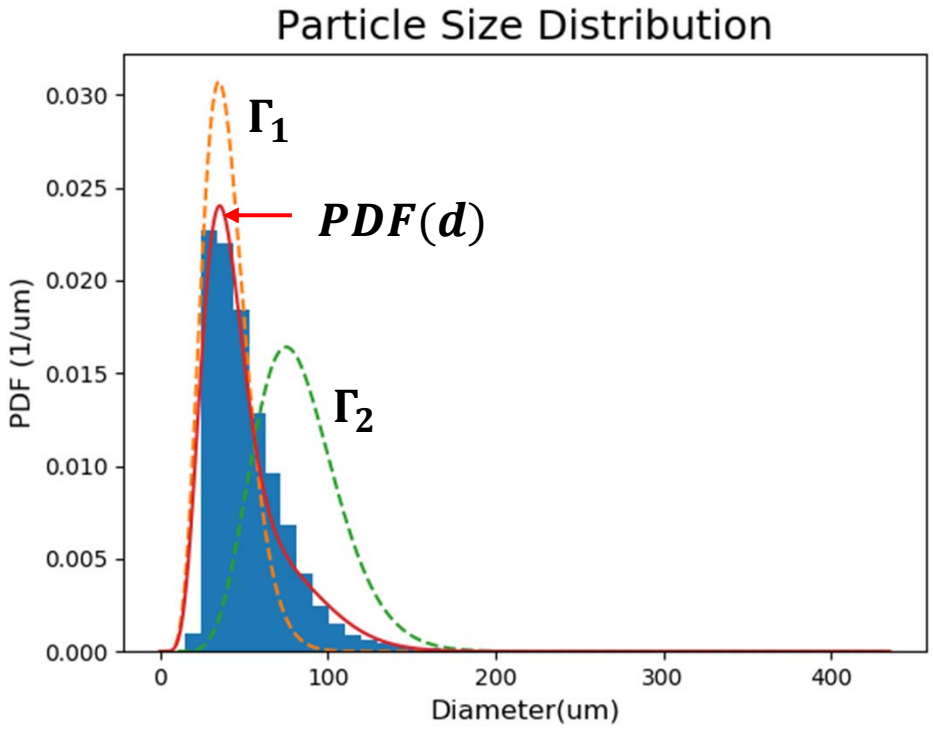

(2) Twin Fluid Nozzle

Isaac Jackiw

Testing Parameters

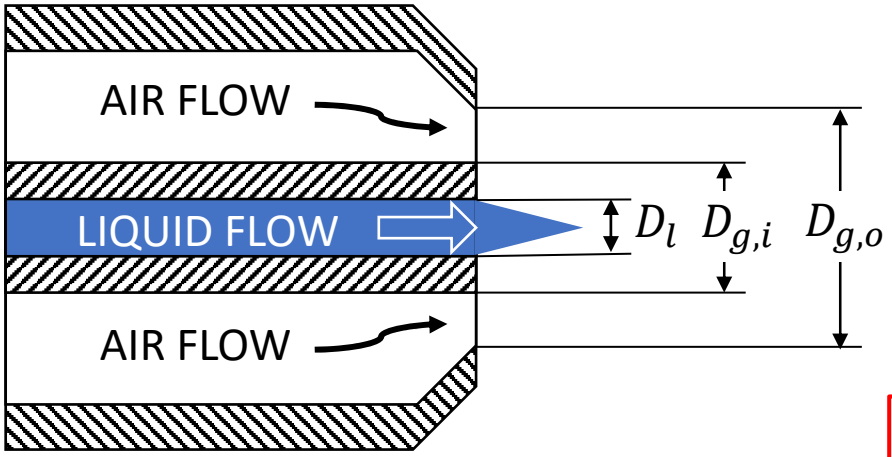

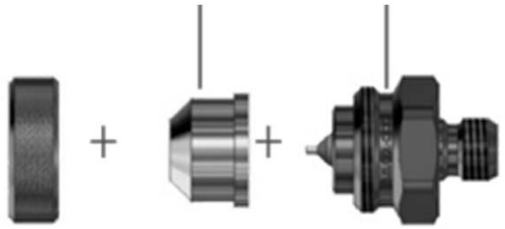

214 test points

Nozzle	D_l [mm]	$D_{g,i}$ [mm]	$D_{g,o}$ [mm]
Spraying Systems, ¼ J 2050-70	0.51	1.27	1.78
Spraying Systems, ¼ J 2850-70	0.71	1.27	1.78

Spraytec system

Nozzle	$\dot{m}_g$ [g/s]	$\dot{m}_l$ [g/s]	ALR	Distance from nozzle tip, Z [mm]	Liquids tested (viscosity)
SS-2050-70	0.22 – 1.28	0.33 – 1.0	0.2 - 4	80	Water and Glycerin mixtures
SS-2850-70	0.22 – 1.28	0.33 – 1.67	0.13 – 3.8	20, 40, 60, 80, 100	

Two-Fluid Nozzle

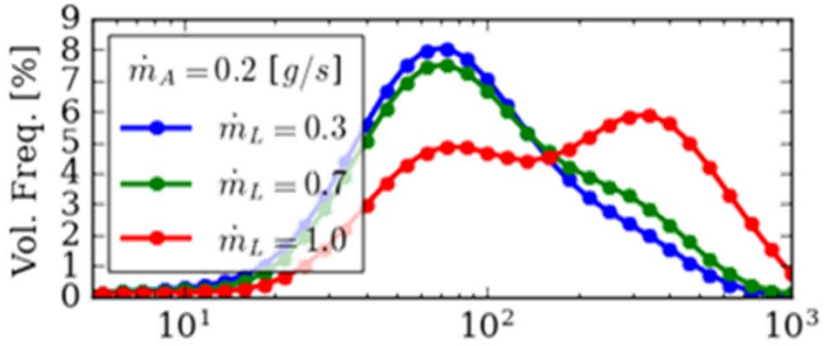

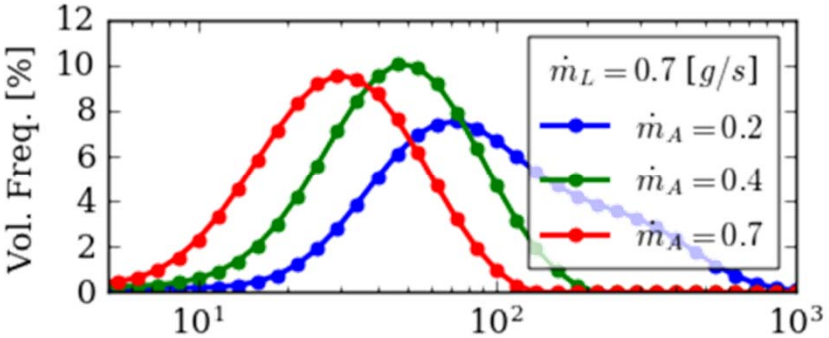

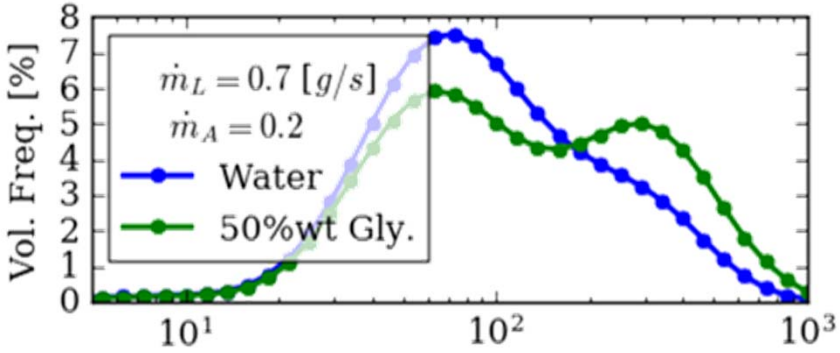

water

$\dot{m}_G$ = 0.2 g/s | $\dot{m}_G$ = 0.4 g/s | $\dot{m}_G$ = 0.6 g/s

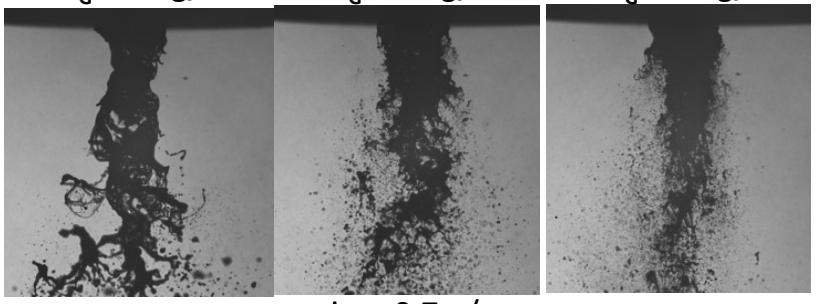

$\dot{m}_L$ = 0.7 g/s

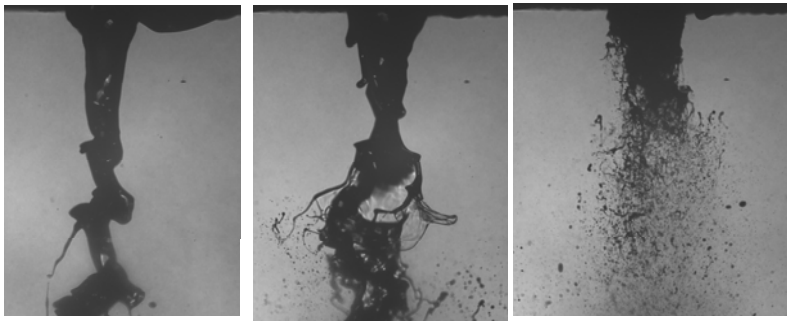

50% wt Glycerin, **μ = 6 mPa.s**

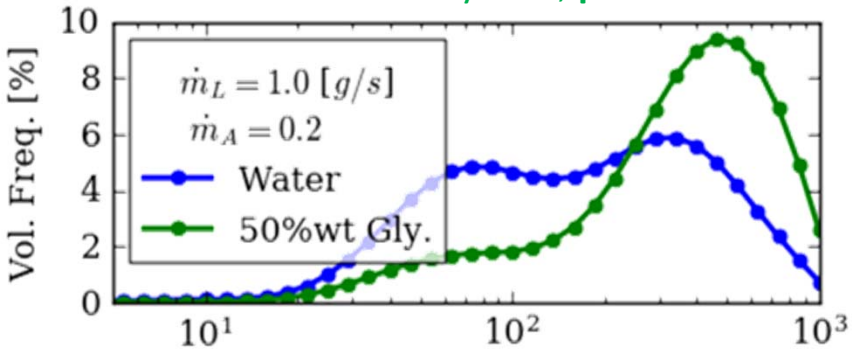

Comparison with Rizk-Lefebvre

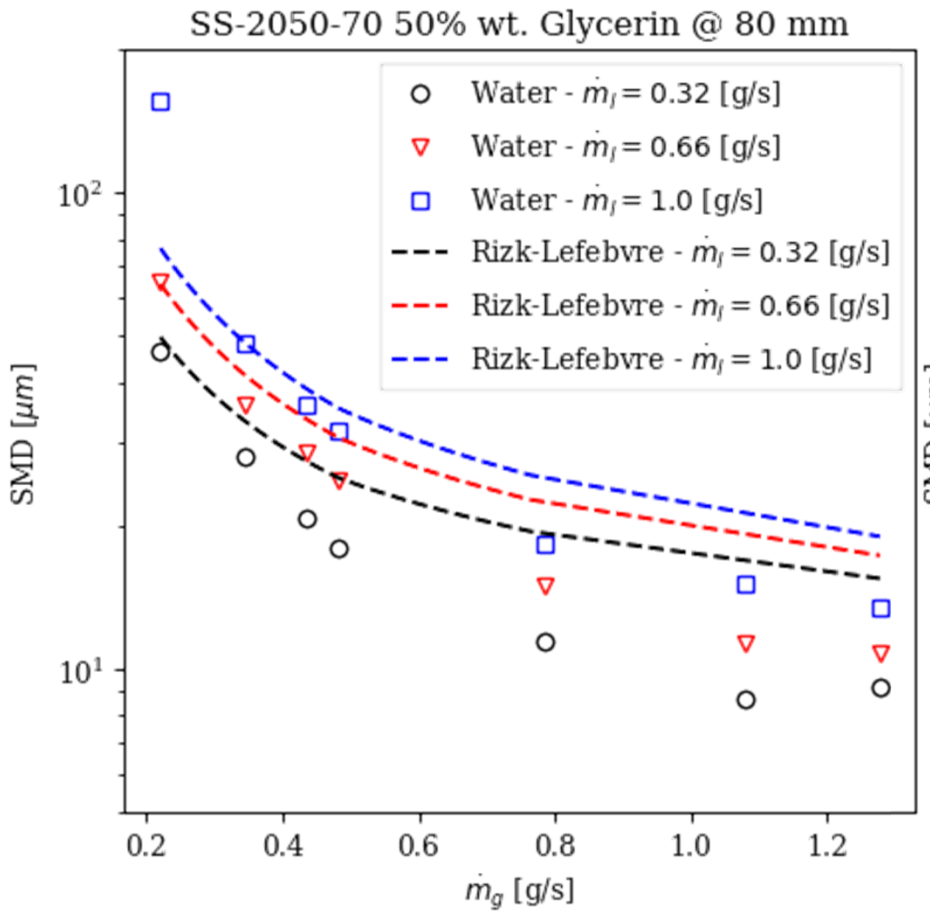

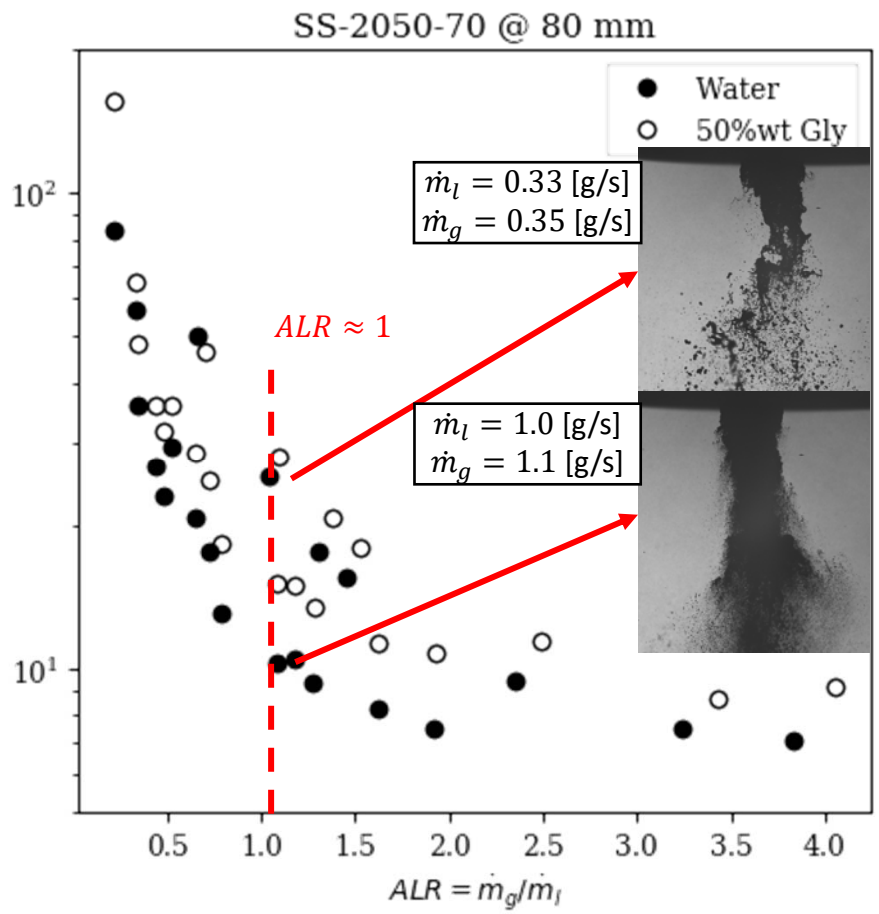

$$\frac{SMD}{D_l} = 0.48\left(\frac{\sigma}{\rho_a U_R^2 D_L}\right)^{0.4}\left(1+\frac{1}{ALR}\right)^{0.4} + 0.15\left(\frac{\mu_l^2}{\sigma\rho_l D_l}\right)^{0.5}\left(1+\frac{1}{ALR}\right)$$

Modelling the atomization physics

Breakup morphologies depend on flow conditions, liquid viscosity, atomizer scale, etc.

Membrane breakup

Shear breakup

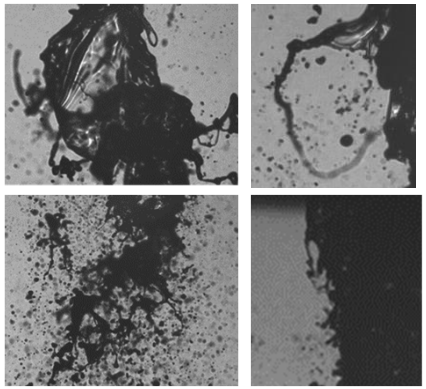

Spray morphology is **not global**

- Different types of **local breakup** can occur

Surface breakup zone

Core breakup zone

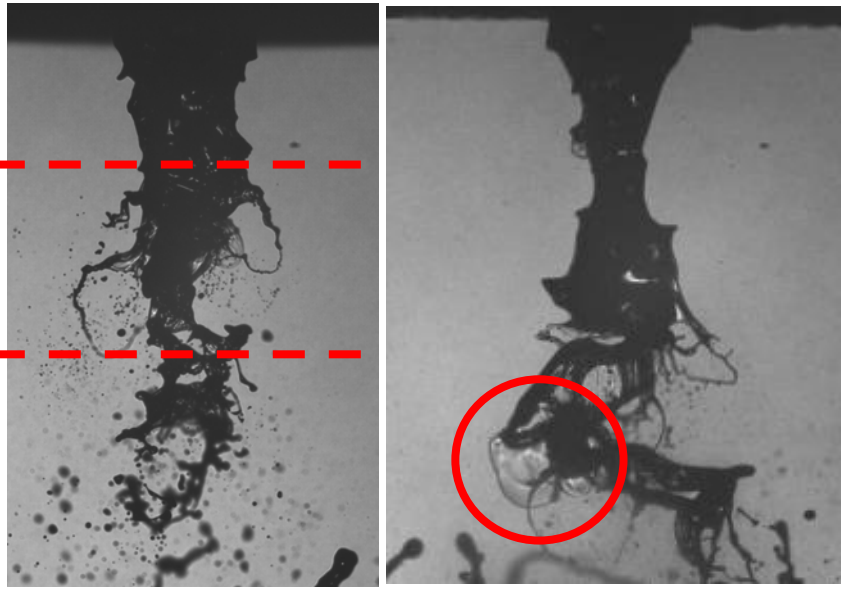

50% wt Glycerin,
μ = 6 mPa.s

Different <u>local</u> breakup morphologies result in distinct breakup sizes, leading to multi-modal PSD.

Droplet Breakup-Based Model

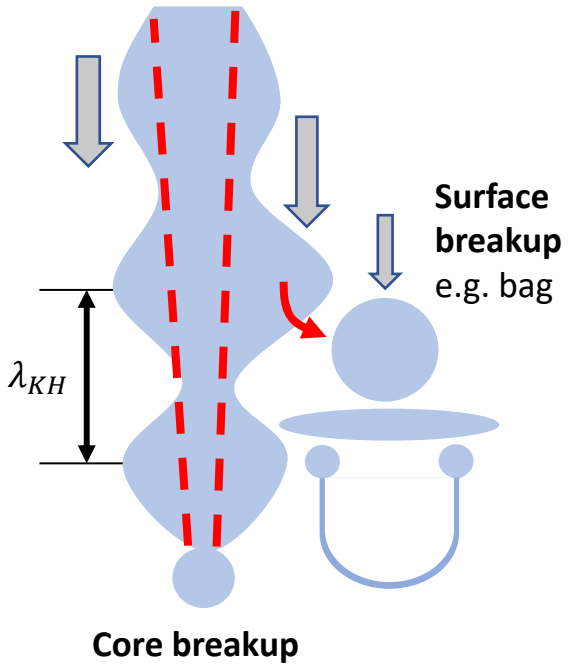

Surface breakup

- Kelvin-Helmholtz (KH) waves form on the liquid
- Each wave forms an *'effective droplet'*
- The effective droplets breaks by a described model

Core breakup

- The remainder of the liquid after surface breakup goes through Rayleigh-Plateau capillary pinching to generate core droplet sizes.

Kelvin-Helmholtz surface waves

Kelvin-Helmholtz surface waves (Finite vorticity thickness derivation)

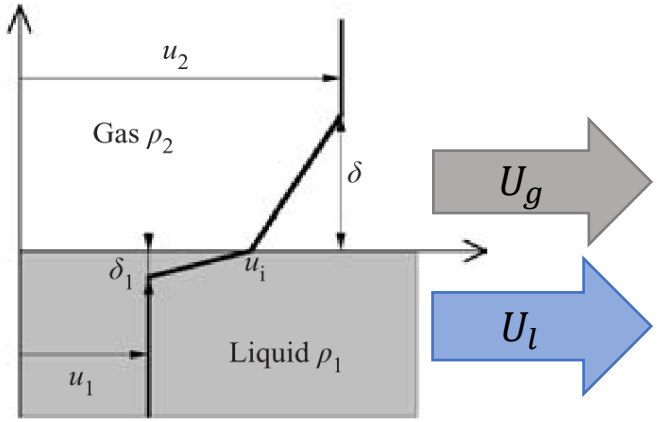

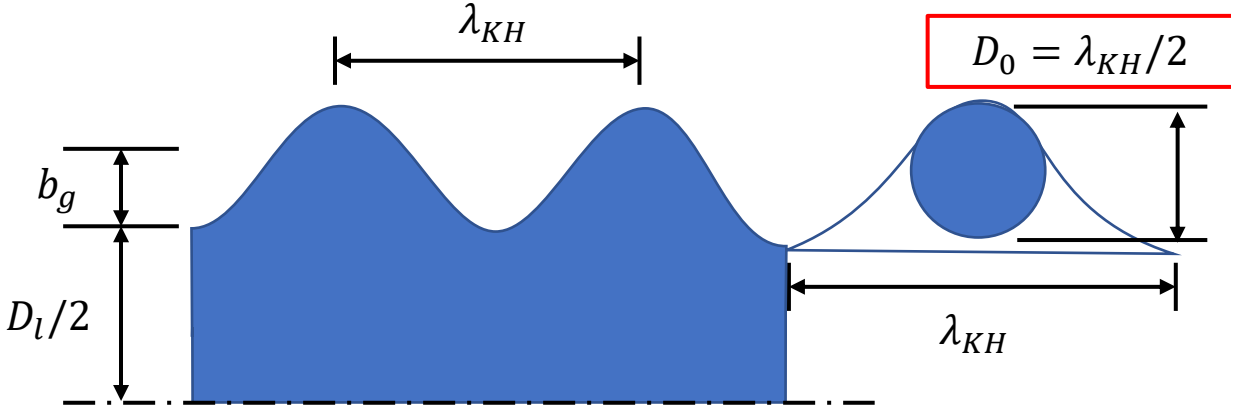

Marmottant & Villermaux (2004)

$$\lambda_{KH} = \frac{2Cb_g}{Re_{bg}^{0.5}}\left(\frac{\rho_l}{\rho_g}\right)^{0.5}, \qquad C \approx 1$$

C is a constant relating to the convergence of the nozzle

A portion of the wave is exposed to the airstream and deforms/breaks as an *'effective droplet'* as per our model described earlier

Droplet breakup Modes

Morphologies

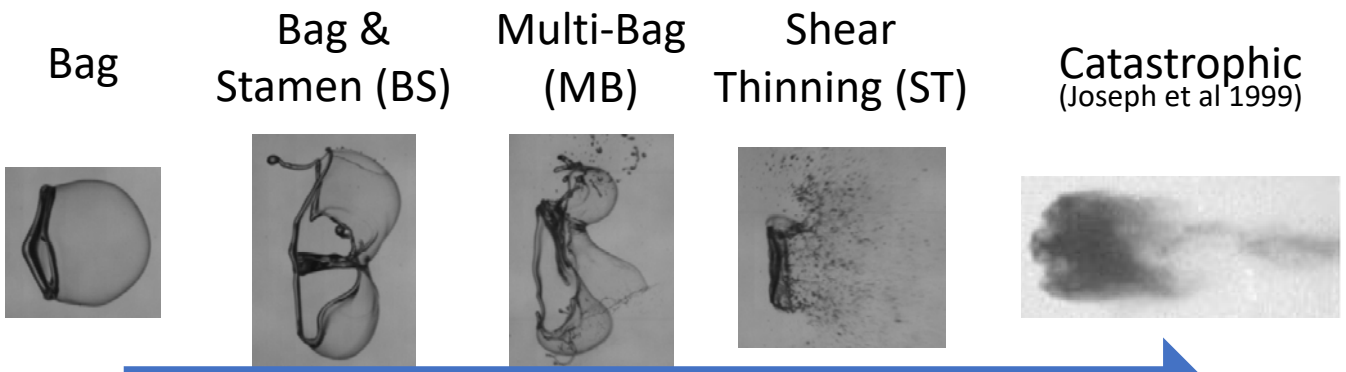

Problem

- Only ST and catastrophic breakup have been modelled well
- Highly viscous fluids tend to break by bag-type morphologies (Bag, BS, MB)
- Breakup of bag morphologies not modelled

Weber number $We = \frac{\rho_a U^2 D}{\sigma}$ Inertia of surrounding gas flow vs. surface tension

Ohnesorge number $Oh = \frac{\mu_l}{\sqrt{\rho_l \sigma D}}$ Viscous vs. liquid inertia & surface tension

Bag Breakup Movies

Bag $We = 11$

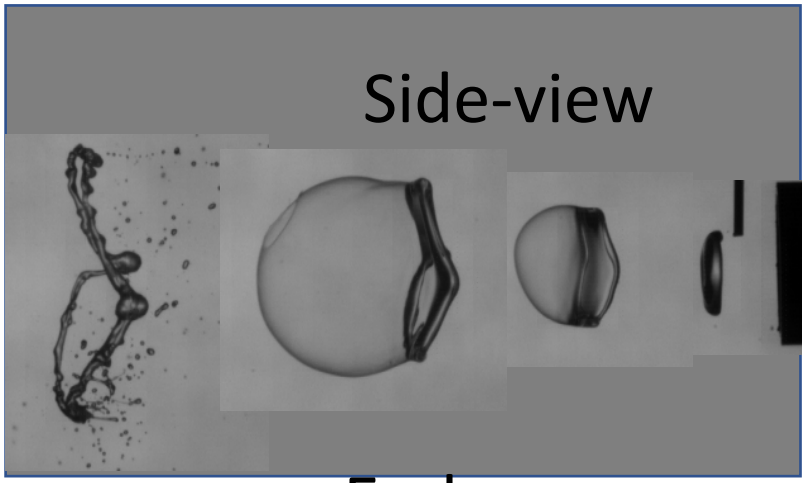

End-on

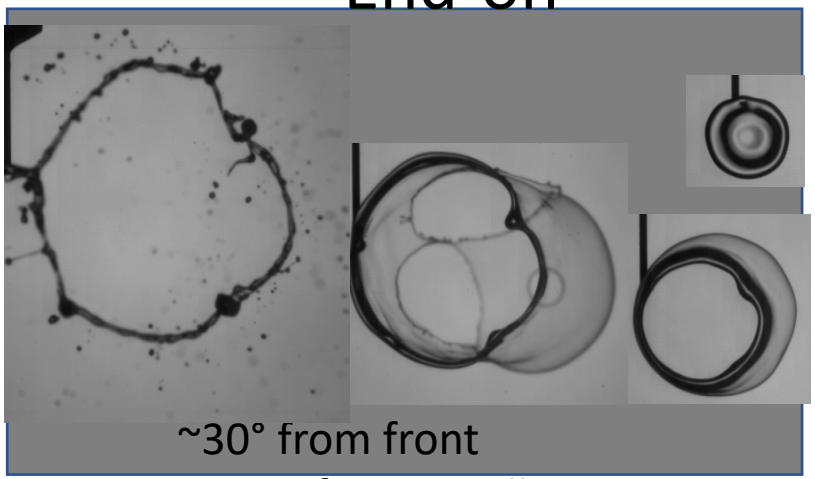

~30° from front

10mm from needle tip

Bag & Stamen (BS) $We = 16$

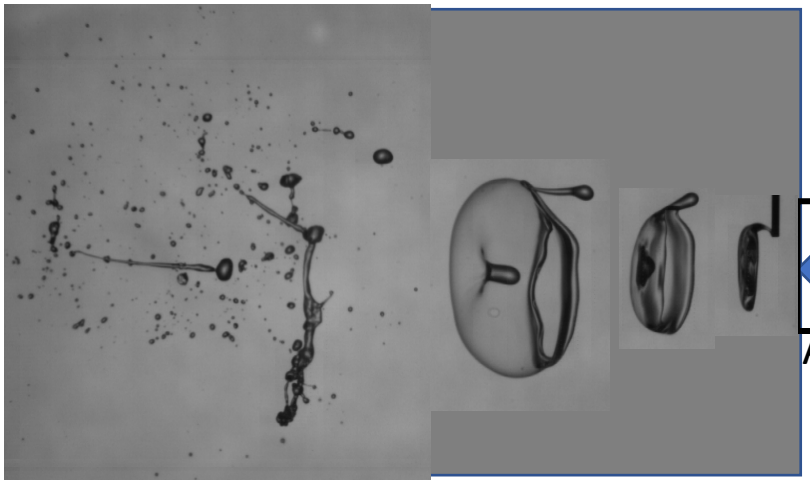

Air flow

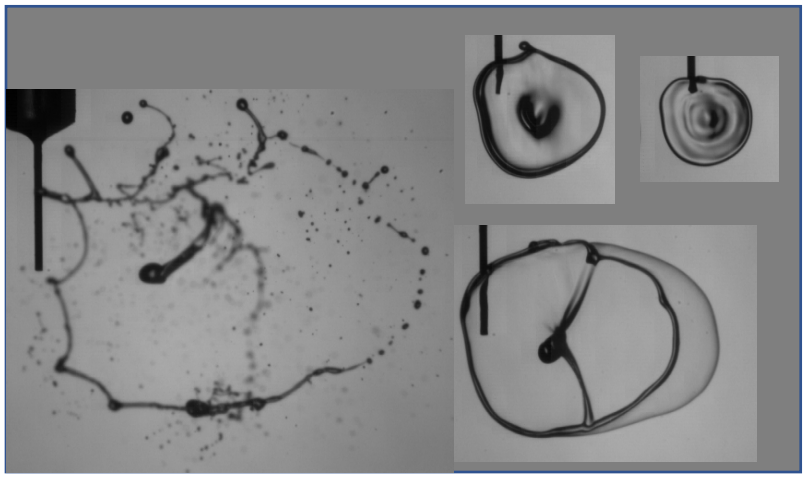

Droplet Breakup Movies

UNIVERSITY OF TORONTO

Multi-Bag (MB)

Shear-thinning (ST)

Side-view

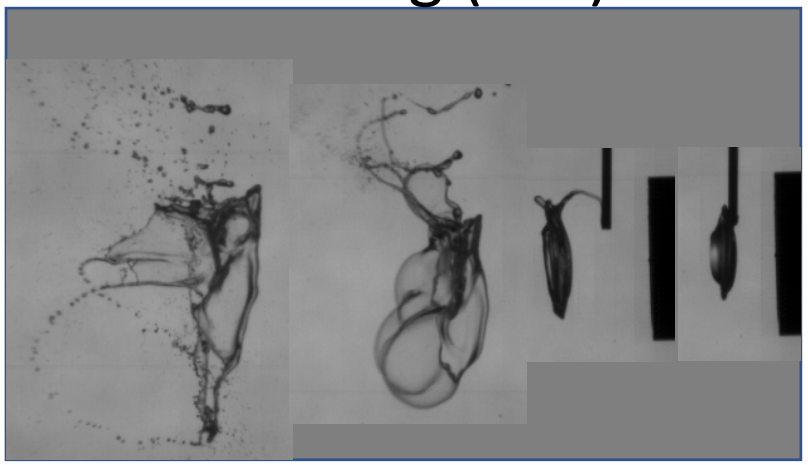

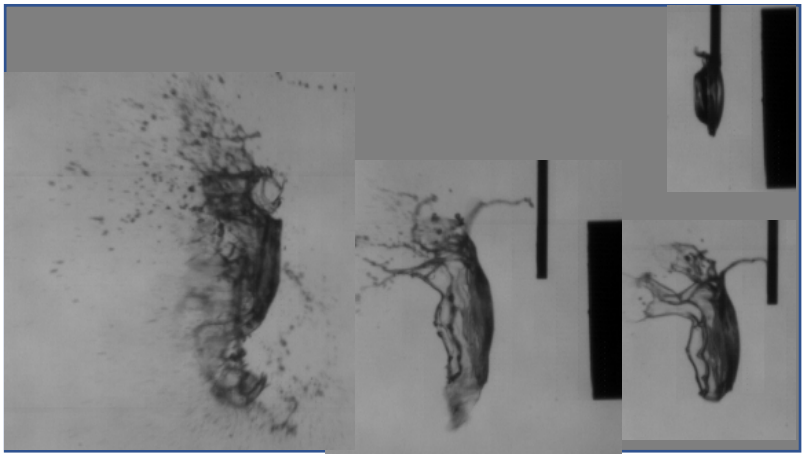

$We = 40$

$We = 108$

End-on

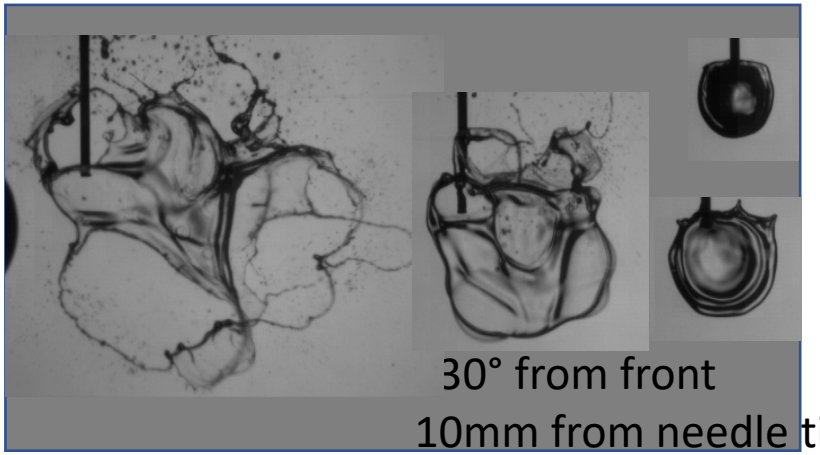

30° from front
10mm from needle tip

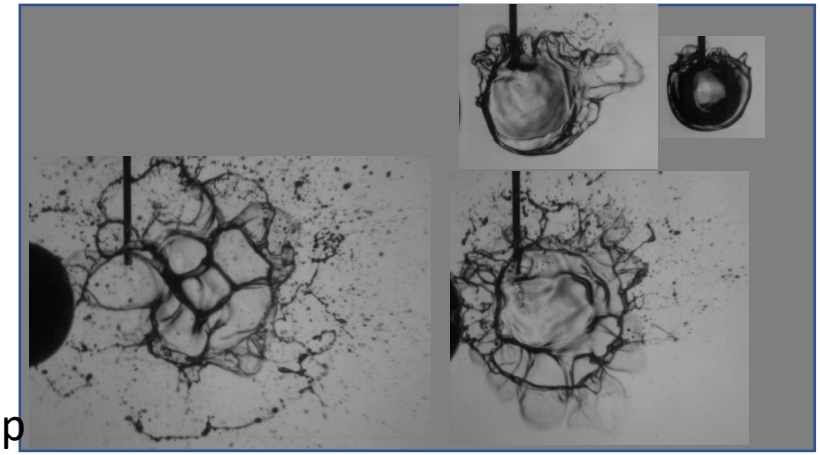

Droplet Breakup-Based Atomization

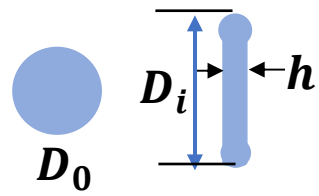

$D_i \approx 1.5D_0$

Empirical

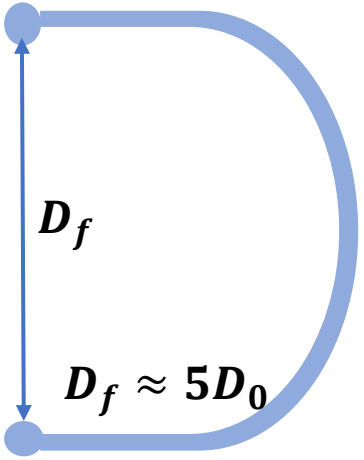

Empirical

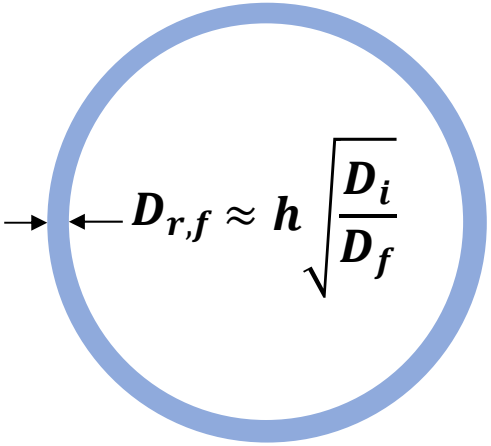

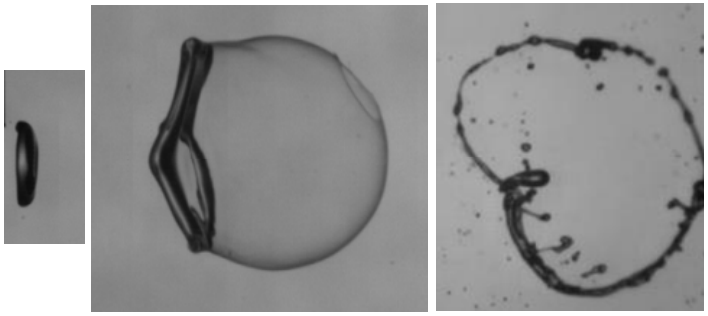

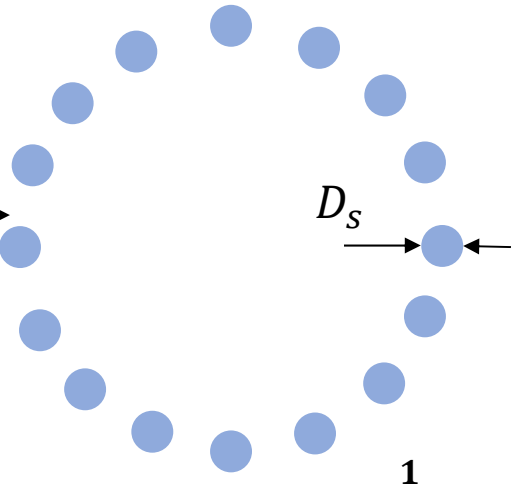

$$D_s = \left(\frac{3}{2} D_{r,f}^2 \lambda_{RP}\right)^{\frac{1}{3}}$$

$$\lambda_{RP} = \frac{\pi}{0.69} D_{r,f}$$

Final Droplet Size:

$$D_s \sim h$$

Droplet Deformation Rate

- Find $\boldsymbol{h}$ based on $\dot{R}$, the expansion rate of the droplet, which is found based on surface tension and inertia balance at the rim.

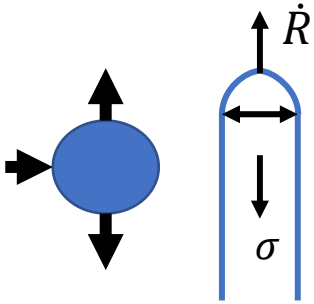

$$h = D_{r,i} \approx \frac{\sigma}{\rho_l \dot{R}^2}$$

$$\dot{R} = \frac{9}{8} U \sqrt{\frac{\rho_g}{\rho_l}} \left(1 - \frac{24}{9We}\right)$$

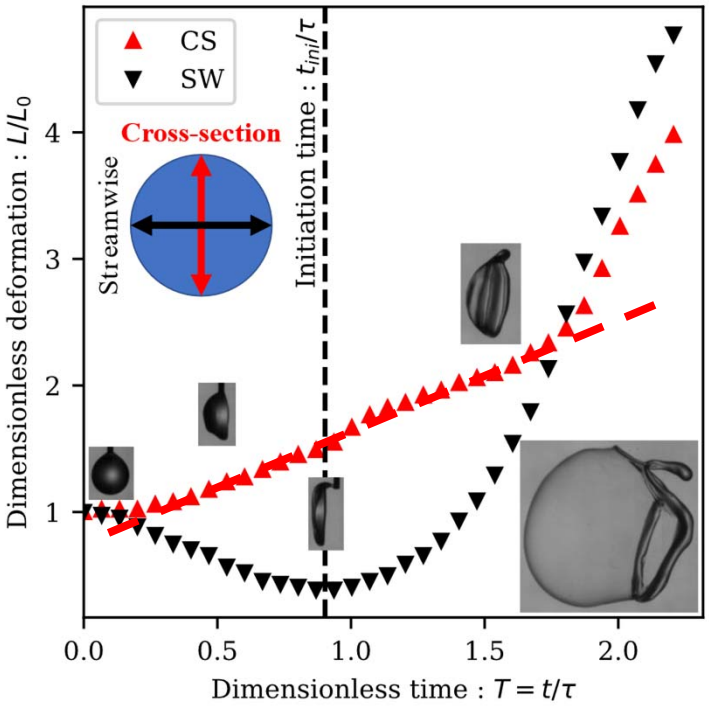

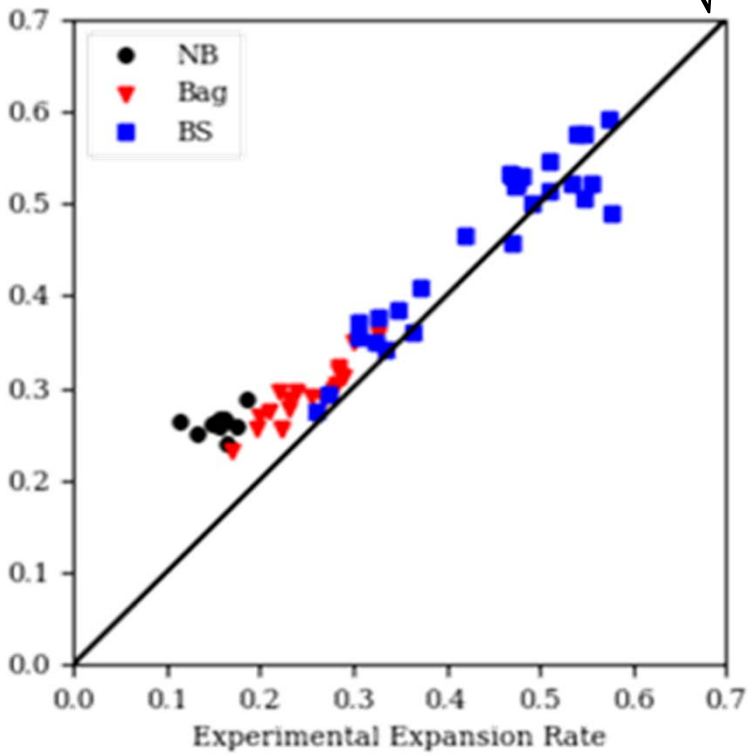

A model for the Spray Droplet Size

- Two modes of breakup; Surface and core
  - Surface breakup by Kelvin-Helmholtz results in droplets of D_s.
  - Core jet thinned by mass loss from surface breakup, breaks by capillary pinch-off mechanism to result in droplets of D_c.

$$\text{SMD} = \frac{\sum nD^3}{\sum nD^2} = \frac{fD_s^3 + D_c^3}{fD_s^2 + D_c^2}, \qquad f = n_s/n_c$$

- Our model will predict relative frequencies, f, as well as D_s and D_c to give SMD (or PSD).

$$f = C\ ALR\ We_{bg}^{n}\ Re_{bg}^{m}$$

$$ALR = \dot{m}_g/\dot{m}_l$$

$$C = 0.158, \qquad n = 1.3, \qquad m = 0.87$$

(empirically from a small set of our data)

Large f → High probability of **small** droplets
Small f → High probability of **large** droplets

SMD Prediction

UNIVERSITY OF TORONTO

U_L = 3.3 m/s, **U_G = 216 m/s**

U_L = 3.3 m/s, **U_G = 168 m/s**

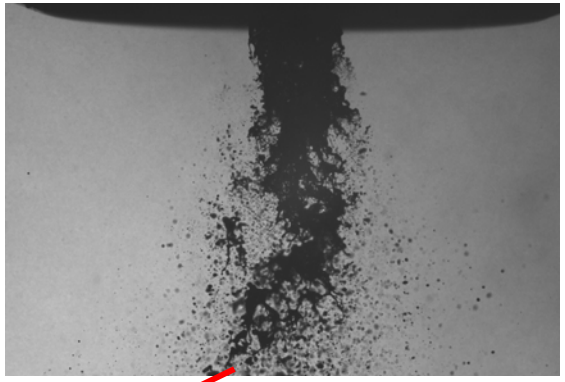

U_L = 3.3 m/s, **U_G = 109 m/s**

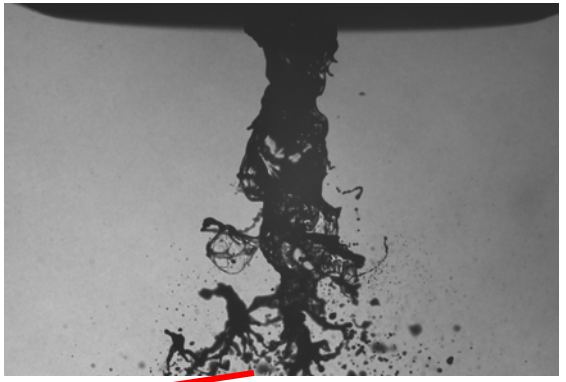

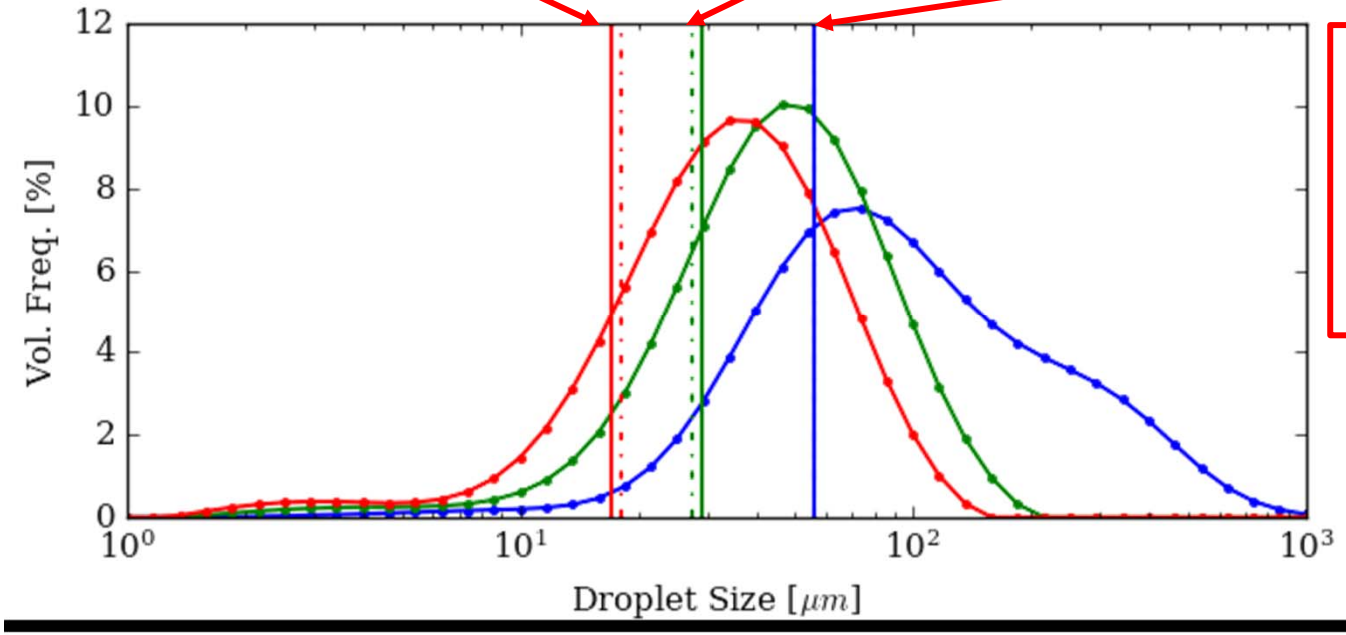

Measured SMD (Solid)
56 µm, 29 µm, 17 µm

Predicted SMD (Dashed)
56 µm, 28 µm, 18 µm

Summary

- A compressive data base for the spray characterization of pressure swirl and twin fluid nozzles for a wide range of viscosities and at high pressures is being developed.
  - Local size distribution and SMD are being measured for all sprays.
- The near nozzle images of the atomization process in pressure swirl nozzles have revealed two different size scales at high pressures.
  - The atomization process is dominated by: formation of waves on the swirling liquid sheet; accumulation of liquid on the wave crests and troughs and thin sheet in between them; breakup of the thick liquid in crests and troughs forming relatively large droplets (the 1st scale); and perforation of the sheet and formation of relatively small droplets (the 2nd scale).
- A sheet preformation-based model is developed for the atomization of pressure swirl nozzles.
- The near nozzle images of the atomization process in twin fluid nozzles have revealed multiple breakup modes.
- A droplet breakup-based model is proposed for the atomization process in twin-fluid nozzles.

END

UNIVERSITY OF TORONTO

Self-Assembled Monolayers as Nucleating Surfaces to Study Early Formation Pathways of Crystal Polymorphs

Hui Du, Lara A. Estroff and Uli Wiesner

Materials Science and Engineering

Hui Du

ubw1@cornell.edu

IFPRI 2020 AGM

Research Project Brief

- Fund project to understand and control crystallinity, polymorphism, and particle morphology in the *early formation stages*.
- Use advanced techniques like cryo-TEM, synchrotron derived pair-correlations, solid-state C^{13} NMR, and in-situ AFM, to visualize these stages.
- High level objectives of this project:

  - *identify appropriate model system(s)* to study, adapt and apply characterization techniques to describe early particle formation stages;

  - collect data that is relevant for the development of molecular dynamic simulation or other computational physics models.

Proposed Approach

- Use self-assembled monolayers (SAMs) to study the relationship between nucleation and polymorph selection.

- Advantages: (i) Enables establishment of scientific correlations between chemistry of nucleation surface and observed polymorph and (ii) may provide access to polymorphs not accessible via solution methods.

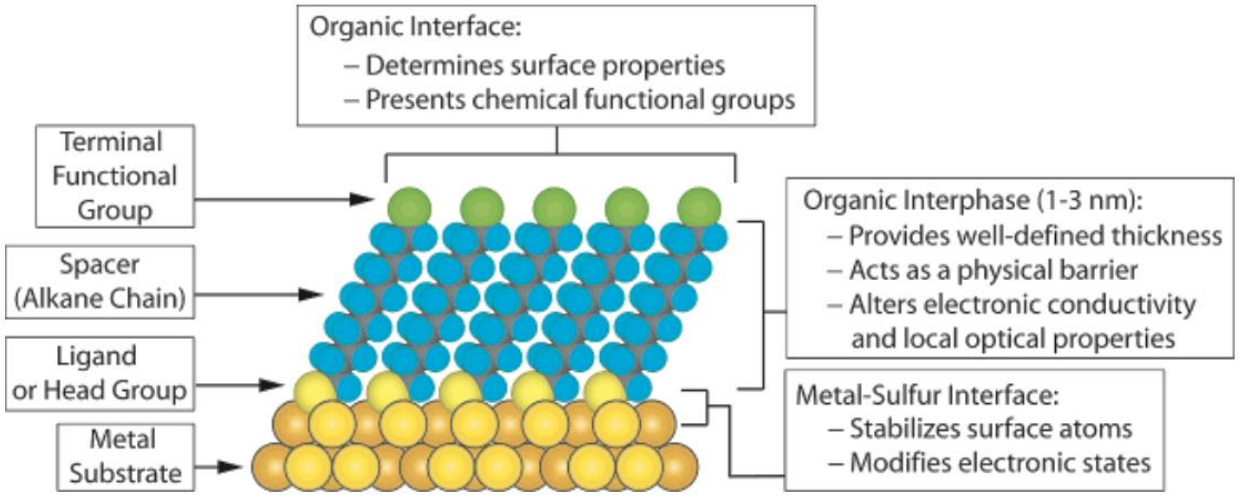

J.C. Love et al., *Chem. Rev.* **2005**, 105, 1103−1169.

Two substrate chemistries: Au and SiO_2

Thiol-gold chemistry

UDT: 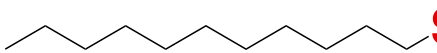

MUOH: **HO** 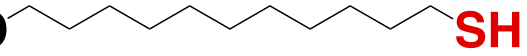

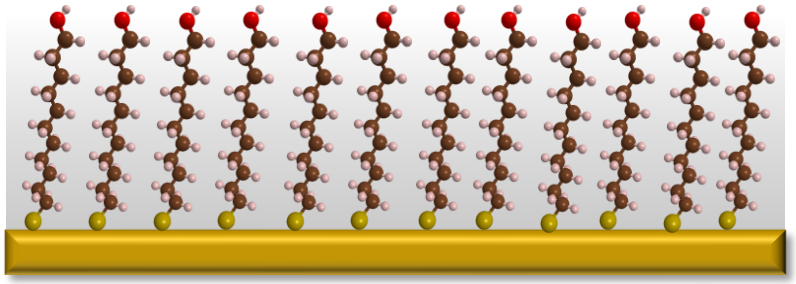

- Highly ordered SAMs
- Poor solution stability
- More expensive

Silane-SiO_2 chemistry

OTS: 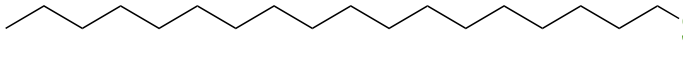

PTS: 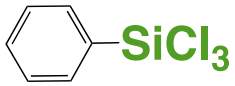

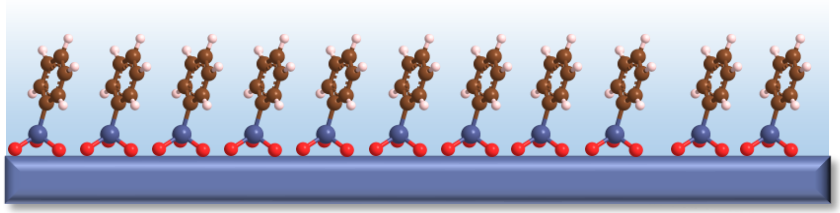

- Less ordered than Au SAMs
- Very good solution stability
- Works on Si-wafers and glass

Past experiences on Acetaminophen:
Both solvent and substrate work together to control crystal polymorph

Solvent	*SAMs*	*n*	*Form I*	*Form II*
Ethanol 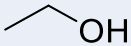	UDT	20	**80%**	20%
	OTS	18	**94%**	6%
	PTS	14	**93%**	7%
	MUOH	11	9%	**91%**
DI water	UDT	9	**93%**	7%
	OTS	18	**89%**	11%
	PTS	10	**90%**	10%
	MUOH	17	**100%**	0%
1,4-dioxane 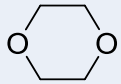	UDT	12	**100%**	0
	OTS	10	**90%**	10%
	PTS	10	**70%**	30%
	MUOH	10	20%	**80%**
DI water/ dioxane 20:80	UDT	11	9%	**91%**
	OTS	11	0	**100%**
	PTS	9	0	**100%**
	MUOH	10	0	**100%**

- Solvent and surface chemistry must be considered in concert for polymorph selection
- Substrate can dictate crystallographic orientation: Form II
- General area X-ray diffraction (GADDS) results & proposed molecular interpretation

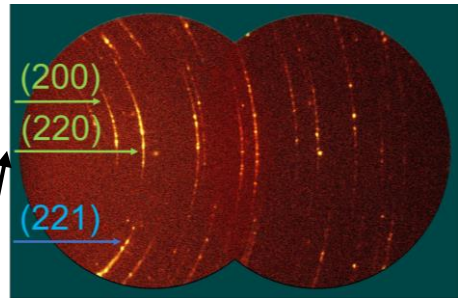

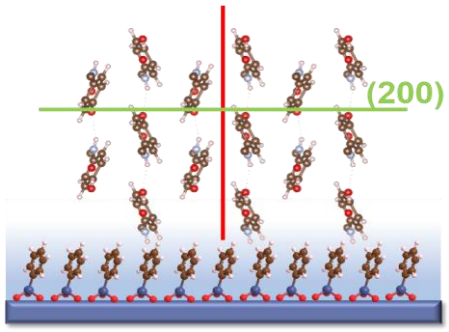

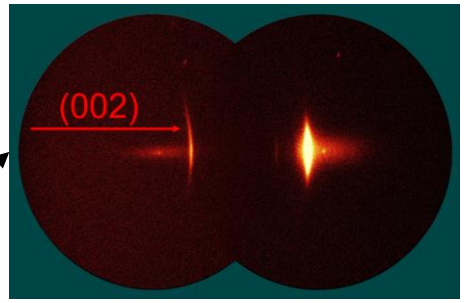

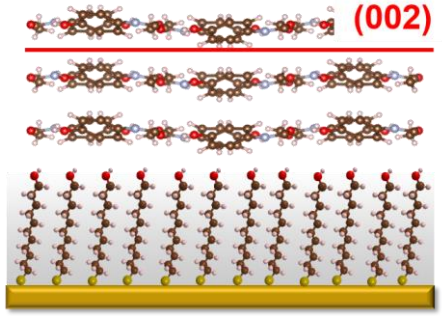

*Unpublished data

Conclusions

- *In-situ* synchrotron studies of crystal nucleation and growth of model compound acetaminophen (ACM) from solution on self-assembled monolayers (SAMs) provided first insights into early formation stages that could be important for polymorph selection.
- Two independent studies of seeded ACM Form II on PTS in dioxane/water revealed crystals growing upwards from the SAM substrate-solution interface with preferred (002) plane orientation perpendicular to substrate supporting SAMs as nucleation sites.
- Two independent studies of spontaneous nucleation & growth of Form 1 on PTS in water revealed unusual peak shifts at the earliest time points in similar q ranges. While details of the observed shift differed, both of these observations were suggestive of structural transformations (versus simple rotations) at early stages of ACM crystal formation.
- Deeper understanding of these early structural transformations likely require molecular dynamics simulations or other computational physics models.

After discussions with several IFPRI members: New model system: 5-Methyl-2-[(2-nitrophenyl)amino]-3-thiophenecarbonitrile (ROY)

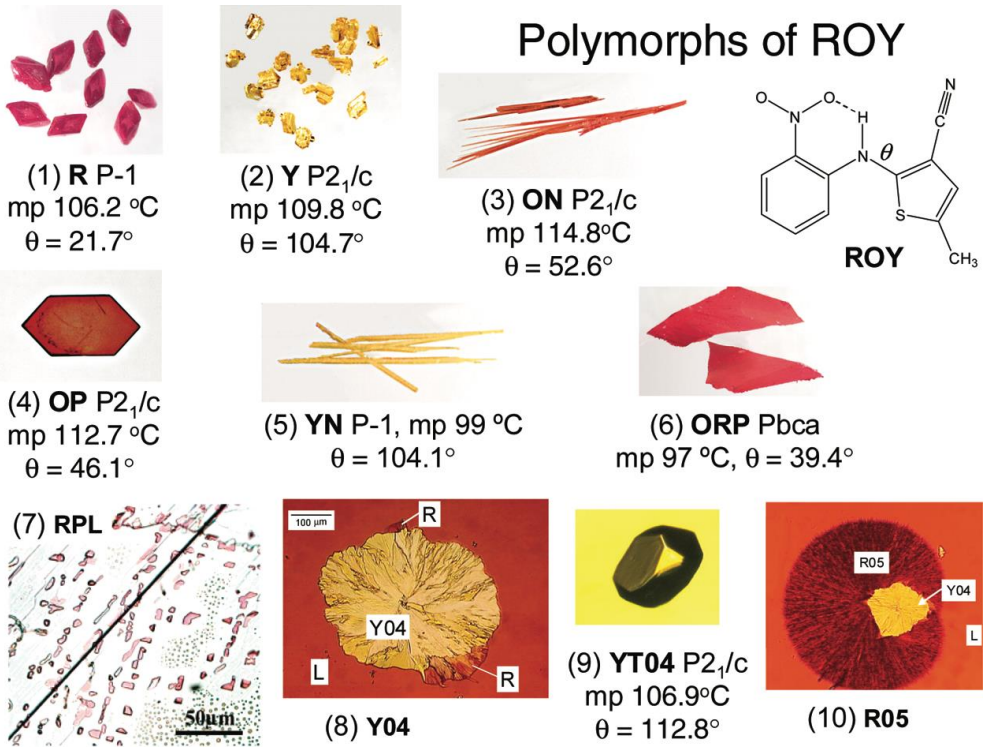

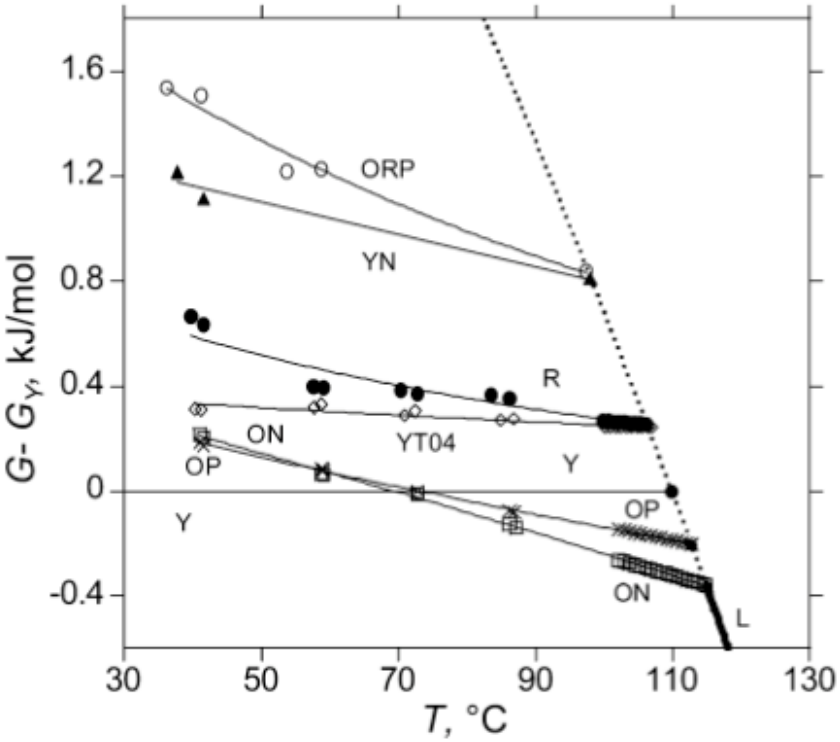

Up to now, ROY has 11 known polymorphs, 9 of which have a fully elucidated crystal structure.

Y is the most stable polymorph below 70 ℃

Yu, L.. *Acc. Chem. Res.* **2010**, *43*, 1257−1266.

Yu, L. et al. *J. Am. Chem. Soc.*, **2000**, *122*, 585– 591

Known dependencies of ROY polymorph selection

Nucleation pathway dependence of polymorph selection via solvent evaporation

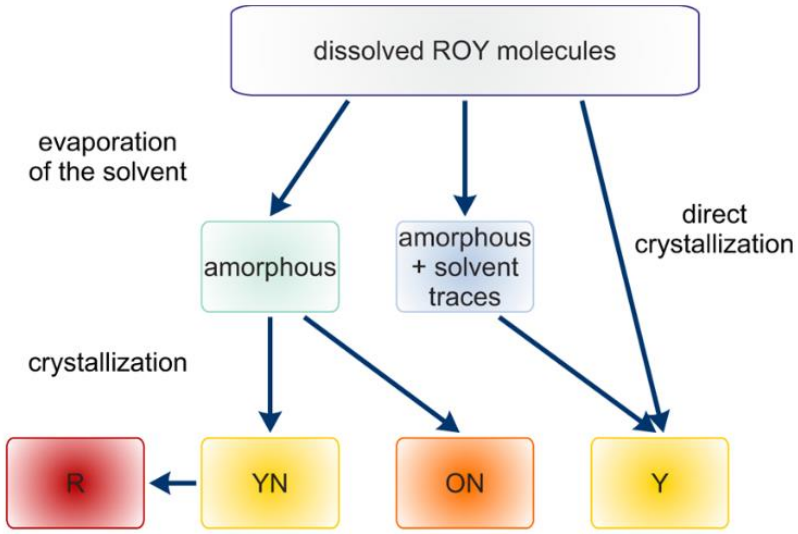

Solvent dependence of polymorph selection due to intermolecular forces

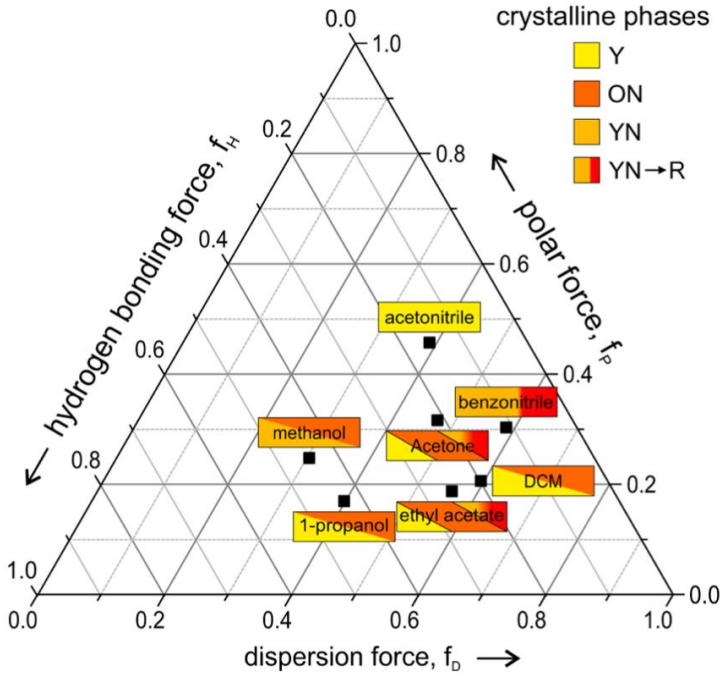

Gnutzmann, T. et al. *Cryst. Growth Des*. **2014**, 14, 6445-6450

Effects on polymorph selection

This time - involve the effect of supersaturation

SAM surface chemistry

Solvent

Supersaturation

Energy Barrier

Polymorphism & Morphology

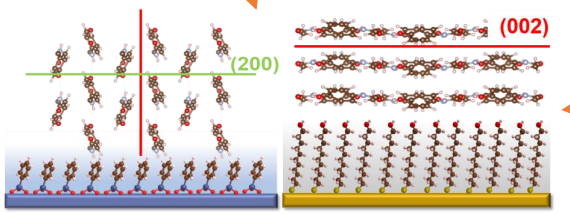

SAMs + solvent effect was studied by ACM

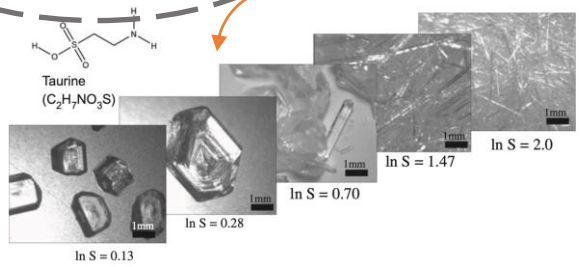

Past experimental setup – no control over degree of supersaturation

Solvent evaporation crystallization

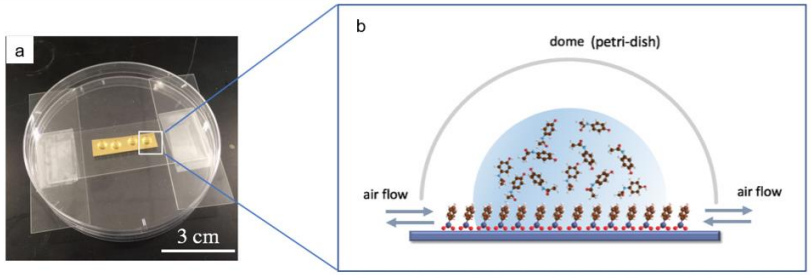

Convenient way to screen conditions

Hard to track solution concentration vs time of nucleation

Direct solution crystallization by cooling

- Concentration is related to **solubility curve**
- Able to know concentration by tracking solution temperature profile

For solution crystallization, solvent needs to have a high boiling point and high ROY solubility.

Possible solvent: **DMSO, Benzyl Alcohol, Toluene…**

Takiyama, H. *Adv. Powder Technol*. **2012**, *23*, 273-278

Results of solubility tests & preliminary direct solution crystallization experiments

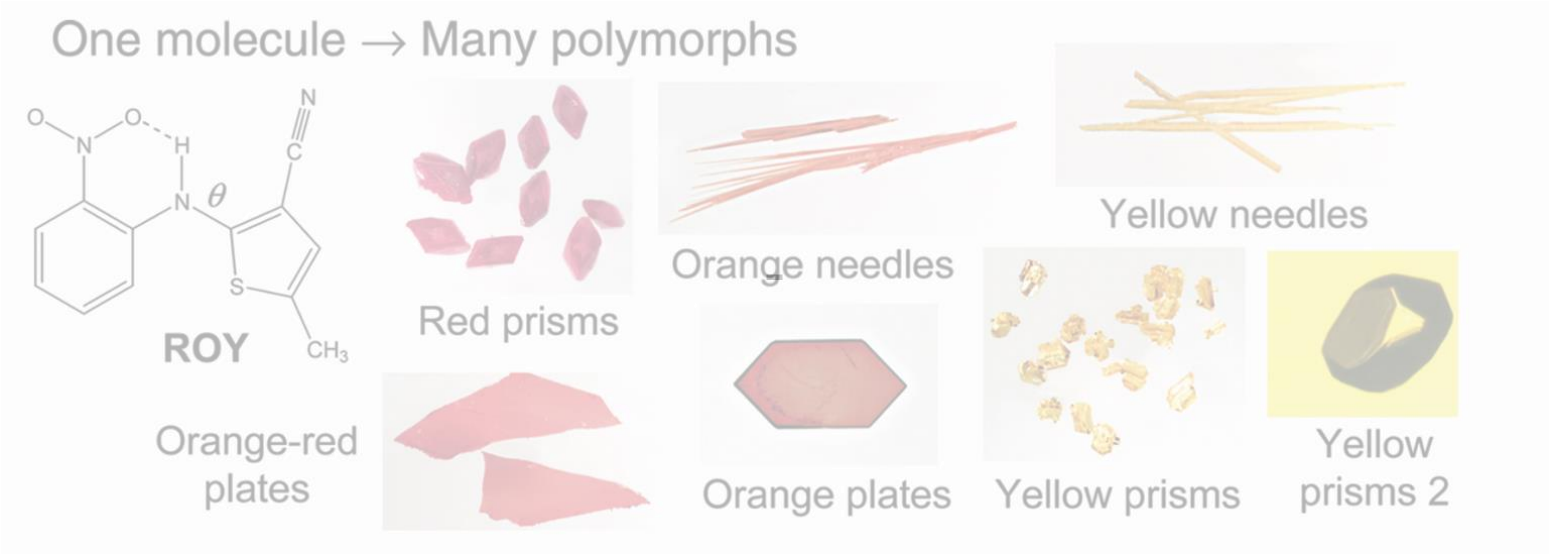

Yu, L.. *Acc. Chem. Res.* **2010**, *43*, 1257−1266.

Calculated solubility of ROY

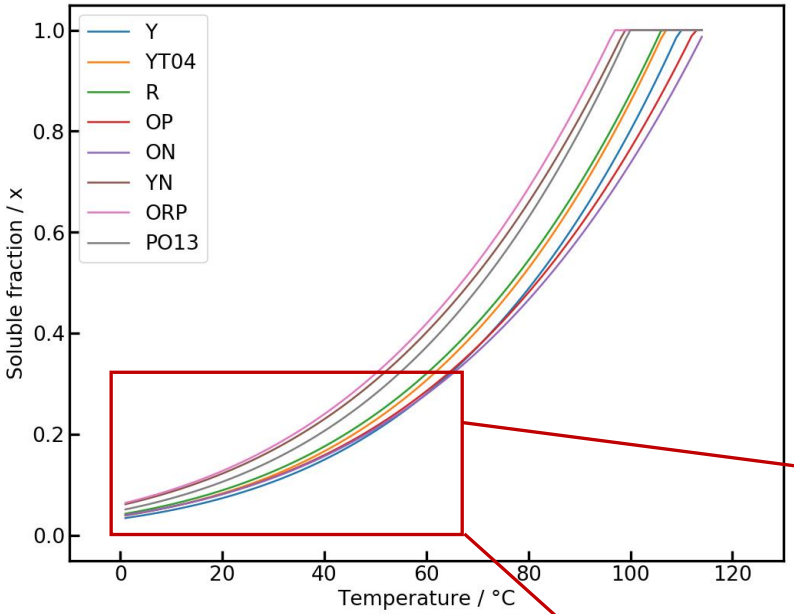

The van't hoff equation:

$$\ln x = \frac{\Delta H_f}{R}\left[\frac{1}{T_f} - \frac{1}{T}\right] = -\frac{\Delta H_f}{RT} + \frac{\Delta S_f}{R}$$

ΔH_f : enthalpy of fusion

ΔS_f : entropy of fusion

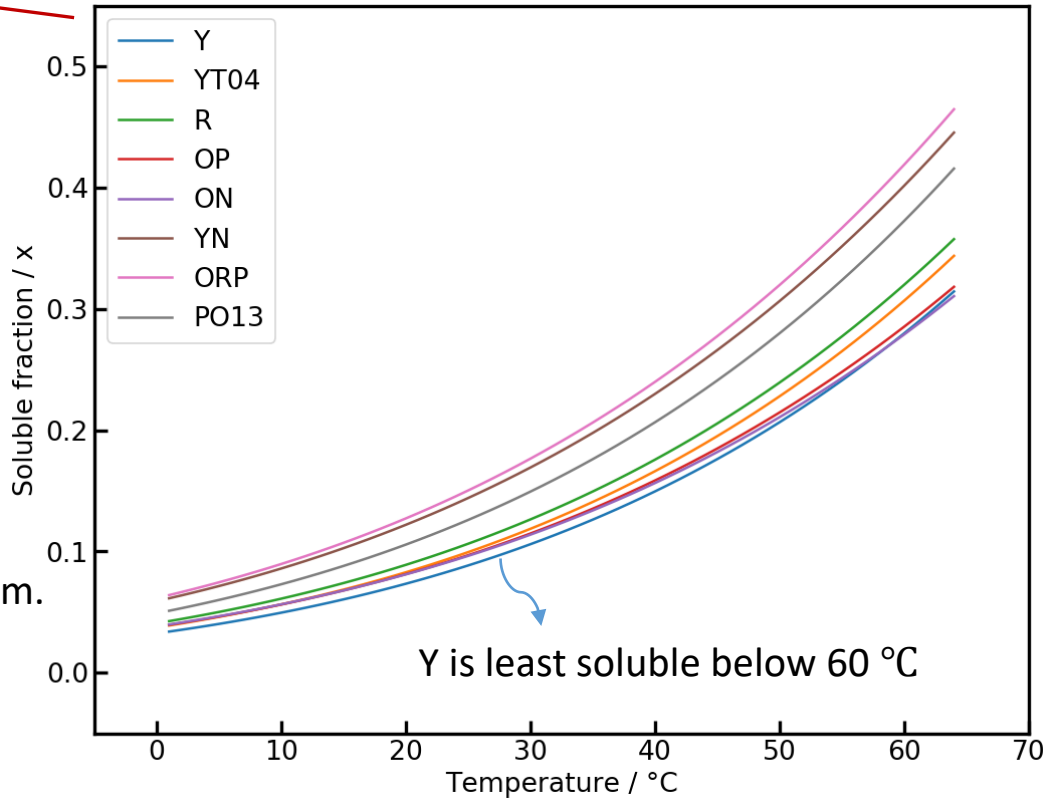

Y is also the most stable polymorph below 70℃.
Therefore, the measured solubility is ROY in Y form.

Yu, L.. *Acc. Chem. Res.* **2010**, *43*, 1257−1266.

Solubility test:

Gravimetric method

Thanks for support by John Hone (Syngenta)

Step 1:

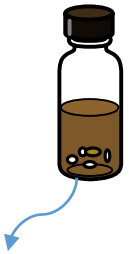

Excess ROY in preheated solvent (supersaturated)

Step 2:

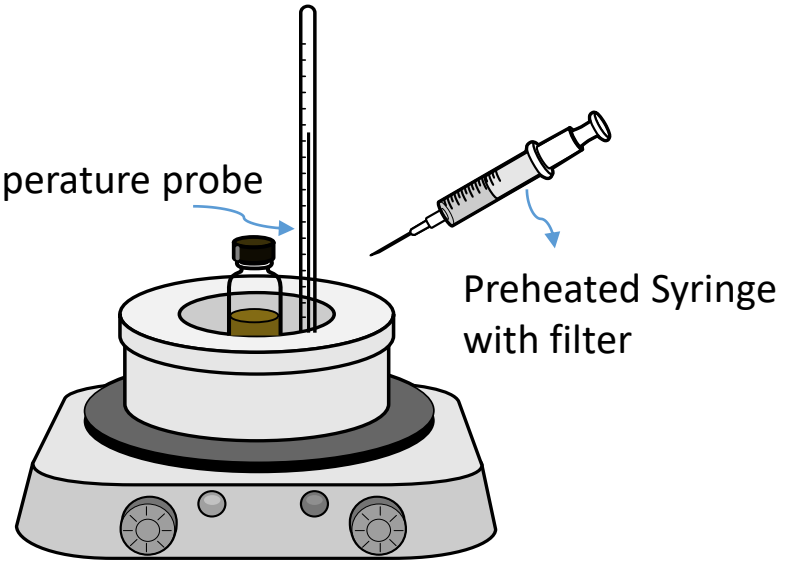

Oil bath

Step 3:

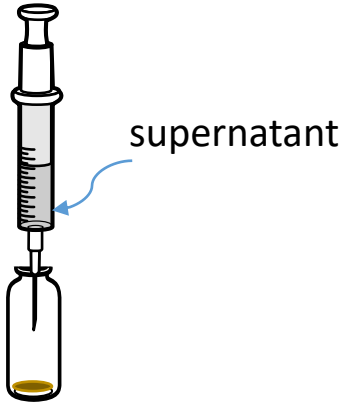

Step 4:

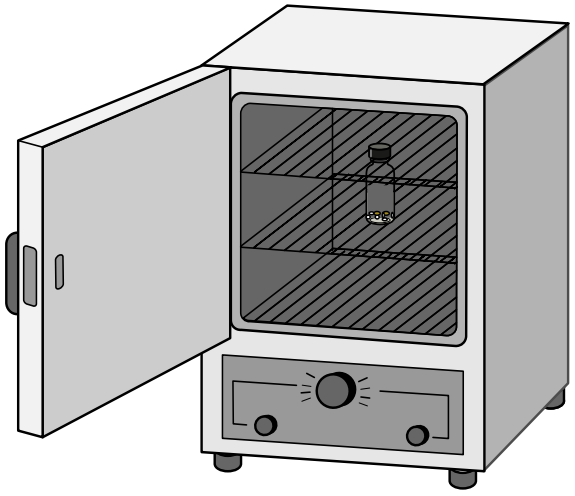

Vacuum dry for more than 8 hrs

Solubility (g/g) = $\frac{m_{dried\ sample} - m_{empty\ vial}}{m_{sample} - m_{dried\ sample}}$

Experimental Results:

Solubility of ROY in DMSO and Benzyl Alcohol

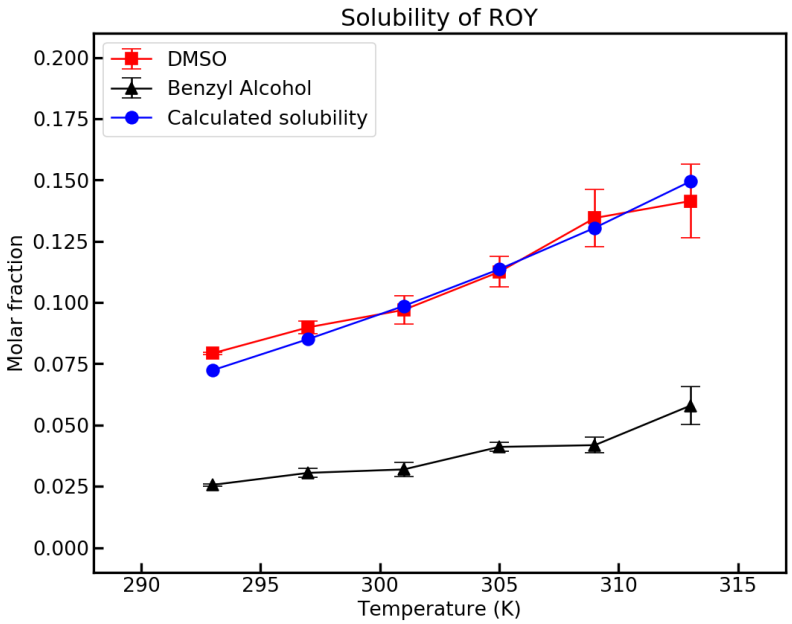

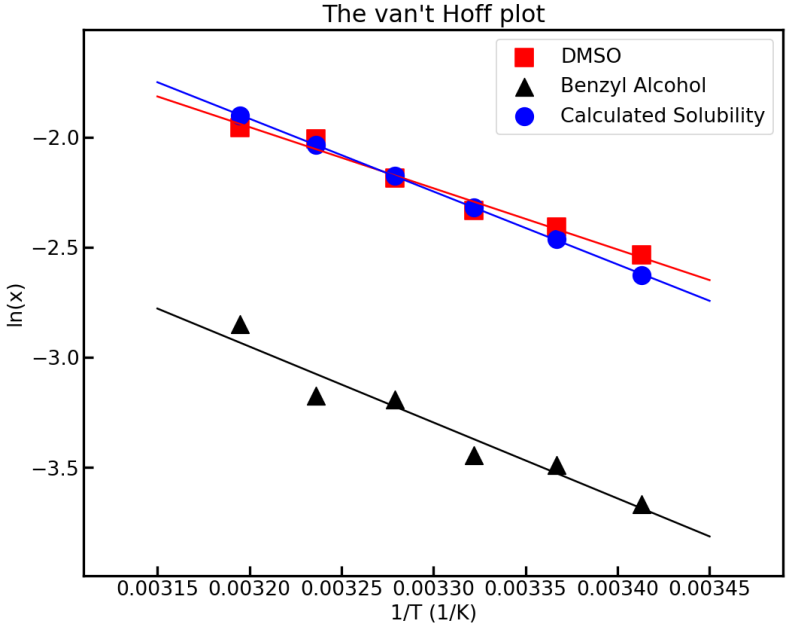

Including solvent effects:

$$\ln x = -\frac{\Delta H_d}{RT} + \frac{\Delta S_d}{R}$$

ΔH_d : enthalpy of dissolution
ΔS_d: entropy of dissolution

Solvent	ΔH_d (kJ/mol)	ΔS_d (J/molK)
Ideal	27.52	72.14
DMSO	23.11	57.74
Benzyl Alcohol	28.69	67.28

ROY Nucleation on cover glass as a func. of supersaturation

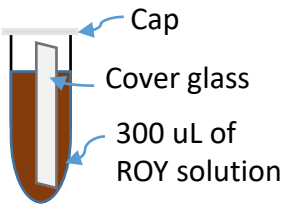

Reference cell

- **Supersaturation: 1.5, 2, 2.5**
- Nucleation surface: cover glass
- Temperature change: 60 ℃ to 20 ℃ natural cooling
- Solvent: Benzyl Alcohol

$$\text{Supersaturation (S)} = \frac{\textit{initial solution concentration}}{\textit{solubility at the crystallization temperature}}$$

Based on literature, Y, R, & ON could be crystallized from benzyl alcohol solutions

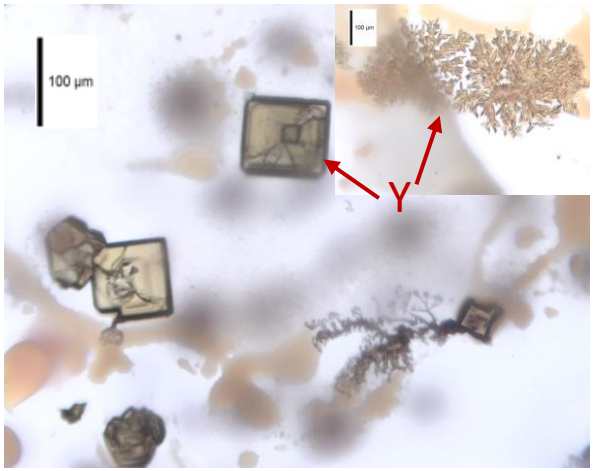

S=1.5

- Only prism shape crystals appear
- Possible polymorph: Y

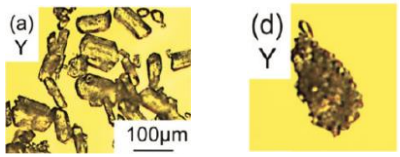

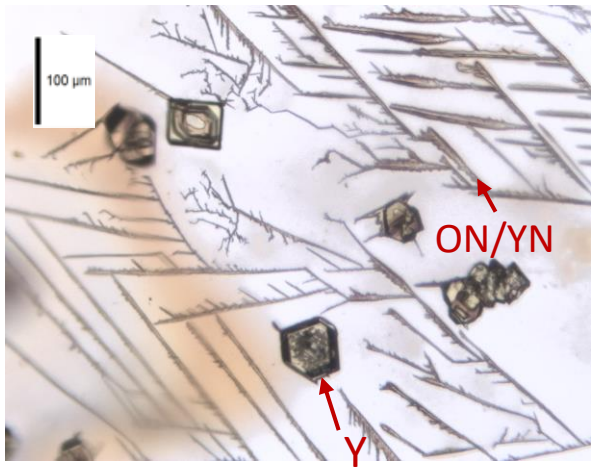

S=2

- Both prism and needle shape crystals appear
- Possible polymorph: Y+ON/YN

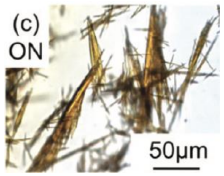

(5) **YN** P-1, mp 99 ºC
θ = 104.1°

S=2.5

- No trace of prism crystals; some needles grown on the large needle crystal
- Possible polymorph: ON

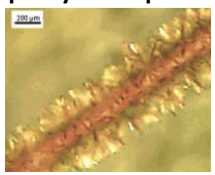

At different supersaturation levels, the dominant polymorph changes.

Diao, Y. et al. *J. Am. Chem. Soc.* **2012**, *134*, 673-684
Chen, S. et al. *J. Am. Chem.* Soc. **2005**, *127*, 17439-17444

ROY Nucleation on SAM as a function of supersaturation

- **Supersaturation: 1.5, 2, 2.5**
- Nucleation surface: Si-OTS
- Temperature change: 60 ℃ to 20 ℃ natural cooling
- Solvent: Benzyl Alcohol/DMSO

Alternative Explanation

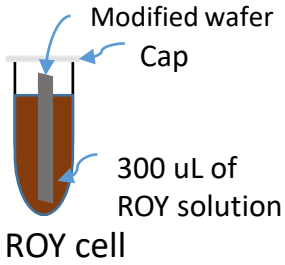

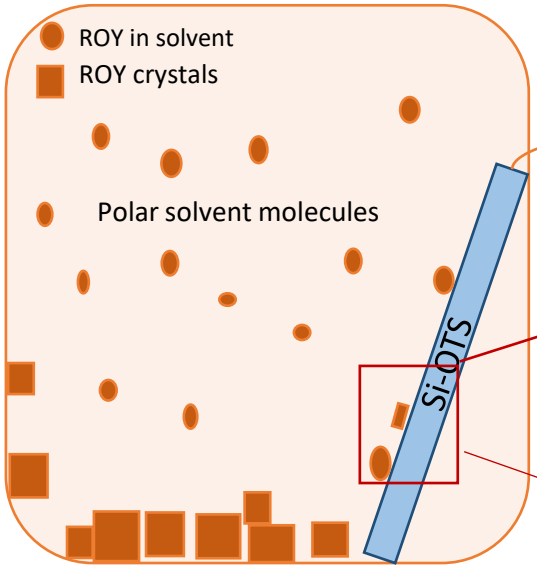

Hydrophobic surface

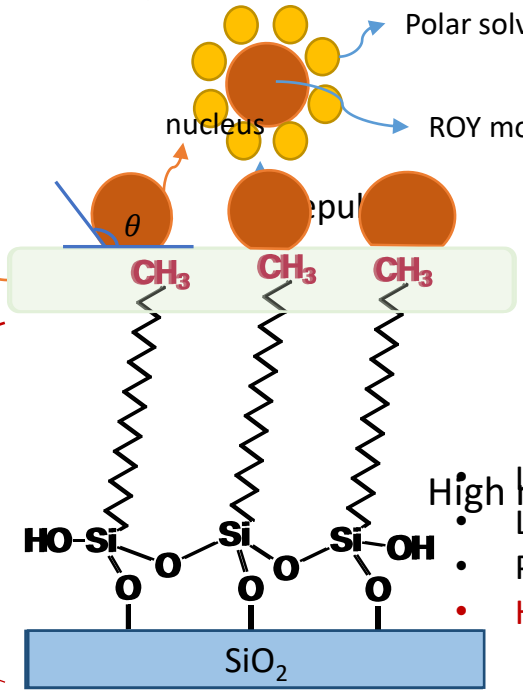

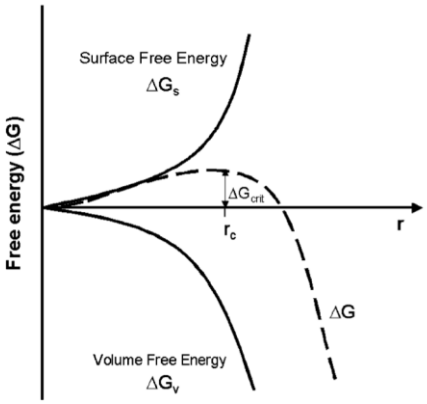

- Large contact angle θ
- Low interfacial free energy
- Poor wetting on the substrate
- High nucleation energy barrier

High nucleation energy barrier

- Little crystallization on SAM surface occurred during 2 days (for all supersaturation levels)
- Crystal clusters appeared at the bottom of the vial
  - → Either preference for homogeneous nucleation in solution or heterogeneous nucleation on container wall

Hydrophobic surface + polar solvent does not favor heterogenous nucleation

Alternative systems:

- Hydrophilic surface (Au-MUOH) + polar solvent (Benzyl Alcohol)
- Hydrophobic surface (Si-OTS) + nonpolar solvent (Toluene)

ROY Nucleation from different SAM + solvent combinations

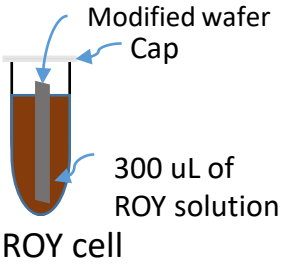

- **Nucleation surface: Au-MUOH (left); Si-PTS (right)**
- **Solvent: Benzyl Alcohol (left); Toluene (right)**
- Supersaturation: 1.5
- Temperature change: 60 °C to 20 °C natural cooling

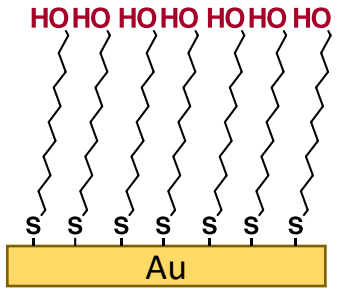

Solvent: Benzyl Alcohol

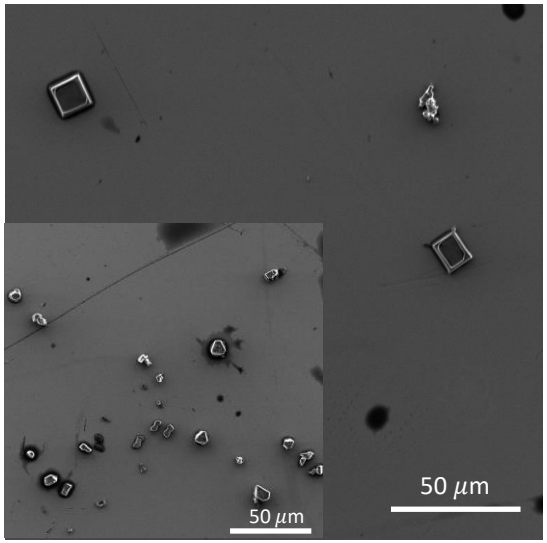

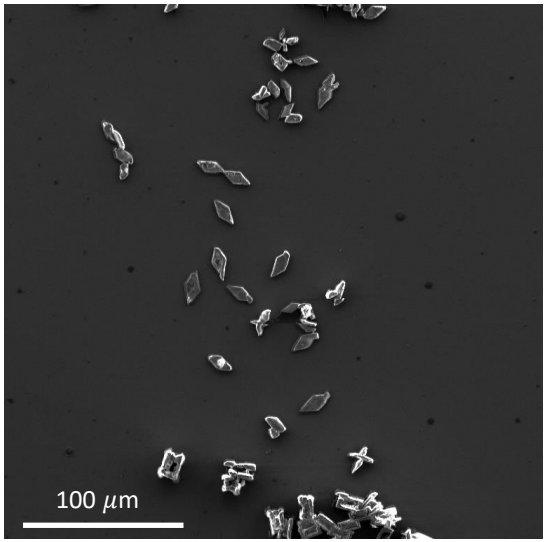

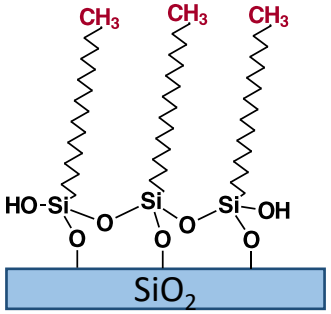

Solvent: Toluene

(2) **Y** $P2_1/c$
mp 109.8 °C
θ = 104.7°

(9) **YT04** $P2_1/c$
mp 106.9°C
θ = 112.8°

(1) **R** P-1
mp 106.2 °C
θ = 21.7°

- Hydrophilic head group + polar solvent
- Cubic shape crystals appear
- Possible polymorph: monoclinic Y/YT04

- Hydrophobic head group + nonpolar solvent
- Rhombic shape crystals appear
- Possible polymorph: triclinic R

There is polymorph selectivity when applying different solvent + SAM surface chemistry combinations

Chen, S. et al. *J. Am. Chem. Soc*. **2005**, *127*, 17439-17444

Conclusions

- In the past funding period we successfully switched our studies of polymorph selectivity from Acetaminophen (ACM) to a more complex system, ROY
- In parallel, rather than driven by solvent evaporation, for ROY we established experimental protocols that enable polymorph selection as a function of the degree of supersaturation, which we heard from industry representatives to be the more relevant parameter.
- Solubility curves for ROY in benzyl alcohol and DMSO were successfully determined
- For ROY in benzyl alcohol, in first proof-of-principle experiments we demonstrated polymorph selection as a function of the degree of supersaturation
- Similar to ACM, first experiments suggest that for ROY again solvent and SAM surface chemistry together control polymorph selection

Possible future directions

- Complete sample characterization (*e.g.* XRD) of existing samples to determine the exact ROY crystal polymorphs formed

- Raman Microscopy may be used to distinguish different polymorphs
  - Different nitrile (C-N) stretch for each polymorph (see figure)

- Work on better ways to control, *e.g.* the temperature jump and monitor the appearance of crystals
  - Cooling rate is an essential parameter for temperature and degree of supersaturation tracking

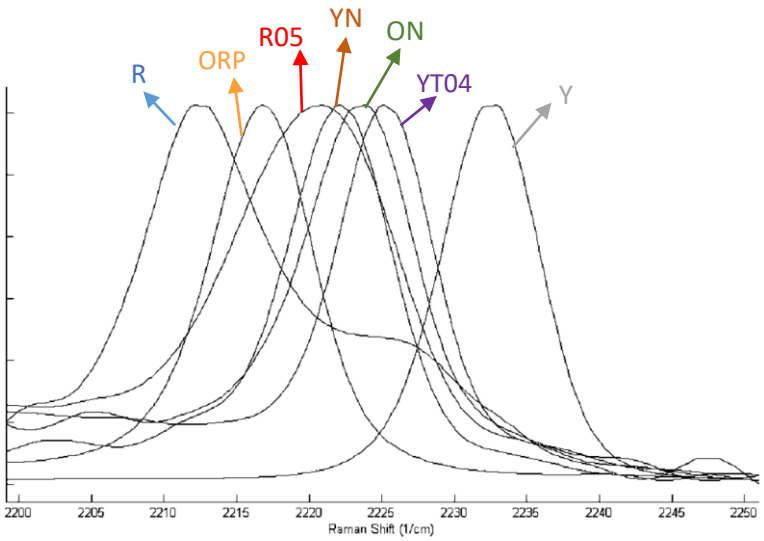

The nitrile stretch (2200-2250 cm^{-1}) of different ROY polymorph

Singh, A. et al. *Cryst. Growth Des*. **2009**, *9*, 1182-1185

Acknowledgement

Controlling Rheology via Boundary Conditions in Dense Granular Flows

Farnaz Fazelpour, Karen E. Daniels
North Carolina State University

IFPRI
International Fine Particle Research Institute

NSF

NC STATE UNIVERSITY

Granular rheology

- **Questions:** for a given set of particles, can we
    - make flow measurements in one geometry
    - determine the constitutive parameters
    - predict flows in other geometries
- **Status:** nonlocal rheology successfully models granular flows across different packing densities, particle sizes and shapes, and shear rates
    - but also need to know wall velocities a priori
- **Aim:** separate which properties are set by the particle properties, and which by the walls
    - develop predictive model for wall slip

Local rheology has some problems

- stress ratio, ratio between:

$$\mu = \frac{\tau(r)}{\mathrm{P}(r)}$$

shear stress: τ

normal pressure: P

- inertial number, ratio between:
  - Microscopic timescale T to squeeze a particle into a hole: $T = \frac{d}{\sqrt{P/\rho}}$
  - Macroscopic timescale of deformation: $\frac{1}{\dot{\gamma}}$

$$I = \frac{\dot{\gamma} d}{\sqrt{P/\rho}}$$

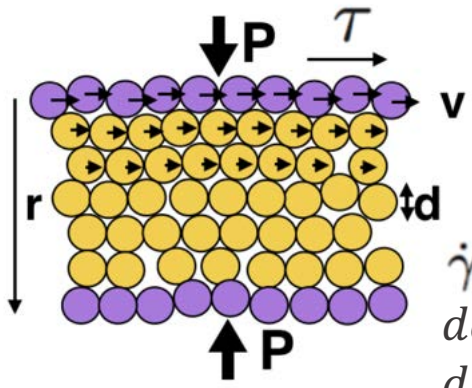

$\dot{\gamma} = dv/dr$

density ρ

diameter d

- Flow can exist below critical stress ratio: $\mu < \mu_s$
- Fails to explain phase transition from inertial to quasistatic regimes
- Fails to describe how shear/vibration in one region can fluidize distant region
- Fails to explain how shear band width depends on geometry

(Forterre et al. *Annu. Rev. Fluid Mech.*, 2008)
(Cheng et al. Phys. Rev. Lett, 2006)
(Nichol et al. Phys. Rev. Lett, 2010)
(Koval et al. Phys. Rev. Lett, 2009)
(Reddy et al. Phys. Rev. Lett, 2011)
(MiDi *Eur. Phys. J. E: Soft Matter Biol. Phys.*, 2004)

Nonlocal rheology (Cooperative model)

Measured values

Model parameters

granular fluidity: $g \equiv \frac{\dot{\gamma}}{\mu}$

- Locally, model the granular material as a Bingham fluid:

$$g_{loc} = \begin{cases} \sqrt{\frac{P}{\rho d^2}} \frac{\mu - \mu_s}{b\mu} & \mu > \mu_s \\ 0 & \mu < \mu_s \end{cases}$$

local parameter + grain parameters + nonlocal parameter

b, μ_s ρ, d A

- The cooperative length scale ξ is set by:

$$\frac{\xi}{d} = A\sqrt{\frac{1}{|(\mu - \mu_s)|}}$$

fluidity is determined by both local fluidity and nonlocal cooperative effect:

$$\nabla^2 g = \frac{1}{\xi^2}(g - g_{loc})$$

(Kamrin and Koval, Phys. Rev. Lett, 2012)

(Hennan et al. PNAS,2013)

Success of nonlocal rheology

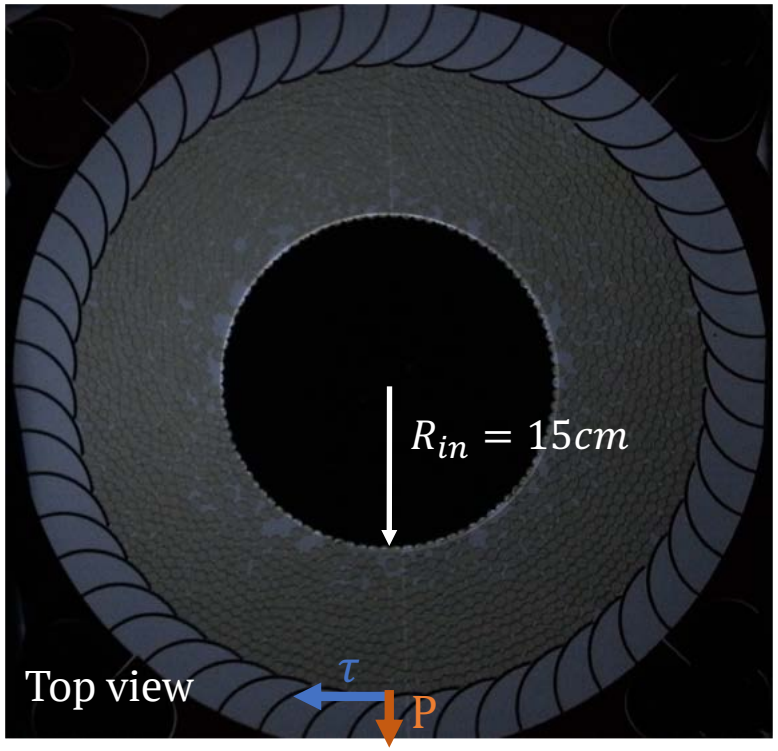

★ The model is able to capture:

1) the measured $\mu(I)$ and $v(r)$ data
2) using a single set of parameters
3) across all packing fraction and shearing conditions

$A(nonlocal)$	$b(local)$	μ_s
0.402 ± 0.003	1.1 ± 0.5	0.26 ± 0.01

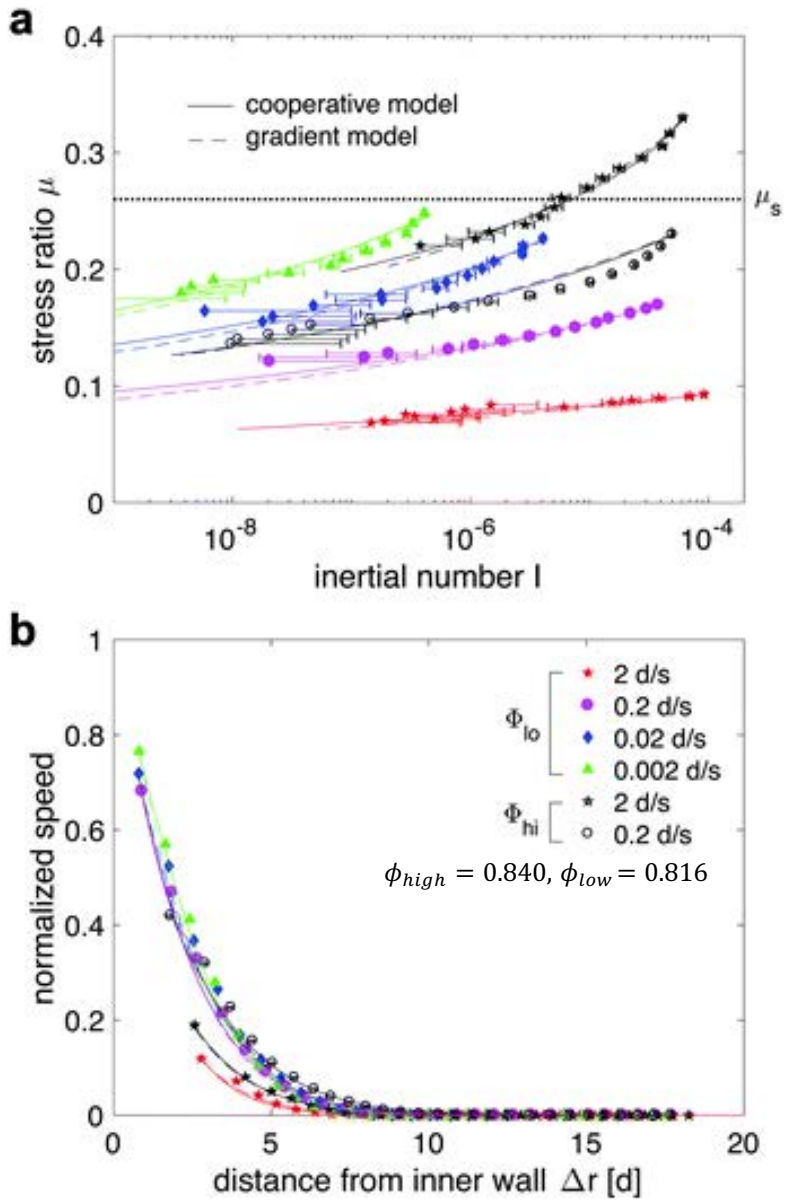

Tang, Brzinski, Shearer and Daniels and , Soft Matter, 2018

Success of nonlocal rheology for particles of different shapes

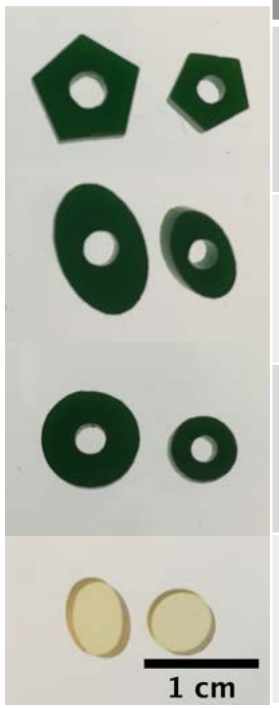

μ_s	b(local)	A(nonlocal)
0.17 ± 0.01	1.1 ± 0.6	0.10 ± 0.001
0.24 ± 0.02	1.1 ± 0.5	0.23 ± 0.003
0.24 ± 0.02	1.1 ± 0.6	0.28 ± 0.003
0.26 ± 0.02	1.1 ± 0.3	0.40 ± 0.003

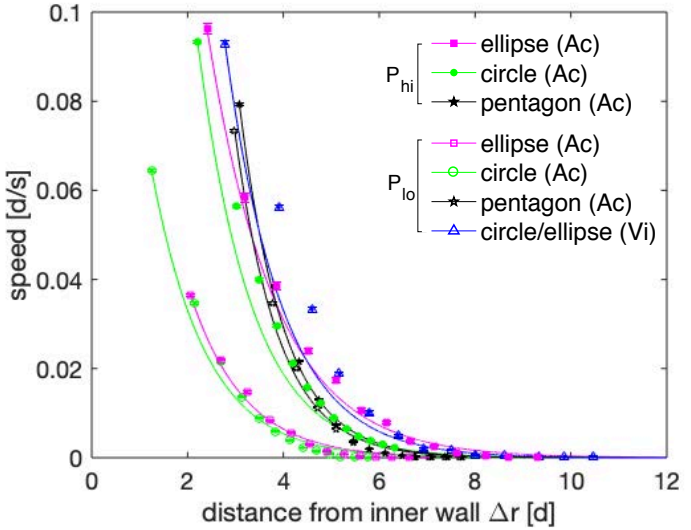

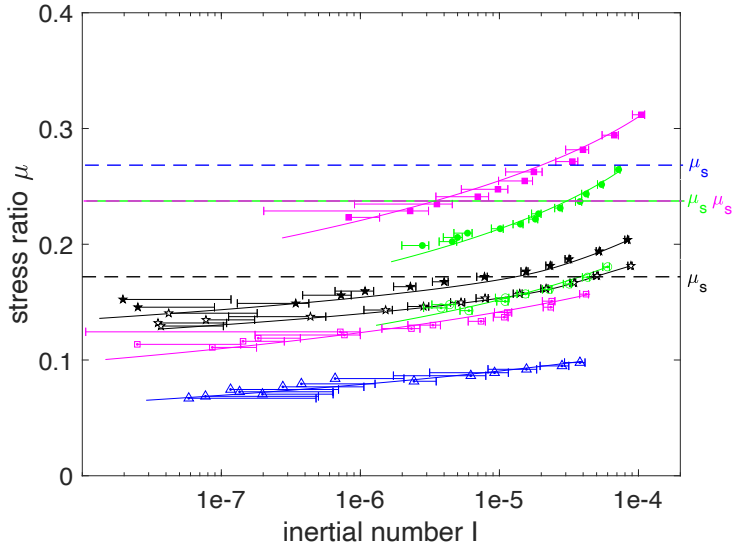

Changing boundary roughness

- Laser-cut boundaries with controlled roughness
- 9 & 11 mm diameter photoelastic particles
- Velocity profile from particle tracking
- Shear and normal stresses from photoelasticity

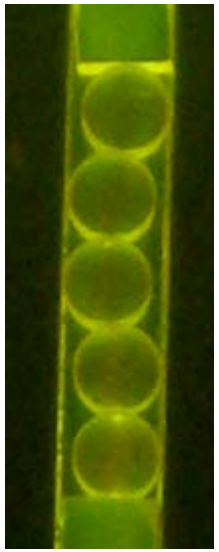

low force

medium force

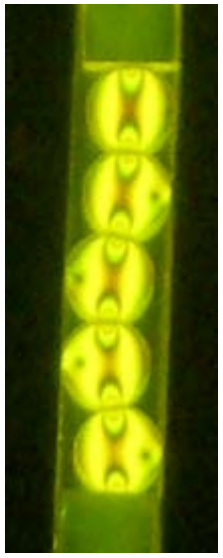

high force

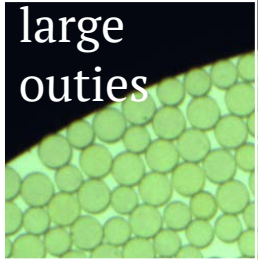

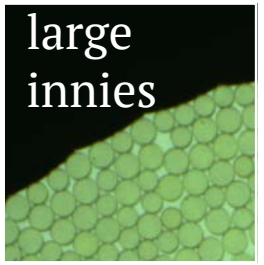

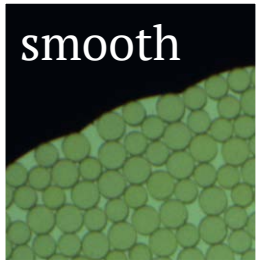

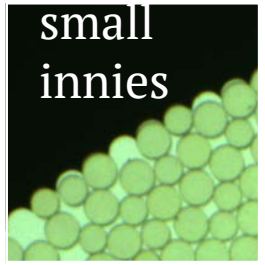

Classic technique: e.g. Frocht 1941

The effect of boundary on flow

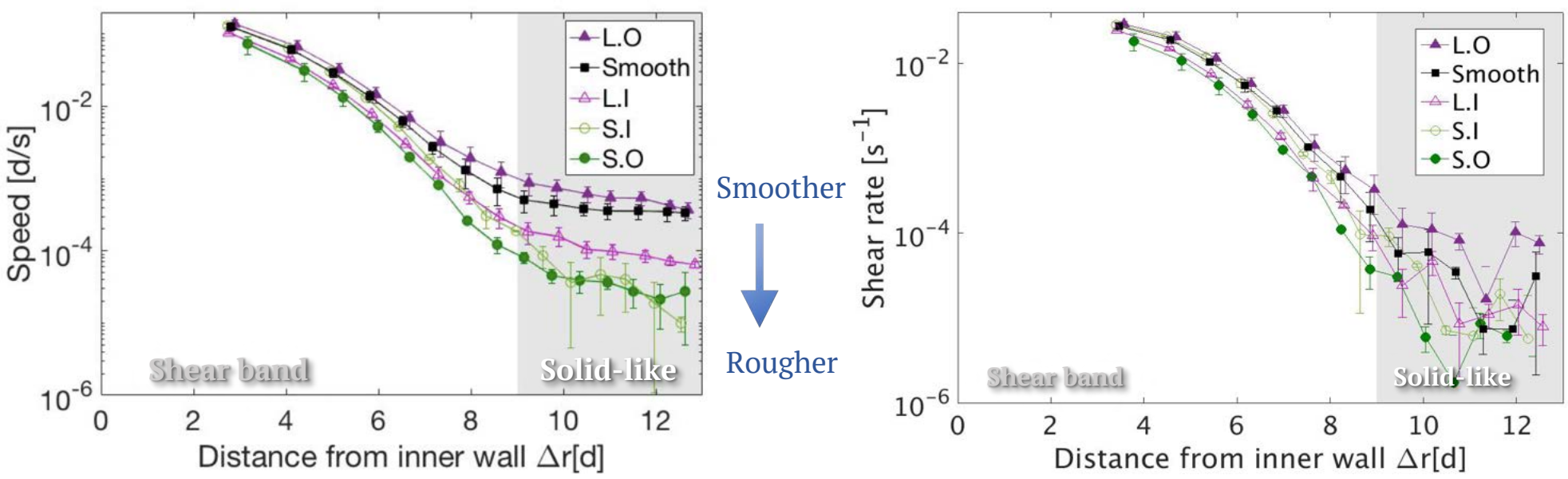

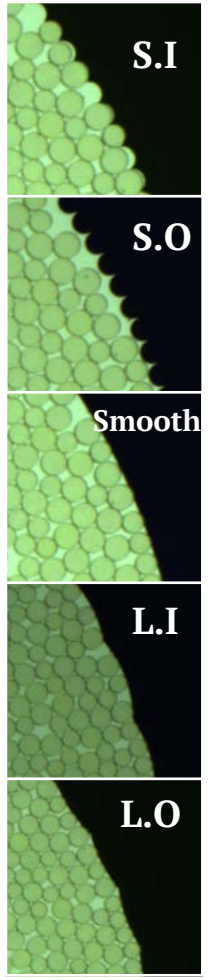

- Smooth boundaries have more than a order of magnitude slip than rough
- Transition to nonlocal regime depends on boundary roughness

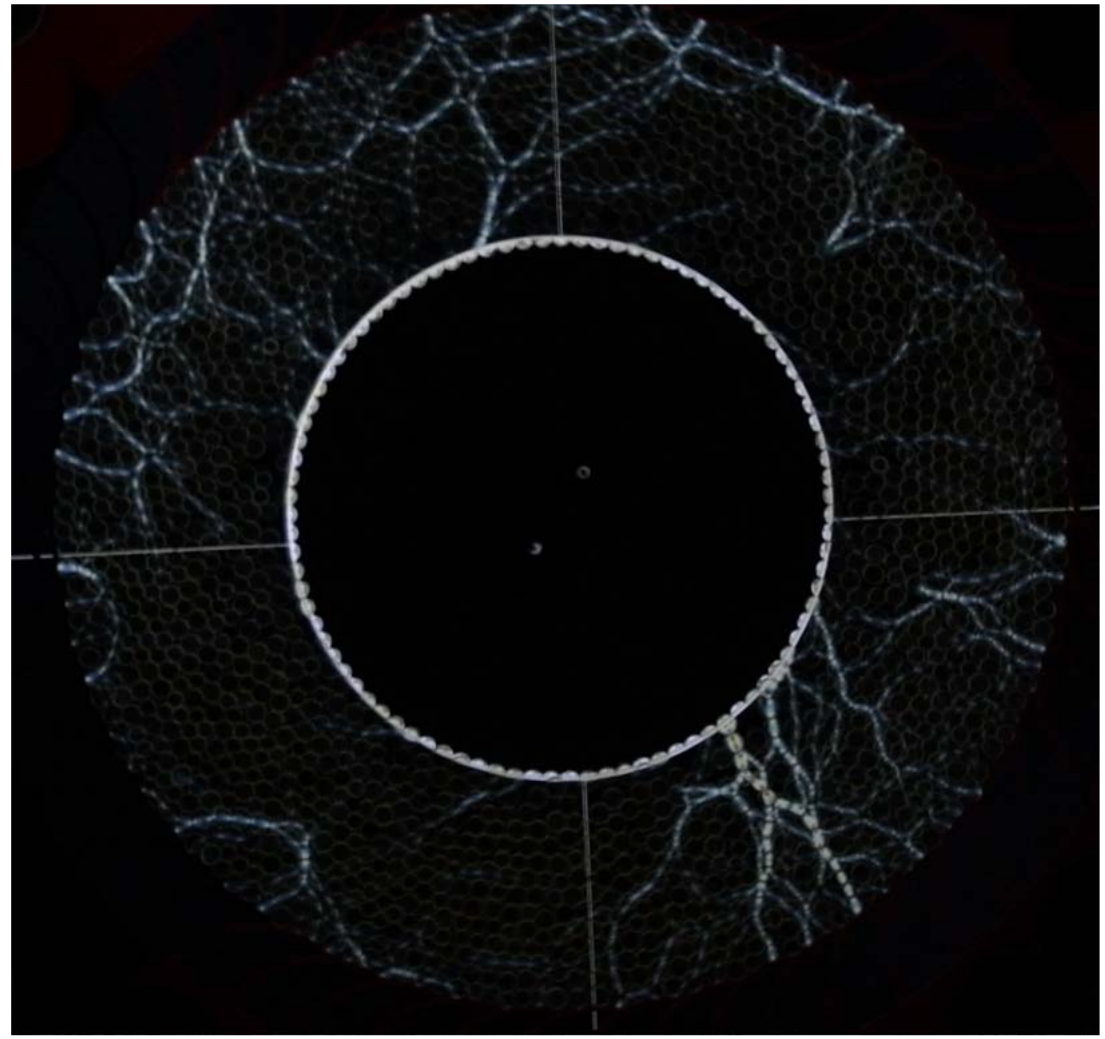

Photoelastic inversion

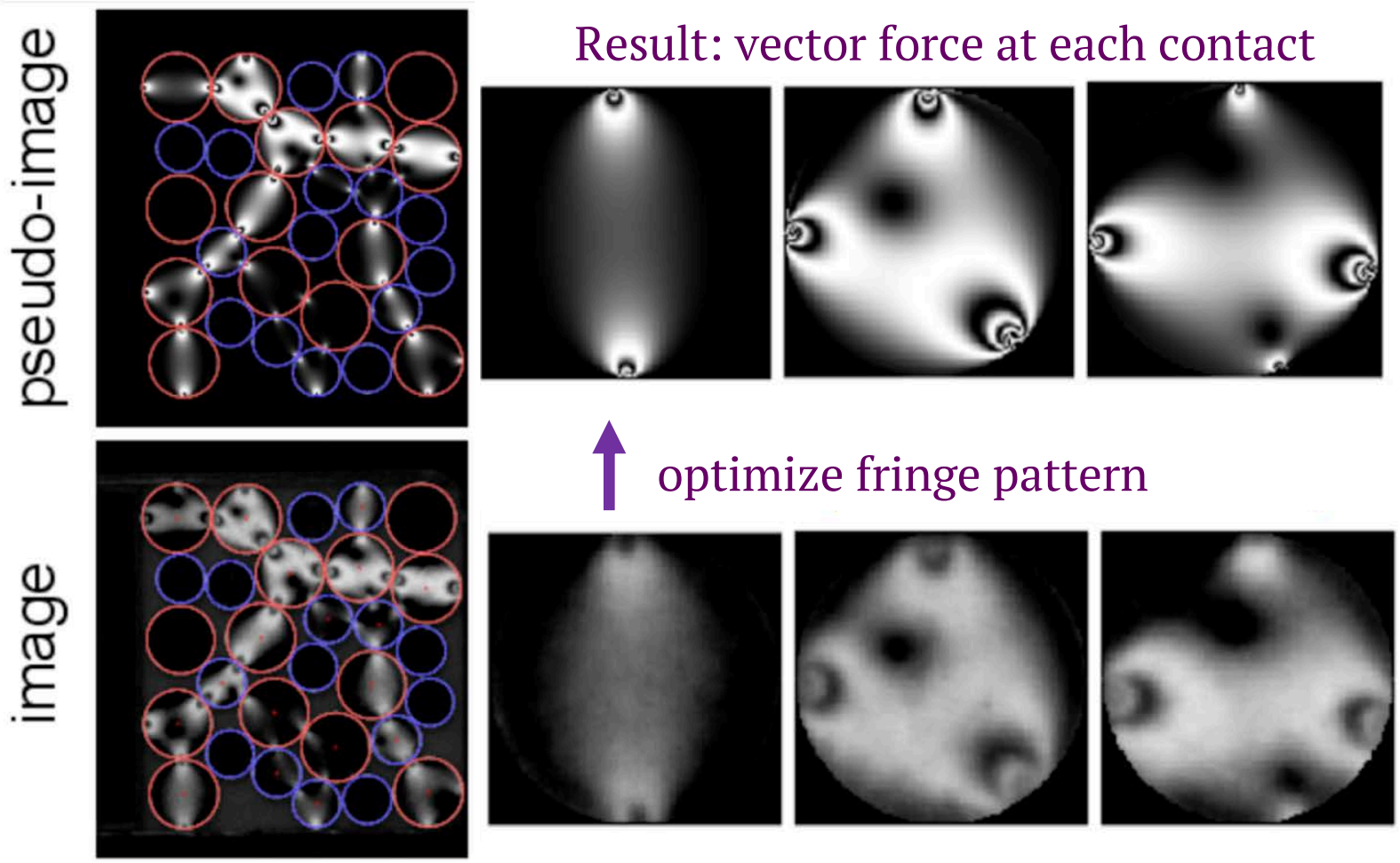

Daniels, Kollmer, Puckett. Rev. Sci. Inst. (2017)
https://github.com/jekollmer/PEGS

Photoelastic inversion

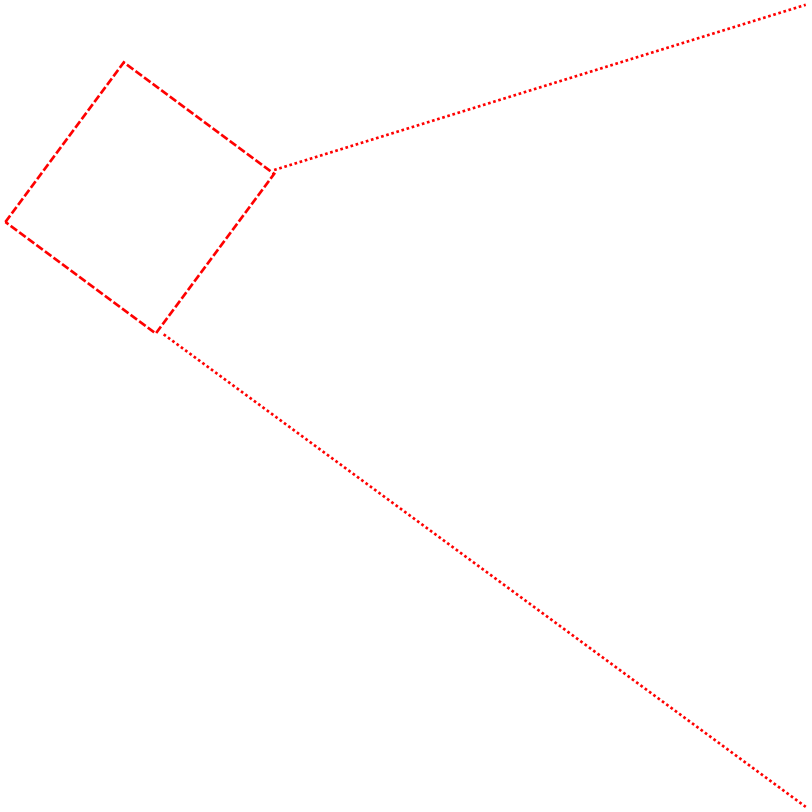

The original image taken on the experiment

Reconstructed pseudo-images, created from fitting the vector contact force at each interparticle contact.

Stress measurement

contact force vector at each contact $dF_i = ds\ \sigma_{ij} n_j$ stress at each contact

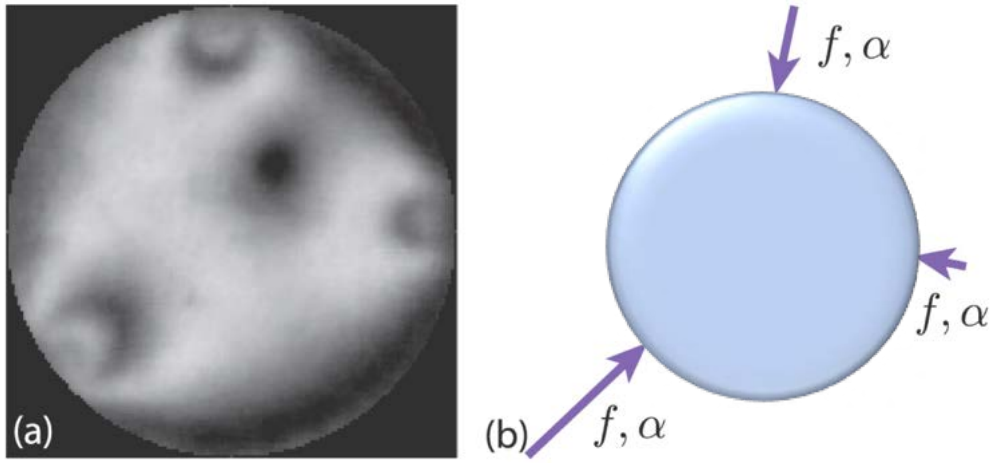

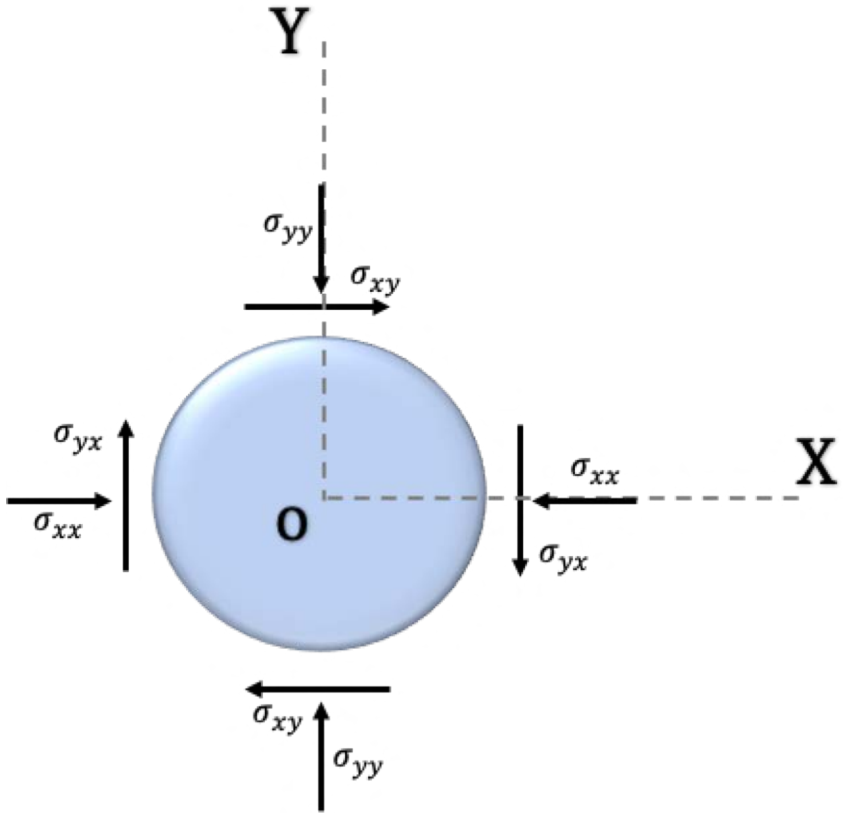

K. Daniels et al Rev, Sci, Inst, 2017

Coarse graining

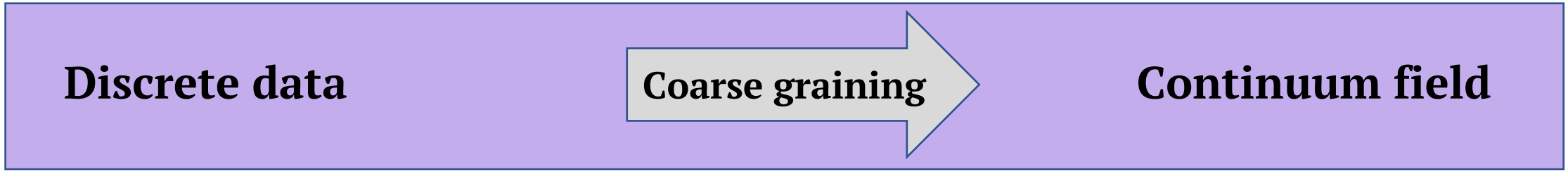

A macroscopic stress field can be extracted from microscopic stress with a coarse graining function(Lucy function):

$$\mathcal{W}(\mathbf{r}) = \frac{105}{16\pi c^3}\left(-3\,(r/c)^4 + 8\,(r/c)^3 - 6\,(r/c)^2 + 1\right), \text{ if } r := |\mathbf{r}| < c, 0 \text{ else},$$

Contact stress is defined:

$$\sigma^c = \sum_{i=1}^{N}\sum_{j=i+1}^{N} f_{ij}\, r_{ij} \int_0^1 \mathcal{W}(r - r_i + s\, r_{ij})\, ds$$

Where r_{ij} is interaction forces and f_{ij} is center to center vector

T Weinhart et al, *Phys. Fluids, 2013*

Code-Development Dataset

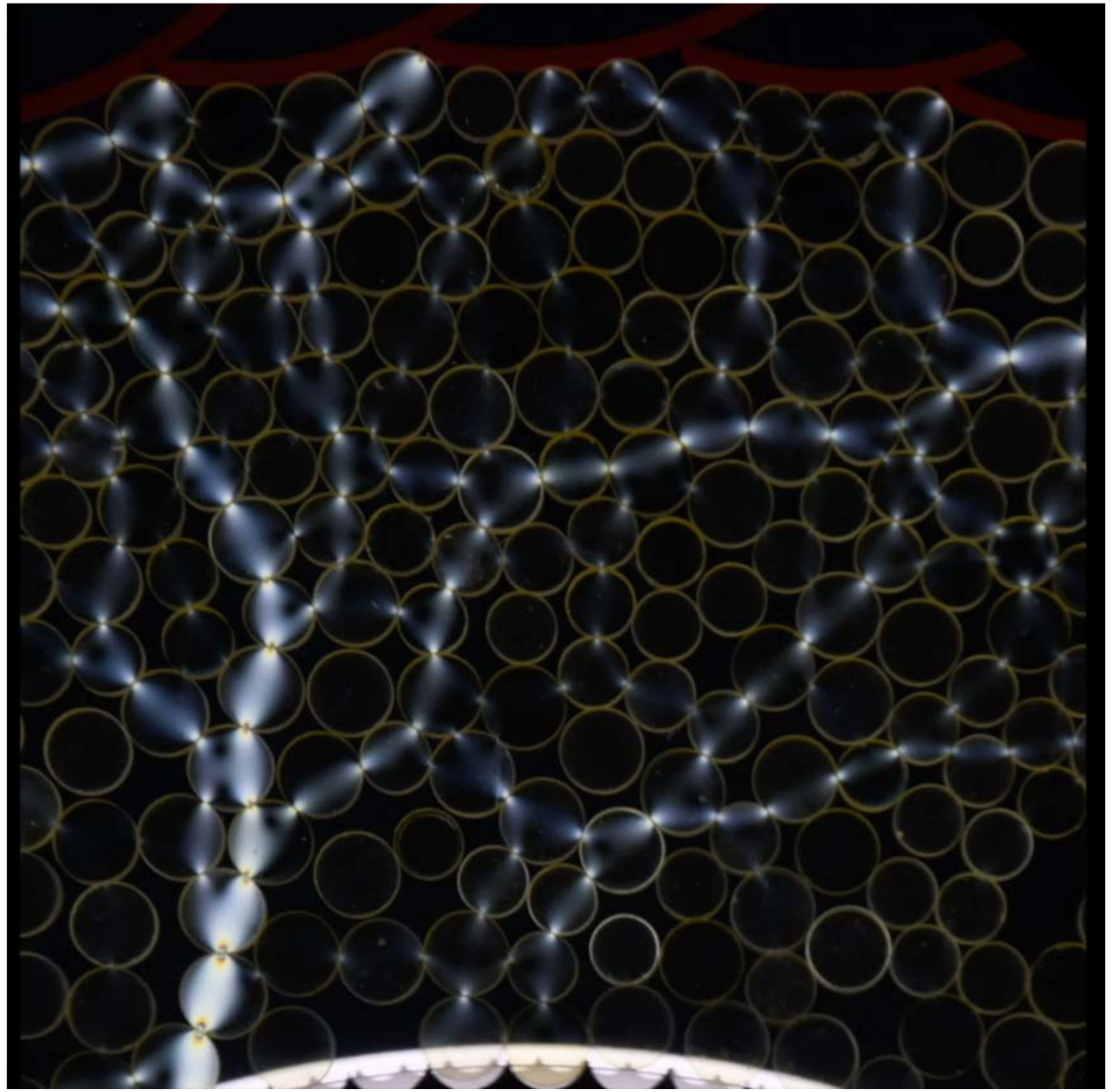

Coarse graining normal stress (pressure)

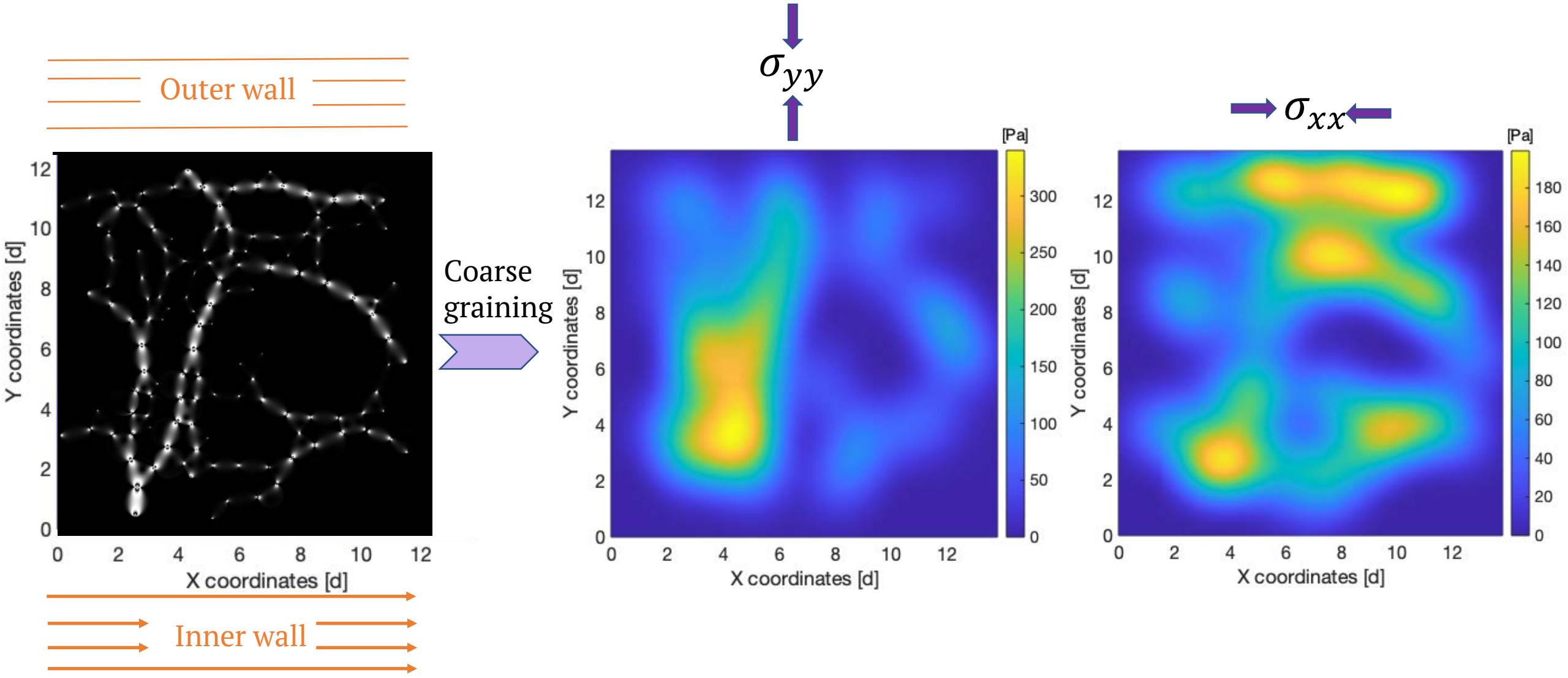

Coarse graining shear stress

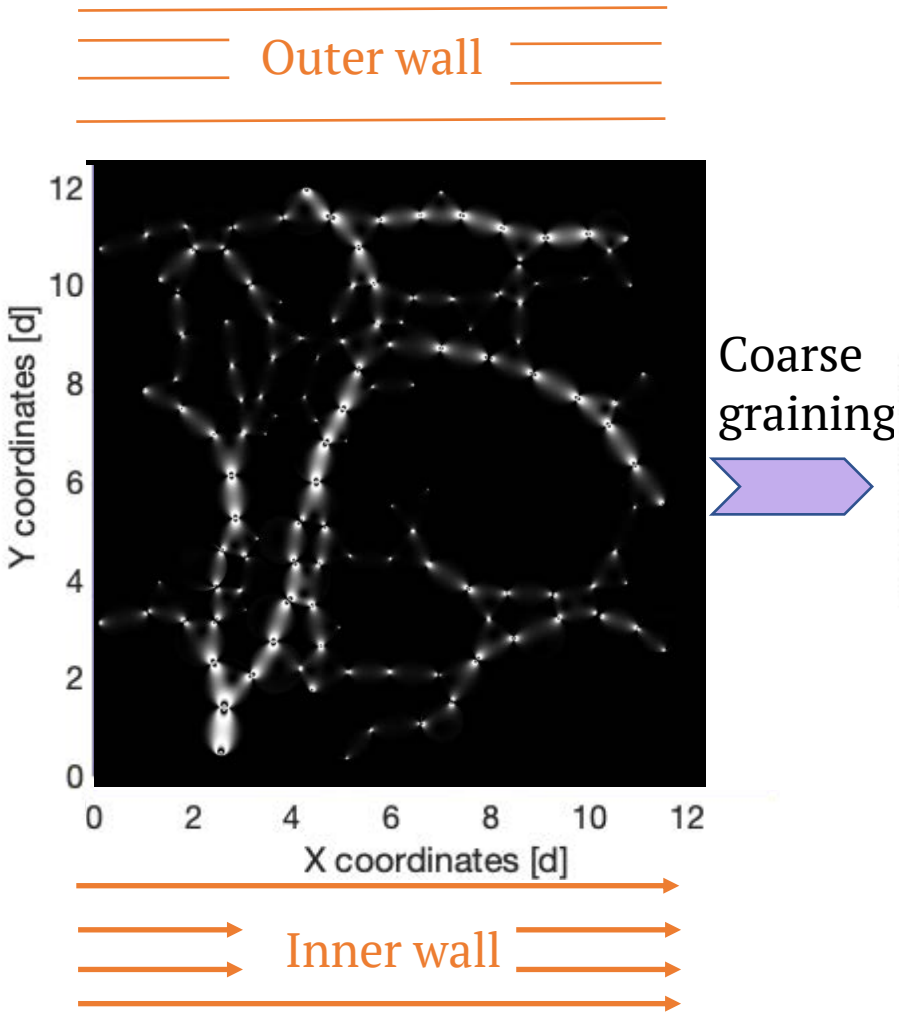

Coarse graining

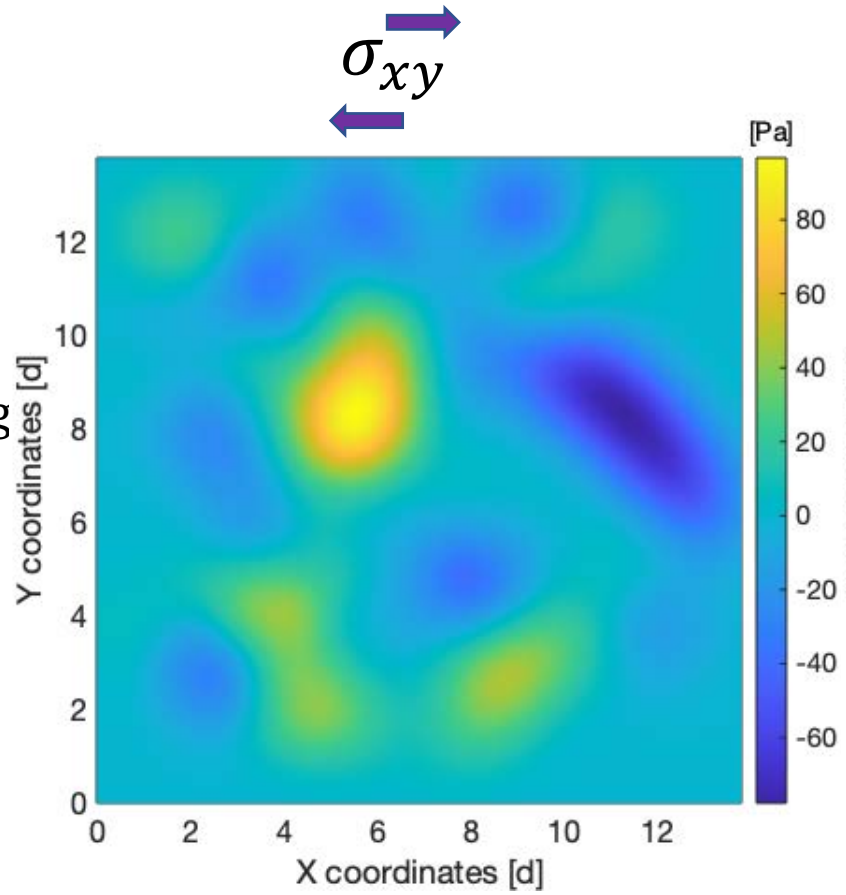

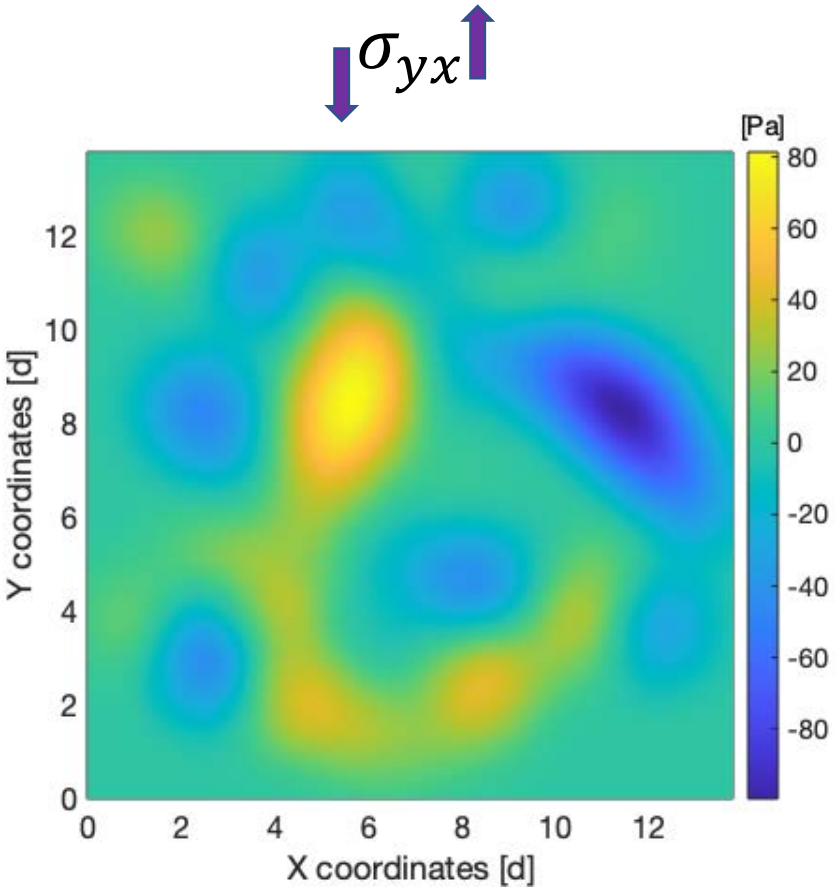

Coarse graining stress, average over 60 frames

Shear stress τ

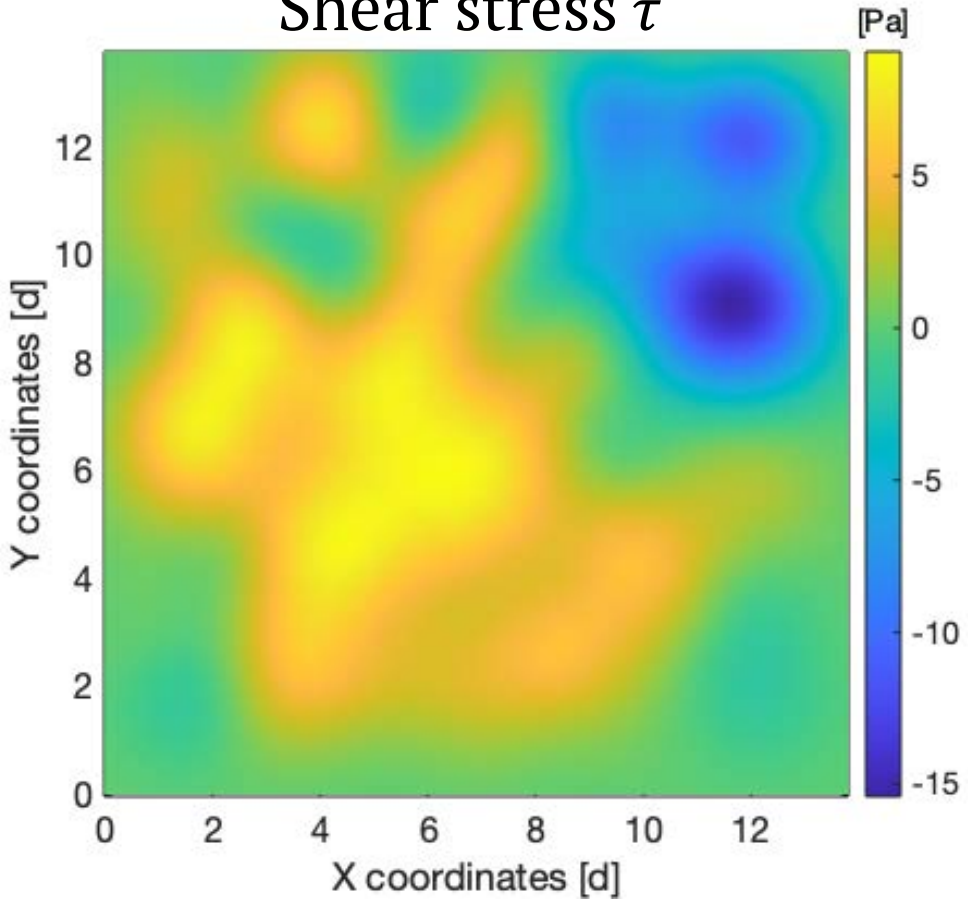

Pressure P

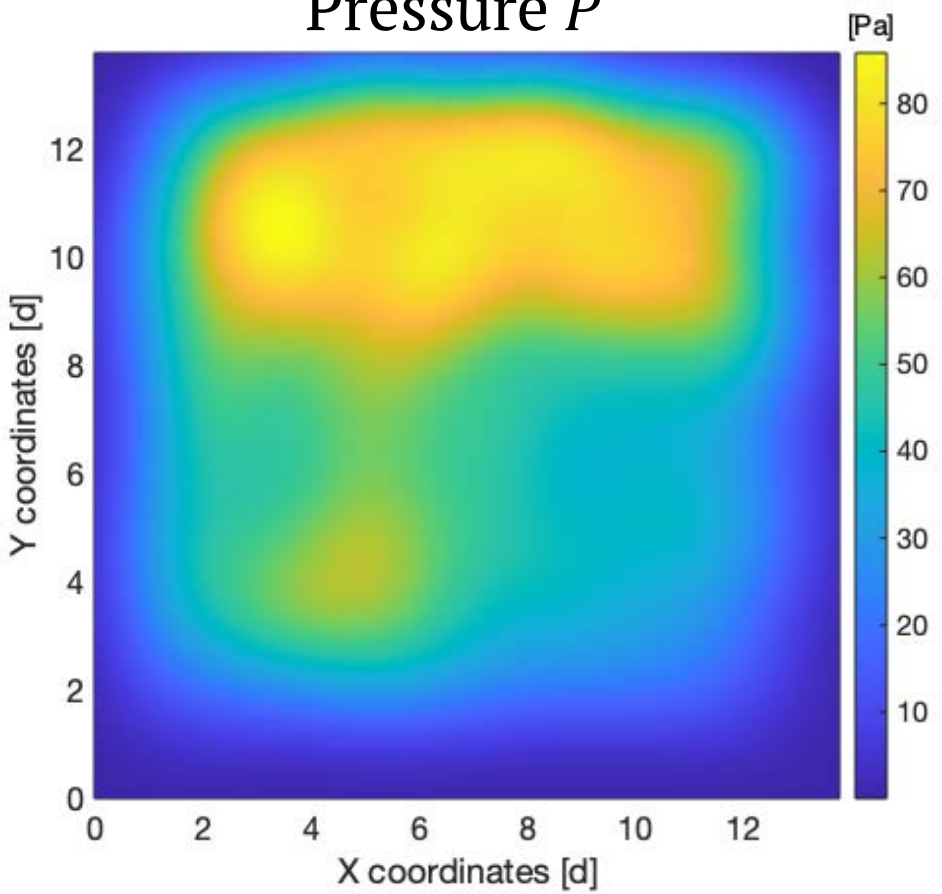

Conclusions & Next Steps

- we have observed that boundary roughness strongly controls both the flow profile $v(r)$ and shear rate profile $\gamma(r)$.
- Successfully measured stress component at grain size level, using photoelastic methods.
- Developed coarse graining pipeline to obtain stress field.
- When we take more data we will be able to:
  1. obtain stress fields and how boundary properties control stress fields
  2. provides all of the information necessary to calculate the local $\mu(I)$ and fluidity $g(r)$
  3. characterize the dependence of the boundary conditions on both the particle-shape and boundary characteristics.

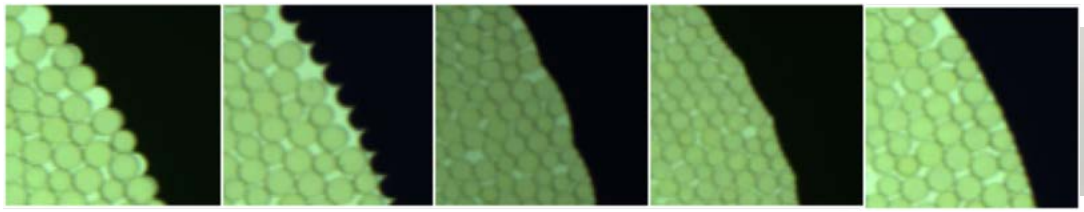

A Holistic Approach for the Model-based Control of Crystal Size, Shape and Purity in Integrated Batch and Continuous Crystallization - Wet Milling Systems

Botond Szilagyi, Zoltan K. Nagy

School of Chemical Engineering

Purdue University, West Lafayette, IN

PURDUE UNIVERSITY

Outline

Project objectives

… and main deliverables

Progress summary

… in a nutshell

Next steps

… given what we know, what could we do

Project objectives

- Many technology and economic drivers
- 70% of all solid products & 90% of APIs involve a crystallization step
- Control of crystalline properties (CSD, shape, polymorphic form, purity, etc.) important
  - Product effectiveness (dissolution, bio-availability, tablet stability)
  - Efficient downstream operations (filtration, drying)

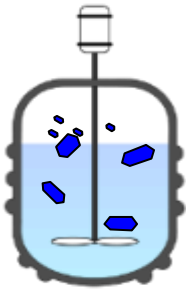

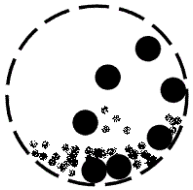

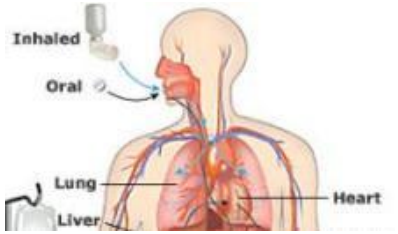

Crystallization → Downstream processes → Final product

Control of crystal properties is critical for product functionality and operational efficiency

1D agglomeration and breakage models and solvers

Agglomeration modeling in crystallization (1D)

- **Agglomeration often spontaneously occurs during crystallization.**
- **“Forced agglomeration”: spherical agglomeration.**
- **Granulation processes fully governed by agglomeration.**

Agglomeration of two primary particles

- Volume conservation
- No shape conservation. Modeling practice: sphere equivalent diameter

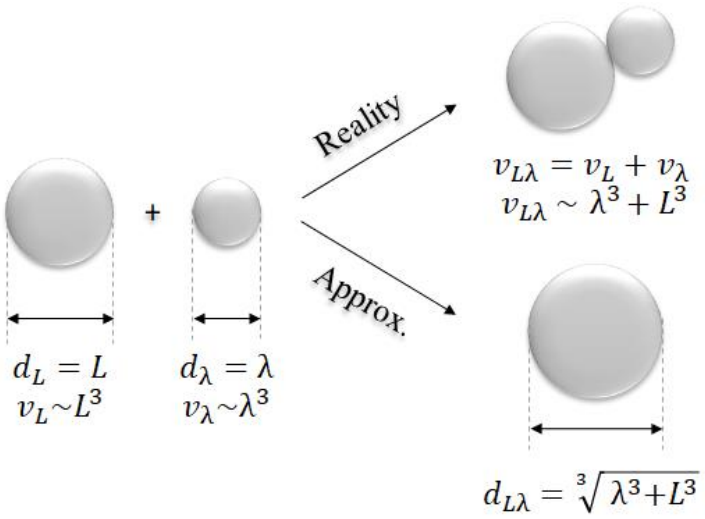

Agglomeration of multiple particles

- Volume conservation
- Quasi shape-conservation. Modeling practice: sphere equivalent diameter

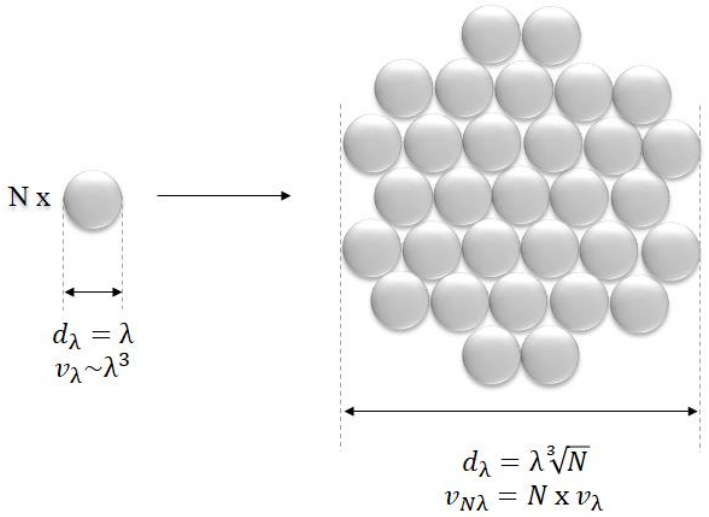

Agglomeration modeling in crystallization (1D)

The agglomeration population balance model-equation:

$$\frac{\partial n(L,t)}{\partial t} = \frac{L^2}{2}\int_0^L \frac{\beta\left[(L^3-\lambda^3)^{1/3},\lambda\right]}{(L^3-\lambda^3)^{2/3}} n\left((L^3-\lambda^3)^{1/3},t\right) n(\lambda,t)d\lambda - n(L,t)\int_0^{L_{max}} \beta(L,\lambda)n(\lambda,t)d\lambda$$

Birth rate of L-size particles by agglomeration

Death rate of L-size particles by agglomeration

$\beta(L,\lambda)$: agglomeration kernel. Implemented:

Name	$\beta(L,\lambda)$
Constant	k_{ag}
Brownian motion	$k_{ag}\frac{(L+\lambda)^2}{L\lambda}$
Sum	$k_{ag}(L^3+\lambda^3)$
Hydrodynamic	$k_{ag}(L+\lambda)^3$
Differential force	$k_{ag}(L+\lambda)^2\lvert L-\lambda\rvert^2$

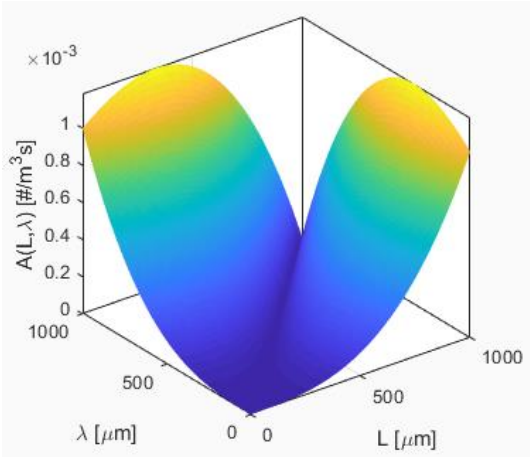

Differential force ($k_{ag} = 10^{-12}$)

k_{ag}: might depend on temperature, stirring conditions, growth rate etc.

Breakage modeling in crystallization (1D)

- **Attrition often occurs during crystallization processes.**
- **Fragmentation might also occur.**
- **Wet milling: governed by particle breakage.**
- **Breakage: volume conserving. Not shape conserving (there are exceptions, as high aspect-ratio crystals)**

The breakage population balance model-equation:

$$\frac{\partial n(L,t)}{\partial t} = \int_{\lambda}^{L_{max}} b(L|\lambda) n(\lambda,t) S(\lambda) d\lambda - S(L) n(L,t)$$

Birth rate of L-size particles by breakage

Death rate of L-size particles by breakage

Breakage modeling in crystallization (1D)

Breakage selection function ($S(L)$)

- Probability that an L size crystal breaks up
- Numerous functions. Implemented: constant, power-law and hyperbolic tangent

$$S(L) = k_{br}\frac{1}{2}\left(\tanh\left(k(L_c - L)\right) + 1\right)$$

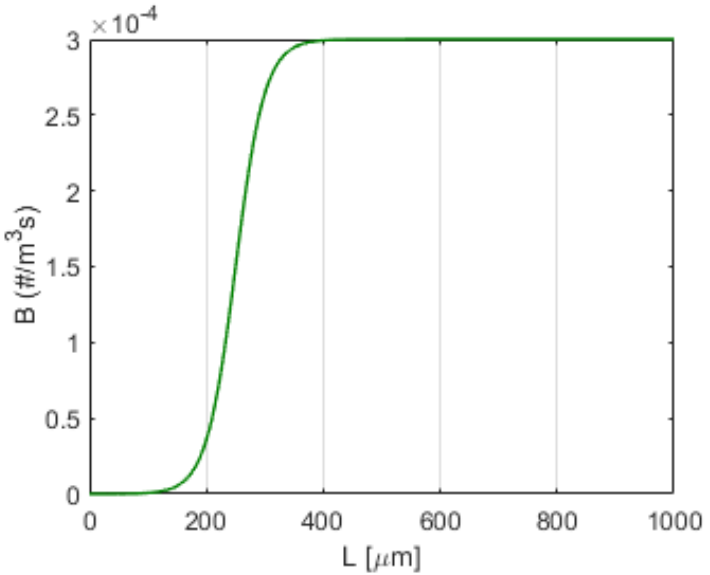

Parameters: k_{br} = 0.0003; k = 0.02; L_c = 250 μm

Fragment distribution function ($b(L|\lambda)$)

- Probability that L sized crystal is produced from the breakage of a λ size crystal
- Implemented: symmetric fragmentation, uniform distribution, normal distribution

$$b(L|\lambda) = \frac{1}{\sigma\sqrt{2\pi}}\exp\left(-\frac{(L-\mu)^2}{2\sigma^2}\right)$$

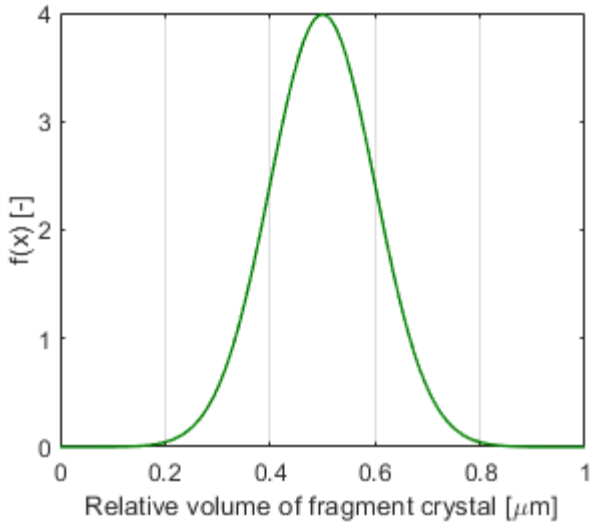

Parameters:σ= 0.1λ; μ= 0.5 λ

Implementation in the generic 1D solver

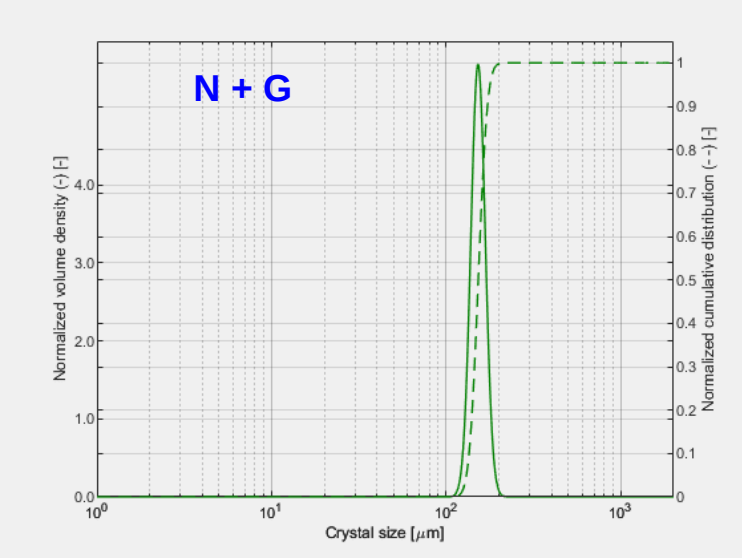

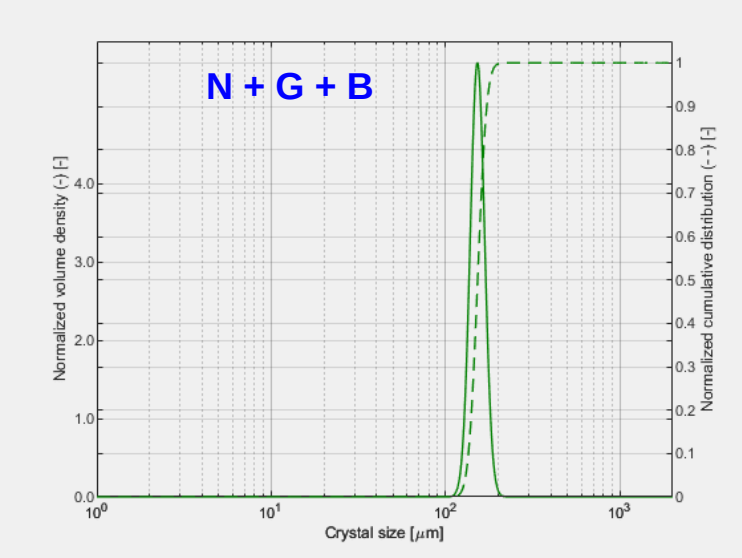

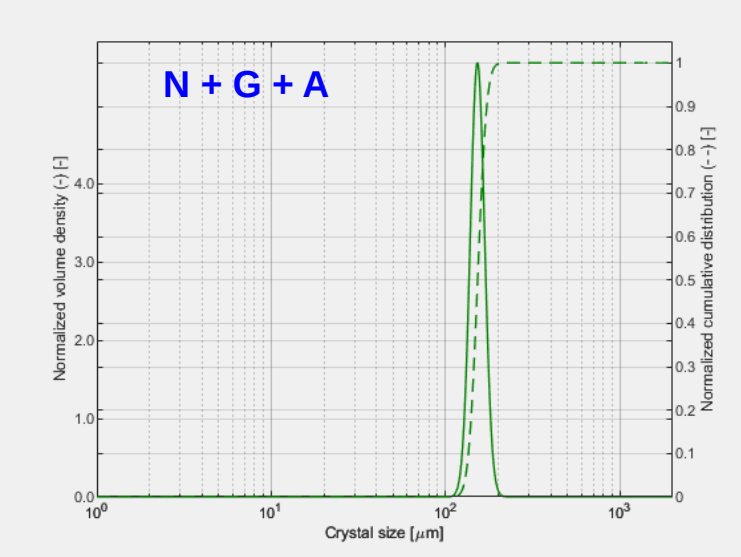

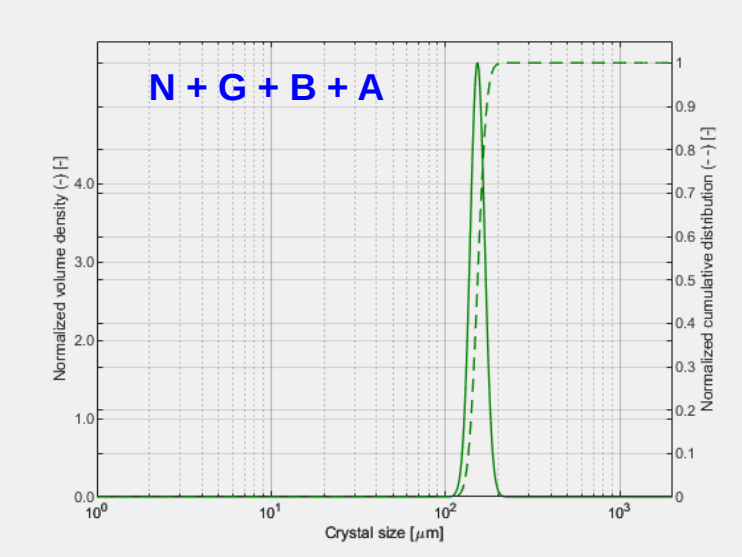

Integrated system model development: MSMPR cascade and it's applications

MSMPR cascades

- First step in the flexible crystallization network development.
- Mechanisms: 1D nucleation, growth, dissolution, breakage, agglomeration
- System types: cooling, antisolvent, combined cooling and antisolvent

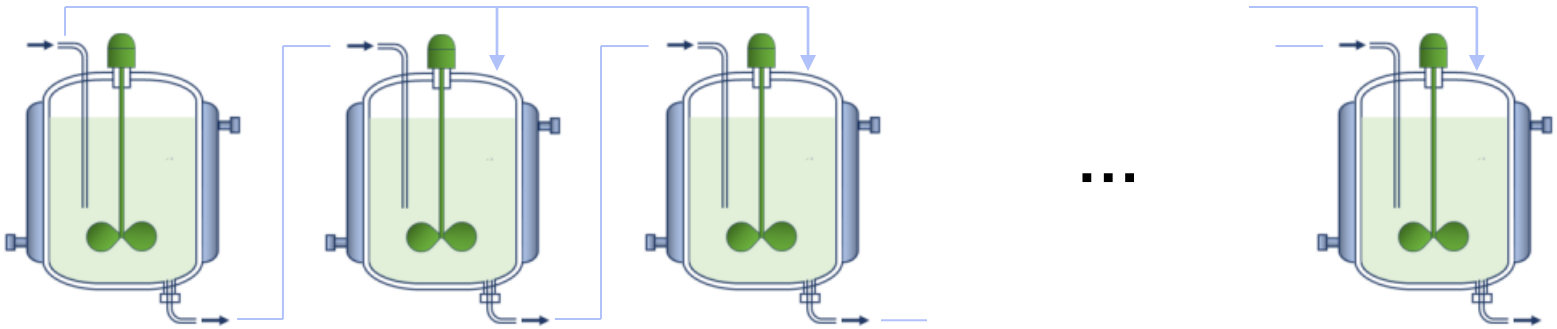

- Flexible number of crystallizers (no upper limit)
- Operating conditions configured individually for each crystallizer

MSMPR cascades: modeling and simulation

- Quick example: pure cascade of four MSMPRs. Model-equations were populated and solved automatically for each crystallizer
- Cooling crystallization with identical yields and mean residence times

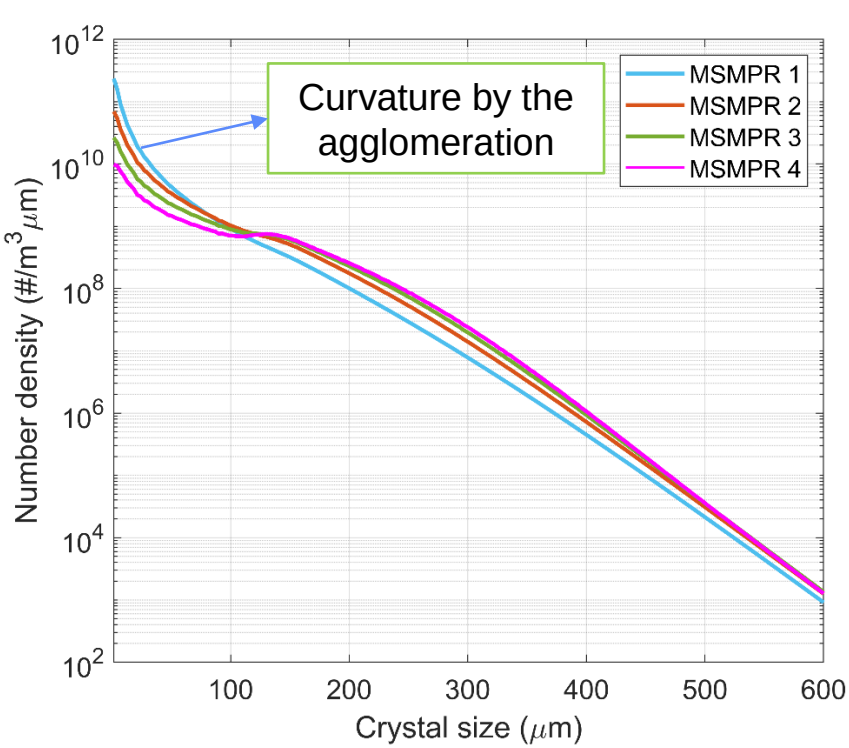

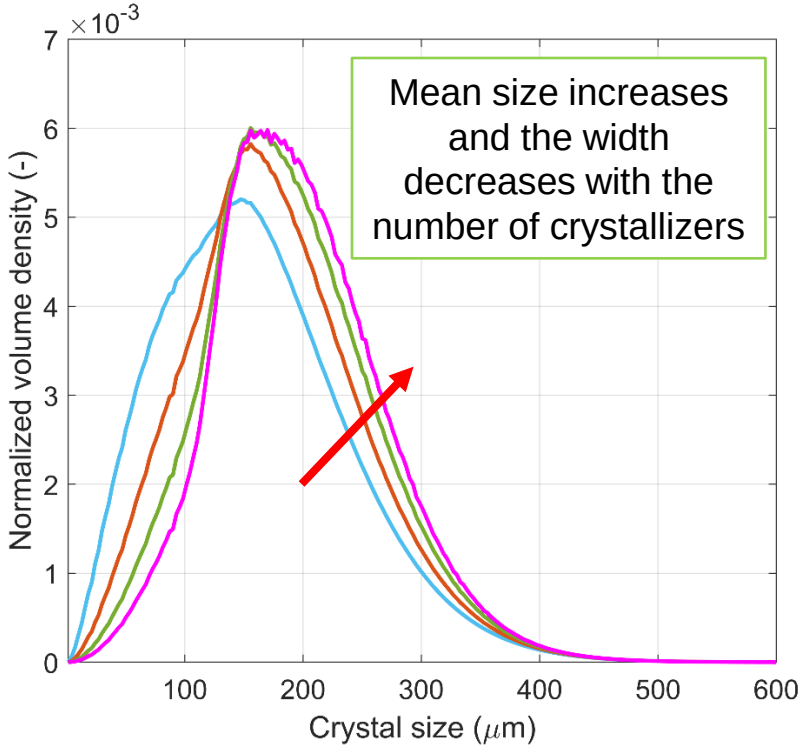

Typical MSMPR cascade simulation with nucleation, growth, agglomeration and size dependent breakage (~10 s, 3 μm grid size, 2400 μm max. size)

Flexible MSMPR cascade model: further applications

- Integrated MSMPR-tubular crystallizers are promising devices. In MSMPR in-situ seed generation happen.

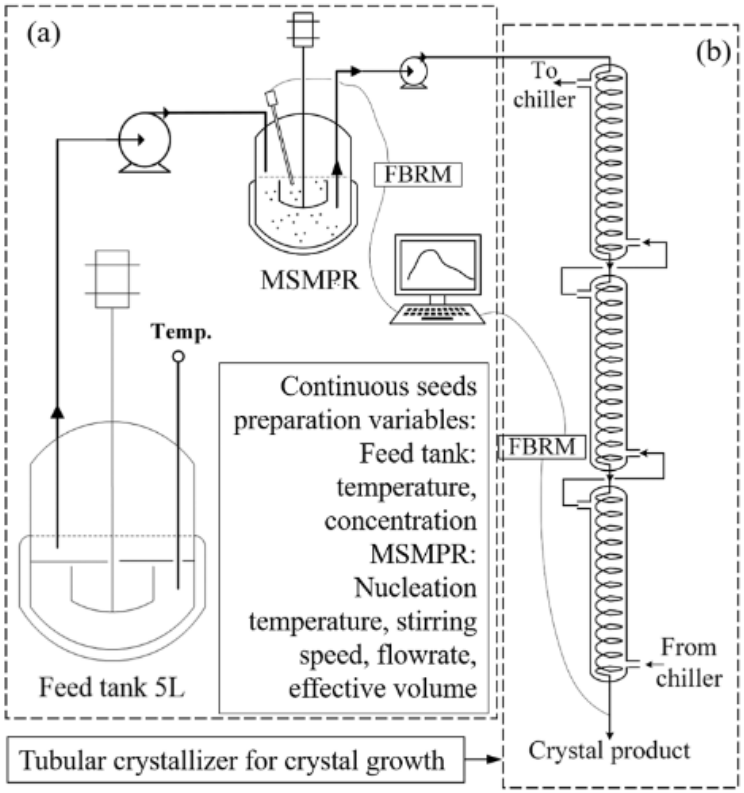

Scheme of an integrated continuous MSMPR-tubular crystallizer system for polymorphic crystallization *

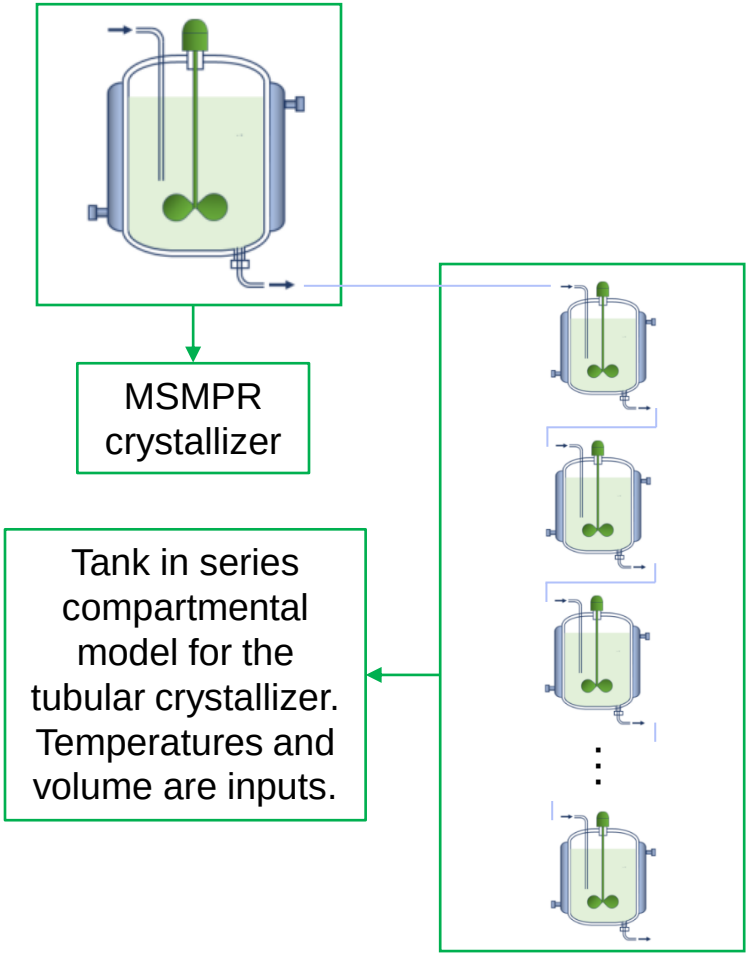

* Z. Gao et al., Journal of Crystal Growth, 507, 334-351

Extension to MSMPR network (in progress)

- Model-equations populated based on adjacency matrices that defines the connectivity
- The active crystallization mechanisms set for each MSMPR

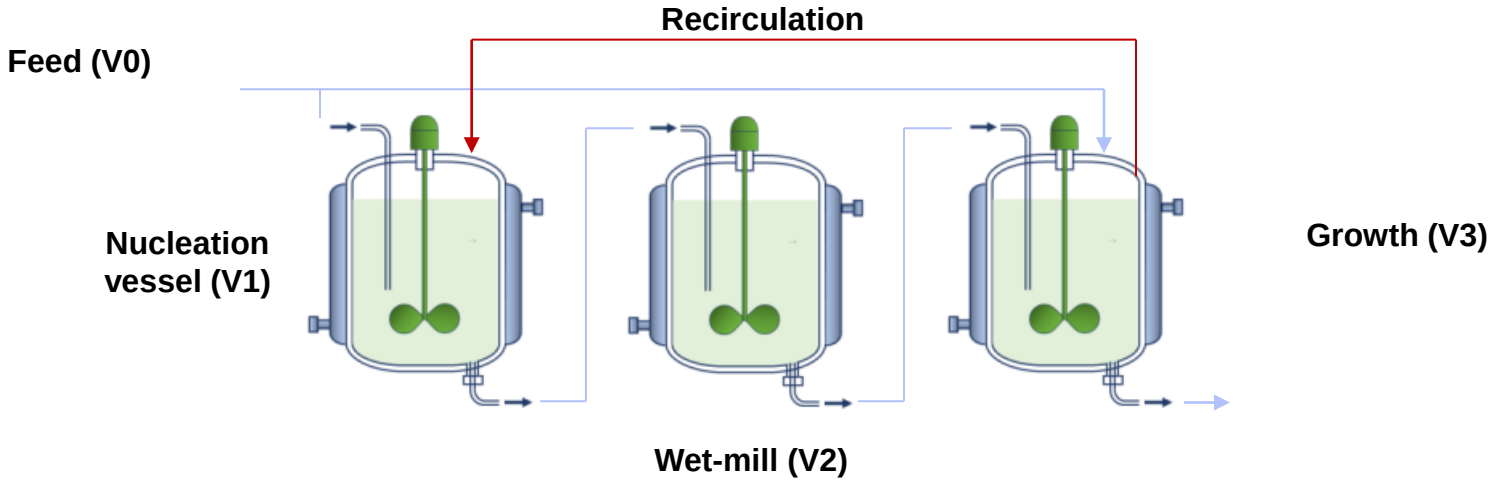

	V0	V1	V2	V3
V0	0	1	0	1
V1	0	0	1	0
V2	0	0	0	1
V3	0	1	0	0

- *Example*: definition of connectivity between the MSMPRs
- "1" in a cell means that there is a flux from the crystallizer in the given line to the crystallizer of the given column
- Similar adjacency matrices are applicable for the definition of other operating conditions (e.g. flowrates)

Parameter estimation: a novel way of using FBRM data and it's application to 1D and 2D crystallization kinetics estimation

How to use the FBRM count data for PE?

Repeating question, because:

- FBRM became routine tool in crystallization monitoring
- Great for qualitative measurements, indirect feedback control on particle size (DNC)
- Difficult to quantify
- Inaccurate CSD-CLD transformations
- Generally not used for PE

$$\boldsymbol{O(KP)} = f(\Delta C) + wf(\Delta D) + uf(\Delta N)$$

ΔC sum-squared error of concentrations

ΔD sum-squared error of CSDs

ΔN FBRM term (generally not used)

Correlation between count and number density?

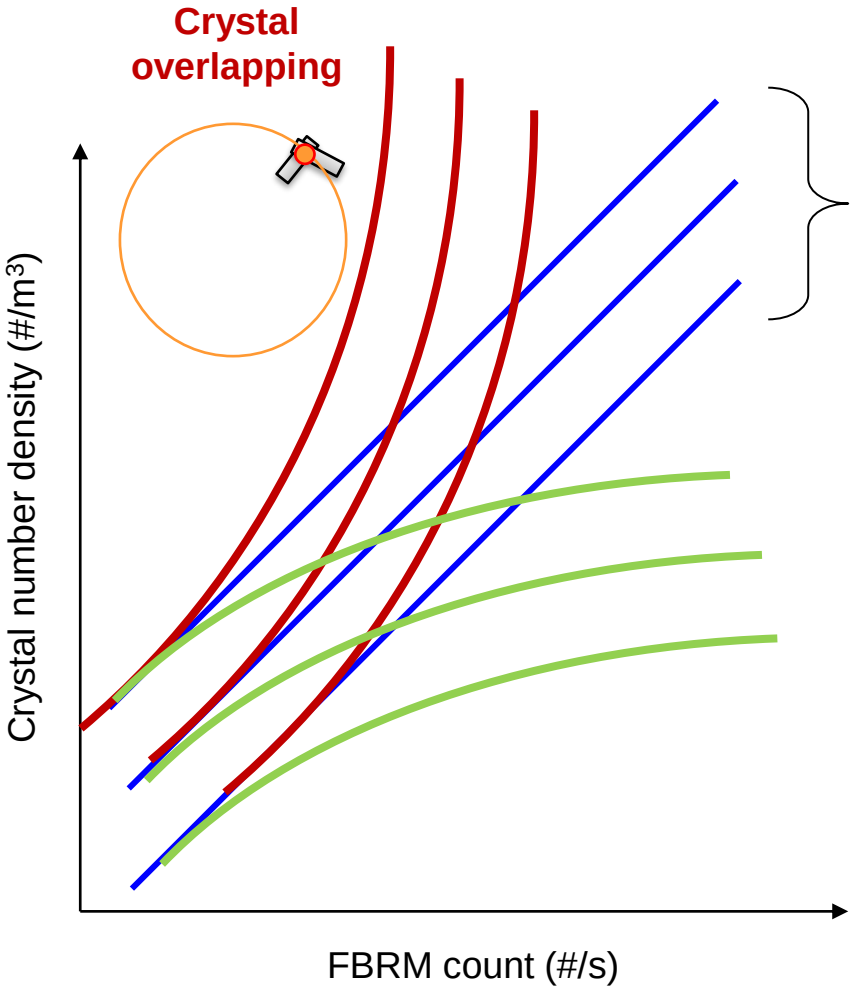

(low solid loading, spherical crystals…)

FBRM placement, stirring rate etc.

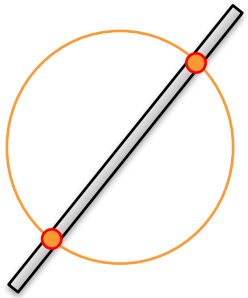

Double counting of high AR crystals

How to use the FBRM data for PE?

Repeating question, because:

- FBRM became routine tool
- Great for qualitative measurements
- Hard to quantify
- Inaccurate CSD-CLD transformations
- Generally not used for PE

$$\boldsymbol{O(KP)} = f(\Delta C) + wf(\Delta D) + uf(\Delta N)$$

ΔC sum-squared error of concentrations

ΔD sum-squared error of CSDs

ΔN FBRM term (generally not used)

$$\Delta N = -\boldsymbol{R^2}$$

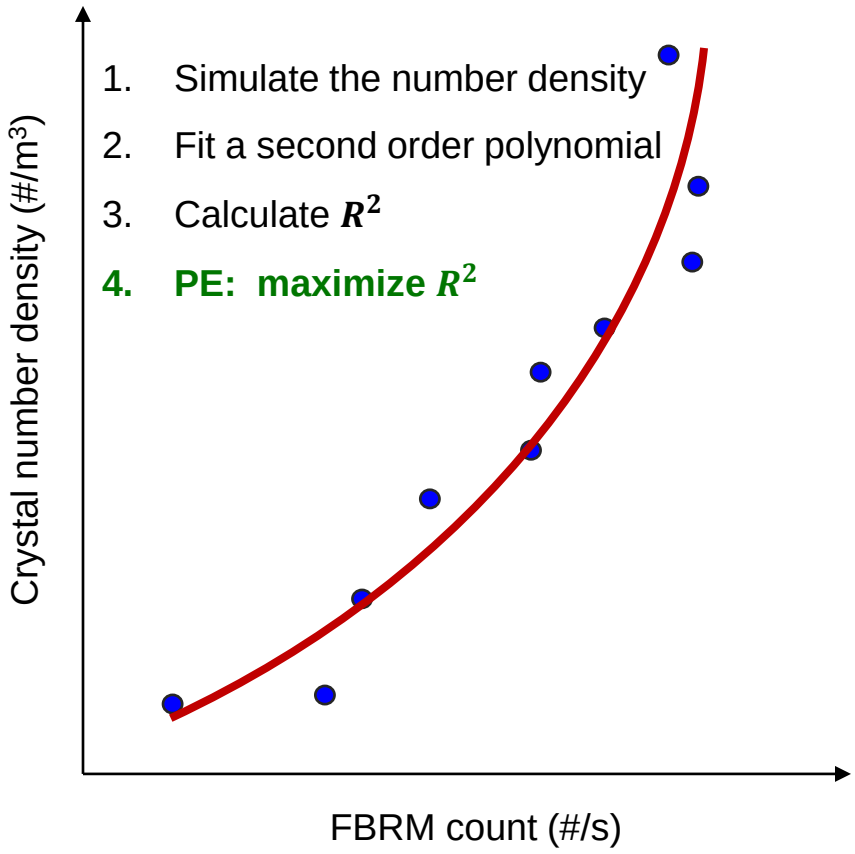

New assumption: The FBRM count correlates with the true number density, which can be captured with a second order equation

Crystallization kinetics of a model API: 1D case

- 1D demonstration to introduce a novel size dependent growth expression and the count correlation based parameter estimation.
- Model API (“Compound A”, real API candidate).
- Slow-growing high aspect ratio crystals, nucleation-dominated process.
- Temperature cycles are required to obtain sufficiently large crystals.
- The model would enable direct optimization and *in-silico* DOEs

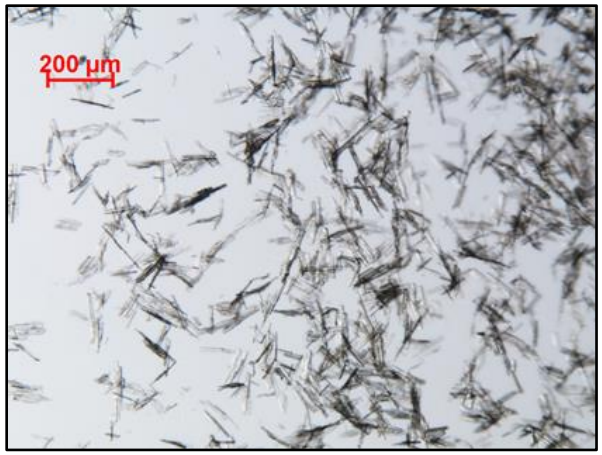

Linear cooling *

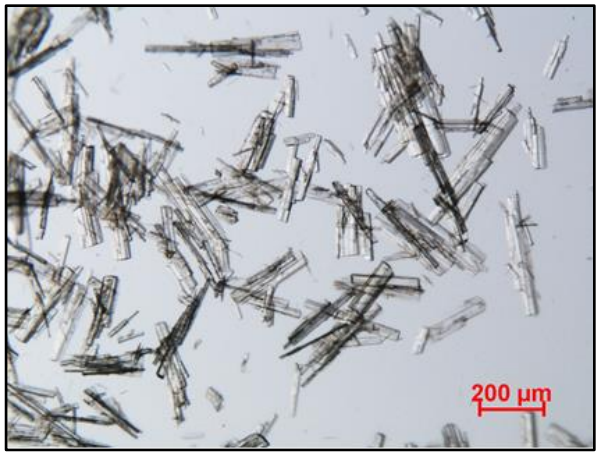

One temperature cycle *

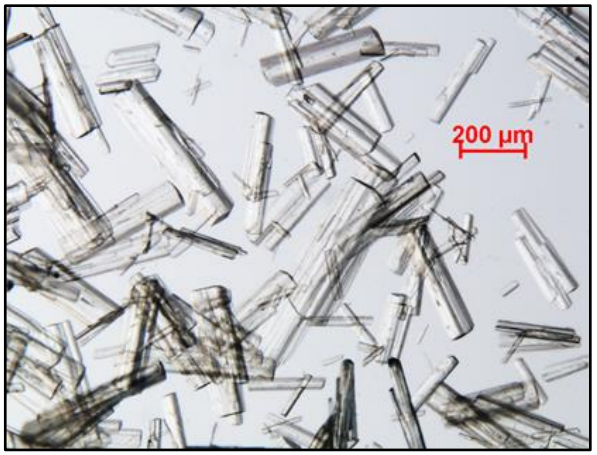

Three temperature cycles *

*** Identical batch time, operating temperature range and initial conditions**

Numerical solution: 2D HR-FVM

- **1D PBM with nucleation and growth**

$$\frac{\partial n(L,t)}{\partial t} + \frac{\partial G(S)n(L,t)}{\partial L} = B(S)\delta(L - L_n)$$

- **Numerical solution: HR-FVM on non-uniform grid**
- **The kinetics** (fitting parameters)

$$B = k_b \sigma^b V_c$$

$$D = k_d \sigma (1 + d_d L)^{-d_e}$$

$$G = k_g \sigma^g \exp\left(-\frac{E_A}{RT}\right) G(L)$$

Size dependent growth models generally used to fit steady-state MSMPR CSD data

Model 1: $G(L) = (1 + c_1 L)^{c_2}$

Model 2: $G(L) = 1 - \exp(-c_1(L + c_2))$

Model 3: $G(L) = 0.5(\tanh(c_1(L - c_2)) + 1)$

Model 4: $G(L) = 0.5(\tanh(c_1(L - c_2)) + 1)(1 + c_3 L^{c_4})$

Size dependent growth models proposed in this case to capture size dependency in the Kolmogorov scale

Crystallization kinetics of a model API: 1D case

- PE using 6 calibration and 2 validation experiments.

$\min_{P \in R_+^0} O(P)$	With FBRM data				Without FBRM data			
	Model 1	Model 2	Model 3	Model 4	Model 1	Model 2	Model 3	Model 4
Calibration	29237.2	2682.7	495.0	232.6	11543.6	1804.3	278.8	129.3
Validation	6018.6	1462.8	212.9	90.0	4593.8	1083.3	145.1	67.1

Much narrower CI-s for Model 4 by FBRM

Parameter	Nominal parameters (± C.I. limits)	
	W.O. FBRM	W. FBRM
$\log10(k_s)$	-2.77 ± 8.6	-3.06 ± 0.21
s	2.19 ± 14.0	2.25 ± 0.37
$\log10(k_g)$	10.83 ± 53.5	10.79 ± 0.79
g	1.12 ± 4.9	1.04 ± 0.17
$\log10(E_A)$	4.91 ± 2.0	4.92 ± 2.4 10^{-2}
$\log10(\mathbf{c_3})$	-0.75 ± 0.74	-0.90 ± 0.39
$\mathbf{c_4}$	0.97 ± 0.17	0.84 ± 0.14
$\log10(\mathbf{c_1})$		
$\log10(\mathbf{c_2})$		
$\log10(k_d)$		
$\log10(\mathrm{d_d})$	-3.10 ± 2.2 10^4	-3.19 ± 105.6
$\mathrm{d_e}$	1.2 10^{-3} ± 61.76	1 ± 237.6

Quasi size-independent dissolution

Different SDG shapes in the small range

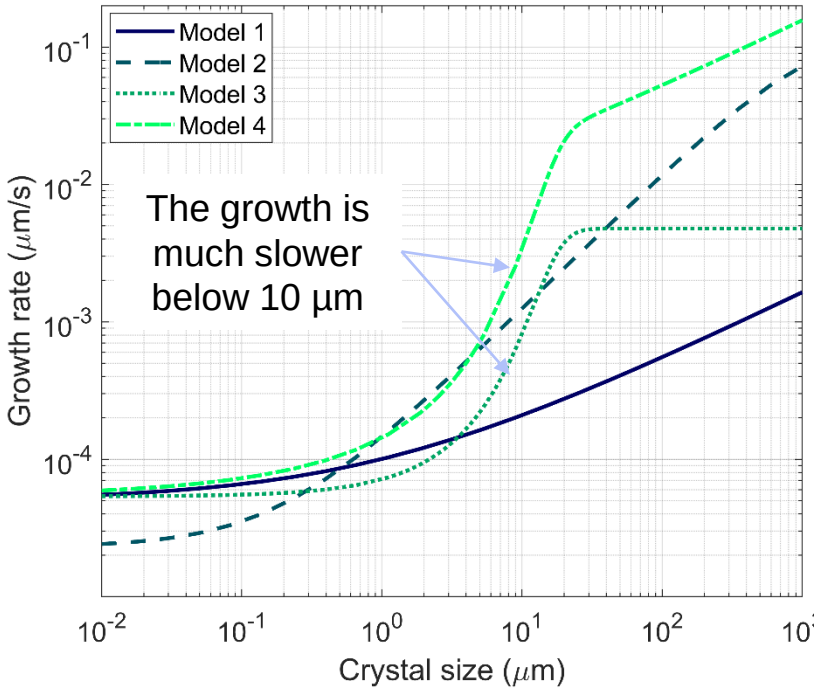

Crystallization kinetics of a model API: 1D case

- Hyperbolic tangent growth models (Model 3 and Model 4) gave superior performance compared to the traditional SDG models.
- Model 1-3 has the same number of parameters (no over-fitting).

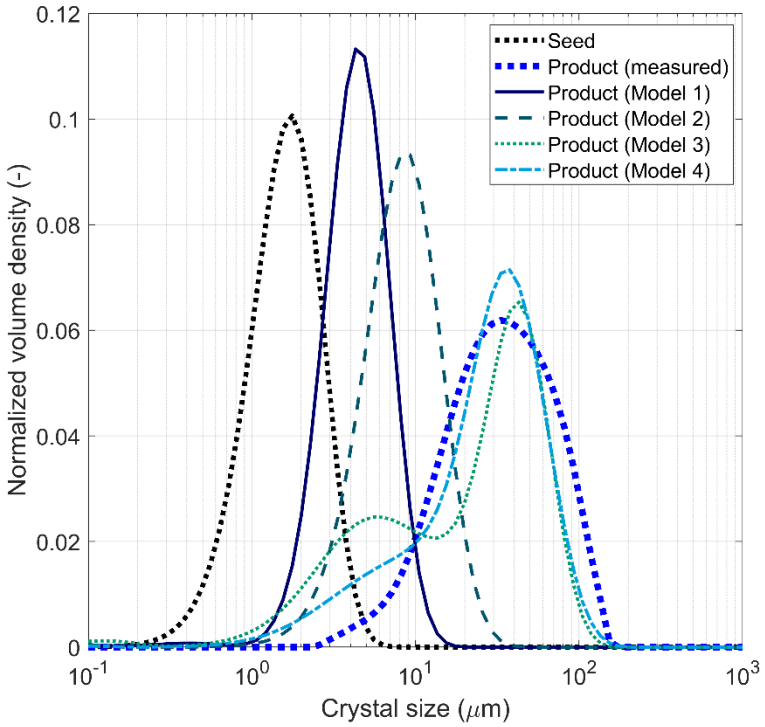

Validation experiment # 1: simulated and measured product CSDs

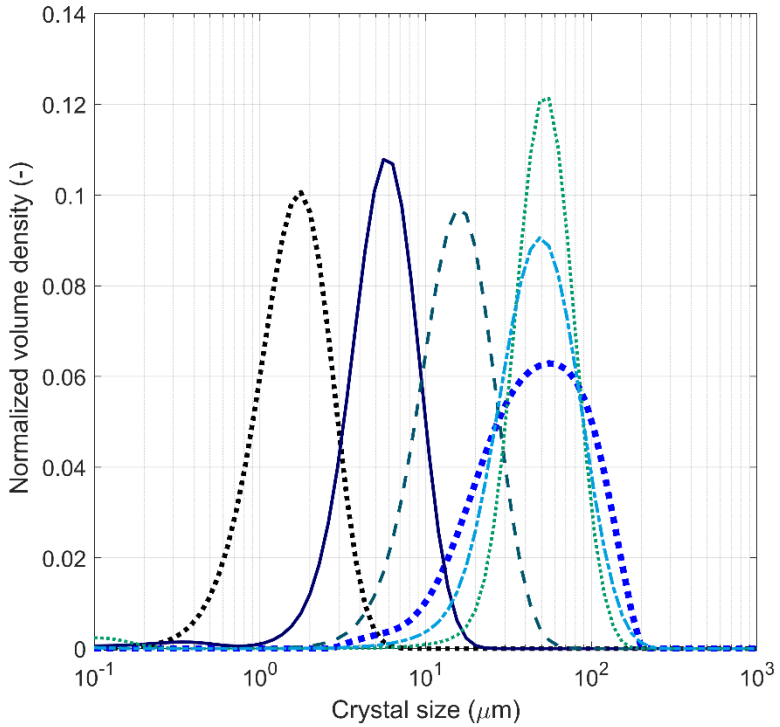

Validation experiment # 2: simulated and measured product CSDs

The need for a 2D model in this case

Mean aspect ratio of product crystals obtained in different experiments. There is a strong variation.

Expt. #	Seed type	Product mean AR
1	Type 1	7.78
2		7.33
3		4.81
4		6.25
5	Type 2	4.79
6		4.41
7		4.48
8		3.62
9	Type 3	4.91
10		5.44

Nucleation:

$$B = k_b \sigma^b V_c$$

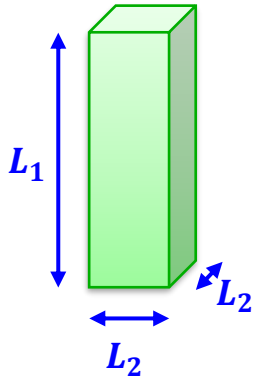

The growth rate equation:

$$G_i = G(L_1, L_2) k_{g,i} \sigma^{g_i} \exp\left(-\frac{E_A}{RT}\right)$$

$$G(L_1, L_2) = 0.5\left(\tanh\left(c_1(D_e - c_2)\right) + 1\right)\left(1 + c_3 D_e^{c_4}\right)$$

$$D_e = \frac{6}{\pi}\sqrt[3]{k_V L_1 L_2^2}$$

Dissolution:

$$D_i = D(L_1, L_2) k_{d,i} \sigma$$

$$D(L_1, L_2) = \frac{1}{(1 + d_d D_e)}$$

Numerical solution: 2D HR-FVM

❑ 2D PBM with Nucleation and Growth

$$\frac{\partial n(L_1,L_2,t)}{\partial t}+\frac{\partial G_1(S)n(L_1,L_2,t)}{\partial L_1}+\frac{\partial G_2(S)n(L_1,L_2,t)}{\partial L_2}=B(S)\delta(L_1-L_{1n})(L_2-L_{2n})$$

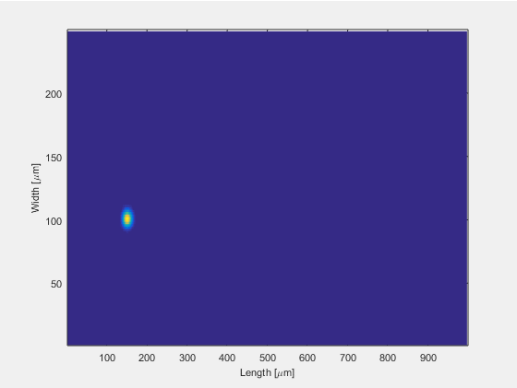

2D CSD dynamics in seeded batch crystallization with N and 2D Growth

❑ Numerical solution: 2D HR-FVM on GPU

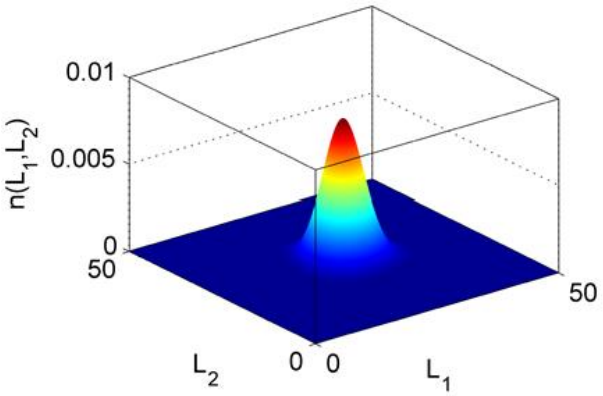

Step 1. Continuous 2D population density function (PDF)

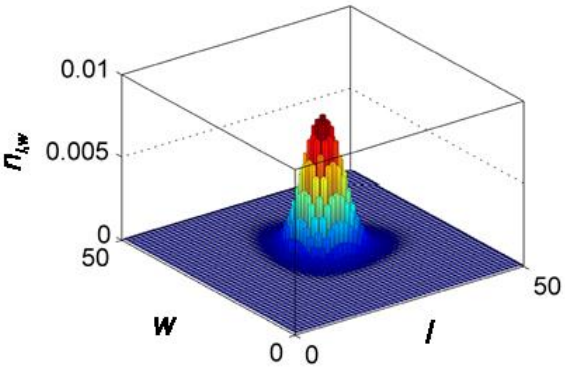

Step 2. Finite volume discretization of the 2D PDF

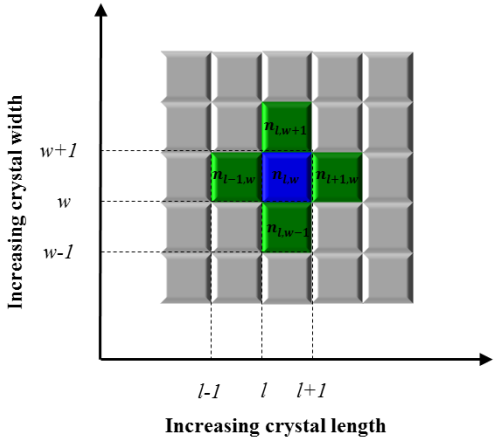

Step 3. Number balance based on PBM for every cell

Crystallization kinetics of a model API: 2D case

Proposed objective function for 2D parameter estimation

$$O(\boldsymbol{KP}) = f(\Delta C) + wf(\Delta D) + uf(\Delta L) + zf(\Delta N)$$

- $f(\Delta C)$: Concentration fit
- $f(\Delta D)$: CSD fit
- $f(\Delta L)$: Shape fit
- $f(\Delta N)$: Count correlation maximization

Why these many terms?

$f(\Delta C)$: coupled N, G_1 and G_2 information

$f(\Delta D)$: partly decouples N from G_1 and G_2

$f(\Delta L)$: provides relative G_1 and G_2 information

$f(\Delta N)$: influenced majorly by N and fines dissolution

However, there is also more sensor-specific error…

$\boldsymbol{KP}$: vector of kinetic parameters to be estimated

Seed CSD approximation

- 2D CSD of seeds must be approximated from 1D size and shape measurement (inverse problem)
- Solved by optimization, assuming sum of 2D correlated normal distributions

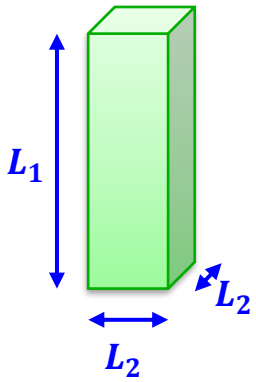

$$V_{Cr} = k_V L_1 L_2^2$$

$$n_0 = n_{0,1} + w n_{0,2}$$

k_V = 0.153

w = 4.98

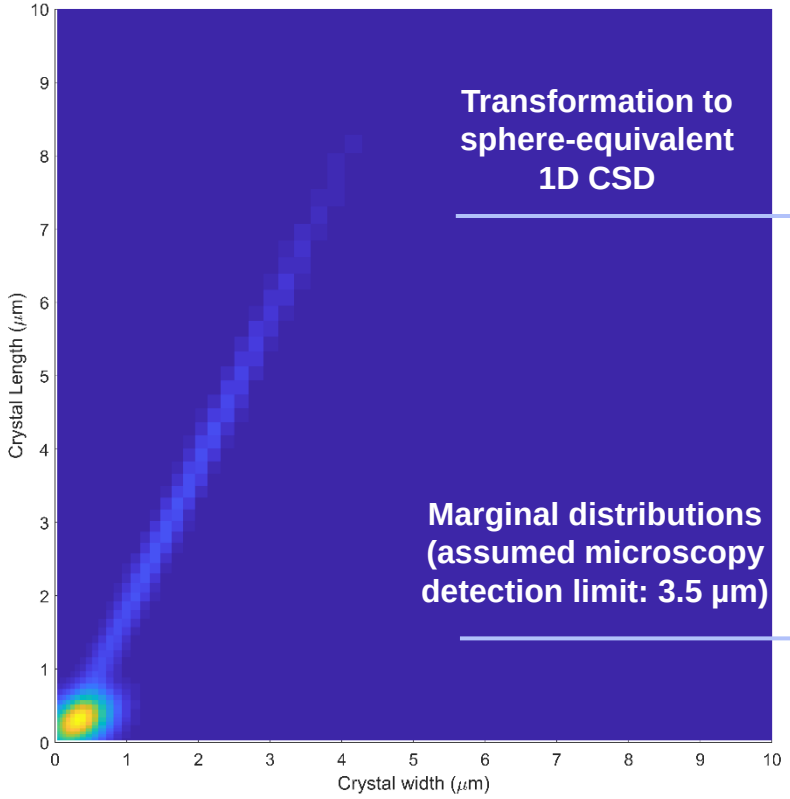

Transformation to sphere-equivalent 1D CSD

Marginal distributions (assumed microscopy detection limit: 3.5 µm)

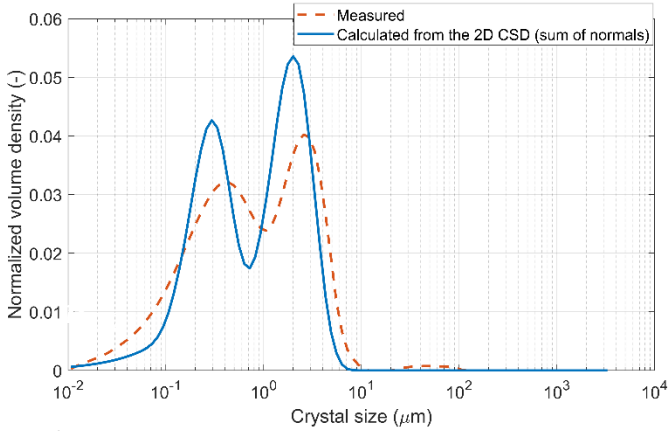

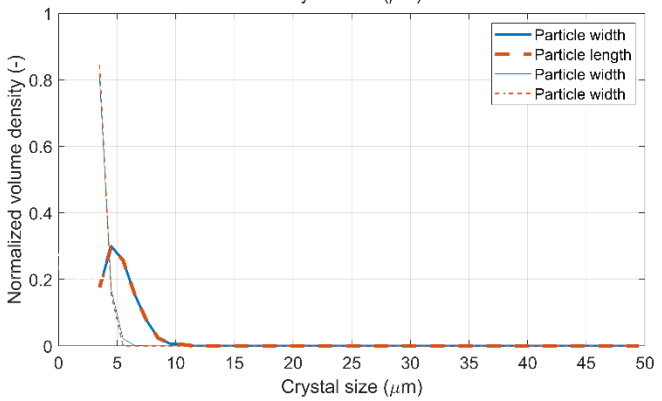

2D case, intermediate results

- 2D crystallization kinetics: dissolution and size dependent growth along the length and with was considered in the first step
- Under extension to nucleation rate model

The considered size dependent growth rates:

$$G_i = G k_{g,i} \sigma^{g_i} \exp\left(-\frac{45000}{RT}\right)$$

$$G = 0.5\left(\tanh\left(c_1(D_e - c_2)\right) + 1\right)\left(1 + c_3 D_e^{c_4}\right)$$

D_e is the sphere-equivalent diameter:

$$D_e = \frac{6}{\pi}\sqrt[3]{k_V L_1 L_2^2}$$

The considered size independent dissolution rates:

$$D_i = k_{d,i}\sigma$$

Nominal values and 95 % confidence interval limits *

P	Nom.	L.B.	U.B.
$k_{g,1}$	110420	37229	327480
$k_{g,2}$	24429	5218	114370
g_1	1.80	1.34	2.25
g_2	1.42	0.98	1.86
$k_{d,1}$	0.032	0.02	0.51
c_1	0.072	0.054	0.097
c_2	14.02	9.60	20.47
c_3	2.99	1.25	7.16
c_4	0.807	0.51	1.14

* $k_{d,2}$ was fixed to 0.005

2D case, intermediate results

- Basic uncertainty analysis (as we have many fitting parameters)
- Monte-Carlo sampling of kinetics assuming multivariable correlated normal CSD (left hand side figure). 150 random kinetic parameter combinations

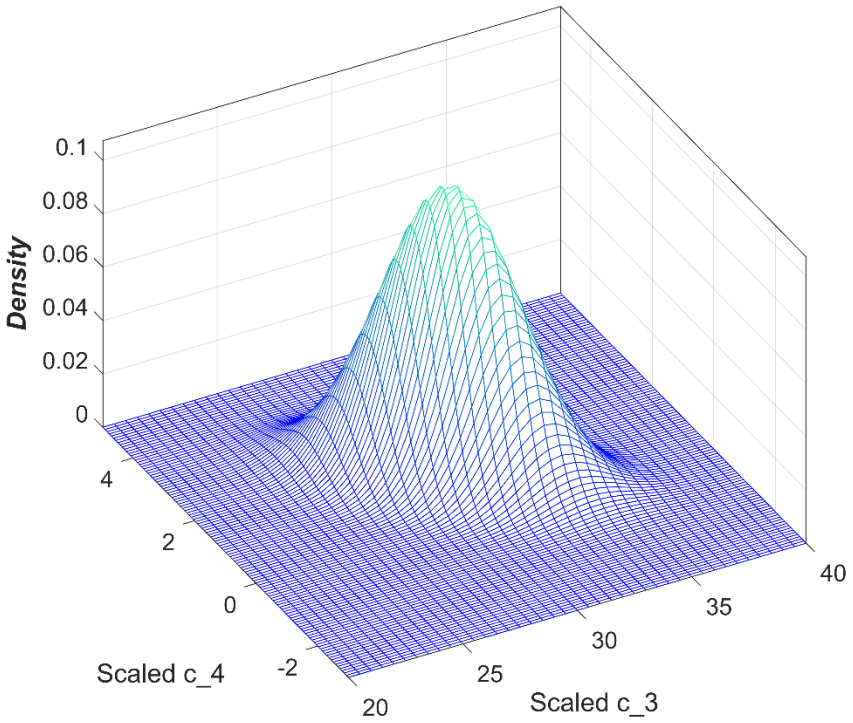

Correlation between c_3 and c_4

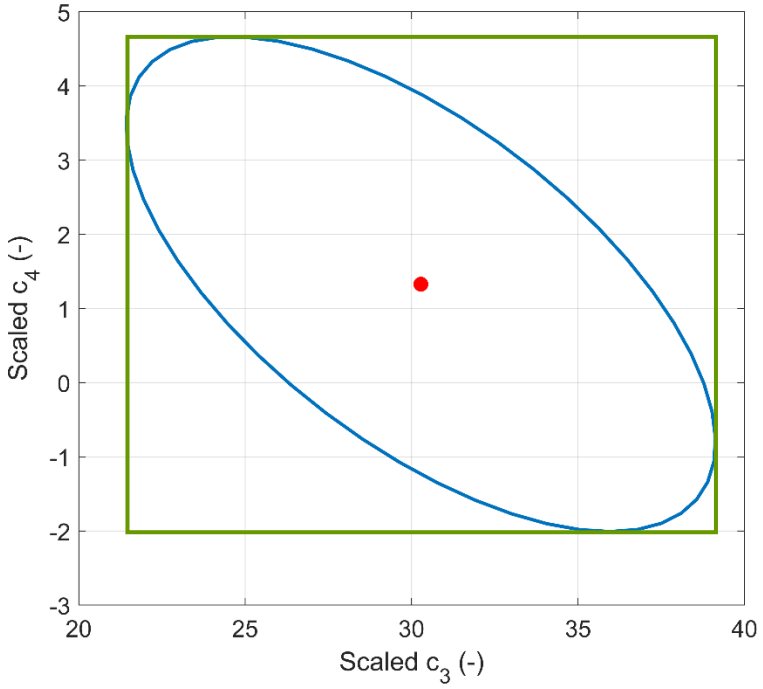

Nominal value, confidence ellipsoid and box (confidence intervals)

2D case, intermediate results. Validation runs

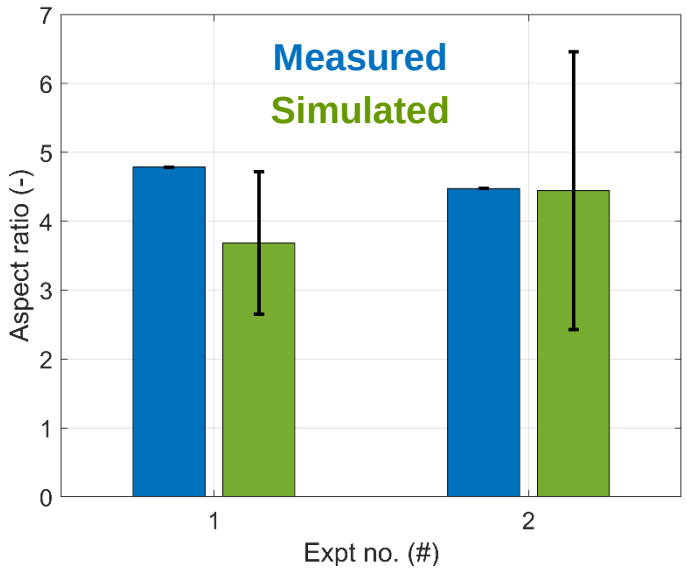

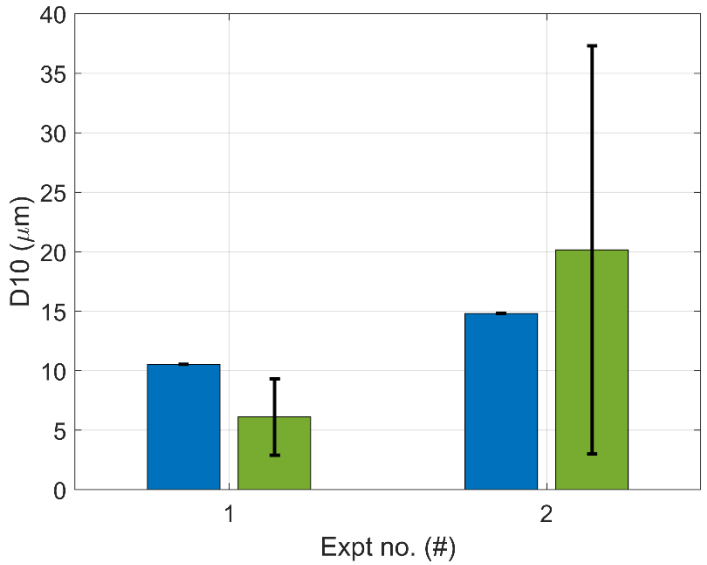

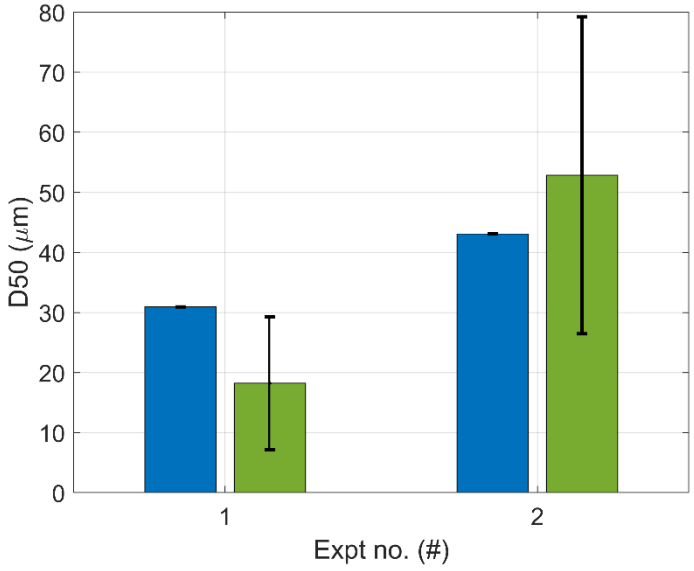

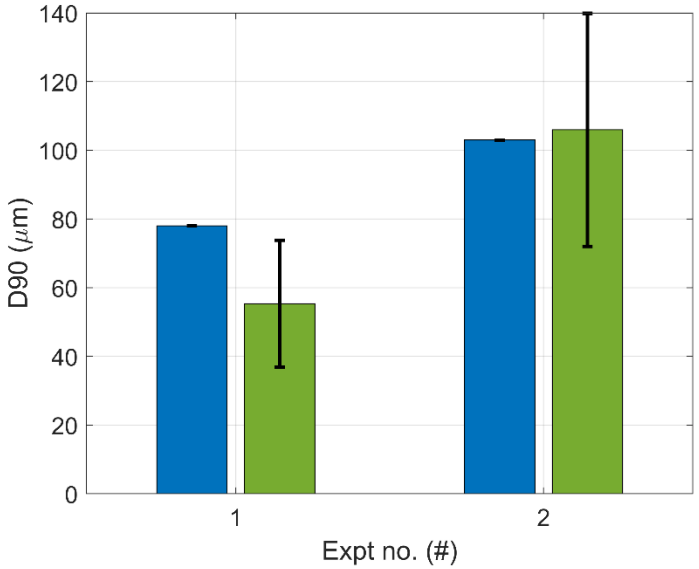

*Mean and standard deviation of 150 simulation with kinetics sampled randomly

Short term plans (~1 year)

Flexible MSMPR network

… with dedicated wet-mills and recirculation streams

2D crystallization

… Finishing the 2D parameter estimation

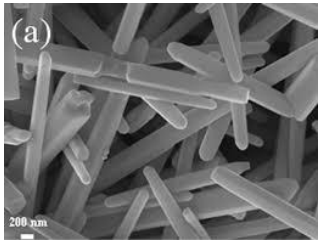

Blaze probe acquisition

… and comparing it to the Metler's EasyViewer probe

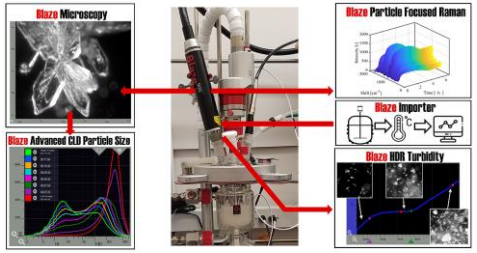

A Holistic Approach for the Model-based Control of Crystal Size, Shape and Purity in Integrated Batch and Continuous Crystallization - Wet Milling Systems

Botond Szilagyi, Zoltan K. Nagy

School of Chemical Engineering

Purdue University, West Lafayette, IN

PURDUE UNIVERSITY

Investigating the Effect of Solvents and Impurities on Crystal Growth

IFPRI AGM 2020

Michael F. Doherty and Tobias Mazal

CHEMICAL ENGINEERING
UC SANTA BARBARA

Project Objective:

The goal of this research is to develop a practical engineering tool for predicting the relative growth rates (growth kinetics) and morphology of solution-grown faceted crystals, including the effects of solvent, and impurities/additives. The methodology will be tested on a variety of systems, including: paracetamol, olanzapine, ammonium acetate and a variety of drug substances, all grown from solution.

Approach:

Our approach is to leverage many years of research & development building our crystal design software tool called ADDICT. Our approach is to develop (fast) mechanistic models of crystal growth validated by experiments and both molecular simulations and KMC simulations.

Background - ADDICT

- Mechanistic framework developed by Doherty group models layered growth
- Predicts crystal morphology for given .cif file and growth conditions[3]

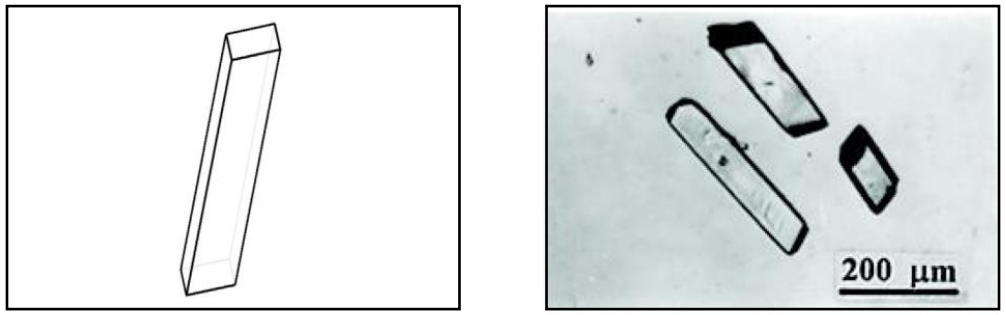

(a) Predicted shape of paracetamol in Vapor ⟷ (b) Observed shape of paracetamol in Vapor

Images adapted from Li et al. (**2016**)

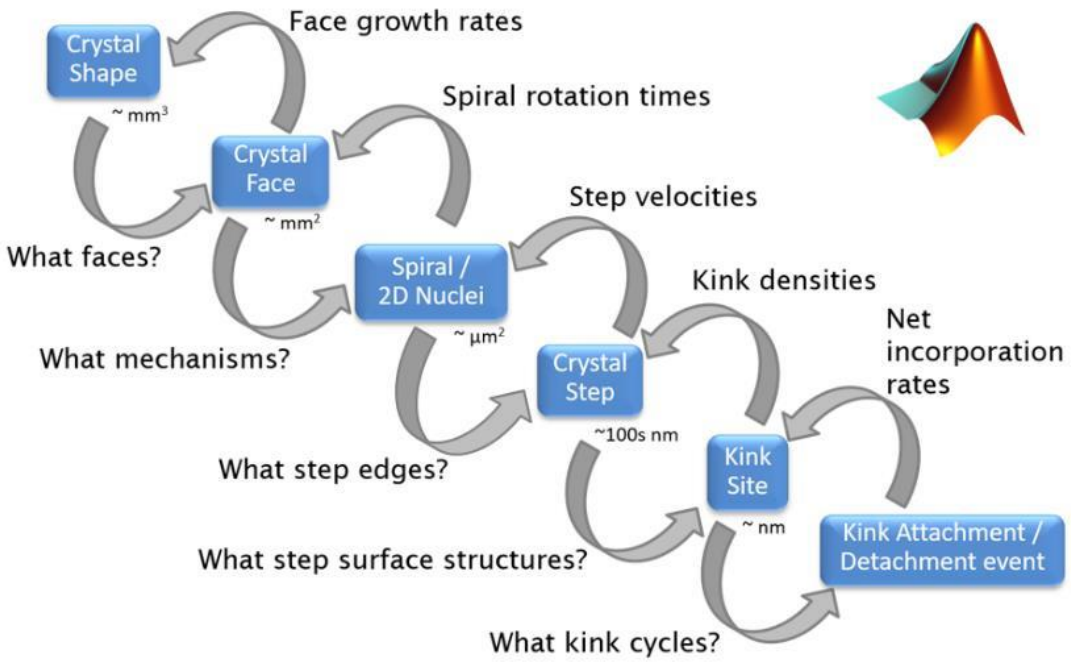

Scheme works well when implemented case-by-case by expert. Software implementation for general user is a challenge.

CHEMICAL ENGINEERING
UC SANTA BARBARA

Background - Impurities

- Anti-freeze proteins within Antarctic fish inhibit ice crystal formation
- Antimalarial medications inhibit β-hematine crystallization
- Inhibition of L-cystine kidney stones through structural mimics
- Metacetamol/PAA inhibition of paracetamol production

- This can occur at **ppb concentrations!**

Background - Impurities

- PAA inhibits growth of **paracetamol** crystals
- Distinct faces inhibited by different amounts by introduction of PAA

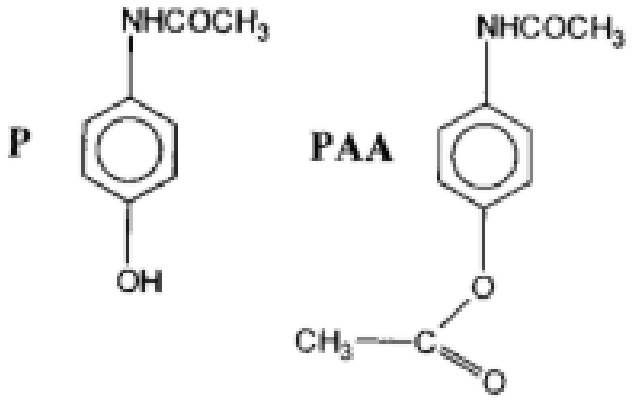

PAA = p-acetoxyacetanilide

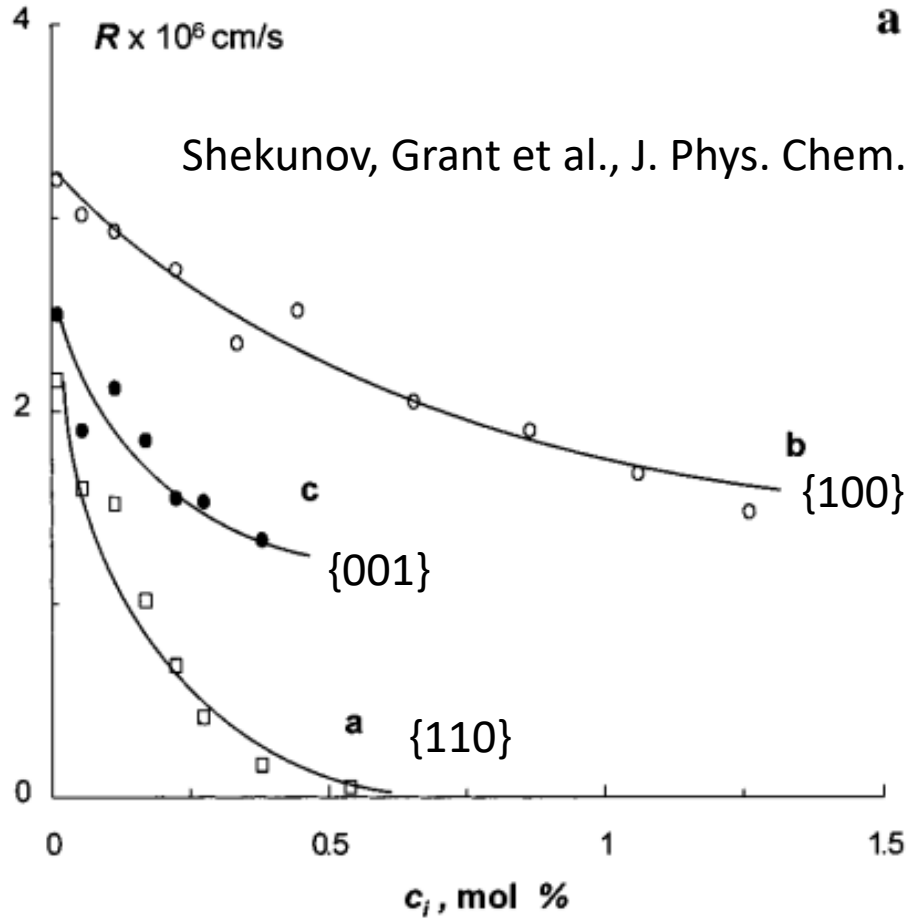

Shekunov, Grant et al., J. Phys. Chem. B, 1997

Figure 1. Dependencies of (a) normal growth rate, R as functions of concentration c_i of PAA in solution. Curves correspond to the crystal faces {110} (a, □), {20$\bar{1}$} (b, ○), and {001} (c, ●). $\sigma = 0.1$. $T = 35.5$ °C.

Three Inhibition Mechanisms

1. Step pinning (main focus of current work). Influences critical length of step front

2. Spiral pinning. Influences critical length of step side

3. Kink blocking. Influences the number of growth sites (kinks)

Step Pinning

- Cabrera and Vermilyea (1958): **Step Pinning Mechanism**[5]
- Segments of the step edge are halted as edge encounters impurities spaced apart distance less than the critical length

$$v = v_\infty (1 - 2 l_c d^{1/2})^{1/2}$$

Critical Length of Step

Density of Adsorbed Impurities

$$d \propto \theta_I$$

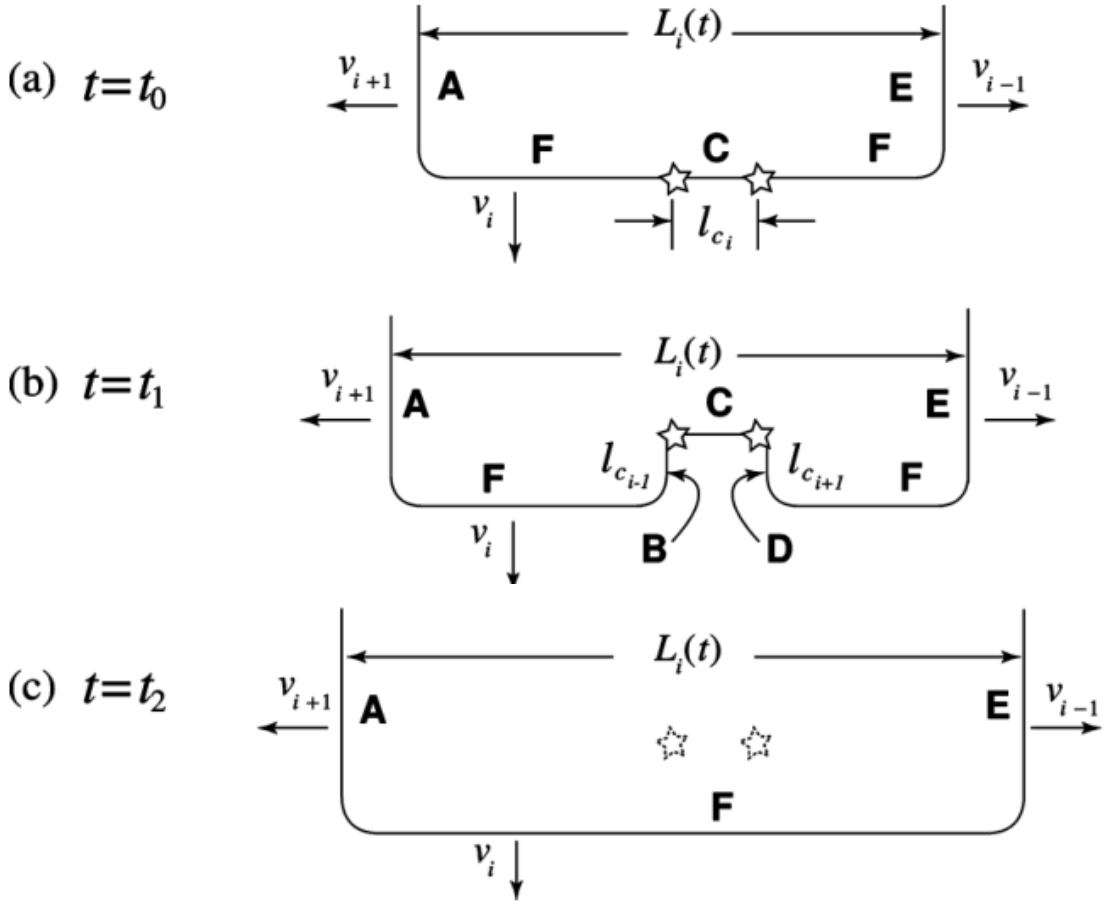

Image adapted from J. Sizemore, M. F. Doherty (**2009**)

Kinetic Monte Carlo (KMC)

- KMC used to simulate growth of a Kossel crystal, starting with a flat step edge[6]
- Attachment and detachment events are defined as transport of growth units:
  - Bulk solution ↔ Terrace
  - Terrace ↔ Edge
  - Edge ↔ Kink
  - Terrace ↔ Kink

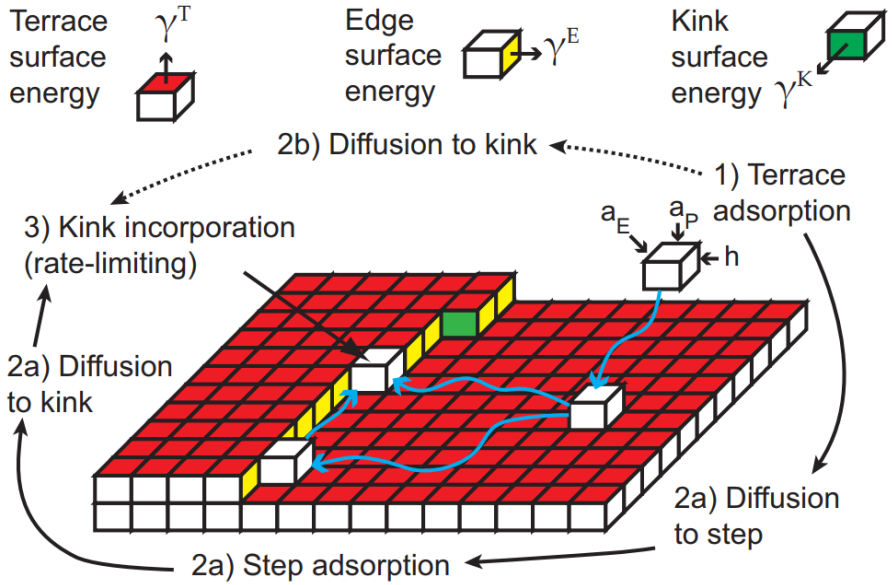

Image adapted from Tilbury et al. (**2016**)

KMC Algorithm

1. Define possible events and their corresponding rates.

KMC - Microkinetic Rate Expressions

	Attachment Rates (1/s)	Detachment Rates (1/s)
Edge ↔ Kink	$j_{K,i}^{+} = k_{K,i}^{+}\ \theta_{E,i} = v_0 \exp\left(\frac{-\Delta U_{K,i}^{\ddagger}}{k_B T}\right)\theta_{E,i}$	$j_{K,i}^{-} = k_{K,i}^{-} = v_0 \exp\left(\frac{-(\Delta U_{K,i}^{\ddagger} + \Delta W_{K,i})}{k_B T}\right)$
Terrace ↔ Edge	$j_{E,i}^{+} = k_{E,i}^{+}\ \theta_{T,i} = v_0 \exp\left(\frac{-\Delta U_{E,i}^{\ddagger}}{k_B T}\right)\theta_{T,i}$	$j_{E,i}^{-} = k_{E,i}^{-}\ \theta_{E,i} = v_0 \exp\left(\frac{-(\Delta U_{E,i}^{\ddagger} + \Delta W_{E,i})}{k_B T}\right)\theta_{E,i}$
Terrace ↔ Kink	$j_{KT,i}^{+} = k_{KT,i}^{+}\ \theta_{T,i} = v_0 \exp\left(\frac{-(\Delta U_{K,i}^{\ddagger} + \Delta U_{E,i}^{\ddagger})}{k_B T}\right)\theta_{T,i}$	$j_{KT,i}^{-} = k_{KT,i}^{-} = k_{KT,i}^{+} \exp\left(\frac{-(\Delta W_{E,i} + \Delta W_{K,i})}{k_B T}\right)$
Solution ↔ Terrace	$j_{T}^{+} = k_{T}^{+}\ x = v_0 \exp\left(\frac{-\Delta U_{T}^{\ddagger}}{k_B T}\right)x$	$j_{T,i}^{-} = k_{T}^{-}\ \theta_{T,i} = v_0 \exp\left(\frac{-(\Delta U_{T}^{\ddagger} + \Delta W_{T})}{k_B T}\right)\theta_{T,i}$

$$x = x_{sat} S$$

CHEMICAL ENGINEERING
UC SANTA BARBARA

KMC Algorithm

1. Define possible events and their corresponding rates.
2. Set initial system state.

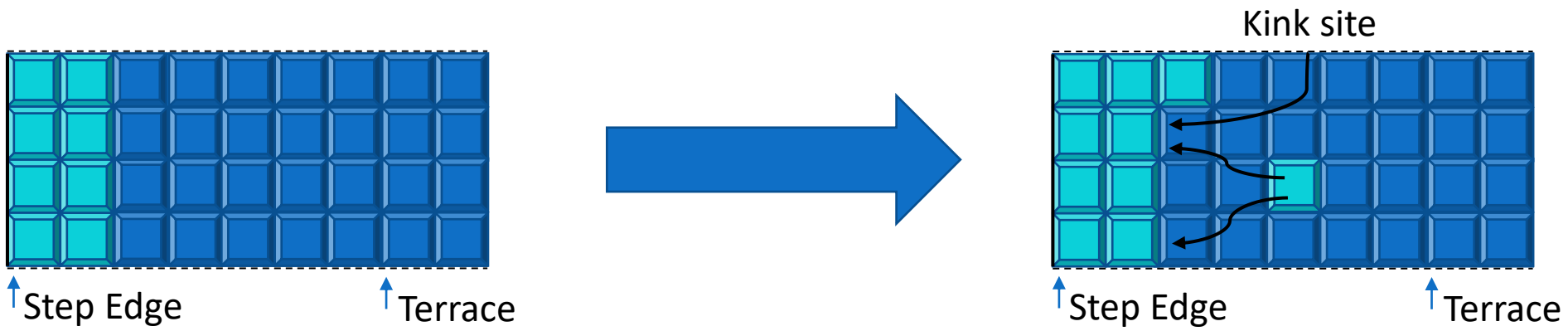

KMC Algorithm

1. Define possible events and their corresponding rates.
2. Set initial system state.
3. At each site, determine the number of nearest neighbors and occupation status. Then, compute cumulative rate functions, Γ_i, and the total rate constant, Γ_{tot}.

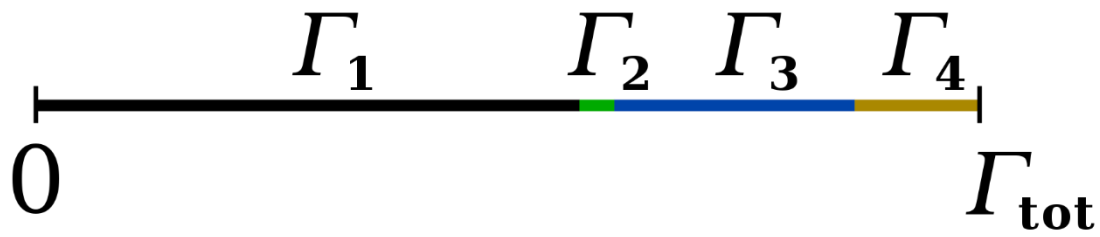

KMC Algorithm

1. Define possible events and their corresponding rates.
2. Set initial system state.
3. At each site, determine the number of nearest neighbors and occupation status. Then, compute cumulative rate functions, Γ_i, and the total rate constant, Γ_{tot}.
4. Draw a random number *n* between 0 and Γ_{tot} to determine which event to execute:

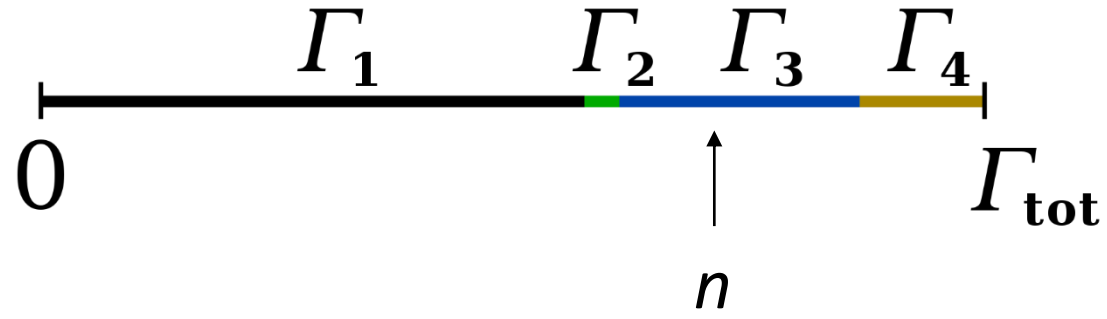

KMC Algorithm

1. Define possible events and their corresponding rates.
2. Set initial system state.
3. At each site, determine the number of nearest neighbors and occupation status. Then, compute cumulative rate functions, Γ_i, and the total rate constant, Γ_{tot}.
4. Draw a random number *n* between 0 and Γ_{tot} to determine which event to execute (e.g., 3). Pick a random site where event 3 is possible and implement event 3 at that site.

KMC Simulation

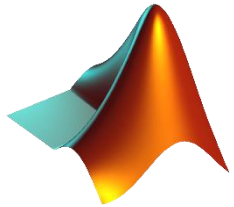

- S = 1.5
- $\phi = 3\ k_B T$
- 15,000 MC steps

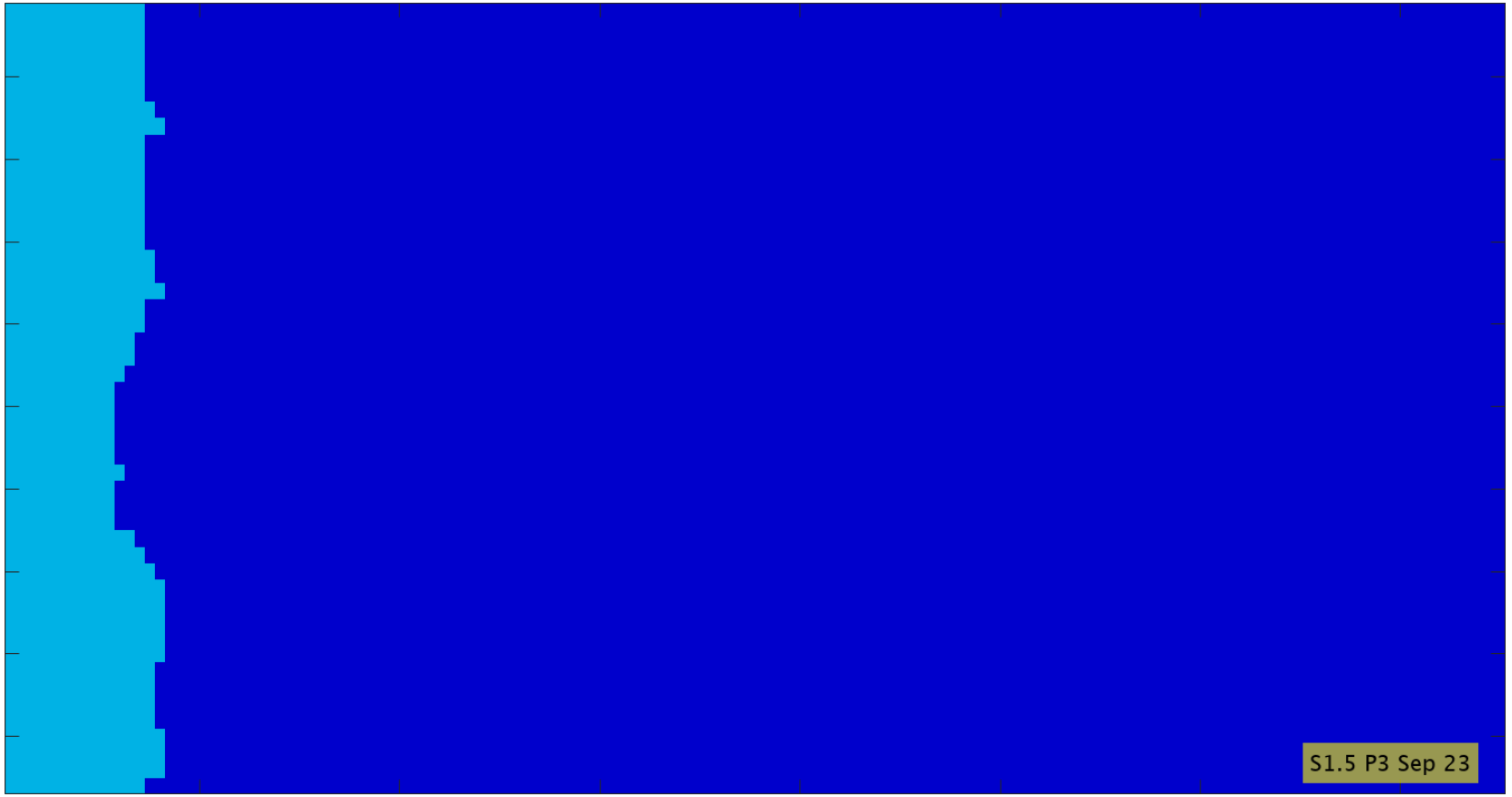

KMC Simulations (production runs)

- Simulations run for 75,000 MC steps at various energies; S = 1.5

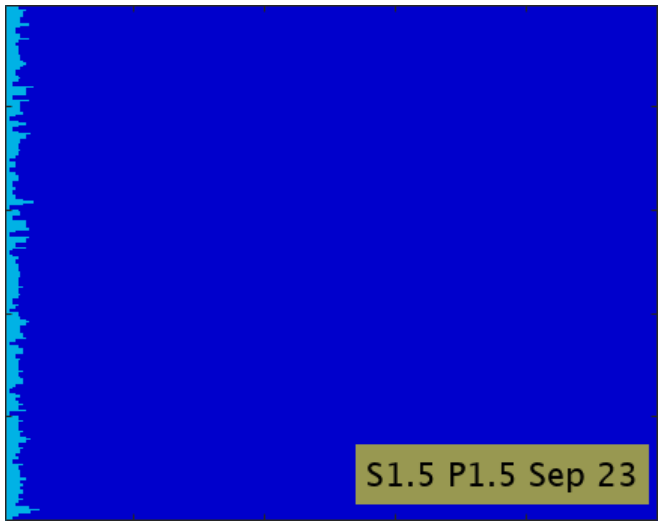

$\phi = 1.5\ k_B T$

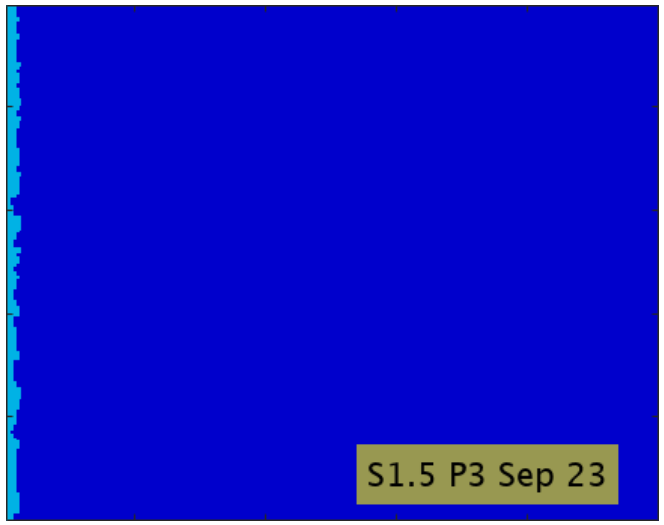

$\phi = 3\ k_B T$

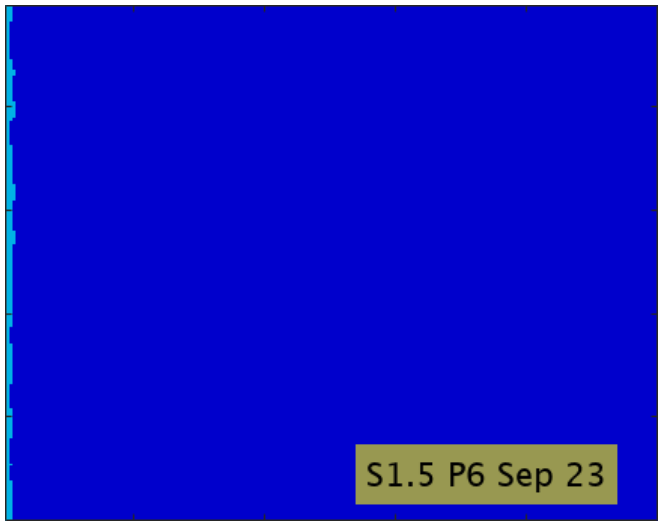

$\phi = 6\ k_B T$

- Higher energy penalty corresponds to slower edge but “smoother” front

Step Velocity Dependence

- Sensible agreement of step velocity with both ϕ and S
- What if we introduce **impurity molecules?**

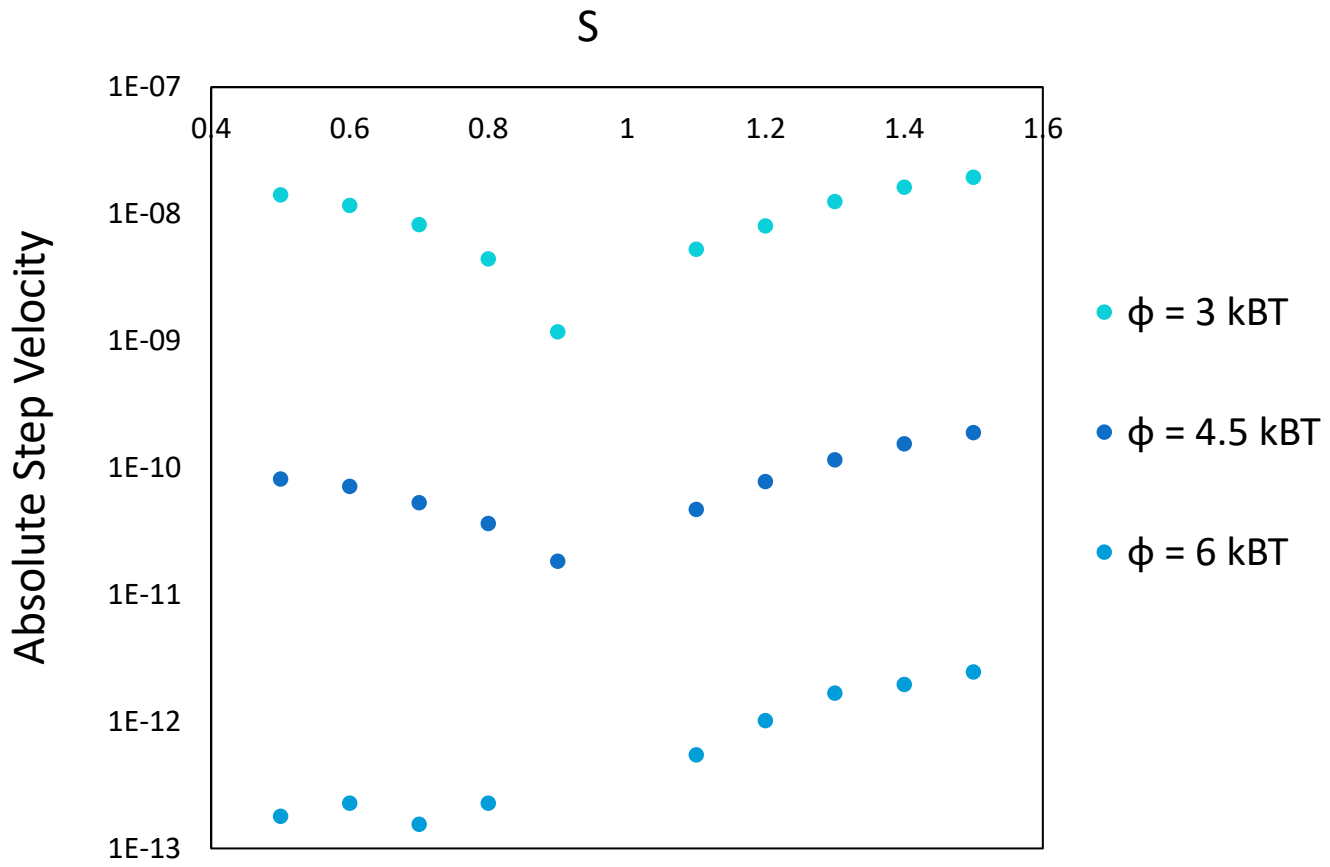

CHEMICAL ENGINEERING
UC SANTA BARBARA

Introducing Impurities

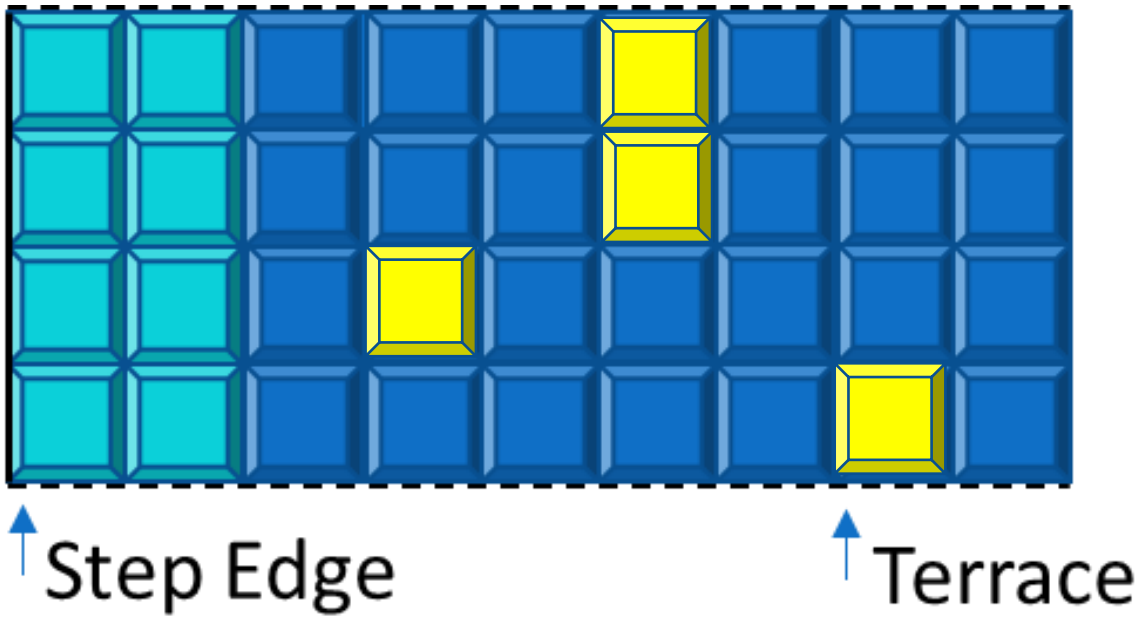

= impurity

θ_I - fractional coverage of impurities on the terrace

Impurities on a Lattice

θ_I - fractional coverage of impurities on the terrace

- S = 1.5
- $\phi = 3\ k_B T$
- 15,000 MC Steps

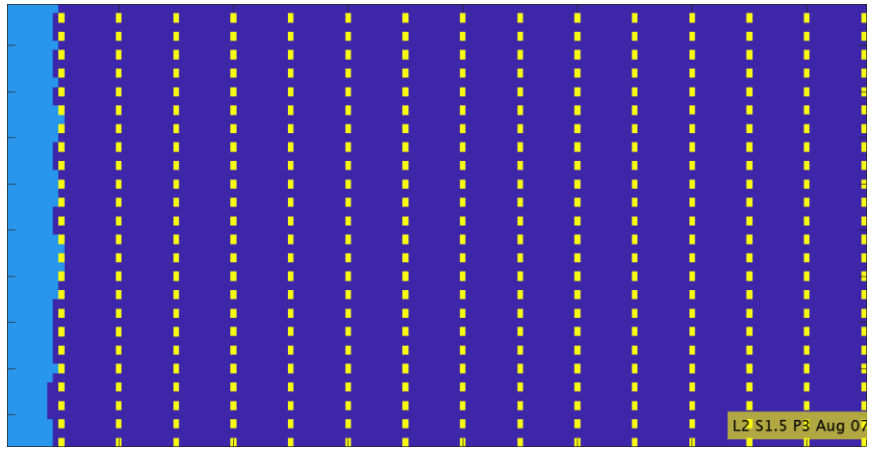

$\theta_I = 0.057$

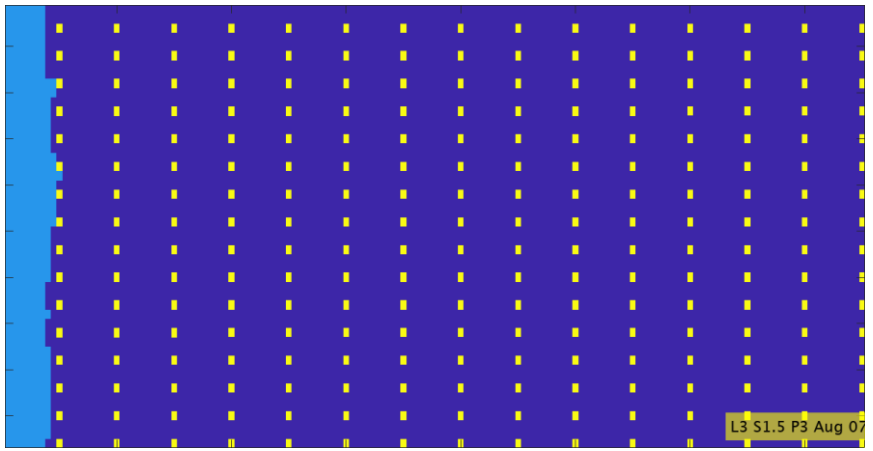

$\theta_I = 0.088$

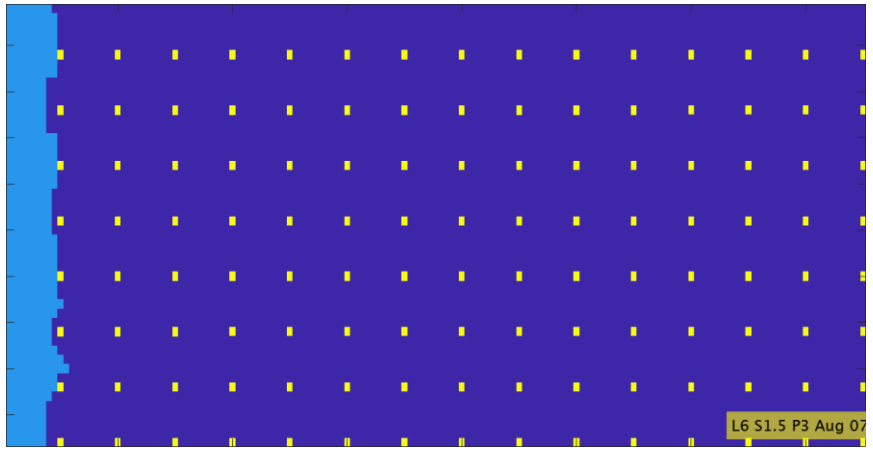

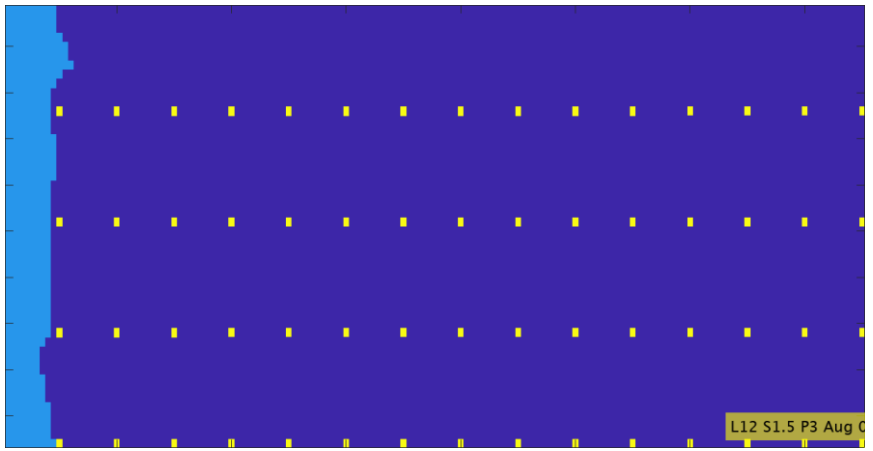

CHEMICAL ENGINEERING
UC SANTA BARBARA

Impurities on a Lattice

- Imposters close together significantly diminish step velocity and thus reduce growth rate
- Monotonic decrease with increasing coverage

CV Model equation:

$$v = v_\infty (1 - 2 l_c d^{1/2})^{1/2}$$

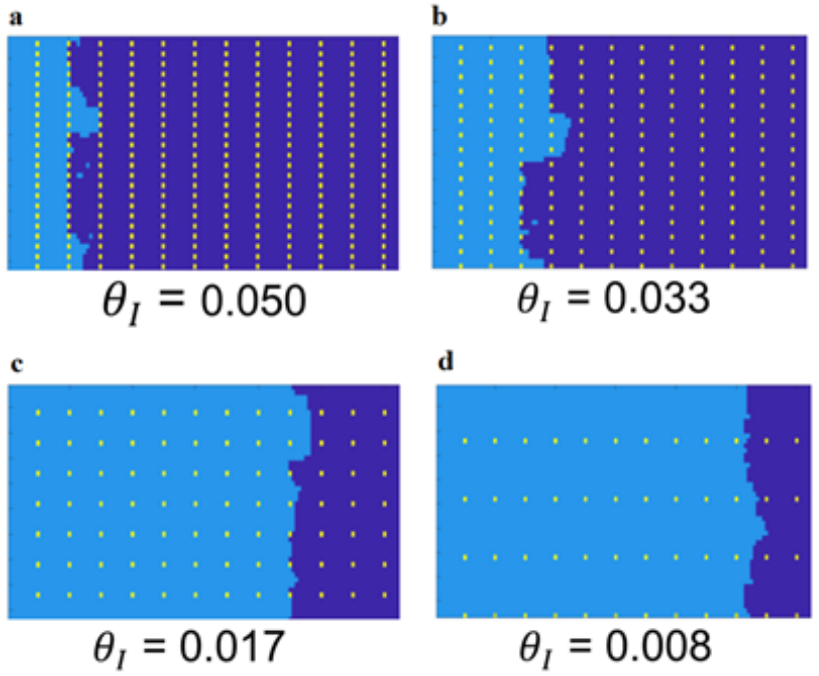

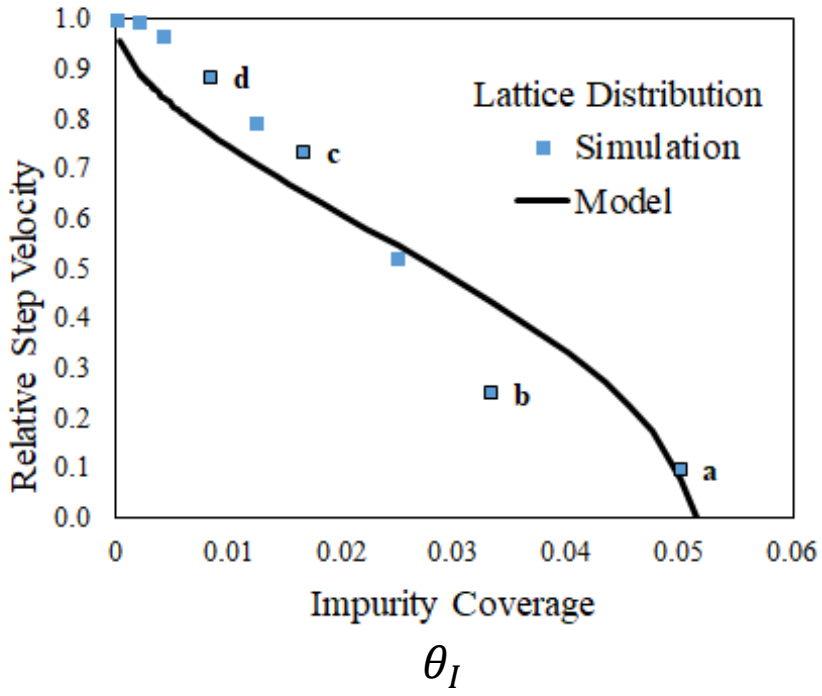

Impurities Distributed Randomly

- S = 1.5
- $\phi = 3\ k_B T$
- 15,000 MC steps

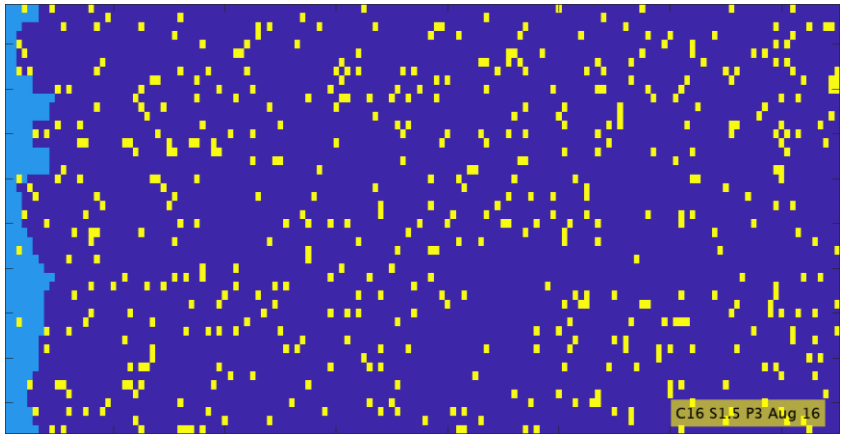

$\theta_I = 0.042$

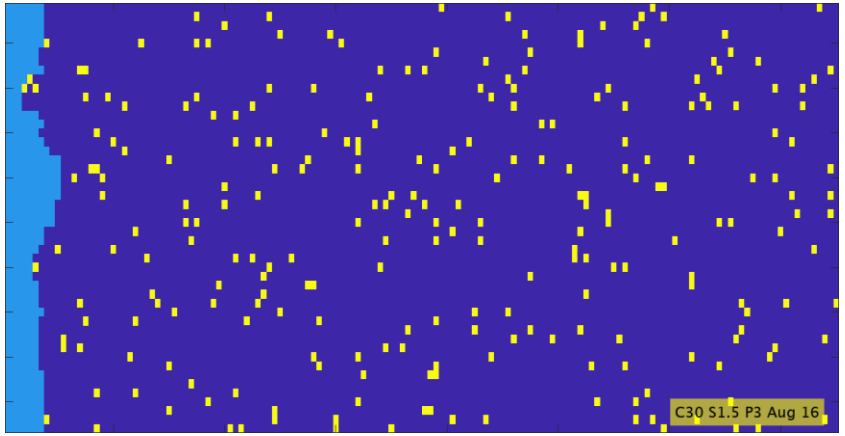

$\theta_I = 0.028$

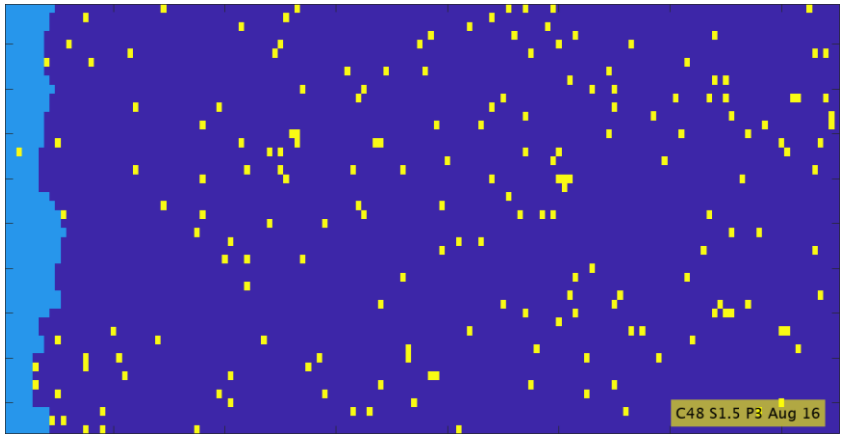

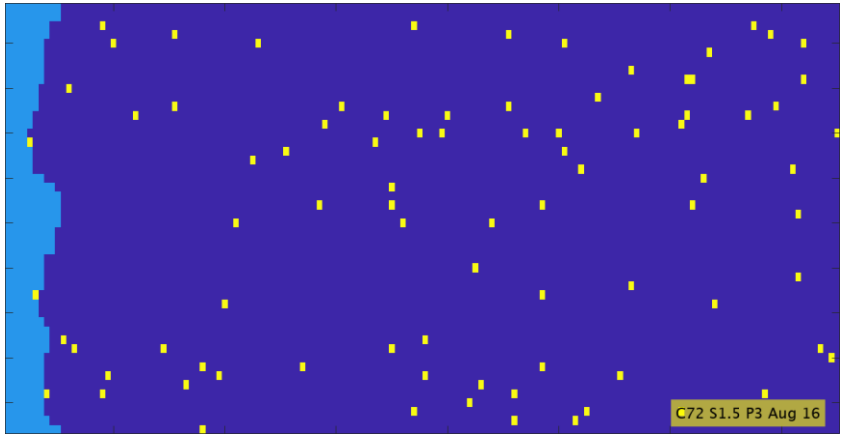

CHEMICAL ENGINEERING
UC SANTA BARBARA

Impurities Distributed Randomly

- Model equation captures monotonic decrease but not all curve characteristics
  - Predicts dead zone prematurely (error bars?)
- Are KMC results & CV model sensitive to the **impurity distribution?**

CV Model equation:

$$v = v_\infty (1 - 2 l_c d^{1/2})^{1/2}$$

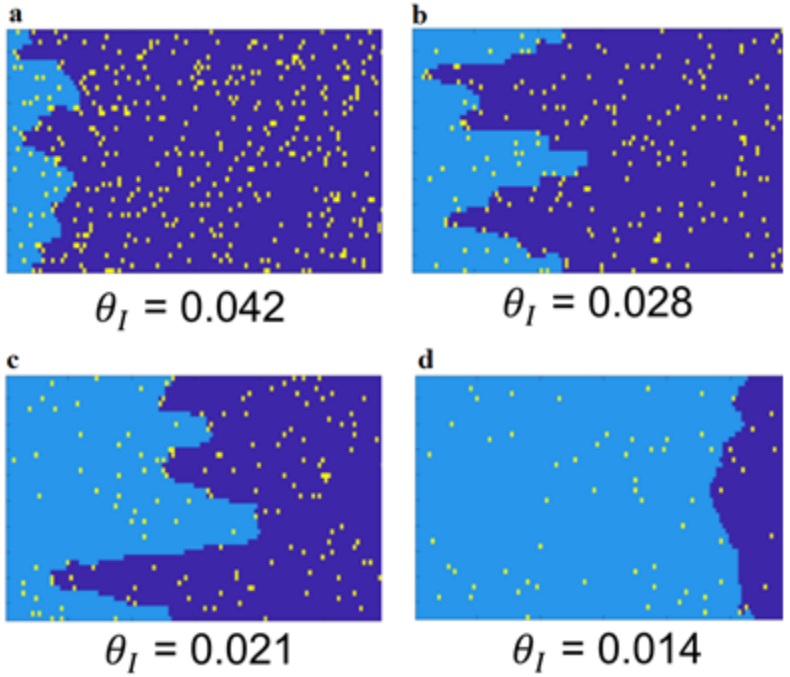

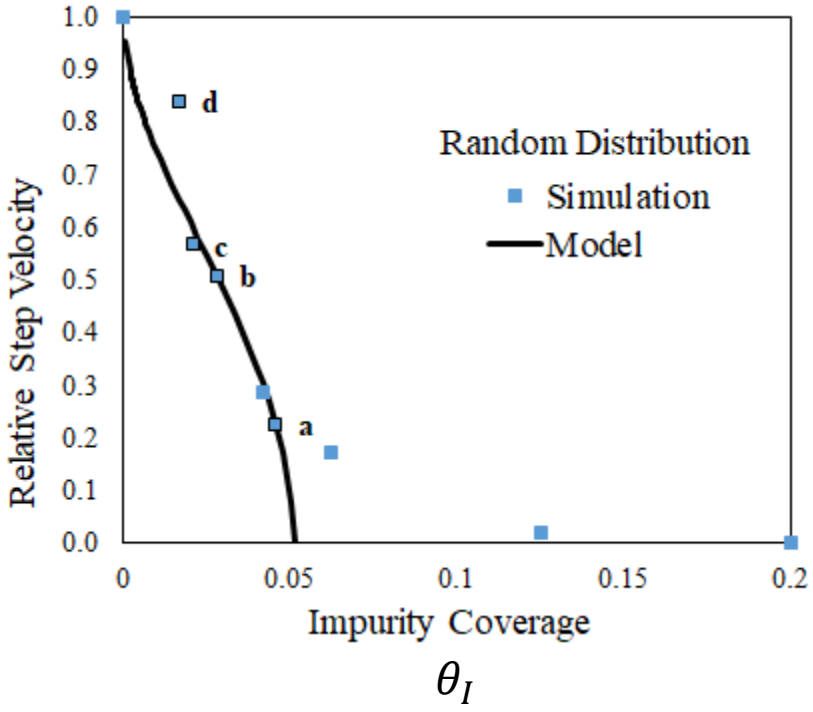

CHEMICAL ENGINEERING
UC SANTA BARBARA

Future Work

- **2020-21:** Implement KMC for more realistic systems
  - Mobile impurities
  - Include finite energetic interactions amongst solute and imposter species
- **2020-21:** Investigate other mechanisms by which impurities may inhibit crystal growth (step-pinning, kink death)
- **2020-21:** Compare inhibitor mechanisms through KMC simulation to determine the range of validity of each mechanism and the transitions between them
  - Compare KMC results to experimental inhibitor results before implementing validated mechanisms into ADDICT
- For mobile impurities consider the formation of inhomogeneous terrace with 2D islands of impurities at higher coverage fractions? MD simulations to examine how impurities affect energetics and surface coverage on the crystal surface

Acknowledgments

- **Doherty Group**
- **IFPRI**
- **BD Fellowship (NSF HRD-1701365)**
- **GEM Fellowship**

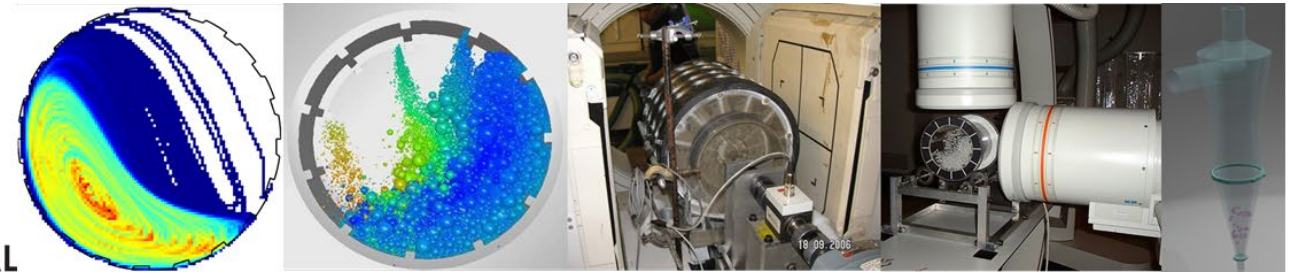

SCALE-UP RULES FOR MIXING MECHANISMS IN ROTATING DRUM FLOWS

By

Indresan Govender & Taswald Moodley

International Fine Particle Research Institute

Aim

To identify a suitable dimensionless number from a fundamentally-derived granular flow model of rotating drum flows that facilitates scale-up of the dominant mixing mechanisms spanning rolling-to-cascading flow regimes

1) Model formulation
2) Validation of the model
3) Identification of an energy proxy for dominant mixing mechanisms
4) Dimensionless number that facilitates scale-up

1. Continuum Model: Preamble

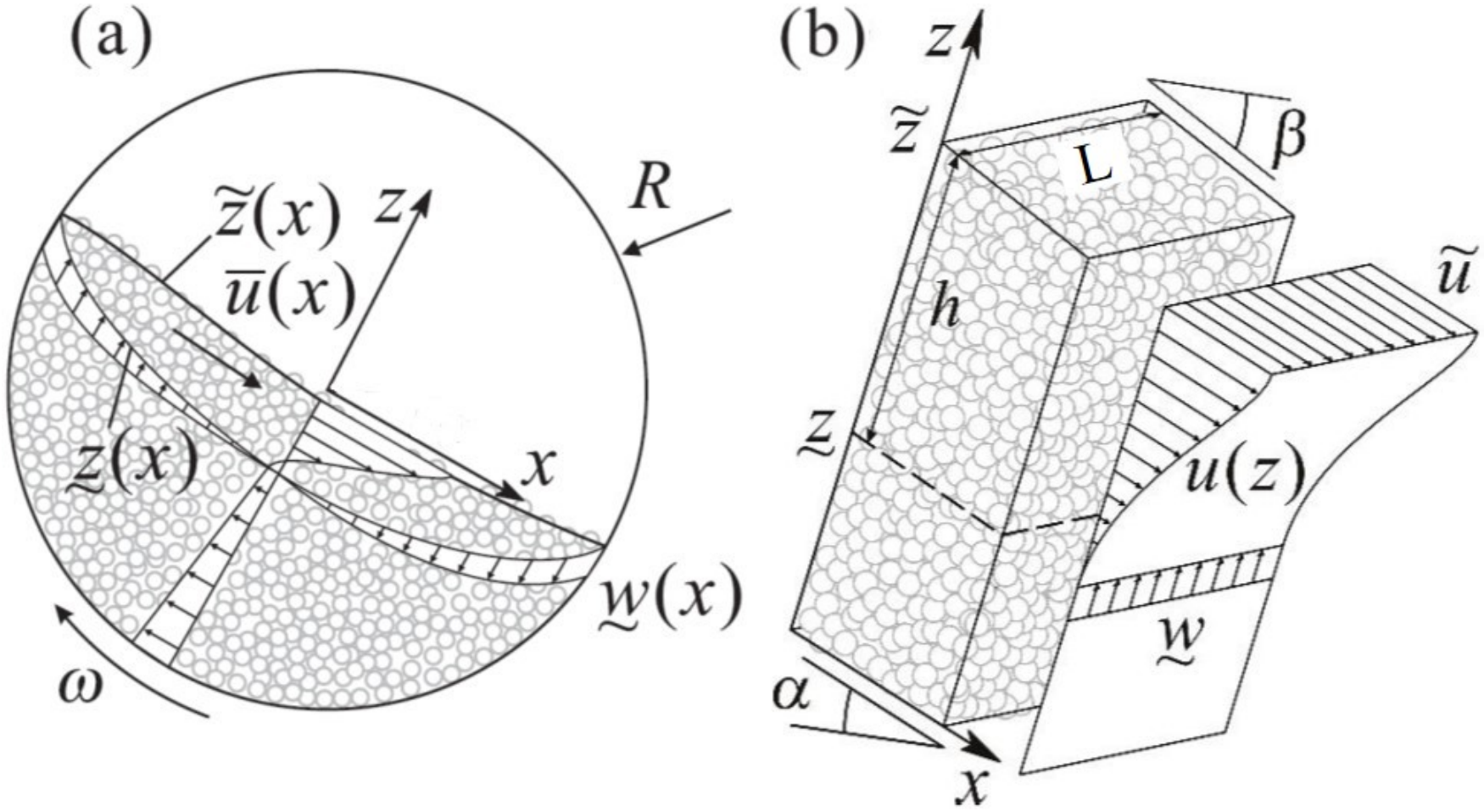

Capart et al. (2015) and Hung et al. (2016)

1. Continuum Model: Assumptions

a) Based on linearized viscoplastic dense granular flow rheology by Jop et al. (2006)

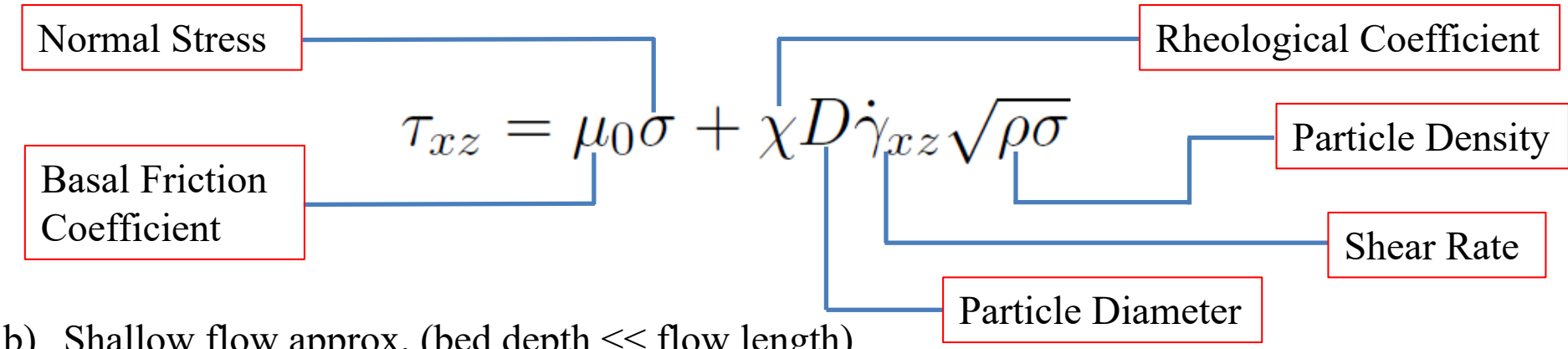

b) Shallow flow approx. (bed depth << flow length)
c) Incompressible flow (Tested with full DEM tensorial analysis across all flow regimes)
d) Uniform axial flow (We are ignoring axial flow for now)
e) Coulomb-like friction along side walls
f) Non-equilibrium velocity profile remains similar to equilibrium velocity profile
g) The following boundary conditions apply:

Free Surface

$$\widetilde{w} = \frac{\partial \widetilde{z}}{\partial t} + \widetilde{u}\frac{\partial \widetilde{z}}{\partial x}$$
$$\widetilde{\sigma} = 0,$$
$$\widetilde{\tau} = 0.$$

Basal Interface

$$\underset{\sim}{u} = 0,$$
$$\underset{\sim}{w} = -\omega x$$
$$\underset{\sim}{\tau} \equiv \tau_0 = \mu_0 \underset{\sim}{\sigma}.$$

1. Model Assumption (c): Incompressibility

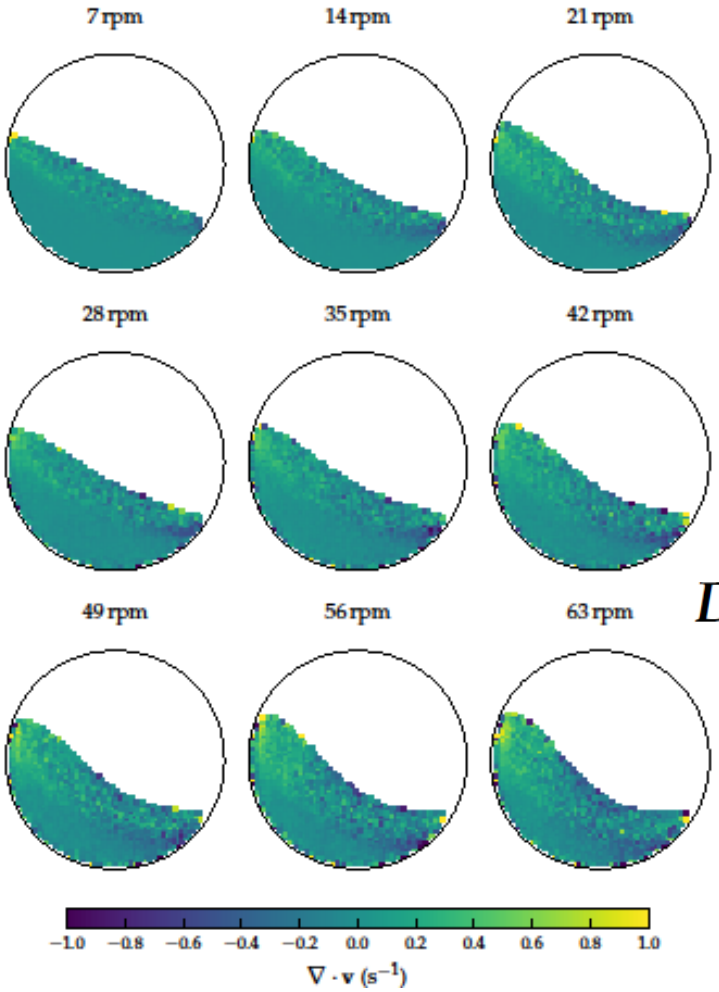

$$D_{\text{vol}} = D - D_{\text{dev}}$$

$$D_{\text{dev}} = D - \frac{1}{3}\text{tr}(D)I$$

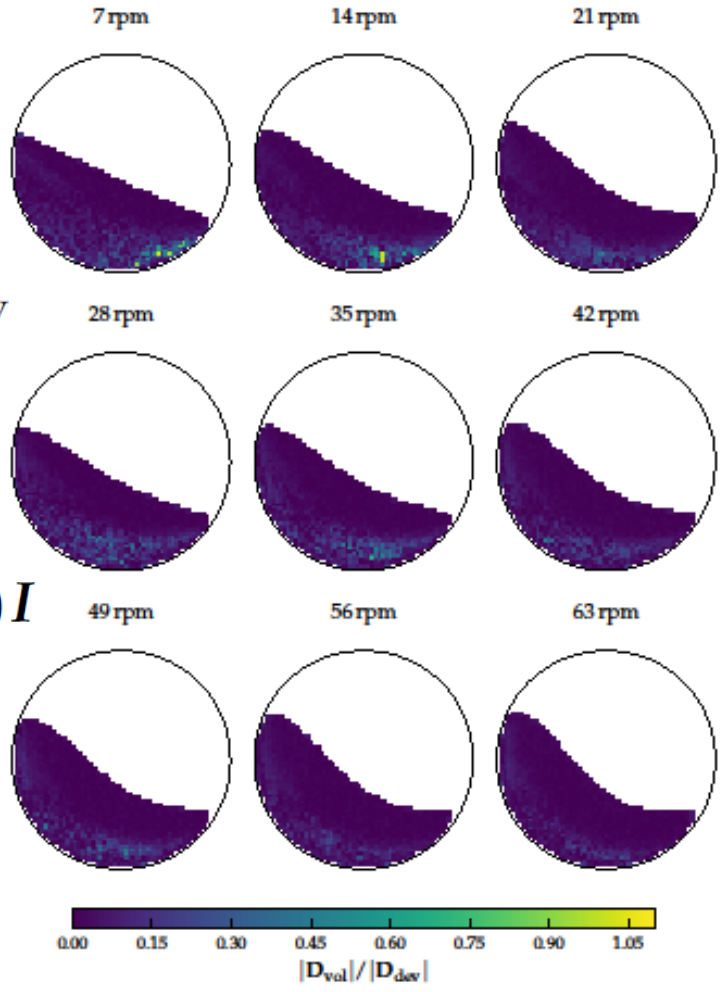

$\boldsymbol{D}$ = symmetric velocity gradient
$\boldsymbol{D}_{\text{dev}}$ = deviatoric component of $\boldsymbol{D}$
$\boldsymbol{D}_{\text{vol}}$ = volumetric component of $\boldsymbol{D}$

- The flowing layer is very slightly incompressible
- The rising layer (below basal interface) is incompressible
- Incompressibility valid over wide Froude range

1. Steady-State Governing Equations

Free Surface Profile

$$\frac{d\hat{\tilde{z}}}{d\hat{x}} = \frac{2695\sqrt{\hat{h}}\hat{q} - \hat{h}^4\left(864\kappa - 385\right) - 693\kappa\hat{q}\hat{h}\left(\frac{d\hat{q}}{d\hat{x}}\right)}{9\hat{h}^3\left(96\kappa - 77\right)}$$

Flowing Layer Depth Profile

$$\frac{d\hat{h}}{d\hat{x}} = \frac{6\left(72\kappa - 77\right)\hat{h}\hat{q}\left(\frac{d\hat{q}}{d\hat{x}}\right) + 560\sqrt{\hat{h}}\hat{q} - 64\hat{h}^4}{3\hat{q}^2\left(96\kappa - 77\right)}$$

Velocity field

$$u(x,z) = \overline{u}(x) f(\hat{\eta}(x,z)) + \omega z \qquad \ldots x\text{-velocity profile}$$

$$w(x,z) = -\frac{\partial \tilde{z}}{\partial x}\overline{u}(x) f(\hat{\eta}(x,z)) - \omega x, \quad \text{with} \qquad \ldots z\text{-velocity profile}$$

$$f(\hat{\eta}(x,z)) = \begin{cases} \frac{7}{3} - \frac{35}{6}\hat{\eta}^{\frac{3}{2}} + \frac{7}{2}\hat{\eta}^{\frac{5}{2}}, & \text{if } 0 \le \hat{\eta} \le 1 \\ 0, & \text{otherwise.} \end{cases}$$

velocity shape function with

$$\ldots \quad \eta = \tilde{z} - z$$

$$\hat{\eta} = \frac{\eta}{h}$$

2. Validation: Velocity Field in Rolling Regime

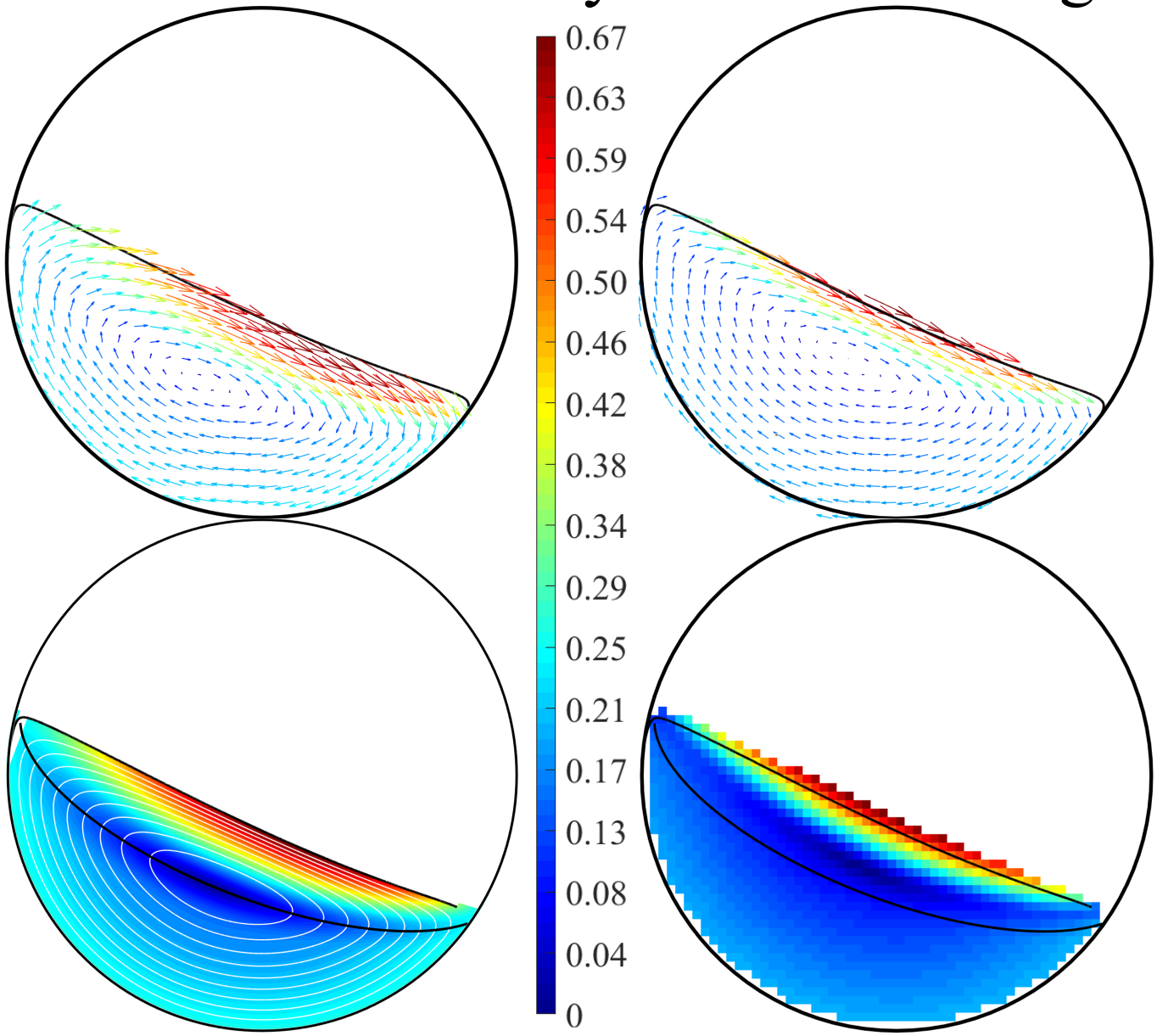

2. Validation: Velocity Field in Cascading Regime

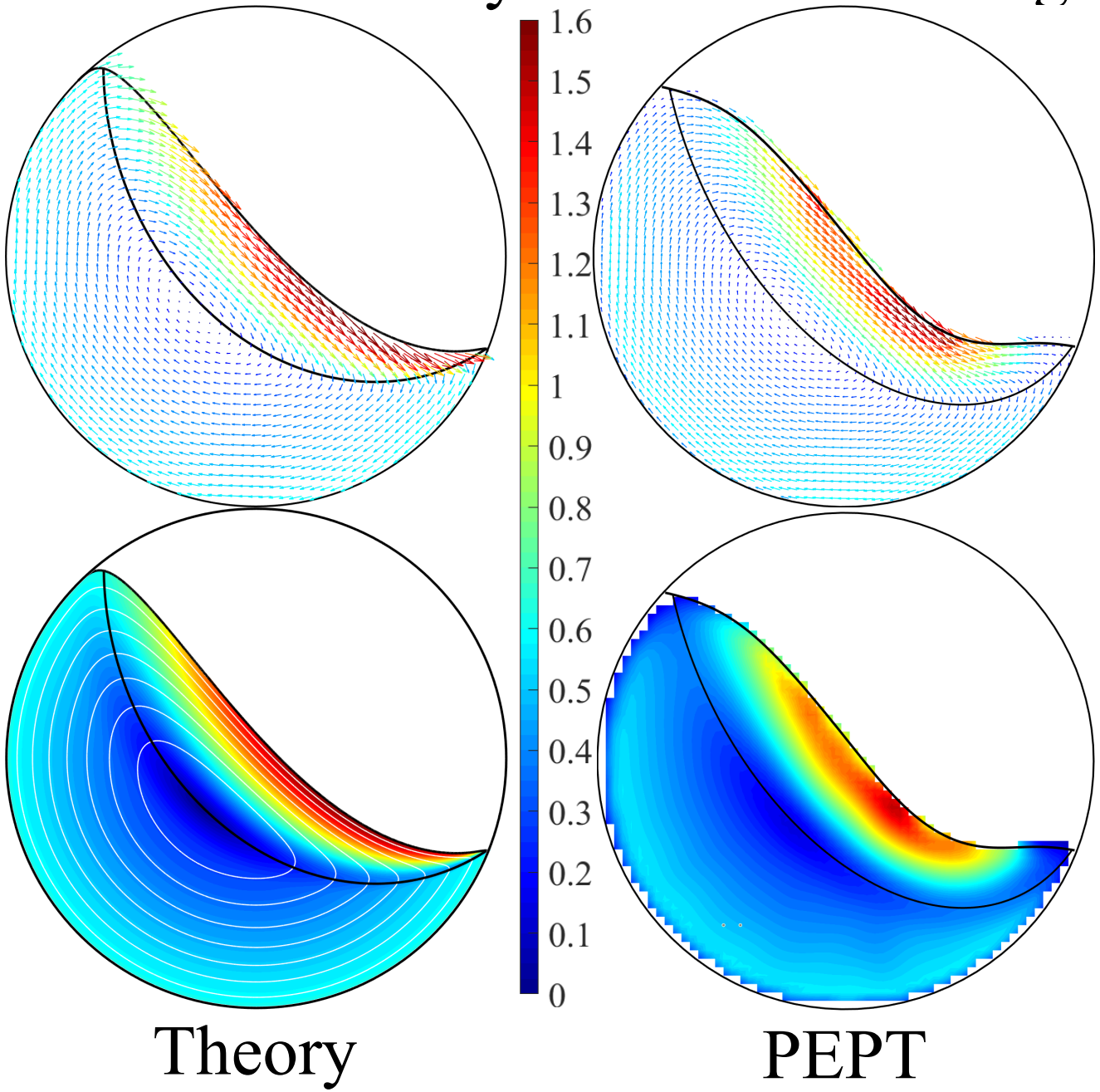

3 Physical Significance of Energy Balance

$$u\rho\frac{\partial u}{\partial t}+\rho\left(u^2\frac{\partial u}{\partial x}+uw\frac{\partial u}{\partial z}\right)=u\rho g\sin(\beta)-u\frac{\partial \sigma}{\partial x}-\frac{2\tau_W}{L}+u\frac{\partial \tau}{\partial z}$$

1st term: Rate of change of kinetic energy.

2nd term: Divergence of the kinetic energy flux.

3rd term: Gravitational energy flux.

4rd term: Work rate of the normal stress gradient.

5th term: Energy dissipation rate due to wall shear stresses.

6th term: Energy dissipation rate by internal shear stresses.

Term 2 describes advective energy dissipation

Term 6 describes shear energy dissipation

Typical Energy Distributions (per unit density): [m^2/s^3]

Shear Dissipation

$$\chi D \sqrt{g_\perp h \hat{\eta}} |\dot{\gamma}|^2$$

- Positive definite
- Monopolar

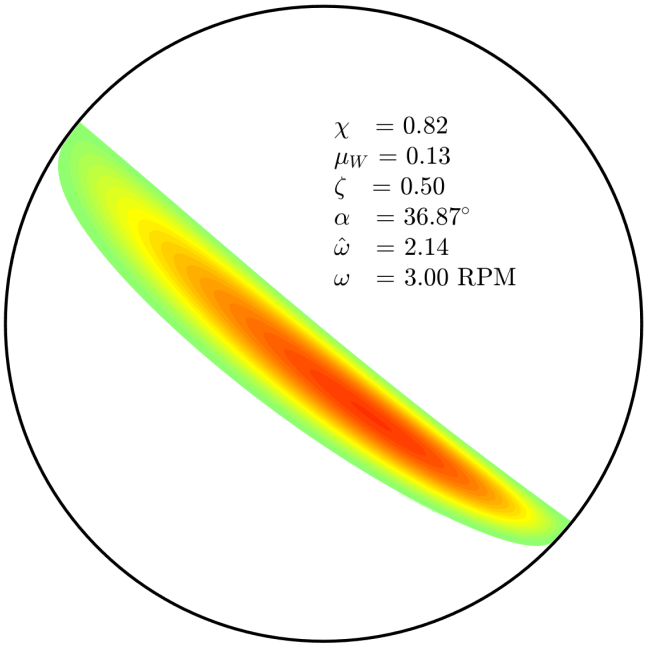

Advective Dissipation

$$\vec{\nabla} \cdot \left(K \rho \vec{V} \right) = \left(\frac{3}{2} \right) u^2 \frac{\partial u}{\partial x} + \left(\frac{1}{2} \right) uw \frac{\partial u}{\partial z}$$

Bipolar distribution

- Positive divergence ⇒ KE source
- Negative divergence ⇒ KE sink

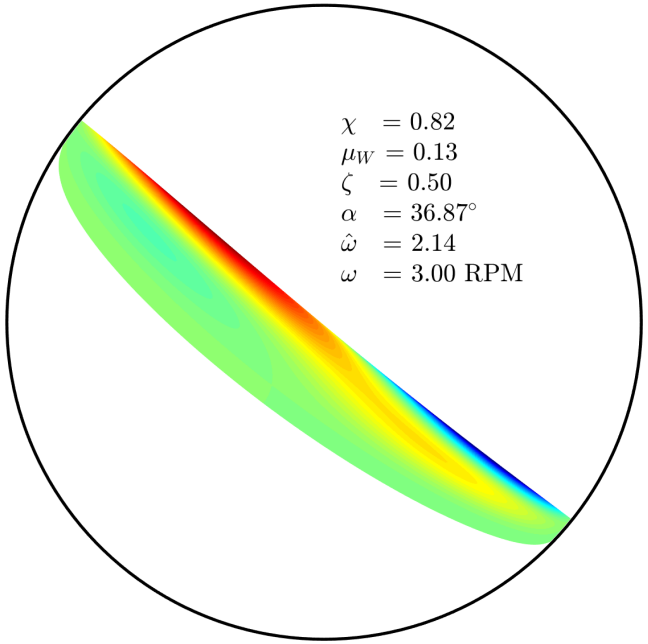

Energy Distributions spanning Rolling-to-Cascading

Shear Dominated

ω = 0.10 RPM
R = 239 mm
Fill Frac (ζ) = 0.5

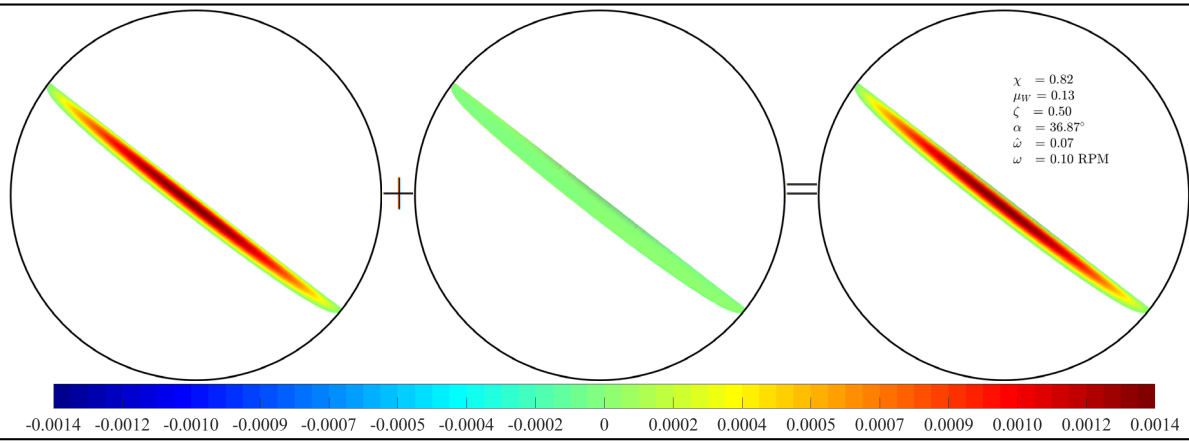

Shear & Advective Dominated

ω = 3.00 RPM
R = 239 mm
Fill Frac (ζ) = 0.5

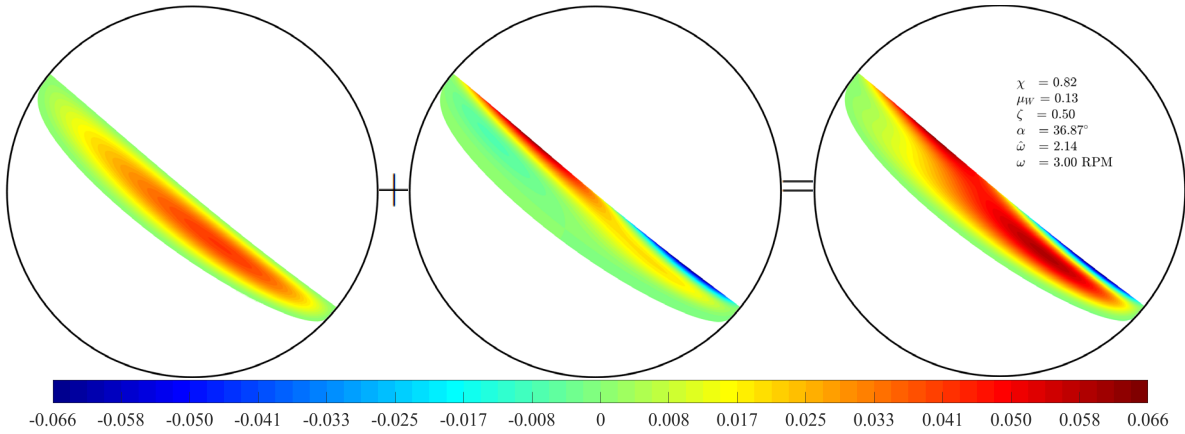

Advective Dominated

ω = 10 RPM
R = 239 mm
Fill Frac (ζ) = 0.5

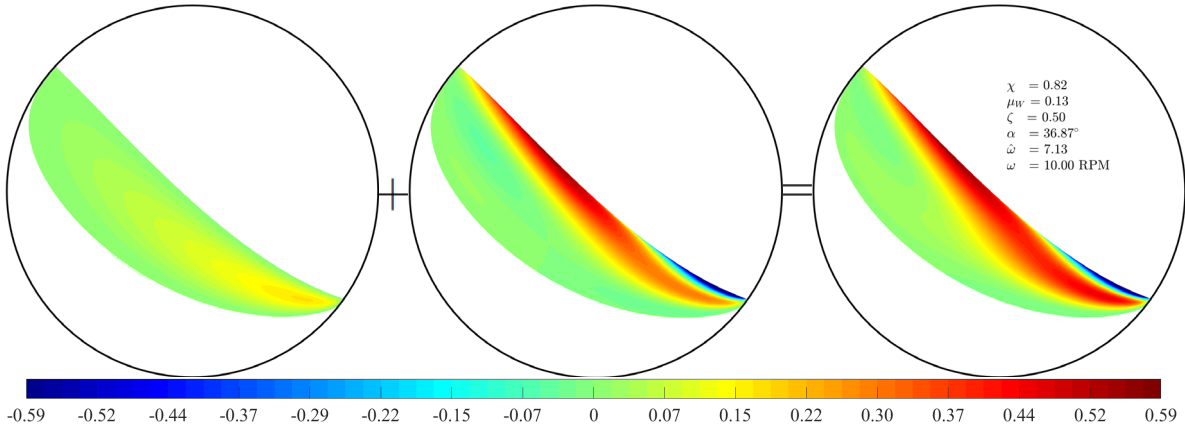

3. Scale-Up Rule of Mixing Mechanism

By dimensional analysis we obtain the ratio of forced-to-free Entrainment:

$$\hat{\omega} = \frac{\omega R^{9/8}}{\sqrt{g_{\perp}}\,(\chi D)^{3/4}} \left(\frac{L}{\mu_W}\right)^{1/8}$$

The Crux of the Scale-Up Rule

- Two rotating drum configurations with the same $\hat{\omega}$ will exhibit the same proportions of advective-to-shear energy dissipation.
- So, a bench-scale configuration with a given proportion of advection-to-shear energy dissipation can be scaled (up) to an industrial drum by keeping $\hat{\omega}$ the same in both configurations.
- To illustrate the scale-up rule, we consider the three basic splits of advection-to-shear flow and mixing

Scale-Up of Shear Dominated Mixing

Scaling Rule	Shear + Advection = Total
R = 239 mm ω = 1.00 RPM Fill Frac (ζ) = 0.5	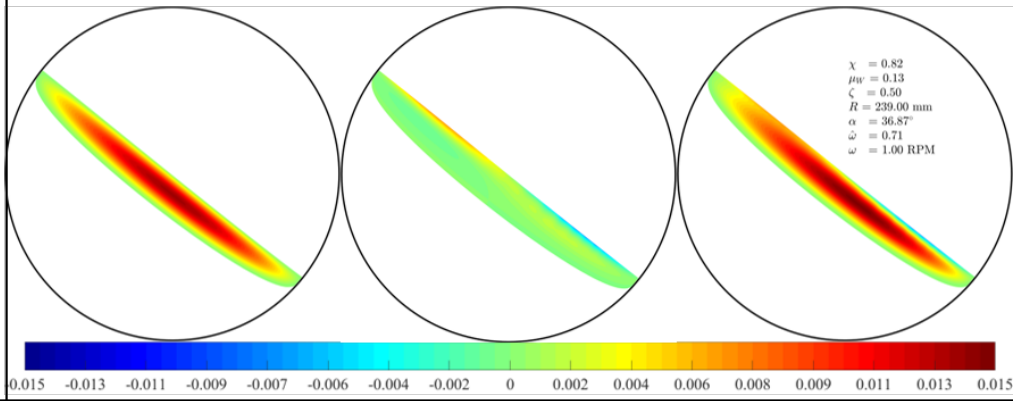
R → 2R ω → ω/($2^{9/8}$) Fill Frac (ζ) = 0.5	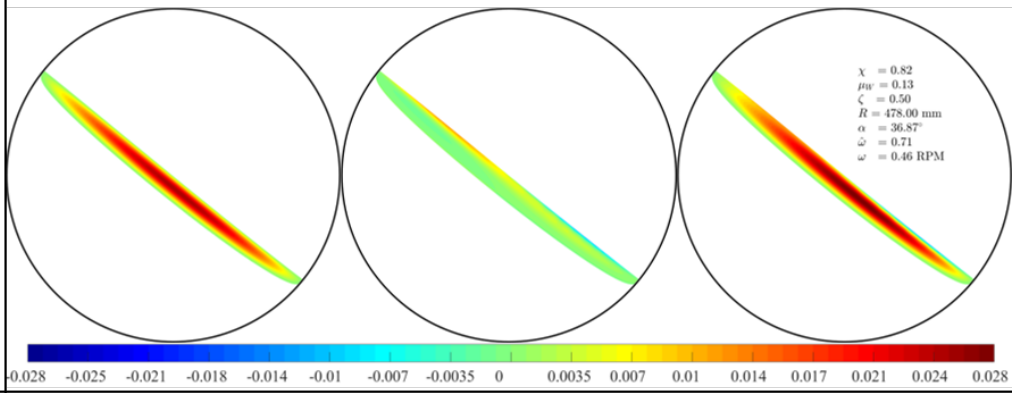
R → 4R ω → ω/($4^{9/8}$) Fill Frac (ζ) = 0.5	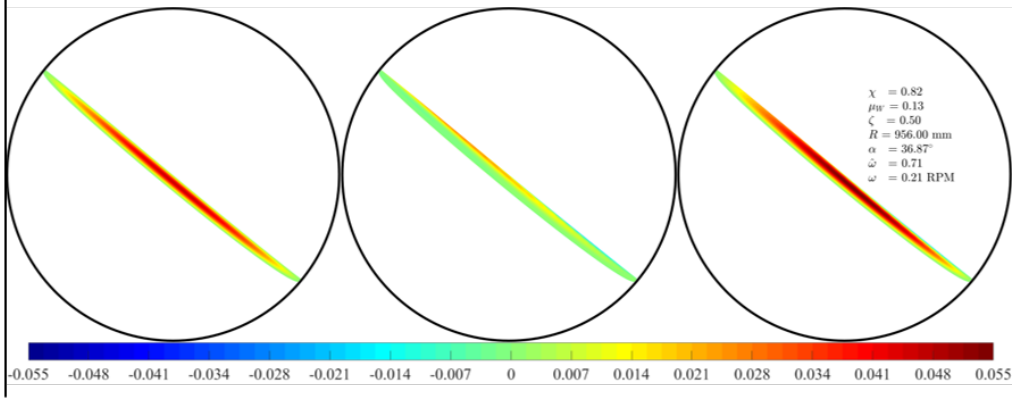

Scale-Up of Shear-&-Advection Mixing

Scaling Rule	Shear + Advection = Total
R = 239 mm ω = 3.00 RPM Fill Frac (ζ) = 0.5	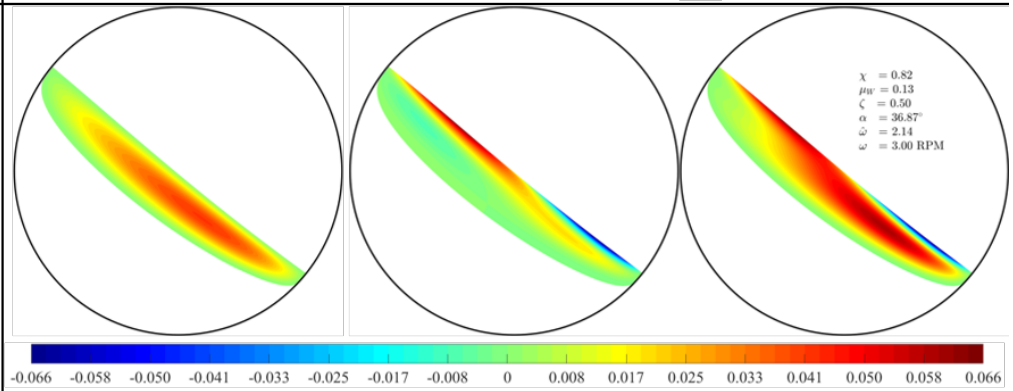
R → 2R ω → ω/($2^{9/8}$) Fill Frac (ζ) = 0.5	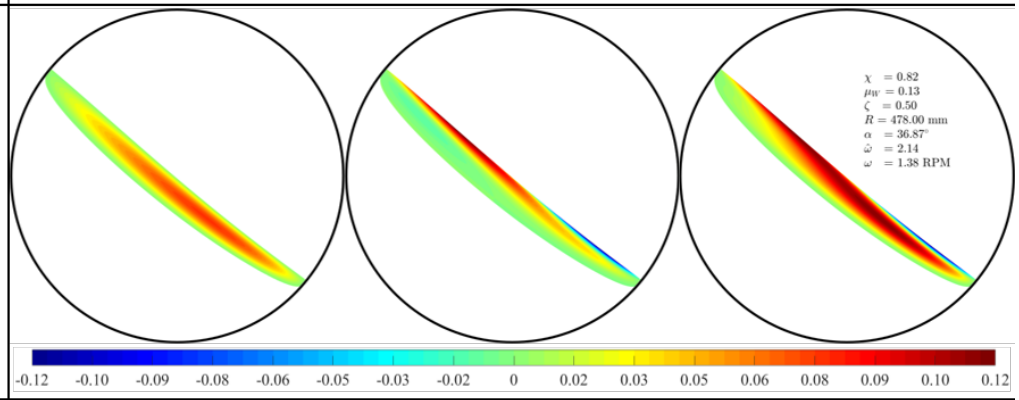
R → 4R ω → ω/($4^{9/8}$) Fill Frac (ζ) = 0.5	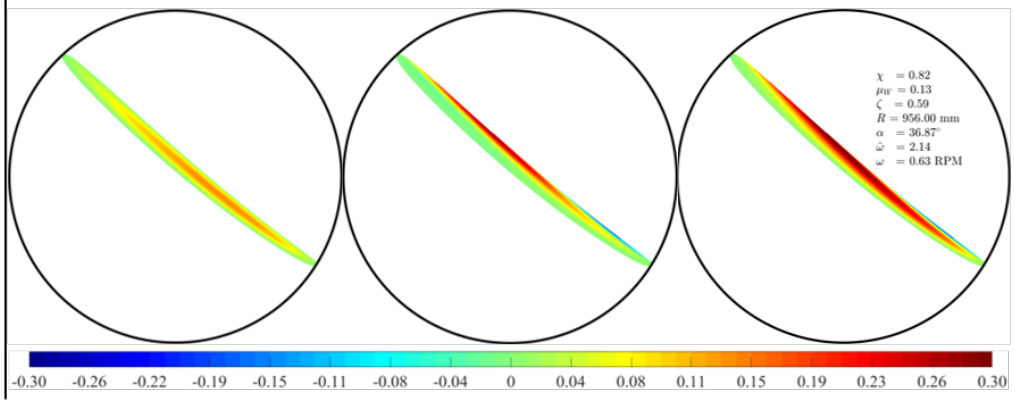

Scale-Up of Advective Dominated Mixing

Scaling Rule	Shear + Advection = Total
R = 239 mm ω = 10.00 RPM Fill Frac (ζ) = 0.5	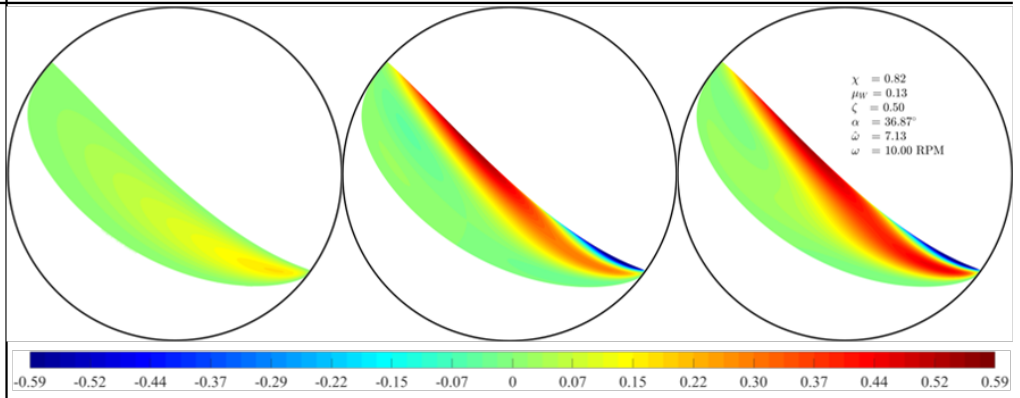
R → 2R ω → ω/($2^{9/8}$) Fill Frac (ζ) = 0.5	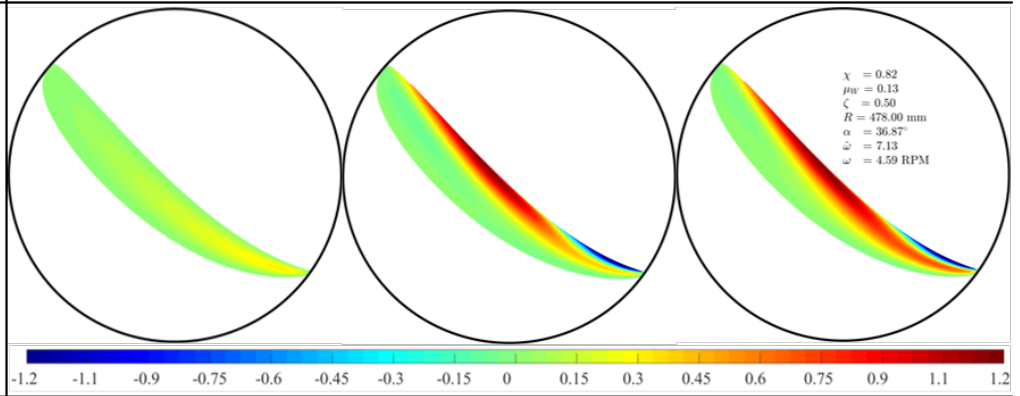
R → 4R ω → ω/($4^{9/8}$) Fill Frac (ζ) = 0.5	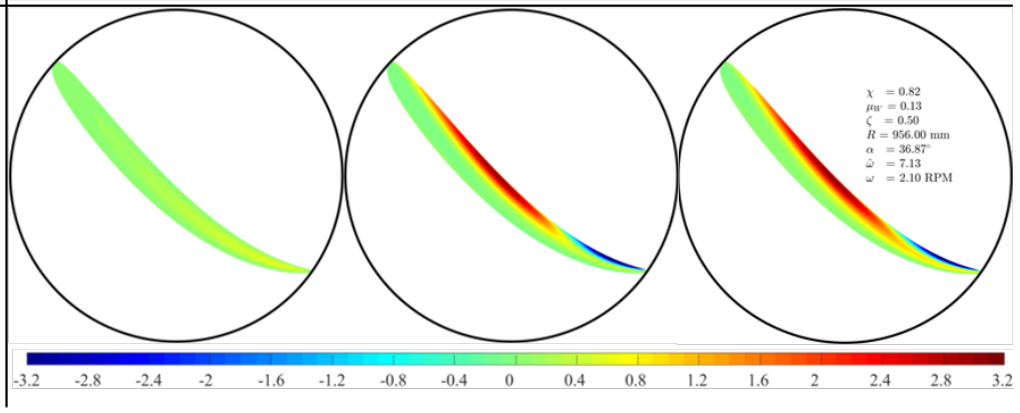

Scale-Up of Fully Cascading Mixing

Scaling Rule	Shear + Advection = Total
R = 239 mm, ω = 24.47 RPM Fill Frac (ζ) = 0.5	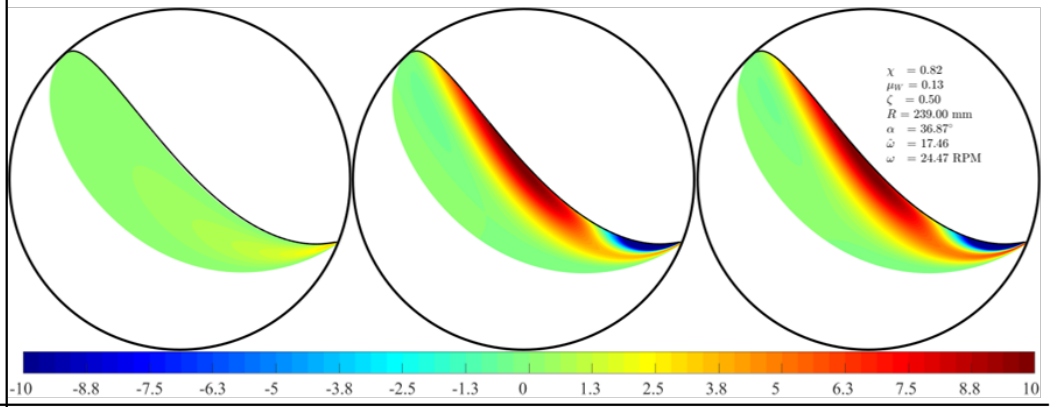
R → 2R ω → ω/$(2^{9/8})$ Fill Frac (ζ) = 0.5	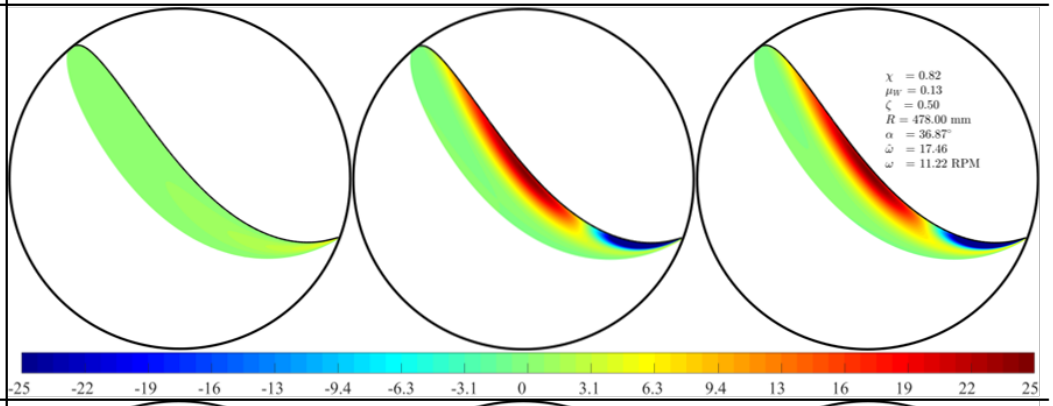
R → 4R ω → ω/$(4^{9/8})$ Fill Frac (ζ) = 0.5	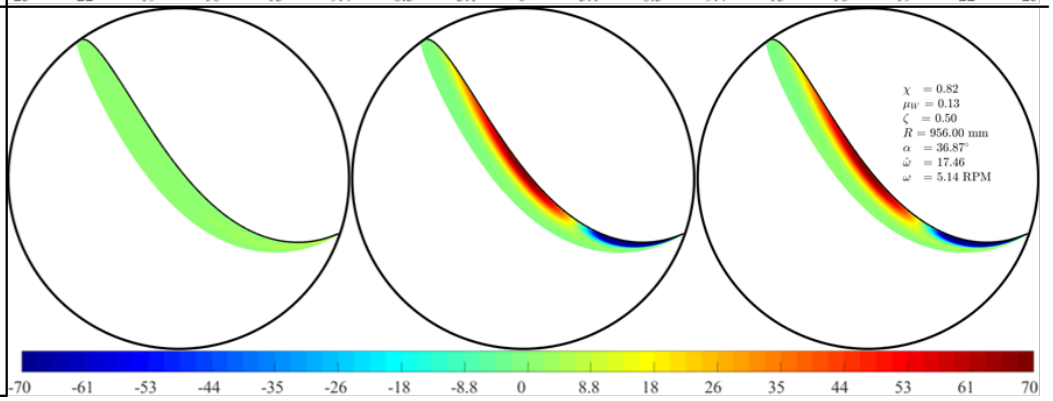

Conclusions & Future Work

- A robust granular flow model of rotating drum flows was developed using the linearized viscoplastic Inertial rheology
- The accurate velocity field predictions have hitherto not been reported in the literature, and for such a wide range of flow regimes
- Shear & Advective Energy dissipation signatures are useful in identifying the dominant mixing mechanisms
- The Entrainment Number allows us to scale-up the dominant mixing mechanisms across the rolling-to-cascading flow regimes

- Future (ongoing) work will include:
- An exploration of other rheologies, including those that incorporate wet systems (Peclet & Visco-Inertial)
- A full tensorial analysis that facilitates comparison between measurements (via PEPT) and simulations (via DEM) is currently underway
- Mixtures beyond bi-disperse systems will be studied using PEPT & DEM

Thank You!

TECHNISCHE UNIVERSITÄT BERGAKADEMIE FREIBERG
Die Ressourcenuniversität. Seit 1765.

INSTITUT FÜR MECHANISCHE VERFAHRENSTECHNIK UND AUFBEREITUNGSTECHNIK

IFPRI International Fine Particle Research Institute

Detailed insight into microscopic phenomena using 3D-tomography data to develop a better model for dead-end filtration

E. Löwer, M. Brockmann, Dr. Th. Leißner, Prof. Dr.-Ing. Urs A. Peuker

Objectives of the project

PARTICLE PROPERTIES
- wettability
- particle-particle interaction

FILTER CAKE PROPERTIES
- integral and local porosity
- pore size
- particle contacts

PROCESS RELEVANT PROPERTIES
- dewatering behavior
- moisture content
- permeability

Influence of wetting properies

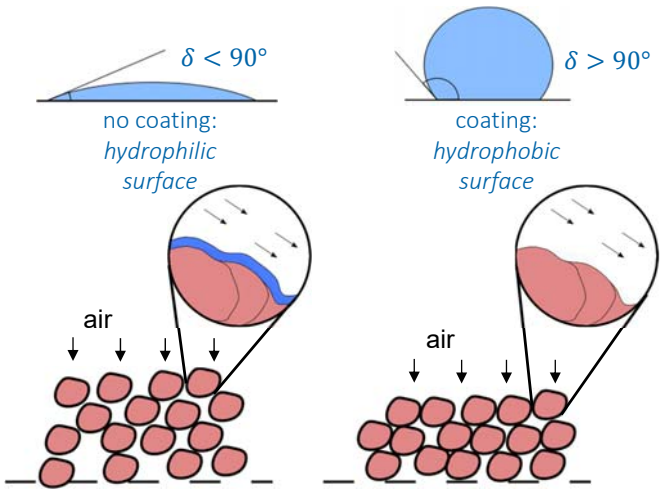

The wetting influences both the particle-particle interactions and the de-watering behavior of a porous network. At poor wetting we observe:

- Gas-bridges (capillary forces) increase the attractive forces between particles
- Liquid repels from solid surface

Methods – parameter to be retrieved, or what can we measure

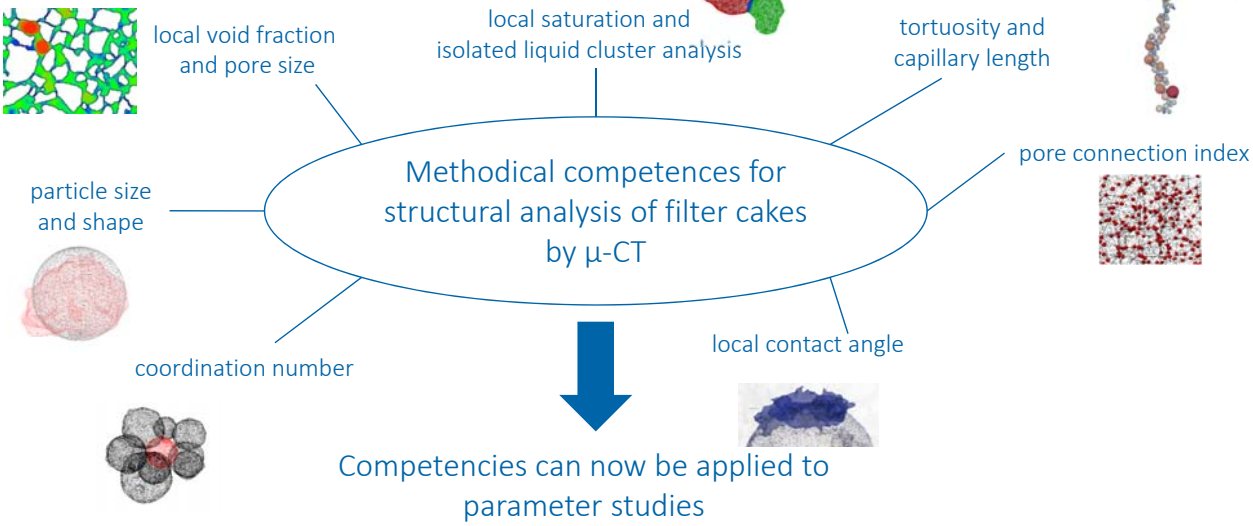

Material and Methods

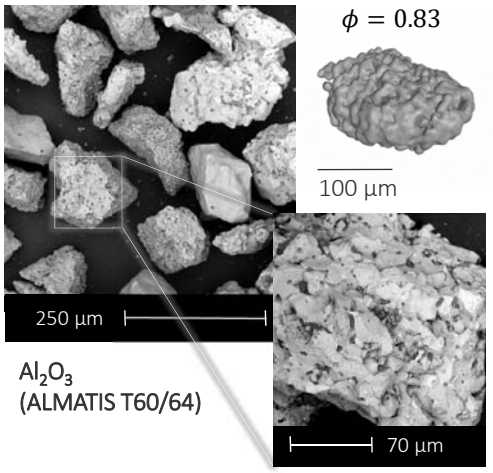

Al_2O_3
(ALMATIS T60/64)

$\phi = 0.83$

VDI 2762

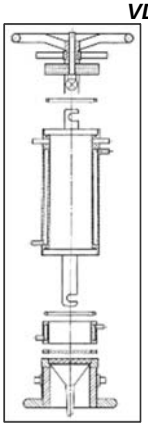

$A_{VDI} = 20\ cm^2$

$A_{VDI}/A_{insitu} = 100$

DOWN-SCALE

insitu flow-cell

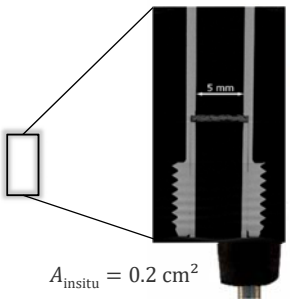

$A_{insitu} = 0.2\ cm^2$

Image processing (segmenation and phase identification)

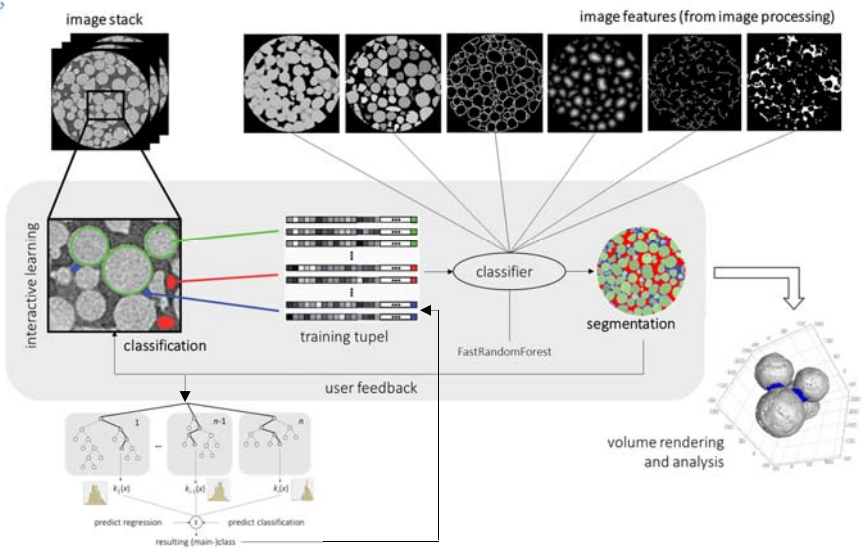

TECHNISCHE UNIVERSITÄT BERGAKADEMIE FREIBERG
Die Ressourcenuniversität. Seit 1765.

INSTITUT FÜR MECHANISCHE VERFAHRENSTECHNIK UND AUFBEREITUNGSTECHNIK

Methods I – determining parameters form the two phase system (solid-liquid)

E. Löwer, M. Brockmann, Dr. Th. Leißner, Prof. Dr.-Ing. Urs A. Peuker

Identification & quantification of the porosity

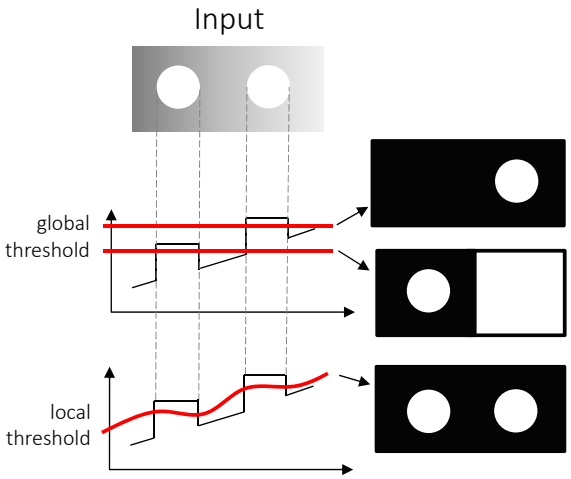

Identification & quantification of the porosity

partial volume correction depending on

- particle size and shape
- x-ray attenuation
- resolution

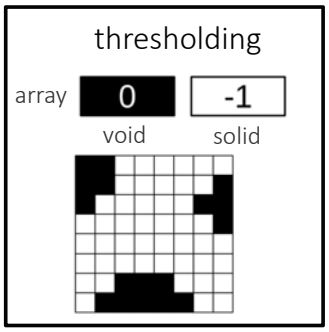

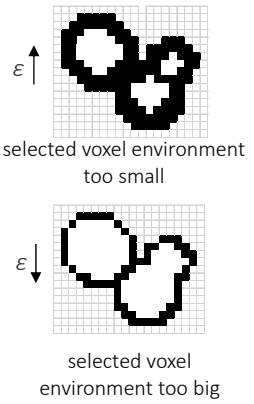

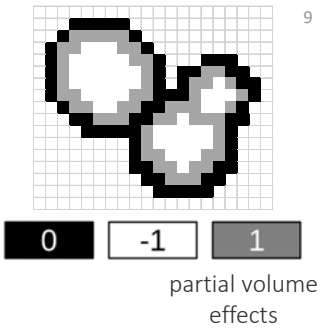

Definition and quantification of contact points within the cake

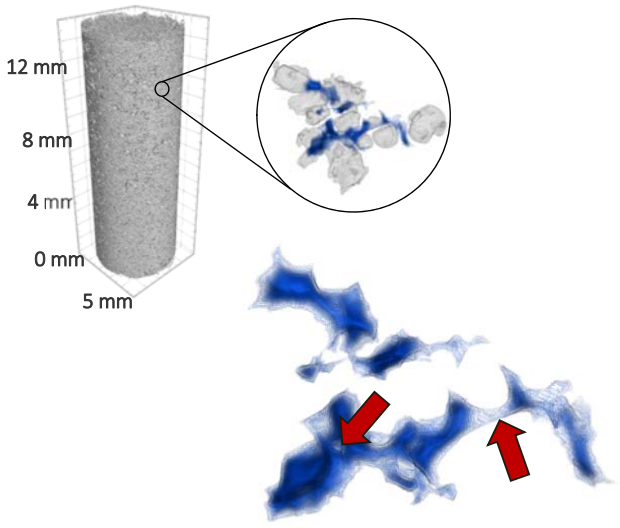

- Resolution of the measurements is not able to correlate several voxels to the particle-particle contact.
- The alternative definition of a contact point uses the distance map between the particles.
- The minimum of distance is defined (threshold) as contact point.

Definition and quantification of contact points within the cake

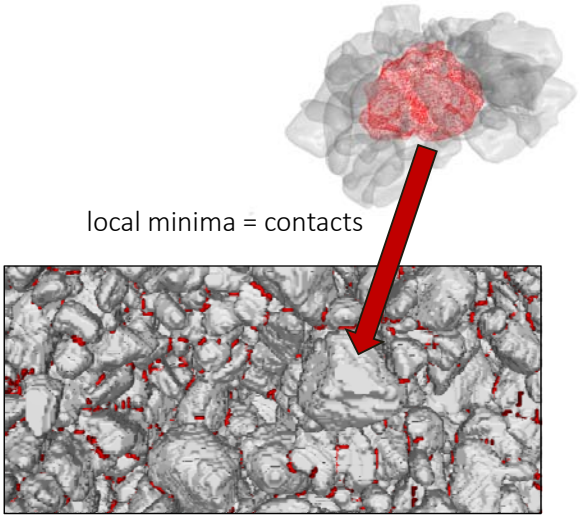

- The visualization of a single irregularly shaped particle shows how it is embedded into the filter cake.
- The red marked positions are the contacts between the individual particles according the definition (minimum of the distance map).

Definition of tortuosity

N identical capillaries with the same alignment in space

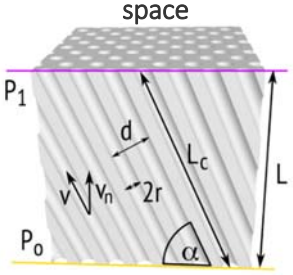

P_i – pressure
L_c – capillary length
α – alignment angle

pressure loss can be determined using the laws of classic fluid dynamics

BUT

disregarding:

a) capillary crosslinking
b) inlet effects
c) changes in cross sectional area
d) surface wettability
e) Always assumption:
   S_V = const.
   ε = const.
   r_C = const.

Determination of the real tortuosity

capillary length L_C

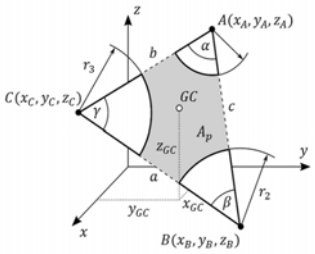

tetrahedron model

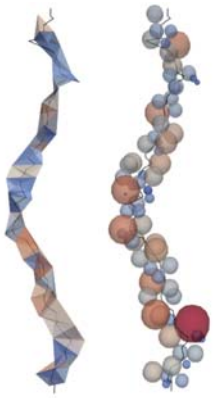

The capillary length, i.e. the tortuosity, depend on the individual way we are walking through the filter cake. This length also differs with the staring point at the filter cake surface. We defined the capillary length, by connecting the balance points of the triangles, which have been constructed between the particle centers.

Capillary pressure – geometric aspects

3D

mercury intrusion

1.

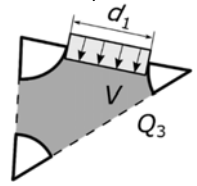

inscribed sphere

2.

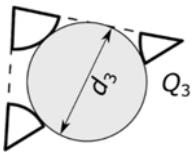

2D

tetrahedron model

3.

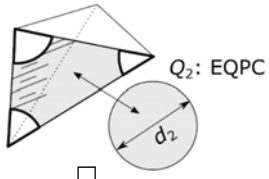

4.

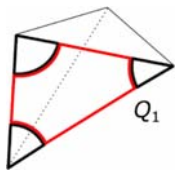

tetrahedron perimeter

To apply the LAPLACE equation

$$\Delta p = \frac{U}{A} \cdot \gamma_l \cdot cos\delta$$

we need a detailed view into the local geometry of the pore. There are different options to quantify the required geometric parameters. U reflects length of the three phase contact line.

TECHNISCHE UNIVERSITÄT BERGAKADEMIE FREIBERG
Die Ressourcenuniversität. Seit 1765.

INSTITUT FÜR MECHANISCHE VERFAHRENSTECHNIK UND AUFBEREITUNGSTECHNIK

Methods II – determining parameters form the three phase system (solid-liquid-gas)

E. Löwer, M. Brockmann, Dr. Th. Leißner, Prof. Dr.-Ing. Urs A. Peuker

Determination of the liquid saturation (balancing)

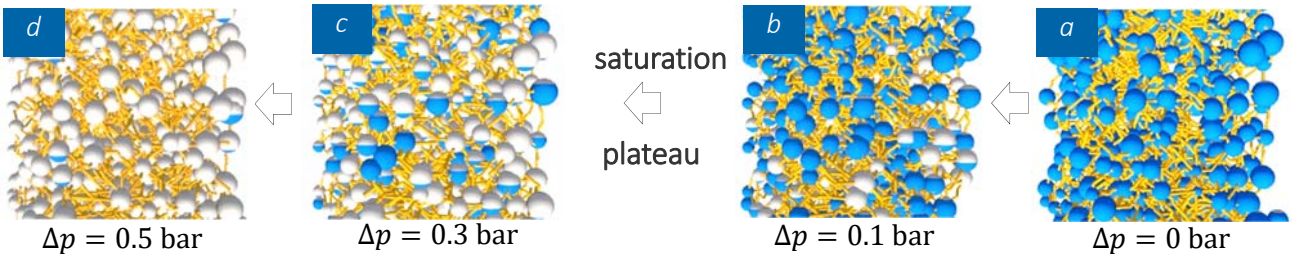

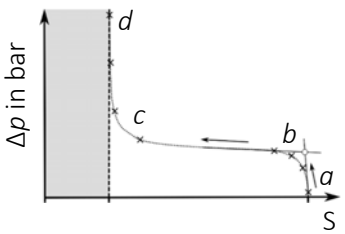

$$S = \frac{V_l}{V_{void}} = \frac{V_l}{V_{cake} - V_s}$$

Definition of the local wetting angle – extraction of liquid phase volume

SINGLE “LIQUID BRIDGE”

surface vector map

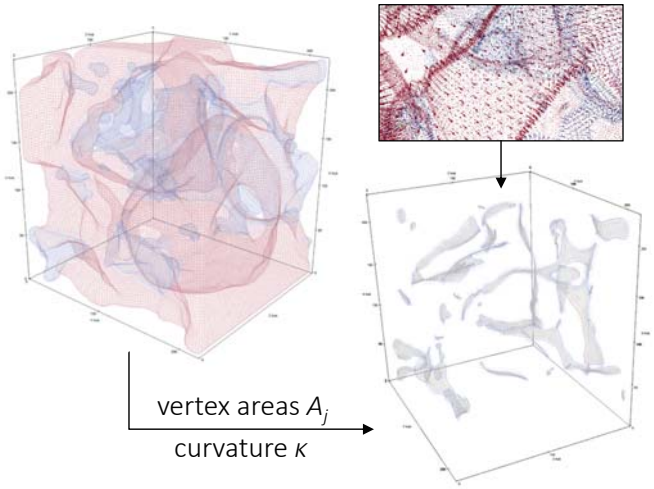

The three phase contact line of the liquid bridges is far below the resolution of the CT-measurements. Therefore, the wetting angle as been extrapolated by using a vectoral approach using the scalar product of the perpendicular vectors on each plane. Due to the local curvature to the liquid we measure a wetting angle distribution.

Quantifying the liquid bridges

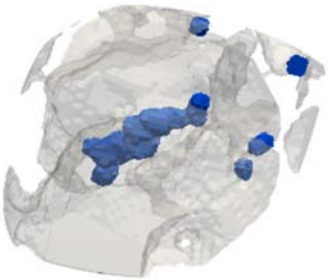

degree of freedom

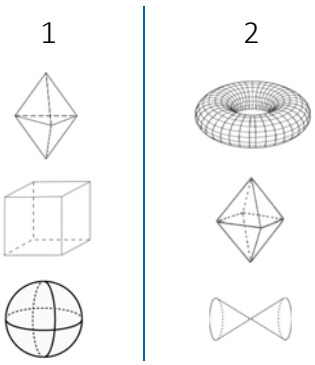

The tomograms show the challenges in the definition of the characteristic size of the pore liquid. The remaining liquid has quite irregular elongated shape, thus we are far form defined liquid bridges, which are common in the 2D-models.

Validation

E. Löwer, M. Brockmann, Dr. Th. Leißner, Prof. Dr.-Ing. Urs A. Peuker

CONCERN	VALIDATION METHOD
structure effects	▪ local particle size ▪ local porosity
particle morphology	▪ 2D and 3D shape parameters
pore size discription	▪ mercury intrusion ▪ inscribed sphere model ▪ pore wetting line
local contact angle	▪ static and dynamic sessile drop
capillary distribution	▪ perculating sphere model ▪ laboratory pressure tests

Validation particle properties (PSD)

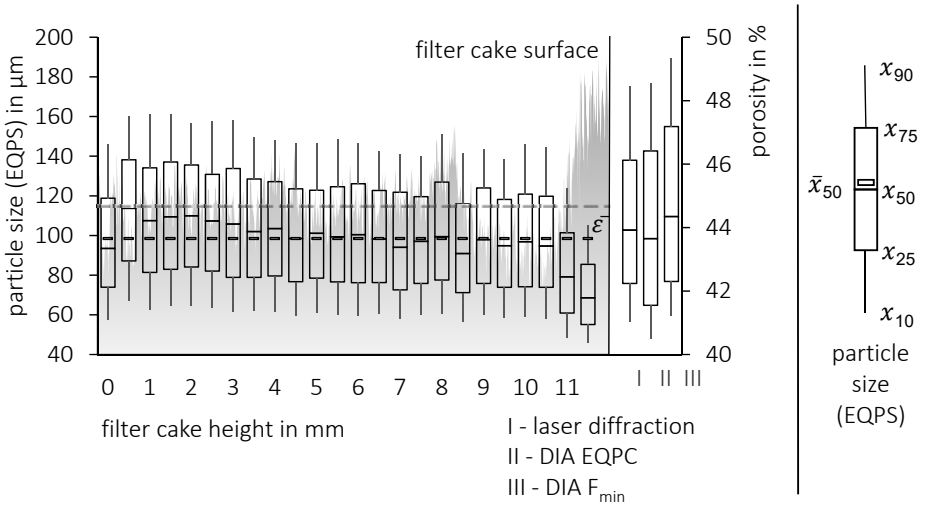

Validation pore properties (PoreSD)

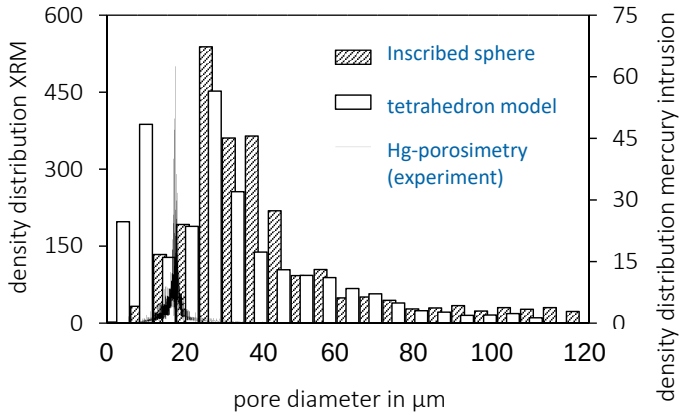

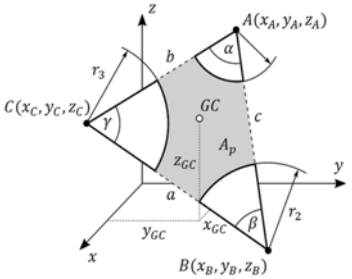

Validation pore properties (CPC)

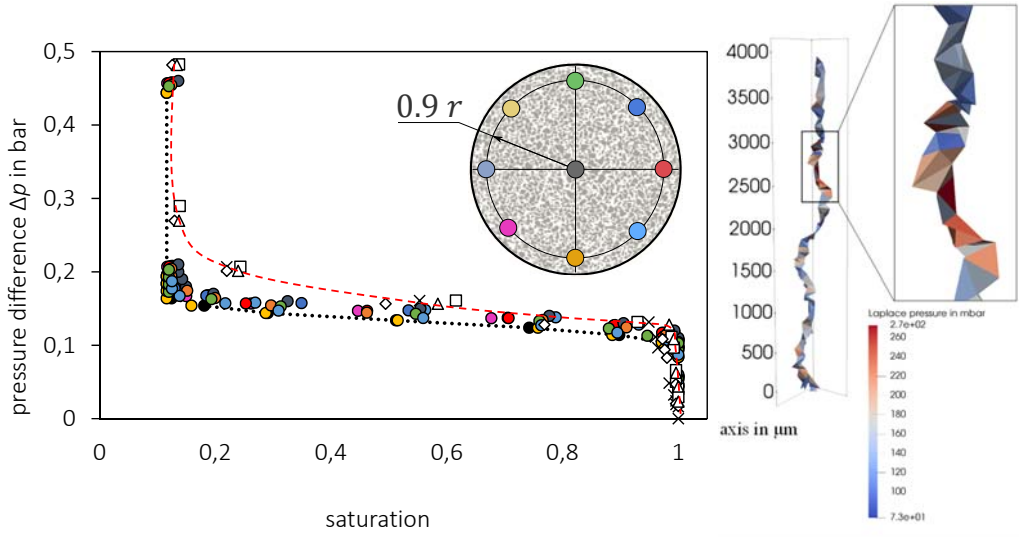

Validation wetting angle

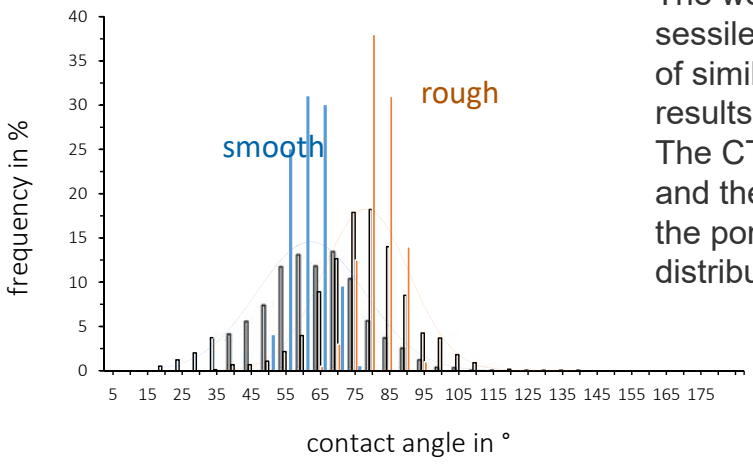

The wetting angle measured with the sessile drop method on a planar surface of similar roughness, fits to the CT-results, especially with the modal values. The CT-results allow a better resolution and therefore and due to the curvature of the pore geometry they have wider distribution.

Results – what we can further learn form CT-data?

E. Löwer, M. Brockmann, Dr. Th. Leißner, Prof. Dr.-Ing. Urs A. Peuker

Saturation – liquid distribution over the cake height.

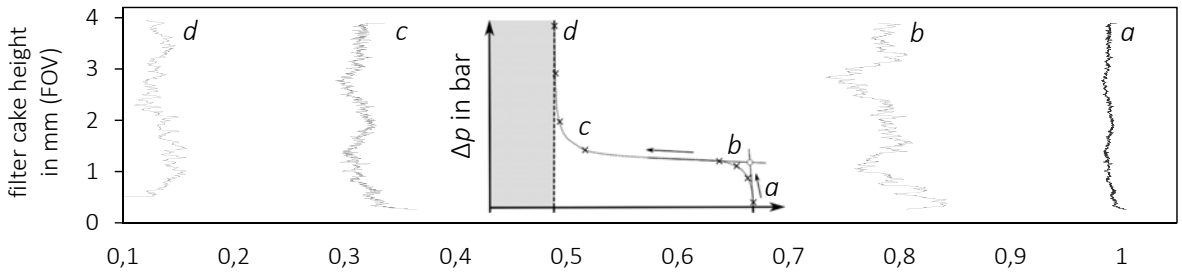

Characteristic length of liquid bridges and their volume distribution.

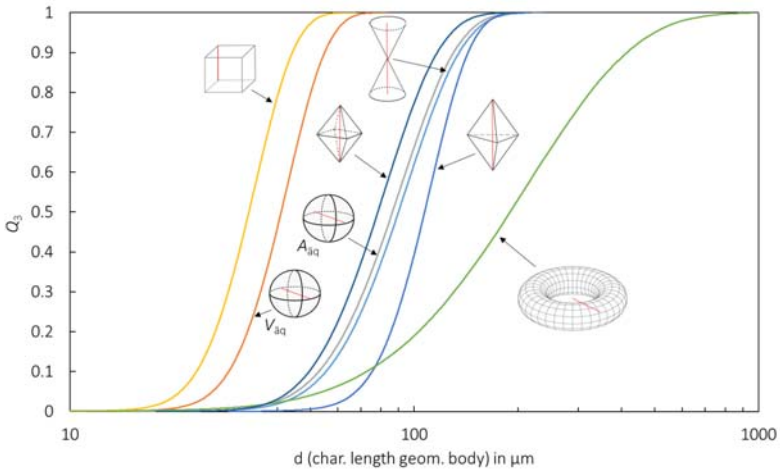

Lateral tortusity distribution

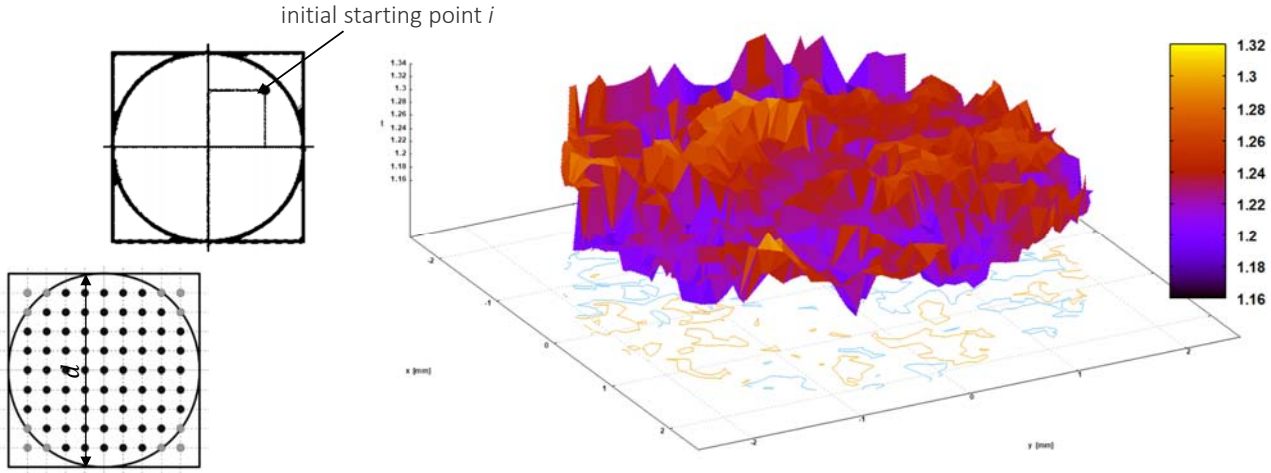

Different definitions of tortuosity and their distribution.

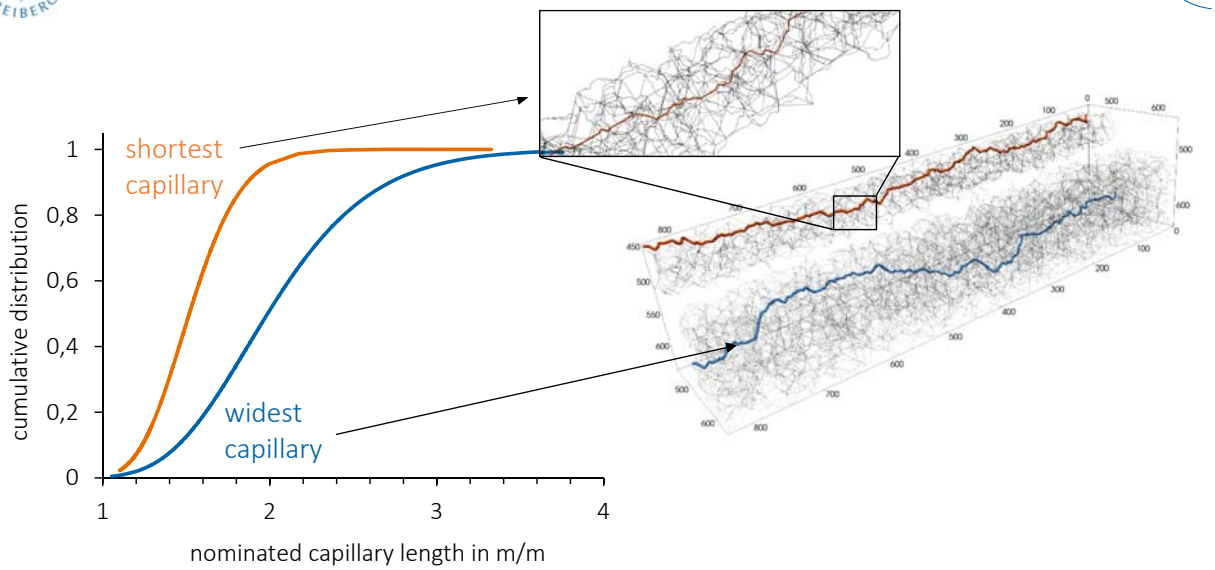

Contact angle distribution

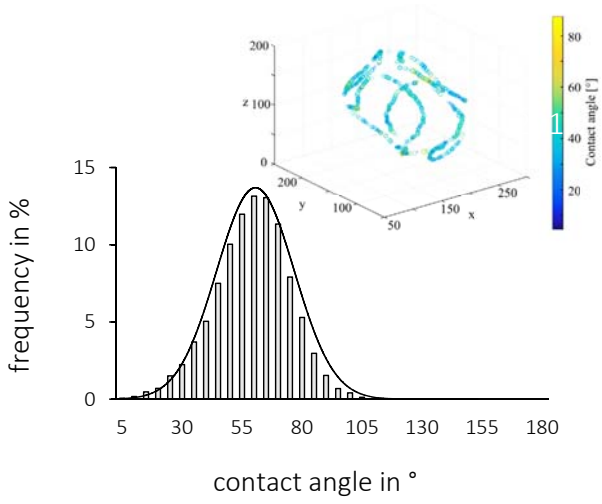

The contact angle on real (rough) curved particle surfaces shows a large variation, which is due to the complex geometry of the pore system formed by the particles.

Results – what we can further learn form CT-data concerning wetting effects.

E. Löwer, M. Brockmann, Dr. Th. Leißner, Prof. Dr.-Ing. Urs A. Peuker

Changing the wetting angle

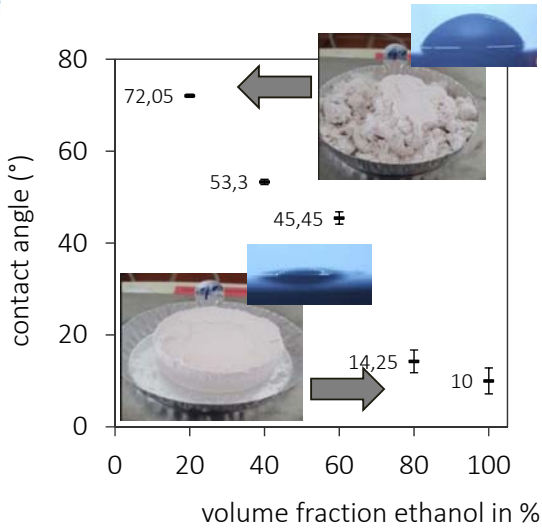

From the macrospoic point of view we see significant changes in the tensile stress and the flowability of a filter cake, when the wetting between mother liquid and solid changes.

(The more ethanol is in the liquid phase the better the wetting becomes.)

Influence of the wetting angle on cake structure

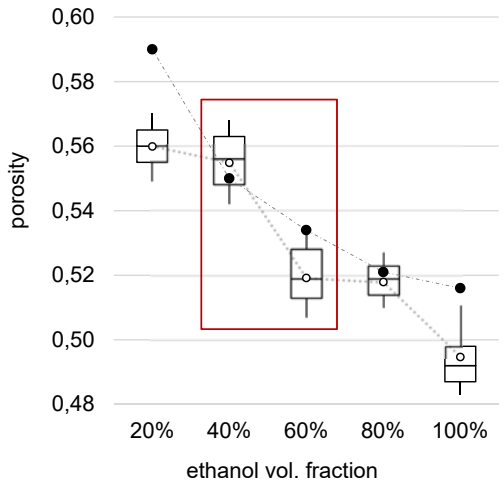

The effect of the wetting also can be seen in the structuring of the cake itself. The integral porosity decreases by about 6 %-points. The fluctuations within the porosity are larger in the range between 40-60 % of ethanol, where the largest change in porosity occurs.

Influence of the wetting angle on pore size

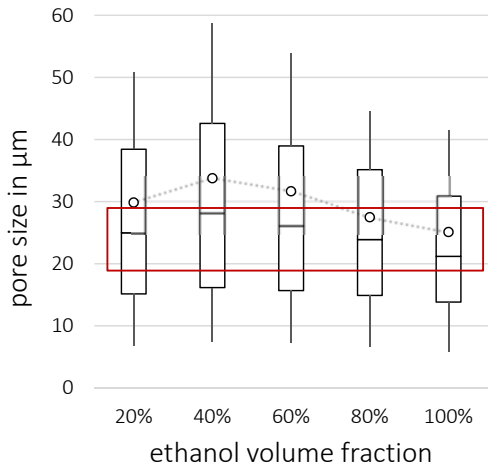

The pore size (using the inscribed sphere model) does not change much as a function of the wetting properties. It just can be stated that the span on the extreme values increases at 40 and 60 % of ethanol. The median (-) of the PoreSD decreases with the higher packing, with the lower porosity, respectively.

Influence of the wetting angle on coordination number

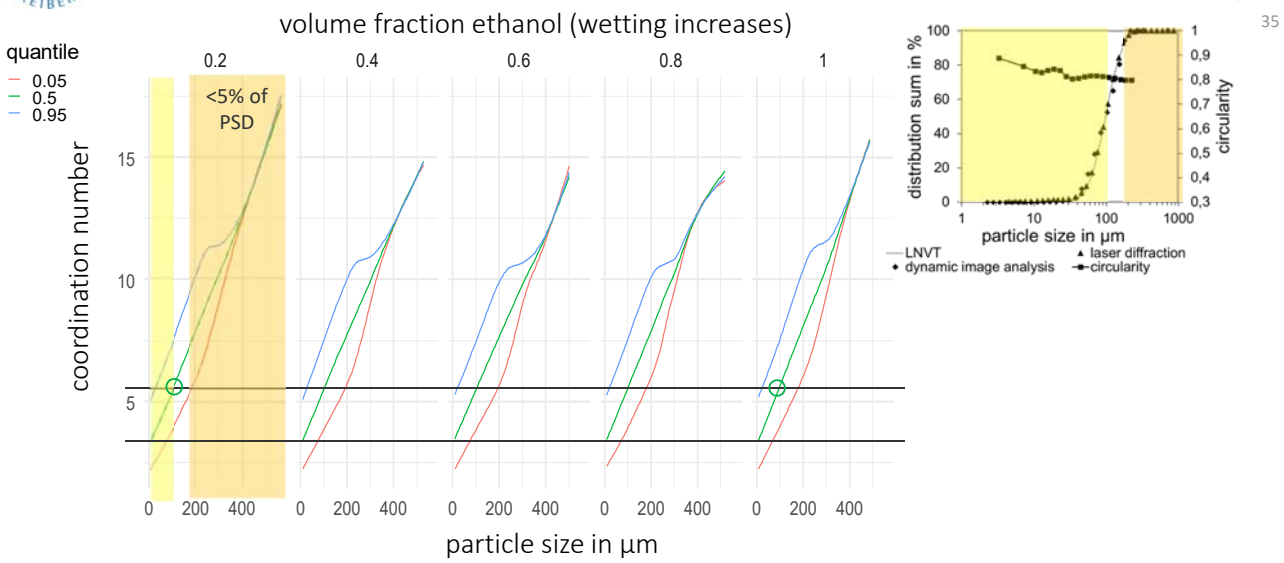

Outlook I -Summary

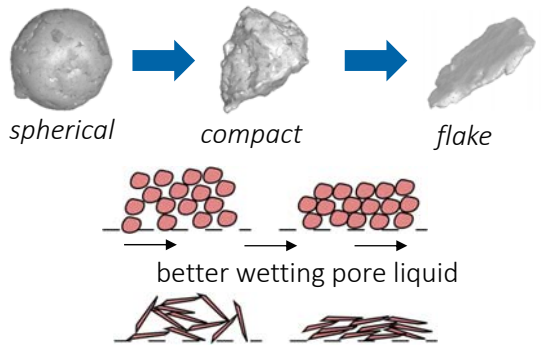

Having now in place a reliable data processing strategy, which bases on self-coded software, we be able to finally address strongly non-ideal particles and their structuring as a function of wetting.

Preliminary work (FIB / filter cake washing)

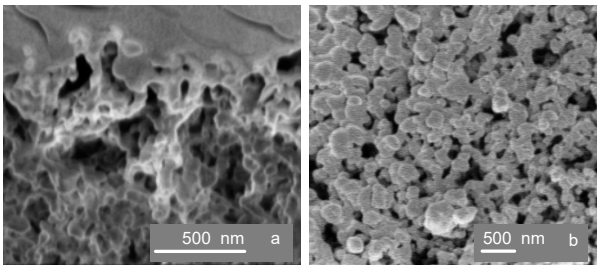

FIB-Analysis of filter cake made of porous particles

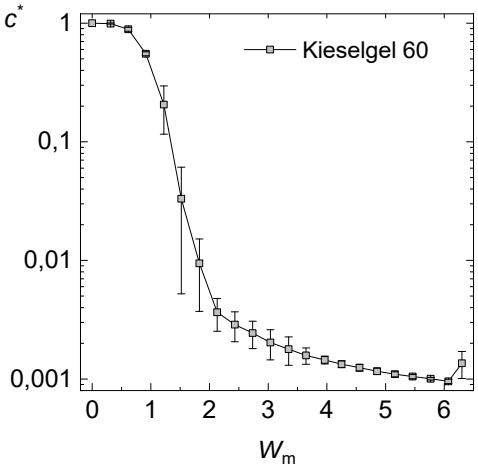

Washing curve for porous product (pore width 6 nm)

Seupel, S 2020 (paper submitted to WFC)

Outlook II

On strategy concerning second period:

- Centrifugal de-watering / sediment formation (sedimentation)
- Centrifugal de-watering (de-watering / Bond-diagram)
- Filter cake washing and structural effects

Multi-Scale structural analysis of pore networks, e.g. combination of FIB and µ-CT

International Fine Particle Research Institute

3D Printing of Perfect Particles

Prof Karen Hapgood

IFPRI AGM, May 2020

School of Engineering,
Deakin University, Australia

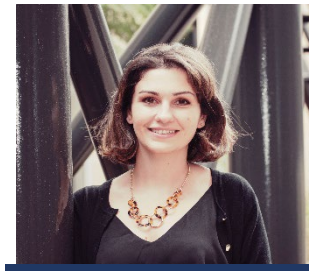

Dr Negin Amini

Dr Jun Zhang

IFPRI Project overview Years 1-6

Brief: Design controlled agglomerates with tuneable properties that can be systematically varied to validate models of granule breakage, flow or dissolution

Years 1-3: 3D Printing Tunable Particles

- 3D Printing approach: CAD design and 3D printed agglomerates in a Stratasys polyjet printer, prints multiple materials simultaneously.
- **Printed multiple identical copies of agglomerates, varying geometries and bridge strength**
- **Focus on breakage**: compared quasi-static deformation and breakage of agglomerate under compression
- **Compared to DEM** simulations of an identically structured agglomerate

Years 4-6: 3D Printing Perfect Particles

- 3D Printing Approach: Making the most of disruptive technology in particle technology applications
- Goal: **A suite of designer particles**, agglomerates and substrates, including "tunable" properties,
- Use these "perfect particles" to validate and advance more realistic models of
  - Powder flow and segregation,
  - Agglomerate breakage
  - Wetting and dissolution.

3D print any* agglomerate

IFPRI
International Fine Particle Research Institute

DEAKIN UNIVERSITY

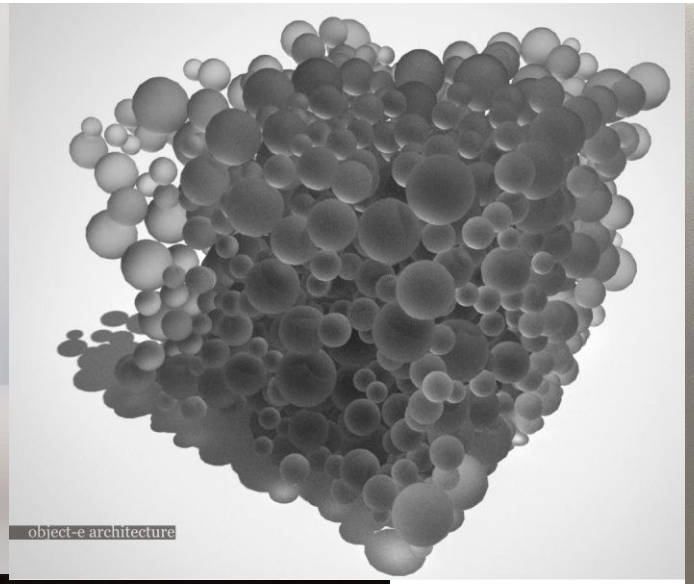

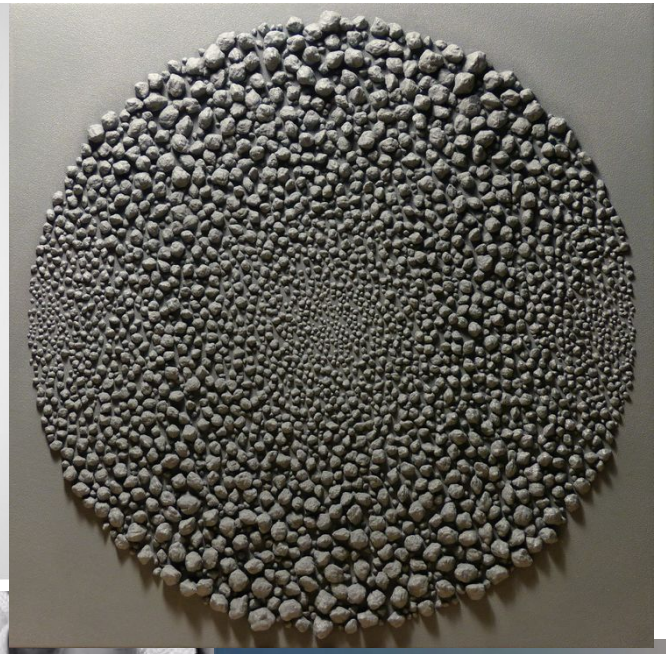

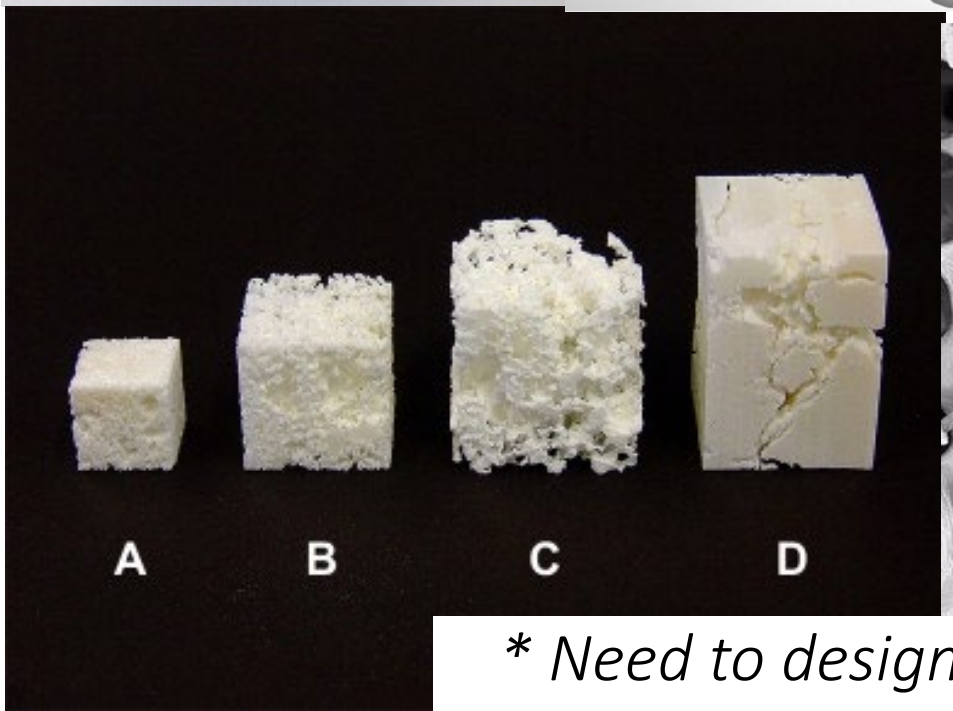

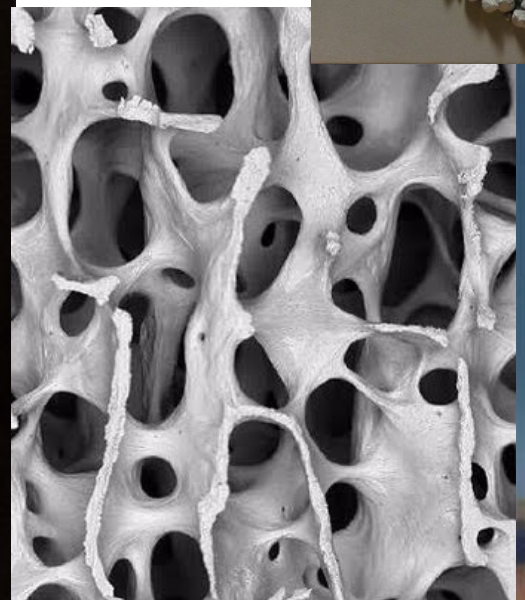

** Need to design and remove the support material*

IFPRI Project overview

Brief: Design controlled agglomerates with tuneable properties that can be systematically varied to validate models of granule breakage, flow or dissolution

Years 1-3: 3D Printing Tunable Particles

- 3D Printing approach: CAD design and 3D printed agglomerates in a Stratasys polyjet printer, prints multiple materials simultaneously.
- **Printed multiple identical copies of agglomerates, varying geometries and bridge strength**
- **Focus on breakage:** compared quasi-static deformation and breakage of agglomerate under compression
- **Compared to DEM** simulations of an identically structured agglomerate

IFPRI International Fine Particle Research Institute

Australian Government Australian Research Council

UNIVERSITY OF LEEDS

Agglomerate design and printing

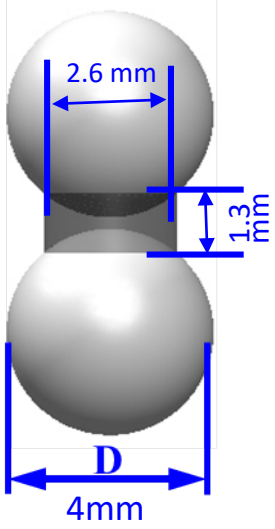

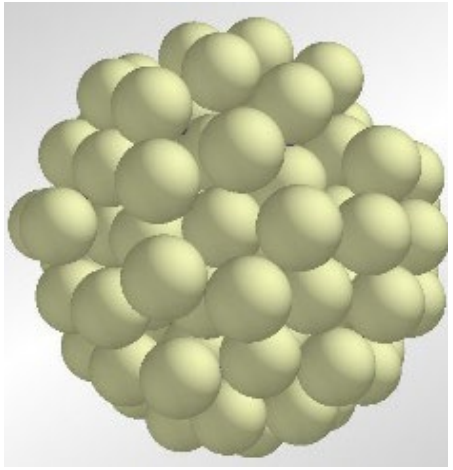

Create agglomerate structures in EDEM

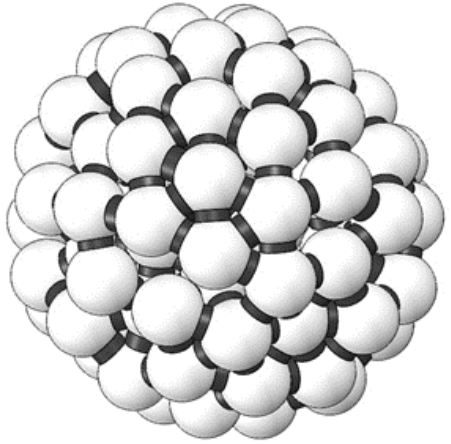

Replicate agglomerates In Solidworks

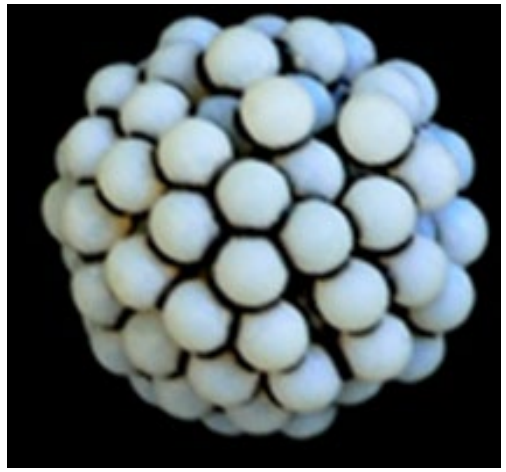

3D printed agglomerates

- Define materials to be used for each particle and bond (rigid or ductile)
- Systematically vary bond strength, geometry, particle size, bond size etc
- Conduct multiple replicate breakage tests
- Print layer orientation can affect results for weaker interparticle bonds

Agglomerate Printing

IFPRI International Fine Particle Research Institute

DEAKIN UNIVERSITY

Design files → Object studio software → Object500 3D printer → 3D printed Agglomerates

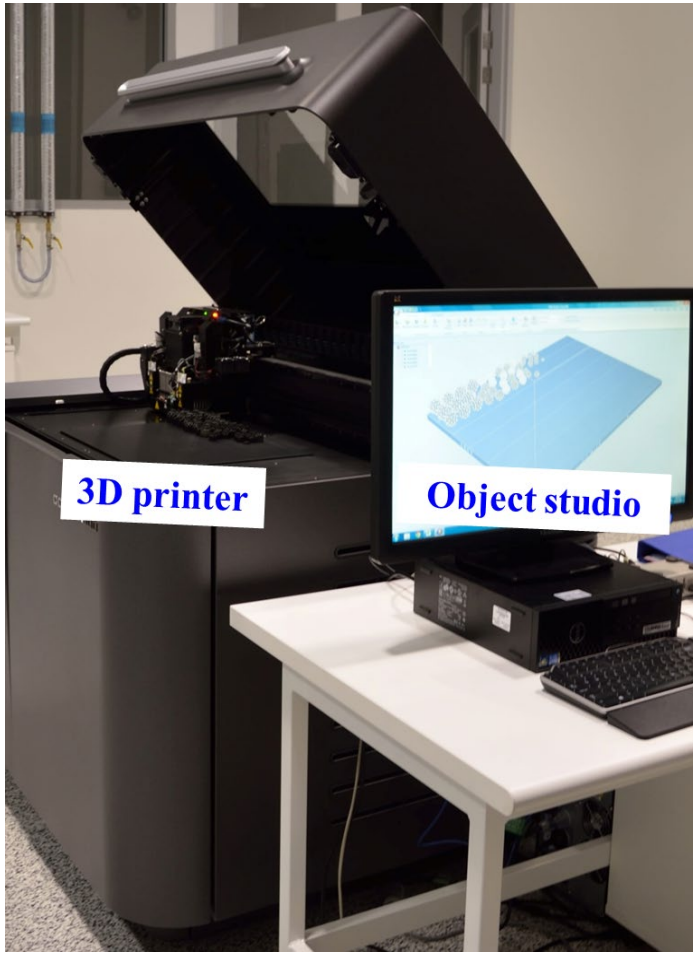

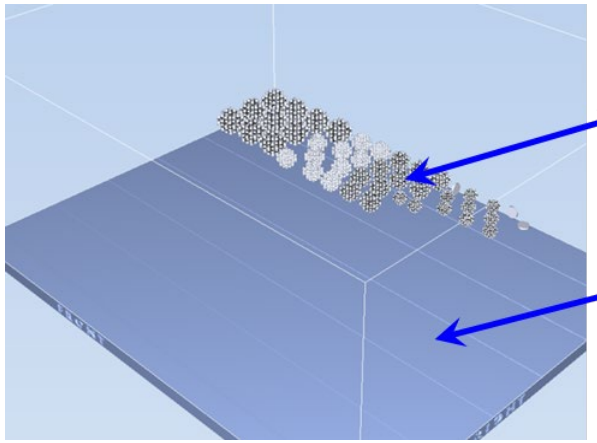

(a) Object studio software

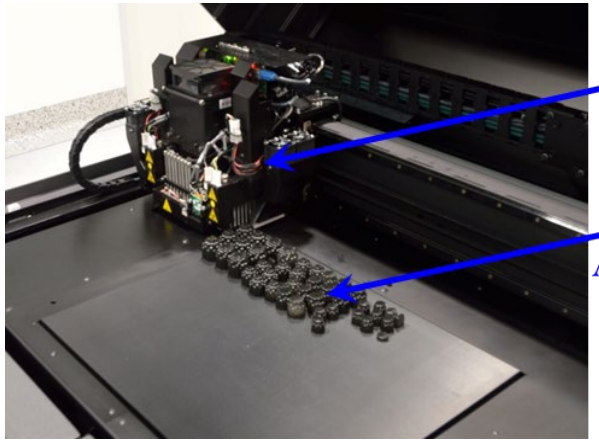

How a Objet500 part is made (YouTube)
https://www.youtube.com/watch?v=Apzlk8RJiqs

Deformation & Breakage

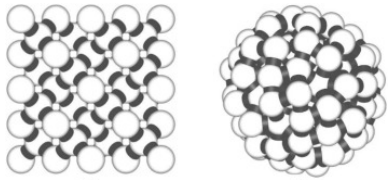

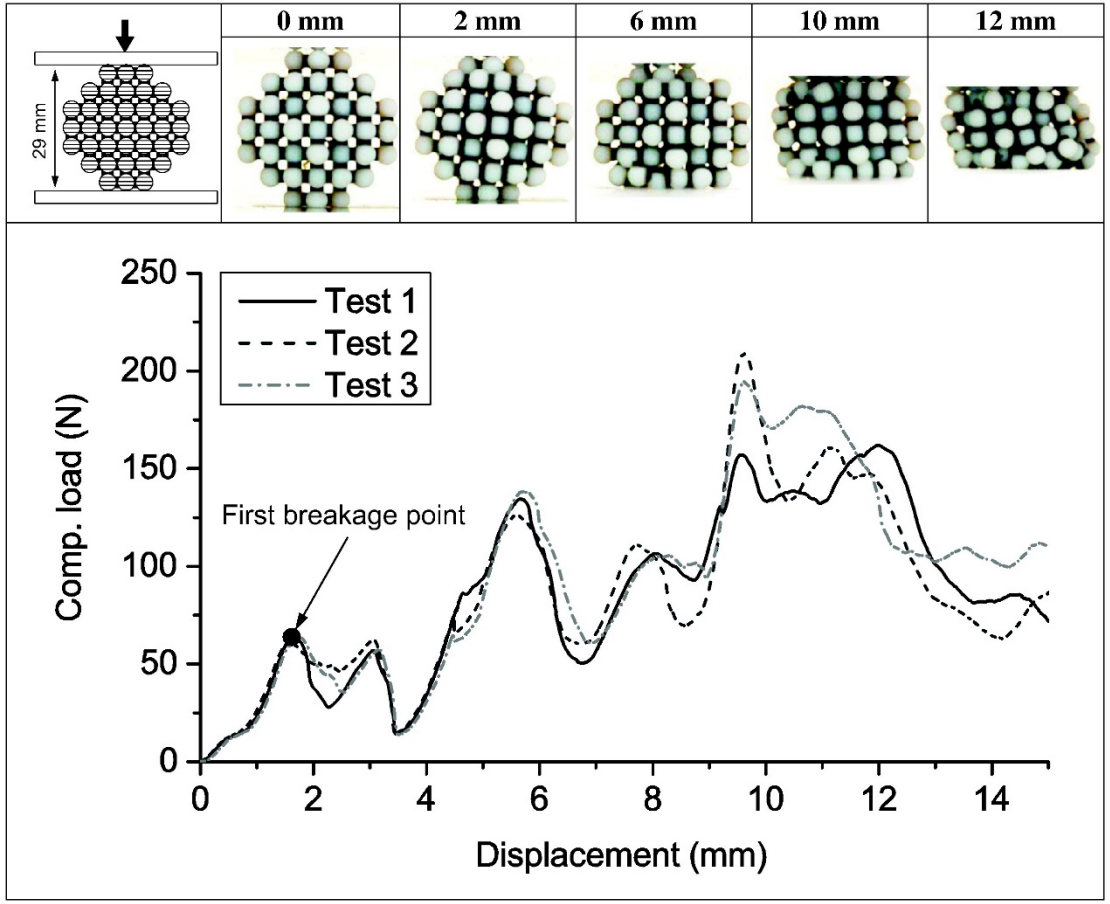

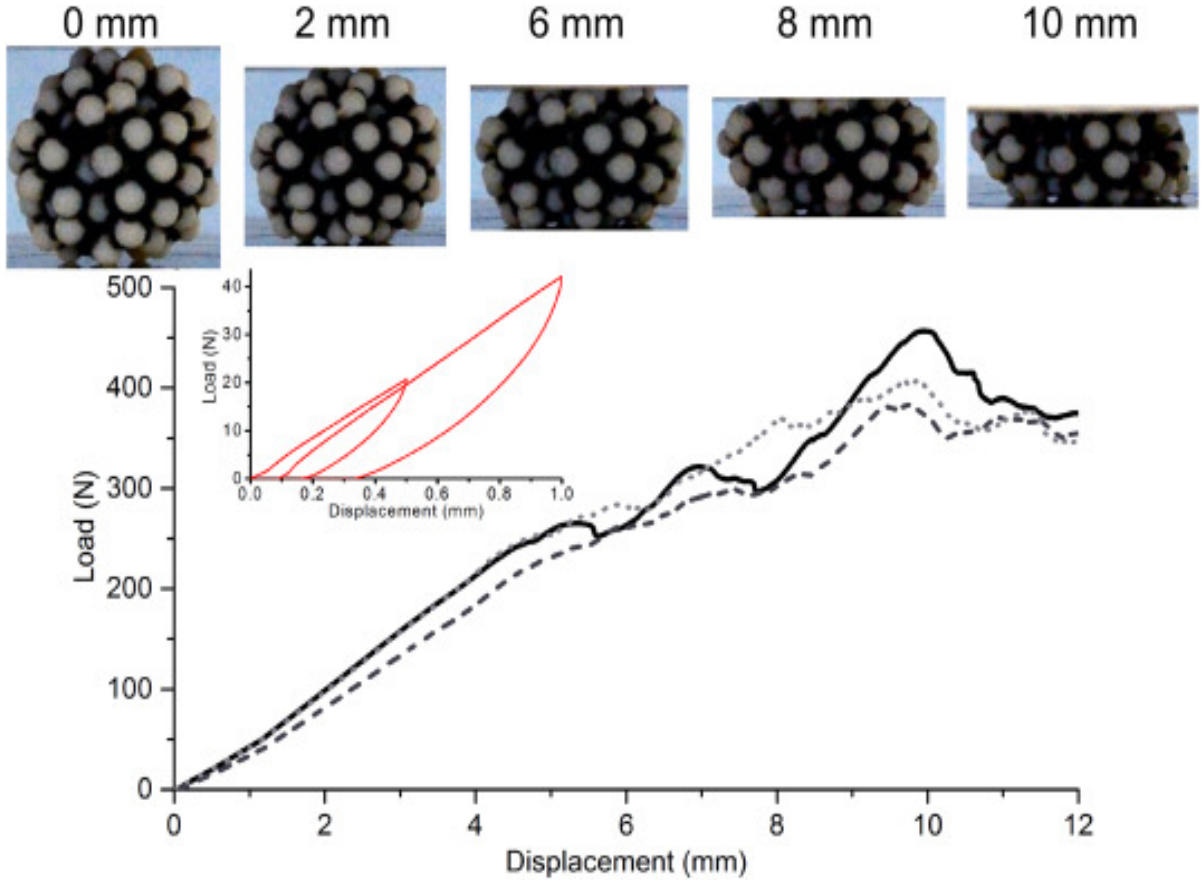

Highly reproducible experimental data for replicates of the same design

Ge et al (2017). 3D printed agglomerates for granule breakage tests. *Powder Technology, 306*, 103-112. doi: http://dx.doi.org/10.1016/j.powtec.2016.10.070

Ge et al . (2018). Experimental study of the deformation and breakage of 3D printed agglomerates: Effects of packing density and inter-particle bond strength. *Powder Technology, 340*, 299-310. doi: https://doi.org/10.1016/j.powtec.2018.09.029

Deformation & Breakage

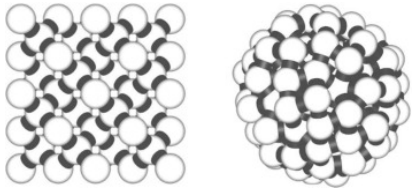

EDEM

TBBM contact model:

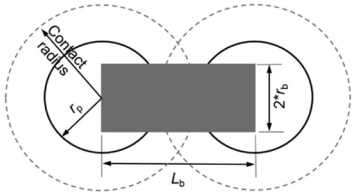

Symmetrical Agglomerate

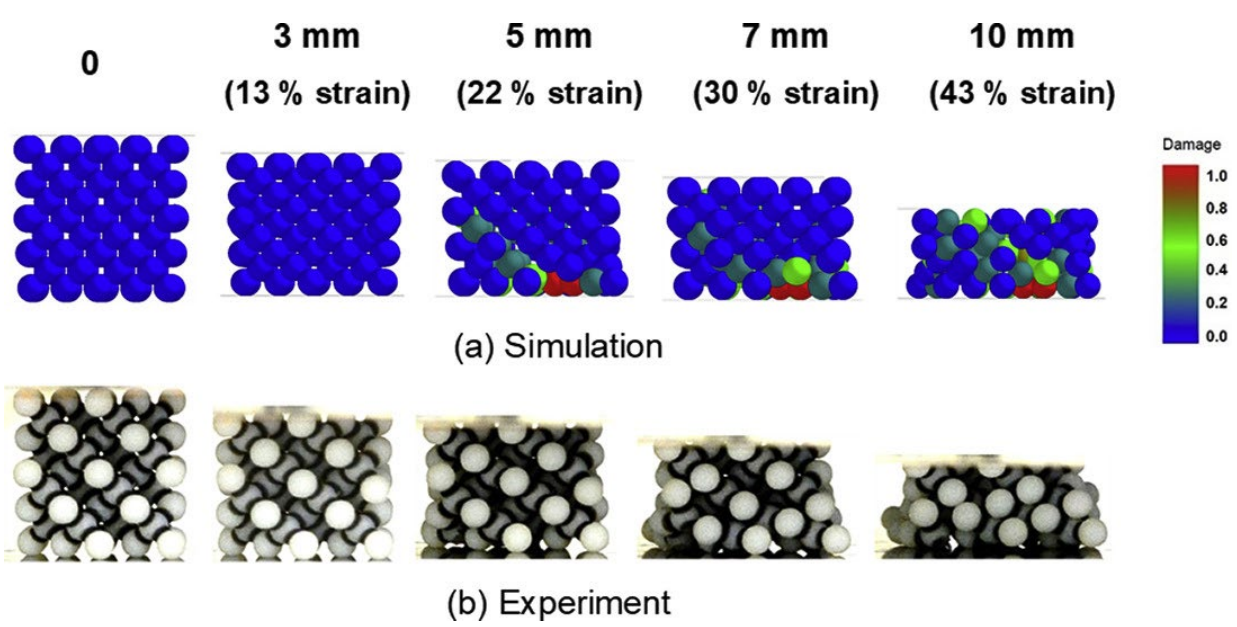

Random Structure Agglomerate

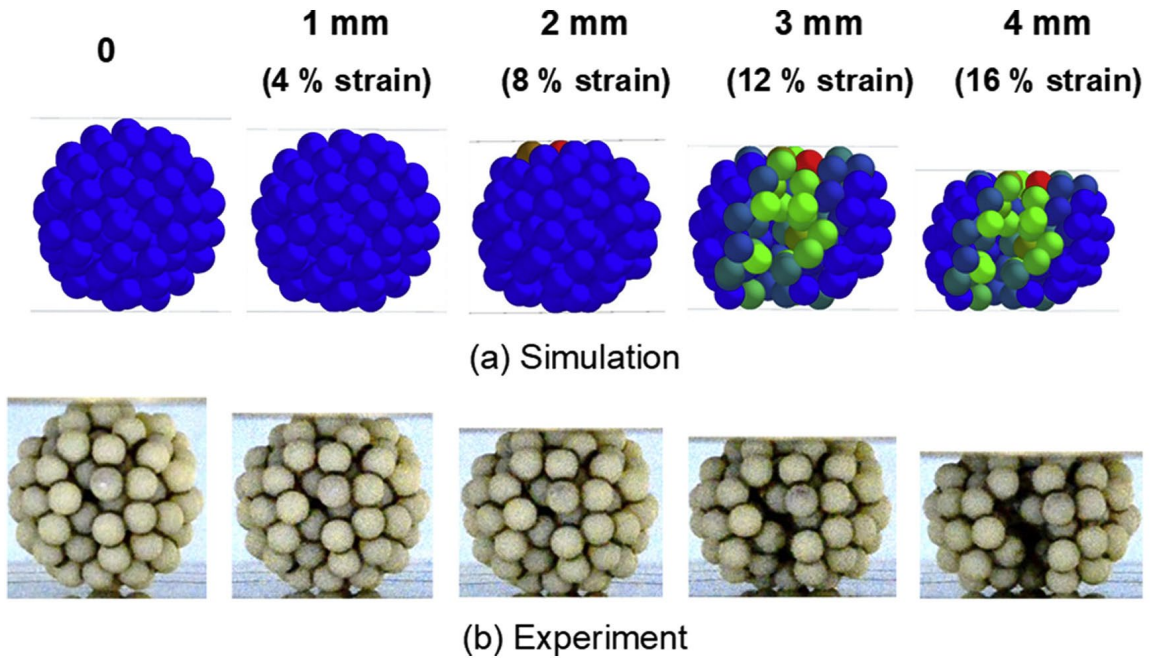

Ge et al (2019). DEM analysis of compression breakage of 3D printed agglomerates with different structures. *Powder Technology, 356*, 1045-1058. doi: https://doi.org/10.1016/j.powtec.2019.08.113

Ge et al. (2020). Deformation of 3D printed agglomerates: Multiscale experimental tests and DEM simulation. *Chemical Engineering Science, 217*, 115526. doi: https://doi.org/10.1016/j.ces.2020.115526

Deformation & Breakage

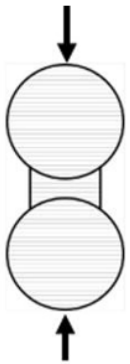

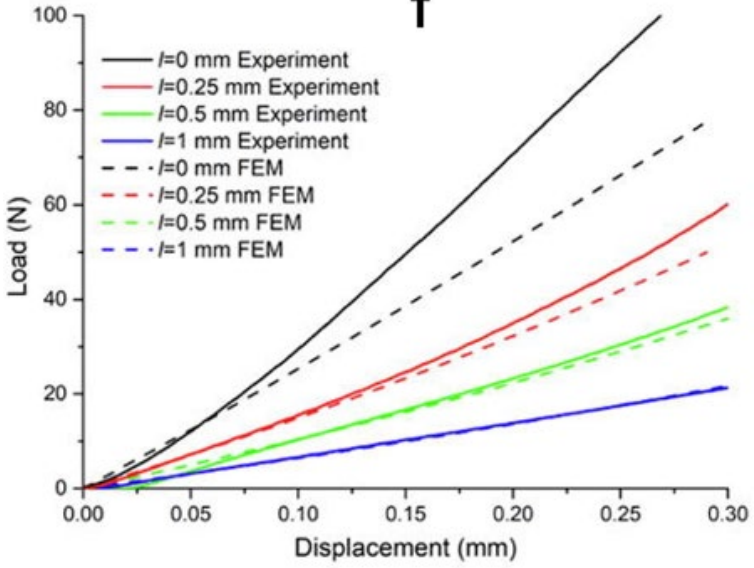

➢ Doublet scale

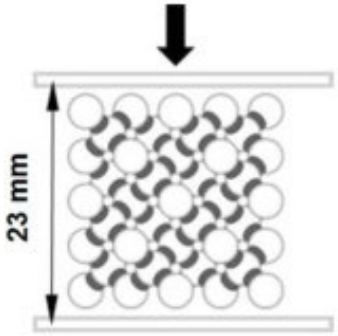

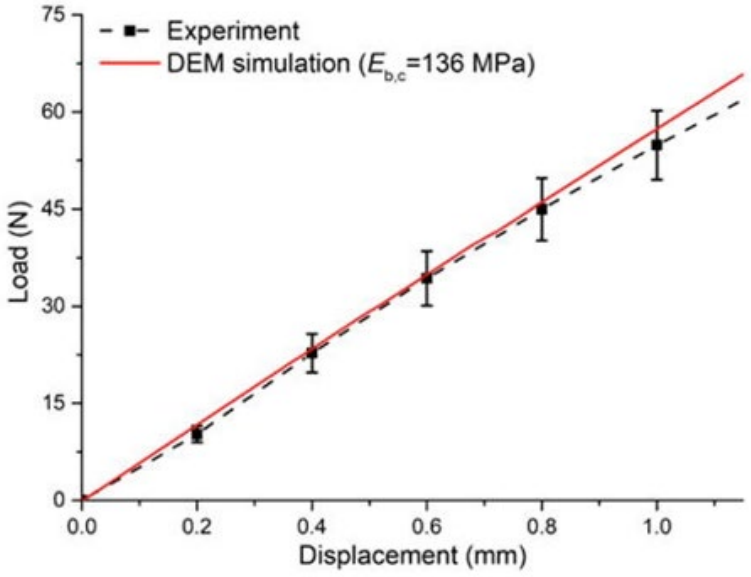

➢ Symmetrical Agglomerate

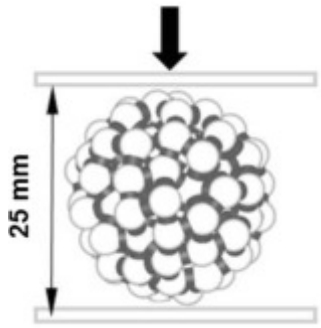

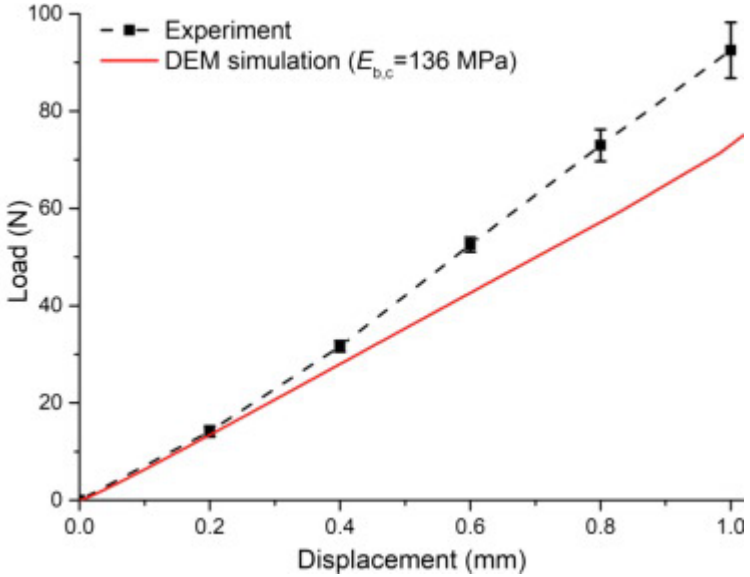

➢ Random structure Agglomerate

Ge et al (2019). DEM analysis of compression breakage of 3D printed agglomerates with different structures. *Powder Technology, 356*, 1045-1058. doi: https://doi.org/10.1016/j.powtec.2019.08.113
Ge et al. (2020). Deformation of 3D printed agglomerates: Multiscale experimental tests and DEM simulation. *Chemical Engineering Science, 217*, 115526. doi: https://doi.org/10.1016/j.ces.2020.115526

IFPRI Project overview Years 1-6

IFPRI International Fine Particle Research Institute

DEAKIN UNIVERSITY

Brief: Design controlled agglomerates with tuneable properties that can be systematically varied to validate models of granule breakage, flow or dissolution

Years 1-3: 3D Printing Tunable Particles

- 3D Printing approach: CAD design and 3D printed agglomerates in a Stratasys polyjet printer, prints multiple materials simultaneously.
- Printed multiple identical copies of agglomerates, varying geometries and bridge strength
- Focus on breakage: compared quasi-static deformation and breakage of agglomerate under compression
- Compared to DEM simulations of an identically structured agglomerate

Years 4-6: 3D Printing Perfect Particles

- 3D Printing Approach: Making the most of disruptive technology in particle technology applications
- Goal: A suite of designer particles, agglomerates and substrates, including “tunable” properties,
- Use these “perfect particles” to validate and advance more realistic models of
  - Agglomerate breakage
  - Wetting and dissolution.
  - Powder flow and segregation,

DEAKIN UNIVERSITY

IFPRI International Fine Particle Research Institute

IFPRI Project overview Years 1-6

IFPRI International Fine Particle Research Institute

DEAKIN UNIVERSITY

Brief: Design controlled agglomerates with tuneable properties that can be systematically varied to validate models of granule breakage, flow or dissolution

Years 1-3: 3D Printing Tunable Particles

- 3D Printing approach: CAD design and 3D printed agglomerates in a Stratasys polyjet printer, prints multiple materials simultaneously.
- Printed multiple identical copies of agglomerates, varying geometries and bridge strength
- Focus on breakage: compared quasi-static deformation and breakage of agglomerate under compression
- Compared to DEM simulations of an identically structured agglomerate

Years 4-6: 3D Printing Perfect Particles

- Agglomerate Breakage
  1. Agglomerate strength extensions
  2. Tracking of deformation and breakage
  3. Photoelastic stress visualisation
- Agglomerate Dissolution
  4. Liquid imbibition into porous substrates
- Flow & segregation of irregular particles
  5. Flow of irregular particles
  6. Density Segregation
  7. DEM Boundary experiments

1a. Multi-coloured agglomerates

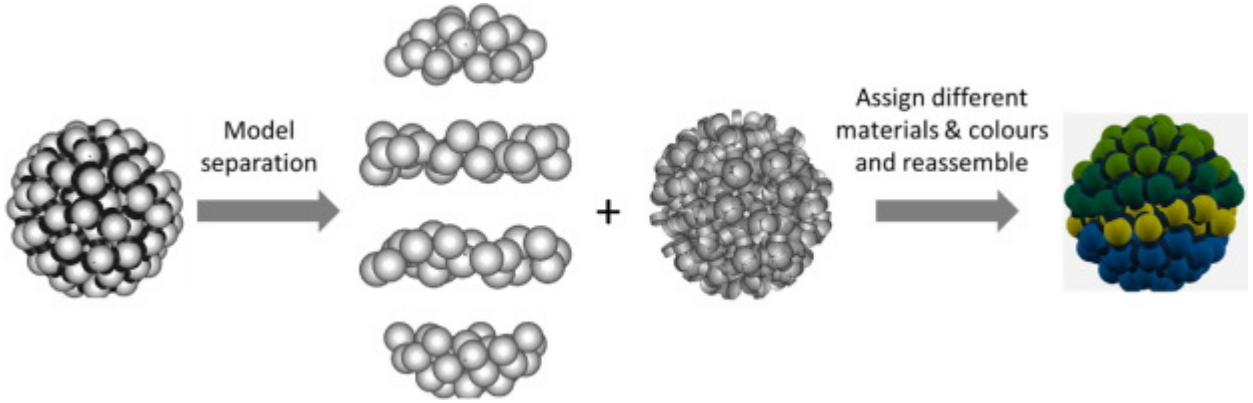

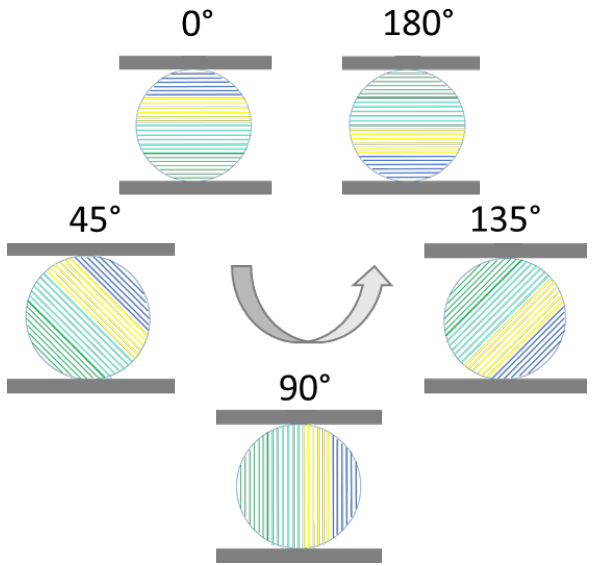

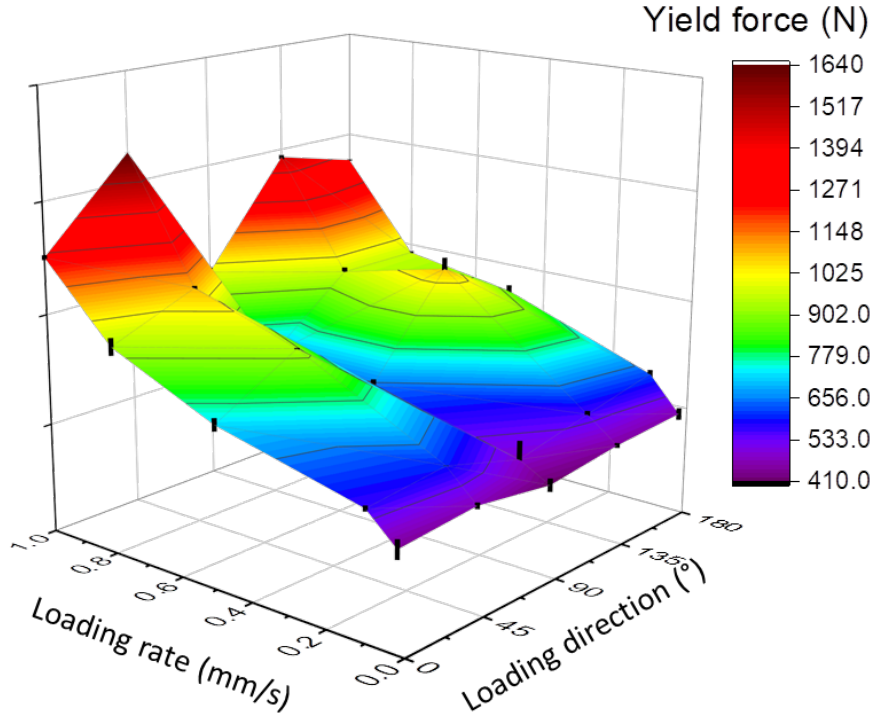

- Compress a single agglomerate at orientations
- Randomly structured bonds
- Loading rate varied
- **Shows a single agglomerate has a range of strengths, depending on orientation.**

Zhang, J., Amini, N., Morton, D. A. V., & Hapgood, K. P. (2020). 3D printing of tuneable agglomerates: Strain distribution and effect of internal flaws. *Advanced Powder Technology*. (in press) doi: https://doi.org/10.1016/j.apt.2020.04.037

1b. Agglomerates with internal flaws

- Inspired by famous paper by Subero & Ghadiri (2000)
- Agglomerates with internal voids
- Removed particle and bridges from midsection of agglomerate
- Removed 1, 3 or 5 particles, various spatial arrangements

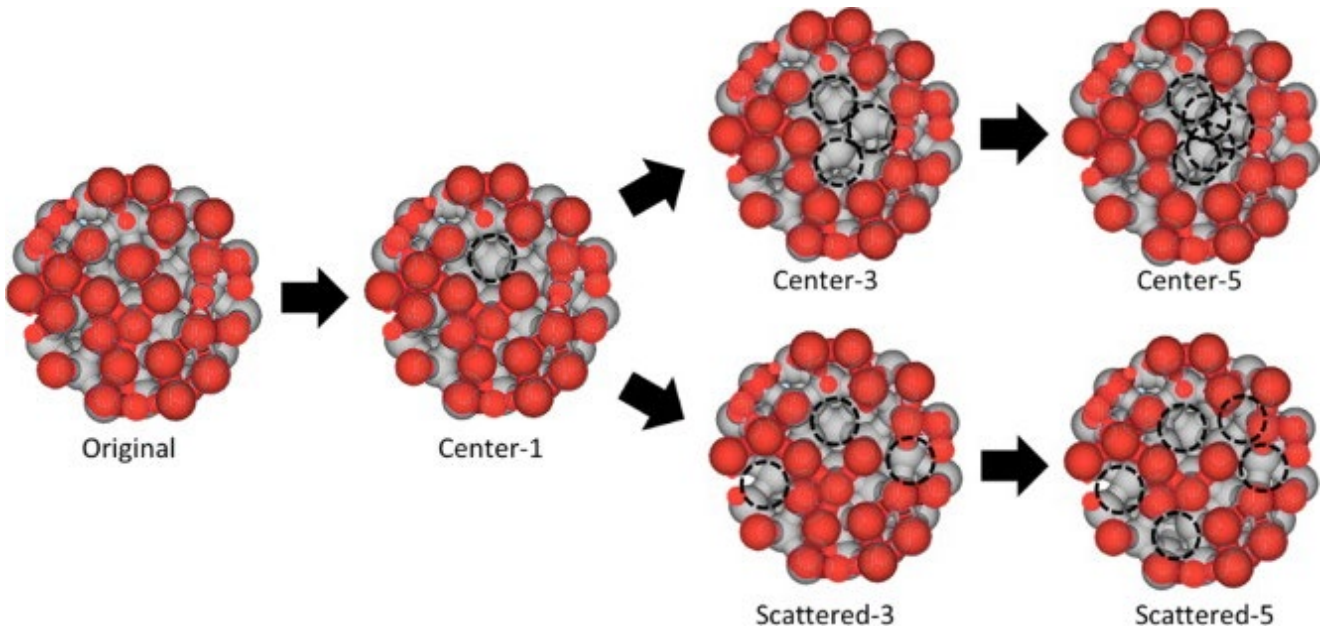

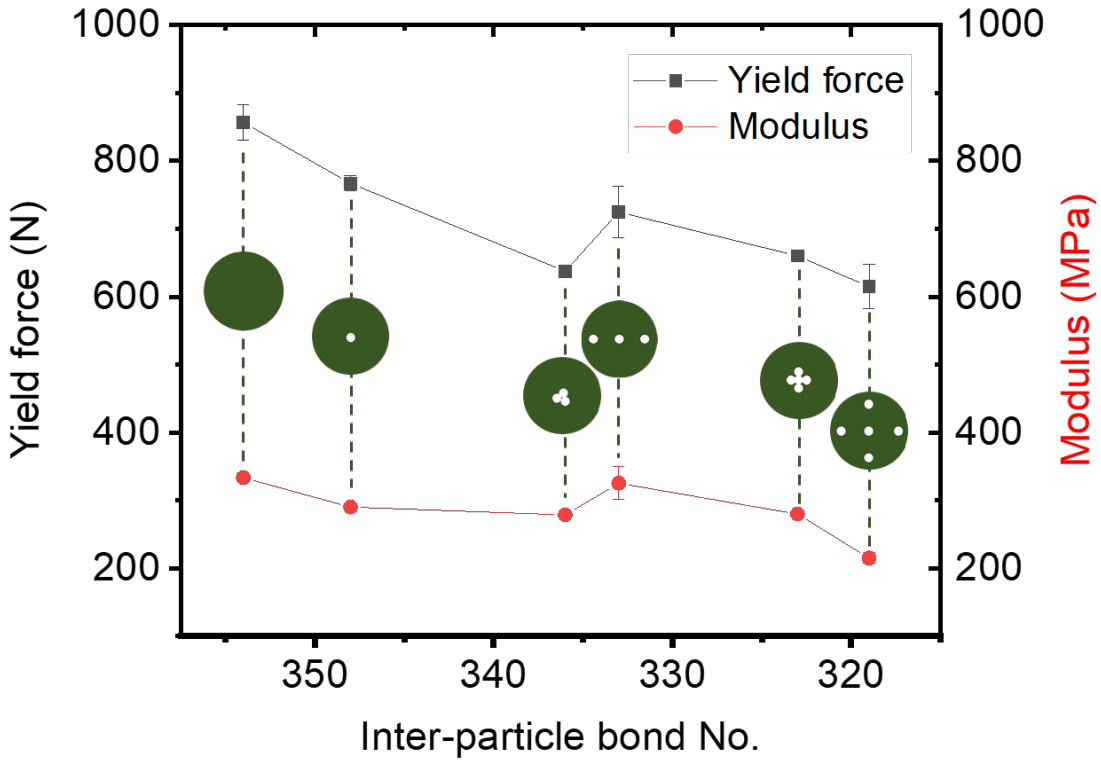

Subero, Pascual, Ghadiri, Production of agglomerates of well-defined structures and bond properties using a novel technique, Chem. Eng. Res. Des., 78 (1) (2000), pp. 55-60

Zhang, J., Amini, N., Morton, D. A. V., & Hapgood, K. P. (2020). 3D printing of tuneable agglomerates: Strain distribution and effect of internal flaws. *Advanced Powder Technology*. (in press) doi: https://doi.org/10.1016/j.apt.2020.04.037

1c. Breakage of Binder jetted agglomerates

Binder jet printing

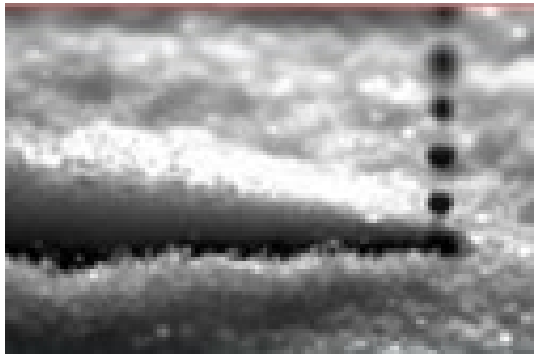

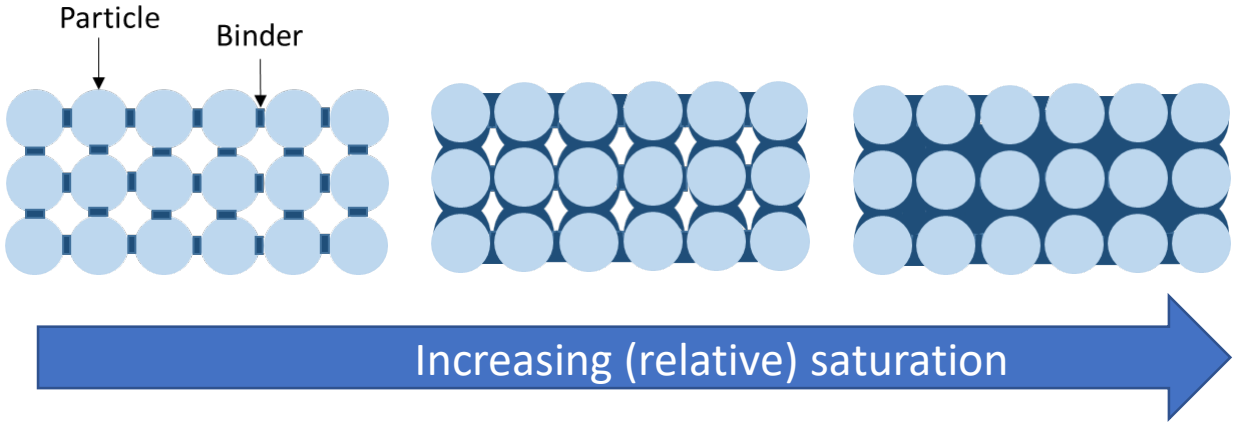

➢ Structure-Property relationship

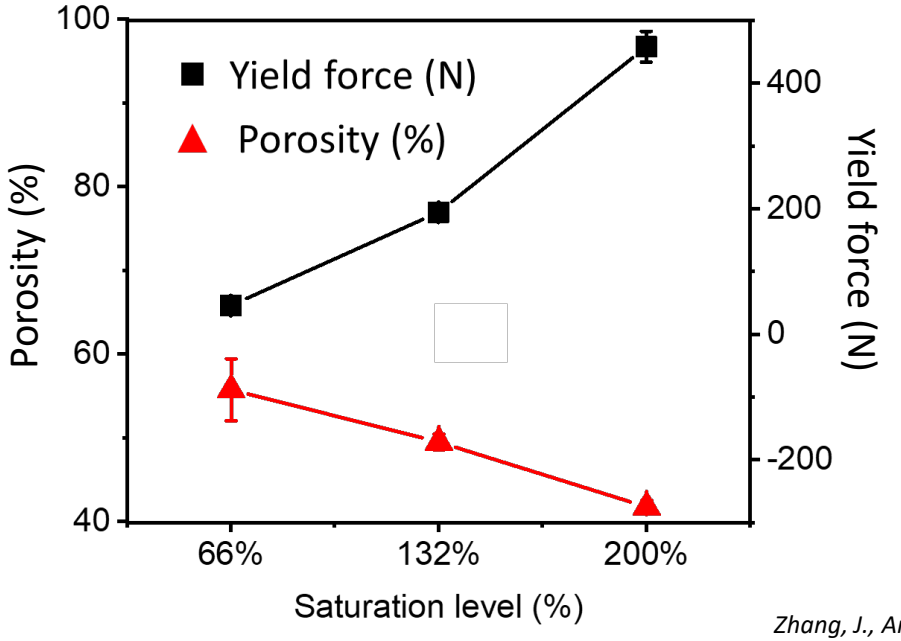

➢ Breakage

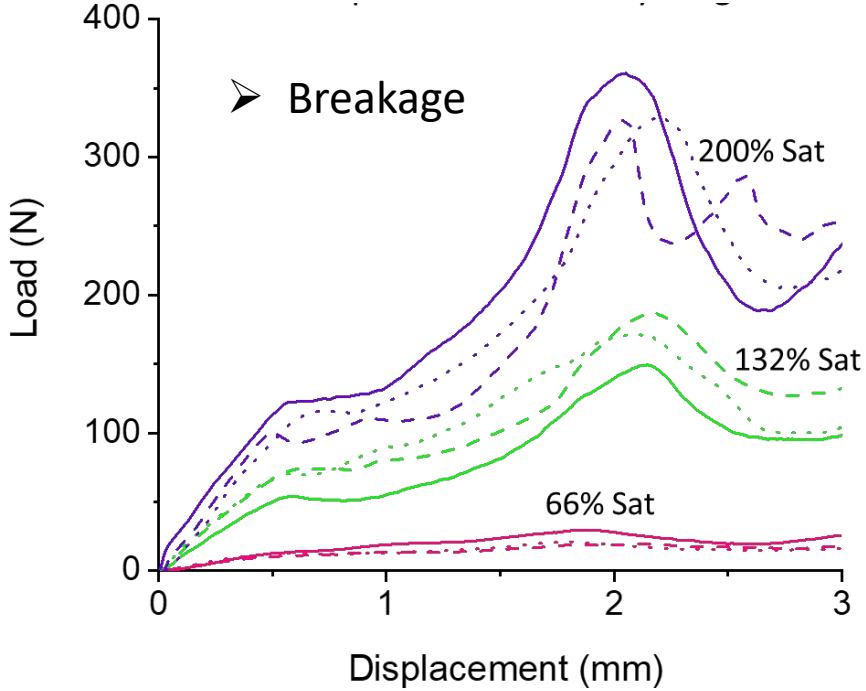

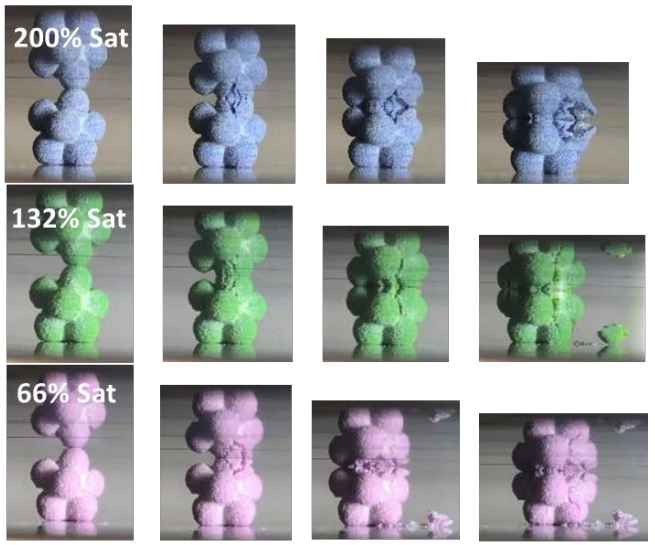

Zhang, J., Amini, N., Morton, D., Hapgood, K. Binder jetting of well-controlled powder agglomerates for breakage study, submitted to Advanced Powder Technology, 2020

2. Tracking of deformation and breakage

- Analyse (in-situ) of the experimental deformation using GOM Correlate software
- Speckle pattern stamped onto surface of 3D printed disc in agilus material

DIC Strain Distribution

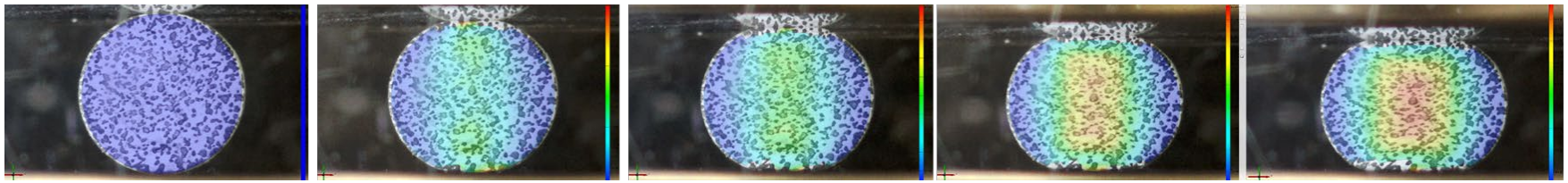

- Mapped 2D speckle images onto the surface of each individual particle (various speckle resolutions)
- 3DPrint showed bleeding of pattern, experiments awaiting access to labs

CAD

3D Print

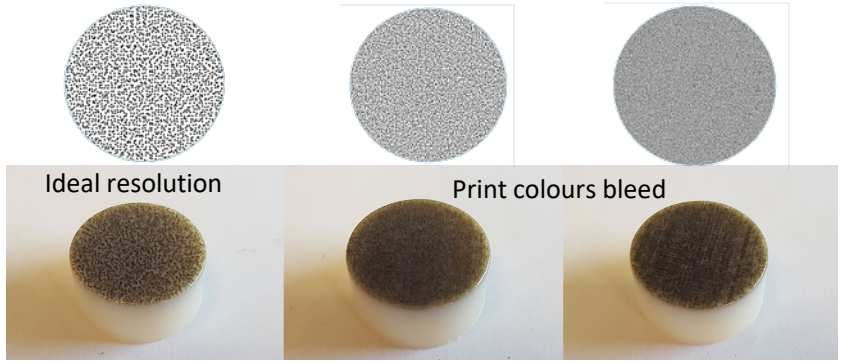

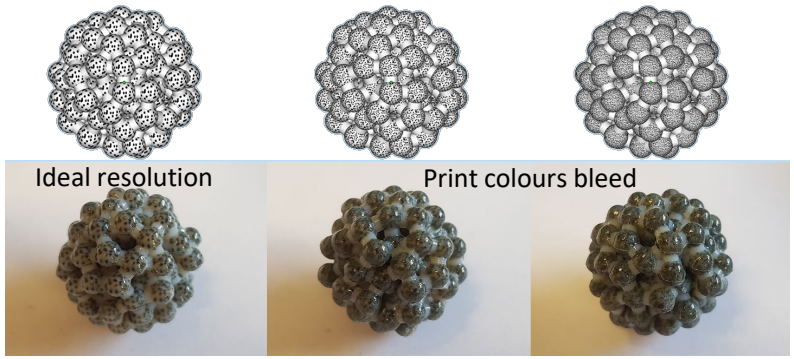

3. Photoelastic stress visualisation

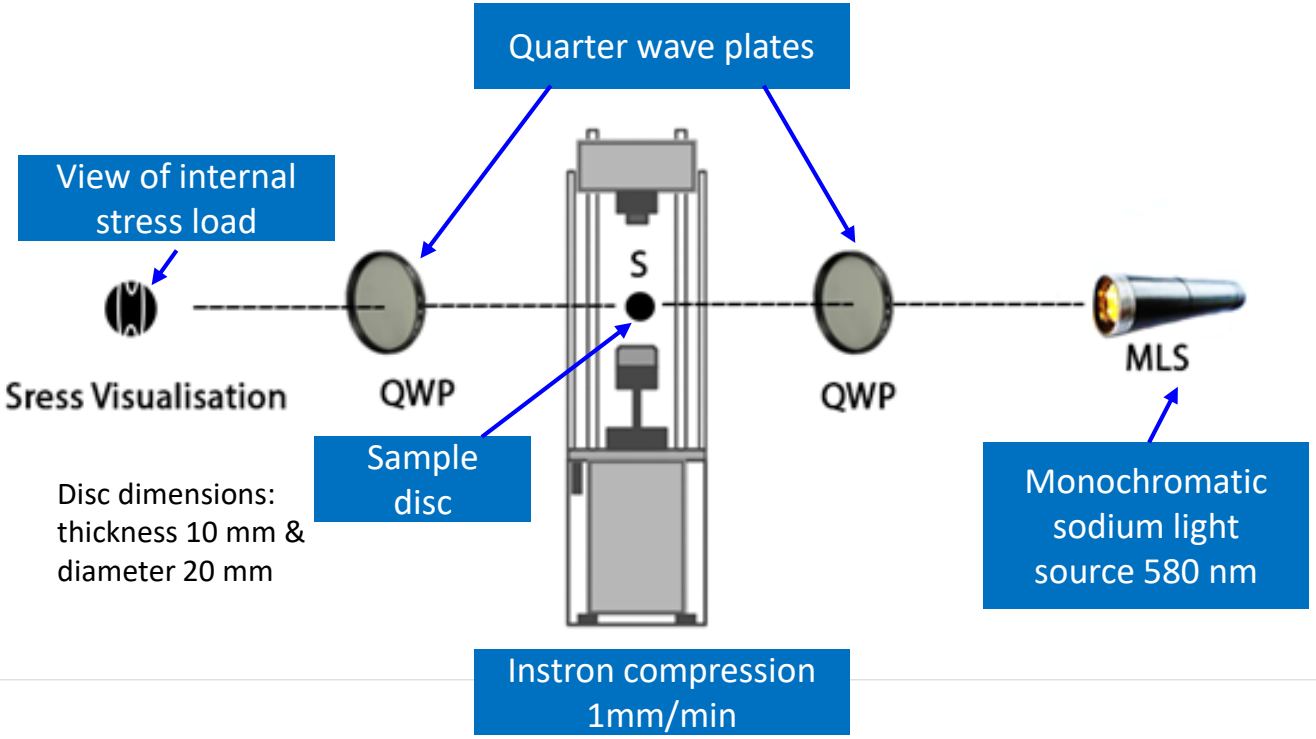

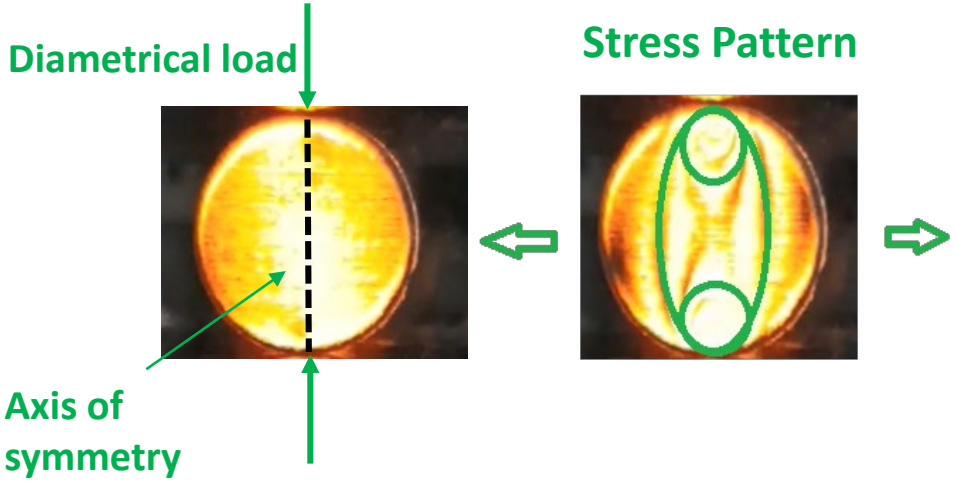

Incremental stress fringes during compression

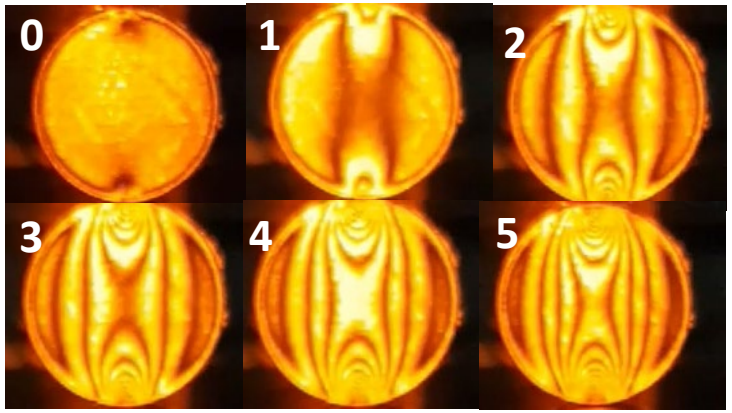

Disc dimensions: thickness 10 mm & diameter 20 mm

- Compression of a simple disc at 1 mm/min
- Successfully observed stress visualisation
- No lines from 3D printing visible
- No residual stress from polyjet print method

3. Photoelastic stress visualisation

- 2D discs: Difference in stress observed but not macroscopic mechanical properties

Layer orientations

Experiment: 1st fringe

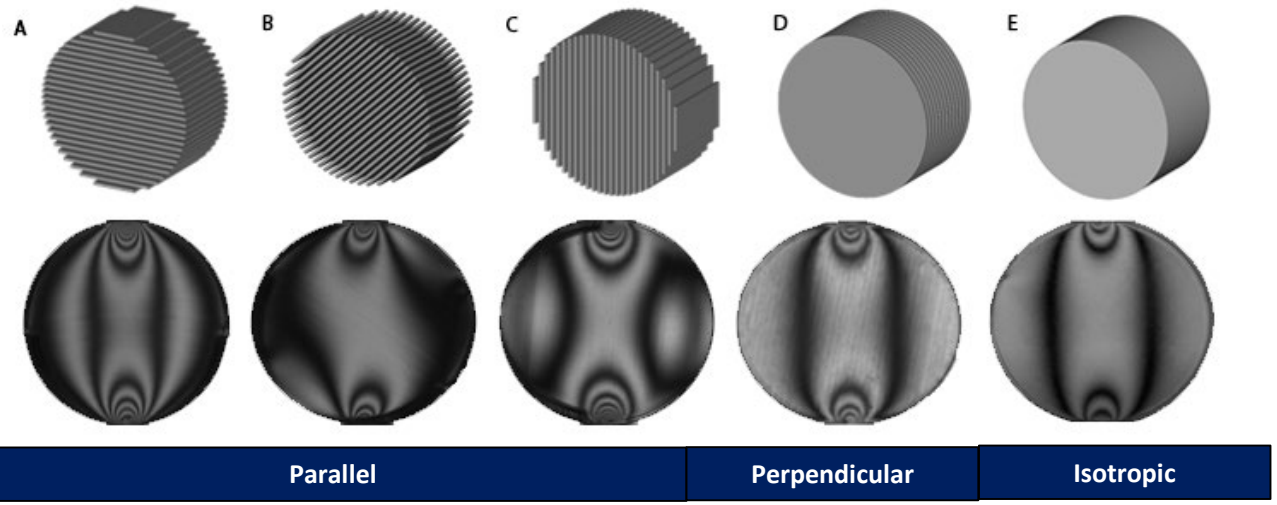

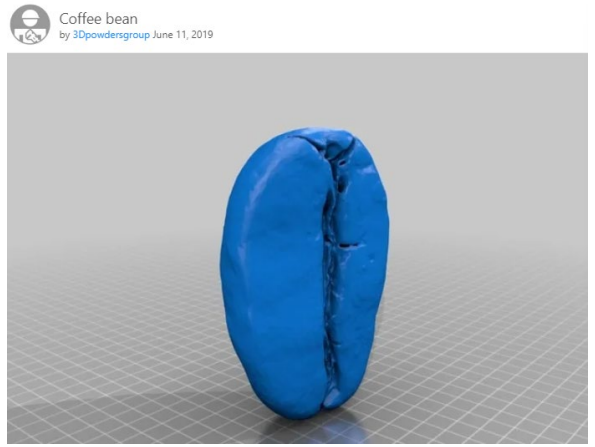

Experimental 3D stress

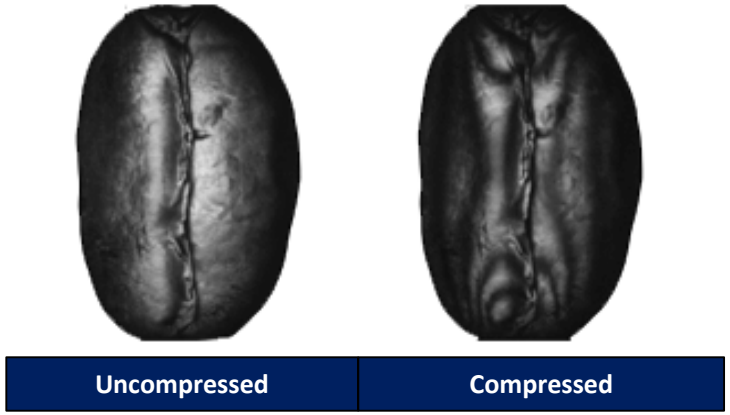

FEA 3D stress analysis

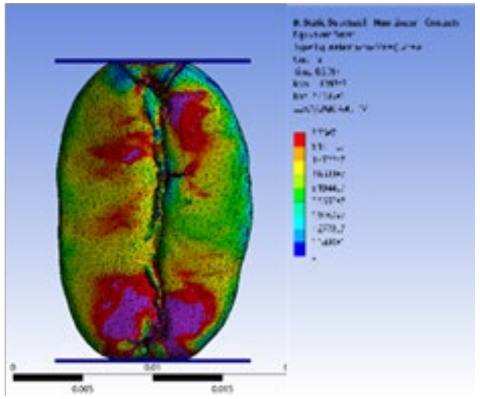

2D bean slice stress comparison

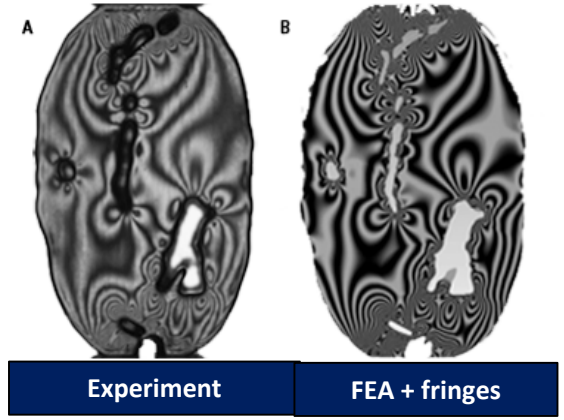

Amini, Long, Zhang, Tuohey, Daniels., Fazelpour, Morton, Hapgood . Photoelastic stress analysis of a 3D printed coffee bean, in preparation for submission to AIChE Journal 2020

5. Flow of irregular shaped particles

- **Angle of repose**

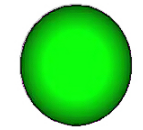

Spherical

Briquette

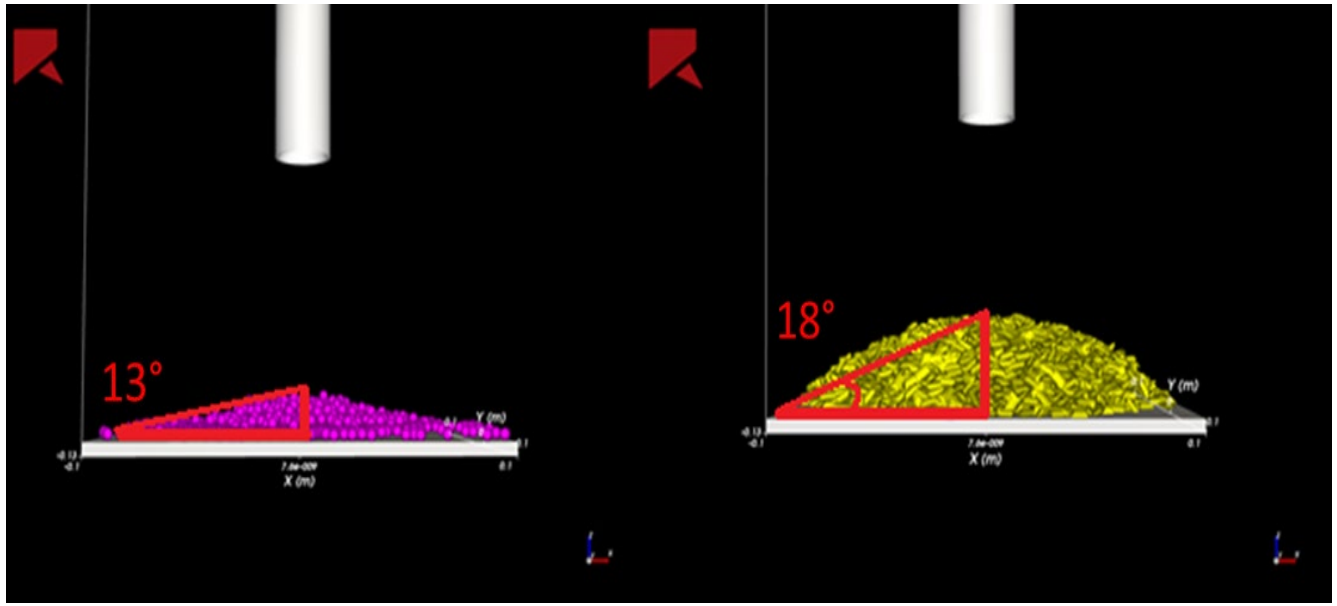

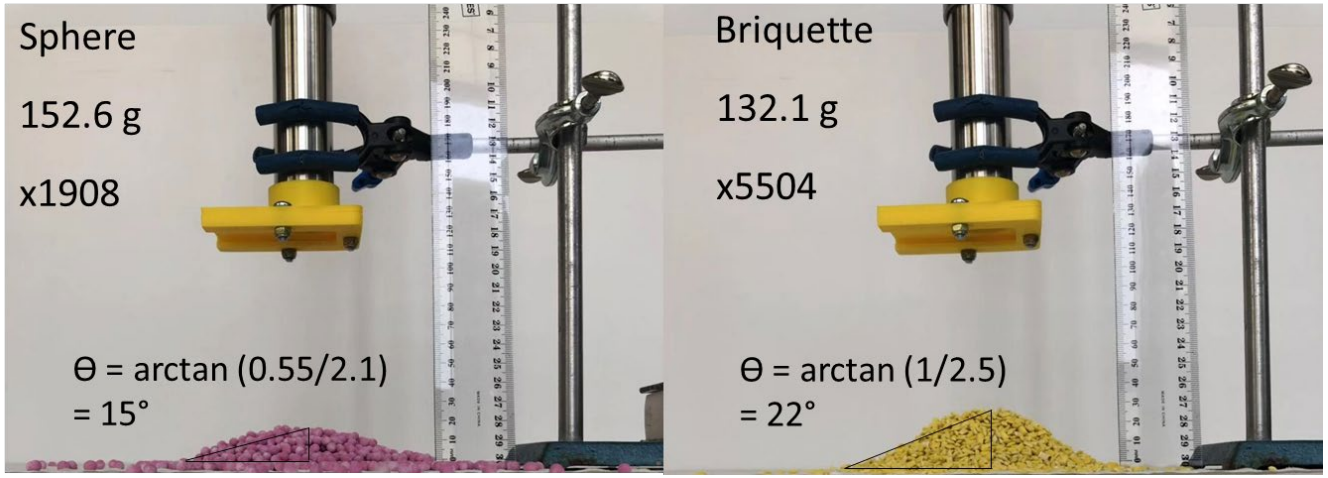

Work in Progress…

3D prints

TBA

EDEM

~ 20 spheres

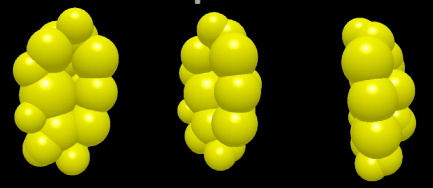

~ 60 spheres

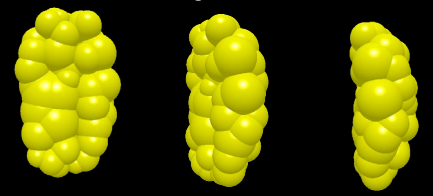

~ 110 spheres

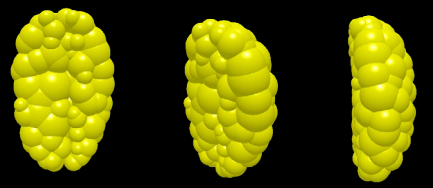

~ 150 spheres

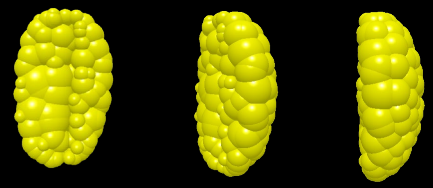

CAD

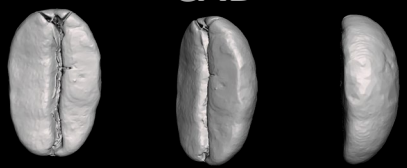

3D printing Overview

IFPRI International Fine Particle Research Institute

DEAKIN UNIVERSITY

➢ Techniques

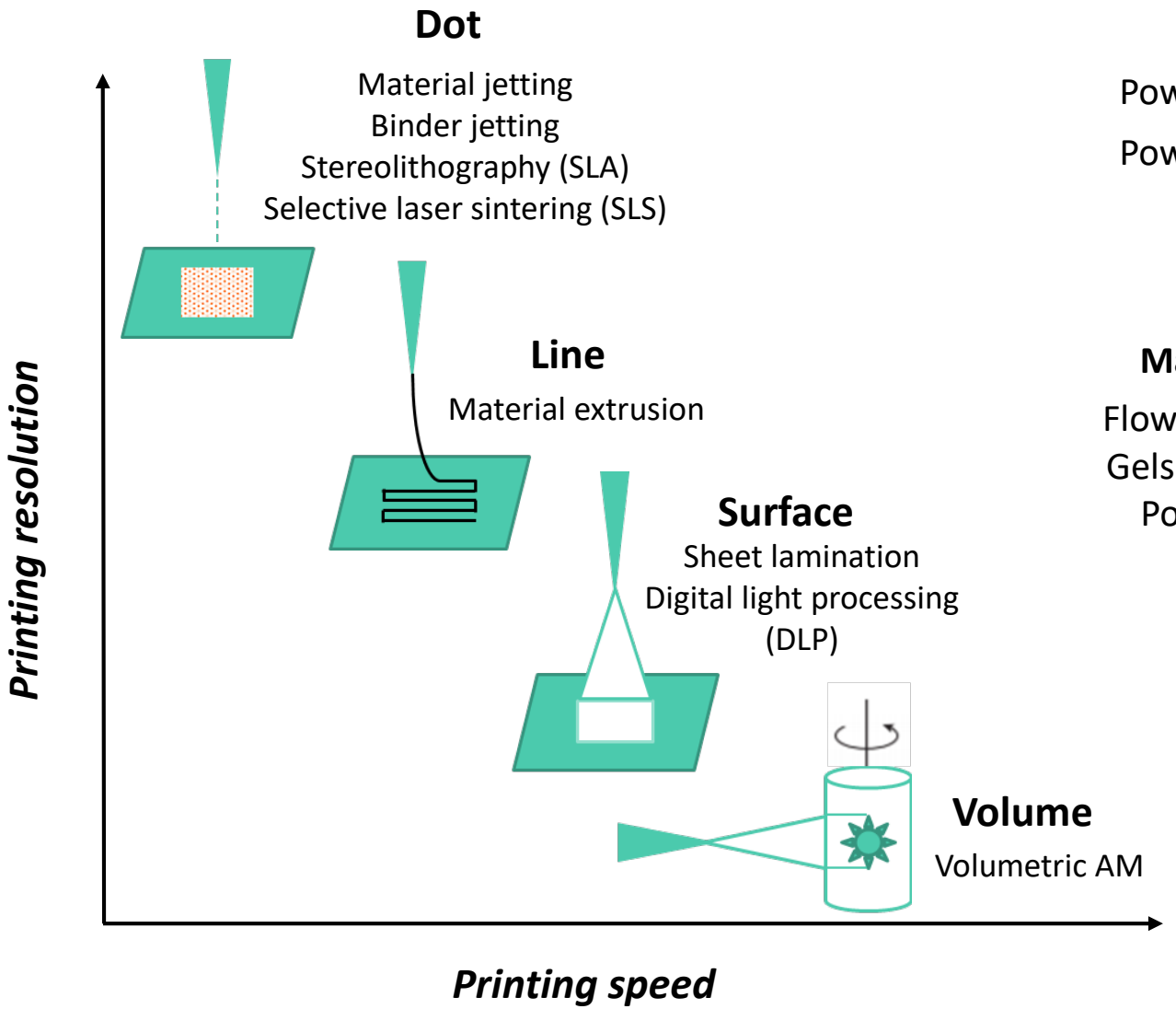

➢ Particulate materials

Dry system →
- Powder flow
- Drop penetration
- Powder engineering

Powder spreading methods

Powder deposition methods

Wet system →
- Ink rheology
- Reinforcement
- Functionality

Matrix	+	Particle
Flowing liquid Gels & Pastes Polymers		Micro particle Nano particle Fibers

➢ Applications

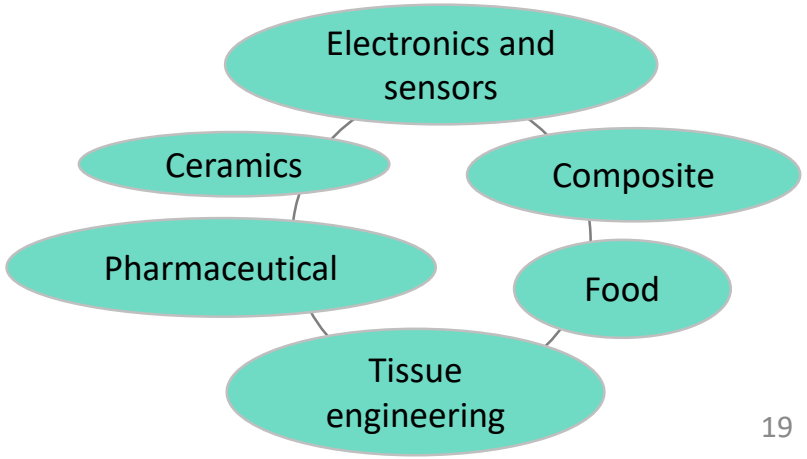

Deakin 3D Powders group

https://blogs.deakin.edu.au/3dpowdersgroup/

Special thanks to:

-IFPRI

- Prof David Morton
- Dr John Long
- Dr Michael Pereira
- Josh Tuohey *(MechE UG)*→

3D printing STL files at Thingiverse

https://www.thingiverse.com/3Dpowdersgroup/designs

-

My last IFPRI Presentation 2015-2020

IFPRI
International Fine Particle Research Institute

DEAKIN UNIVERSITY

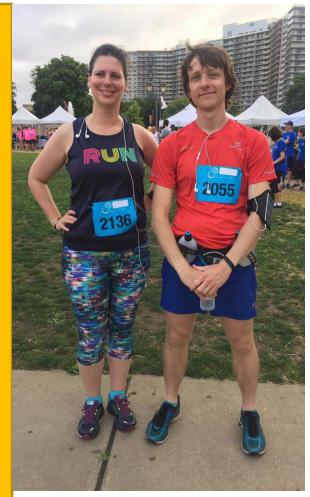

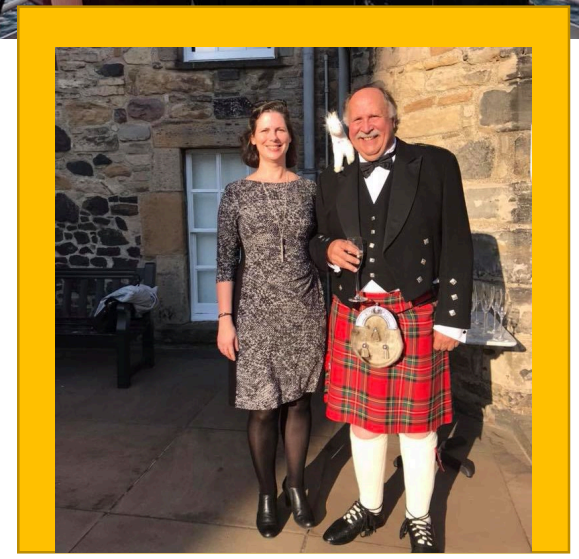

Exploiting a Framework
for the Development of Segregation Rate Models

J. J. McCarthy

Department of Chemical Engineering
University of Pittsburgh

June, 2019

Quantitative Prediction of Segregation at Process Scale

- Identify critical **material and process parameters** that control the *extent* of powder segregation
- Develop **quantitative models that predict** segregation and possible re-homogenization within a process train
- **Validate** models with appropriate experiments
- Demonstrate that the models are applicable to **full-scale** processes
- In scope:
  - Dense flows
  - Formulated (i.e. multicomponent) mixtures
- Additional considerations:
  - Cohesive powders
  - Particle shape effects

Competing Timescales

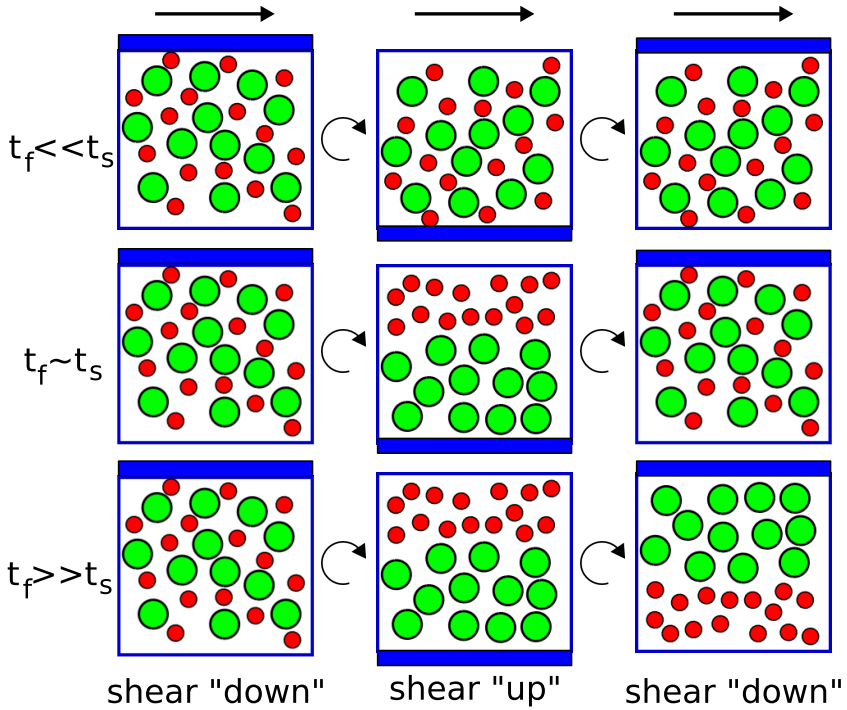

- If $t_{seg} \approx t_{forcing}$ balance of rates
  - We control $t_{forcing}$
  - Sensitive test of t_{seg} model
  - "Collapse" complex dynamic experiment onto "steady state" measurement

Shear Cell Simulations

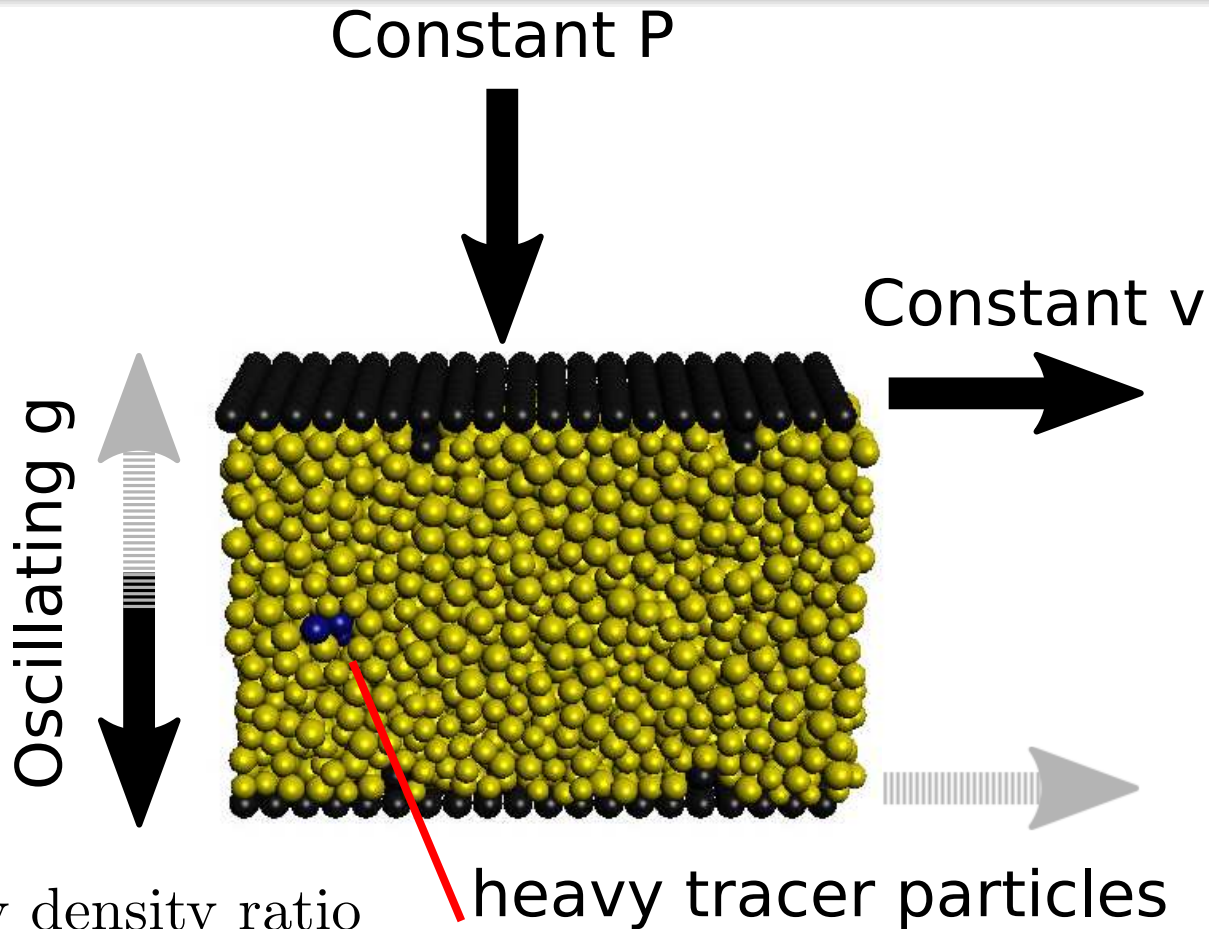

- Vary density ratio
- Vary shear rate (velocity)
- (Mostly) Constant pressure BC

Shear Cell Results

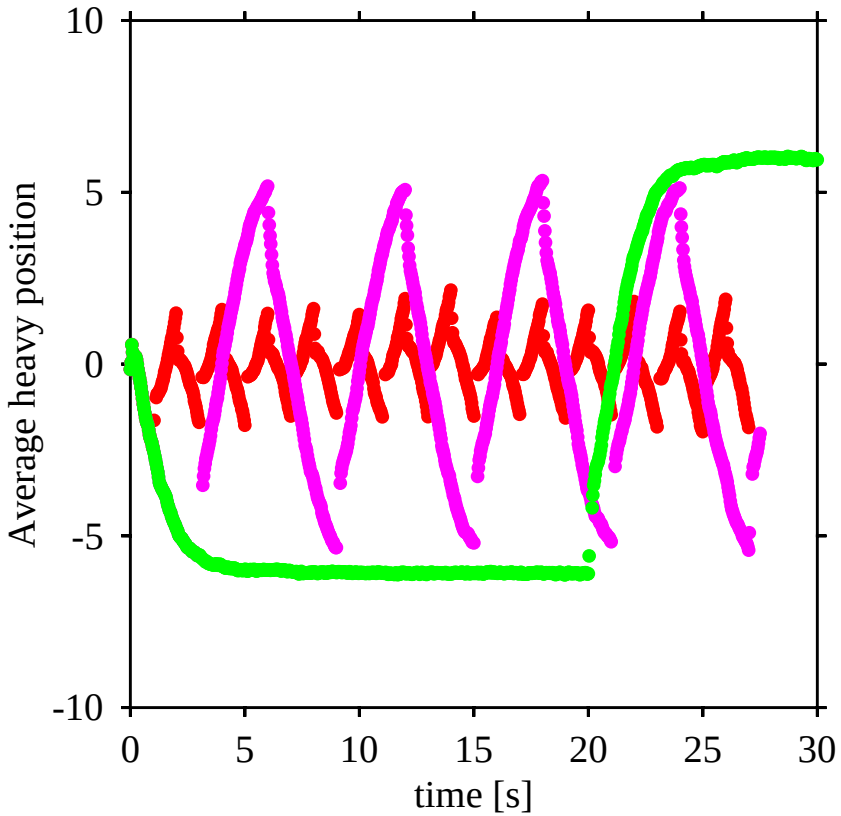

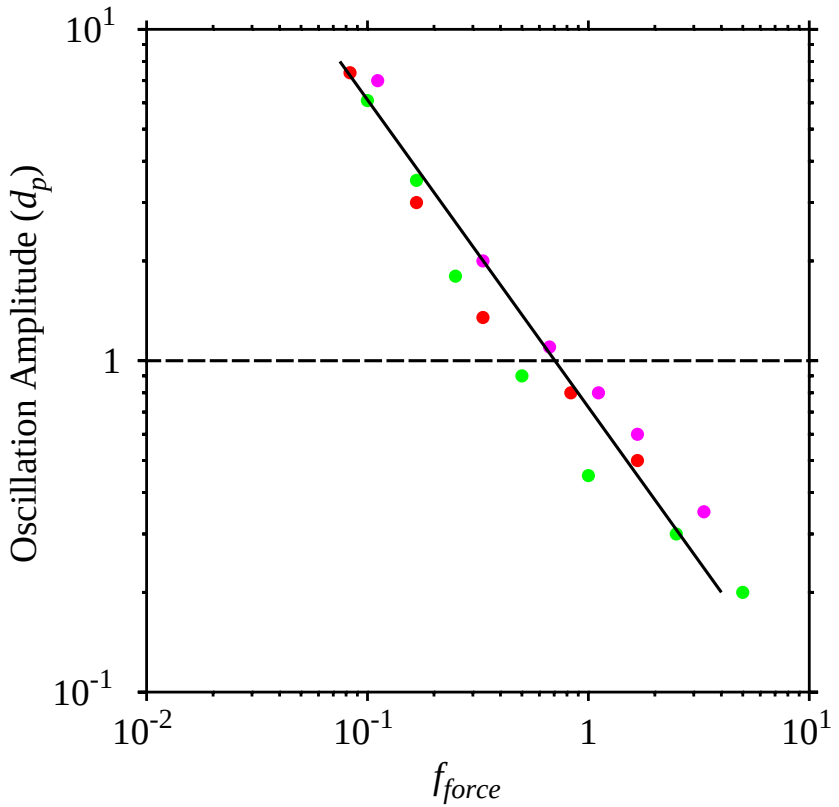

- "Asymptotic" segregation ↓ with ↑ forcing frequency
- Choose threshold segregation value to ID critical frequency
- Scaled segregation rate collapses onto single critical curve

Indirect Forcing in a Baffled Tumbler

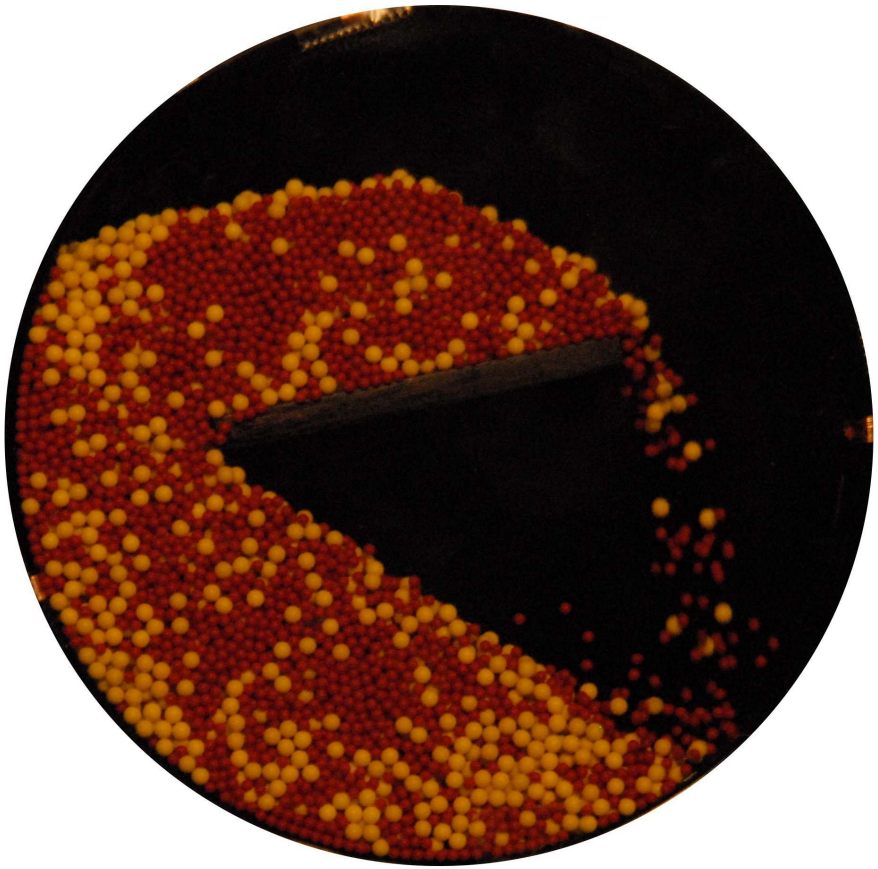

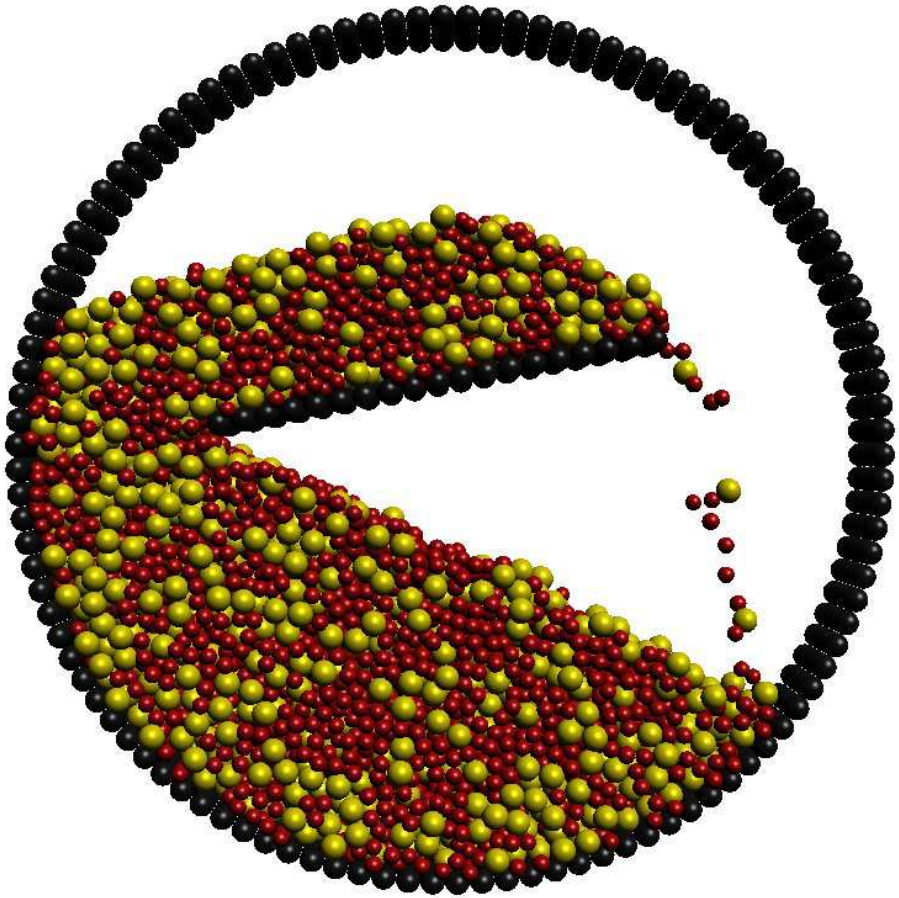

- Changing the rotation rate changes $t_{forcing}$

Calculating the Effective/Critical Forcing Frequency

- Mean residence time $\rightarrow f$ (effective forcing frequency)

$$f = \frac{1}{\tau_{mean}} = \frac{\sqrt{\omega\dot{\gamma}}}{2\pi}, \text{ where } \dot{\gamma} = \left[\frac{g\sin(\beta_m - \beta_s)}{cd\cos(\beta_s)}\right]^{1/2}$$

Khakhar and Ottino, 2002

- Obtain critical frequency from theory to be tested, e.g.:
- Size segregation velocity

$$v_s = [K_S + (1-\phi)K_T](1-\bar{d})$$

for fixed total concentration, ϕ, $v_s = [K_\phi](1-\bar{d})$

where $K_\phi \propto \dot{\gamma}$, thus, $f_{crit} \propto (1-\bar{d})\dot{\gamma}$

- Frequency ratio

$$\frac{f}{f_{crit}} \propto \frac{\sqrt{\omega}}{\sqrt{\dot{\gamma}}(1-\bar{d})}$$

$$\frac{f}{f_{crit}} = \frac{K_2\sqrt{\omega}(d_1\cos_{\beta_S})^{1/4}}{(1-\bar{d})[g\sin(\beta_m - \beta_s)]^{1/4}}$$

Hajra, Bhattacharya and McCarthy, *Powder Tech.*, 2012

Model Predictions (Density Segregation)

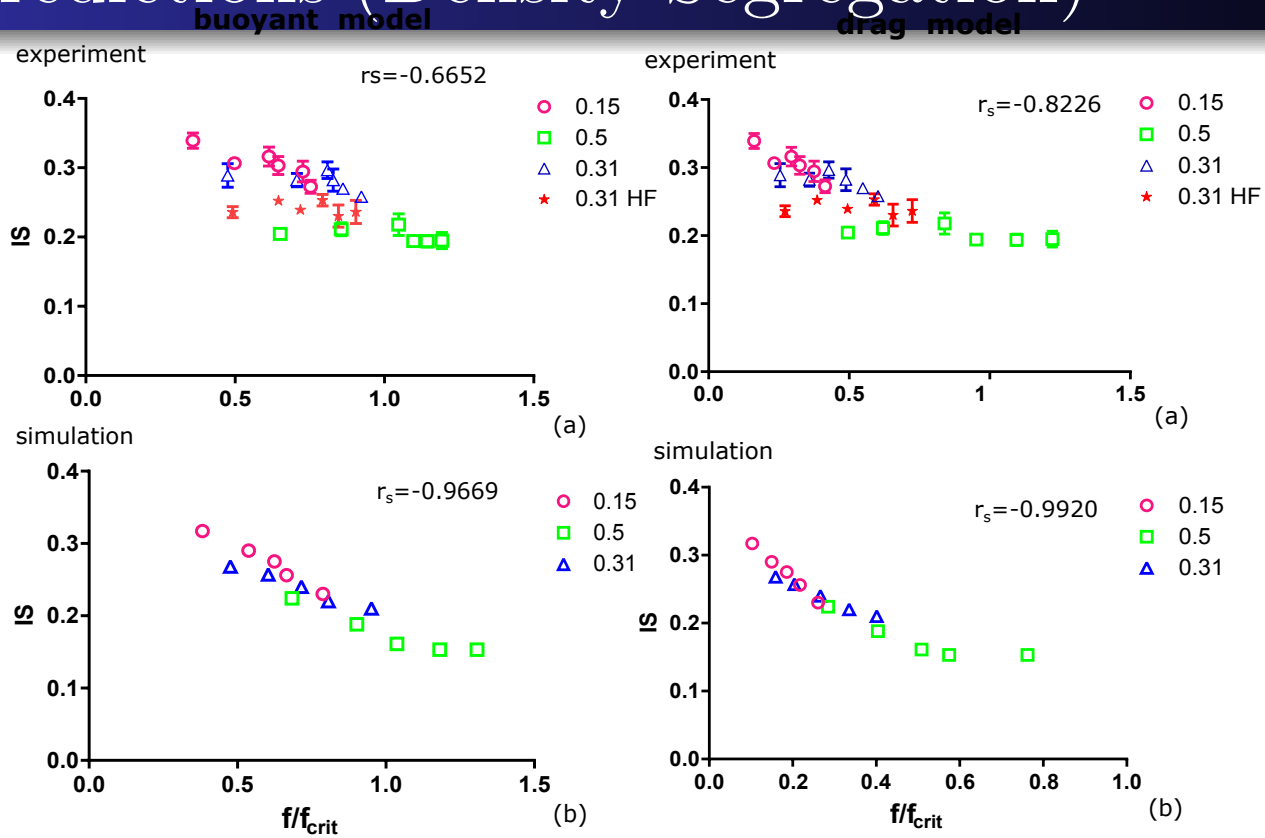

- Particle roughness suggested at AGM 2015
- "Proper" model will yield monotonic change in IS vs f/f_{crit}
- r_s for quantitative measure ($1 \rightarrow$ monotonic)

Model Predictions (Size Segregation)

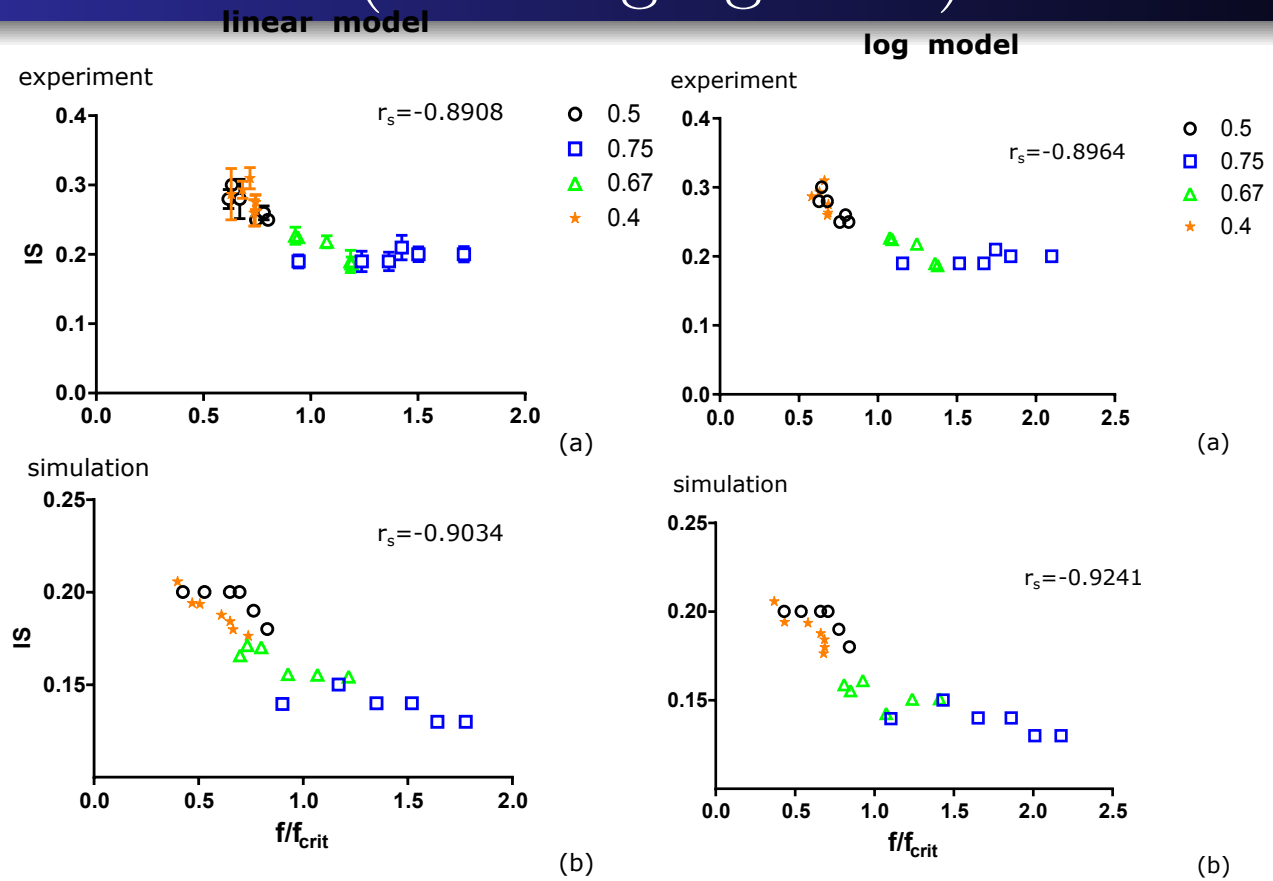

- "Proper" model will yield monotonic change in IS vs f/f_{crit}
- r_s for quantitative measure ($1 \rightarrow$ monotonic)

Density Segregation Under Varying Conditions

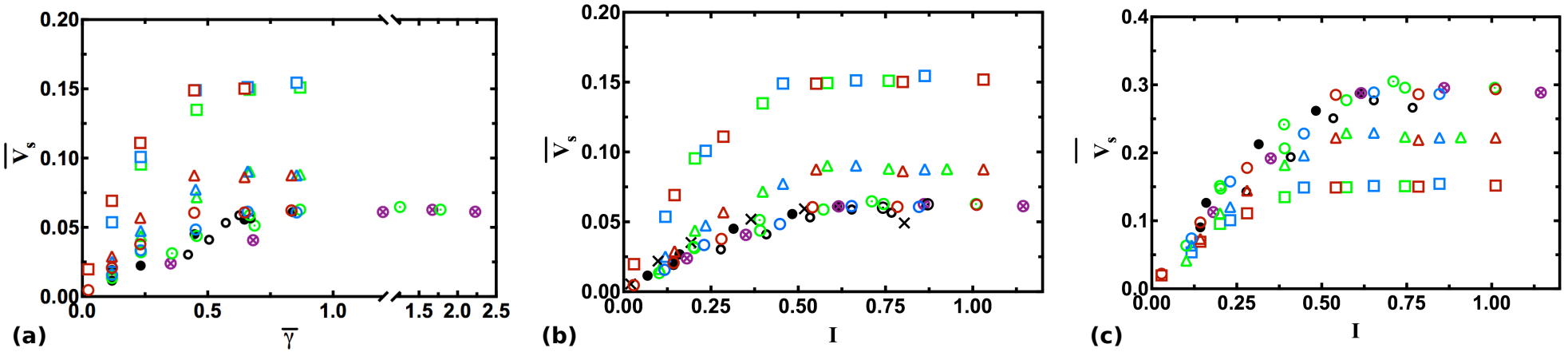

- Segregation under different confining pressure (or constant volume)
- Also varying shear rate, particle size, and density ratio
- Rheological quantity, $I = \dot{\gamma} d_p \sqrt{\frac{\rho}{P}}$, collapses data

A Unified Model, Based on Rheology

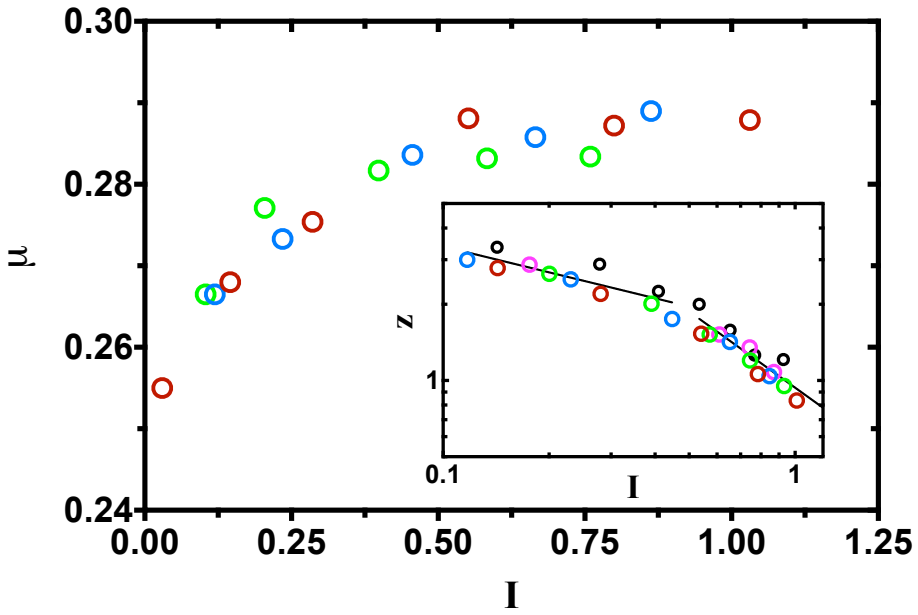

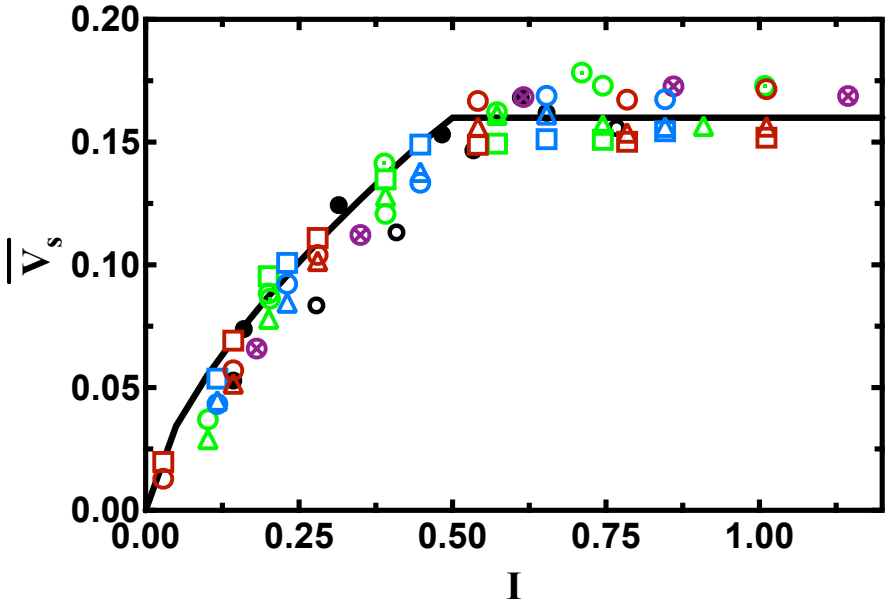

- Segregation saturation occurs at same location as frictional saturation
- Model based on coordination number fits **all** data

Experimental Validation of Density Model

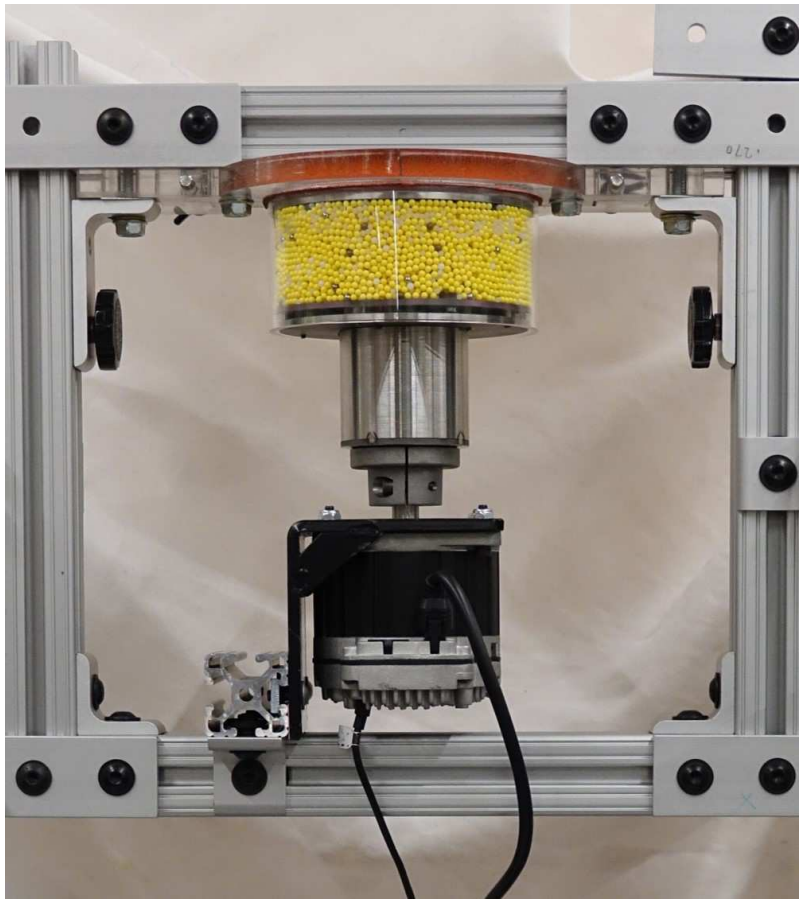

- Experimental apparatus for continuous shearing
- Run with tracer particles that are visually tracked

Experimental Validation

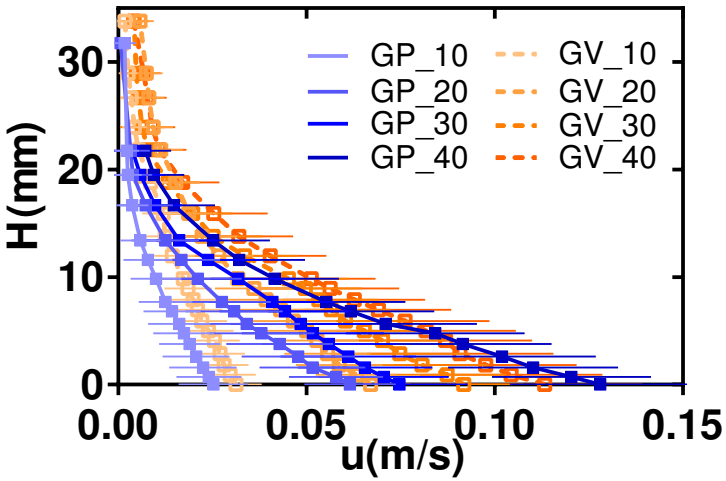

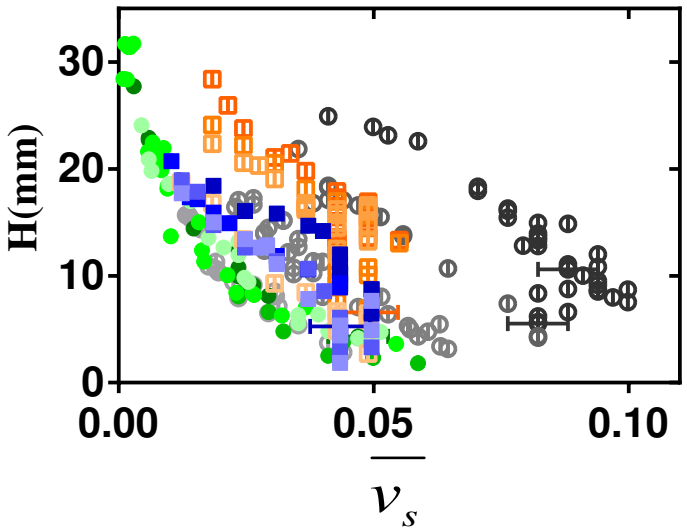

- Measurements of velocity vs height for varying conditions
- Matched to segregation measurements at same locations

Experimental Validation

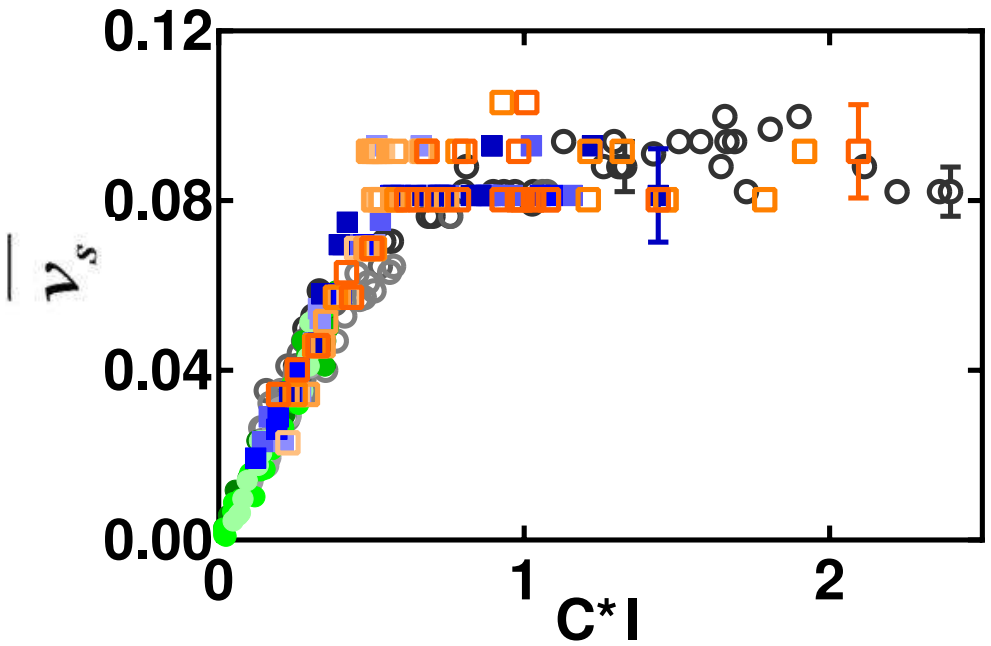

- Inhomogeneous shear means that the inertia number, I, varies with height
- Can easily measure v_s vs I for a range of conditions
- Results confirm novel segregation saturation model

Testing Size Segregation

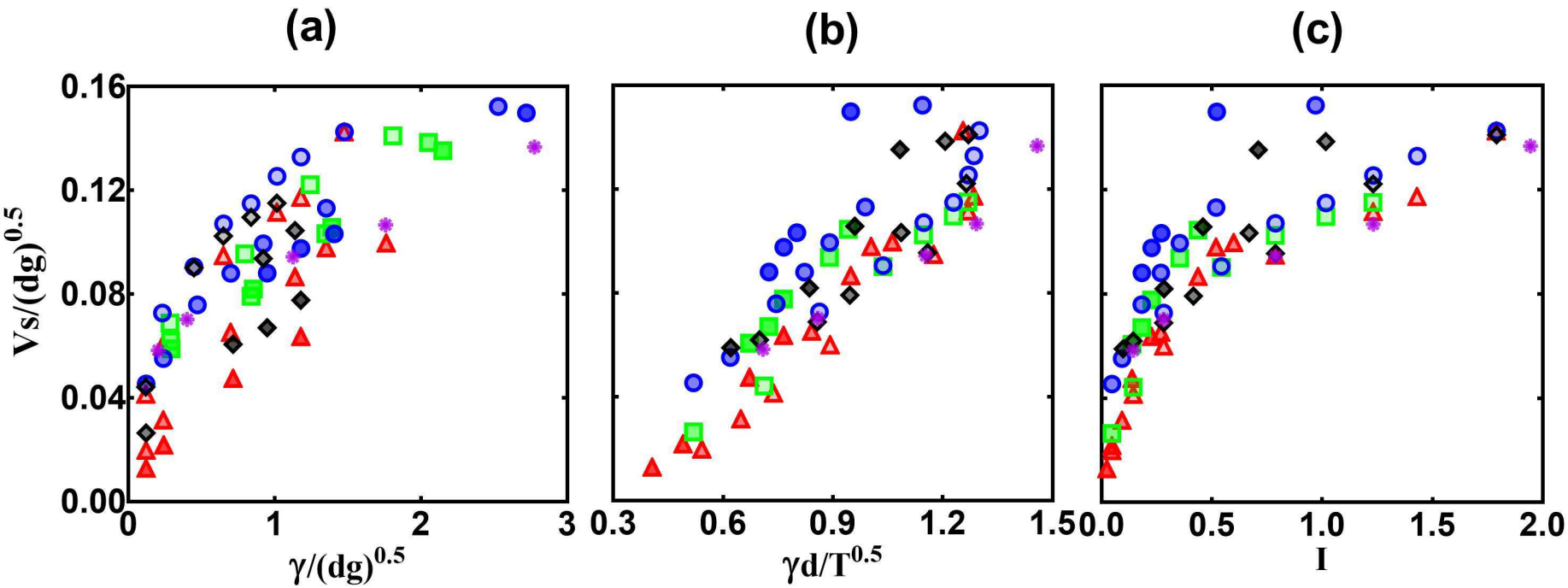

- No simple scaling of shear rate collapses size data
- Tried gravity, granular temperature, and inertia number

Impact of Rheology on Size Segregation

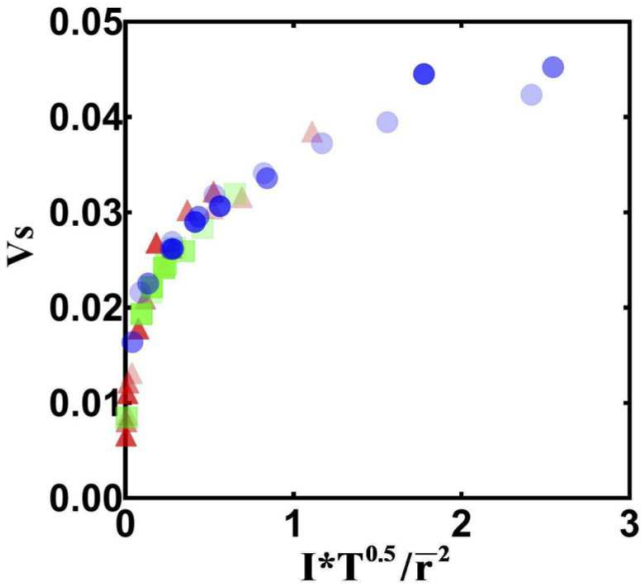

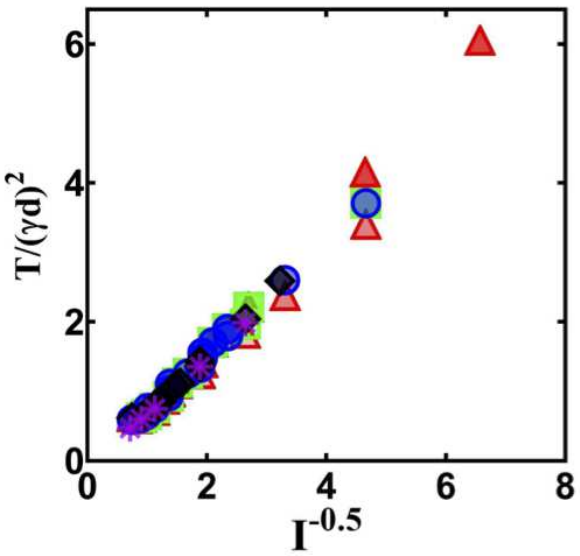

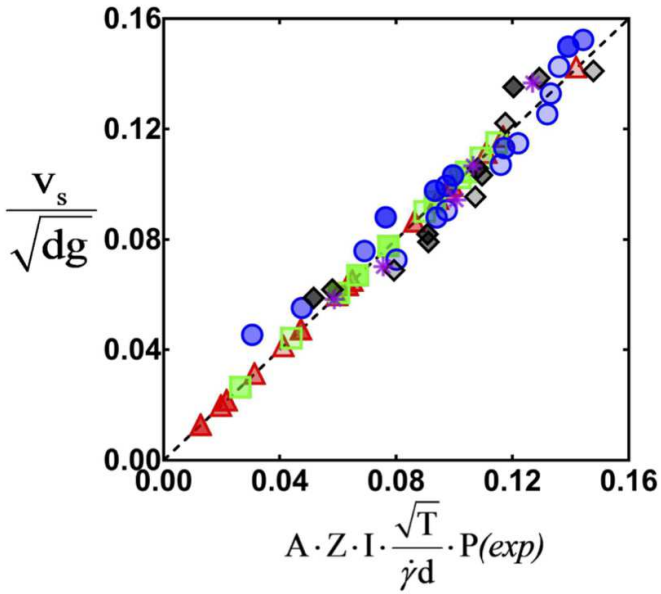

- Size segregation involves a more complex interplay between segregation and rheology
- Combining I and T captures both creation and finding of voids
- Novel observation: size ratio squared!

Cohesive Segregation

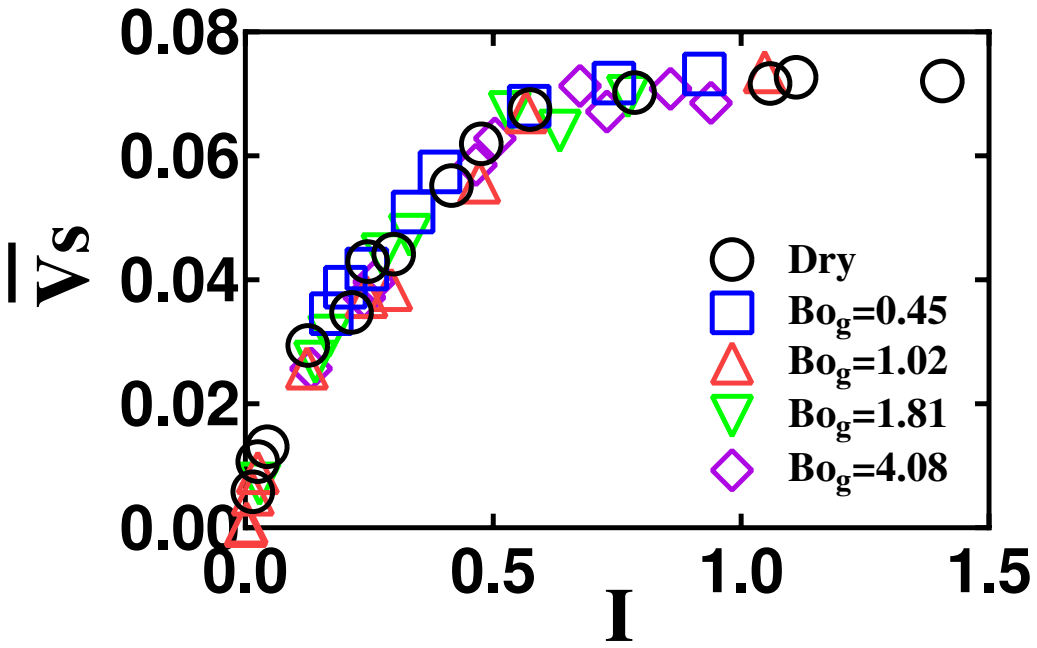

- $\bar{v}_s = \frac{z_{adj}(\bar{\rho}-1)}{6\beta\sqrt{\bar{\rho}}} I$ works for **both** cohesive and non-cohesive systems

Cohesive Segregation Works: How?

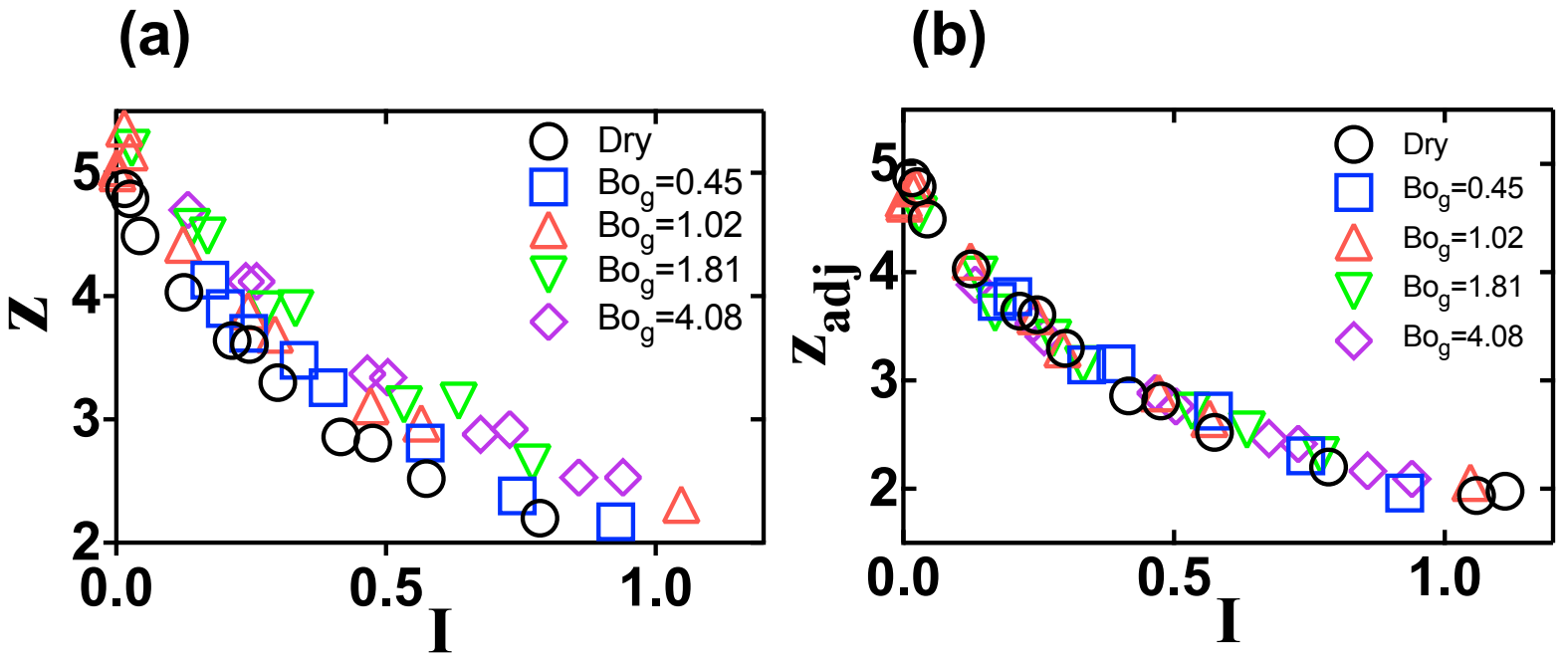

- $z_{adj} = z \cdot (1 - \frac{F_c}{F_z}) = z \cdot (1 - \frac{4\gamma}{\alpha P d_p})$
- Cohesion is important, but effective collisions still lead to segregation

Experimental Exploration of Shape Segregation

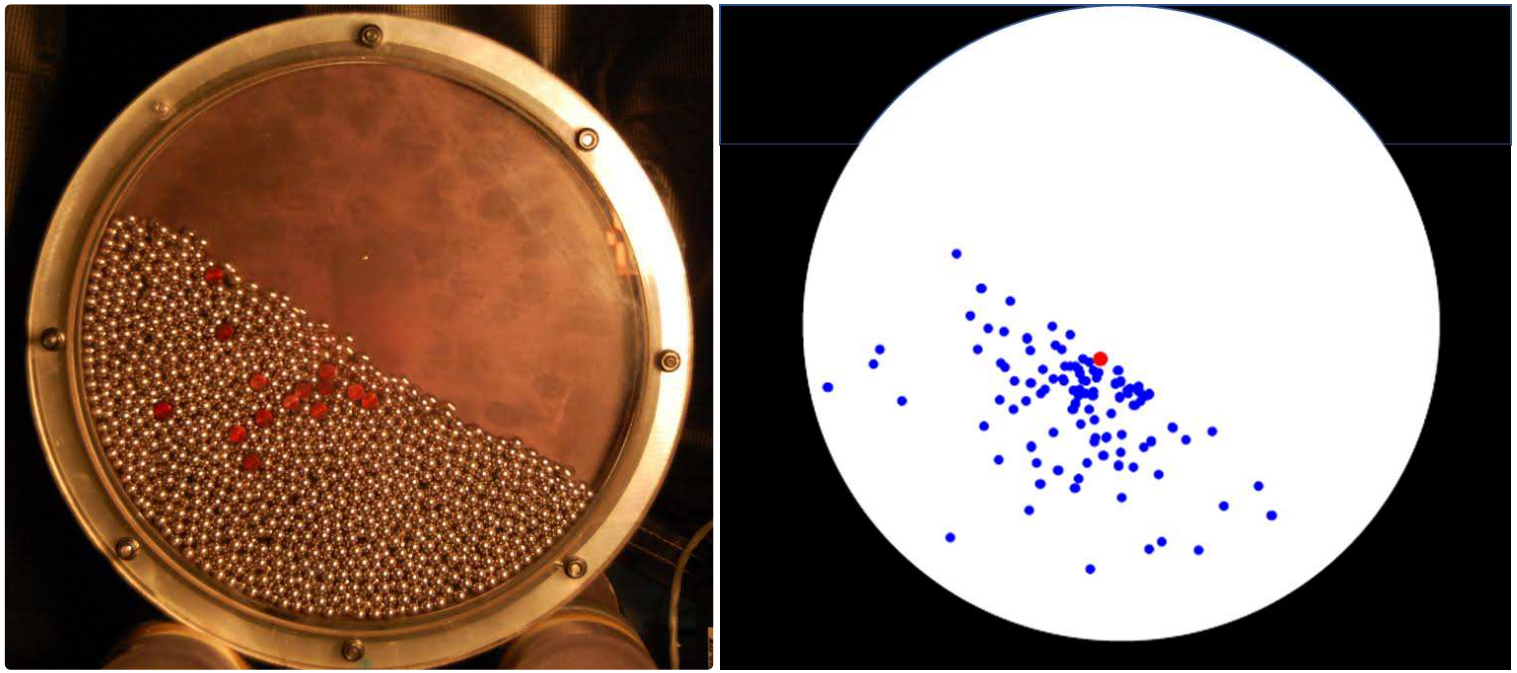

(a) (b)

- Tracking the periodic observed location of tracers allow a measure of segregation based on "distance to center"
- Comparing to sphere-sphere systems → equivalent size parameter

Effective Size of Cylinders/Discs

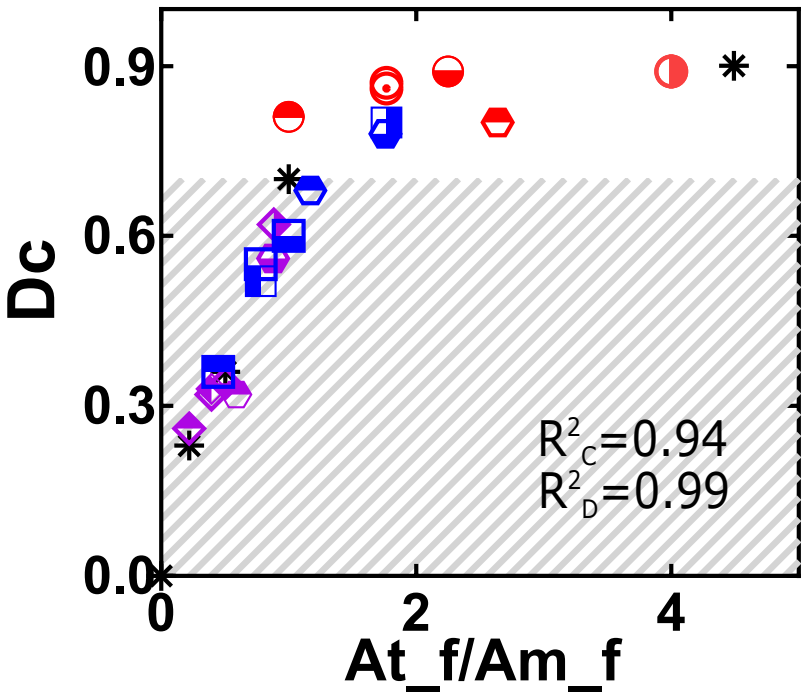

Shape descriptor # / Classification #	Shortest L / 1D	Average L / 1D	"Lay down" A / 2D	"Spinning" A / 2D	Volume / 3D	**"Flowing" A / 2D**
R^2 Cylinder	0.94	0.79	0.77	0.77	0.65	**0.94**
R^2 Disc	0.74	0.94	0.99	0.57	0.57	**0.99**

Using van der Waals Cohesion

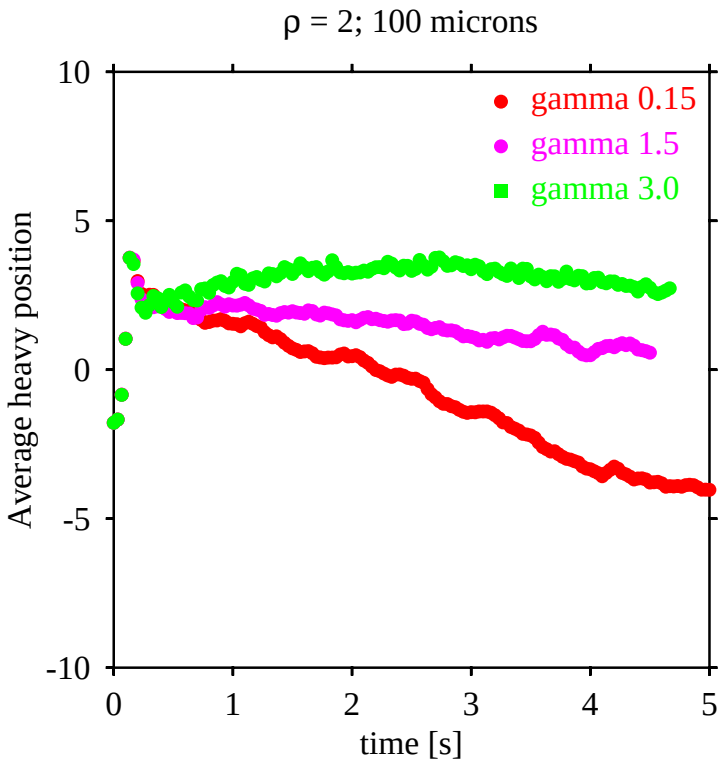

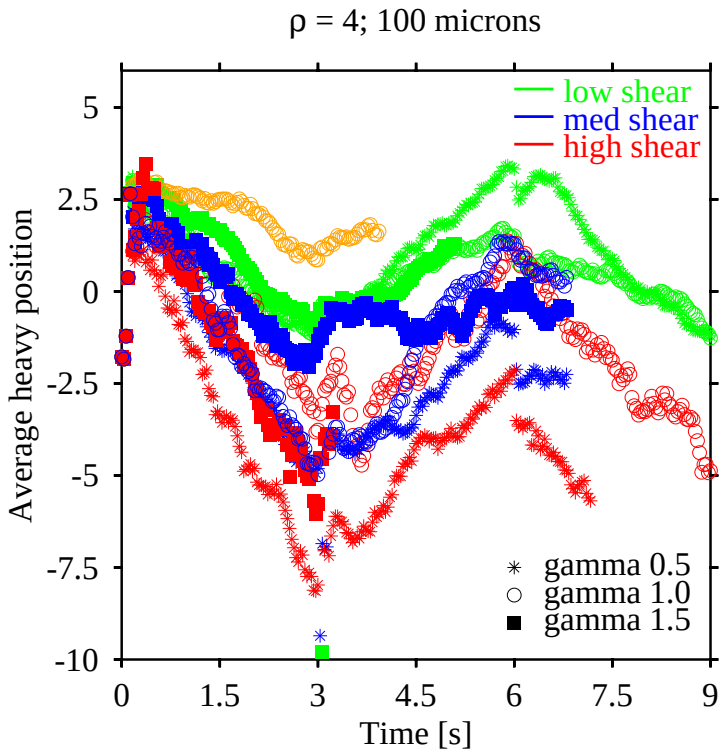

- Continuing simulations
- Formal analysis to come

Transport Modeling (Density)

$$\frac{\partial c_i}{\partial t} + u\frac{\partial c_i}{\partial x} + w\frac{\partial c_i}{\partial z} + \frac{\partial v_s c_i}{\partial x} = \frac{\partial}{\partial z}\left(D\frac{\partial c_i}{\partial z}\right)$$

- Route to "scale up" of models to relevant-scale usage
- Our model combines rheology and segregation; perfect for transport equations

Flowability Assessment of Weakly Consolidated Powders

Colin Hare[1], Ali Hassanpour[2], Azza Mahmoud[1], Alexandros Stavrou[1]

[1]Department of Chemical and Process Engineering, University of Surrey
[2]Institute of Particle Science & Engineering, University of Leeds

Introduction

- In traditional flowability measurement devices:
  - Reproducibility of unconfined yield strength is greatly reduced at low stresses.
  - Or inconsistent with observed behaviour.
  - Materials found to be cohesionless may have practical differences.
  - Onset of flow is measured – may not be complete flow description.

- IFPRI seek to develop a theoretical understanding of flow of weakly consolidated & weakly cohesive powders.
  - Development of practical means of making measurement to support theory.
  - Results should be generalisable to broad class of powders.

Ball indentation[1]

- Spherical indenter driven into powder bed[2]

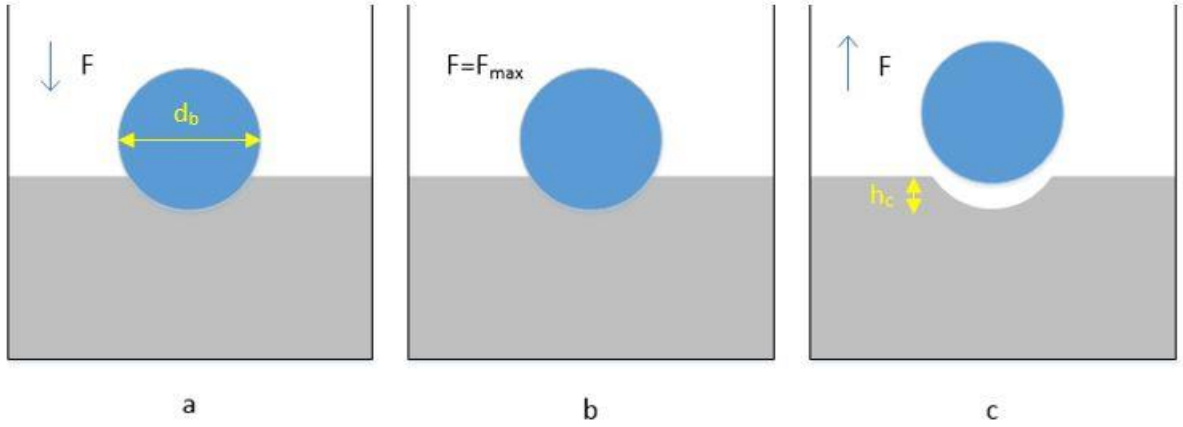

- Force & displacement measured throughout
  - Hardness determined:

$$H = \frac{F}{A} = \frac{F}{\pi(d_b h_c - h_c^2)}$$

- Indentation zone is confined by powder
- Hence, hardness related to unconfined yield stress by **constraint factor, C**:

$$H = C \cdot \sigma_c$$

- The value of C is not known a priori for a given powder
- Can be determined by complimentary σ_c measurement

[1]Hassanpour, A., Ghadiri, M., 2007, *Particle & Particle Systems Characterization*, 24 (2), 117-123.
[2]Stavrou, A., Hare, C., Hassanpour, A., Wu, C-Y., 2020, *Chemical Engineering Science*, 211, 115307.

Ball indentation dimensions

- Criteria established by Zafar *et al.* (2017)[3]

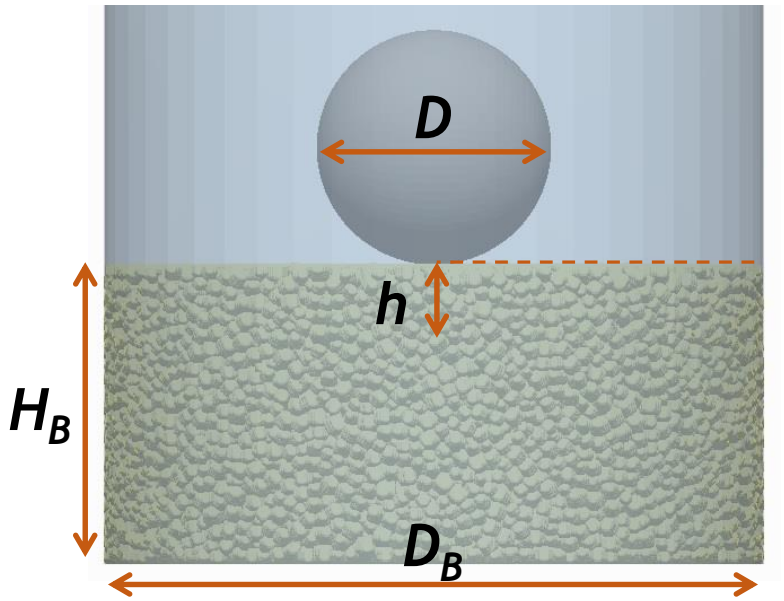

$$D \geq 16d_p$$

$$D_B \geq 45d_p$$

$$H_B \geq 20d_p$$

- Suitable penetration depth required
- Dimensionless penetration depth,

$$h_d = \frac{h}{R}$$

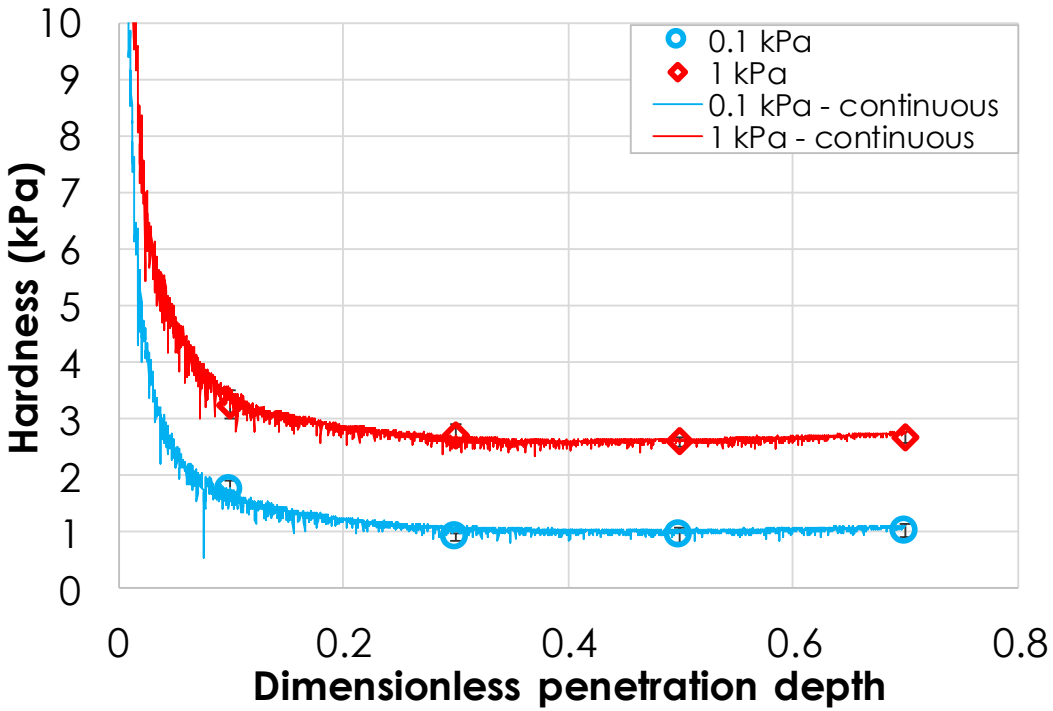

- Stable hardness region found[2]
- Negligible elastic recovery
  - ❑ *H* determined without unloading (<1 % error)

[2]Stavrou, A., Hare, C., Hassanpour, A., Wu, C-Y., 2020, *Chemical Engineering Science*, 211, 115307.
[3]Zafar, U., Hare, C., Hassanpour, A., Ghadiri, M., *Powder Technology*, 310, 300-306.

Flow measurement methods used

	Shear cell	Uniaxial compression	Ball indentation (original method)[1]	Ball indentation (critical method)
Consolidation	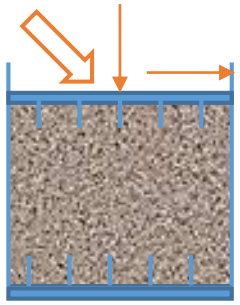	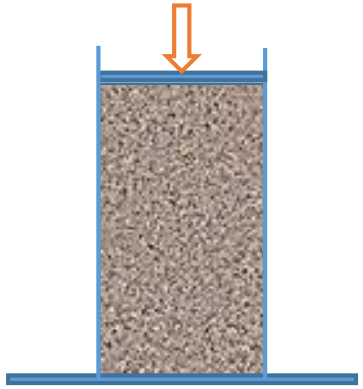	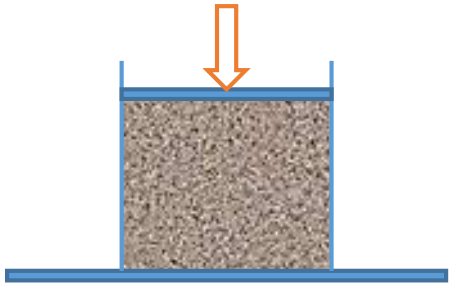	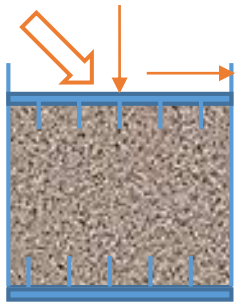
Failure	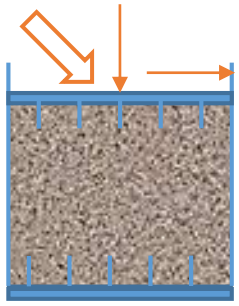	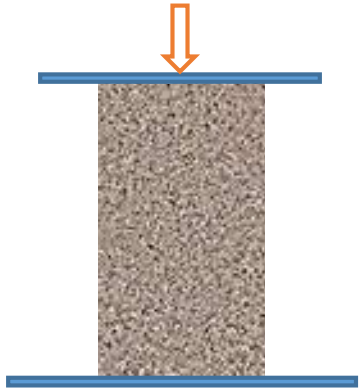	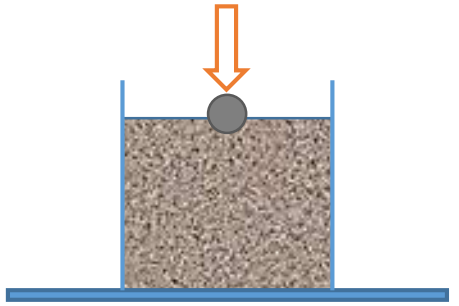	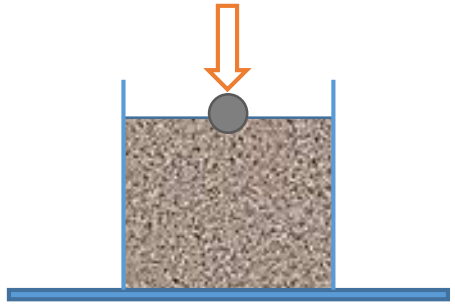
Measurement	Control: σ Measure: τ Determine: σ_1 & $\boldsymbol{\sigma_c}$	Control: σ (σ_1) Measure: $\boldsymbol{\sigma_c}$ (uUYS)		

[1]Hassanpour, A., Ghadiri, M., 2007, *Particle & Particle Systems Characterization*, 24 (2), 117-123.

Cohesive glass beads: size effect

- Effect of particle size

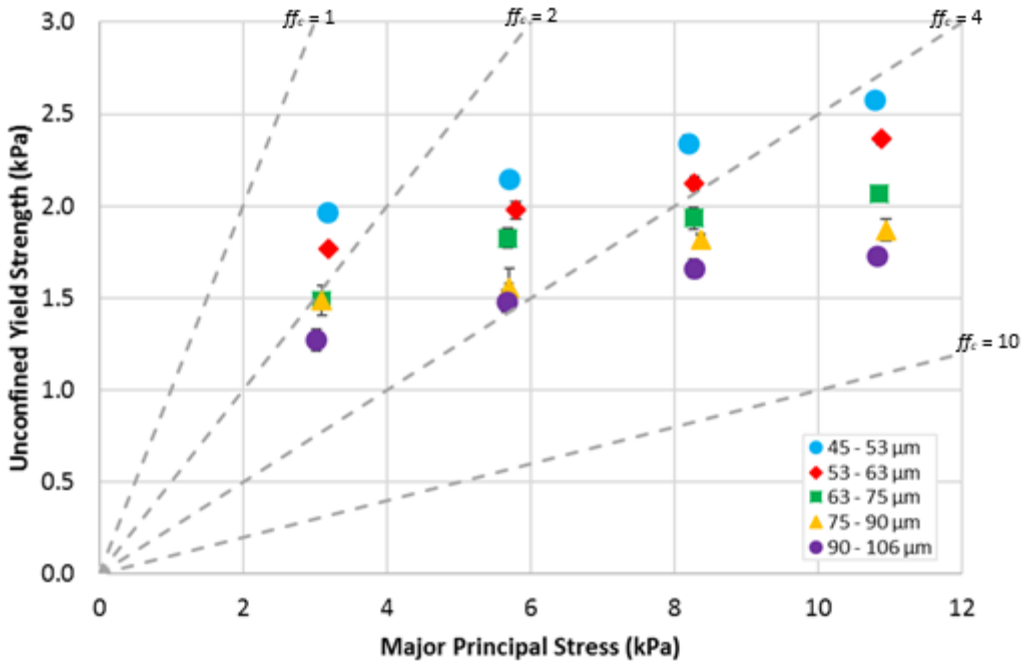

- Increase in size → decrease in σ_c

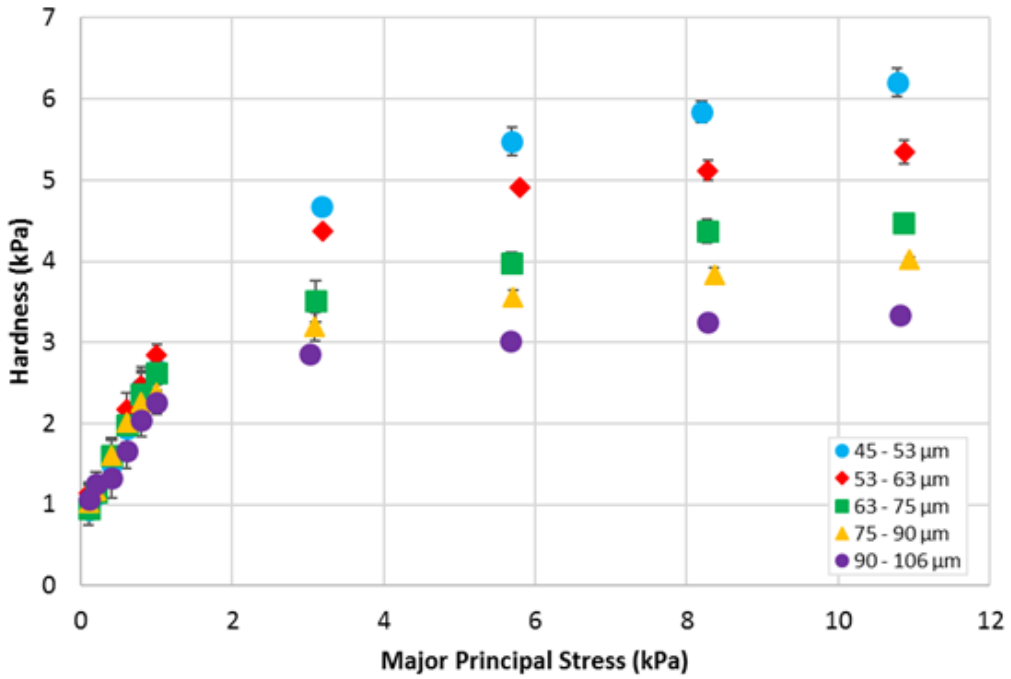

- Increase in size → decrease in *H*
- *H* increase is much steeper at low stress

- Constraint factor found: $C = H/\sigma_c$

[4]Stavrou, A., Hare, C., Hassanpour, A., Wu, C-Y., 2020, *Powder Technology*, 364, 98-114.

Cohesive glass beads: low stress behaviour

- Shear cells often not reliable at such low stresses
- Yield loci reliable for 45-53 μm sample

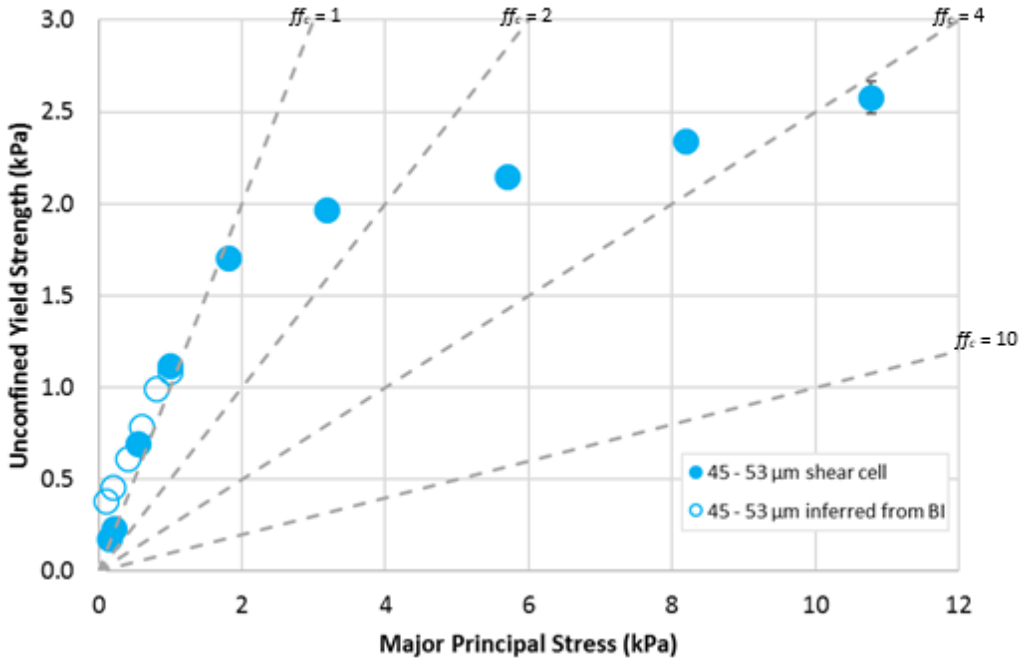

- σ_c agrees with that inferred from ball indentation

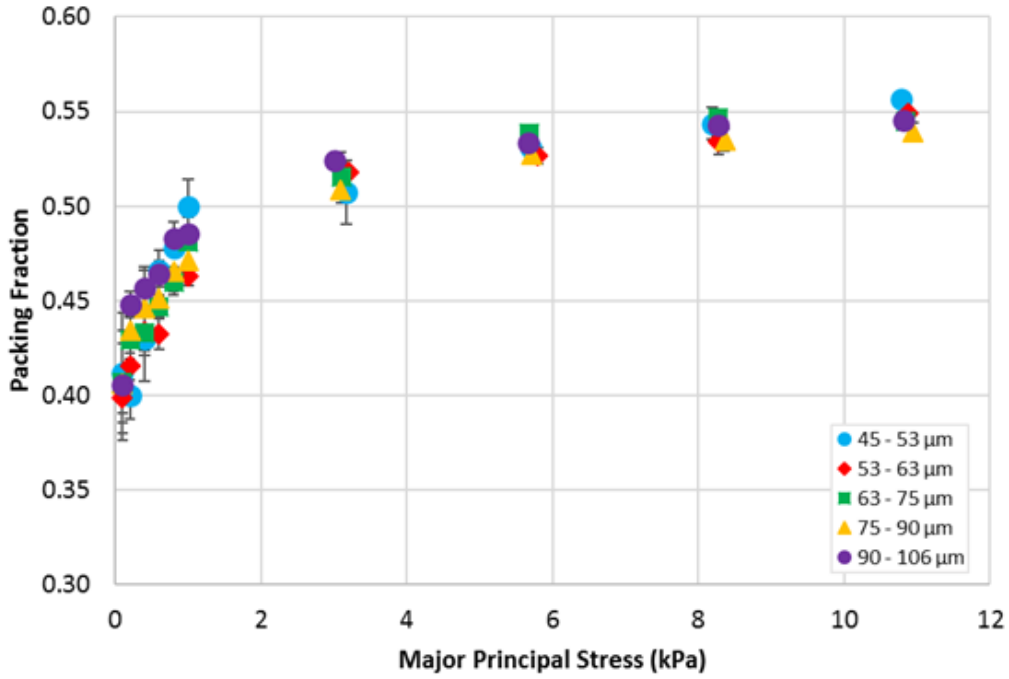

- Low stress behaviour:
  - H, σ_c increase sharply with stress
  - Corresponds with sharp increase in packing fraction

[4]Stavrou, A., Hare, C., Hassanpour, A., Wu, C-Y., 2020, *Powder Technology*, 364, 98-114.

Cohesive glass beads: size distribution effect

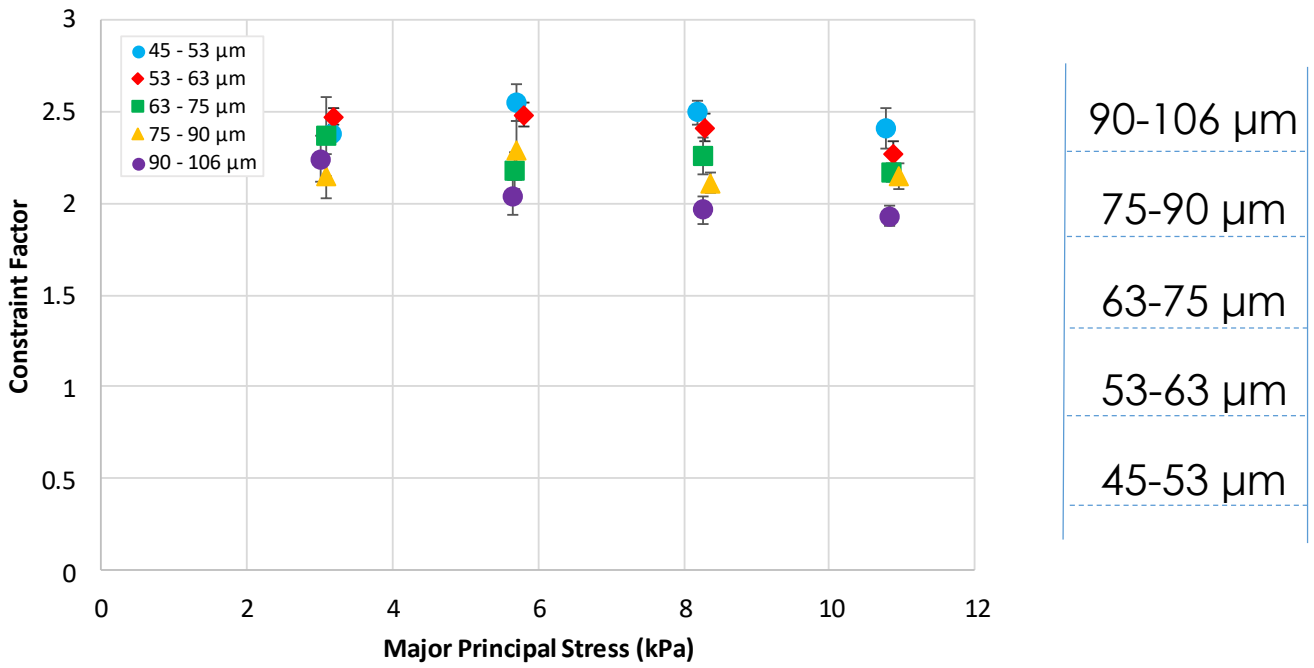

90-106 µm

75-90 µm

63-75 µm

53-63 µm

45-53 µm

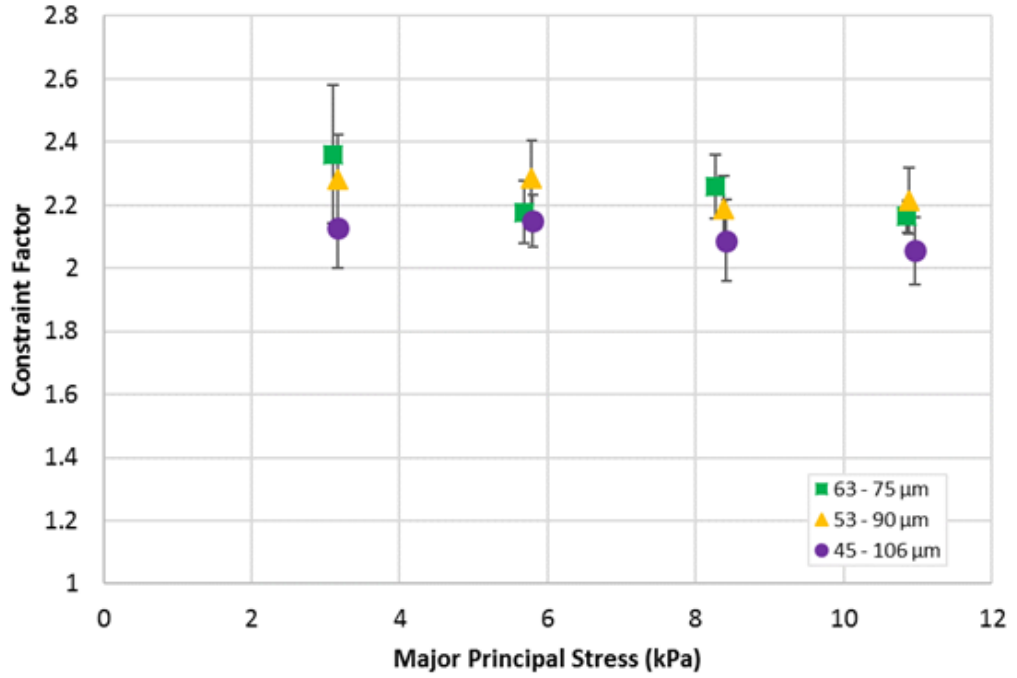

- C generally decreases with increasing size
- C decreases as distribution span increased

[4]Stavrou, A., Hare, C., Hassanpour, A., Wu, C-Y., 2020, *Powder Technology*, 364, 98-114.

Cohesive glass beads: size distribution effect (2)

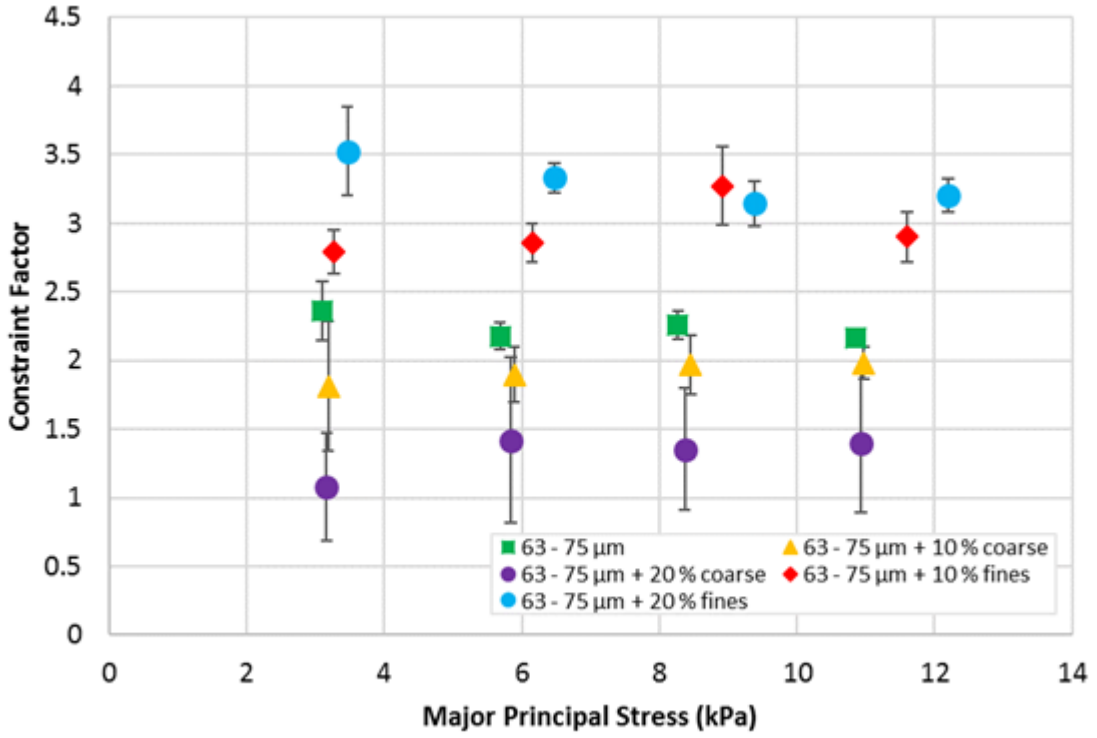

150-180 µm	**(coarse)**
63-75 µm	
<20 µm	**(fines)**

- Increased fines → C increases
- Increases coarse → C reduces
- Competing effects led to less pronounced C changes for wider span

[4]Stavrou, A., Hare, C., Hassanpour, A., Wu, C-Y., 2020, *Powder Technology*, 364, 98-114.

Simulation results

- Discrete Element Method (DEM) used to manipulate particle properties[2]

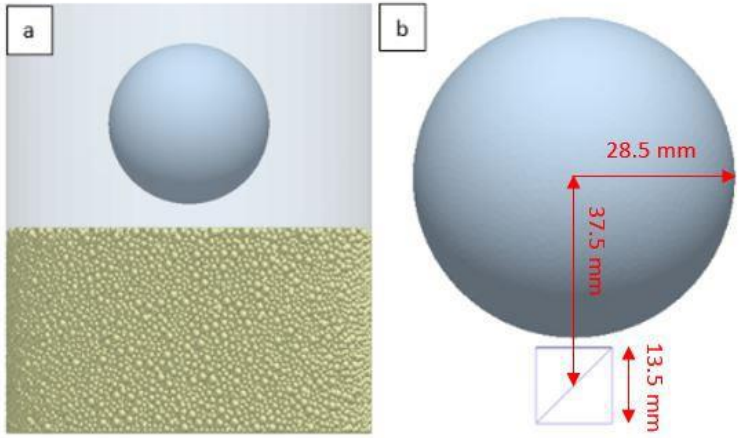

- Stresses determined below indenter:

$$\sigma_{ij} = -\frac{1}{V}\sum_{N_p}\sum_{N_c}\left|x_i^c - x_i^p\right| n_i F_j$$

$$\tau_D = \sqrt{\frac{(\sigma_1-\sigma_3)^2 + (\sigma_1-\sigma_2)^2 + (\sigma_2-\sigma_3)^2}{6}}$$

- $C' = H/\tau_D$

- Pasha *et al.* (2014)[5] model, accounts for:
  - Plasticity
  - Adhesion

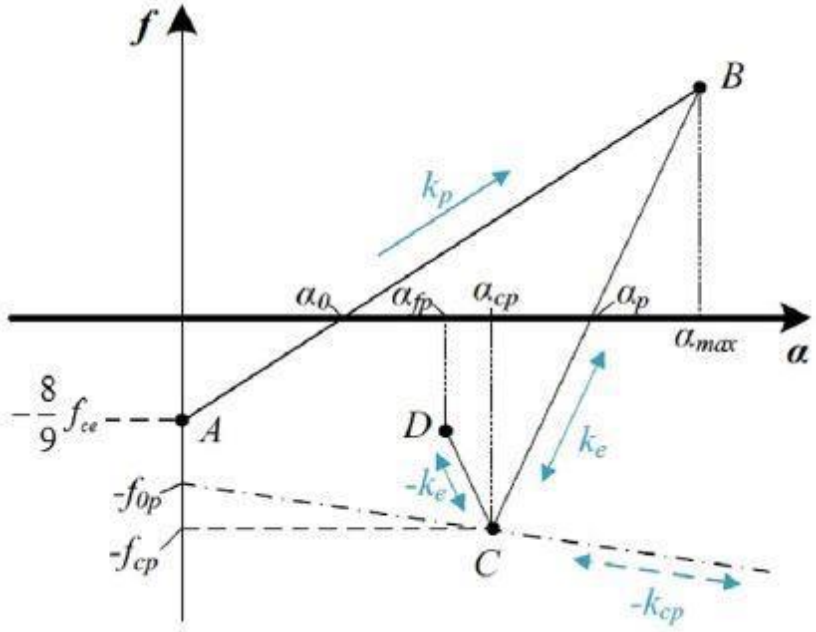

[2]Stavrou, A., Hare, C., Hassanpour, A., Wu, C-Y., 2020, *Chemical Engineering Science*, 211, 115307.
[5]Pasha, M., Dogbe, S., Hare, C., Hassanpour, A., Ghadiri, M., 2014, *Granular Matter*, 16, 151-162.

Stability of constraint factor

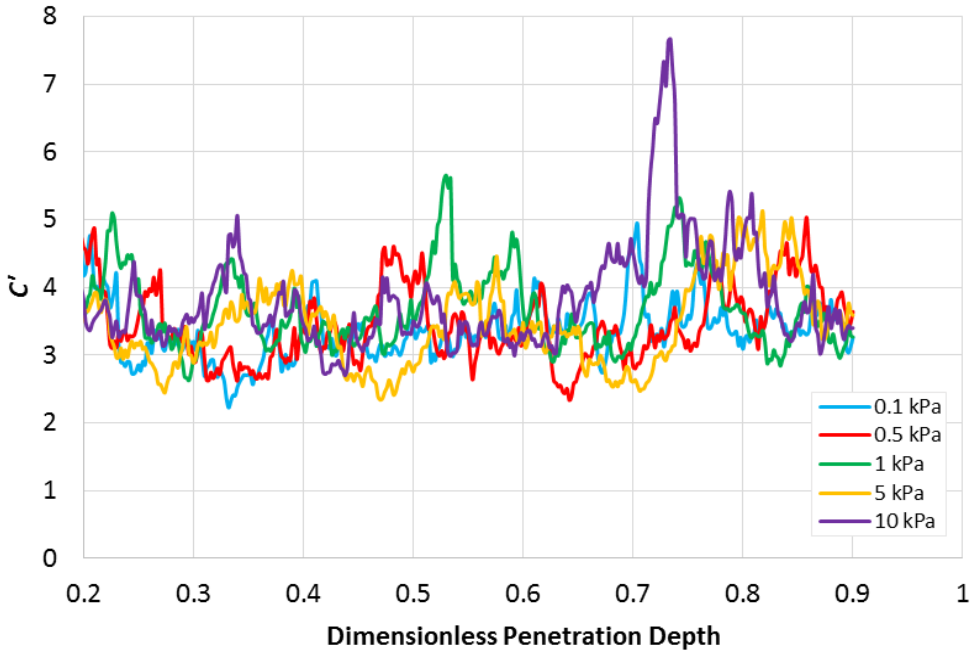

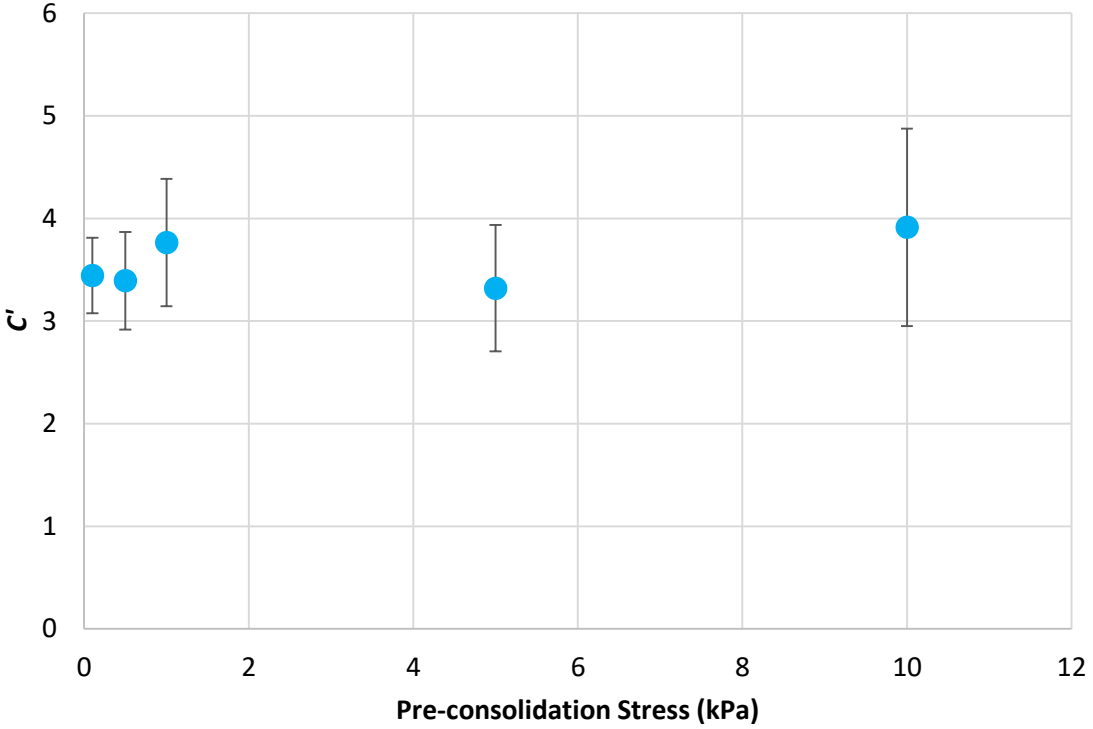

- Significant C' fluctuations with depth
- Average C' independent of stress

[2]Stavrou, A., Hare, C., Hassanpour, A., Wu, C-Y., 2020, *Chemical Engineering Science*, 211, 115307.

Effects of surface energy & friction

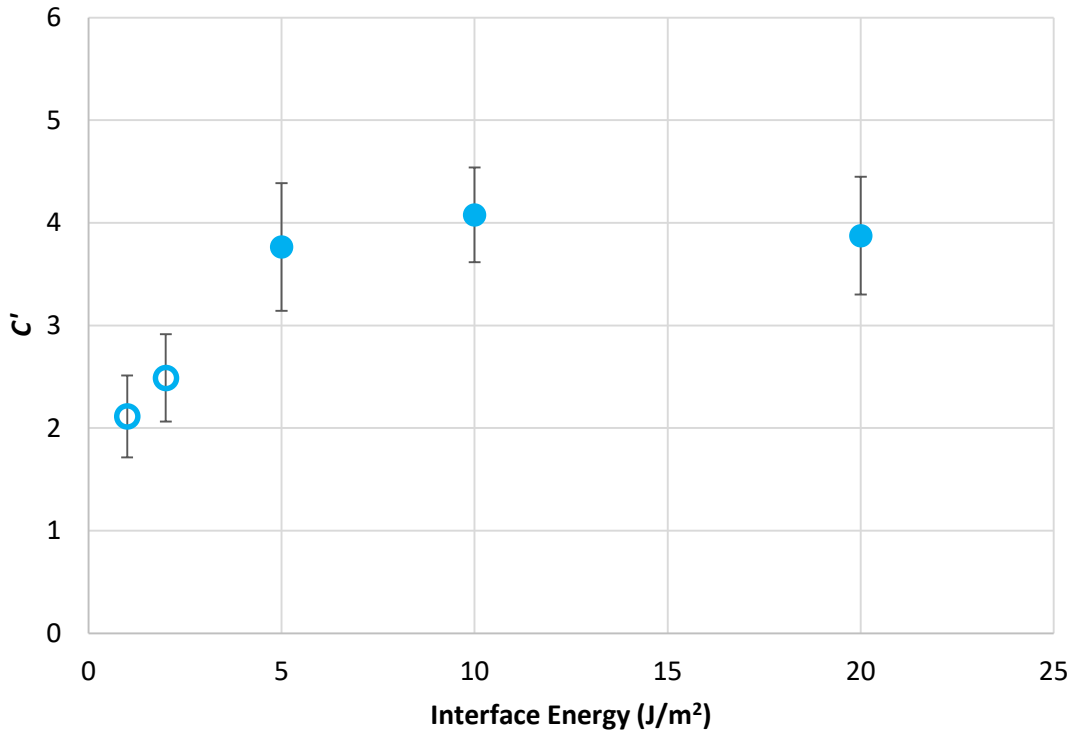

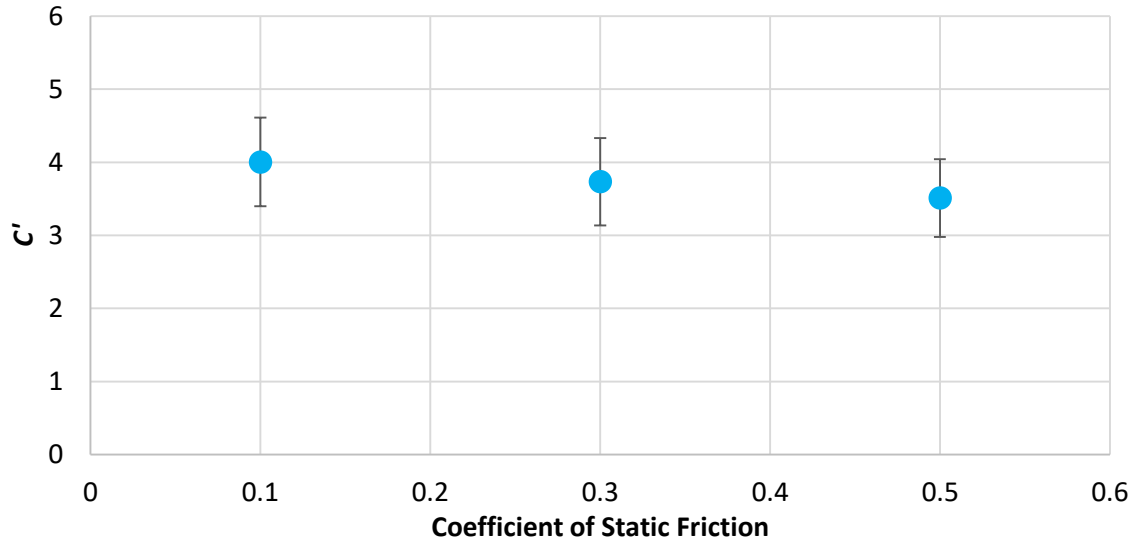

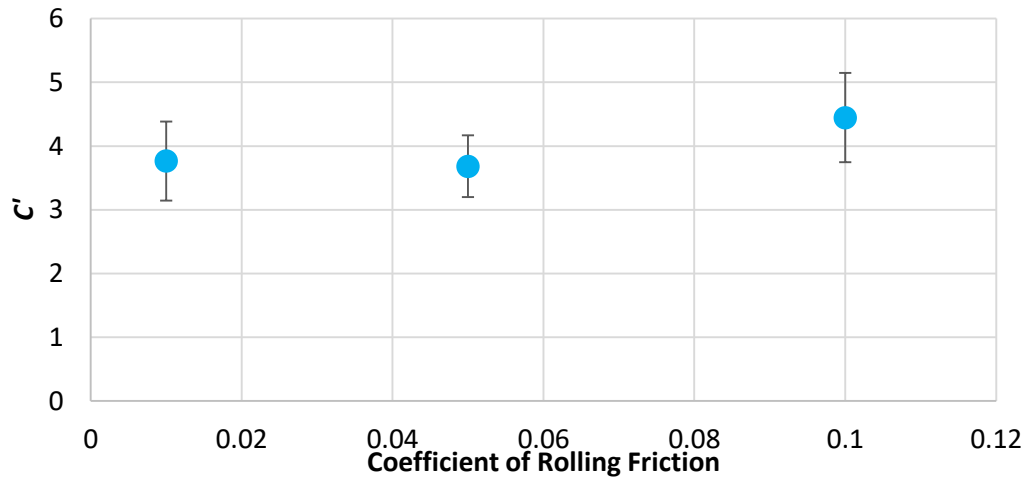

- C' increases with Γ for slight cohesion
- C' virtually independent of μ_s
- C' increases slightly for increasing μ_r

[2]Stavrou, A., Hare, C., Hassanpour, A., Wu, C-Y., 2020, *Chemical Engineering Science*, 211, 115307.

Real materials

- Methods applied to non-ideal powders
  - Shear cell measurements at σ_{pre} – 2, 4, 6, 8 kPa
  - Indentation at σ_1
- Constraint factor stable for most
  - Pea protein exhibited slip-stick behaviour
- Value of C ranges from 2-6
  - For materials tested
- Actual value of C depends on method used to determine σ_c

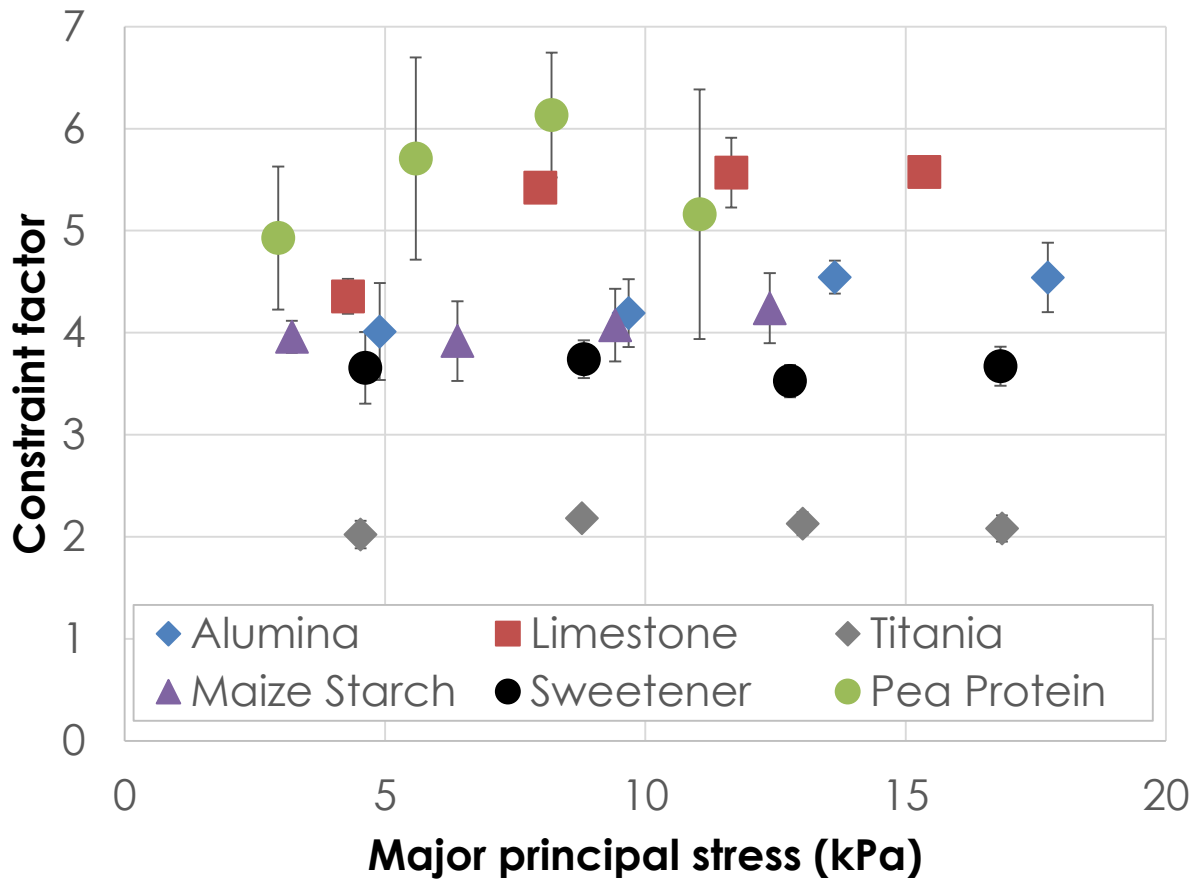

[6]Stavrou, A., 2019, Doctoral Thesis, *University of Surrey*.

Influence of mean flow function coefficient

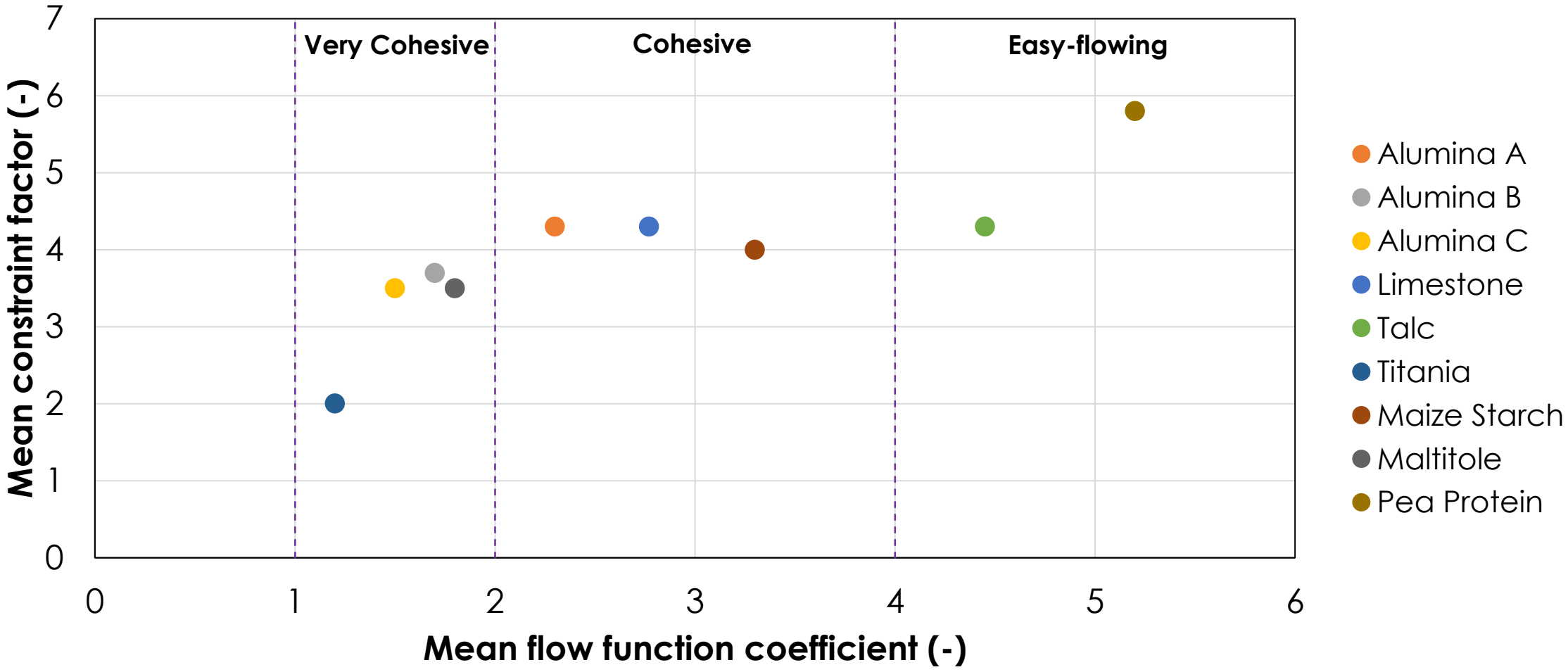

Relationship between C and ff_c

- Since: $ff_c = \frac{\sigma_1}{\sigma_c}$ (1),

$$C = \frac{H}{\sigma_c} \quad (2)$$

- Then: $$\boldsymbol{C = \frac{H}{\sigma_1} ff_c} \quad \textbf{(3)}$$

- Constraint factor (C) will be constant if:
  - $\boldsymbol{ff_c}$ and $(\boldsymbol{H/\sigma_1})$ are independent of consolidation stress,

or

  - $\boldsymbol{ff_c}$ increases, while $(\boldsymbol{H/\sigma_1})$ decreases at the same rate, with increasing stress

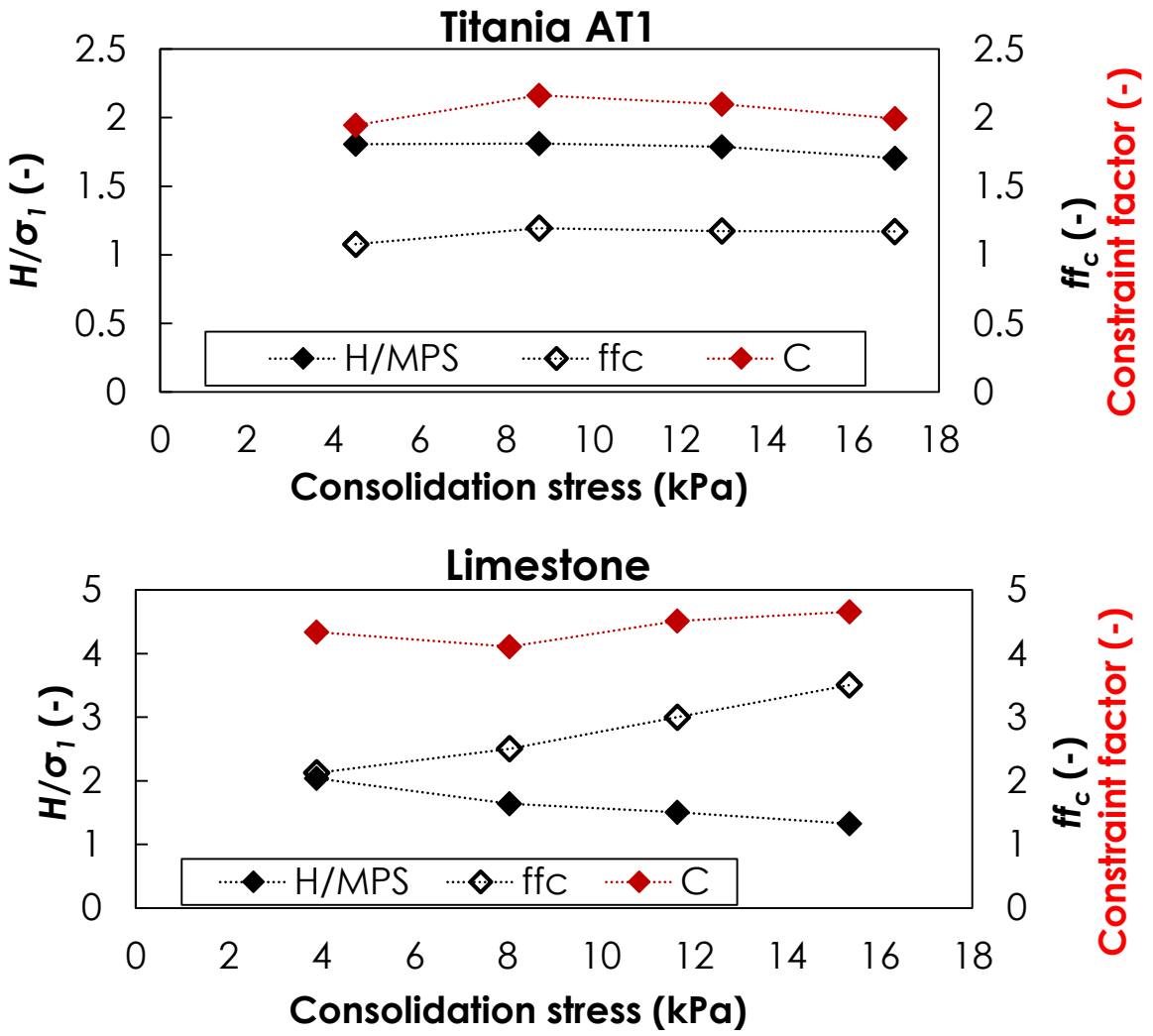

Influence of flow function coefficient and friction angle

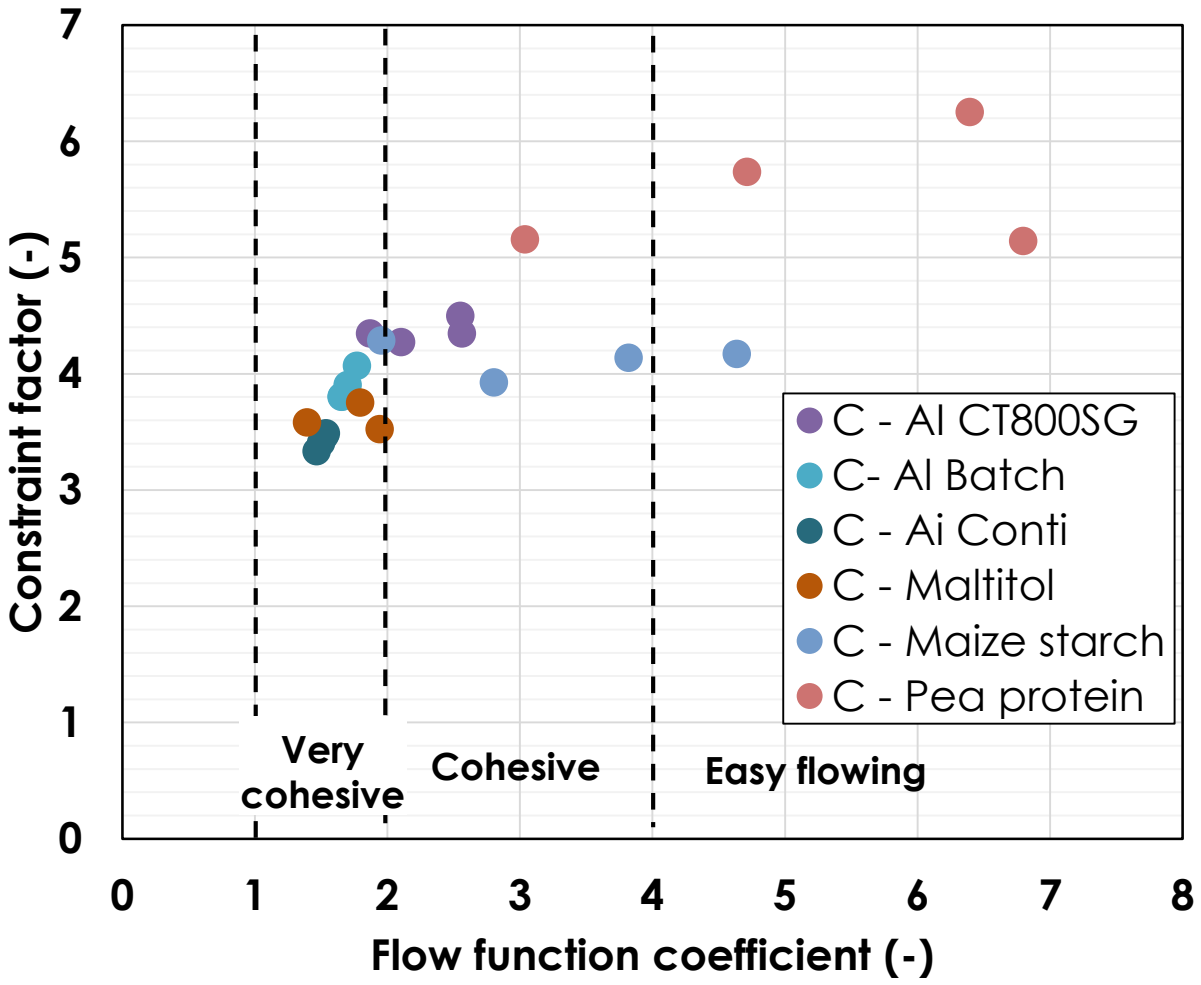

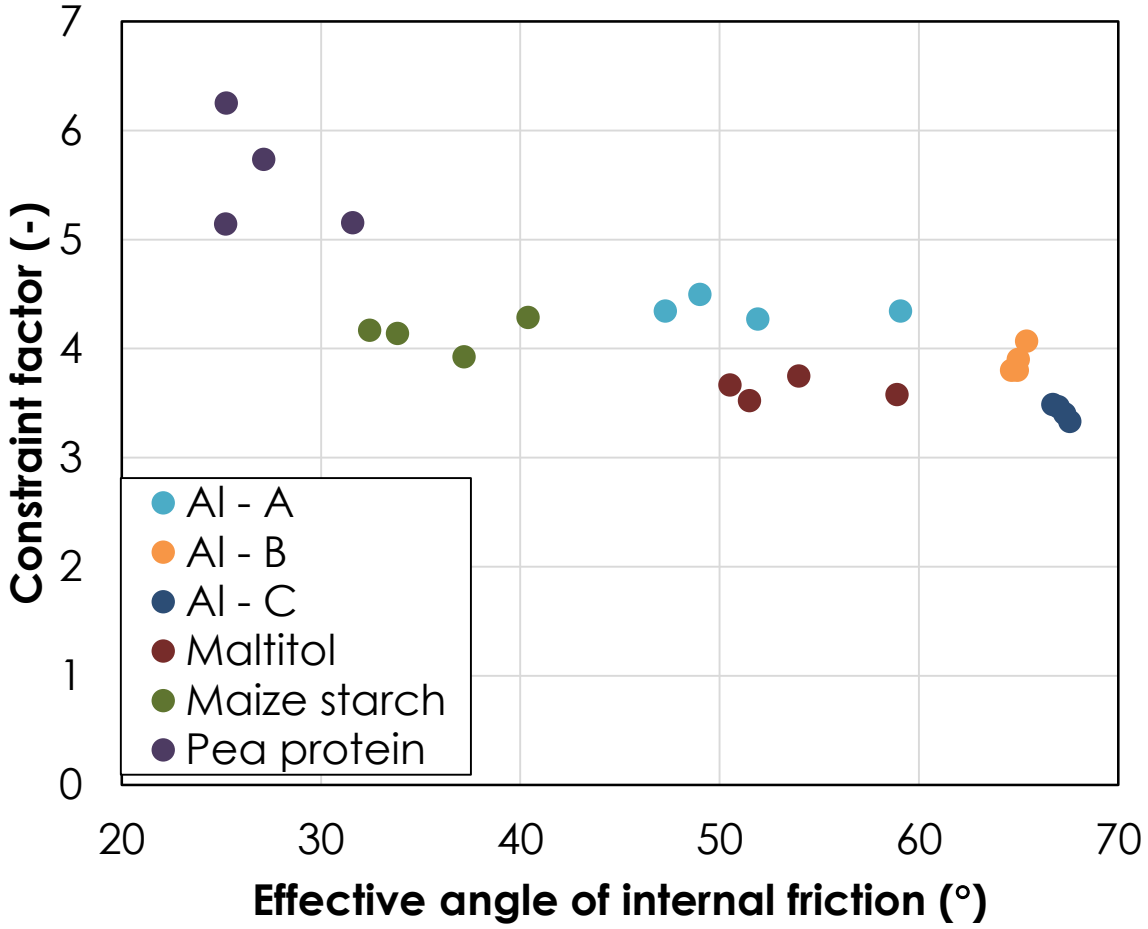

Critical method

	Shear cell	Uniaxial compression	Ball indentation (original method)[1]	Ball indentation (critical method)
Consolidation	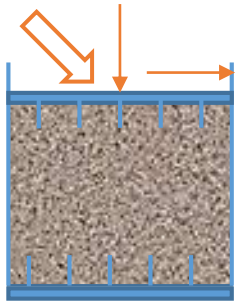	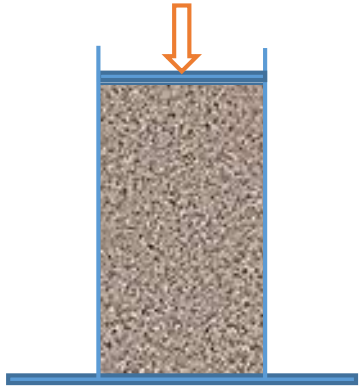	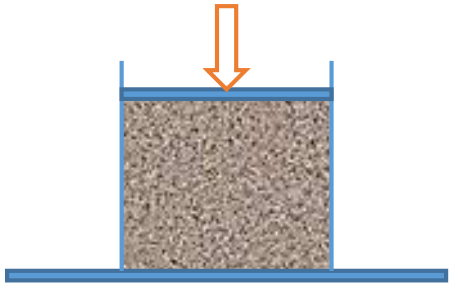	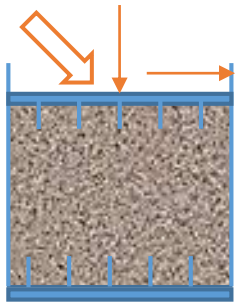
Failure	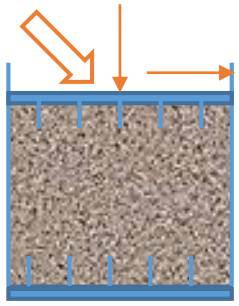	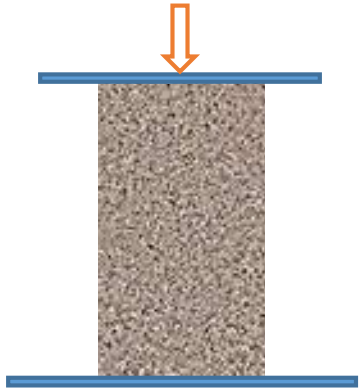	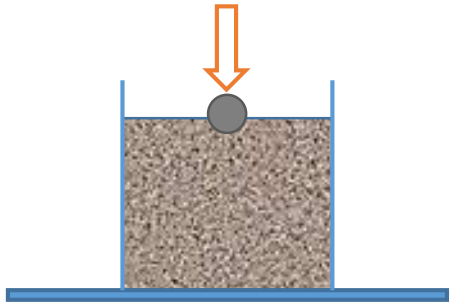	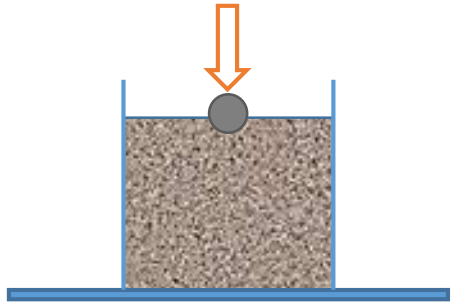
Measurement	Control: σ Measure: τ Determine: σ_1 & $\boldsymbol{\sigma_c}$	Control: σ (σ_1) Measure: $\boldsymbol{\sigma_c}$ (uUYS)	Control: σ (σ_1) Measure: $\boldsymbol{H}$ Determine: C, σ_c	

[1] Hassanpour, A., Ghadiri, M., 2007, *Particle & Particle Systems Characterization*, 24 (2), 117-123.

Indentation onto sheared beds

Standard shear test: requires extreme cohesion

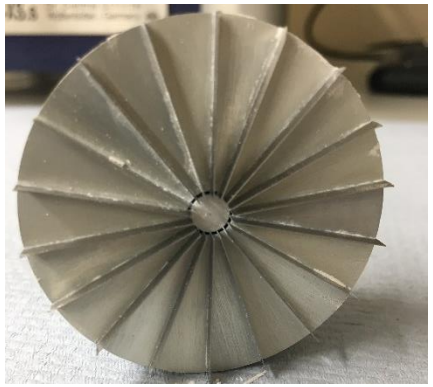

Shear test using wall friction head: insufficient pre-shear

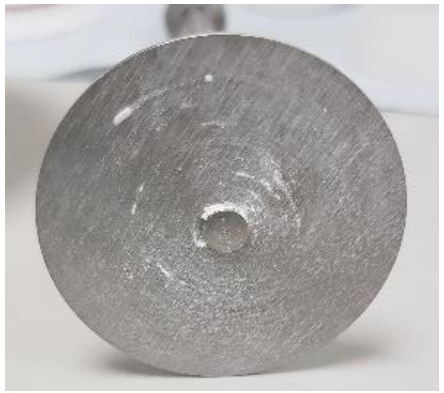

Splitting after shear test: induces unknown shear stress

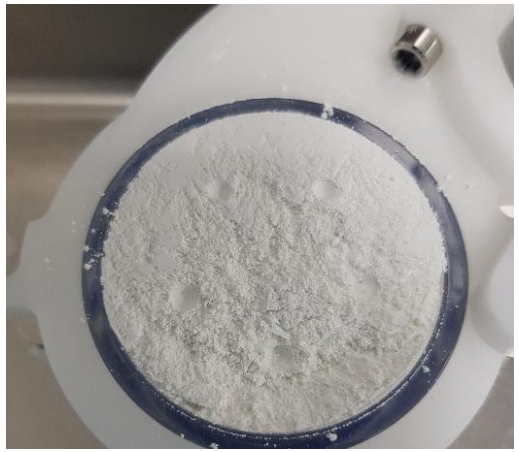

Vacuum suction after shear test: unknown suction force

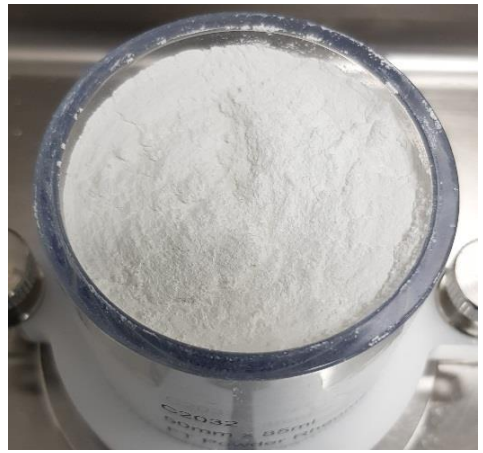

Defining constraint factor

	Mixed method	Critical method	Vertical method
Unconfined yield strength	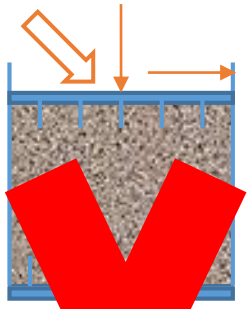	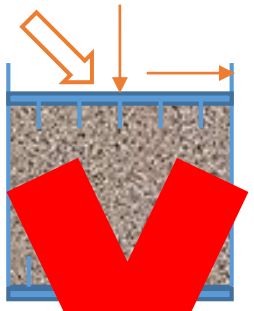	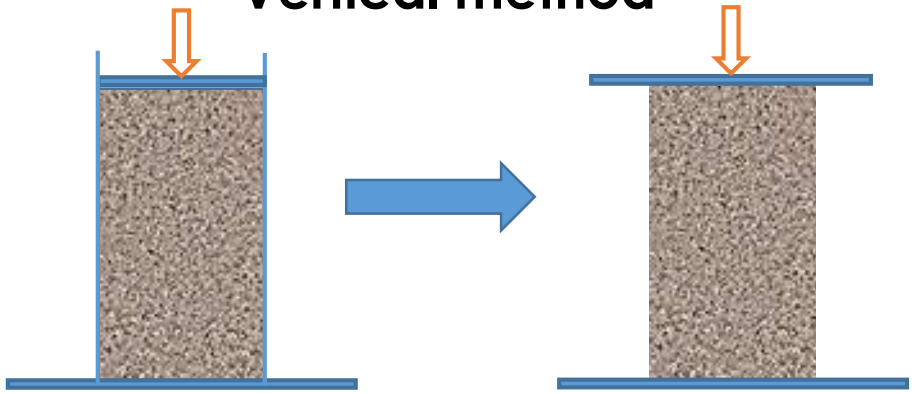 Uniaxial compression
Bed preparation for indentation		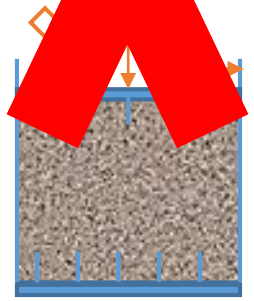	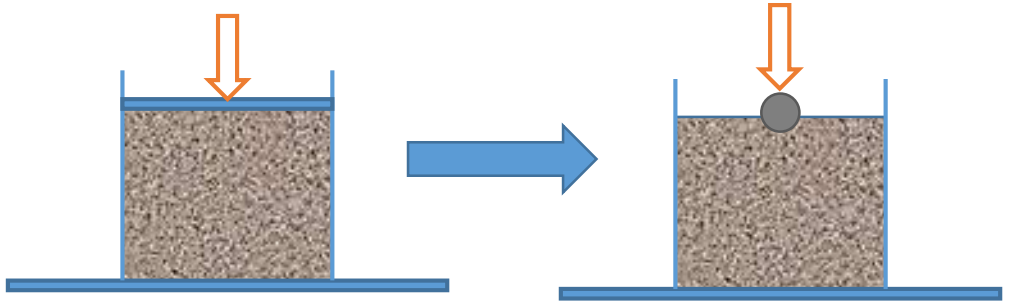
Comment	Packing state differs	Difficult to provide a flat surface for indentation	Packing state replicated in indentation test uUYS < σ_c, though reliable as flow indicator

Bed preparation

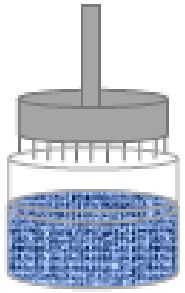

Pre-shearing

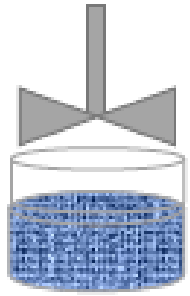

Blade conditioning

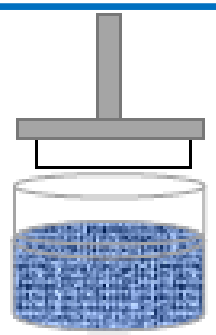

Wire conditioning

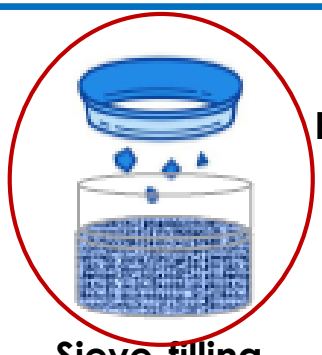

Sieve-filling

Best reproducibility (CV < 5%)

Variation for 3 indents on a single bed

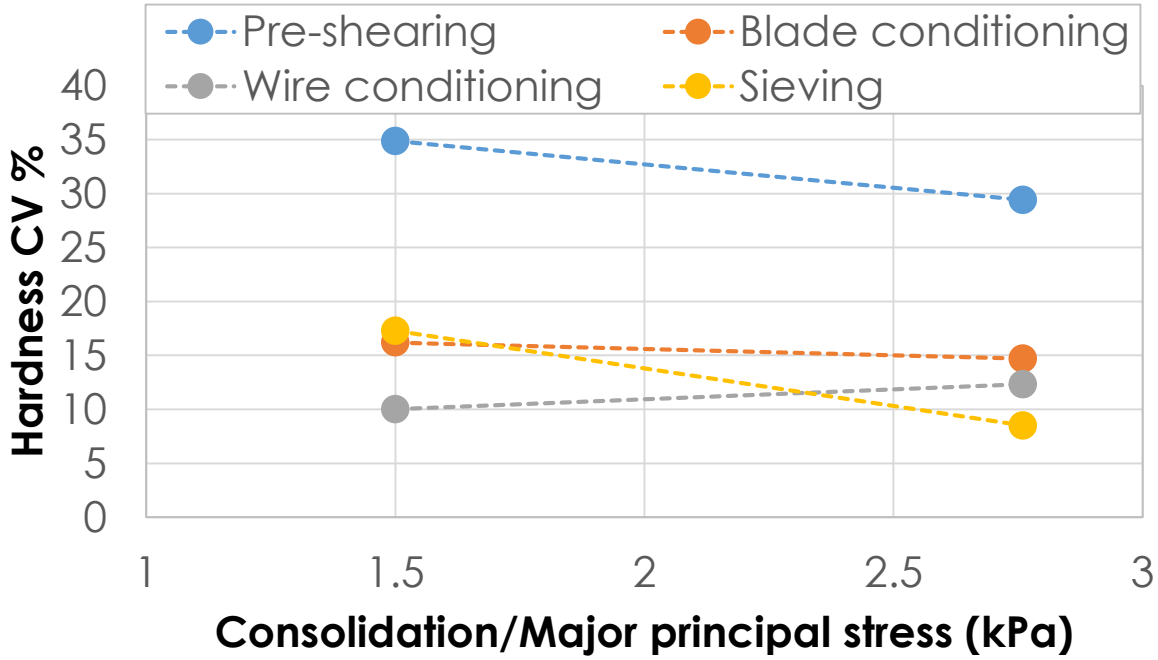

Variation for indents on 5 separate beds

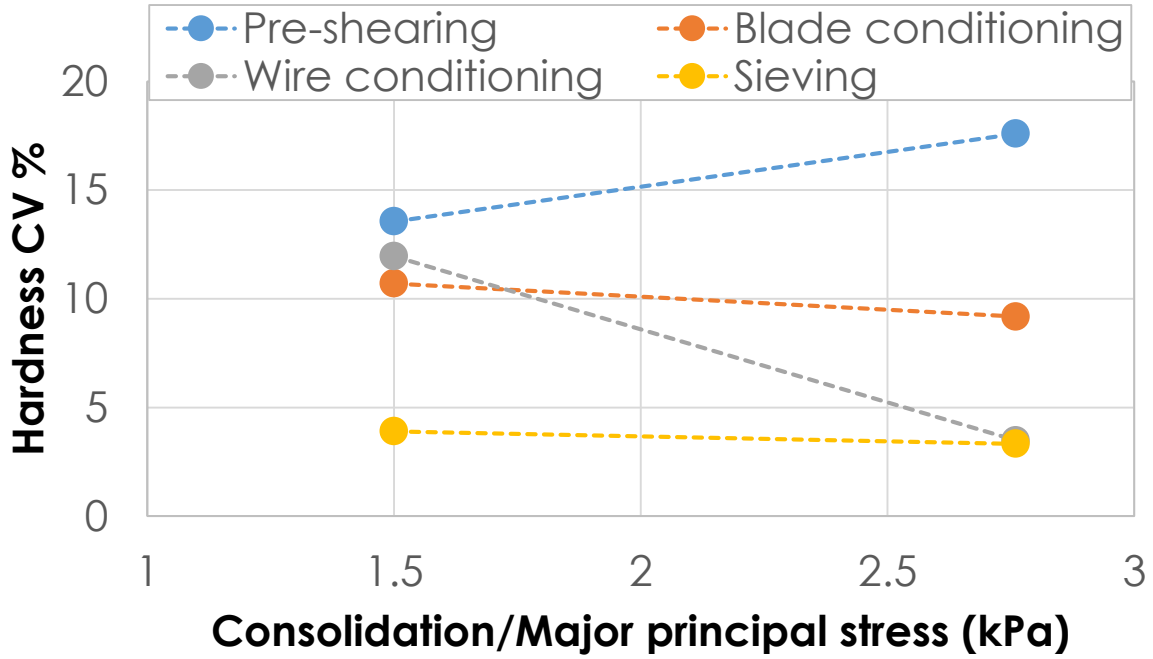

Influence of indentation method setup

How indentation test arrangements may affect

- ❑ Bed hardness
- ❑ C value
- ❑ Inferred σ_c

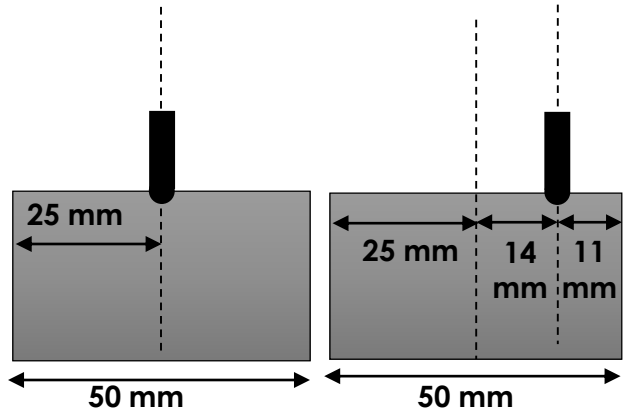

➢ **Indentation position**

- ❑ At central and radial positions (4 mm indenter)

➢ **Indenter size**

- ❑ 4, 6 and 10 mm indenters, indenting at the centre

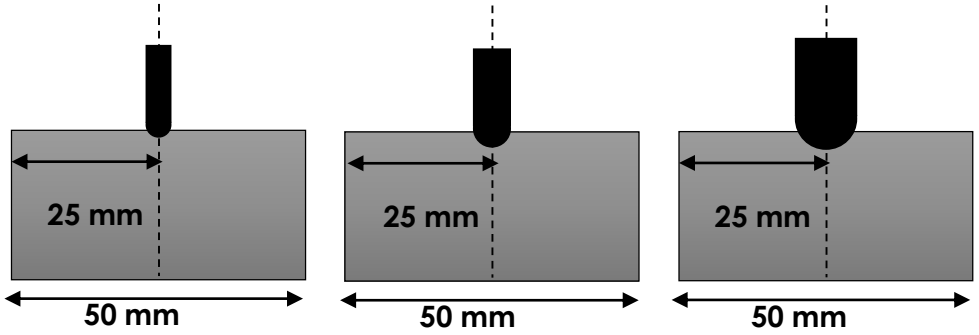

➢ **Penetration depth**

- ❑ At penetration depths of **20%** and **50 %** of indenter radius (4 mm indenter)

Indenter position

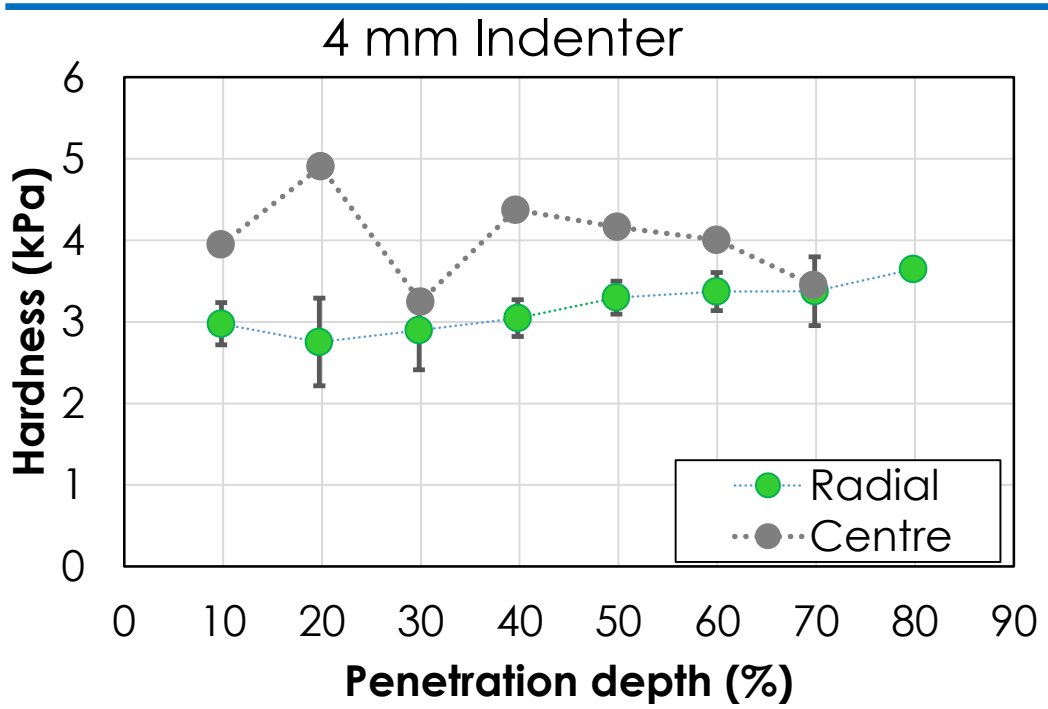

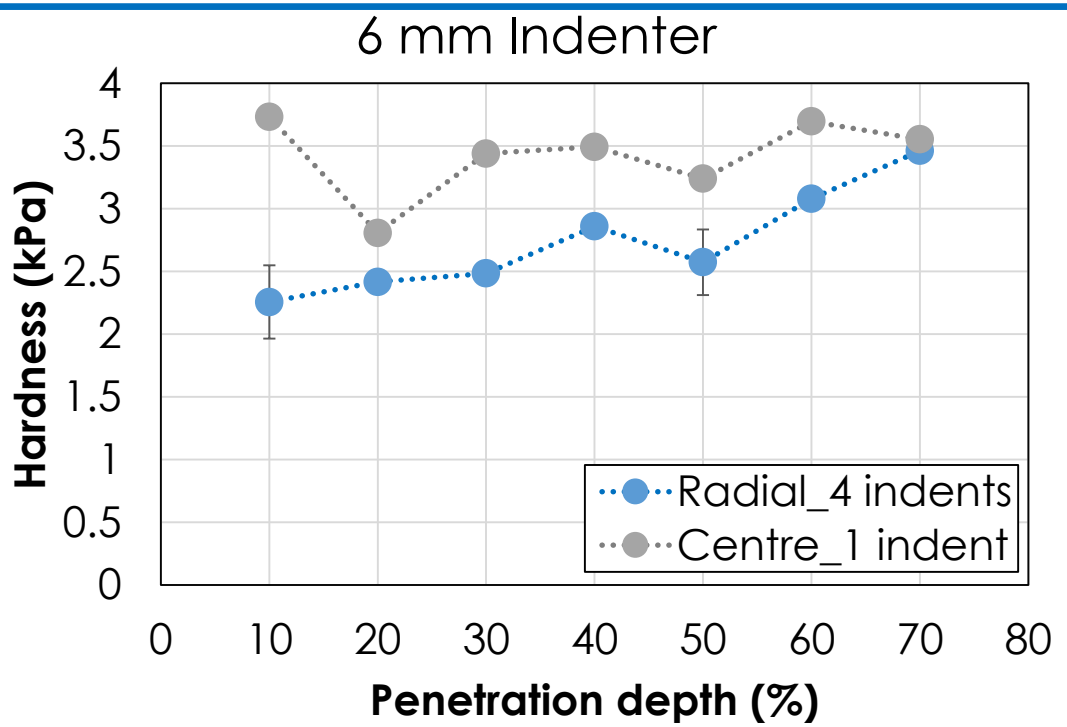

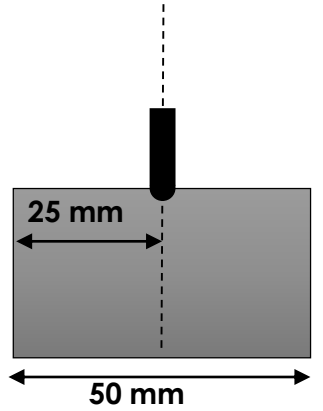

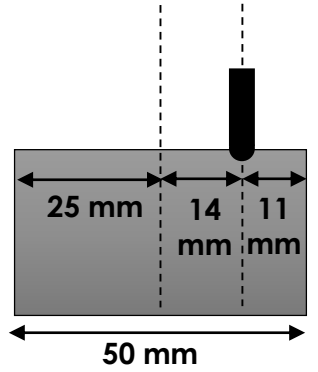

- Hardness greater in the centre
  - Agrees with findings of Hassanpour and Ghadiri (2007)[1]
- This may be due to greater packing fraction in the centre

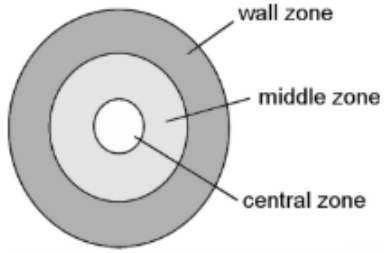

Indentation zone classification[1]

[1] Hassanpour, A., Ghadiri, M., 2007, *Particle & Particle Systems Characterization*, 24 (2), 117-123.

Penetration depth: influence on hardness

Silanised glass beads 63-75mm[4]

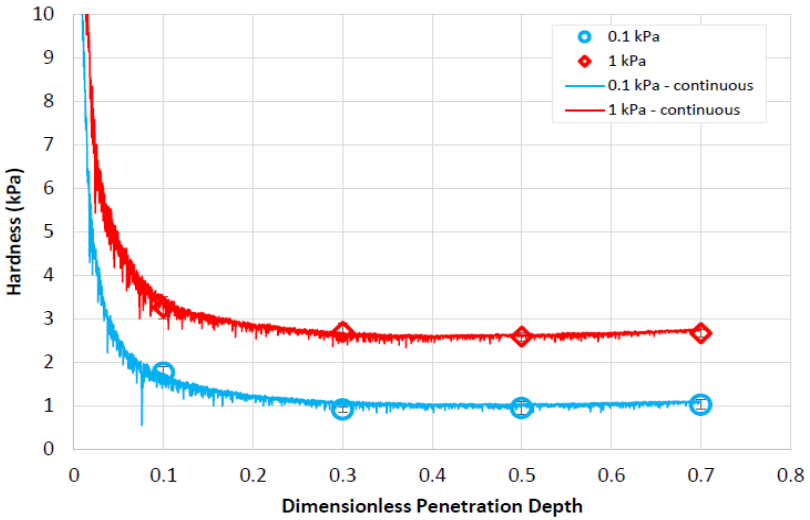

Alumina[6]

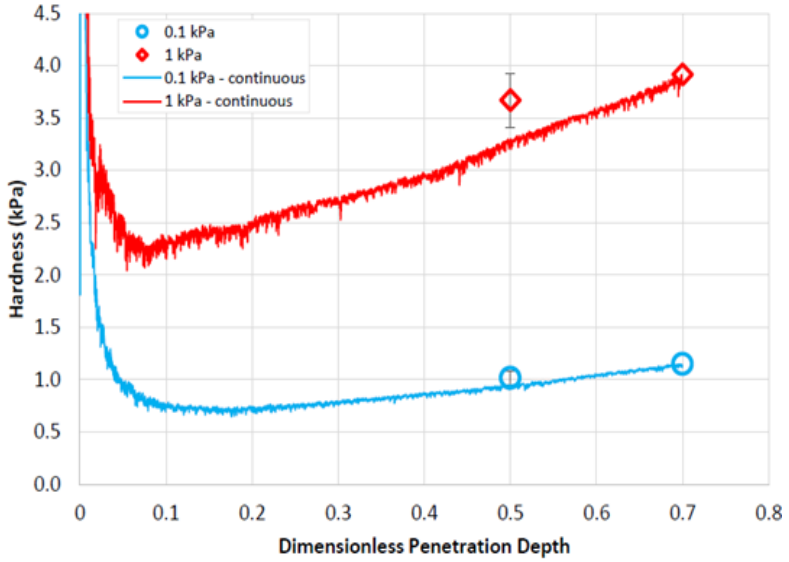

Titania – at 1 kPa

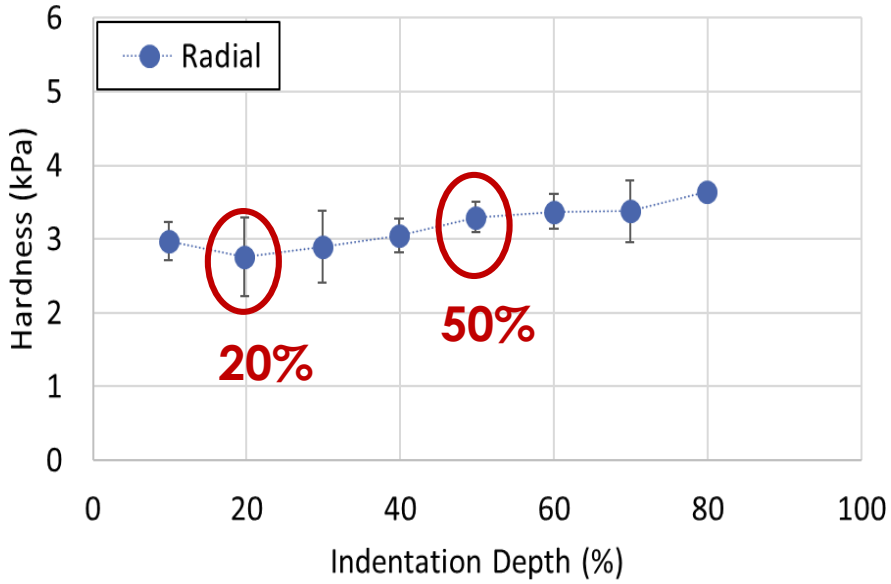

[4]Stavrou, A., Hare, C., Hassanpour, A., Wu, C-Y., 2020, *Powder Technology*, 364, 98-114.
[6]Stavrou, A., 2019, Doctoral Thesis, *University of Surrey*.

Penetration depth: influence on C and *uUYS*

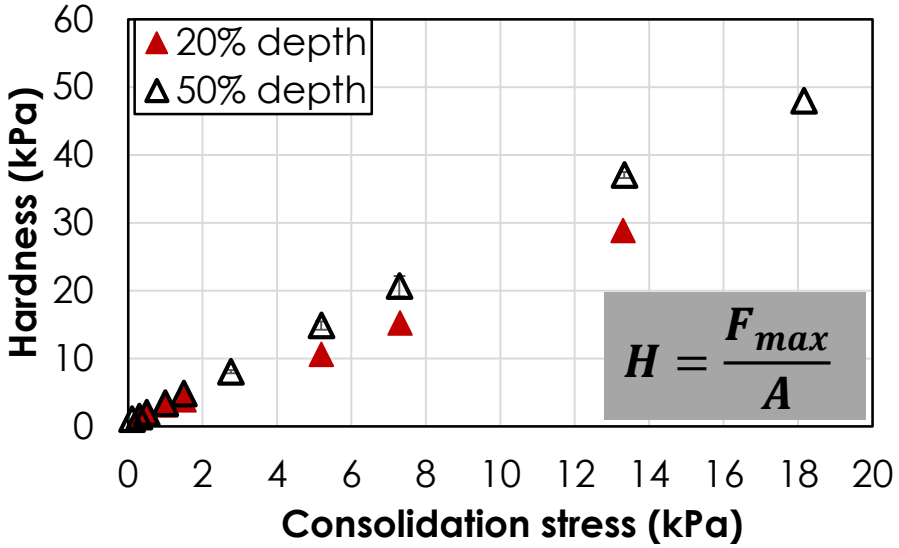

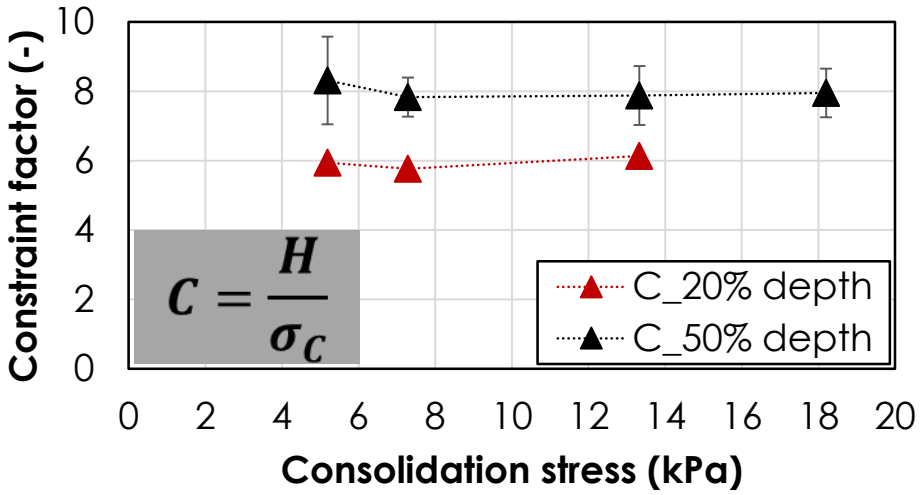

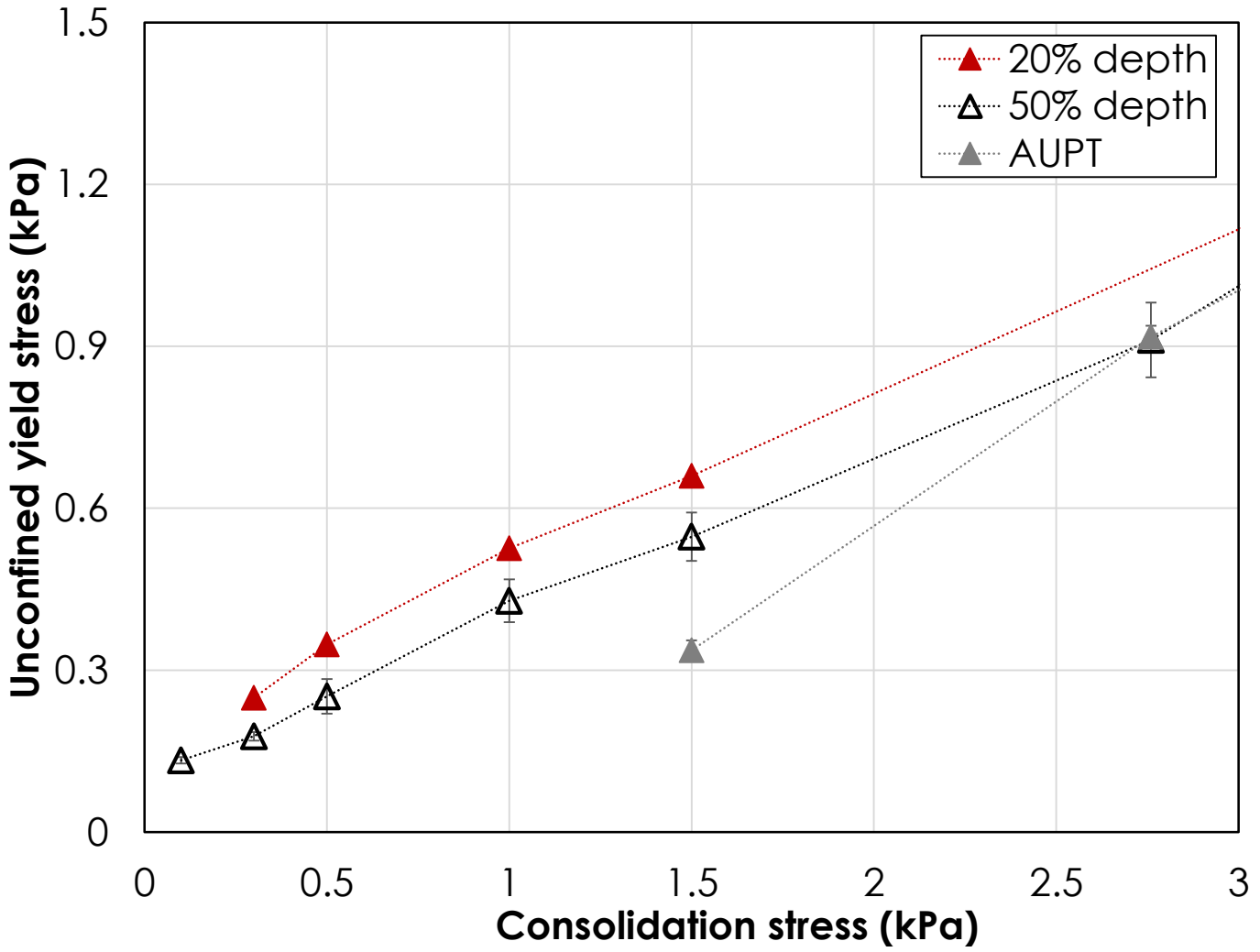

Indenter size

d_{Ind}	Depth	10 %		20 %		30 %		40 %		50 %		60 %		70 %	
		h (mm)	F_{max} (mN)	h	F_{max}	h	F_{max}	h	F_{max}	h	F_{max}	h	F_{max}	h	F_{max}
4 mm		0.2	9.23	0.4	22.1	0.6	20.8	0.8	34.9	1	39.2	1.2	42.3	1.4	39.4
6 mm		0.3	19.9	0.6	28.5	0.9	50	1.2	63	1.5	68.7	1.8	87.7	2.1	91.4
10		0.5	32.7	1	81.7	1.5	112.1	2	139	2.5	160	3	211	3.5	248.6

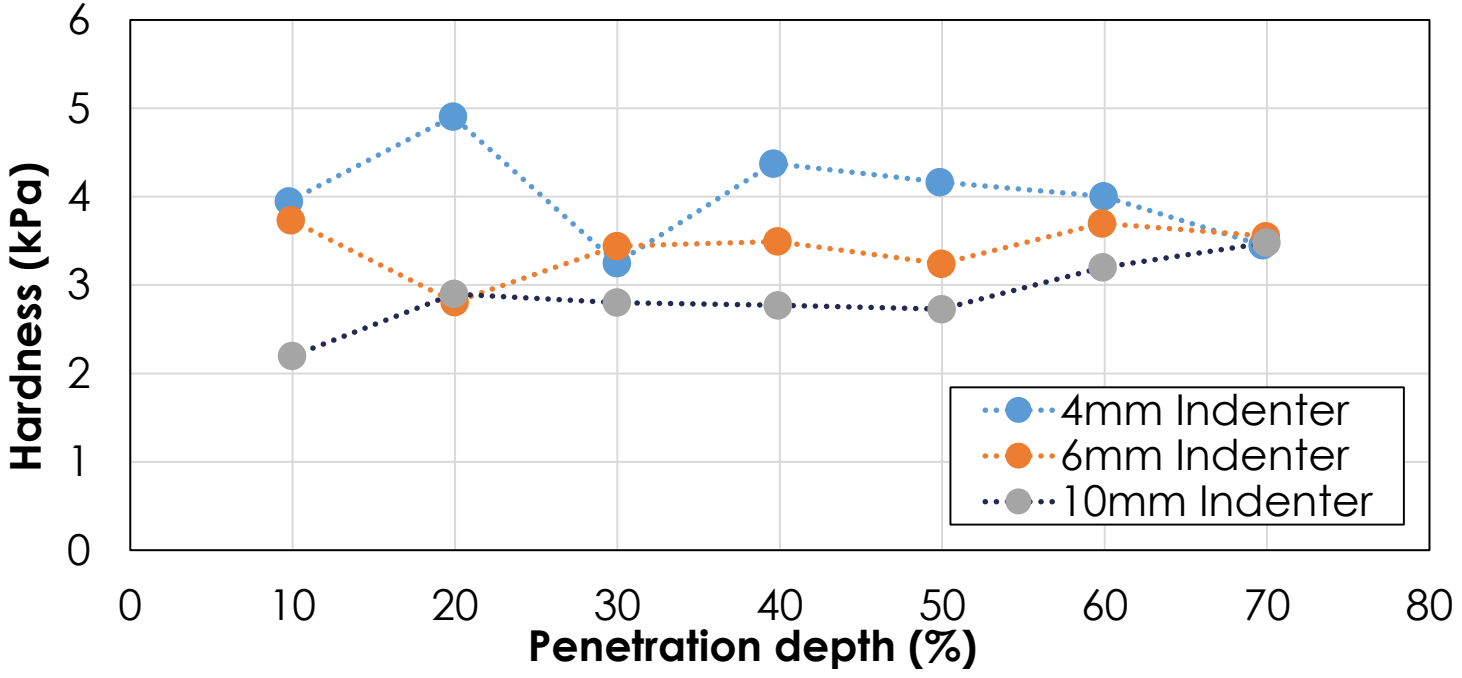

- Fluctuations largest for smallest size
  - Smaller force measured
- Largest indenter gives most consistent results
- *H* is lower for larger indenters
  - Suggests F_{max} is overestimated for small indenters

Measurement accuracy: consolidation stress

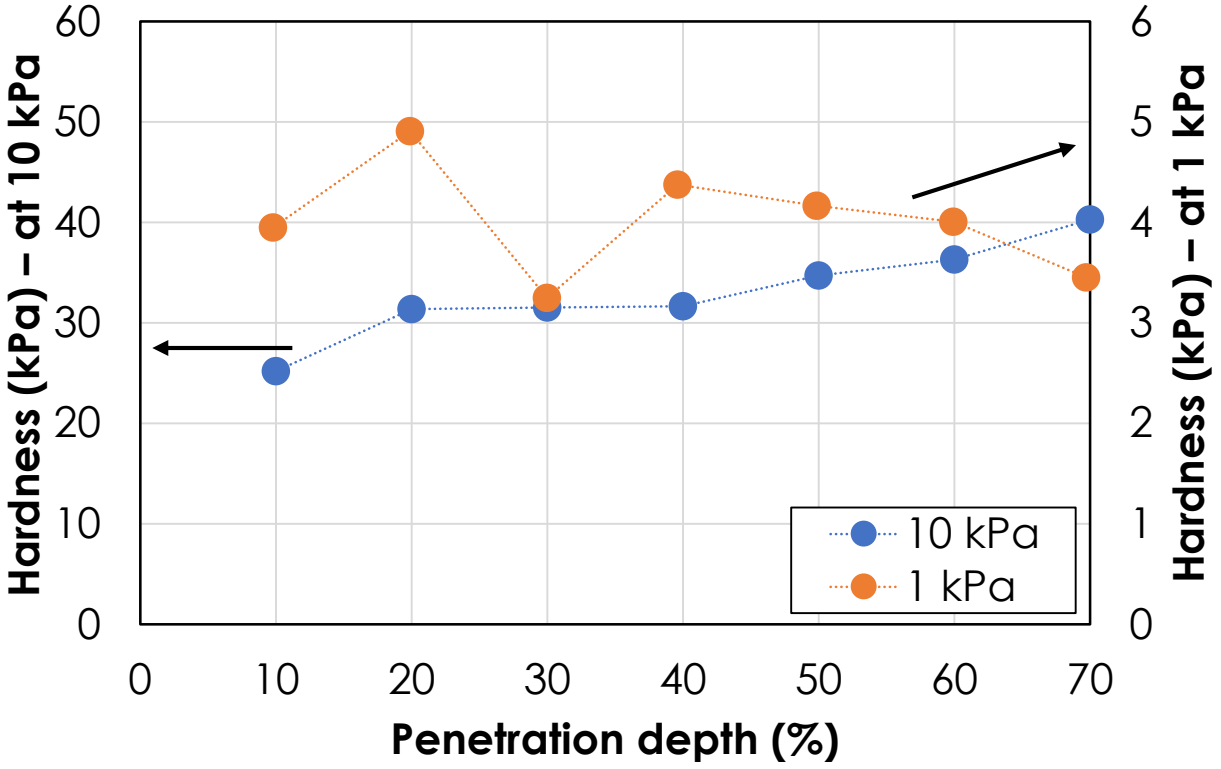

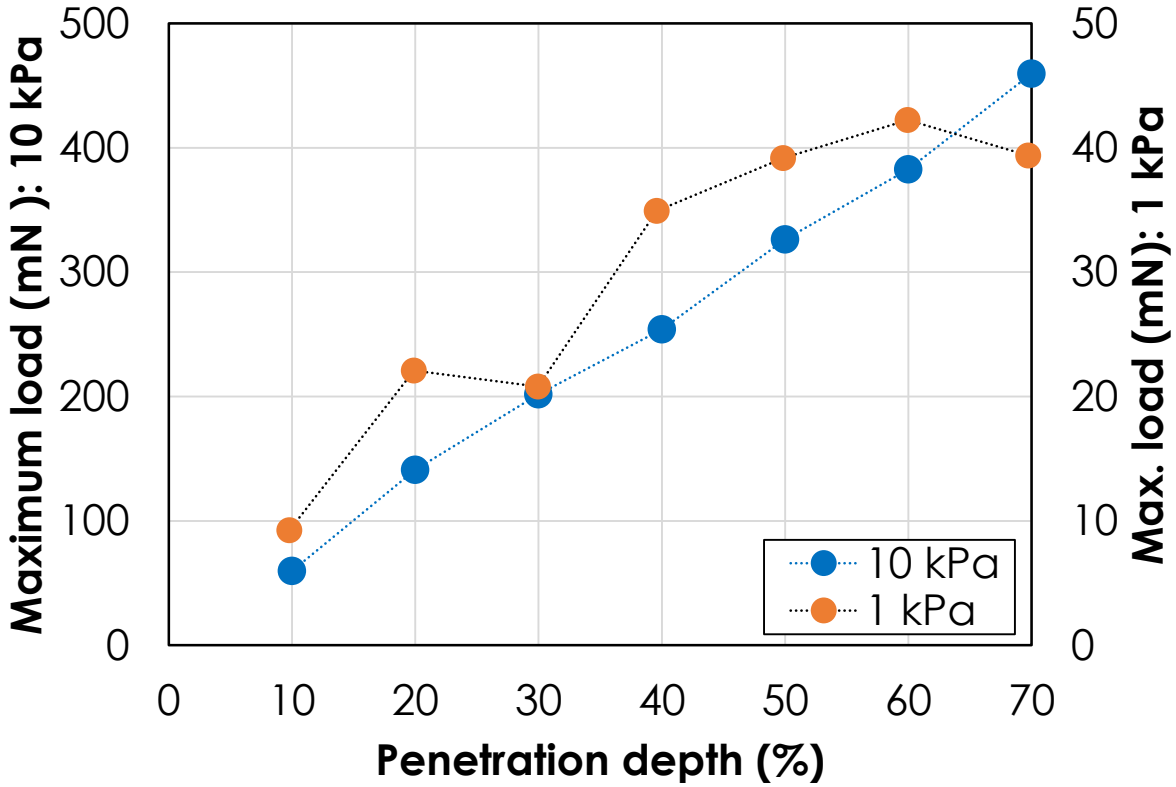

- Lower force measured at low consolidation stress
  - Hence greater fluctuations in hardness with depth

$$H = \frac{F_{max}}{A} = \frac{F_{max}}{\pi(dh - h^2)}$$

Measurement accuracy: indenter size

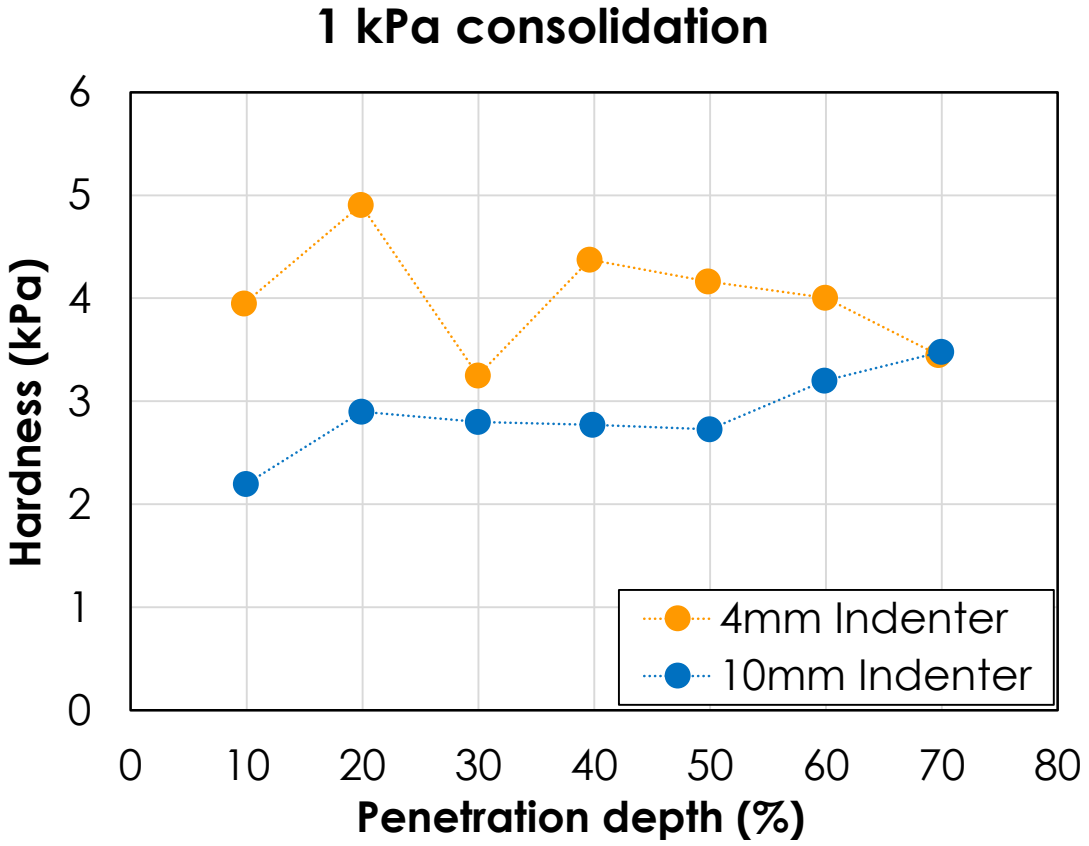

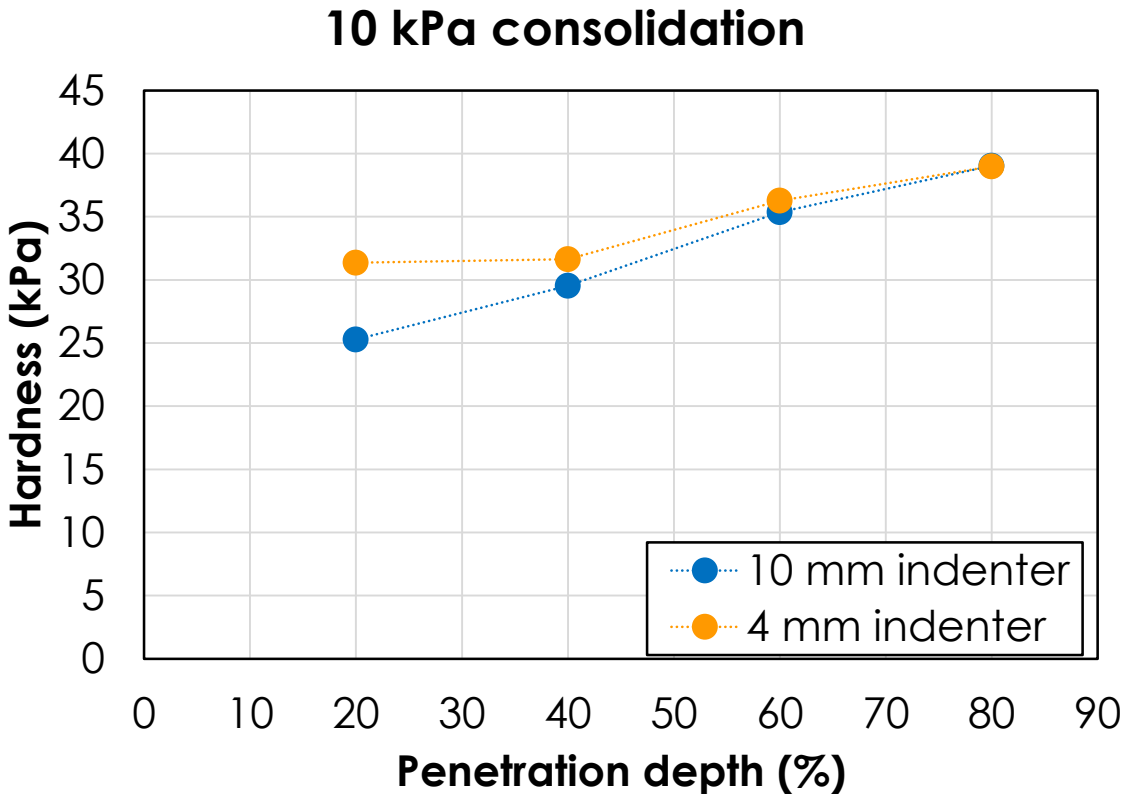

- For given dimensionless penetration depth, force increases with indenter size & consolidation stress
  - At higher consolidation the 4 & 10 mm indenters agree

Indentation onto sieved beds - titania

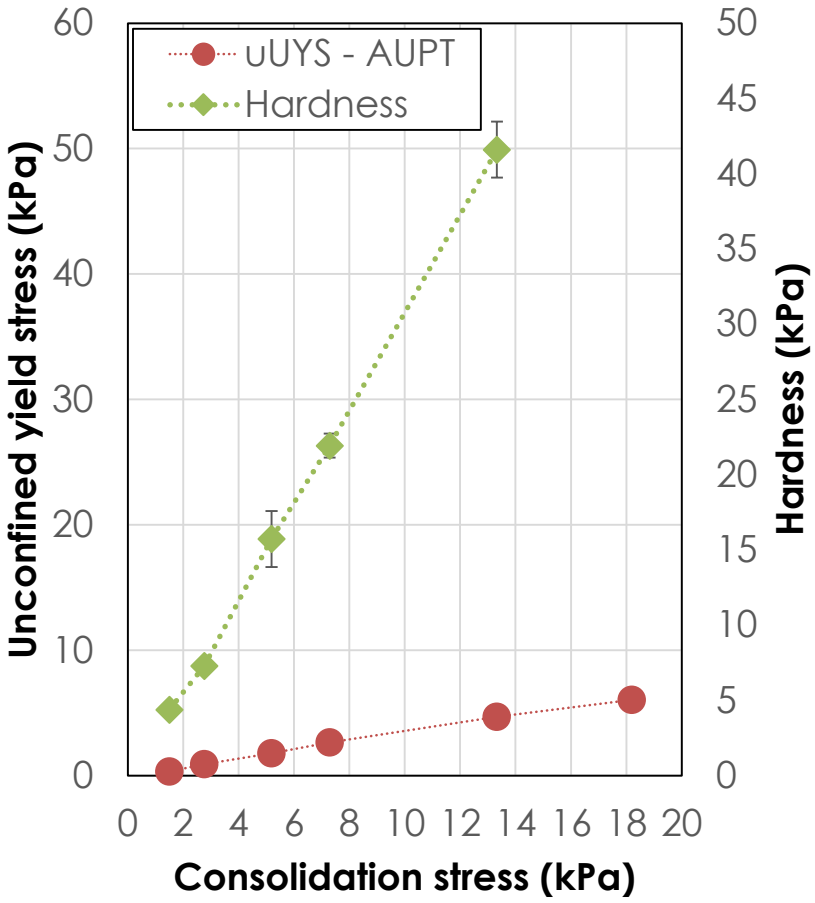

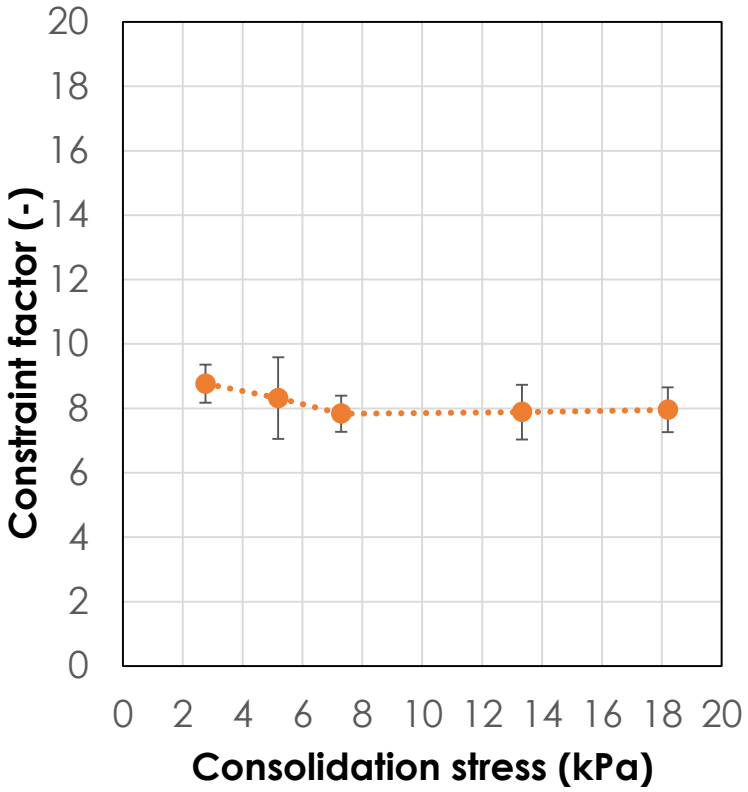

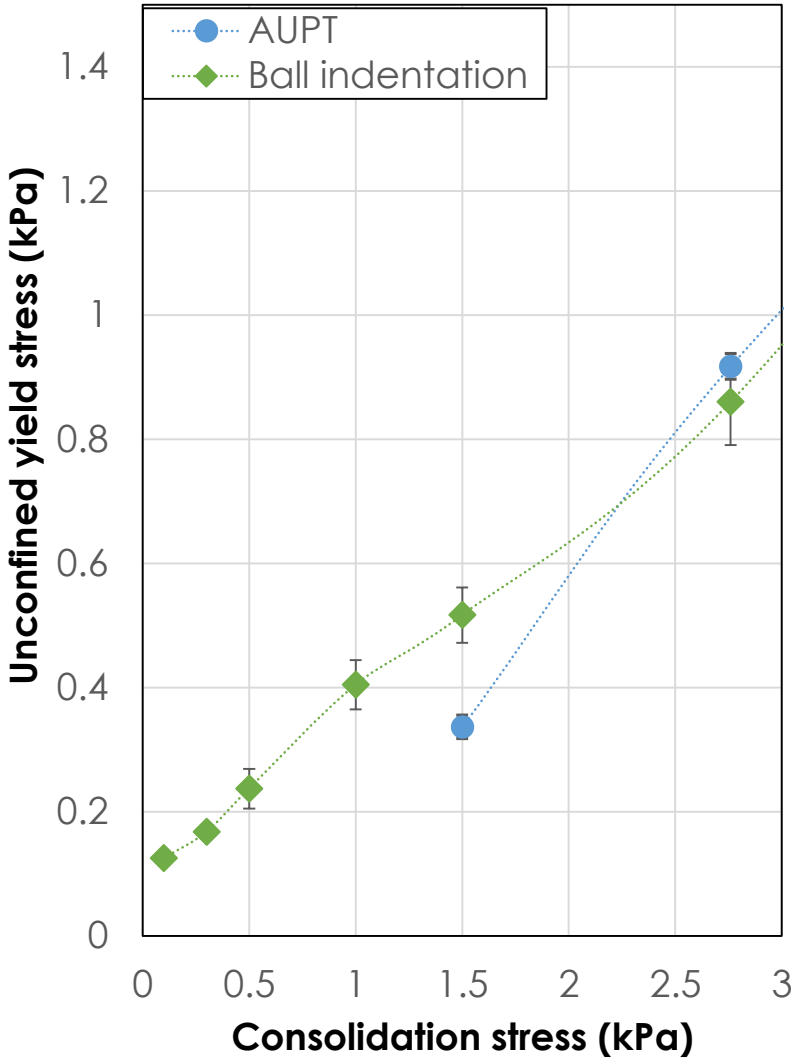

Comparison of techniques

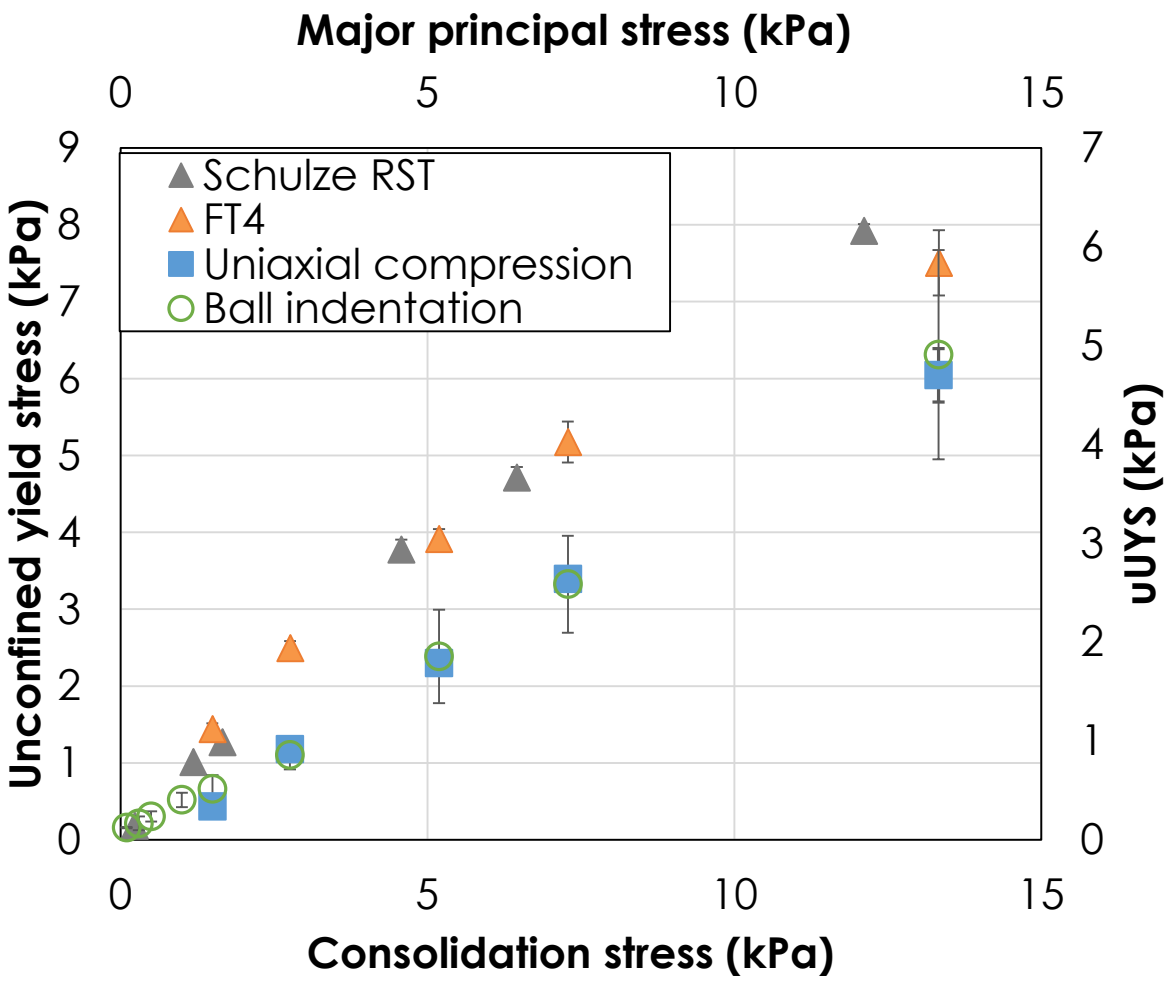

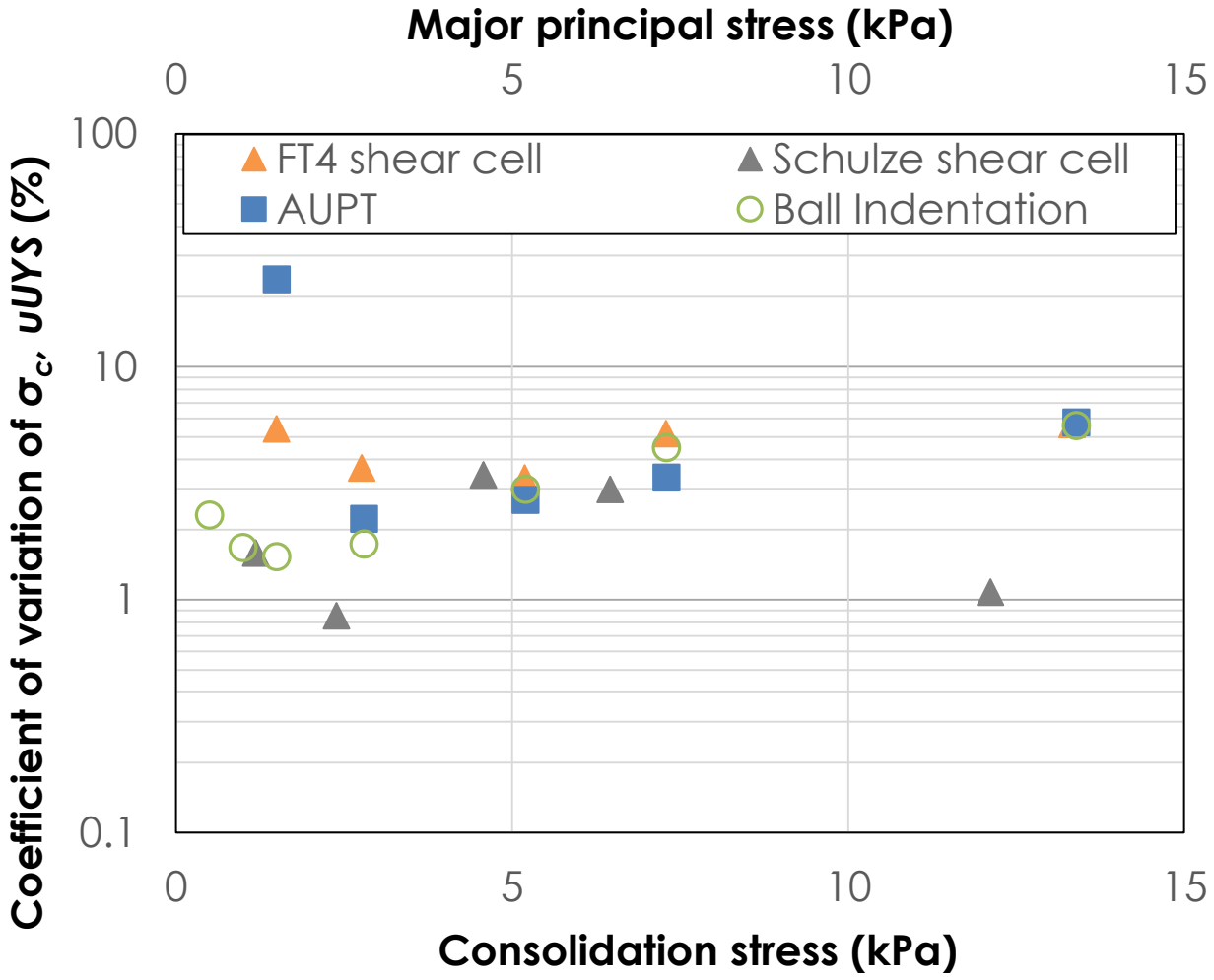

Measurement accuracy: test flow through a hopper

- Powder flow properties required for the design:
  - **Flow function** (from **shear cell tests**) – or from **ball indentation**
  - **Effective angle of friction** (from shear cell test)
  - **Wall friction angle** (wall friction test)
  - **Bulk density** (compressibility test)
- Need to determine:
  - **Hopper half angle, θ (from vertical)**
  - **Outlet size, *B***

Critical mass flow hopper angle depends on:

- The hopper geometry (conical or planner)
- The powder's **effective angle of friction, δ_e**
- The powder's **wall friction angle, ϕ**

Analytical description of the theoretical boundary between the mass flow and funnel flow regions for conical hoppers[7,8]:

$$\theta = \frac{\pi}{2} - \frac{1}{2} cos^{-1}\left(\frac{1 - sin\delta_e}{2sin\delta_e}\right) - \beta$$

Where β is the angle formed between the major principal axis and a line normal to the hopper wall

$$2\beta = \varphi + sine^{-1}\left(\frac{sin\varphi}{sin\delta_e}\right)$$

[7] Mehos, G., Hopper Design Principles for Chemical Engineers.
[8] Enstadt, G., *Chemical Engineering Science*, 30, 1273-1283.

Hopper design:

- Jenike (1961)[9] defined ratio of σ_1 to the arch support stress ($\bar{\sigma}$) as the flow factor, *ff*
- The flow factor is a function of θ, ϕ, and δ:

$$ff = \frac{Y(1+sin\delta_e)H(\boldsymbol{\theta})}{2(X-1)(sin\boldsymbol{\theta})}$$

$$X = \frac{2^{\boldsymbol{m}}sin\delta}{1-sin\delta}\left[\frac{\sin(2\beta+\theta)}{sin\theta}+1\right]$$

$$Y = \frac{[2(1-\cos(\beta+\theta))]^{\boldsymbol{m}}sin\theta(\beta+\theta)^{1-\boldsymbol{m}}+sin\beta sin^{1+\boldsymbol{m}}(\beta+\theta)}{(1-sin\delta)sin^{2+\boldsymbol{m}}(\beta+\theta)}$$

where ***m*** is equal to 1 for circular outlets and 0 for slotted outlets

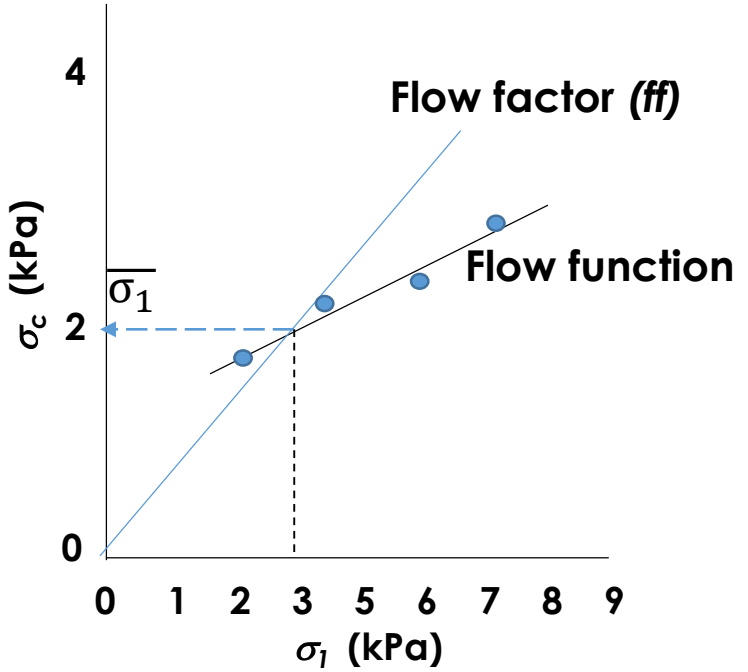

Hopper design – Outlet size (B):

$$B = H(\theta).\frac{\overline{\sigma_1}}{g.\rho_b}$$

$$H(\theta) = \left(\frac{130° + \theta}{65}\right)^{m}\left(\frac{200° + \theta}{200°}\right)^{1-m}$$

$\boldsymbol{B}$: minimum outlet diameter to avoid arching (m)

H(θ): Factor depends on angles of internal friction and wall friction

$\overline{\boldsymbol{\sigma_1}}$: Critical unconfined yield strength (Pa)

$\boldsymbol{\rho_b}$: bulk density (kg/m^3)

[9] Jenike, A. W., 1961, *University of Utah Engineering station*, Bulletin 108.

Actual outlet size required for flow

- We aim to use a small volume of powder ~ 5 litres
  - Require small outlet size
- Require arch support stress, $\bar{\sigma}$ = 0.1-1 kPa

- Therefore need powder to be:
  - Cohesive
  - Moderately high bulk density

- Preferably
  - Hopper angle should be fixed
  - Outlet size free to vary
    - Without significant change in hopper height
    - Requires hopper angle > 20°

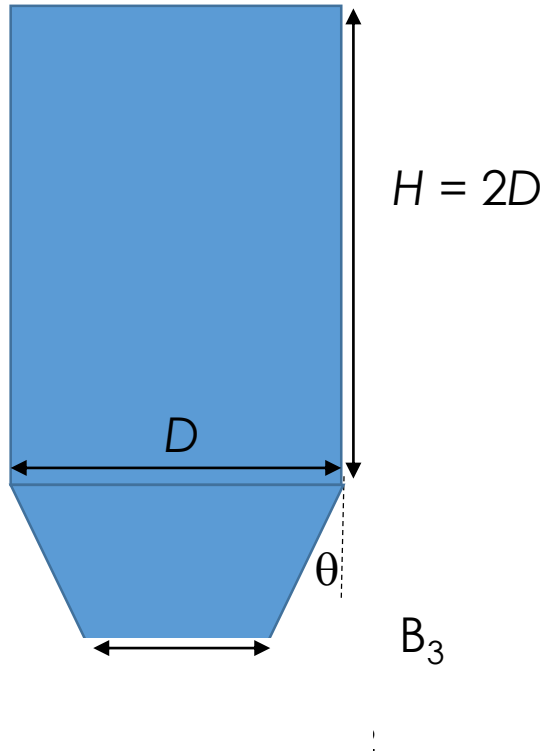

Hopper design for tested powders

	Stress range (σ_{pre}, kPa)	FF_c (-)	Loose Bulk density (g/ml)	δ_e (°)	ϕ (°)	$\overline{\sigma_1}$ (kPa)	ρ (g/ml)	θ (°) before subtracting safety factor	Outlet size, B (cm)
Titania moderate σ_{pre}	2-16	1.8 – 5	0.34	51	**25.9**	3.24	0.5	19	145
Titania low σ_{pre}	0.2 - 1.6	1.1 – 1.2	0.34	66.5	**33.7**	0.43	0.38	10.8	25
Gypsum	0.2-0.8	1.2 – 1.7	**0.74**	67	38.2	0.34	0.85	5.1	10
Flour	0.1-0.8	1.1 - 2	0.54	66	35.4	0.24	0.61	9	9
MCC	0.1-1	2.5-4.2	0.32	44.4	25.2	0.06	0.37	19.8	4
MCC - coated disc	0.1-1	-	0.32	44.4	17.6	0.06	0.37	**29**	4

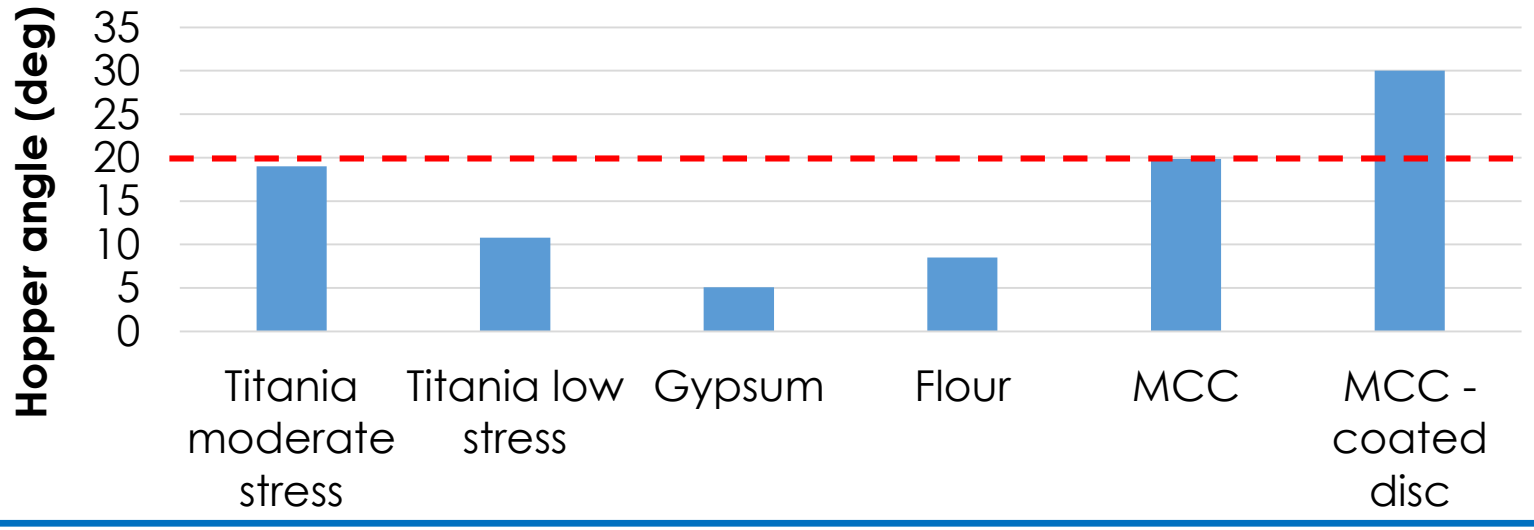

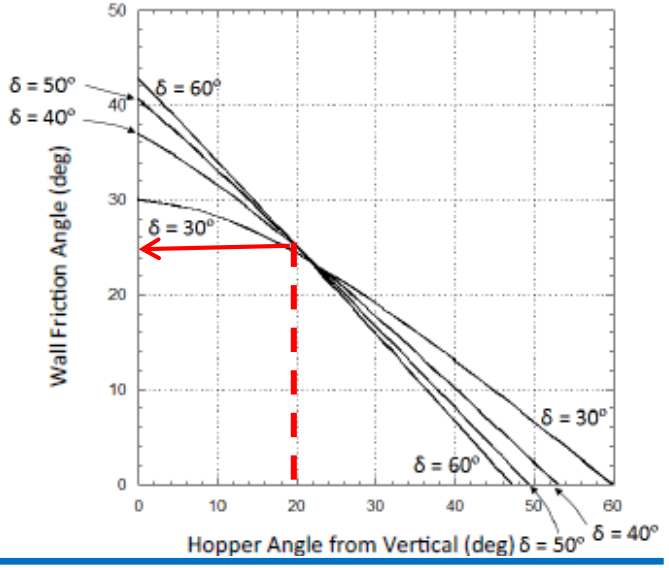

Conclusions

- For ball indentation, constraint factor correlations found for:
  - Particle properties: size, size distribution, surface energy, friction
  - Flow properties: flow function coefficient, angle of internal friction

- Challenges of powder flow measurement at low stress
  - Reproducibility of bed preparation method
  - Resolution & accuracy of the force sensor

- Reproducible measurements provided by:
  - Indentation – sieve-filled bed, vertical consolidation, multiple indents on bed
  - Schulze RST.XS.s with low stress cell

Future work

- Accuracy of the measurement to be tested by hopper flow behaviour
  - Based on flow functions from
    - Ball indentation
    - Schulze RST.XS.s
- Packing fraction distribution in ball indentation measured by X-Ray tomography
- Ball indentation, uniaxial compression and shear cell measurements carried out for further materials, to:
  - Determine constraint factor
  - Compare the measurements
  - Establish the operability range

Environmentally Responsive "Smart" Particles

Presented: IFPRI 2020 Virtual AGM

IFPRI
International Fine Particle Research Institute

Southwest Research Institute

James Oxley, Ph.D.
Staff Scientist
James.Oxley@swri.org
Prepared May 22nd, 2020

Objectives & Scope

The Search

- Resources:
  - Scopus
  - Google Scholar
  - Patents, Company websites
- Terms:
  - ‘smart particles’, ‘sensor particles’
  - Variations: microspheres, microparticles, environmental, etc.
- Target: academia and industry

The Details

- Operating principles
- Detection
- Analysis
- Control methodologies
- Size range
- Response sensitivity
- Manufacturing

Results

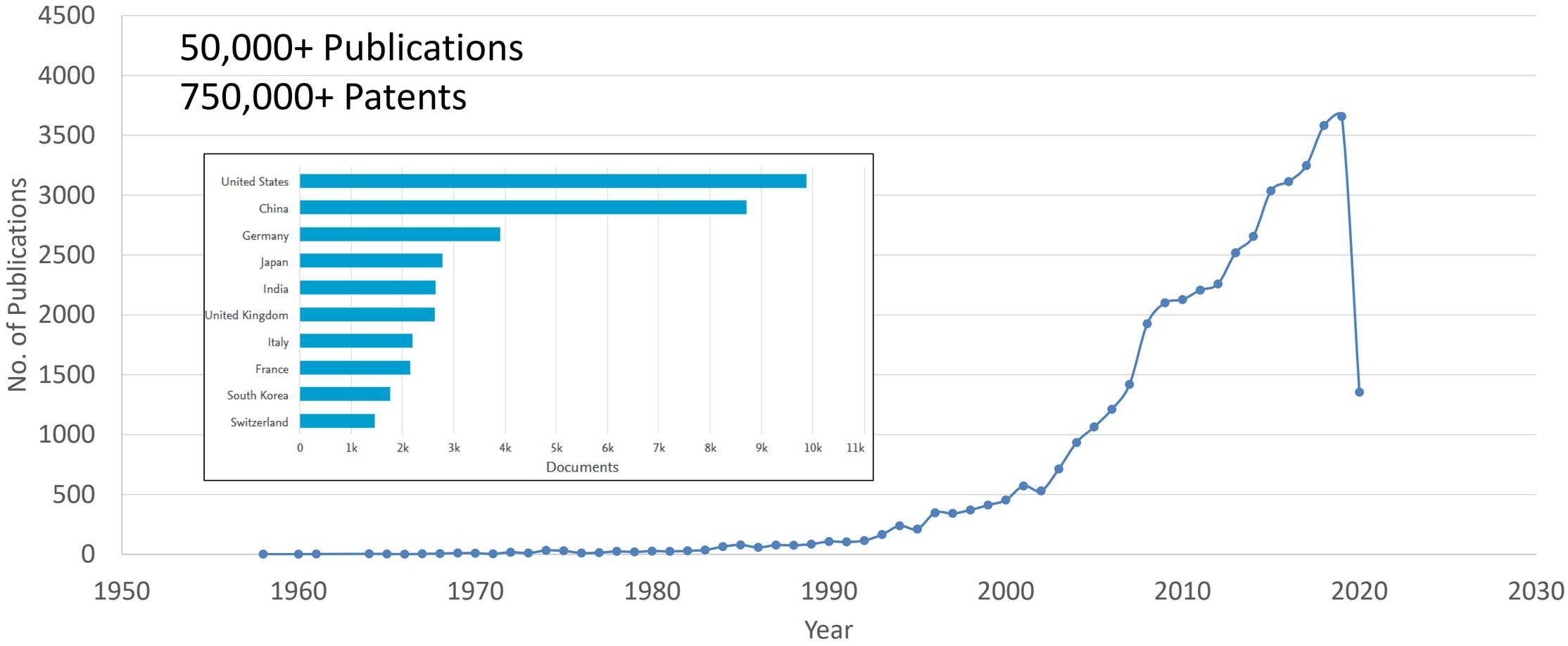

Focusing on publications; filtering based on citation index and keywords.

Organization by Trigger/Stimuli

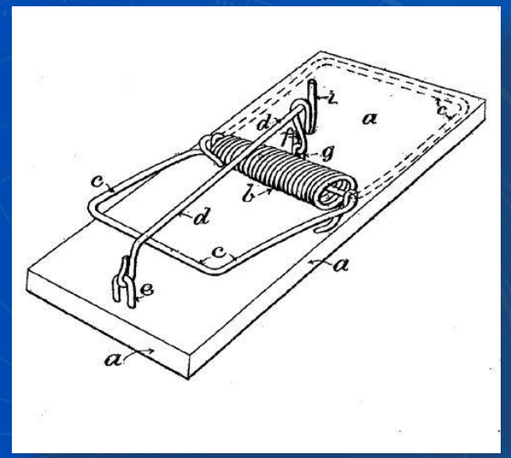

Mechanical

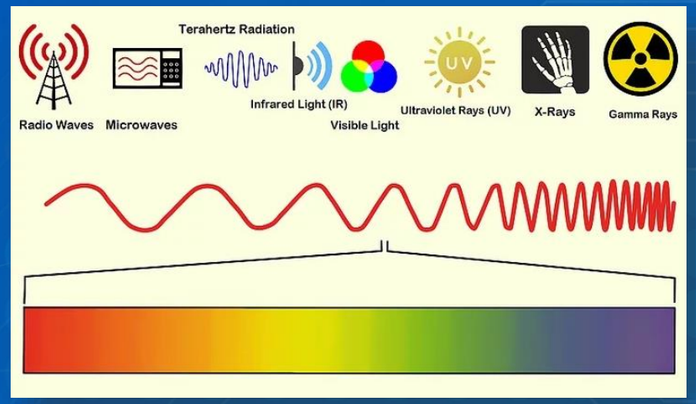

Electromagnetic

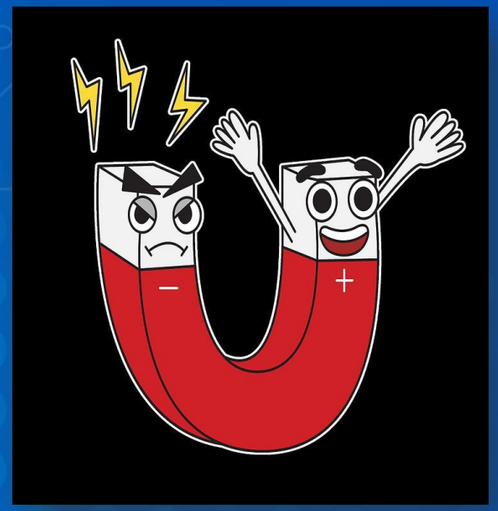

Magnetics

Thermal

Chemical/pH

Other/Misc

Mechanical

- Applications:
  - Carbonless copy paper
  - Pressure mapping
  - Scratch N' Sniff
  - Adhesives
- Mode of Action
  - Core-shell microcapsules
  - Mechanical fore releases capsule contents
  - Contents: color chemistry, fragrance, adhesives

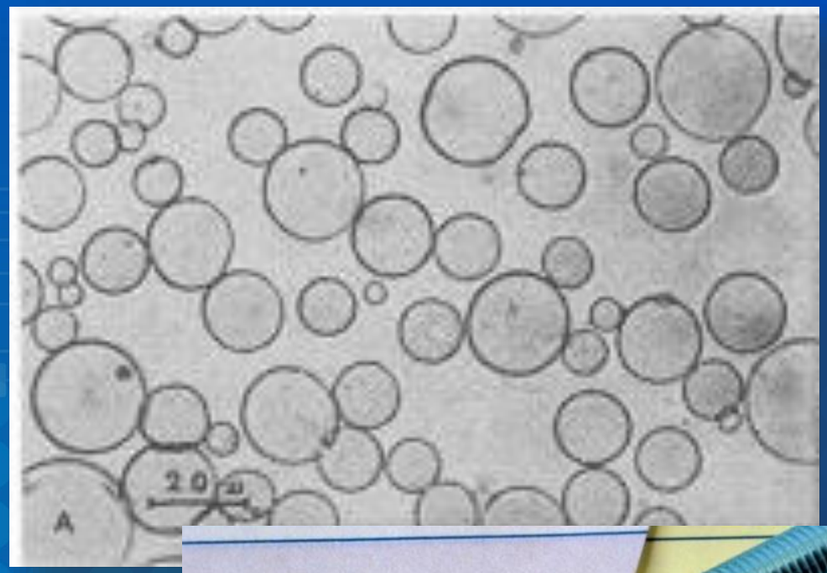

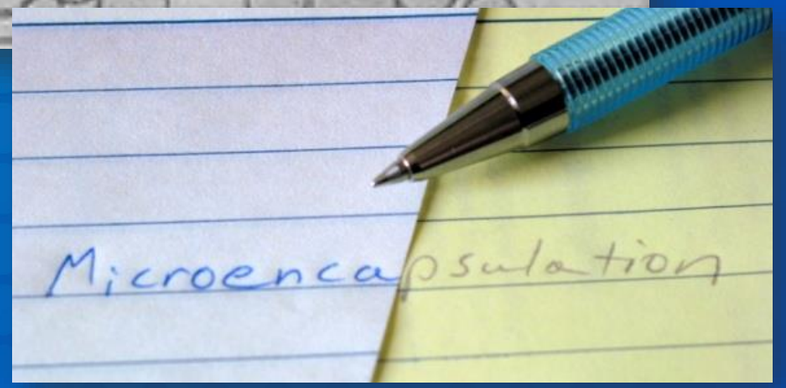

Mechanical Example

- FujiFilm Prescale
- Pressure sensing film applications
- Encapsulated color chemistry activated with microcapsule rupture
- Range: 7.25 to 43,500 psi
- Resolution (spatial): 5-15 µm
- Detection: colorimetric
- Control: color intensity, orientation of developer sheet and capsules
- Manufacturing: interfacial polymerization, polyurea

https://www.fujifilm.com/products/prescale/prescalefilm/

Mechanical Example, cont.

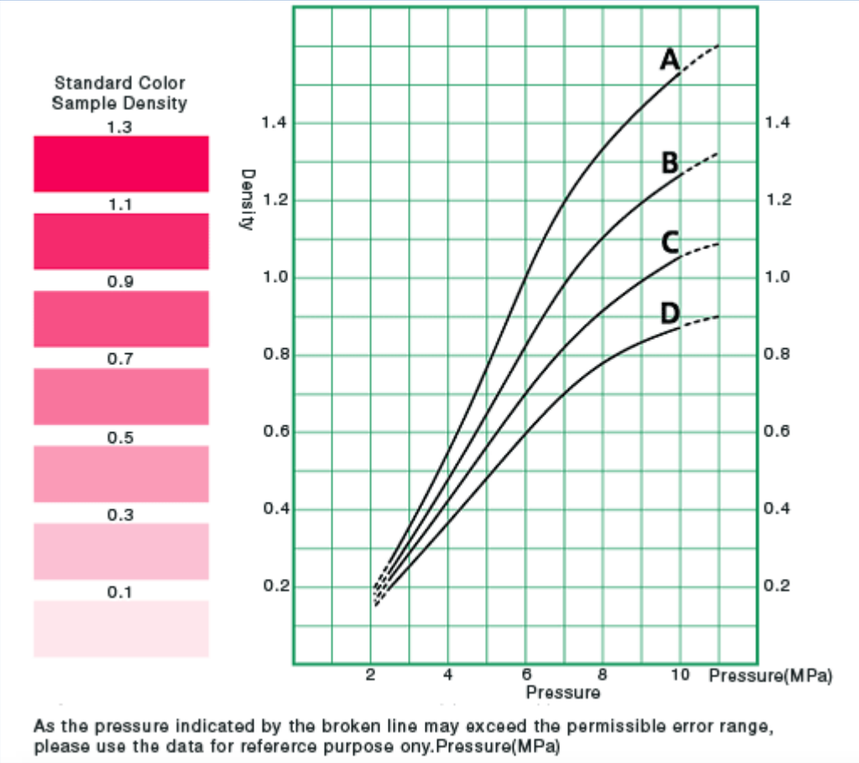

Gasket/seal

Pressure Film Type	Code	Alternative Code	Pressure Range
Ultra Extreme Low	5LW	UXL310	0.87 - 7.3 PSI (0.06 - 0.51 kg/cm^2)
Extreme Low	LLLLW / 4LW	XL310	7.2 - 28 PSI (0.5 - 2 kg/cm^2)
Ultra Low	LLLW	UL270	28 - 85 PSI (2 - 6 kg/cm^2)
Super Low	LLW	SL270	70 - 350 PSI (5 - 25 kg/cm^2)
Low	LW	L270	350 - 1,400 PSI (25 - 100 kg/cm^2)
Medium	MS	M270	1,400 - 7,100 PSI (100 - 500 kg/cm^2)
High	HS	H270	7,100 - 18,500 PSI (500 - 1,300 kg/cm^2)
Super High	HHS	SH270	18,500 - 43,200 PSI (1,300 - 3,000 kg/cm^2)

Physical Specifications	
Operating Temperature	68°F - 95°F (20°C - 35°C) *much higher for brief exposure*
Humidity Range	20% to 90% RH
Gauge (Thickness)	4 - 20 mils
Spatial Resolution	From 5 - 15 microns
Substrate	Polyethylene Terephthalate (PET)
Accuracy	± 10% visual, ± 2% *Utilizing optional optical measurement systems*
Shelf Life	2 Years

https://www.fujifilm.com/products/prescale/prescalefilm/

Thermal

- Applications
  - Energy phase change materials
  - Expancel
  - Display phase change material (e.g. liquid crystals)
- Mode of action
  - Thermal absorption
  - Triggers phase change
  - Solid → liquid
  - Liquid → gas

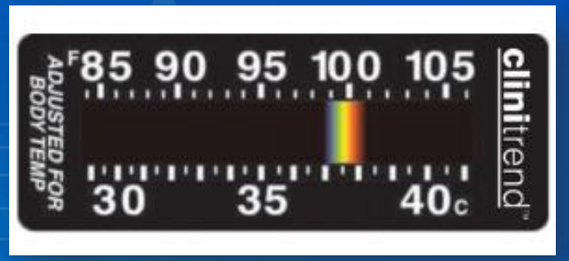

Thermal Example

- LCR Hallcrest microcapsules
- Liquid crystal containers
- Phase change activated by heat
- Range: -30 °C to 120 °C
- Precision: +/- 0.1 °C
- Accuracy: +/- 1 °C
- Detection: colorimetric, observation
- Control: liquid crystal chemistry
- Manufacturing: complex coacervation with gelatin/gum acacia shell

https://www.lcrhallcrest.com/

Chemical/pH

- Applications:
  - Gases
  - Ions
  - Chemical-specific sensor
- Mode of Action
  - Surface-modified particles
    - Higher surface area
    - Better suspension stability, solution homogeneity
  - Disruption/alteration of surface-bound functional groups
    - Change in optical properties (e.g. fluorescence)
    - Change in electrical properties

Chemical Example

- Luminex xMAP
- Detection and quantitation of proteins, genes, etc.
- Multiple products:
  - MagPlex
  - MagPlex-TAG
  - MicroPlex
  - MagPlex-Avidin
  - SeroMAP
- Particles: carboxylated polystyrene
- Size: 5-6 µm
- Variety: >100 unique spectral signatures
- Manufacturing: Dyeing and surface functionalization of polystyrene beads

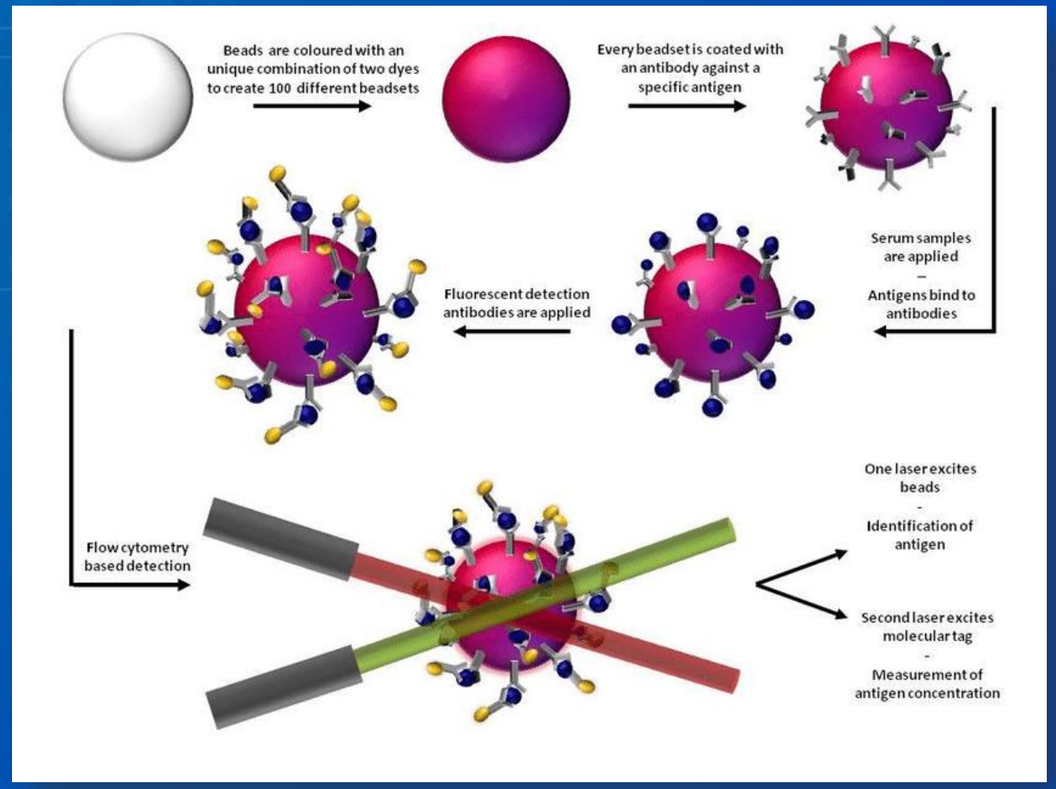

Chemical Example, cont.

- Gas detection (H_2S, formaldehyde, EtOH)
- $ZnSnO_3$ particles
- Size: ~500 nm
- Variations for sensitivity
  - 14-facted polyhedron[1]
  - Octohedron[2]
- Synthesis:
  - controlled precipitation of $ZnAc_2$ and $SnCl_4$
  - Varied surfactants and NaOH soln.
- Voltage measured across particles deposited on ceramic tube

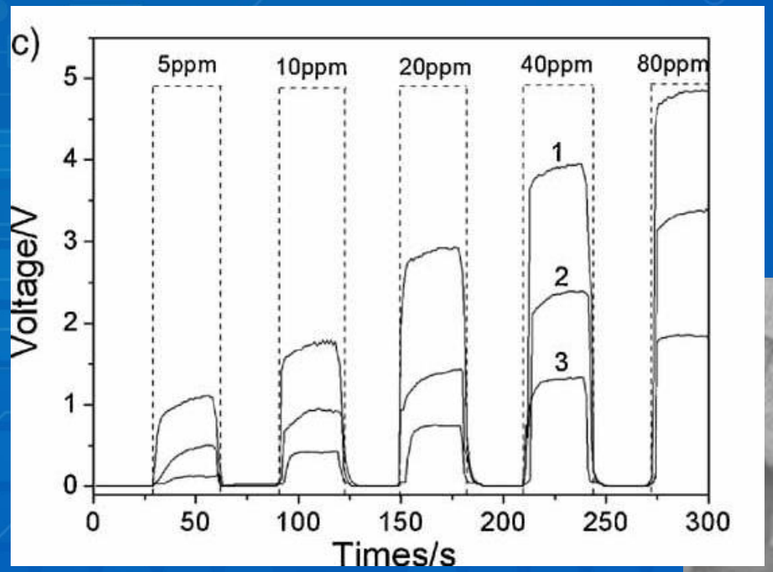

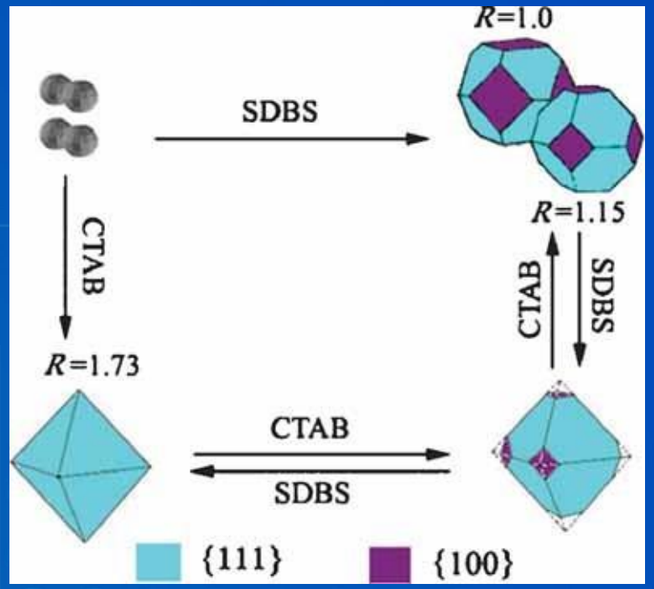

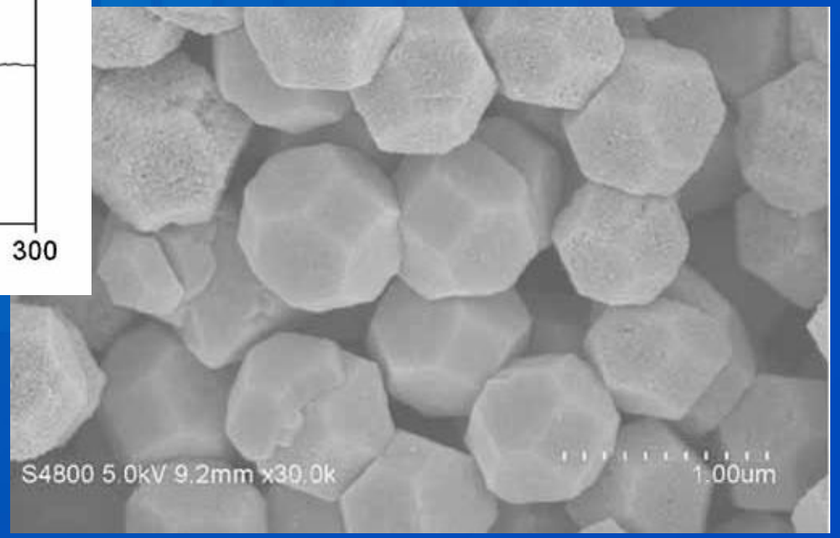

Geng, B.; Fang, C.; Zhan, F.; Yu, N. Synthesis of Polyhedral ZnSnO3 Microcrystals with Controlled Exposed Facets and Their Selective Gas-Sensing Properties. *Small* **2008**, *4* (9), 1337–1343. https://doi.org/10.1002/smll.200701177.

pH Example

- Sugar-Responsive Pickering Emulsion
- Functionalized poly(*N*-isopropylacrylamide) microgel
- Synthesis: aqueous free-radical precipitation polymerization
- Pickering with dodecane as model core oil
- Microgel size: 300-900 nm (soln. dependent)
- Emulsion size: ~200 µm
- Sensitivity: 0-20 mM

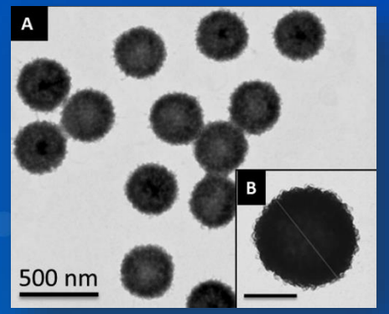

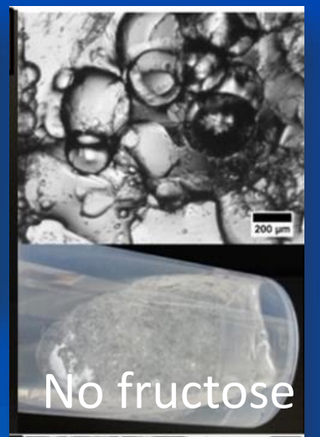

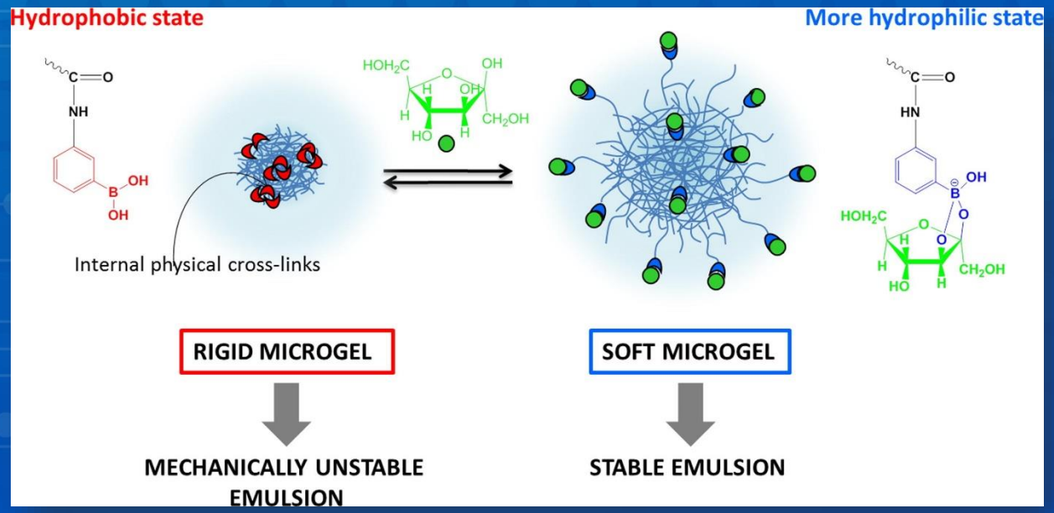

Tatry, M.-C.; Qiu, Y.; Lapeyre, V.; Garrigue, P.; Schmitt, V.; Ravaine, V. Sugar-Responsive Pickering Emulsions Mediated by Switching Hydrophobicity in Microgels. *J. Colloid Interface Sci.* **2019**, *561*, 481–493. https://doi.org/10.1016/j.jcis.2019.11.023.

Electromagnetic Radiation

Applications

- Near-IR Thermal Therapy
- Quantum Dots
- Photoresponsive release

Mode of Action

- UV/Visible absorbance → Fluorescence
- IR absorbance → heat
- UV absorbance → degradation

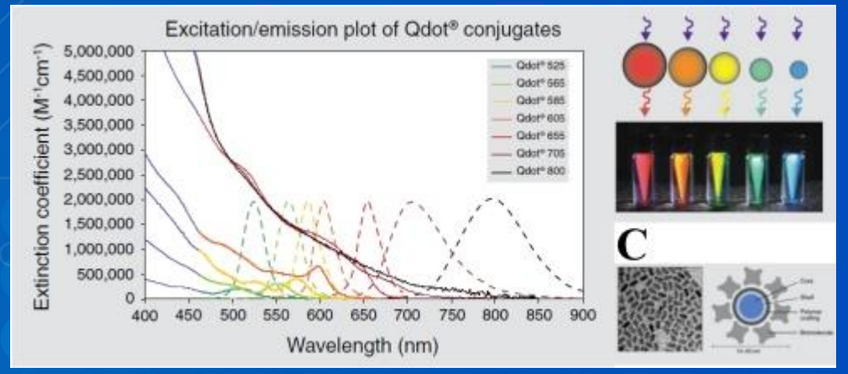

Invitrogen Qdots®

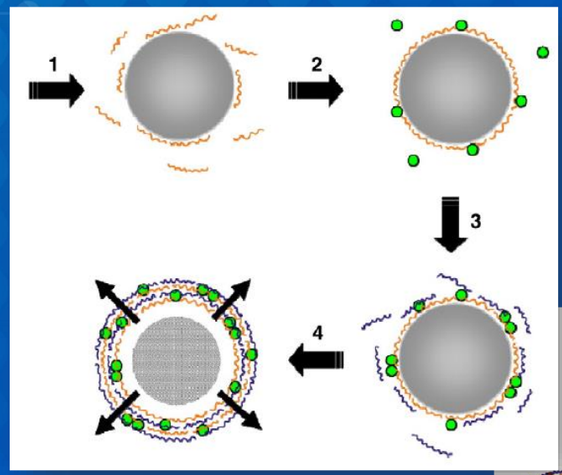

Bédard, 2010

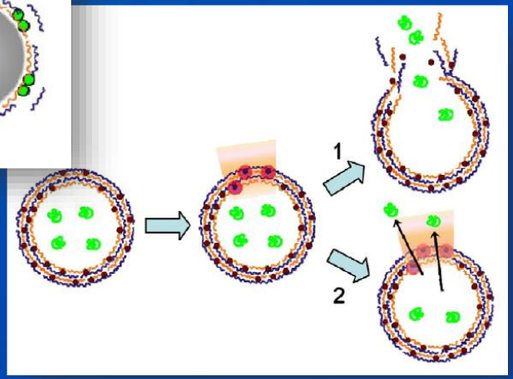

Electromagnetic Radiation Example

- Nanospectra Biosciences
- Technology: AuroLase® tumor ablation
  - Aminated silica particles prepared via Stöber process
  - Colloidal gold adhered to amine surface
  - Shell growth via $HAuCl_4$
  - Functionalized with thiolated PEG
  - IV injection; accumulate in tumor
- Size: 110 ± 11 nm core, 10 nm shell
- 820 nm laser irradiation, irreversible tumor damage

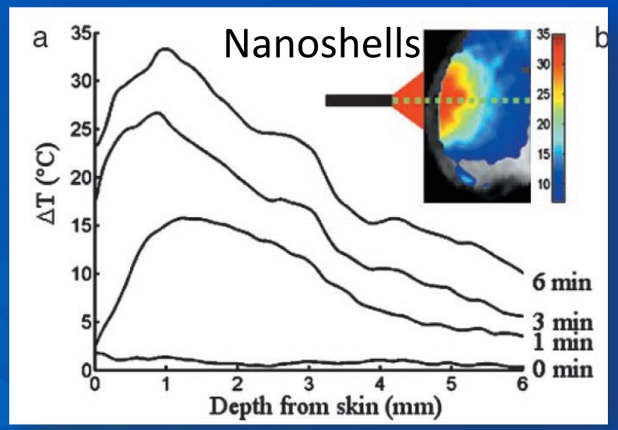

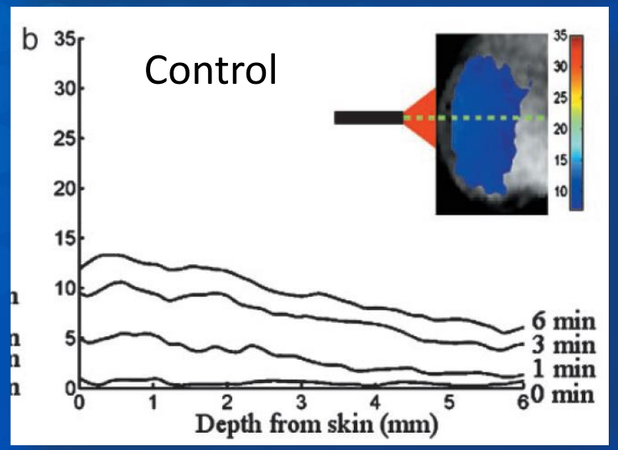

NANOSPECTRA

Hirsch, L. R.; Stafford, R. J.; Bankson, J. A.; Sershen, S. R.; Rivera, B.; Price, R. E.; Hazle, J. D.; Halas, N. J.; West, J. L. Nanoshell-Mediated near-Infrared Thermal Therapy of Tumors under Magnetic Resonance Guidance. *Proc. Natl. Acad. Sci. U. S. A.* **2003**, *100* (23), 13549–13554. https://doi.org/10.1073/pnas.2232479100.

Magnetic/Electric Fields

Applications

- Electrophoretic displays
- Magnetic particle actuation
- Oil/Water separation
- MRI contrast agents
- Chemical/Biosensors

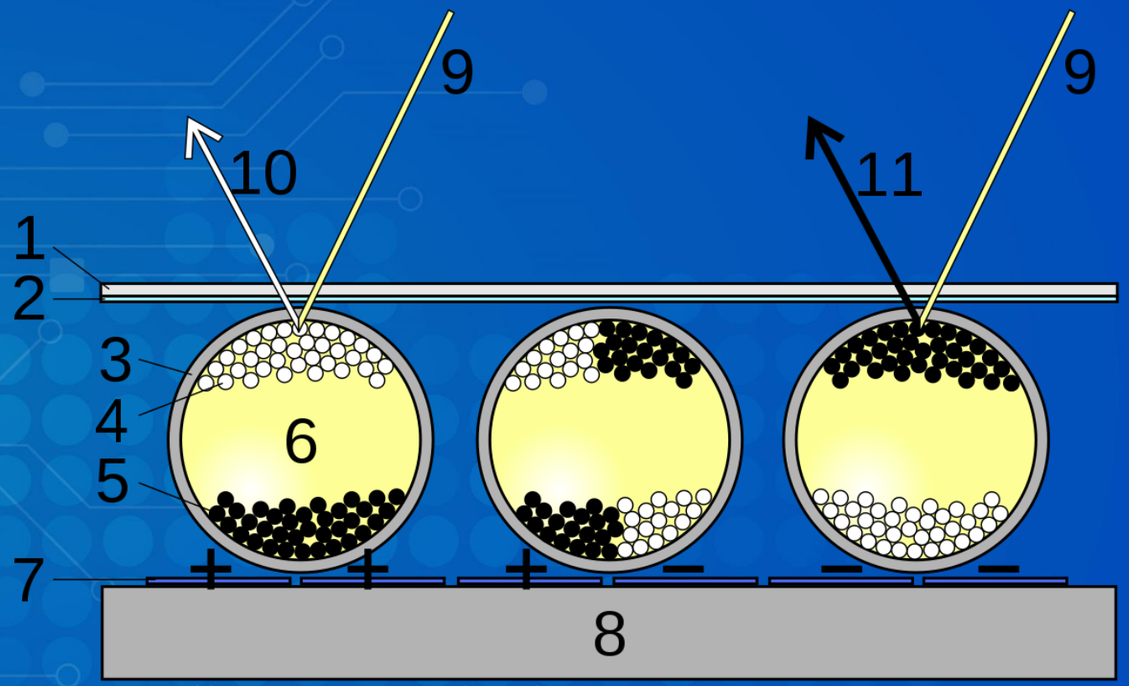

https://en.wikipedia.org/wiki/E_Ink

Mode of Action

- Particles composed of magnetically or electrically sensitive materials
- Oscillation or introduction of field alters particle behavior

Magnetic/Electric Field Example

- Magnetically induced oil/water separation w/ Janus particles
- Technology: Janus iron oxide particles
- Preparation:
  - Iron-Oxide core
  - Carboxymethyl cellulose/ethyl cellulose shell
- Size: ~100 nm
- Saturation magnetism: 69.7 emu/g
- Emulsion displacement via strong hand magnet
- Demonstrated recycling/reuse

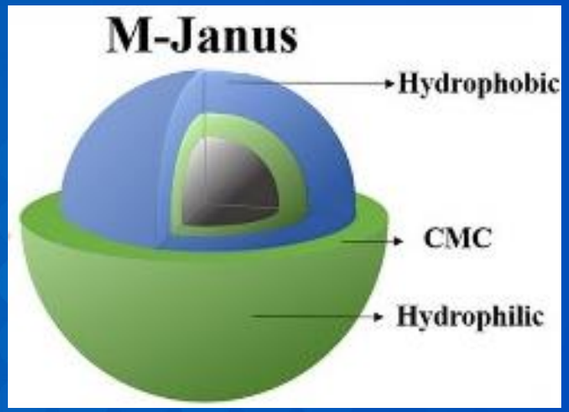

He, X.; Liang, C.; Liu, Q.; Xu, Z. Magnetically Responsive Janus Nanoparticles Synthesized Using Cellulosic Materials for Enhanced Phase Separation in Oily Wastewaters and Water-in-Crude Oil Emulsions. *Chem. Eng. J.* **2019**, *378*. https://doi.org/10.1016/j.cej.2019.122045.

Other Systems: Microencapsulation

Applications

- Pharmaceuticals
- Nutraceuticals
- Food
- Cosmetics
- Consumer Products
- Agriculture
- Paints & Coatings
- Other Industrial Applications

Mechanisms

- Mechanical
- Thermal
- pH
- Dissolution
- Diffusion
- Biodegradation
- Osmotic
- No release

Indoor Applications

Cleaning products

Deodorant

Fragrances

Hair care

Toothpaste

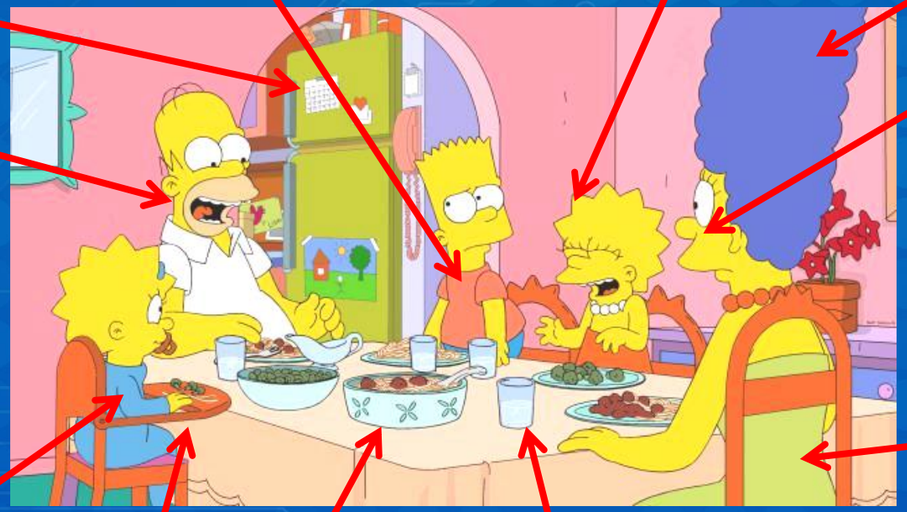

Cosmetics

Laundry

Vaccines

Flavors & nutrients

Beverages

Outdoor Applications

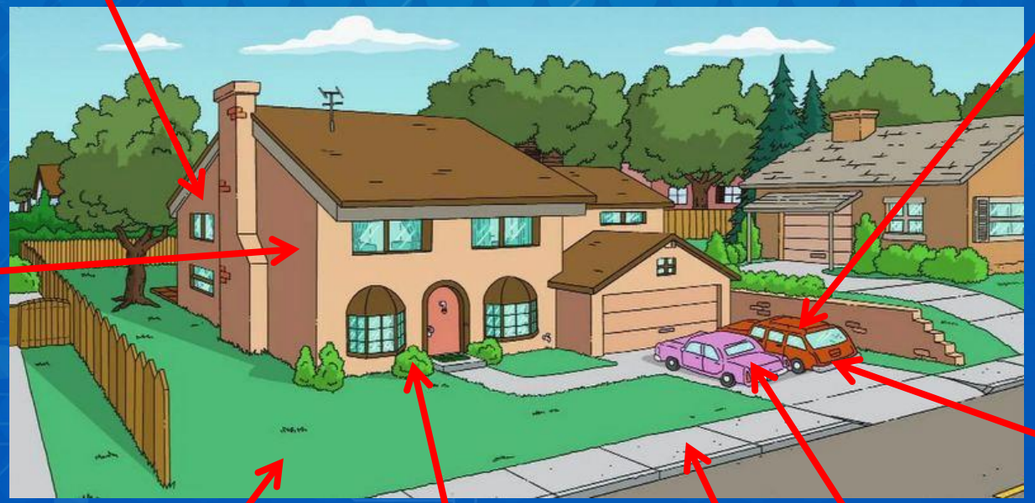

Conclusions and Next Steps

Conclusions

- Variety of particles, applications, triggers, and responses
- Mechanical, thermal, chemical, electromagnetic, magnetic, etc.
- Successful commercial examples, and emerging academic solutions

Next Steps

- Collect feedback from IFPRI membership
- Complete written review
- Final goals:
  - Balance of commercial and academic examples
  - Not intended to be a catalog; rather survey of different approaches/applications

Thank You

Independent, Non-Profit Contract R&D
+3000 Employees
2 Million Sq. Ft. Laboratory Space

$600 Million Annual Revenue
Established 1947
San Antonio, TX

Advanced Particle Sensors LLC

particle characterization for the real world ™

Review: In-Process Characterization of Suspensions and Slurries

David M. Scott

Advanced Particle Sensors

david.scott@particlesci.com

Presentation to IFPRI– 5/22/20

Abstract

This presentation provides highlights of a comprehensive literature review of new and emerging methods for in-process characterization of suspensions and slurries. Most of the 165+ reviewed publications (selected from a field of over 3200 search hits) describe variations of known methods or ideas but nonetheless represent current applications. Innovative or otherwise noteworthy developments are identified in this presentation and will be described more fully in the report.

Outline of Presentation

2 Introduction

2.4 Scope of Review

4 Particle Size and Particle Size Distribution

4.1 Acoustic Methods

4.4 Optical Methods

5 Particle structure

5.2 Density

5.3 Fractal dimension

5.5 Shape

6 Properties of Suspension / Slurry

6.1 Density / Concentration

6.2 Gas volume fraction

6.3 Phase distribution

6.4 Rheological properties

9 Conclusions

(Numbering follows the outline presented at the Winter meeting in Philadelphia.)

Scope of Review

New and emerging methodologies for in-process characterization of suspensions and slurries, encompassing

- Particle size distribution: from nm to mm, including detection of very small particles in the presence of large particles
- Particle structure: shape, porosity, fractal dimension, density, etc.
- Suspension/slurry density, gas volume fraction, phase distribution
- Rheological properties

Automated methods for taking and preparing samples for analysis are also in scope.

4.1 PSD via Acoustic Methods

High level of activity in this area, with few recent innovations

Acoustic Emission (from particle impacts, larger particles create louder sound)

- AE is well-established in minerals processing, with intrusive and non-intrusive clamp-on sensors. A recent patent to CiDRA (Newton and Fernald 2019) measures particle size in a grinding circuit by comparing the power spectrum of the sound to an empirical model. Percent oversize is estimated.

CiDRA PST mounted on hydrocyclones (cidra.com)

- A more rigorous approach was investigated at Strathclyde using a finite element code and Hertz contact theory to analyze particle collisions with the vessel wall (Tramontana et al. 2015). Experimental validation was provided using 3 broad size classes covering 0-850 μm. There have been no follow-up studies citing this work.

PSD via Acoustic Methods, cont'd

Dynamic Sound Scattering (ultrasonic analog of Dynamic Light Scattering)

- Proposed conceptually by Bodner and Inozemtsev (1977)
- Various authors have discussed measurement of particle velocity
- Norisuye (2018) patented an implementation that can monitor particle size over 3-30 μm in opaque, concentrated, sedimenting systems.

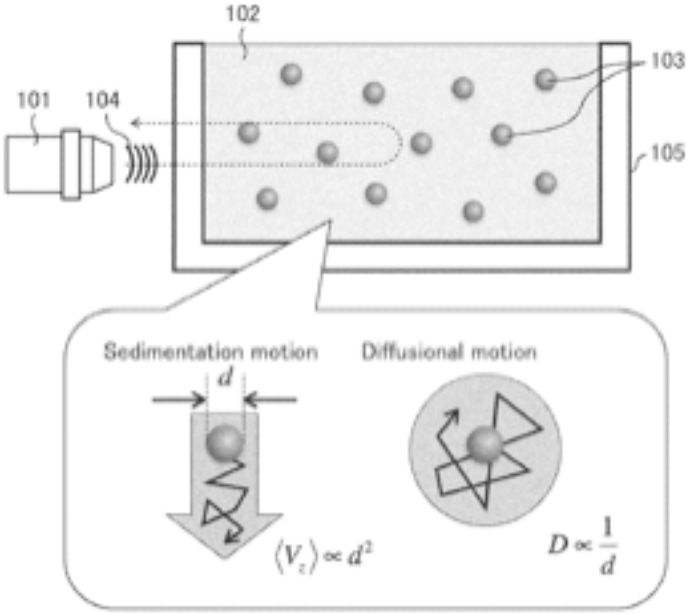

Norisuye, Fig. 16

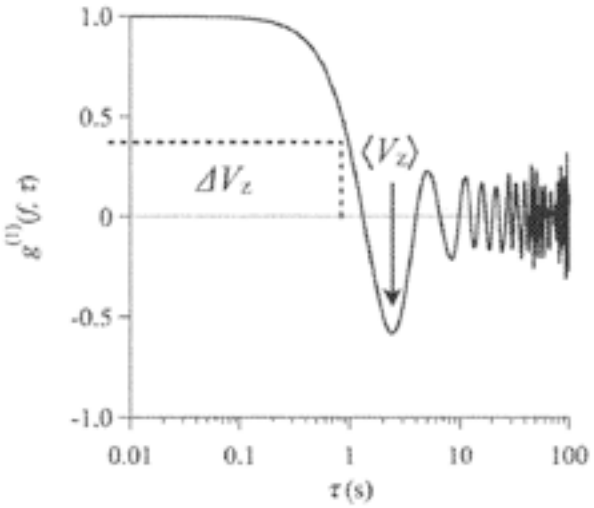

Norisuye, Fig. 3c

4.4 PSD via Optical Methods

4.4.1 Absorption and spectroscopy

- Statistical Extinction Method (Dannigkeit et al. 2016; Schwarz et al. 2018) measures mean size (1-1000 μm) up to 30 vol%, by analyzing transmission fluctuations in a collimated light beam with a spatial filter or pinhole detector.
- Raman spectroscopy has been used to measure size in suspensions and emulsions (Owen 2018; Houben et al. 2015).

4.4.3 FBRM & 1-D Optical Scanners (chord length distributions)

- Deconvolving the PSD from CLD data requires an instrument response model that is typically empirical (e.g. Kernick 2018). Irizarry et al. (2017, 2020) create such models based on the response for 5 different size fractions.
- Szilaǵyi and Nagy (2018) provide a fast simulation of CLD for a given PSD (the “forward problem”) for control of crystallization.
- Other applications include contamination detection in drilling mud and monitoring flocculation in a minerals grinding circuit.

PSD via Optical Methods, cont'd

Interferometry

- InProcess-LSP (www.inprocess-lsp.com) introduced "NanoFlowSizer" based on Spatially Resolved Dynamic Light Scattering (Besseling et al. 2019) to measure size in turbid flowing nanosuspensions.

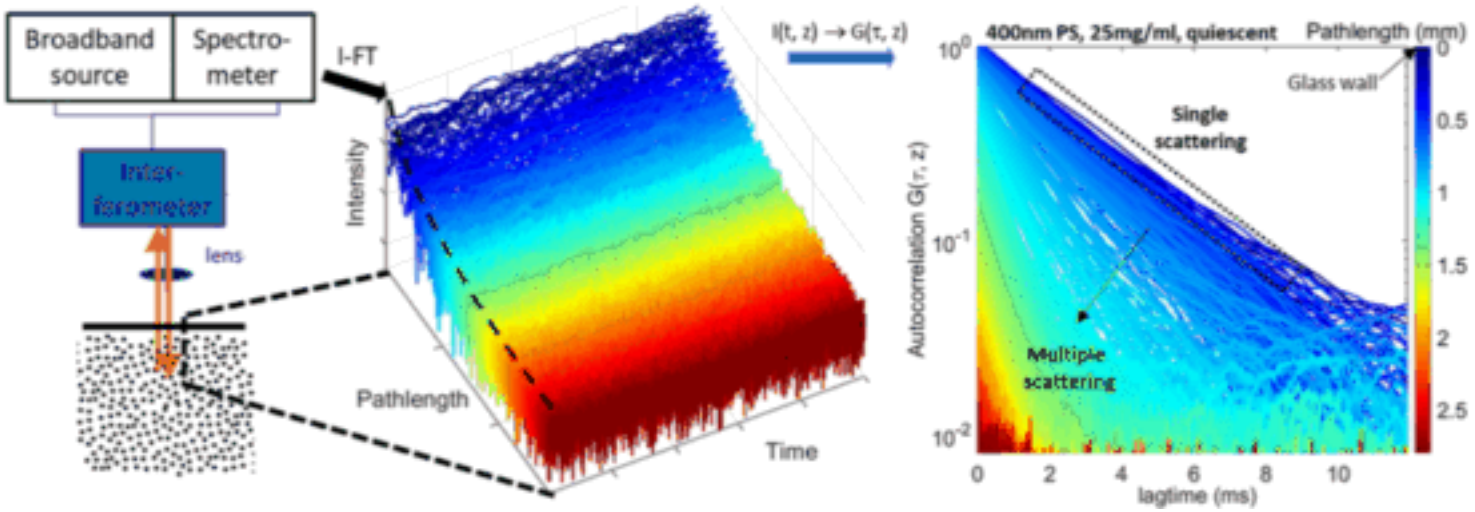

Besseling et al., Fig. 1

- A similar approach is described by Guzman-Sepulveda et al. (2015), who used a fiber coupler rather than an interferometer (fixing the path length).

PSD via Optical Methods, cont'd

Scattering / Diffraction

- Hussain et al. (2020) propose a cheap and compact size analyzer based on a custom Angular Spatial Filter (Pruneri et al. 2018) and a CMOS camera. Sizes 13μm to 150μm at concentrations up to 4 wt% were measured.

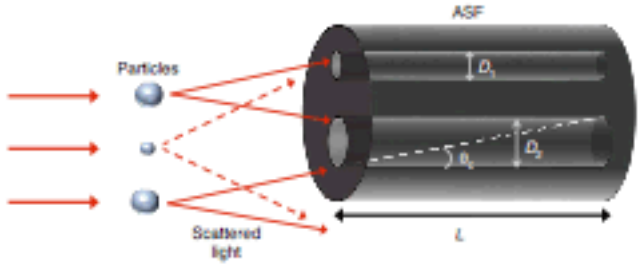

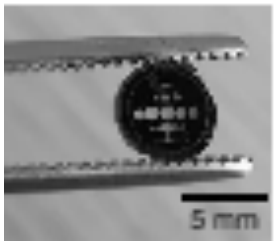

Hussain et al., Figs. 1 & 2

- Wyatt (2018) describes how to extend the Rayleigh-Gans approximation (usually limited to sizes <50 nm) to 2000 nm by extrapolating the forward ($\theta=0°$) intensity from measurements at multiple scattering angles.
- Several patents were filed or issued on "next generation" improvements to existing diffraction instruments (to be listed in the report).

5.2 Particle Density

- Guzman-Sepulveda et al. (2015) use low-coherence DLS to determine the Stokes' settling velocity in colloids, from which mass density is calculated. See also Ishii et al. (2010). Time scale is hours!
- Al-Lashi and Challis (2015) discuss the application of ultrasonic spectroscopy to suspensions of solid particles in order to estimate density, if the other properties are known.
- For oceanographic applications, Hurley et al. (2016) use a Sequoia Scientific (sequoiasci.com) submersible laser diffraction system to estimate the mass density of particles by assuming beam attenuation is proportional to density.

5.3 Fractal Dimension

Imaging Techniques

- Fractal dimension is commonly determined by image analysis, e.g. of flocced sediment in vessels (MacIver & Pawlik 2017); capillary suspensions (Bossler & Koos 2016, Bossle et al. 2018); and coagulation of wastewater (Ratnaweera & Fettig 2015, Ren et al. 2017).
- Yu (2014) demonstrated the use of a 3-layer artificial neural network to analyze output from an imaging system and predict suspended solids removal efficiency for chemical coagulation in wastewater treatment plants.
- Cao et al. (2014) have extracted fractal dimension with digital holography to monitor flocculation of algal blooms with clay.

Fractal Dimension, cont'd

Optical Methods

- Small-angle light scattering (Jung et al. 1995) is an established technique for estimating fractal dimension. Kuśnierz & Wiercik (2016) applied it to diluted sludge, and Bowers et al. (2017) used it to study marine flocs.
- Expósito et al. (2019) have proposed a new method to estimate fractal dimension of microalgal cultures by correlating the suspension chord length distribution with the flocs average geometry through a machine learning model.

5.5 Shape

Imaging Methods

- Huo et al. (2016) propose a strategy for in-situ crystal shape and size measurement for monitoring crystallization, including a new shape feature index based on the COV of distance from perimeter points to the centroid.
- Cardona et al. (2018) tackle the issue of removing out-of-focus objects from the particle statistics, using the Gaussian derivative method of Geusebroek et al. (2000) to assess the focus.
- Lu et al. (2018) address the challenge of image segmentation in the presence of varying backgrounds and bubbles in a 4 L crystallizer.
- ★ Heisel et al. (2019) built a neural network to discriminate between single crystals and agglomerates independent of shape.
- Several groups have used stereo imaging to obtain 3D crystal shape (Rajagopalan et al. 2017), measure agglomeration (Huo et al. 2017), or estimate growth kinetics (Zhang et al. 2017).

Shape, cont'd

Optical Methods

- Mostafavi et al. (2014) noted that particle shape can influence the results of many on-line characterization techniques. Turning this to advantage, aspect ratio has been measured from laser diffraction data (Scott & Matsuyama 2014, Villa et al. 2016) and – in theory – angularly-resolved Vis-NIR spectroscopy (Stoliarskaia et al. 2019).
- Aspect ratio of gold nanorods was estimated via DLS by taking the ratio of the rotational and translational decay rates (Muschol 2014).
- ★ Häne et al. (2019) used Photon Density Wave spectroscopy (Fishkin et al. 1996, Bressel et al. 2013) to monitor particle formation of zeolites in a highly turbid suspension, noting that the reduced scattering coefficient becomes constant when no changes occur in particle size, number, or shape.

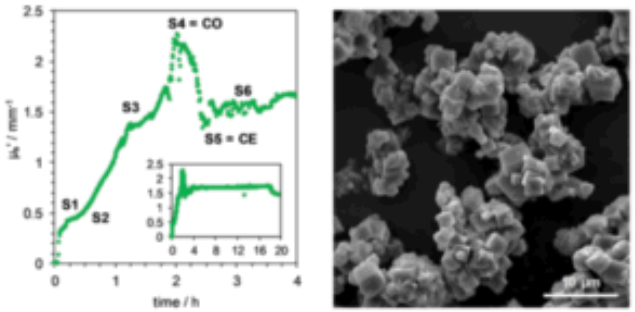

Häne et al. Fig. 2

Shape, cont'd

Optical Methods, cont'd

- Petrak et al. (2015) applied geometric reasoning to extract particle shape and aspect ratio from hypothetical chord length distributions generated by the Parsum probe (not taking instrumental bias into account). Parsum has a patent on this approach (Dietrich et al. 2018).

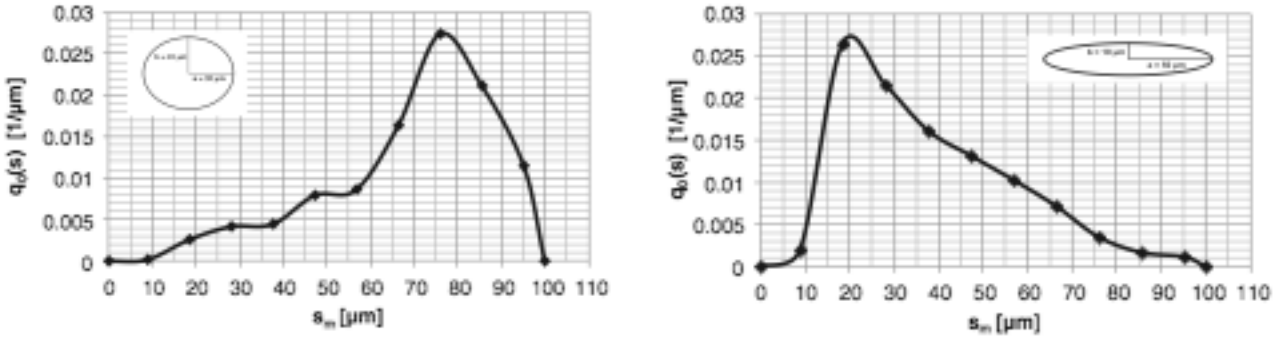

Petrak et al.
Figs. 6 & 7

Ultrasonic Method

- Ivanov et al. (2017) measured the diameter and aspect ratio of carbon nanotubes by comparing attenuation spectra of the colloid at rest (isotropic orientation) and in laminar flow (aligned particles).

6.1 Density of Suspension/Slurry

- Mechanical methods include measuring the weight of the slurry (Moth 2019) and monitoring the resonance frequency of a piezoelectric tuning fork in contact with the process slurry (Gonzalez et al. 2017).
- Recently, Lin et al. (2020) used a Neural Network to extract slurry density from Raman spectra in a 25 wt% paracetamol / ethanol suspension. [This approach requires an enormous effort to set up new applications.]
- Density can be measured from the ultrasonic reflection coefficient, which depends on the acoustic impedance (density x sound speed) of the slurry. Recent advances include a spool piece deign for large (<70 cm) steel pipe (Greenwood 2015) and application to cement slurry in undersea drilling (Cordeiro et a. 2016).

6.2 Gas Volume Fraction in Slurry/Suspension

- An interesting approach (Figueiredo et al. 2016) recorded ultrasound scattered at 45, 135, and 180 degrees in a mutiphase flow experiment, then used a 4-layer neural network to extract gas volume, with surprisingly good results. [Note: the Atkinson-Kytömaa attenuation model they use is invalid over their range of frequency and particle size! Since they mention "the solids concentration is very small", one assumes the particles contributed little to the total ultrasonic attenuation.]

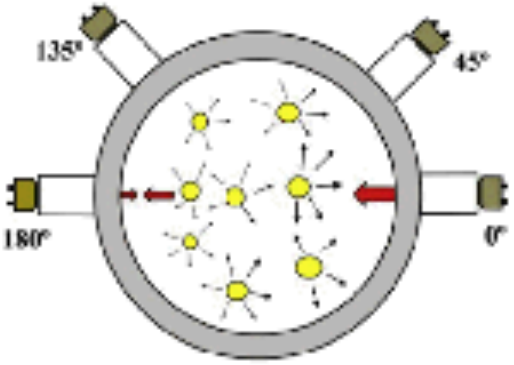

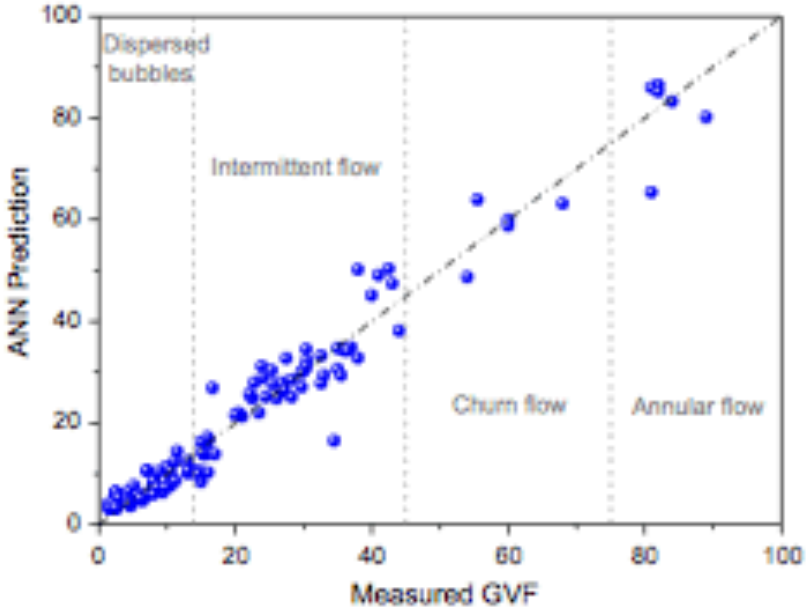

Figueiredo et al., Figs. 8 & 22

Gas Volume Fraction, cont'd

- Forte et al. (2019) demonstrated that a linear-probe ERT system (Industrial Tomography Systems, itoms.com) can measure axial profile of gas fraction and the global gas hold-up in a stirred tank, with minimal influence from the presence of particles in a gas/solids/liquid system.

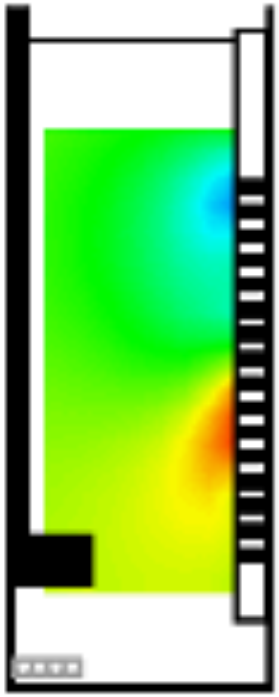

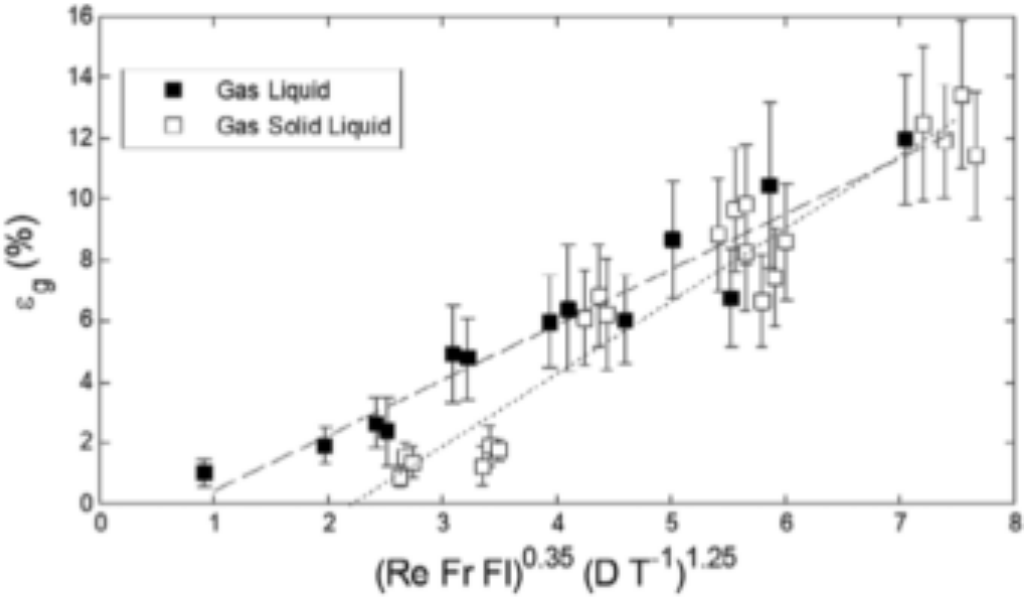

FIGURE 11 Global gas hold-up trend for two-phase and three-phase systems Solids concentration is 5 wt%

Forte et al., Figs. 6e & 11

6.3 Phase Distribution in Slurry/Suspension

Electrical Sensing

- Dos Santos et al. (2015) used invasive electrical mesh sensors to measure solid concentration distribution in slurries at 4000 frame/s with a spatial resolution of 6.25 mm. Tests used 250 micron sand at 1-35 vol%.

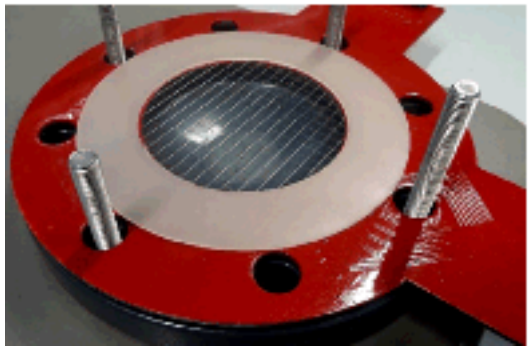

Dos Santos et al., Fig. 4

- Electrical Resistive Tomography (ERT) has long been used to measure concentration profile and homogeneity of mixing (e.g. Mann et al. 2001). A recent example is the measurement of slurry concentration profiles in a reactor to evaluate mixing performance of a particular impeller design (Mishra & Ein-Mozaffari 2016).

Phase Distribution in Slurry/Suspension , cont'd

Optical Method

- Fiber optic backscatter probes calibrated to give local solids (Mokhtari & Chaouki 2019)

Heat Transfer Method

- Ilgner (2017, 2018) noninvasively monitors sedimentation in slurry pipelines by measuring rate of heat removal from heated spots strategically placed along the line. Additional work (Ilgner & Kruger 2018) is aimed at monitoring dune height along the pipeline (simulation shown below).

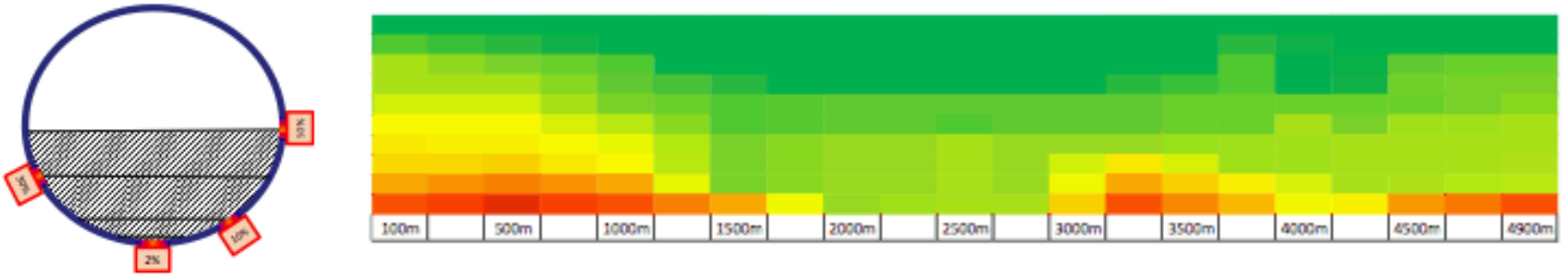

Ilgner & Kruger, Figs. 8 &13

Phase Distribution in Slurry/Suspension , cont'd

Ultrasonic Method

- Hunter et al. (2020) recently demonstrated the use of ultrasonic backscatter from a 5x7 transducer array to monitor the settled layer in a pilot scale sedimentation tank.

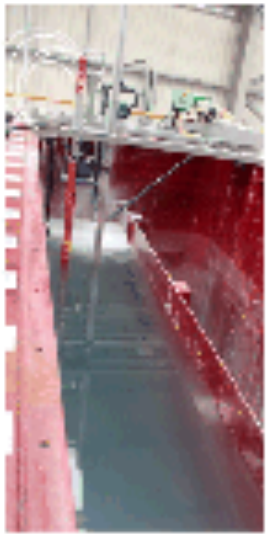

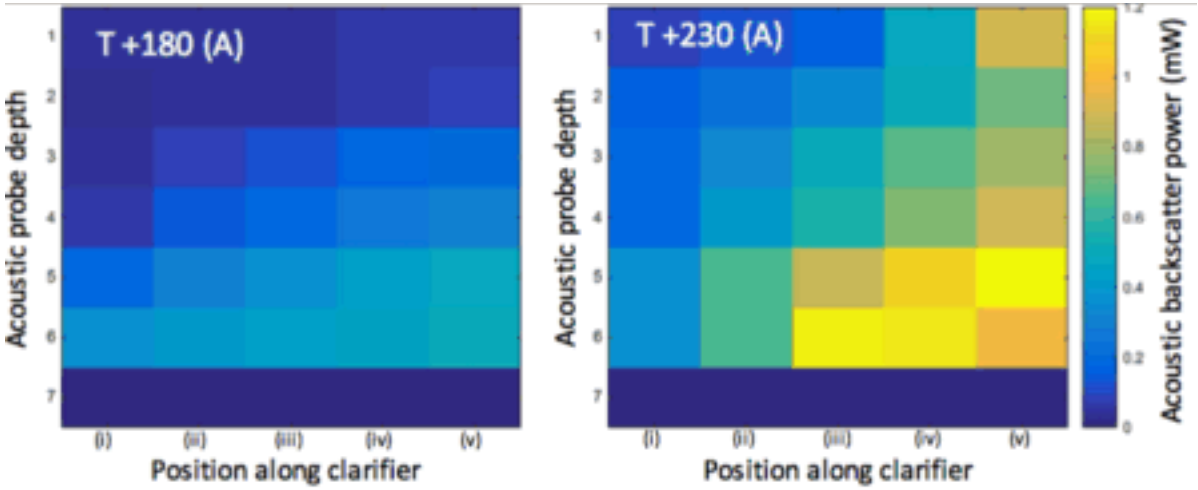

Hunter et al., Figs. 3 & 11 (Clarifier dimensions: 4.86 m long, 2.46 m high, 0.75 m wide)

6.4 Rheology

- Pressure drop across an innovative flow cell design (Okkels 2017a,b) is the heart of the on-line rheometer sold by Fluidan (fluidan.com).

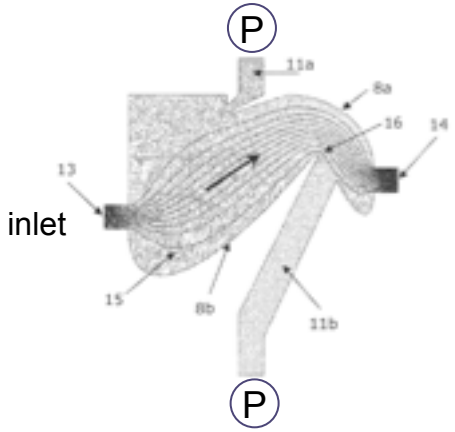

Okkels (2017b) Fig. 4

- Kotzé et al. (2008) combined ultrasonic velocity profiling (to get shear rate), measure the pressure differential (to get stress), and take the ratio to find viscosity. Kotzé et al. (2015) apply this technique to characterize wastewater sludge.

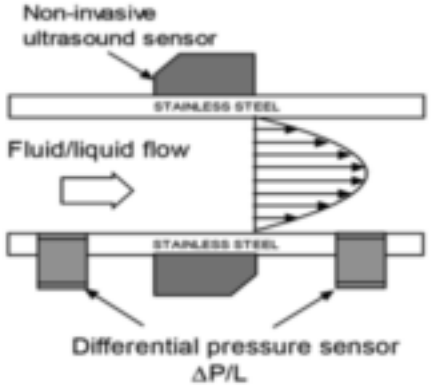

Kotzé et al. (2015) , Fig. 2

Conclusions

- A comprehensive search of the scientific and patent literature revealed a few innovative characterization methods (and several instances of “rediscovering the wheel”). Some of these recent innovations have been commercialized.
- The bulk of the papers reviewed have demonstrated useful, and often new, applications of known methods (or variations of known methods).
- Many particle characteristics of interest can be measured by multiple modalities, including electrical, mechanical, optical , imaging and ultrasonic sensors.
- Characterization gaps still exist; for instance detection or measurement of small particles in the midst of large ones.

UNIVERSITY OF BIRMINGHAM | COLLEGE OF ENGINEERING AND PHYSICAL SCIENCES

DEM Round Robin: Toward a Best Practice for Powder Flow Simulation

Dr. Kit Windows-Yule

School of Chemical Engineering

The University of Birmingham

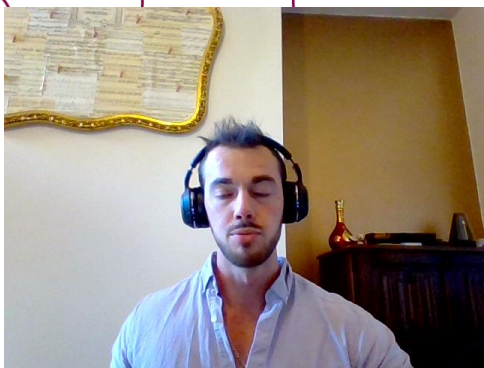

Background: What is DEM, and why do we care?

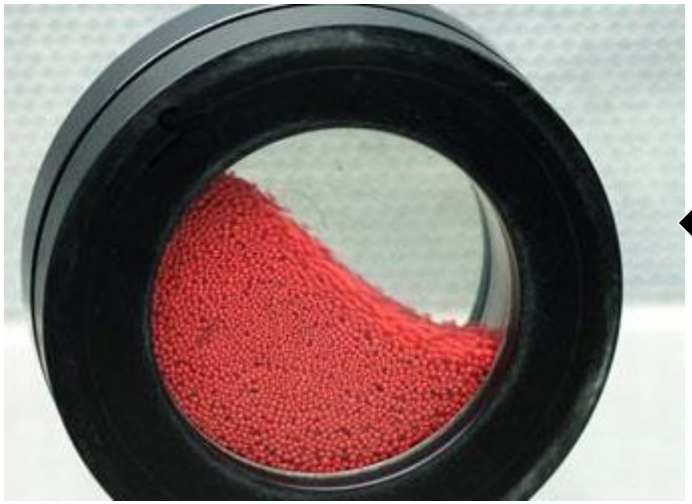

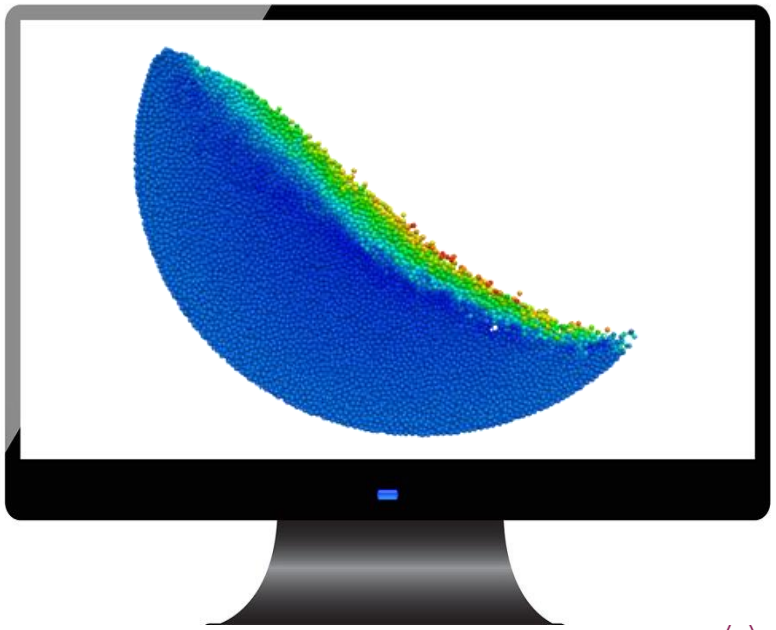

DEM is a tool for numerically modelling powders and particulates

Provides **more information**, **more cheaply** than any experimental

Background: What is DEM, and why do we care?

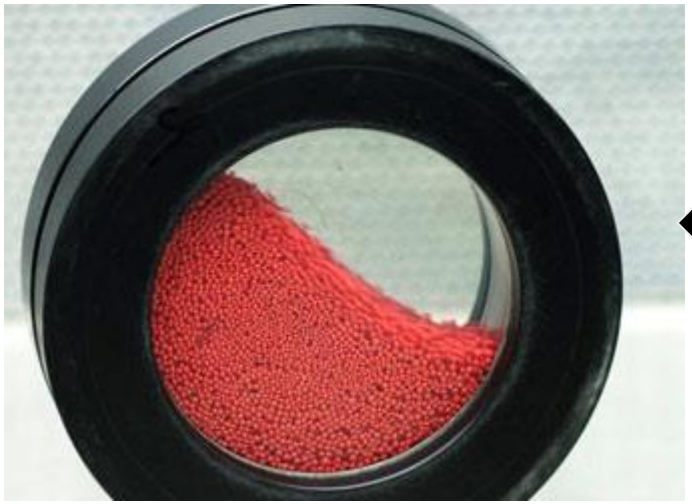

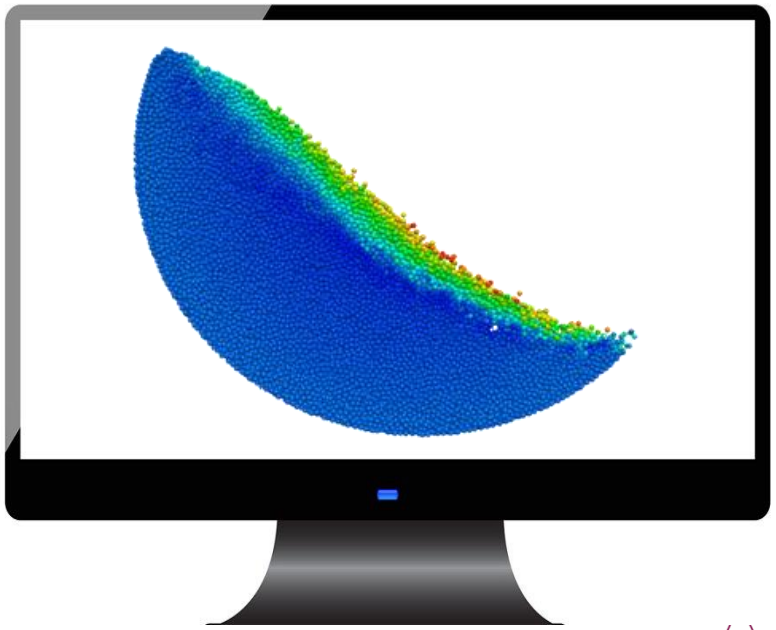

If well calibrated, DEM is capable of quantitatively reproducing dynamics of ‘real’ systems, making it a powerful tool for
and optimisation of industrial equipr

Background: What is DEM, and why do we care?

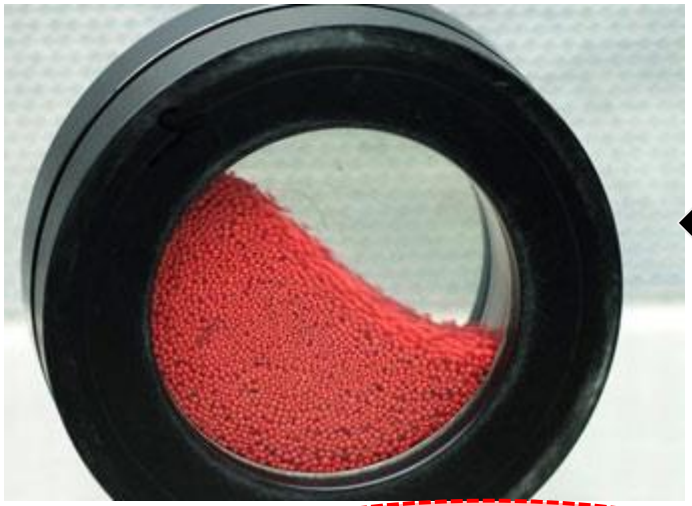

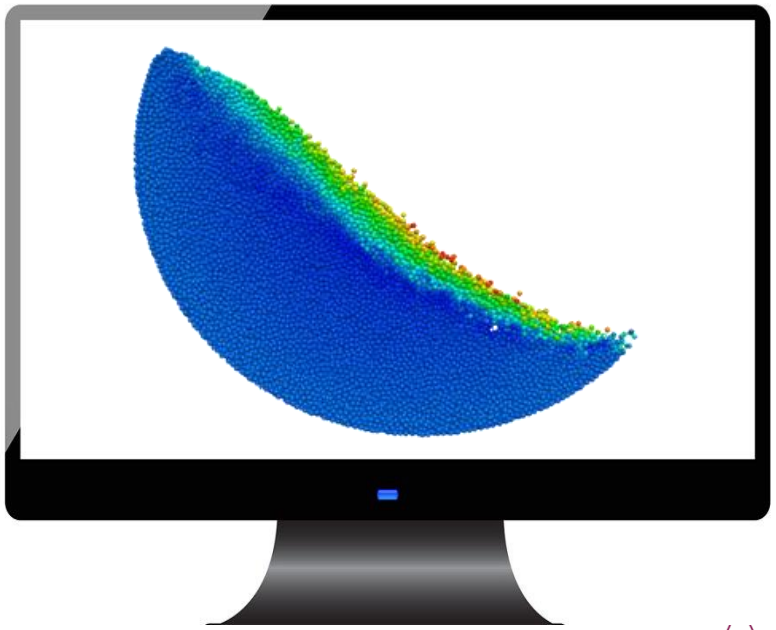

If well calibrated, DEM is capable of quantitatively reproducing dynamics of 'real' systems, making it a powerful tool for [illegible] and optimisation of industrial equipm[illegible]

This is a **big if!**

Background: DEM's Limitations

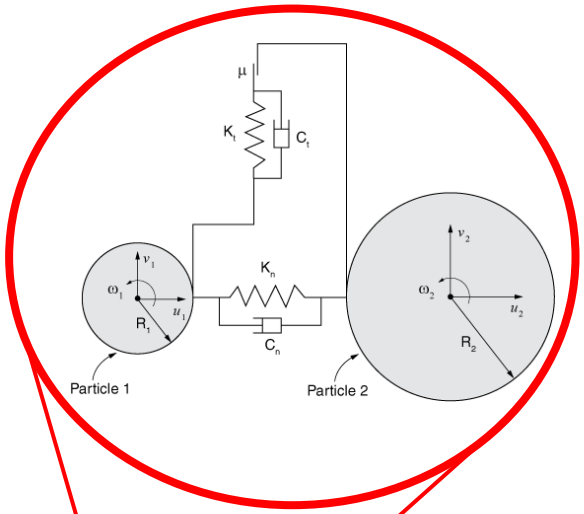

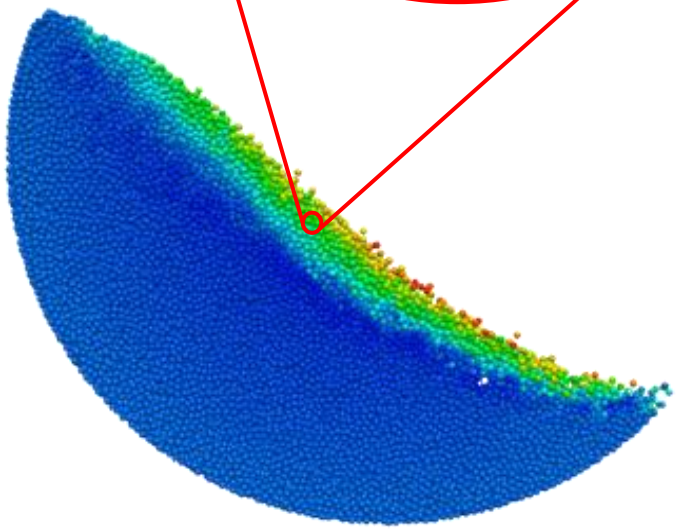

DEM's main limitation is that it is *just a model*

Like any model, it requires certain **assumptions** and **simplifications**

To make an **accurate model**, we require **detailed calib**

Background: DEM's Limitations

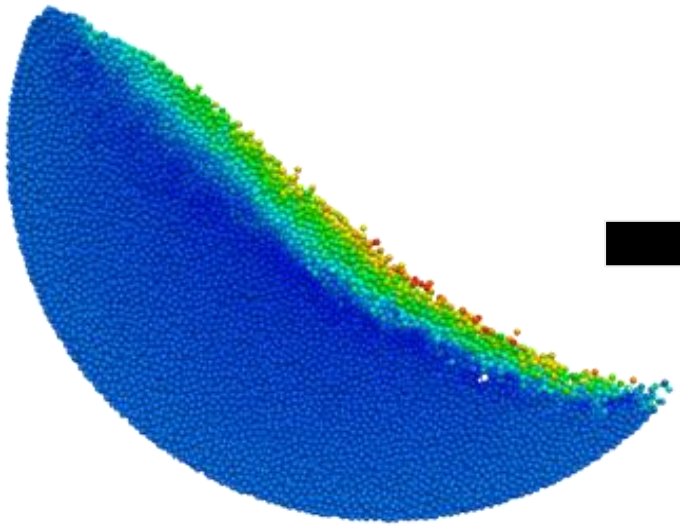

?

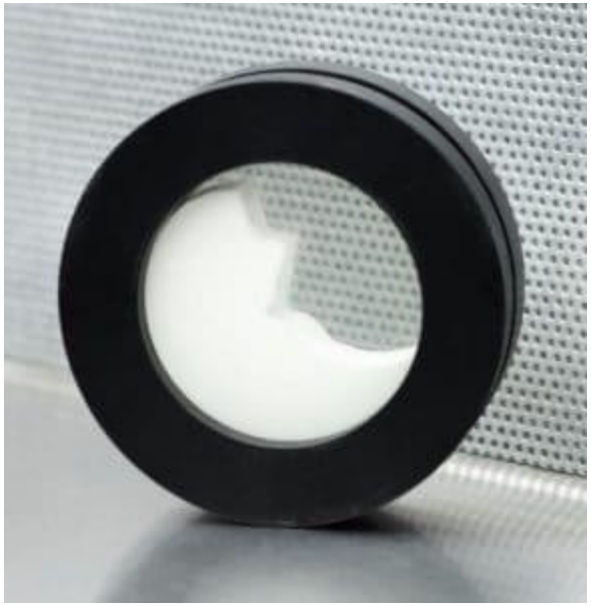

The problem:

1) Calibration is **not simple** – certain properties (e.g. cohesion, particle shape) are both **characterise** and hard to **model**

Background: DEM's Limitations

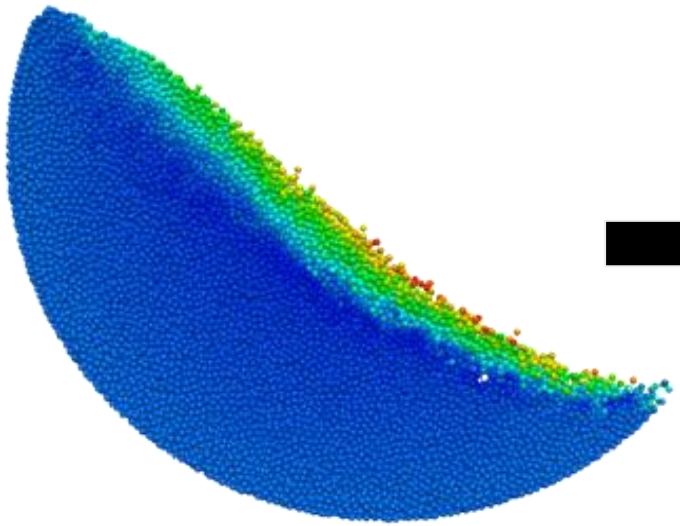

?

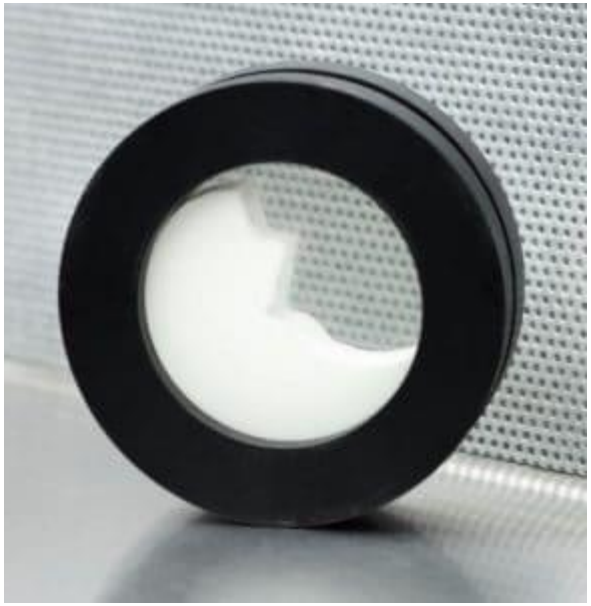

2) There is **no reliable, standard procedure** for DEM calibration – different companies & i
take very different approaches

Project Aim: To determine a "Best Practice" for DEM calibration

→ What to measure
→ How best to measure it
→ How best to model it

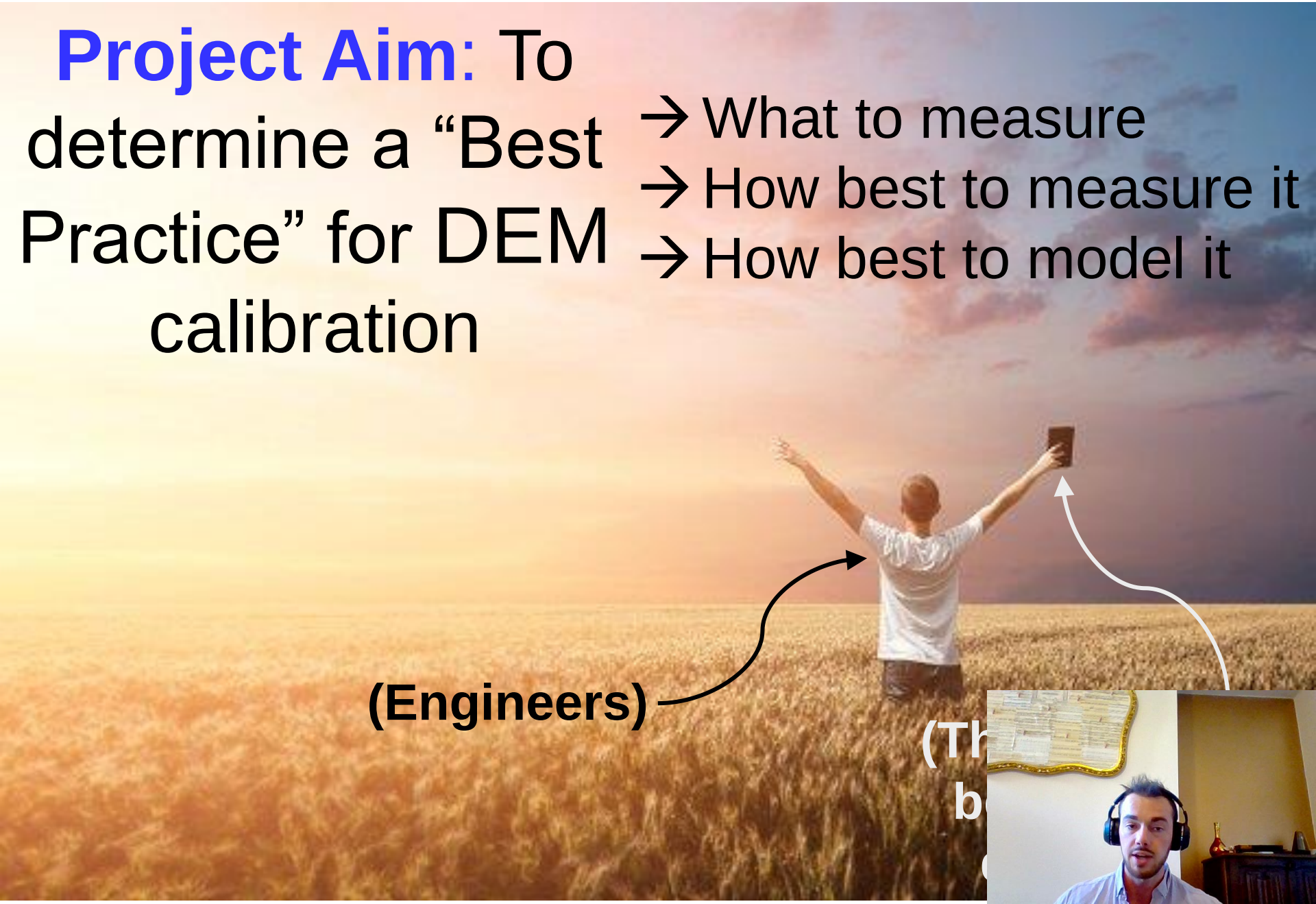

How to Determine Best Practice?

- Need to be able to **objectively** and **quantitatively** assess how well a given methodology reproduces the dynamics of a given system.
- We require the **direct, detailed comparison** of simulation data to experimental data
- This requires both
  - a suitable system
  - a suitable experimental technique

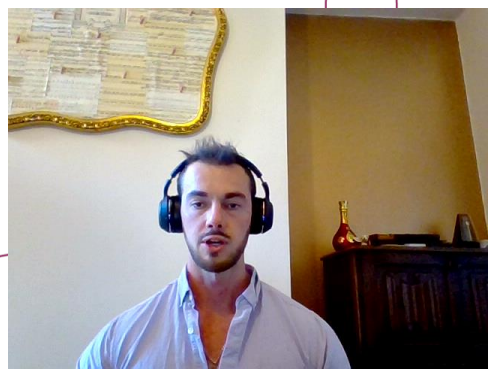

How to Determine Best Practice?

Choose experimental system(s) to model

Acquire experimental data using suitable technique

Produce simulations following current industry practices

Compare simulations to experiment → **best practice**

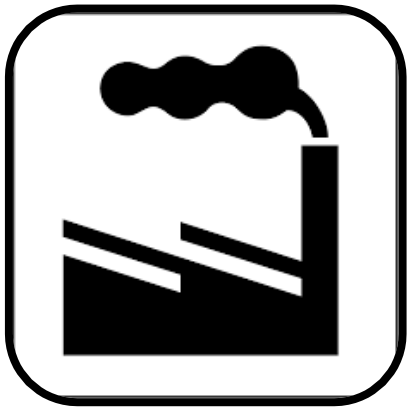

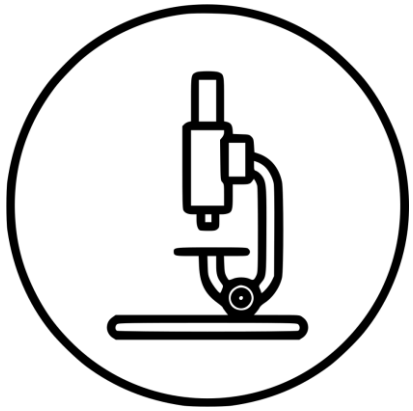

System Selection

- Criteria:
  1. Industrially-relevant systems
     - (→ meaningful outcome)
  2. Suitable for imaging
     - (→ steady state, interesting dynamics)
  3. Explore all regimes (frictional, collisional, intermediate)
     - (→ ensure models suitable for **all** li states)

System Selection 1 – Granutools GranuDrum

PEPT Data
(45rpm – "cataracting" state)

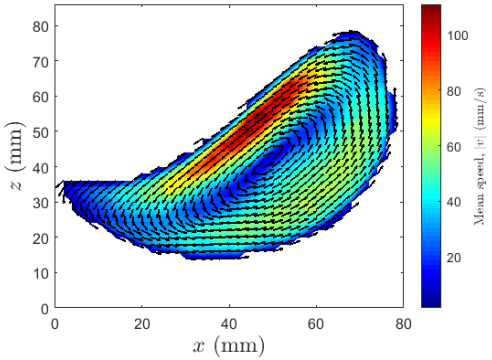

Criterion 3: Can explore both frictional *and* collisional regimes by altering rotation rate ✓

Criterion 1: Rotating drum geometry – common in industry ✓

Same material, varying RPM

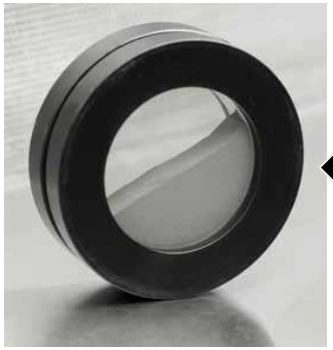

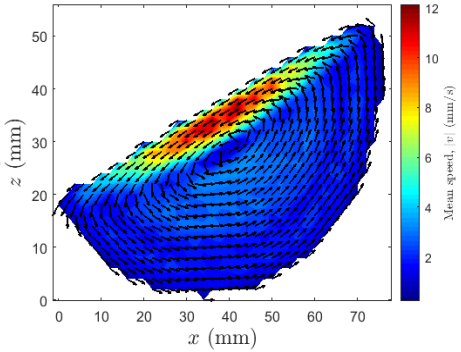

PEPT Data
(5rpm – "rolling" state)

Criterion 2: Interesting and well-researched ste dynamics ✓

System Selection 2 – High Shear Mixer-Granulator

Criterion 3: “High shear” nature and large size complements relatively small, “low shear” rotating drum systems ✓

Criterion 1: Common industrial process equipment ✓

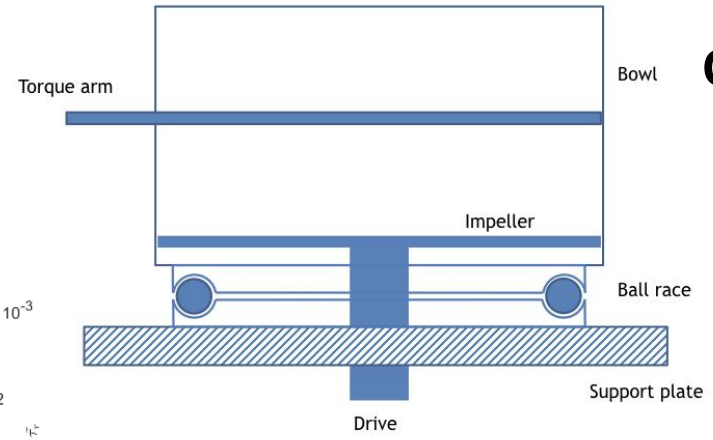

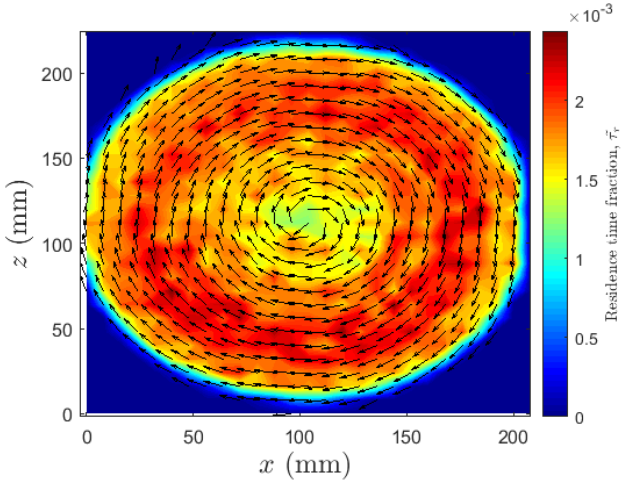

Criterion 2: Interesting and well-researched steady-state dynamics ✓

System Selection: Progress

- Systems agreed and chosen
- Tests conducted to ensure:
  - Compatibility with chosen materials
  - Compatibility with PEPT
- Experiments conducted for Phase 1 materials
- Experiments conducted for Phase 2 materials
- Phase 3 experiments scheduled for April cancelled due to Covid-19 closure
  - Will perform as soon as lab re-opens.

Material Selection

Why these choices?

1. Test fundamental abilities

2. Test ability to model particle shape

3. Test ability to model cohesion

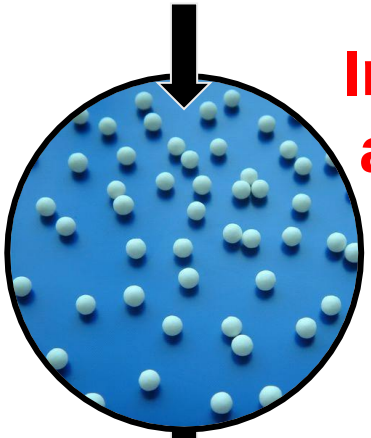

In case we are doing it *really badly*

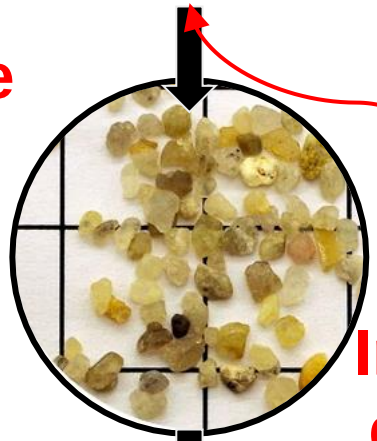

Infamously difficult to model

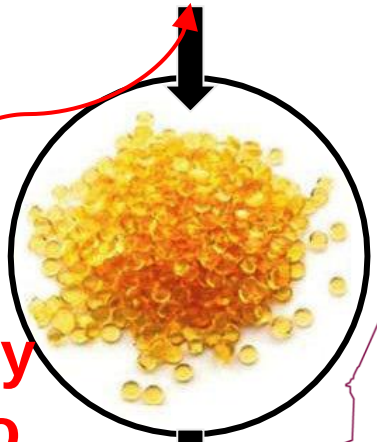

MCC
Simple, spherical geometry
Non-cohesive

Angular Sand
Complex, angular geometry
Non-cohesive

Si
Va

Material Selection

Why these choices?

1. Test fundamental abilities

2. Test ability to model particle shape

3. Test ability to model cohesion

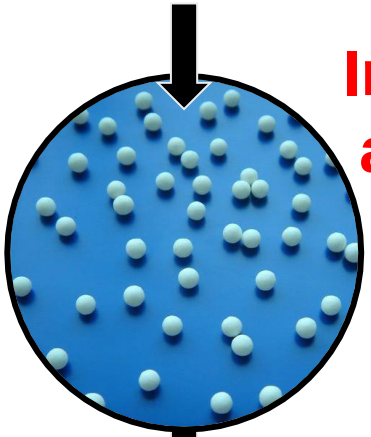

In case we are doing it *really badly*

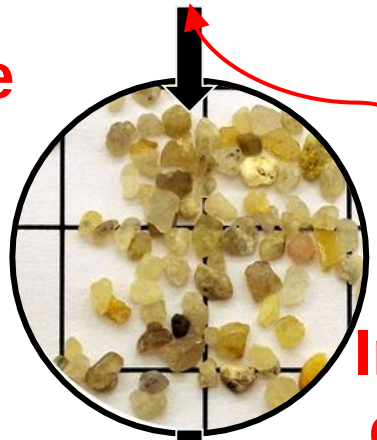

Infamously difficult to model

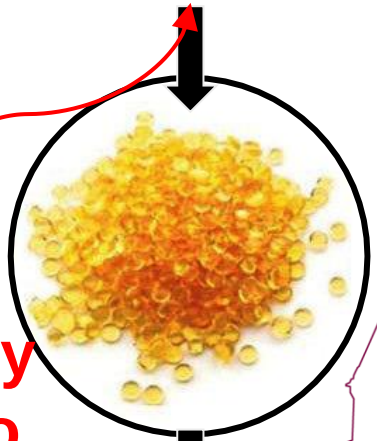

$d \in [1000,1400]\mu m$
$\rho = 1.58\ g/cm^3$

$d \in [1200,2400]\mu m$
$\rho = 2.65\ g/cm^3$

d

Material Selection: More on Material 3

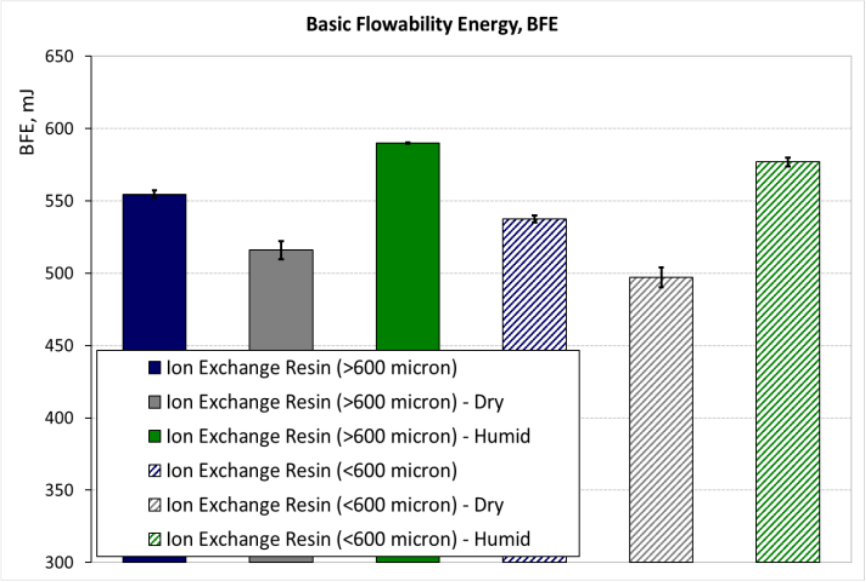

- Tests performed by Freeman Technology show cohesion varies with humidity.

- Tests will be performed with identical particles under both dry and humid conditions
- → Provide clear and rigorous test of ability of DEM m to simulate cohesion.

Material Selection: More on Material 3

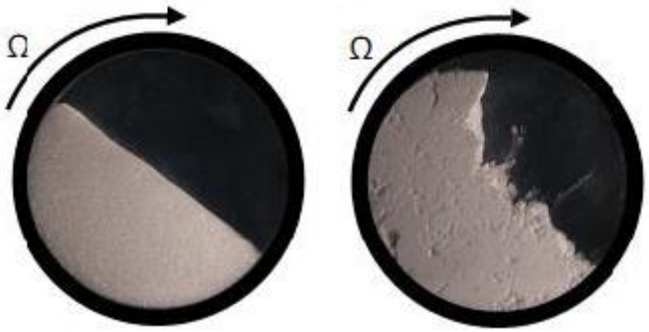

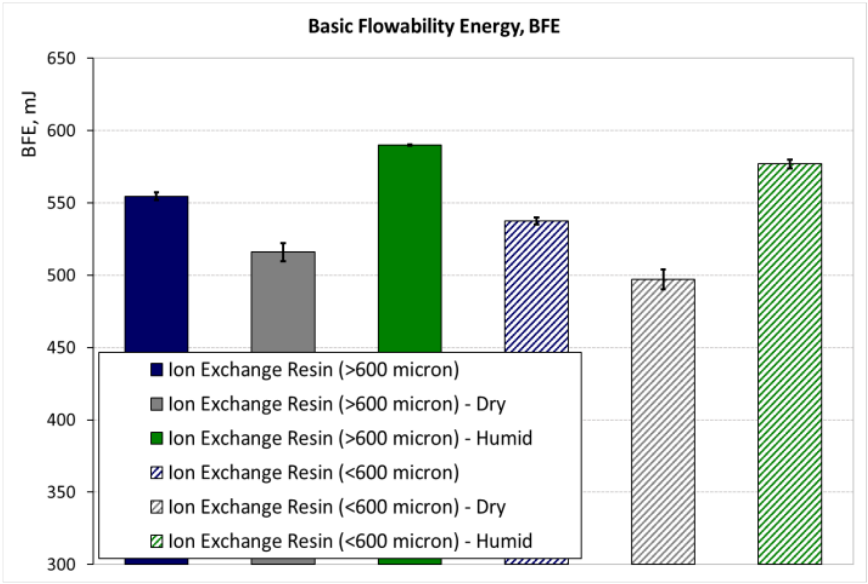

- Use of (air-tight) GranuDrum
- Samples prepared in glove box at desired humidtity
- → allows experiments to be performed under caref controlled conditions

Material Selection: Progress

- All 3 materials agreed, chosen and acquired
- Samples sent to “Characterisation Partners” Freeman Technology and Granutools
- Full, detailed characterization received
- Participants at various stages of characterization

freemantechnology
a micromeritics® company

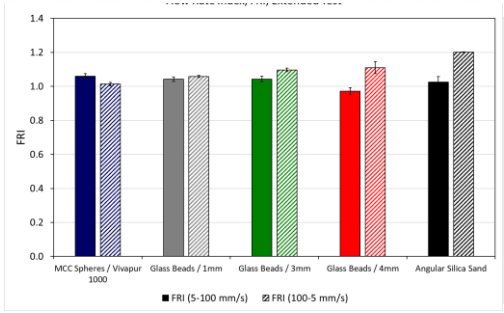

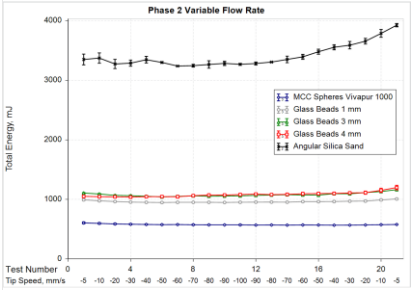

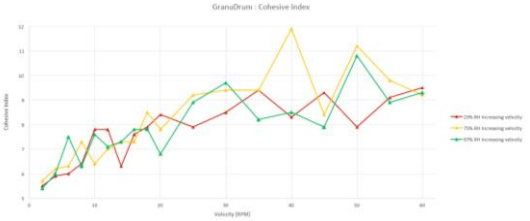

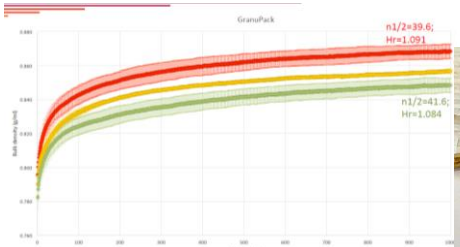

How to Determine Best Practice?

Choose experimental system(s) to model

Acquire experimental data using suitable technique

Produce simulations following current industry practices

Compare simulations to experiment → **best practice**

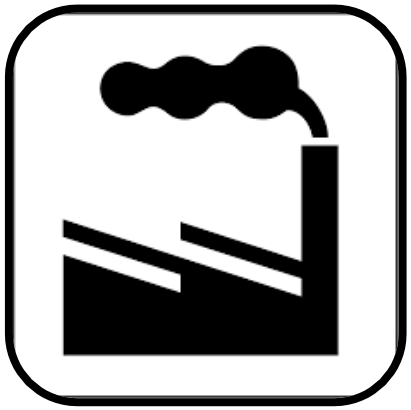

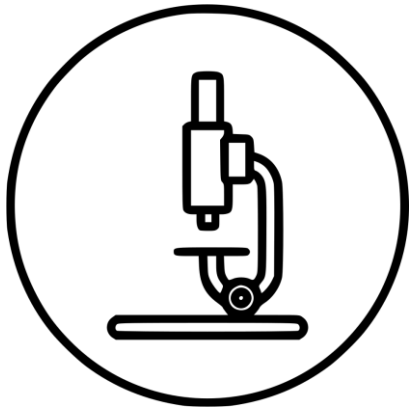

How to Determine Best Practice?

Choose experimental system(s) to model

Acquire experimental data using suitable technique

Produce simulations following current industry practices

Compare simulations to experiment → **best practice**

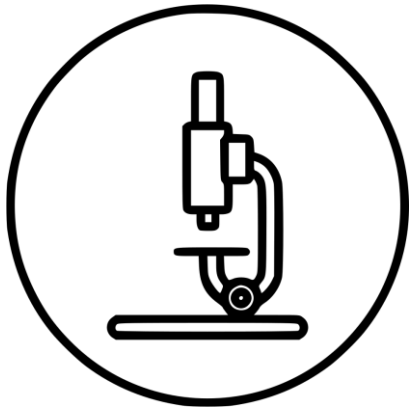

Experimental Method Selection

- Requirements:
  1. Can acquire full, three-dimensional data from opaque systems
  2. Both particle-level (microscopic) and bulk (macroscopic) information
  3. Dynamical data and force data
  4. Detailed, multi-point validation

Experimental Method Selection

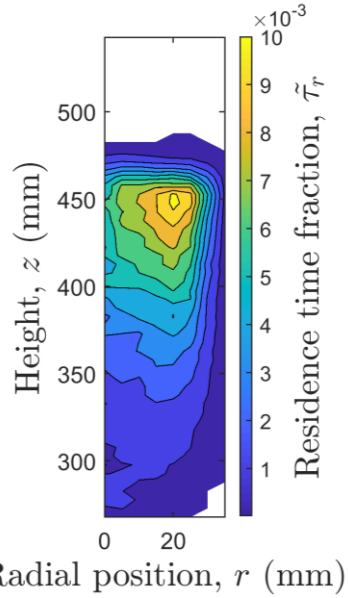

Criterion 2: Both micro- and macro-scale information ✓

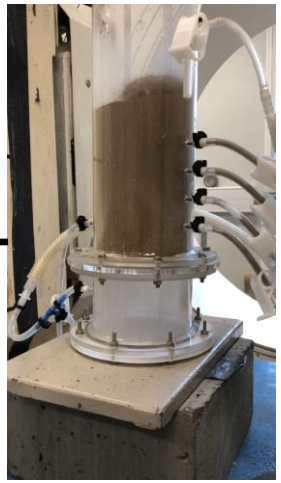

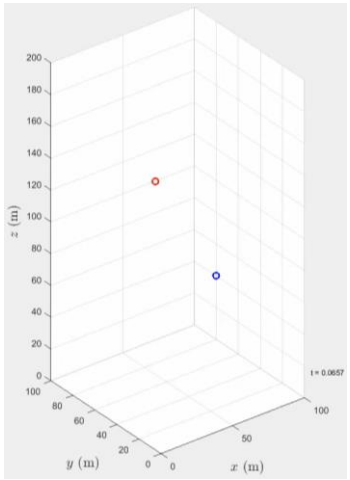

Criterion 1: Full, high-resolution imaging of opaque, 3D systems ✓

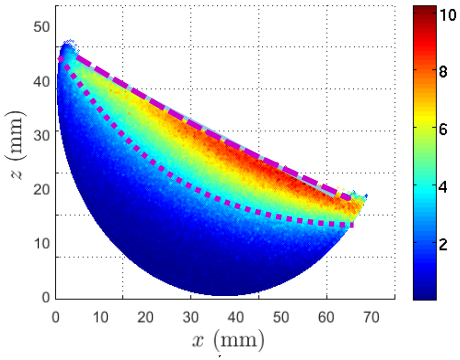

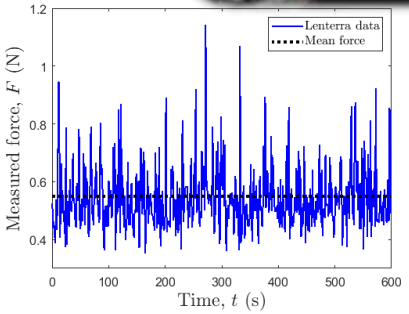

Criterion 3: Additional force data from Freeman Technology's Lenterra force sensor ✓

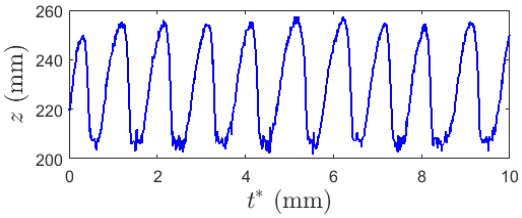

Criterion 4: Detailed multi-point data

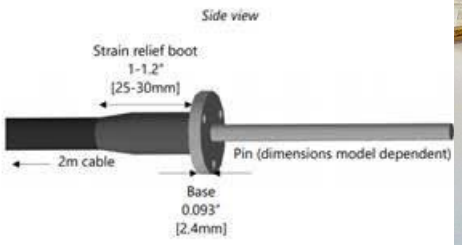

How to Determine Best Practice?

Choose experimental system(s) to model

Acquire experimental data using suitable technique

Produce simulations following current industry practices

Compare simulations to experiment → **best practice**

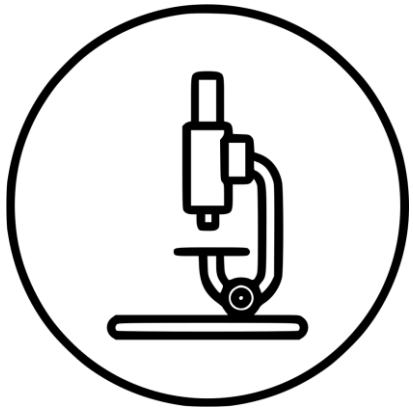

How to Determine Best Practice?

Choose experimental system(s) to model

Acquire experimental data using suitable technique

Produce simulations following current industry practices

Compare simulations to experiment → **best practice**

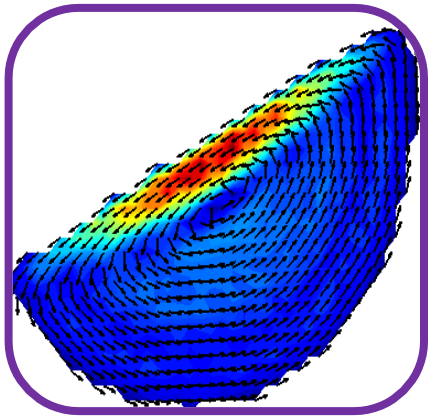

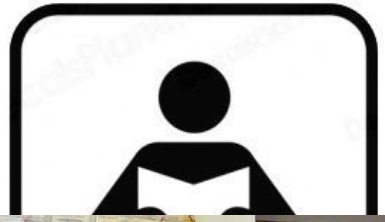

Replicating current industry practice

- The best way to replicate industry practice?
  - Let industry practice!
- Industry participants will:
  - Simulate the 2 systems & 3 materials chosen
  - Provide precise details of their calibration methods
  - Provide their simulation data for comparison with experiment

Simulation: Progress

- Participants at various stages of progress (see below)
  - Covid-19 and other issues have delayed participant progress
- EngD student recruited to aid participants and add additional simulation data
  - → More comprehensive & detailed analysis

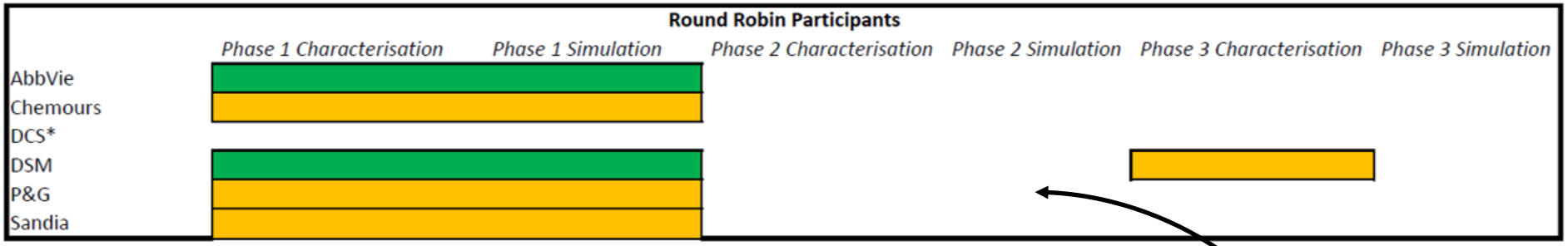

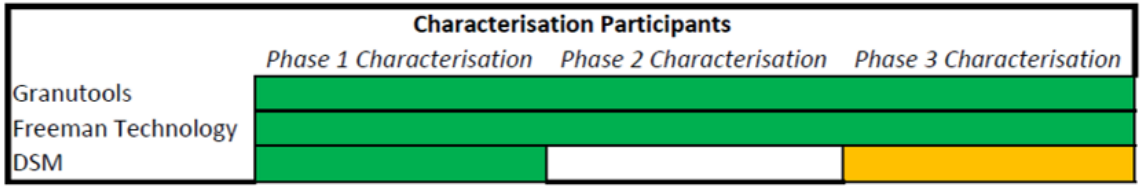

*Due to time and manpower constraints, DCS have had to step down from the Round Robin

M
Pharı

How to Determine Best Practice?

Choose experimental system(s) to model

Acquire experimental data using suitable technique

Produce simulations following current industry practices

Compare simulations to experiment → **best practice**

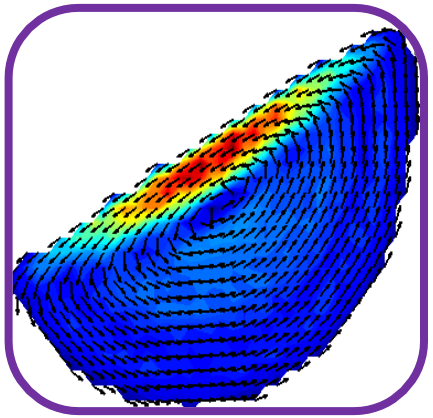

How to Determine Best Practice?

Choose experimental system(s) to model

Acquire experimental data using suitable technique

Produce simulations following current industry practices

Compare simulations to experiment → **best practice**

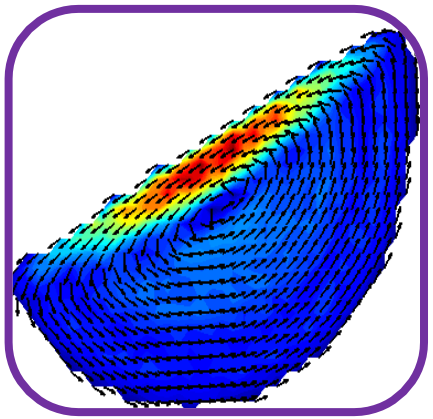

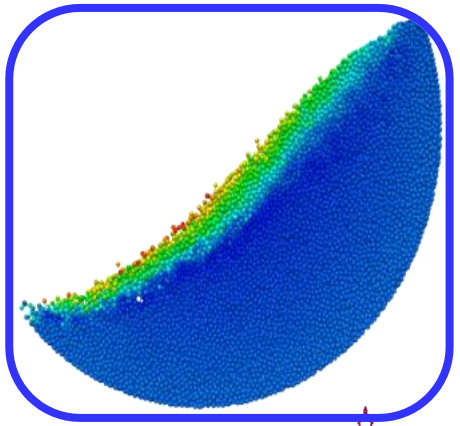

Toward a Best Practice

- Clearly, the chosen **inputs** to a model will influence the accuracy of the **outputs**.
- Our goal is to determine how the choice of each given input affects each given output…
- …and thus identify the **best choices**

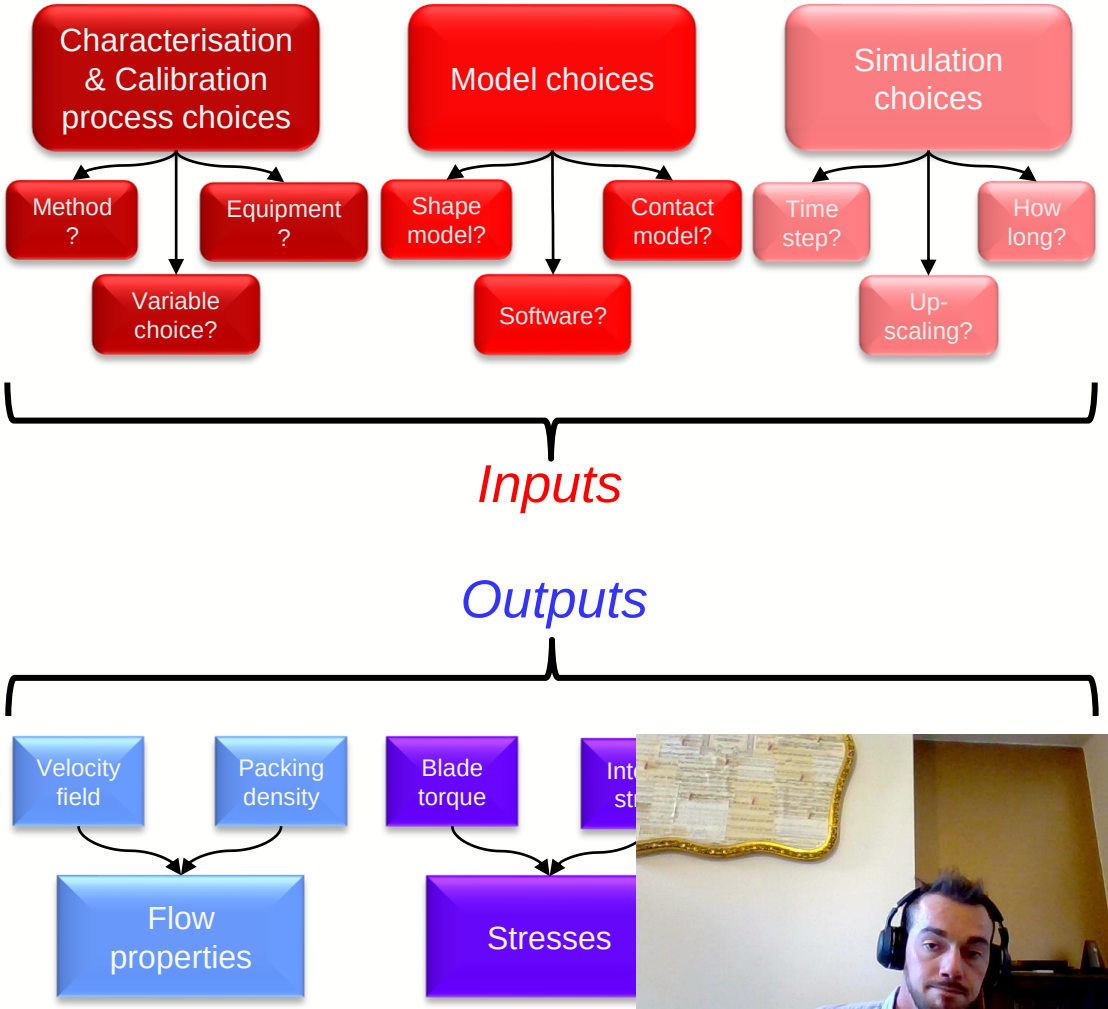

Toward a Best Practice

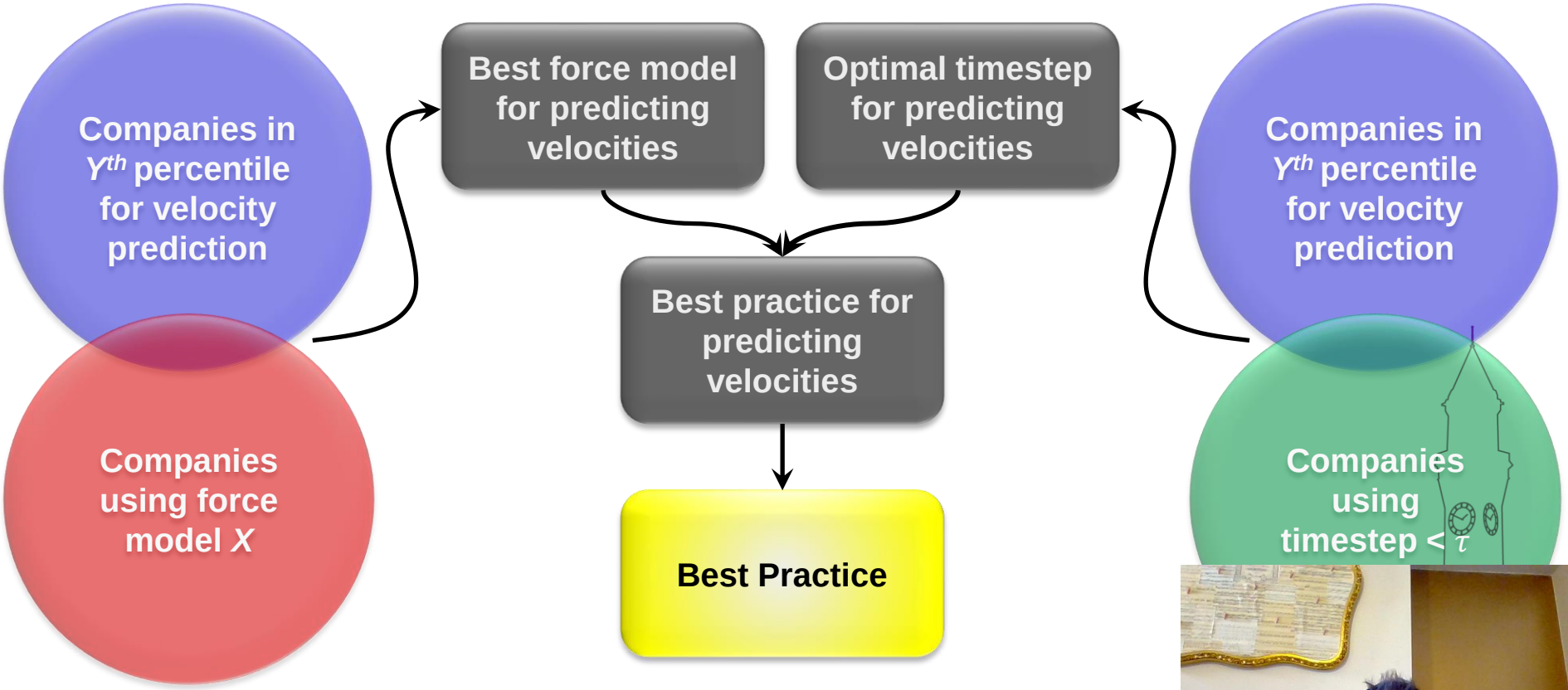

How to determine best practice

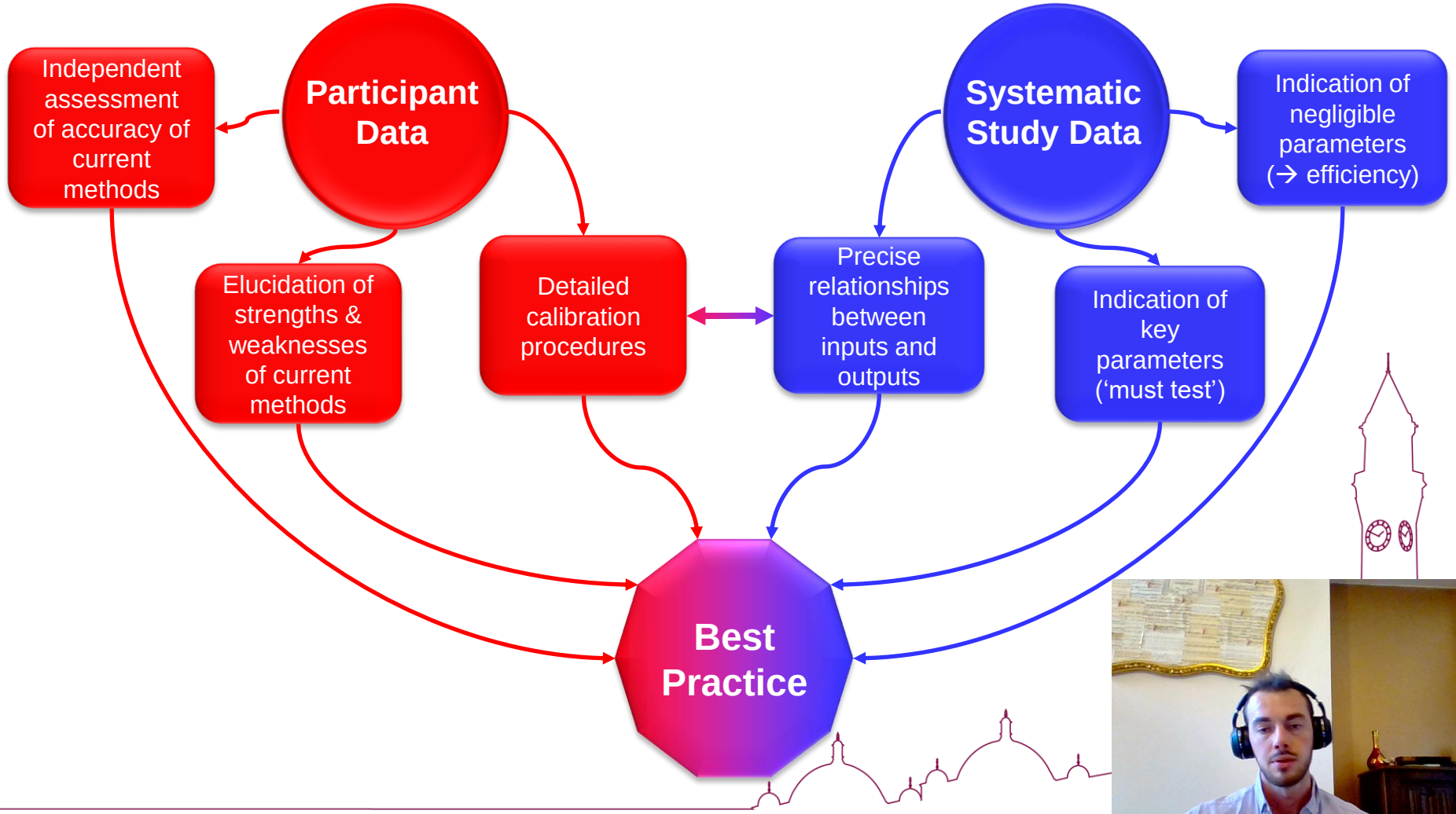

How to Determine Best Practice?

Choose experimental system(s) to model

Acquire experimental data using suitable technique

Produce simulations following current industry practices

Compare simulations to experiment → **best practice**

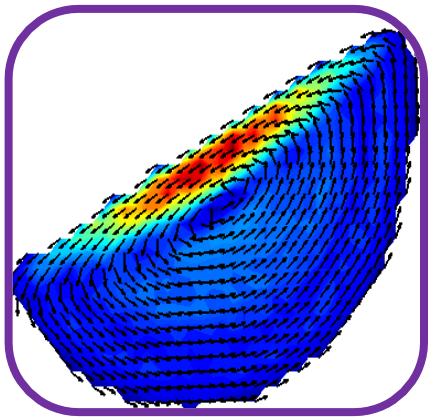

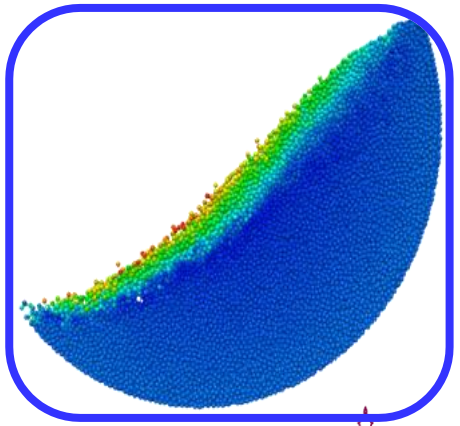

How to Determine Best Practice?

Choose experimental system(s) to model

Acquire experimental data using suitable technique

Produce simulations following current industry practices

Compare simulations to experiment → **best practice**

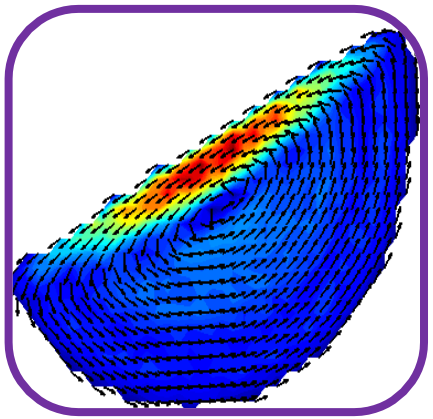

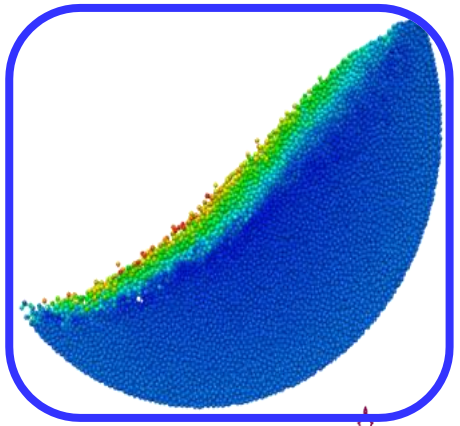

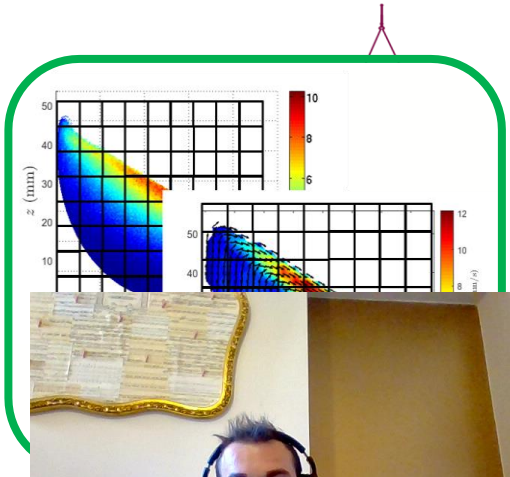

Roadmap

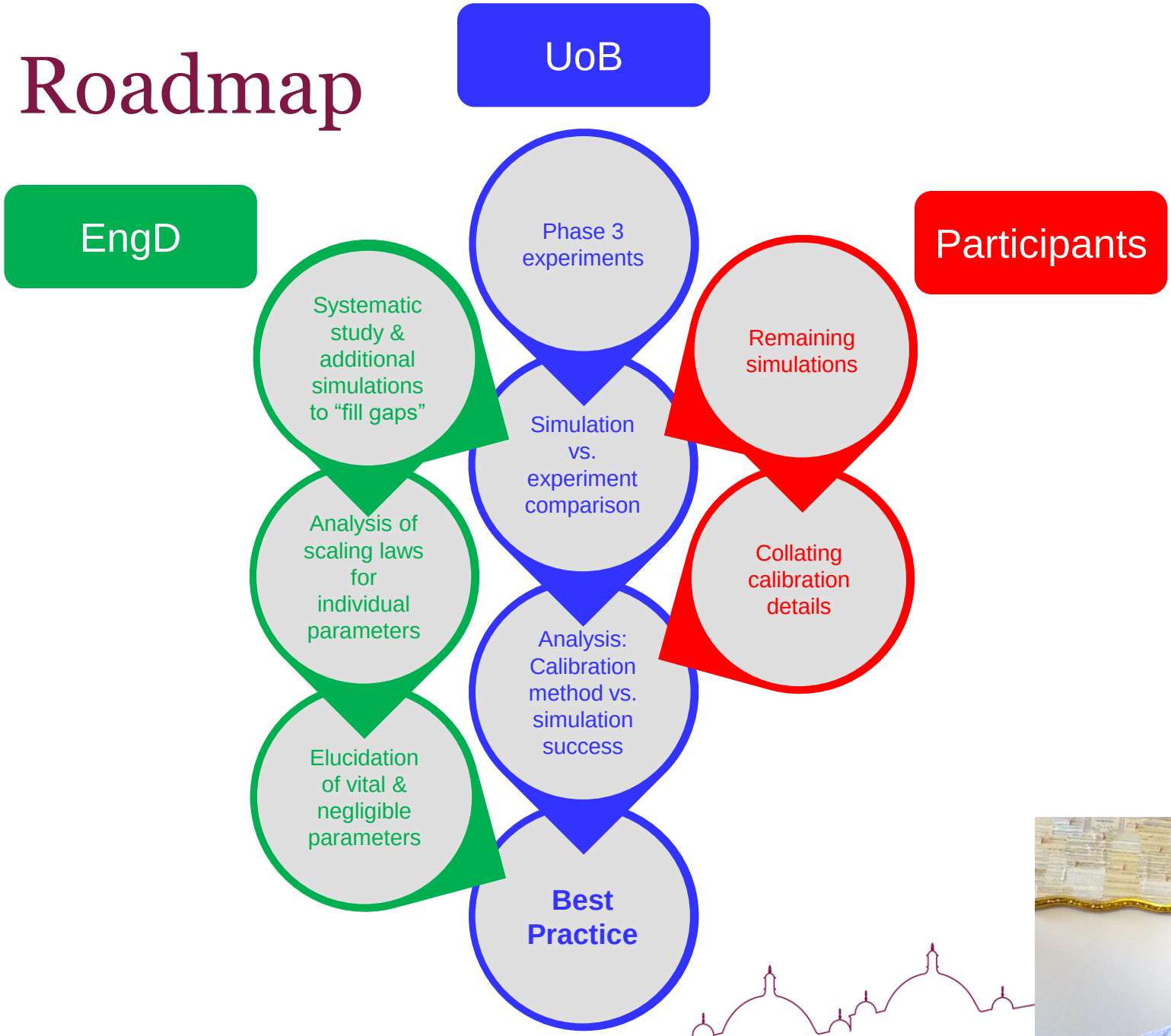
UoB
EngD
Participants
Phase 3 experiments
Systematic study & additional simulations to “fill gaps”
Remaining simulations
Simulation vs. experiment comparison
Analysis of scaling laws for individual parameters
Collating calibration details
Analysis: Calibration method vs. simulation success
Elucidation of vital & negligible parameters
Best Practice